1. Report No. FHWA/TX-07/0-4378-1	2. Government Accession No.	3. Recipient's Catalog No.
4. Title and Subtitle ESTABLISH GUIDANCE FOR SOILS PROPERTIES–BASED PREDICTION OF MEANDER MIGRATION RATE		5. Report Date January 2007 Published: April 2007
		6. Performing Organization Code
7. Author(s) Jean-Louis Briaud, Hamn-Ching Chen, Kuang-An Chang, Young-An Chung, Namgyu Park, Wei Wang, and Po-Hung Yeh		8. Performing Organization Report No. Report 0-4378-1
9. Performing Organization Name and Address Texas Transportation Institute The Texas A&M University System College Station, Texas 77843-3135		10. Work Unit No. (TRAIS)
		11. Contract or Grant No. Project 0-4378
12. Sponsoring Agency Name and Address Texas Department of Transportation Research and Technology Implementation Office P.O. Box 5080 Austin, Texas 78763-5080		13. Type of Report and Period Covered Technical Report: August 2001 - December 2006
		14. Sponsoring Agency Code

15. Supplementary Notes
Project performed in cooperation with the Texas Department of Transportation and the Federal Highway Administration.
Project Title: Establish Guidance for Soils Properties–Based Prediction of Meander Migration Rate
URL: http://tti.tamu.edu/documents/0-4378-1.pdf

16. Abstract
Meander migration costs the Texas Department of Transportation (TxDOT) millions of dollars to protect affected bridges and highway embankments, as illustrated by the case histories accumulated by this research team in phase 1 of this work. These histories include the SH 105 bridge over the Brazos River, the US 90 bridge over the Nueces River, the SH 105 bridge over the Trinity River, the US 59 bridge over the Guadalupe River, and the SH 80 bridge over the Guadalupe River. One recent meander migration threat (FM 787 at the Trinity River) required a $300,000 emergency countermeasure and a $5.6 million replacement bridge.

Several solutions for predicting the movement of meanders have been proposed in the past. This report shows these solutions to be unreliable. The solution outlined in this report considers soil erodibility as an independent parameter influencing meander migration. Other conventional parameters such as flow velocity, meander radius of curvature, river width, and others are part of the proposed solution.

Through a combination of well-instrumented large-scale flume tests, quality numerical simulations, and fundamental laboratory erosion tests, a simple and reliable solution is developed.

17. Key Words Meander Migration, Bank Erosion, Rate of Bankline Movement, Sediment Transport	18. Distribution Statement No restrictions. This document is available to the public through NTIS: National Technical Information Service Springfield, Virginia 22161 http://www.ntis.gov		
19. Security Classif.(of this report) Unclassified	20. Security Classif.(of this page) Unclassified	21. No. of Pages 338	22. Price

Form DOT F 1700.7 (8-72)   Reproduction of completed page authorized

ESTABLISH GUIDANCE FOR SOILS PROPERTIES–BASED PREDICTION OF MEANDER MIGRATION RATE

Jean-Louis Briaud, Hamn-Ching Chen, Kuang-An Chang, Young-An Chung, Namgyu Park, Wei Wang, and Po-Hung Yeh

Zachry Department of Civil Engineering
Texas A&M University

January 2007
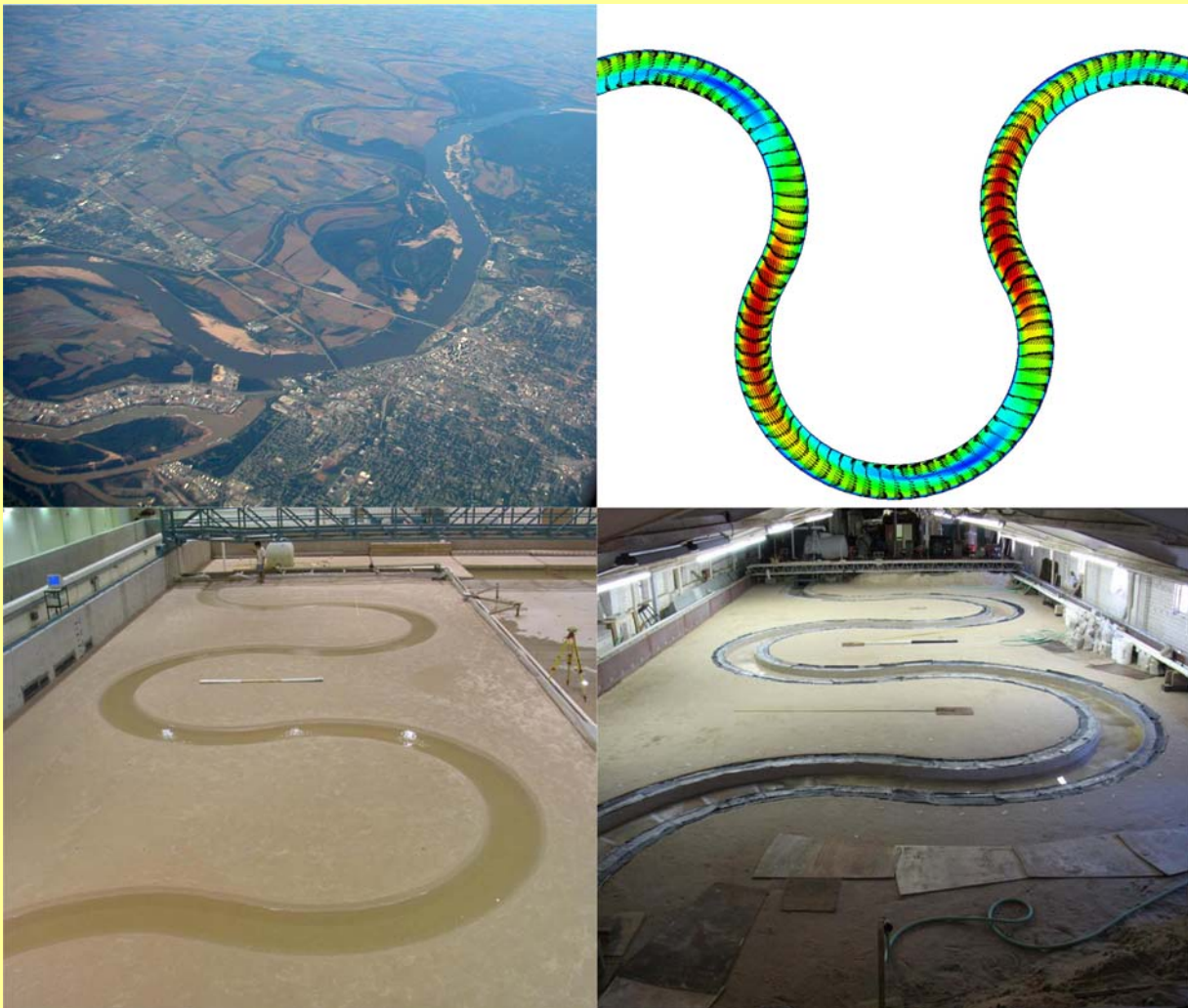
ESTABLISH GUIDANCE FOR SOILS PROPERTIES–BASED PREDICTION OF MEANDER MIGRATION RATE

by

Jean-Louis Briaud
Research Engineer
Texas Transportation Institute

Hamn-Ching Chen
Professor
Texas A&M University

Kuang-An Chang
Associate Professor
Texas A&M University

and

Young-An Chung, Namgyu Park, Wei Wang, and Po-Hung Yeh
Graduate Students
Texas A&M University

DISCLAIMER

The contents of this report reflect the views of the authors, who are responsible for the facts and the accuracy of the data presented herein. The contents do not necessarily reflect the official view or policies of the Federal Highway Administration (FHWA) or the Texas Department of Transportation (TxDOT). This report does not constitute a standard, specification, or regulation. The engineer in charge of the project was Dr. Jean-Louis Briaud, P.E., (Texas, # 48690).

ACKNOWLEDGMENTS

TABLE OF CONTENTS

LIST OF FIGURES

LIST OF TABLES

NOMENCLATURE

A	Meander amplitude
A_w	Cross-sectional flow area
β	Correction factor in M_{max} equation
c_1	Coefficient in τ_{max} equation
c_2	Geometry-dependent coefficient in τ_{max} equation
D	Pipe diameter
D_{50}	Mean particle diameter for the soil
ε	Average height of roughness elements
ε/D	Relative roughness
f	Friction factor obtained from Moody chart
Fr	Froude number
Frc	Critical Froude number
ϕ	Bend angle
g	Gravitational acceleration
h	Water depth
H_w	Water elevations
L_t	Project design life
M	Channel migration distance
$\dot{M}_i$	Initial erosion rate
M_{max}	Maximum erosion distance
μ_w	Dynamic viscosity of water
n	Manning's roughness coefficient
ν_w	$\nu_w = \mu_w / \rho_w$ the kinematic viscosity of water ($10^{-6} \, \mathrm{m}^2$/s at 20˚C)
p	Probability of exceedance
P	Wetted perimeter
Q	Flow rate
Q_{100}, Q_{500}	100/500 year flood
θ	Relative angle ($0 \leq \theta \leq \phi$) within each bend
R	Radius of curvature of the channel bend
Re	Reynolds number
ρ_w	Mass density of water
s	Channel bed slope
S_i	Initial slope of the EFA curve
t	Time
U	Average flow velocity
τ	Shear stress
τ_{avg}	Depth average shear stress
τ_c	Critical shear stress

τ_{max} Maximum shear stress

τ_{max_max} Maximum shear stress of a bend

W Channel width

$\dot{z}$ Erosion rate

EXECUTIVE SUMMARY

INTRODUCTION

Meander migration is a process in which water flow erodes soil on one bank and deposits it on the opposite bank. Therefore, a gradual shift of bank line occurs over time. Bank erosion undermines bridge piers and abutments, scours the foundations of parallel highways, and causes loss of useful land. For example, a recent meander migration threat for FM 787 at the Trinity River as shown in Figure 1 required $0.3 million for emergency countermeasures and $5.6 million for replacement of the bridge.

In order to avoid costly countermeasures for new bridges, TxDOT sponsored the project "Establish Guidance for Soils Properties–Based Prediction of Meander Migration Rate." The research was conducted at Texas A&M University, College Station. The purpose of this project was to develop a methodology that can be used to do site-specific predictions of meander migration. The methodology selected to solve the problem of predicting the meander migration distance at the end of a project life was based on a combination of review of existing knowledge, large flume experiments in two different soil types (i.e., sand and clay), three-dimensional numerical simulations, a hyperbolic model, and a risk analysis.
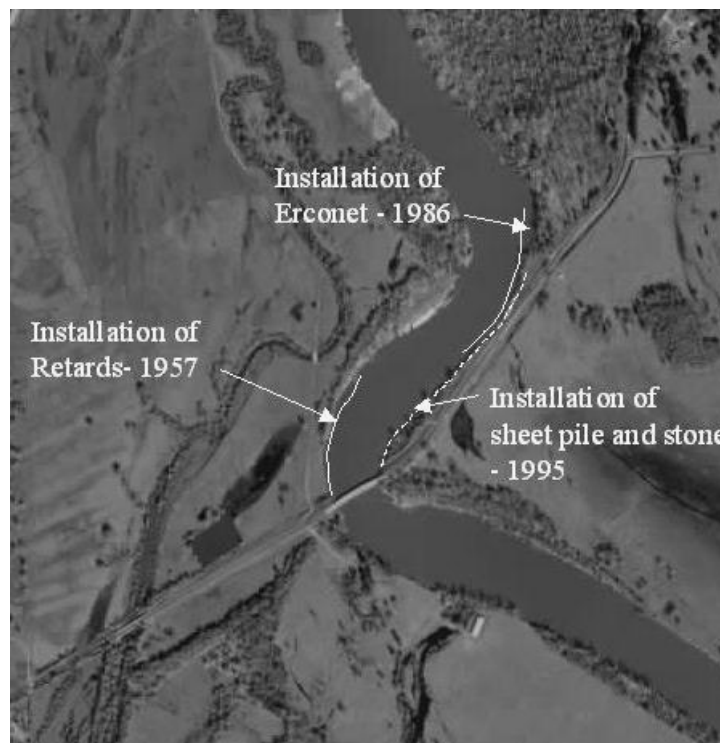
Figure 1. Trinity River at Highway 787 (Briaud et al., 2001).

LITERATURE REVIEW

Researchers studied existing knowledge with respect to prediction of meander migration and summarized the knowledge by topic: meander migration predictions, meander migration flume tests, risk analysis for meander migration, and meander migration software.

Meander migration can be predicted by using empirical equations (Keady and Priest, 1977; Hooke, 1980; Brice, 1982; Nanson and Hickin, 1983), fundamental modeling (Nagata et al., 2000; Duan et al., 2001), or time-sequence maps and extrapolation (Lagasse et al., 2004b).

The most remarkable set of flume tests on behavior of self-formed meandering rivers was conducted by the U.S. Army Corps of Engineers (1945) as shown in Figure 2. They conducted these flume tests in different conditions to investigate the effect of discharge, angle of attack, bed slope, initial cross section, material types, and not feeding sand at the entrance. These studies were not based on a quantitative approach but rather on a qualitative approach.

A good example of risk analysis is the SRICOS-EFA (Scour Rate In Cohesive Soils-Erosion Function Apparatus) method (Briaud et al., 2003). This method predicts the scour depth in clay as a function of time by modeling the erosion process at the water-soil interface and projecting it into time by using future hydrographs. A number of equally possible future hydrographs are generated by the random number generating scheme and a probabilistic post-process provides a probability of the maximum scour depth with a certain confidence level.

A computer program, RVR MEANDER, was developed to predict meander migration (Abad and Garcia, 2006). The RVR MEANDER program is a toolbox to assist in predicting meander migration. Two versions of the program were developed: stand-alone Microsoft Windows-based and geographical information system (GIS)-based versions. The main difference between these two versions is the input process of the coordinates of the river center lines. The GIS-based version provides an automatic import of the river geometry data from existing GIS line data within ESRI ArcMap.
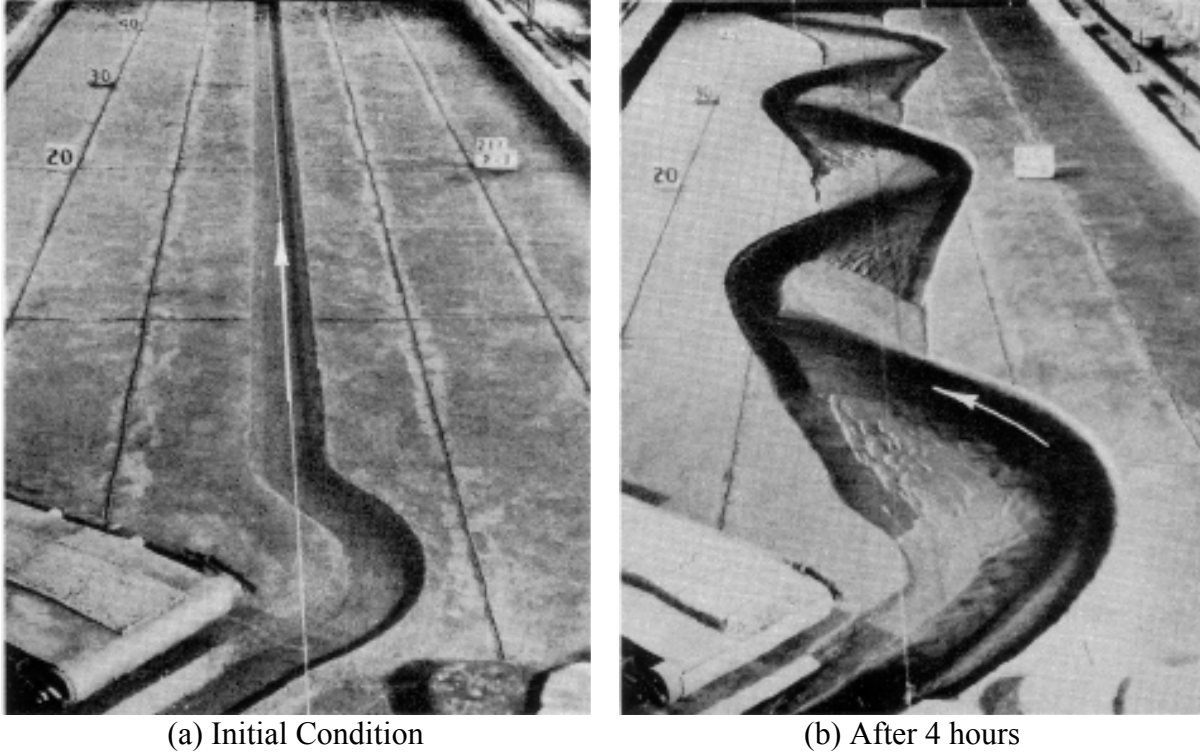
(a) Initial Condition   (b) After 4 hours

Figure 2. Photos from Sand Flume Test with Feeding Sand at the Entrance (U.S. Army Corps of Engineers, 1945).

RESEARCH OBJECTIVES

The overall goal of this research is to develop soil-based guidelines to predict channel meander migration. The main objectives are as follows:

- Apply a soil erosion model to estimate the channel migration distance.
- Evaluate the factors that affect meander migration: channel geometry configurations, soil properties, and flow hydraulic conditions.
- Develop a maximum shear stress equation from three-dimensional numerical simulations.
- Develop prediction equations of maximum migration distance from large-scale flume tests in sand and clay.
- Develop a risk analysis scheme and incorporate it into the new prediction method so that the prediction of meander migration can be made on a probabilistic approach.
- Develop a computer program to integrate all the components.

METHODOLOGY

Under a high flow rate, a river will erode its bankline and rework the flood plain continuously. The bankline displacement usually contains two components: cross-valley expansion and down-valley translation. Both components make the river more sinuous and extend the length between two reference stations. The increasing channel length increases the friction force on the channel boundaries, decreases the velocity, and lessens the erosion process. As the river flow rate remains constant, it is expected that the river bankline displacement from its original place will attain an equilibrium state. A hyperbolic function was used to estimate the channel bankline erosion distance of a cross section. Two physical parameters, the initial migration rate and the maximum migration distance, were determined by numerical simulation with the EFA (Erosion Function Apparatus) test and large-scale physical models, repectively.
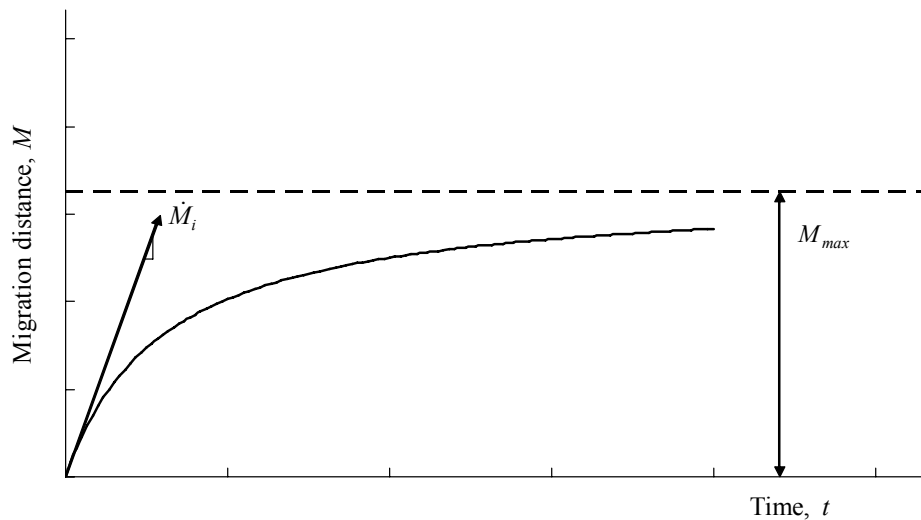
Figure 3. The Hyperbolic Model in Channel Bankline Migration Distance.

NUMERICAL SIMULATION

Similar to the maximum scour rate z_{max} in an earlier TXDOT project (Project 0-2105) same concept and procedure were applied to predict meander migration. The maximum shear stress τ_{max} corresponds to a certain flow condition, soil property, and channel geometry. Numerical simulation calculates the maximum shear stress τ_{max} along the channel under different flow and geometry conditions. Researchers quantitatively analyzed the influence of these factors on maximum shear stress and developed an empirical formula. Along with the EFA test results, the initial migration rate of a channel bankline can be determined.

Shear Stress: φ = 65°
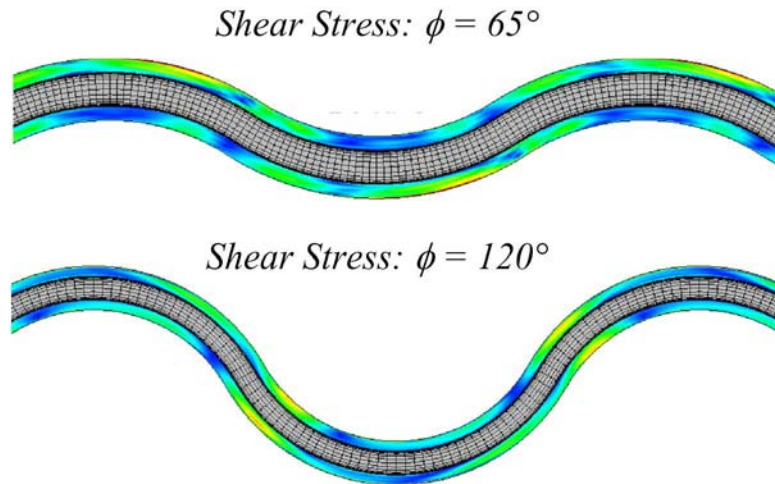
Shear Stress: φ = 120°

Figure 4. Shear Stress Distribution Obtained from Numerical Simulations.

FLUME TEST IN SAND

A series of large-scale experiments were conducted in a basin that is 36.6 m (120 feet) long, 20.9 m (69 feet) wide, and 1.5 m (5 feet) deep located in the Haynes Coastal Engineering Laboratory at Texas A&M University. The test area is 27.4 m (90 feet) long, 13.7 m (45 feet) wide, and 0.30 m (1 foot) deep in the basin, which was filled with sand. An idealized channel was molded from the sand bed to mimic the natural river erosion process. A trapezoidal cross section was chosen with bottom width of 40.0 cm (15.8 inches), top width of 74.6 cm (29.4 inches), bank slope of 30°, and depth of 15.6 cm (6.1 inches). The experiments were run with different controlling variables: five different bend radius-to-channel width ratios, four different bend angles, and four different Froude numbers. Researchers found that the distribution of the maximum migration distance along the channel can be described by a Gaussian distribution function. Parameters of the Gaussian distribution function were also examined with the controlling variables. An equation of the maximum migration distance along the channel was proposed.

Figure 5. Water Basin and Flume Test Setup in Sand Test.

FLUME TEST IN CLAY

This second part of flume tests investigates the channel meander migration in clay by conducting physical modeling. The approach is to vary each primary parameter obtained from dimensional analysis while keeping the remaining parameters constant. The effect and impact of each individual parameter can therefore be examined to provide a basis for parametric study. The approach is similar to that in Chapter 5, except Grande clay was used. A total of eight cases including the three pre-tests were conducted in a large basin that is 22.0 m (72.6 feet) long, 10.0 m (33.0 feet) wide, and 0.9 m (3 feet) deep located on the second floor of the Hydromechanics Laboratory at Texas A&M University. The initial cross section of the channel is of rectangular shape with a width of 60.0 cm (23.6 inches) and a depth of 12.0 cm (4.7 inches). Plywood plates were laid at the bottom of the channel so only the banks were erodible. The channel plan form evolution with respect to each factor was quantified and evaluated. The channel bankline displacement was modeled by a hyperbolic function with the inclusion of the initial migration rate and the maximum migration distance estimated in the model. It was found that the distributions of maximum migration distance along the channel display Pearson IV distributions.
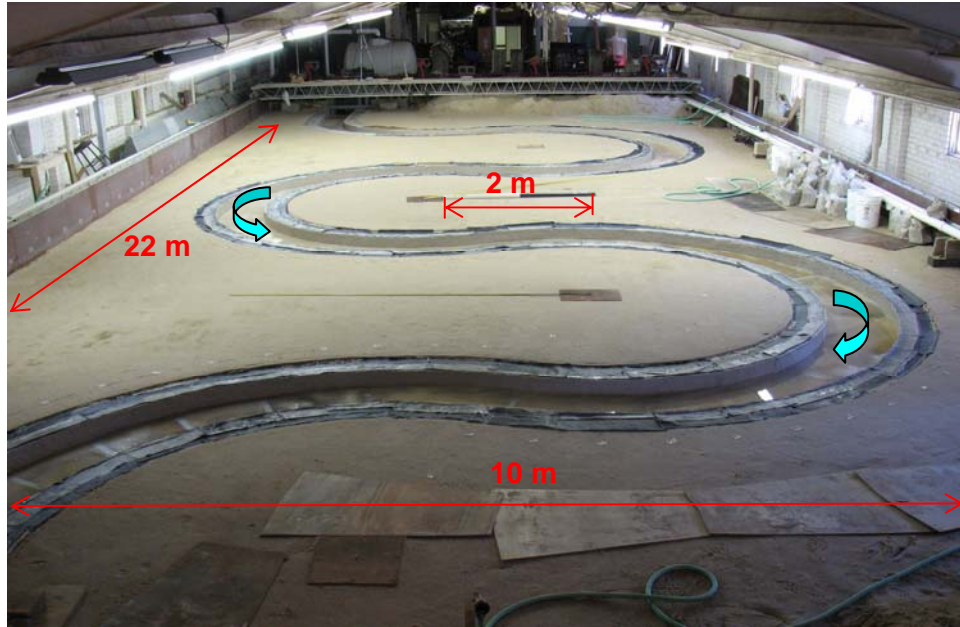
Figure 6. Experimental Setup in the Hydromechanics Laboratory.

RISK ANALYSIS

A meander migrates at a rate controlled by the erosion rate of the soil at the interface between the water and the bank. The hydraulic shear stress imposed by the water is controlled by the velocity of the flow, which is dependent on the hydrograph of the river. A meander migration prediction process must therefore consider the hydrograph of the river. This hydrograph is not known because it will occur in the future during the design life of the bridge or highway embankment. Because it is not realistic to make a deterministic prediction of a future hydrograph, it is more desirable to make predictions of many equally possible hydrographs in a probabilistic manner. Each hydrograph then moves the river toward a predicted position of the meander and a probabilistic post-process provides a cumulative density function (CDF) map that shows the general trend of the meander migration of the river with the associated likelihood levels, as shown in Figure 7. In the figure, each line represents a certain probability that the initial river will move to the location of the line or further at the end of project life (e.g., 75 years).

The common concern of meander migration problems might be a specific location as well as a direction of bank movement. Although the CDF map gives the global picture of the predicted migration movement over the chosen period, it is often insufficient information regarding a specific location and direction. Therefore, a separate CDF for a given location and direction is needed and is determined by interpolation of the CDF map. This feature will be very helpful for the bridge engineers when planning a new bridge.
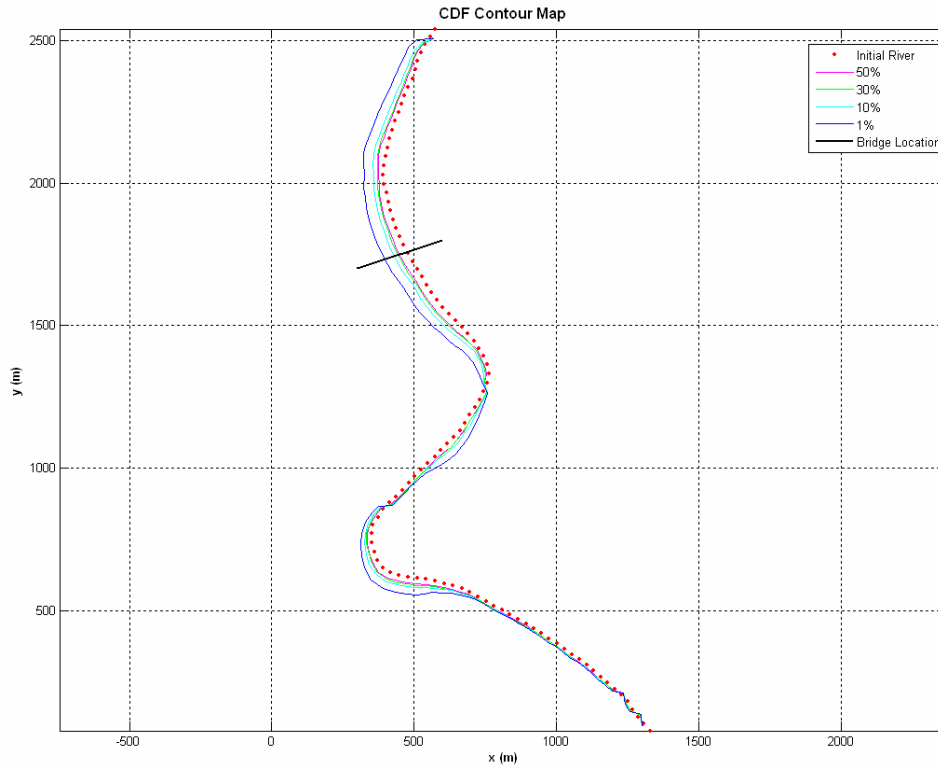
Figure 7. Cumulative Density Function Map.

MEANDER PROGRAM

The MEANDER computer program implements all the methods developed in this project to predict meander migration. It consists of two major components: graphic user interface (GUI) and numerical implementation. This part gives a general view of the MEANDER program regarding GUI, some programming techniques, and implemented modules. These items are introduced in order.
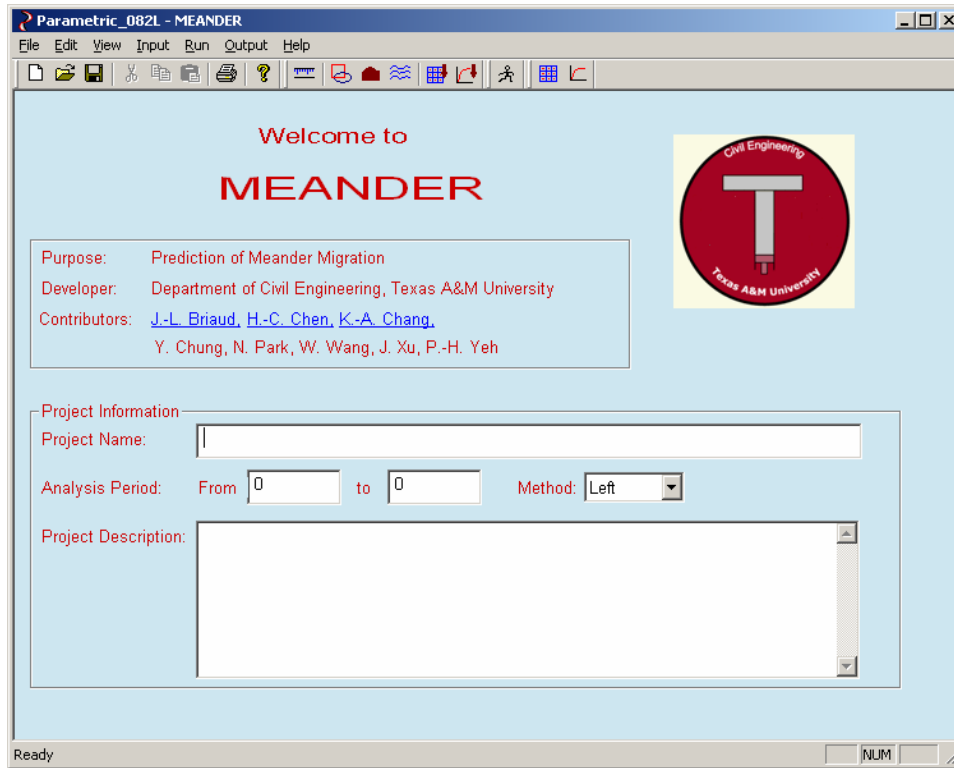
Figure 8. Main Interface of the MEANDER Program.

CHAPTER 1. INTRODUCTION

1.1 INTRODUCTION

This report is the result of a project sponsored by the Texas Department of Transportation (TxDOT) to establish guidance for soils properties–based prediction of meander migration rate.

Meander migration is a process in which water flow erodes soil on one bank and deposits it on the opposite bank. Therefore, a gradual shift of bankline occurs over time. Bank erosion undermines bridge piers and abutments, scours the foundations of parallel highways, and causes loss of useful land. Bridges crossing meandering rivers are often endangered due to the loss of pier or abutment foundations. This problem costs TxDOT millions of dollars to protect affected bridges and highway embankments. One recent meander migration threat at the Trinity River as shown in Figure 1.1 has required a $0.3 million emergency countermeasure and a $5.6 million replacement bridge.
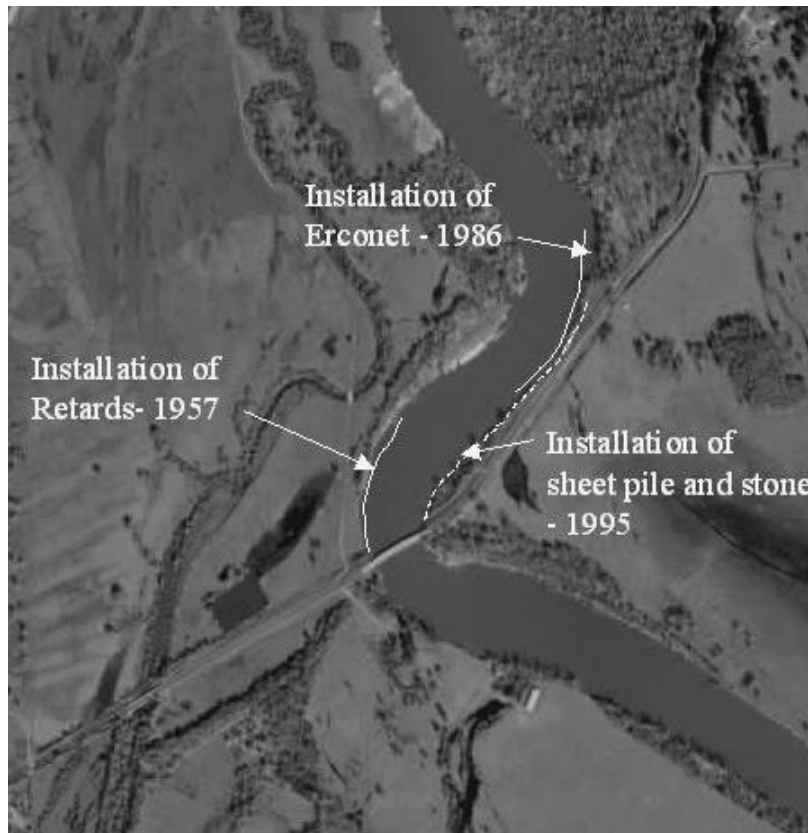
Figure 1.1. Trinity River at Highway 787 (Briaud et al., 2001).

In order to avoid costly countermeasures for new bridges, TxDOT sponsored the project "Establish Guidance for Soils Properties–Based Prediction of Meander Migration Rate." The research was conducted at Texas A&M University, College Station. The purpose of this project was to develop a methodology which can be used to do site-specific predictions of meander migration. Using this methodology, piers and abutments of new bridges can be constructed away from risky locations.

The methodology selected to solve the problem of predicting the meander migration distance at the end of project life was based on a combination of review of existing knowledge, large flume experiments in two different soil types (i.e., sand and clay), three-dimensional (3D) numerical simulations, selection of a hyperbolic model to describe meander migration versus time, and a risk analysis.

1.2 RESEARCH OBJECTIVES

This research is aimed at developing soil-based guidelines to predict meander migration. The main objectives are:
- Apply a soil erosion model to estimate the channel migration distance.
- Evaluate the factors that affect meander migration: channel geometry configurations, soil properties, and flow hydraulic conditions.
- Develop a maximum shear stress equation from three-dimensional numerical simulations.
- Develop prediction equations for the maximum migration distance from large-scale flume tests in sand and clay.
- Develop a risk analysis scheme and incorporate it into the new prediction method so that the prediction of meander migration can be made on a probabilistic basis.
- Develop a computer program to integrate all the components.

1.3 FUNDAMENTAL CONCEPT OF MEANDER MIGRATION

1.3.1 Channel Pattern and Stability

Meander migration occurs as a response to natural or man-made disturbances of the fluvial system. Meander migration and related processes cause problems such as bridge scour, scour of highway foundations, and loss of land. In order to predict changes in channel morphology, location, and behavior, it is important to understand the relative stability of a channel, which is revealed by its patterns.

Alluvial channels are dynamic systems subject to changes of different types and at highly variable rates. Alluvial channel movements are the cumulative result of a combination of climatic, geological, topographic, hydrologic, and human disturbance factors. There are basically three types of channel patterns: straight, meandering, and braided. Rivers with different patterns behave differently; therefore, pattern identification should be the first step toward evaluation of river stability.

Brice (1975) developed a descriptive classification of channel patterns for alluvial rivers. He selected the following channel properties as important for classification: the degree of sinuosity, braiding and anabranching, and the character of meandering, braided, and anabranched streams (Figure 1.2).

Brice and Blodgett (1978) classified streams according to Figure 1.3, which is based on stream properties observable on aerial photographs and in the field. This figure is intended to facilitate the assessment of streams for engineering purposes, with particular regard to lateral stability.

Figure 1.2. Channel Pattern Classification (Brice, 1975).
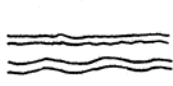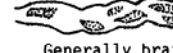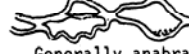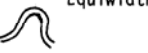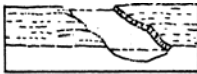
CHANNEL WIDTH	Small (<100 ft or 30 m wide)	Medium (100-500 ft or 30-150 m)	Wide (>500 ft or 150 m)
FLOW HABIT	Ephemeral (Intermittent)	Perennial but flashy	Perennial
CHANNEL BOUNDARIES	Alluvial	Semi-alluvial	Non-alluvial
BED MATERIAL	Silt-clay Silt	Sand Gravel	Cobble or boulder
VALLEY; OR OTHER SETTING	Low relief valley (<100 ft or 30 m deep)	Moderate relief (100-1000 ft or 30-300 m) High relief (>1000 ft or 300 m)	No valley; alluvial fan
FLOOD PLAIN	Little or none (<2x channel width)	Narrow (2-10x channel width)	Wide (>10x channel width)
DEGREE OF SINUOSITY	Straight (Sinuosity 1-1.05)	Sinuous (1.06-1.25) Meandering (1.26-2.0)	Highly meandering (>2)
DEGREE OF BRAIDING	Not braided (<5 percent)	Locally braided (5-35 percent)	Generally braided (>35 percent)
DEGREE OF ANABRANCHING	Not anabranched (<5 percent)	Locally anabranched (5-35 percent)	Generally anabranched (>35 percent)
VARIABILITY OF WIDTH AND DEVELOPMENT OF BARS	Equiwidth Narrow point bars	Wider at bends Wide point bars	Random variation Irregular point and lateral bars
APPARENT INCISION	Not incised		Probably incised
CUT BANKS	Rare	Local	General
BANK MATERIAL	Coherent Resistant bedrock Non-resistant bedrock Alluvium		Non-coherent Silt; sand gravel; cobble; boulder
TREE COVER ON BANKS	<50 percent of bankline	50-90 percent	>90 percent

Figure 1.3. Stream Properties for Classification and Stability Assessment (Brice and Blodgett, 1978).

15

Shen et al. (1981) presented five basic patterns (Figure 1.4) to aid highway engineers in establishing the relative stability of the channel and in identifying hazards that can affect bridge stability. Figure 1.4 is more meaningful than a purely descriptive classification of channels because it is based on cause and effect relations and it illustrates the differences to be expected when the type of sediment load, flow velocity, and other factors differ among rivers.
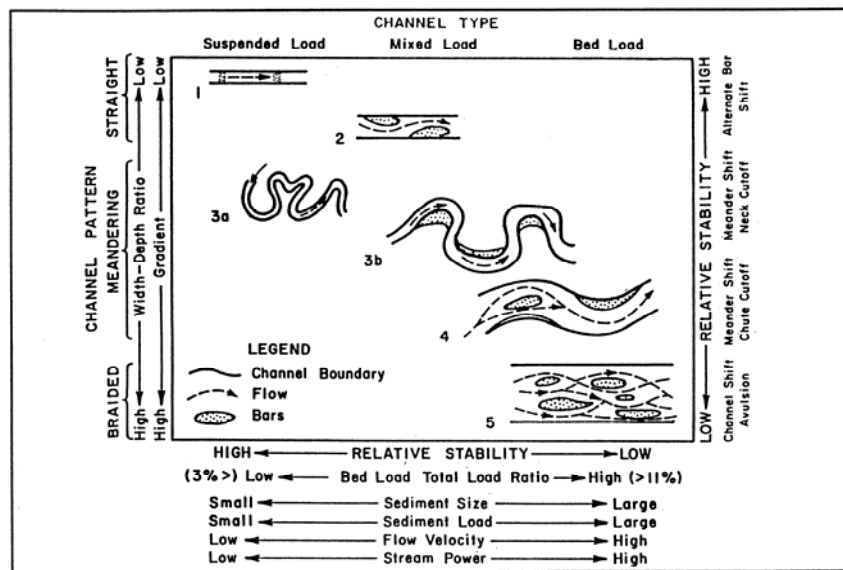
Figure 1.4. Channel Classification Showing Stability and Types of Hazards Encountered with Each Pattern (Shen et al., 1981).

1.3.2 Meander Migration

It has been observed in many flume tests and in real rivers that bank erosion occurs by either a grain-by-grain movement or by mass movement (slumping or toppling). The following factors can cause mass failure: undercutting of the toe of the bank, steepening of the slope, surcharging the bank by construction or dumping, or seepage forces and pore water pressures related to increased water movement through bank sediment. Bank erosion in cohesionless materials usually involves the following processes as shown in Figure 1.5:

1. bed scouring at the side bank;
2. bank collapse due to instability of the scoured bank;
3. deposition of the collapsed bank materials at the front of the bank; and
4. transportation of the deposited materials.
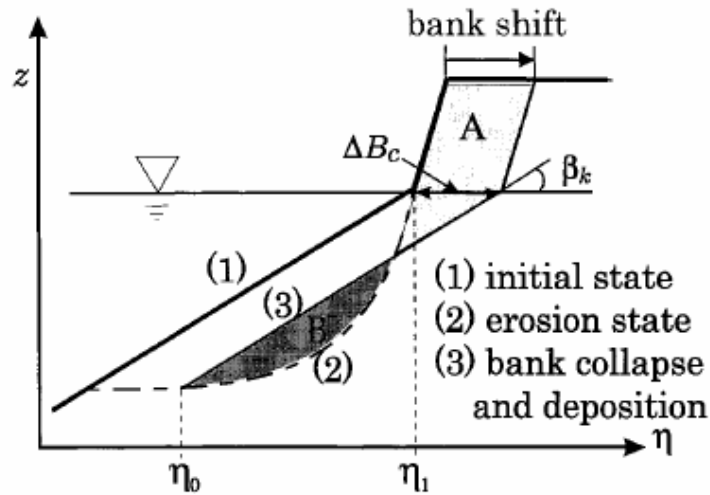
Figure 1.5. Bank Erosion Process (Nagata et al., 2000).

The removal of bank materials on one side is often accompanied by deposition of materials on the opposite bank and a shift of the river channel. If both banks erode at the same cross section, the channel widens.

Meander growth involves a change in the dimensions of a meander. Meander amplitude and width increase as a meander enlarges. At the same time, the radius of curvature of the bend increases. Meander shift involves the displacement of the meander in a downstream direction. Although rare, some parts of the bend can actually shift upstream. Figure 1.6 shows the various modes of meander loop behavior.
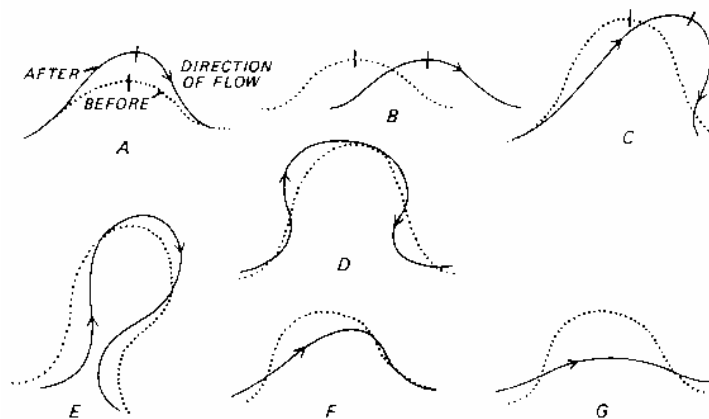
A. Extension, B. Translation, C. Rotation, D. Conversion to a Compound Loop, E. Neck Cutoff by Closure, F. Diagonal Cutoff by Chute, G. Neck Cutoff by Chute.

Figure 1.6. Modes of Meander Loop Behavior (Brice, 1975).

1.4 FACTORS AFFECTING MEANDER MIGRATION

Meander migration is an interactive process between water flow and soil erodibility. The conditions of the flow and the properties of the soil are major factors affecting meander migration. Significant research has been performed to identify influential factors. A list of such factors was prepared for previous TxDOT Project 0-2105 (Briaud et al., 2001b):

- soil properties (soil erosion function),
- flow condition (discharge, velocity, water depth),
- meander geometry (width, depth, radius of curvature, sinuosity),
- stream pattern (straight, meandering, braided),
- free surface slope,
- channel roughness (Manning's roughness coefficient n, Darcy-Weisbach friction factor f),
- sediment load,
- vegetation,
- debris problem,
- channel relocation, and
- human activities on the floodplain of river.

Flow, soil, and geometry are considered to be the most important factors affecting meander migration and are addressed in detail in this study.

1.5 MEANDER PARAMETERS TO DESCRIBE GEOMETRY

Geometry of real rivers is often very complicated. In order to reduce the complexity to an acceptable level but with sufficient precision, channel bends are treated as arcs. The parameters to describe meander geometry are shown in Figure 1.7 and the definitions of these parameters are as follows:

A = meander amplitude

W = channel width

M = channel migration distance

R = radius of curvature

ϕ = bend angle

θ = relative angle ($0 \leq \theta \leq \phi$) within each bend

t = time
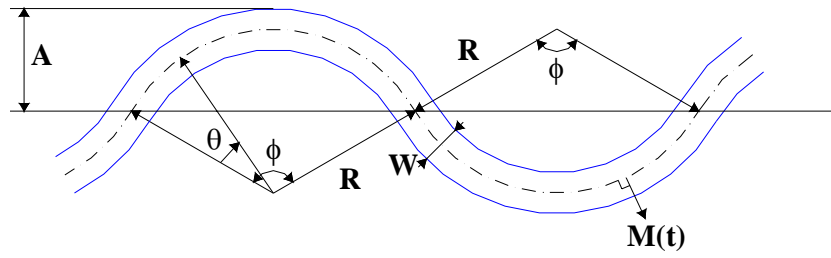
Figure 1.7. Parameters Defining Meander Geometry.

CHAPTER 2. LITERATURE REVIEW

This chapter describes some of the existing knowledge on the prediction of meander migration. This information is divided into four categories: meander migration predictions, meander migration flume tests, risk analysis for meander migration, and meander migration software.

2.1 MEANDER MIGRATION PREDICTIONS

2.1.1 Keady and Priest (1977)

Keady and Priest (1977) consider the rate of downstream migration to be a function of the free surface slope of the river, the meander amplitude, and the specific weight of water. They express this rate by the following formula:

$$\frac{V}{\sqrt{gA}} = \phi(s) \tag{2.1}$$

where, V = migration rate, (ft/yr) = dM/dt in Figure 1.7

g = acceleration of gravity, (ft/sec^2)

A = meander amplitude, (ft) in Figure 1.7

s = free surface slope

ϕ = function of s given in Figure 2.1

The graph presented in Figure 2.1 is based on data from the Red River in Arkansas and Louisiana, the Red Deer River in Alberta, Canada, and other rivers, as shown in Table 2.1. The points corresponding to the case histories in a previous study (Briaud et al., 2001b) are also plotted on the graph.

The free surface slope is very close to the channel bed slope, which is determined by the slope of the terrain. Water flows to a lower elevation. The slope of the terrain provides potential energy to keep water flowing and determines how fast water flows. Keady and Priest (1977) correctly identified the importance of channel slope. But channel slope is not the only factor affecting flow condition. Rainfall is another important factor influencing flow conditions. Usually a large portion of the total migration distance occurs during a few big floods. Soil properties are another important issue ignored by the authors. Different rivers have neither the same precipitation nor

the same soil properties. The usefulness of this method is limited by the extent of the database used to develop it.

Table 2.1. Data Used by Keady and Priest (1977).

Identification	Velocity of Migration (ft/yr)	Meander Amplitude (ft)	Slope
Mississippi R (LA)	60	13,000	0.0000436
Mississippi R (MS)	111	11,000	0.0000588
Mississippi R (TN)	225	13,200	0.0000777
Red R (ARK)	350	2,900	0.000132
Pearl R (LA)	20	1,050	0.000200
Red Deer R (Canada)	20	1,200	0.000275
Tombigdee R (MS)	13	800	0.000421
Buffalo R (MS)	17	1,560	0.000689
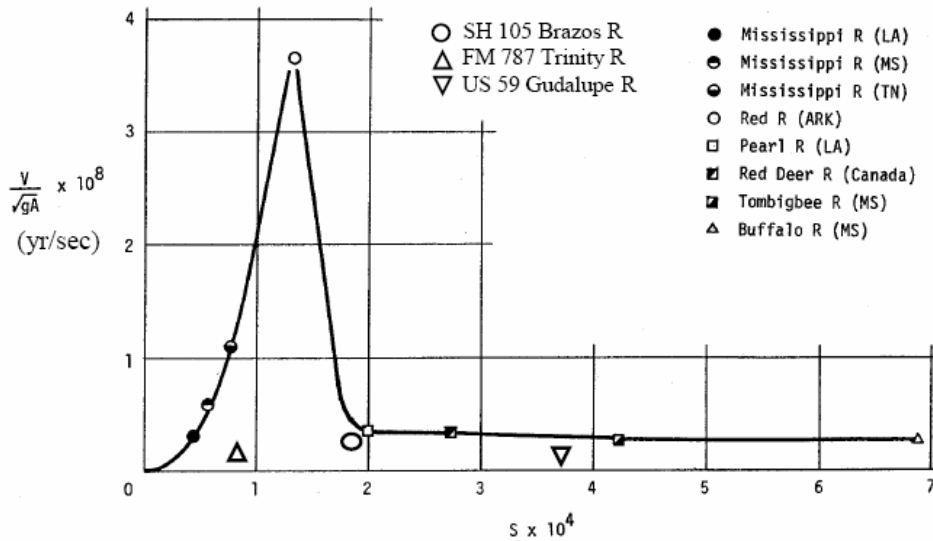
Figure 2.1. Graph for Determining Rate of Meander Migration (Keady and Priest, 1977; Briaud et al., 2001b).

2.1.2 Hooke (1980)

Hooke (1980) proposed that the erosion rate is most closely related to the catchment area (as a surrogate of discharge and width). He determined rates of bank erosion from field measurements and historical maps for 11 streams in Devon, England. He then compared the rates of bank erosion with worldwide published rates in 43 streams. He derived the equation through multiple regression analyses using the 54 data points as follows:

$$Y(\text{m/year}) = 8.67 + 0.114A(\text{km}^2) \quad (r = 0.73)$$
$$Y(\text{m/year}) = 2.45A^{0.45} \qquad\qquad (r = 0.63) \tag{2.2}$$

where, Y = bank erosion rate

A = catchment area

Figure 2.2 shows the data and regression for Hooke's equation. The data points from Briaud et al. (2001b) are added to this figure.
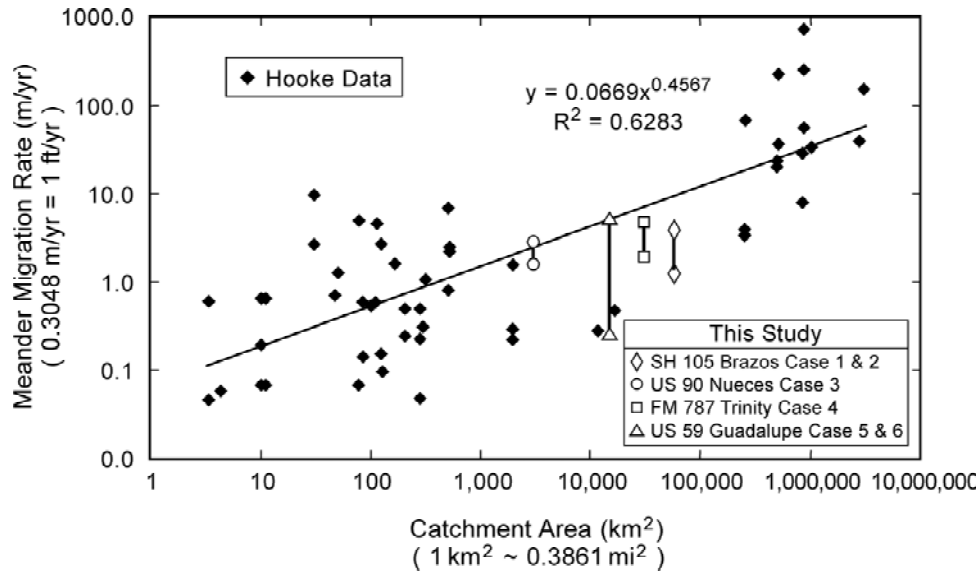
Figure 2.2. Relationship between Catchment Area and Migration Rate
(Hooke, 1980; Briaud et al., 2001b).

The catchment area for a reach of a river is the area catching all the runoff going to that reach. Rainfall is an importance source of river flow. For the same amount of rainfall, the larger the catchment area, the larger the flow rate. For the same river, it is reasonable to assume that the migration rate of different reaches is related to their catchment area. For different rivers it might not be a good idea to relate migration rate to catchment area only and disregard varying precipitation levels. Rivers having the same catchment area might have quite different flow rates due to different amounts of precipitation. Soil properties are also ignored here. Although both axes in Figure 2.2 are in logarithmic scale, there is still significant scatter.

2.1.3 Brice (1982)

Brice (1982) proposed that the rate of bank migration increases with increasing channel width.

$$Y = 0.01B \qquad\qquad (2.3)$$

where, Y = mean erosion rate, (m/yr)

B = channel width, (m)

Brice's data consisted of 43 data points from four different stream types (equiwidth, wide bend, braided point bar, braided) as shown in Figure 2.3. The data points from Briaud et al. (2001b) were added to Figure 2.3. There are several points for each site because there are several periods of observation for each site.
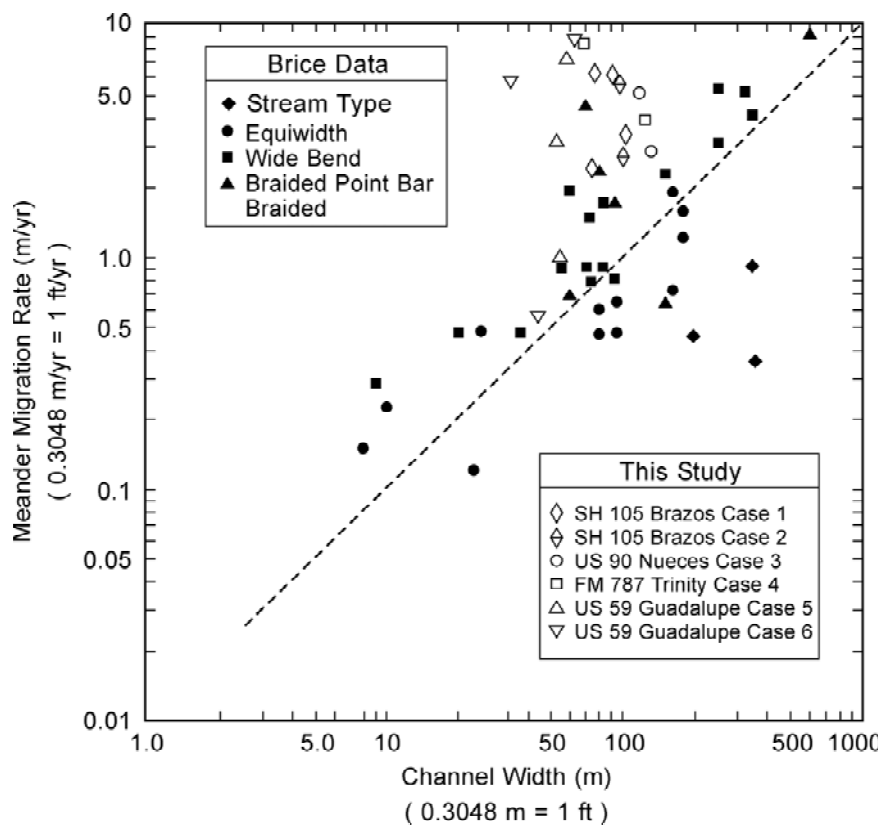
Figure 2.3. Relationship between Migration Rate and Channel Width
(Brice, 1982; Briaud et al., 2001b).

This formula is very simple, probably too simple. Brice only related migration rate to channel width. Almost all the important factors are missing in this formula. Figure 2.3 shows the value 0.01 is meaningful for only a few points in the data set. The migration rate is normally not constant along a river or over time. The ratio of migration rate to channel width is not constant either. The average ratio of migration rate to channel width can roughly predict the amount of

migration within a short period of time for the same river with no guarantee of precision. It is not likely that a universal formula like the author proposed can be applied to all rivers.

2.1.4 Nanson and Hickin (1983)

Nanson and Hickin (1983) showed that the ratio of radius of curvature of a bend (R_c) to channel width (W) influences the lateral migration rate of a meandering river. The relationship between channel migration rate (MR) and the ratio of radius of curvature to channel width for the Beatton River, Canada, and other rivers is shown in Figure 2.4. The normalized migration rate (MR/W) is highest when the ratio of radius of curvature to channel width (R_c/W) is about 3. Data points from a previous study (Briaud et al., 2001b) were added to the figure. The data from Nanson and Hickin (1983) conform, approximately, to the following relations:

$$MR(\text{m/year}) = 0.2\left(R_c/W\right) \quad \text{for } \left(R_c/W\right) < 3$$
$$MR(\text{m/year}) = 2.0\left(R_c/W\right)^{-1} \quad \text{for } \left(R_c/W\right) \geq 3$$

(2.4)

where, MR = mean erosion rate, (m/year)
W = channel width, (m)
R_c = radius of curvature, (m)

This relationship between migration rate and geometry is widely cited, but the data points are widely scattered and the best fit line is not obvious. Geometry is only one factor affecting meander migration. Other important factors such as velocity and soil properties were ignored in the authors' conclusion. This study described the relation between migration rate and geometry qualitatively rather than quantitatively.
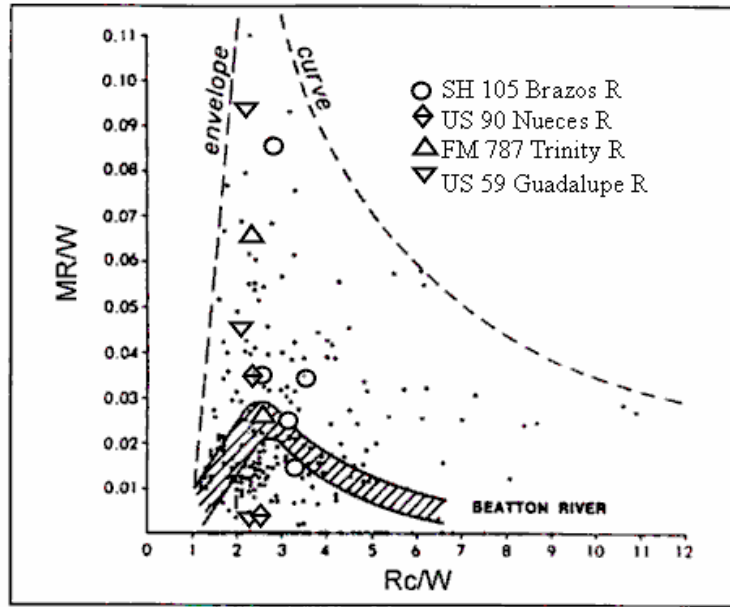
Figure 2.4. Relationship between Migration Rate and Geometry (Nanson and Hickin, 1983, 1986; Briaud et al., 2001b).

2.1.5 Odgaard (1987)

Odgaard (1987) solved constitutive equations by assuming that the rate of bank erosion is proportional to the difference between the near-bank depth-averaged mean velocity and the reach-averaged mean velocity at bank full discharge. The resulting equation indicates that the erosion rate correlates with channel characteristics such as width, depth, curvature, bend angle of channel center line, channel slope, friction factor, and degree of vegetation on the banks. The predictions using this equation agreed well with data measured using historical records (air photos, maps, and stream flow records), field measurements, and soil analysis in the East Nishnabotna River and Des Moines River in Iowa.

$$\bar{v}/u = 2E\frac{b}{r_c}\left(1+\frac{b}{2r_c}\right)^{-1}F \tag{2.5}$$

where, $\bar{v}$ = the average rate of erosion, (m/yr)

u = reach-average mean velocity, (m/s)

$$E = \frac{e}{8}\left(\frac{3\alpha}{2}\frac{\sqrt{\theta}}{k}\frac{m+1}{m+2}F_{Dc}-1\right)$$

26

e = erosion constant

α = 1.27

θ = Shields' parameter (= 0.06)

m = friction parameter

k = Karman's constant (= 0.40)

F_{Dc} = particle Froude number

b = bank-full width of channel (m)

r_c = radius of curvature (m)

$$F = 1 - \exp\left(-B\frac{r_c\phi}{b}\left(1-\frac{\beta}{\phi}\right)\right)$$

ϕ = bend angle

β = angle from crossover to first outer bank erosion occurrence

$$B = \frac{2k^2}{(m+1)^2}\frac{b}{d_c}$$

d_c = center line flow depth

In the calculations, two variables were assumed: the friction factor (m) was taken as 3 and particle Froude number (F_{Dc}) as 10 (Odgaard, 1987). In addition, the erosion constant was taken as $e = 6.4 \times 10^{-7}$ and $e = 4.4 \times 10^{-7}$ for the case of light or no vegetation and dense vegetation on outer bank, respectively.

This method considers flow (u), soil (e), and geometry (b/r_c). If the right erosion constant is picked, the predicted migration rate is close to the measured one. Although soil erodibility is a fundamental property of soil, it is treated as an empirical coefficient here. An e value can be chosen based on existing records, but there is no guarantee that the value will work for a true prediction case. Soil erodibility can be obtained using the erosion function apparatus (EFA) to test the erosion function of the soil (Briaud et al., 2001a). It would be worthwhile to study how to replace the erosion constant e here with the EFA function.

The above method was a simplified version of a more complex solution developed by the same author (Odgaard, 1986). A modified version came later (Odgaard, 1989a). But unfortunately the answer is very sensitive to some parameters. In the example given in another article (Odgaard, 1989b), the calculated migration rate of a hypothetical river is 11 m/yr. If the flux factor B is changed from 6 to 4.8, the migration rate will be 17 m/yr. If the factor f is changed from 0.08 to

0.07, the migration rate will be 12.1 m/yr. So this method, while more fundamentally sound, might not be good for practical use.

2.1.6 Hudson and Kesel (2000)

These authors examined the channel migration and meander-bend morphology for the lower Mississippi River between 1877 and 1924, prior to channel cutoffs, revetments, and change in sediment regime. The average migration rate was 45.2 m/yr in the upper alluvial valley and increased to 59.1 m/yr in the lower alluvial valley. The highest migration rate occurred when the ratio of radius of curvature to channel width was between 1.0 and 2.0. They did not proposed a prediction method.

2.1.7 Ikeda et al. (1981) and Parker et al. (1982)

Although these authors did not propose a method for predicting meander migration, they developed a theory explaining the formation of meanders. They identified alternate-bar instability as the cause of meander migration. Bend instability in sinuous channels is different from the instability of alternate bars in straight channels. These two mechanisms work at the same characteristic wavelengths. They developed an expansion technique involving the Stokes expansion for water waves to perform a nonlinear stability analysis, which explains the skewing and fattening and shows that the lateral and downstream migration rates are proportional to the bend amplitude.

2.1.8 Blondeaux and Seminara (1985)

These authors developed and applied a two-dimensional (2D) model of flow and bed topography in sinuous channels with erodible boundaries in order to study the mechanism of meander initiation. A "resonance" phenomenon uncovered by Ikeda et al., 1981) was detected when the values of relevant parameters fall within a certain range. It was proposed that resonance controls the bend growth and is connected with bar instability. Comparison with experimental observations showed that resonance is associated with meander formation.

2.1.9 Pizzuto (1990)

This author developed a 2D numerical model to predict the distribution of boundary shear stress, cross-channel sediment transport rates, and evolution of bed topography. The equilibrium values of a dimensionless depth increase as the bed slope decreases.

2.1.10 Darby and Thorne (1994, 1996), Darby et al. (1996) and Darby et al. (2002)

Darby and Thorne (1994, 1996) solved the governing equations of flow continuity, flow resistance, conservation of flow momentum, sediment transport, bank stability, and conservation of sediment mass. A physically based 2D numerical model was developed to simulate channel widening. Comparison was made with a 13.5 km (8.44 mi) reach of the South Fork of the Forked Deer River in west Tennessee (Darby et al., 1996). Qualitative agreements were observed, but quantitative predictions are not reliable.

Darby et al. (2002) developed a numerical model and tested river morphology for cohesive erodible banks. The model couples a 2D depth-averaged model of flow and bed topography with a mechanistic model of bank erosion. Deposition and removal of failed bank material were simulated. The authors also solved the governing conservation equations in a moving boundary fitted coordinate system. Model performance was encouraging in regard to agreements between simulations results with data from two flume tests and from a real river.

2.1.11 Mosselman (1998)

Mosselman's (1998) prediction method consists of a 2D depth-averaged flow model and a bank erosion model. The prediction method is applied to a reach of the meandering gravel-bed River Ohre in the former state of Czechoslovakia. Poor agreement was observed. The author claims that inclusion of a 3D flow model, a sediment transport model, will improve the prediction results.

2.1.12 Sun et al. (2001a, 2001b)

Sun et al. (2001a, 2001b) used the linear theory of Johannesson and Parker (1989) to develop a 2D computer model for meandering rivers that couples water flow, bed topography, and sorting of sediments with different grain sizes. The model for bed load sediment transport and sorting came from the theory of Parker and Andrews (1985). Simulation results showed that curvature-related instability is a primary factor affecting the initial growth of meandering rivers and that alternate bars have little impact on the initial development of meander loops.

2.1.13 Duan et al. (2001), Duan and Julien (2005) and Duan (2005)

Duan et al. (2001), Duan and Julien (2005), and Duan (2005) developed a numerical-empirical model called Enhanced CCHE2D (EnCCHE2D) to simulate alluvial channel migration phenomena. The EnCCHE2D model is capable of predicting quasi-3D flow field and shear stress

distribution on the bed. The process of sediment transport and meander migration were predicted based on these quasi-3D flow solutions. The advance or retreat of bank is calculated by considering not only the hydraulic erosion of bank surface and toe but also the mass balance of sediment flux in the near-bank zone.

The flow field was initially obtained by the 2D depth-averaged hydrodynamic model, CCHE2D. A set of empirical functions were then used to transform the flow and the bed shear stress field into quasi-3D ones. Details are explained in Duan (1998).

The sediments consist of bed load and suspended load. The authors used the formula of Meyer-Peter and Muller (1948) for bed load sediment transport. The primitive definition indicates that the volumetric sediment transport rate per unit width and length is equal to the integration of the product of velocity and concentration along the flow depth. They adopted the original formula of Rouse (1938) for calculating sediment concentration profile. Van Rijn's formula (1989) was found to give the best results in computing the reference concentration.

Basal erosion and bank failure occur in the process of bank erosion. Basal erosion caused by flow-induced shear stresses within the submerged part of the bank surface was calculated. Duan (2005) studied bank failure at a later time. The bank erosion rate is determined by the flow and sediment transport fluxes near the bank, and not just by the excessive velocity. After some improvements were made, this prediction model was used to simulate the inception of channel meandering (Duan et al., 2005a).

Figure 2.5 is a simulation result showing that the channel widens and bars and pools form. Because flow field and bed profile measurements are not available, it is not possible to compare simulated flow field and bed configurations with experimental data. Good agreement was observed in the comparison of simulated bank lines with those measured, as shown in Figure 2.6.
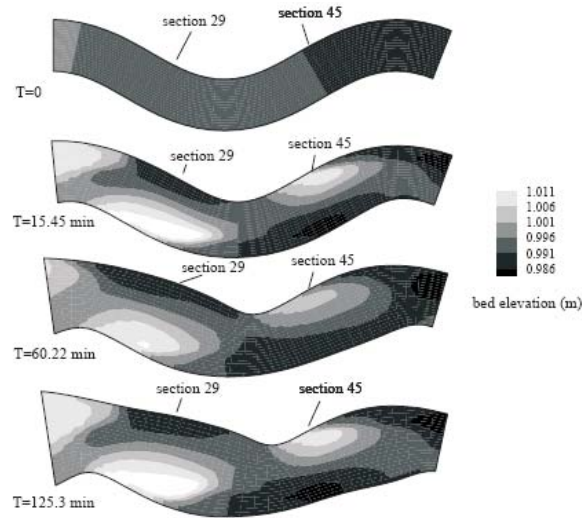
**Figure 2.5. Simulation of Meandering Channel Widening Due to Bank Erosion
(Duan et al., 2001).**
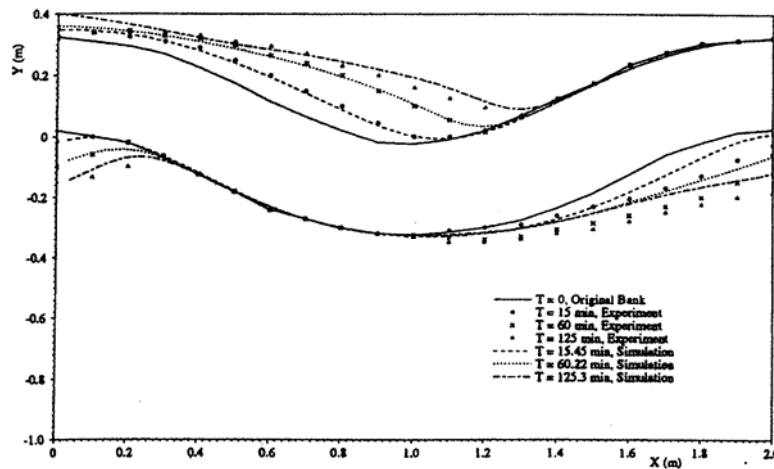
Figure 2.6. Comparison of Experimental and Simulated Results (Duan et al., 2001).

The authors demonstrated that the model is capable of predicting the alternate bars in a straight reach of channel and simulating the initiation process of a meandering channel. No quantitative comparison of the formation of bed form was made due to lack of data. The application of the model is still at the stage of experimental testing.

2.1.14 Chen (2002)

Chen (2002) used a Reynolds-Averaged Navier-Stokes (RANS) method together with a scour rate equation to calculate scour around simple piers. Unsteady RANS equations were solved in a

general curvilinear coordinate system. The same method is used to calculate maximum shear stress for the prediction of meander migration in this project.

2.1.15 Olsen (2003)

Olsen developed a 3D CFD model which was based on the finite volume method using an unstructured grid with dominantly hexahedral cells. The κ-ε model was used to predict turbulence. Sediment transport was computed as bed load in addition to solving the convection-diffusion equation for suspended sediment transport. The CFD model computes the erosion as a function of the sediment transport formulas and the computed 3D flow field.

Verification was done on a laboratory experiment conducted by another researcher. Figure 2.7 displays how a straight channel developed into a meandering channel in the simulation. No comparison with the test results was made.
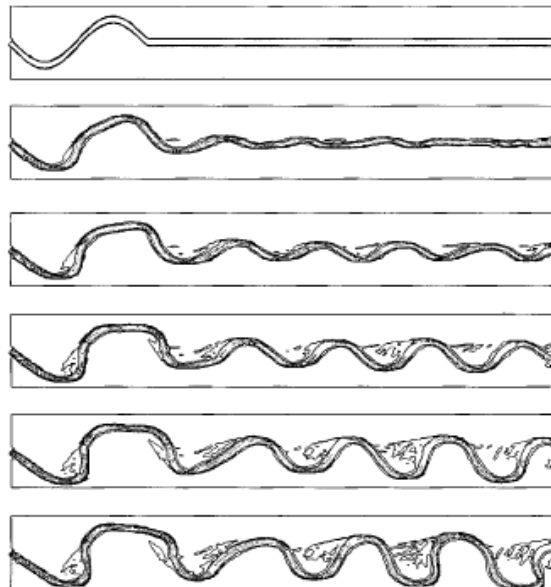
Figure 2.7. Simulated Meandering Process of Laboratory Case (Olsen, 2003).

2.1.16 Abad and Garcia (2004)

Abad and Garcia (2004) introduced a simplified river model for predicting river morphodynamics processes, including river migration. The methodology consists of components such as designing stream restoration, linear and nonlinear analyses, and a plan form migration

model. The mean annual flood discharge was used for the verification of a real river. Partial agreement was observed. This method can be classified as a quasi-2D model.

2.1.17 Rodriguez et al. (2004)

Rodriguez et al. (2004) developed two high-resolution models to simulate the flow field: a depth-averaged model with secondary flow correction and a full 3D computational fluid dynamics (CFD) model. Comparison with field data showed a successful simulation of the main flow features.

2.1.18 Jang and Shimizu (2005)

Jand and Shmizu (2005) modeled the flow field using the cubic interpolated pseudoparticle method. Secondary flow was considered in the sediment transport equation for the streamline and transverse transport to assess bed and bank evolution over time. In the 2D simulation, bank erosion occurs when the cross-sectional slope of the banks is larger than the submerged angle of repose. The model can reproduce phenomena such as bar growth and channel widening. It can also reproduce the features of braided rivers. Good agreements with laboratory experiments were observed.

2.2 MEANDER MIGRATION FLUME TESTS

2.2.1 U.S. Army Corps of Engineers (1945)

The U.S. Army Corps of Engineers (1945) performed a series of flume tests on the behavior of self-formed meandering rivers as shown in Figure 2.8. The flume tests were conducted in different conditions to investigate the effects of not feeding sand at the entrance, discharge, the angle of attack, bed slope, the initial cross sections, and material types. However, the studies were not based on a quantitative approach but rather on a qualitative approach.

(a) Initial Condition   (b) After 4 hours
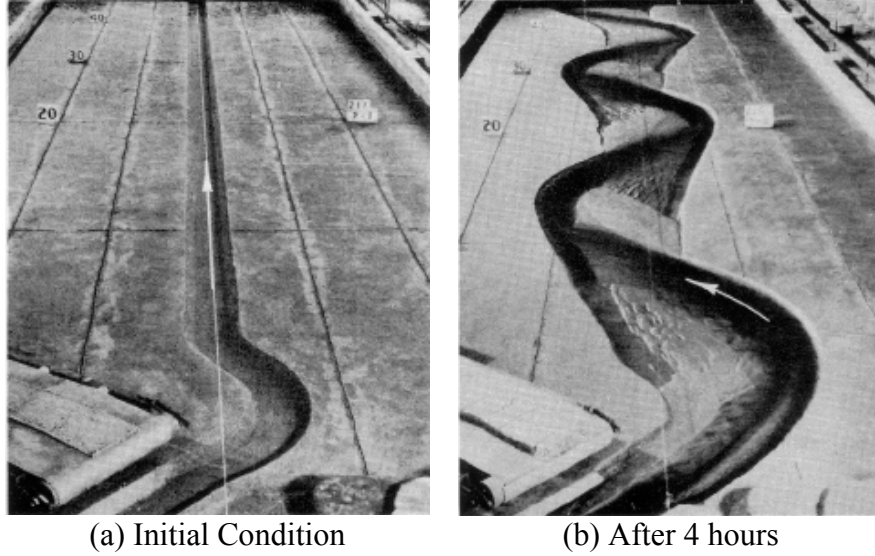
Figure 2.8. Photos from Sand Flume Test with Feeding Sand at the Entrance
(U.S. Army Corps of Engineers, 1945).

The effect of not feeding sand at the entrance to balance the sediment transport was not noticeable at the beginning of the test. The lack of sediment supply at the entrance of the channel gradually caused the channel to flatten with decreasing velocity, so this change slowly progressed downstream as shown in Figure 2.9.
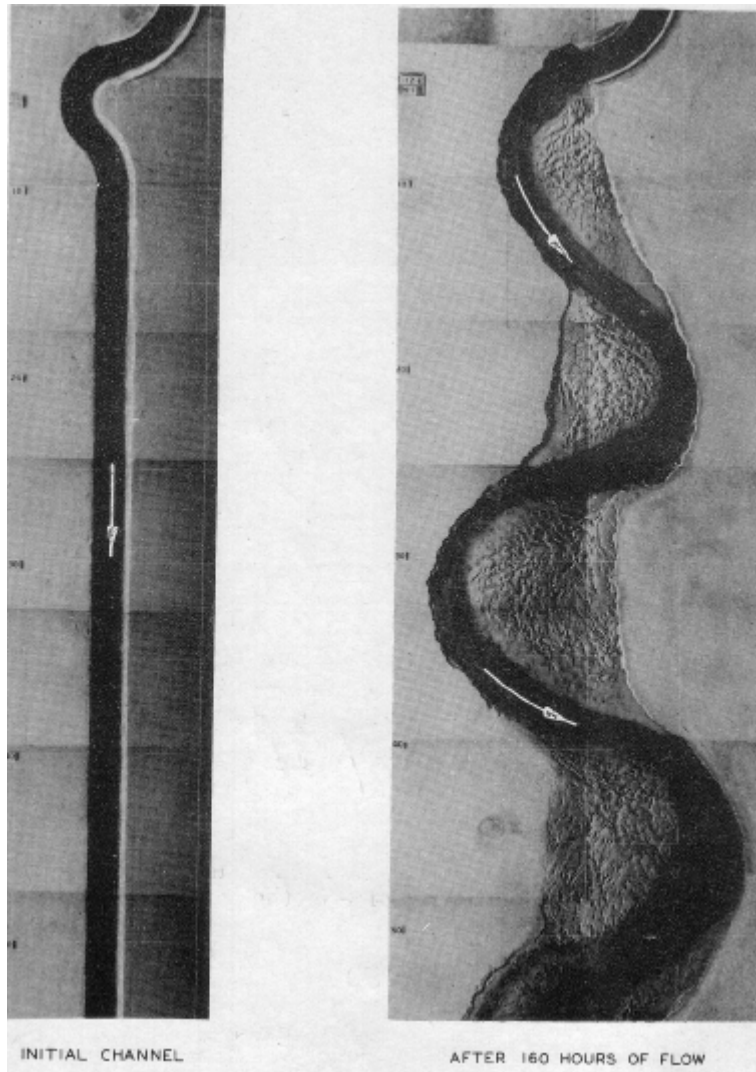
Figure 2.9. Photos from Sand Flume Test without Feeding Sand at the Entrance
(**U.S. Army Corps of Engineers, 1945**).

The size of the simulated meandering bends in the tests depends on the discharge and on the axial slope as shown in Figures 2.10 and 2.11: the higher the discharge or axial slope, the bigger the bends. This trend is reasonable since both discharge and slope are function of the energy of a stream.
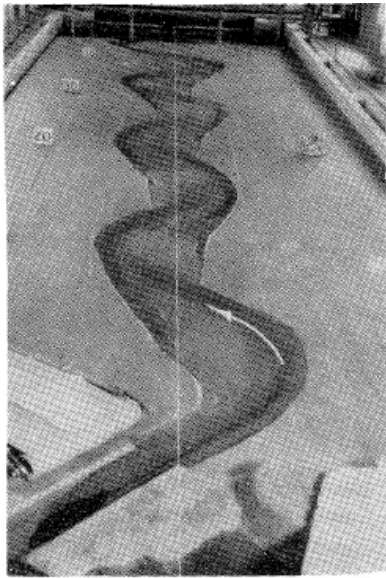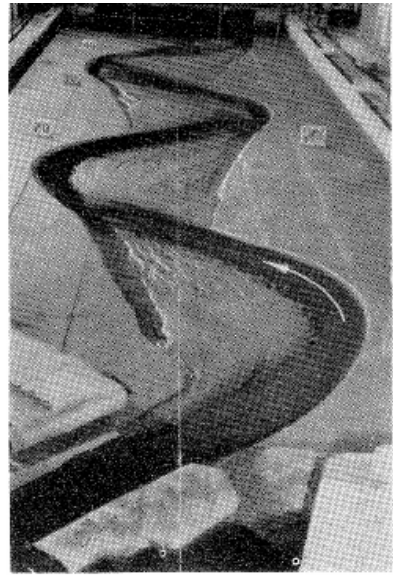
0.05 CFS   0.10 CFS   0.15 CFS

Figure 2.10. Effect of Discharge on the Size of Bend (U.S. Army Corps of Engineers, 1945).
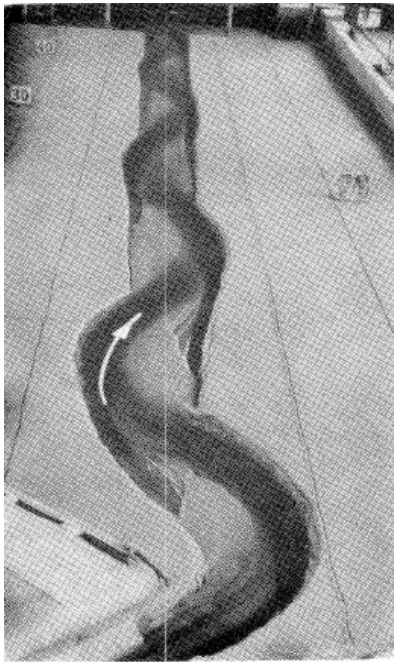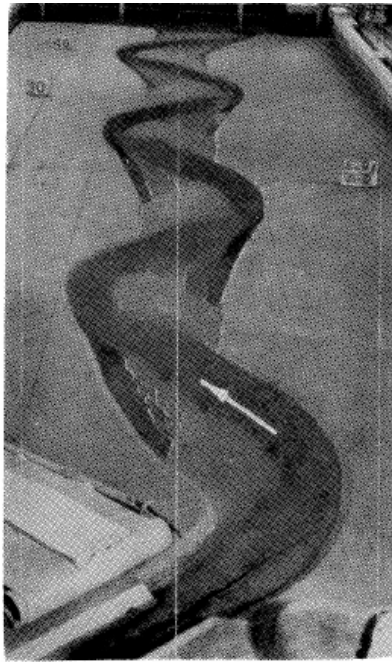
VALLEY SLOPE 0.0060   VALLEY SLOPE 0.0075   VALLEY SLOPE 0.0090
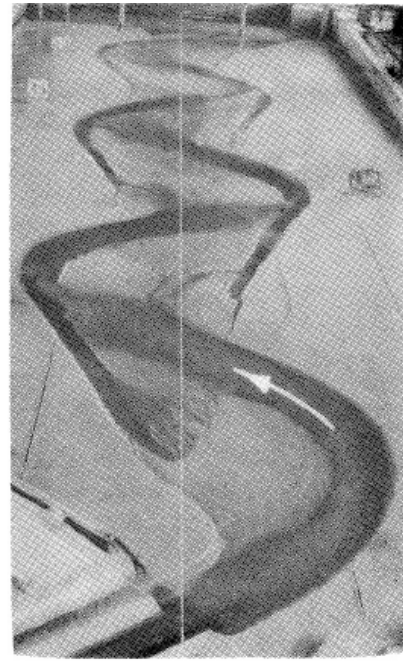
Figure 2.11. Effect of Valley Slope on the Size of Bend
(U.S. Army Corps of Engineers, 1945).

The effects of changes in the initiating angle of attack were studied by varying angles from 30° to 45°, and then to 60° (see Figure 2.12). All other conditions were the same. It is quite obvious that the larger attack angle created the larger meandering bend.

INITIAL ANGLE OF ATTACK – 30°   INITIAL ANGLE OF ATTACK – 45°   INITIAL ANGLE OF ATTACK – 60°
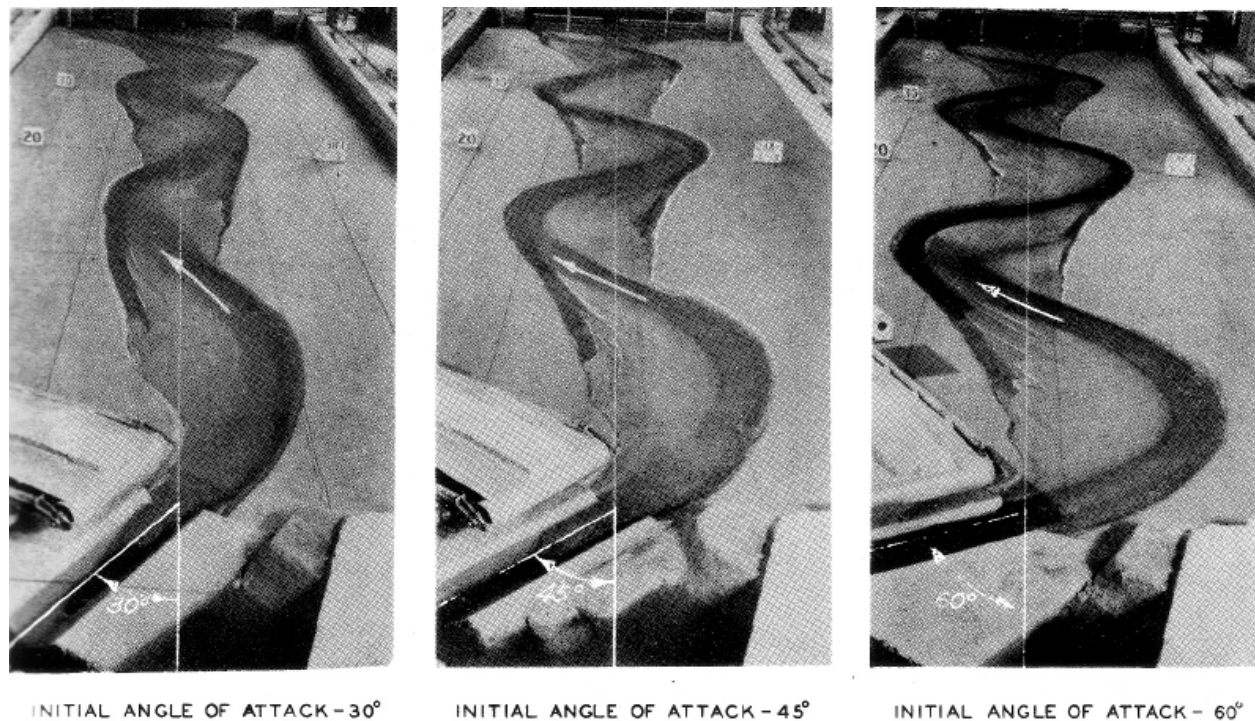
Figure 2.12. Effect of Attack Angle on the Size of Bend
(U.S. Army Corps of Engineers, 1945).

2.2.2 Nagata et al. (2000)

Nagata et al. (2000) presented a numerical model to investigate bed deformation and bankline shifting in 2D plan form. The governing equations are composed of 2D continuity and momentum balance equations in a moving boundary-fitted coordinate system. The authors developed a sediment transport model that included the theory of non-equilibrium sediment transport proposed by Nakagawa and Tsujimoto (1980). An intermittent bank erosion model proposed by Hasegawa (1981) was used, in which a bank slide event with noncohesive materials is evaluated.

The authors also conducted laboratory experiments to verify the model proposed. The experiments used a tilting flume which was 10 m (33 feet) long, 1 m (3.3 feet) wide and 0.2 m (0.7 feet) deep, as shown in Figure 2.13. The initial channel plan form in the experiments was set

as a sine-generated curve with 2 m (6.6 foot) wavelength and a 30° attack angle at the entrance of the channel. The cross-sectional shape was trapezoidal with 14 cm (5.5 inch) bottom width, 30 cm (11.8 inch) top width and 4 cm (1.6 inch) bank height. Sediment was fed manually during the experiments from upstream. Temporal bankline variations and channel bed profiles were measured in the tests.
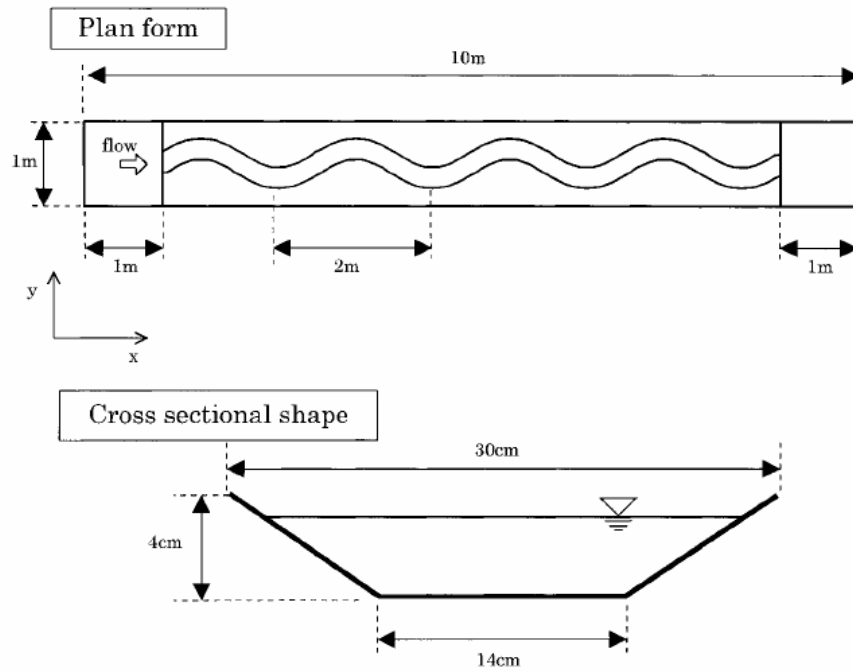
Figure 2.13. Experimental Setup (Nagata et al., 2000).

Figures 2.14 and 2.15 are the results of bankline evolutions and cross-section profiles in calculations and experiments. Comparison between the calculated and experimental results shows good agreement.
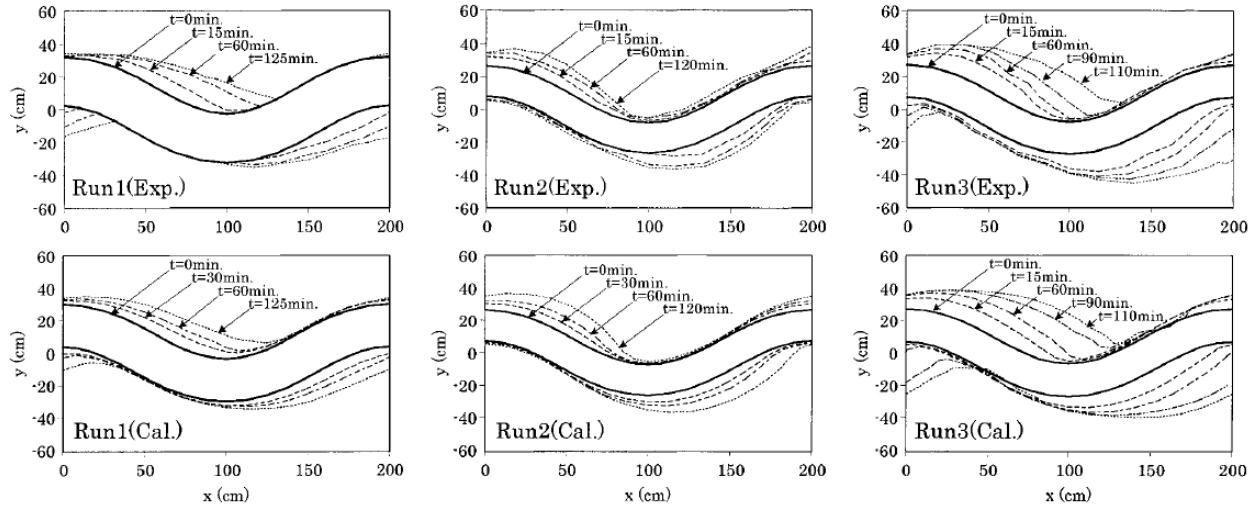
Figure 2.14. Temporal Changes in Plan Forms (Nagata et al., 2000).
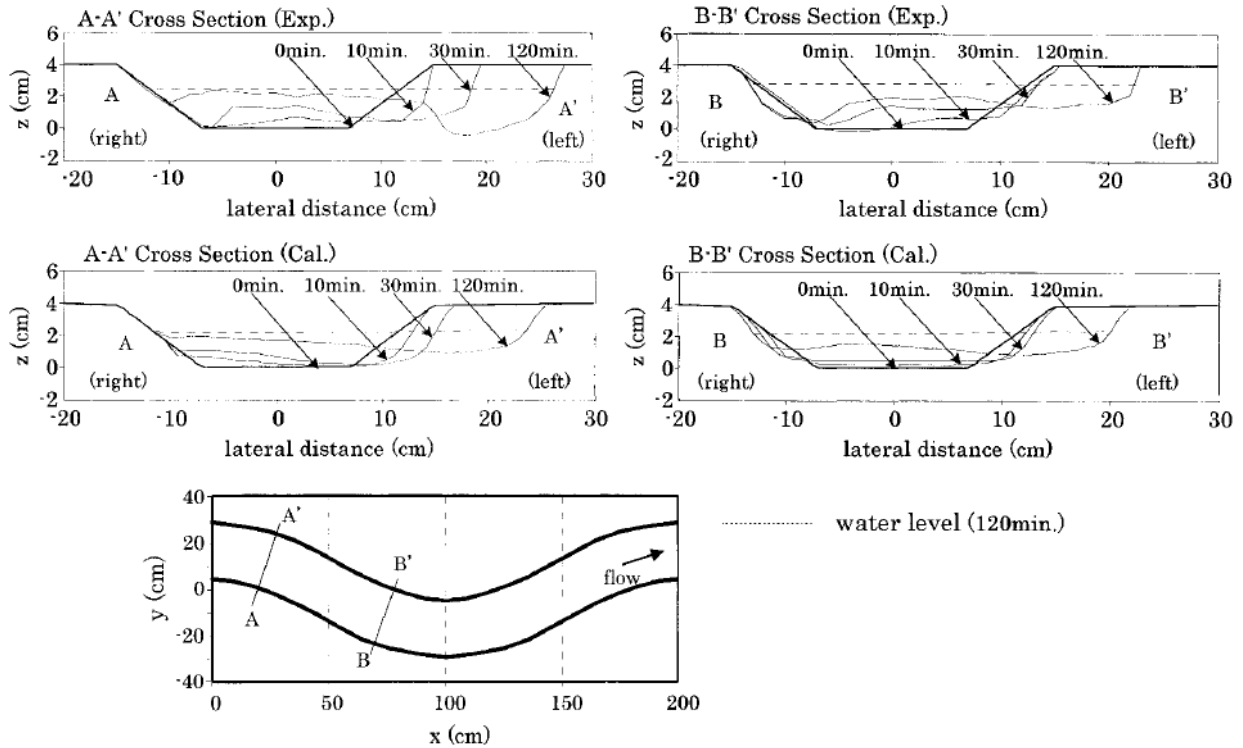
Figure 2.15. Temporal Changes in Cross-Sectional Profiles (Nagata et al., 2000).

2.3 RISK ANALYSIS FOR MEANDER MIGRATION

2.3.1 Briaud et al. (2003)

Briaud et al. (2003) developed the SRICOS-EFA method which predicts the scour depth in clay as a function of time. This is a fundamental modeling approach which consists of modeling the erosion process at the water-soil interface and projecting it into time by using future hydrographs (daily discharge versus time). This approach has the advantage of simulating the real phenomenon on a site-specific basis. It has the drawback of being more complicated because it requires site-specific measurement of soil properties and selection of future hydrographs.

Since the future hydrograph is unknown and it is not realistic to make a deterministic prediction, they developed a new technique to generate equally possible future hydrographs in a probabilistic manner. This technique consists of using a past hydrograph, preparing the frequency distribution plot for all the floods within that hydrograph, sampling the distribution randomly, and preparing a future hydrograph, for the required period, which has the same mean and standard deviation as the measured hydrograph. This process is repeated 10,000 times and, for each hydrograph, a final scour depth (the depth reached after the design life) is generated. These 10,000 final depths of scour are organized in a frequency distribution plot with a mean and standard deviation, as shown in Figure 2.16.
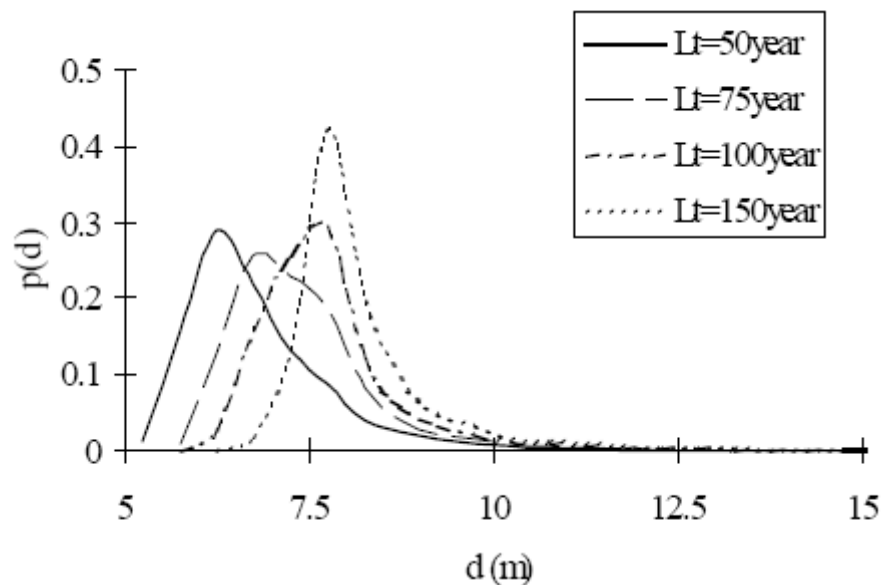
Figure 2.16. Probability Distribution of Scour Depth, *d*, for Different Lengths of the Project Life, *L*$_t$ (Briaud et al., 2003).

This analysis can be used to estimate the probability of exceedance R associated with the choice of different design values of scour depth and project lives. By definition, R is the probability that the design conditions are exceeded in the course of the life of the structure. From the probability distribution of d (Figure 2.16) it is possible to determine the CDF of d (Figure 2.17). R is then estimated as the probability of exceedance (Figure 2.17). This analysis provides a statistical framework that can be used in a cost-benefit study of bridge foundation design.
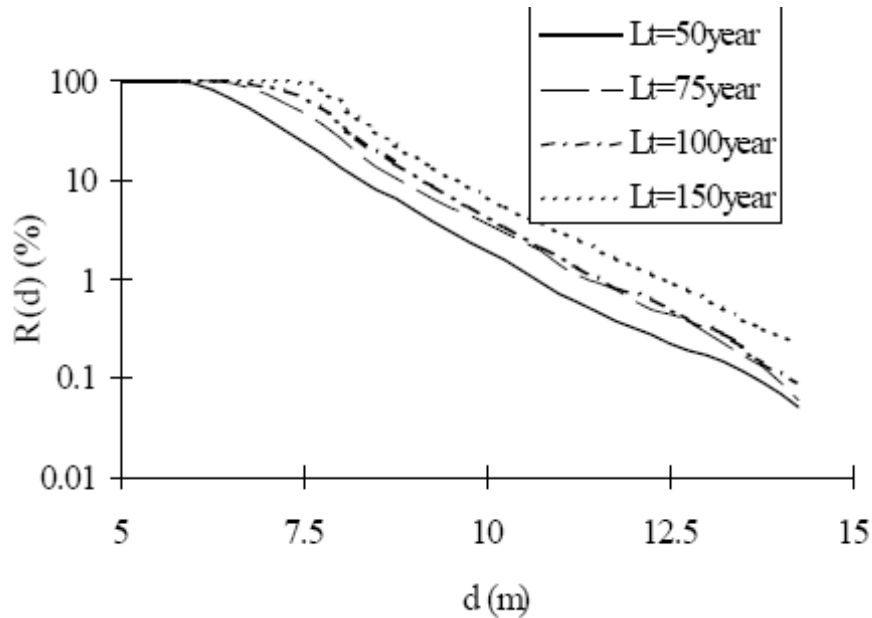
Figure 2.17. Risk Associated with Different Design Values of the Final Scour Depth, *d*, and Different Lengths of the Project Life, *L*$_t$ (Briaud et al., 2003).

2.3.2 Lagasse et al. (2003, 2004a, 2004b)

Lagasse et al. (2003, 2004a, 2004b) conducted National Cooperative Highway Research Program (NCHRP) research Project 24-16. The principal product of this research was a stand-alone handbook for predicting stream meander migration using aerial photographs and maps. The handbook deals with the problem of incremental channel shift and provides a methodology for predicting the rate and extent of lateral channel shifting and down-valley migration of meanders. The methodology is basically on using time-sequence maps and extrapolation. First, circles at two different times are fitted for a given bend. Then, the location of the center and the magnitude of the radius are linearly extrapolated with respect to time. The direction of new migration increment can also be extrapolated based on the direction of the two previous increments. The

process is shown from Figure 2.18 to 2.20, and the equations for the extrapolation are Eqs. 2.6 to 2.8. A program, "The Data Logger and Channel Migration Predictor," was developed to assist this process. It is an ArcView extension and was written in Visual Basic for Application (VBA) for ArcView.
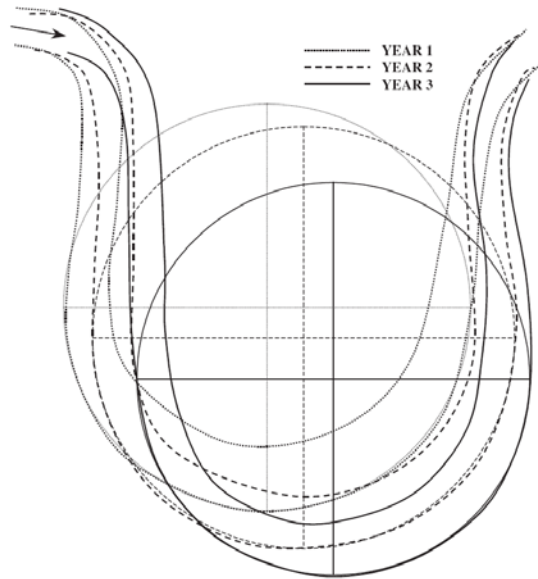
Figure 2.18. Banklines and Circles Drawn along Outer Bankline Positions for a Hypothetical Channel in Three Different Years (Lagasse et al., 2004b).
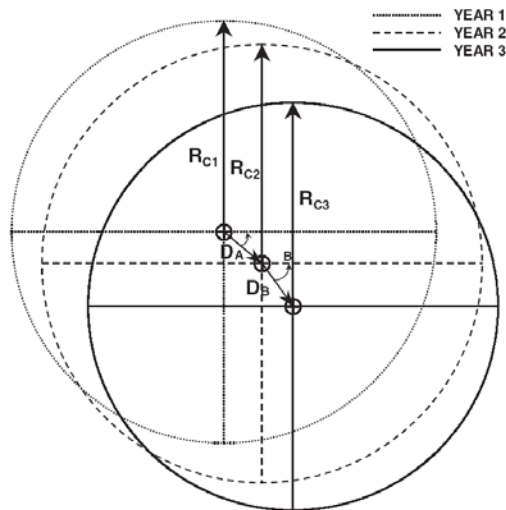
Figure 2.19. Diagram Defining the Outer Bank Radius of Curvature in Years 1, 2, and 3 (R_{c1}, R_{c2}, and R_{c3}) and the Amount (D_A and D_B) and Direction (θ_A and θ_B) of Migration of Bend Centroid during Periods A and B (Lagasse et al., 2004b).
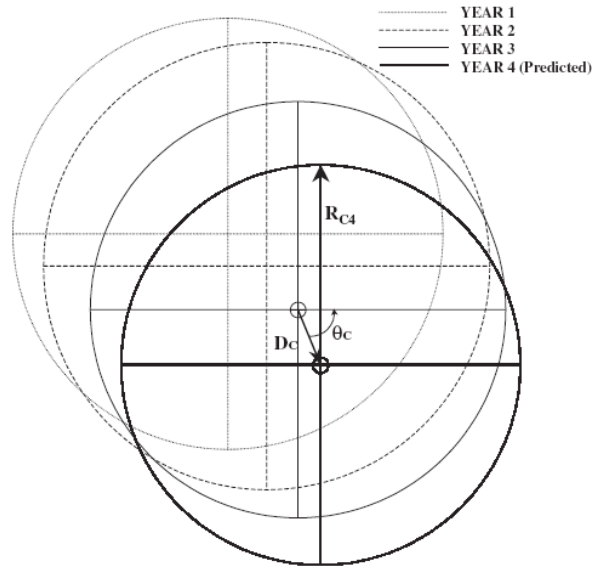
Figure 2.20. Predicted Position and Radius of Curvature of the Circle that Defines the Outer Bank of the Hypothetical Channel in Year 4 (Lagasse et al., 2004b).

$$R_{C4} = R_{C3} + \left[\left(\frac{(R_{C3} - R_{C2})}{(Y_B)} \right) (Y_C) \right] \tag{2.6}$$

$$D_C = \left(\frac{(D_B)}{(Y_B)} \right) (Y_C) \tag{2.7}$$

$$\theta_C = \left[\left(\frac{(\theta_B - \theta_A)}{(Y_B)} \right) (Y_C) \right] + \theta_B \tag{2.8}$$

As part of this study, a database of measured bend migration was generated and a statistical analysis was performed to develop guidance in estimating the normalized extension and translation migration with respect to the channel width for sites where aerial photos are not available. The procedures and guidance are in the form of a cumulative percentage plot, and two separate graphs are shown in Figures 2.21 and 2.22. There are four different categories of the channel such as Brice Class A, B_1, B_2, and C. For example, for meanders of the type Brice C sites, the probability of the normalized extension migration reaching 0.02 river width per year or less is 79 percent, according to Figure 2.21. For the same probability of 79 percent, the normalized translation migration according to Figure 2.22 is 0.036 river width per year. Figure 2.23 shows example movements in percentages for a 30-year time period. This approach can be meaningful for the site at which the historical record is not available. The drawback of this method is that it cannot incorporate a change in soil condition and a future hydrograph different from the past hydrograph. The advantage is its simplicity and its field-scale soil specifications.
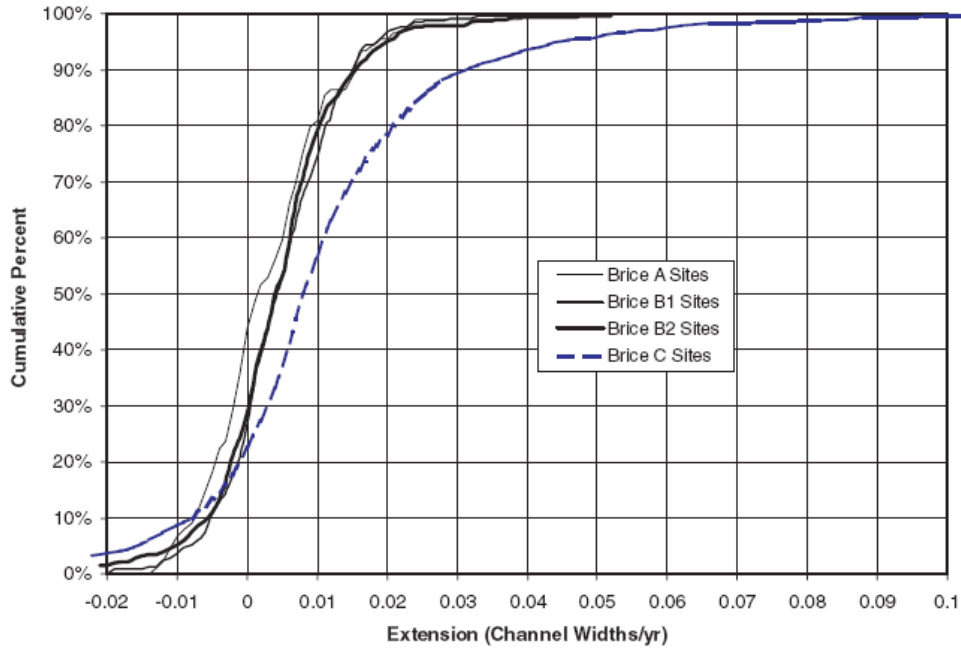
Figure 2.21. Cumulative Percentage of Extension Migration (Lagasse et al., 2004b).
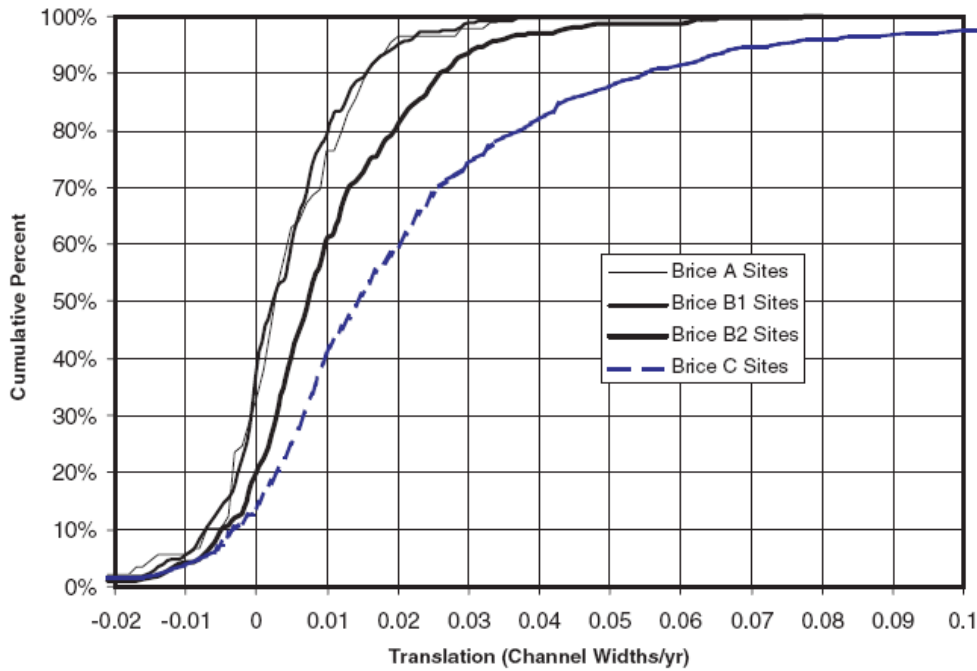
Figure 2.22. Cumulative Percentage of Translation Migration (Lagasse et al., 2004b).
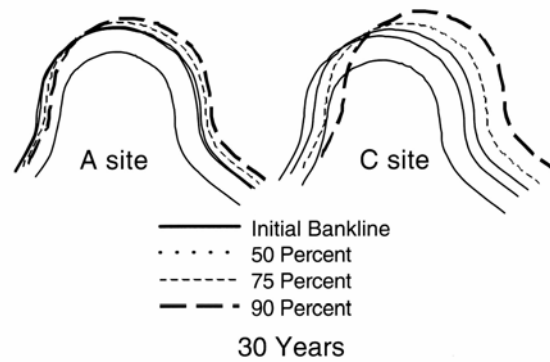
**Figure 2.23. Example Movement Percentages for a 30-Year Time Period
(Lagasse et al., 2004b).**

2.4 MEANDER MIGRATION SOFTWARE

2.4.1 Abad and Garcia (2006)

Abad and Garcia (2006) developed the RVR MEANDER program as a toolbox to assist the prediction of meander migration. The flowchart for the model is shown in Figure 2.24. Two versions of the program were developed: stand-alone Microsoft Windows-based and geographical information system GIS)-based versions.

The stand-alone version as shown in Figure 2.25 was written in Microsoft Visual C++ and Microsoft Foundation Classes (MFC). The geometry input can be done by typing manually, utilizing a spreadsheet, or importing from an ArcMap-DXF file.

The GIS-based version as shown in Figure 2.26 was written in Microsoft Visual C++ and MFC like the stand-alone version. In addition, Visual Basic and the ArcObjectsTM Developer Kit were used as well. The user can import the river geometry data from existing GIS line data within ESRI ArcMap.

Figures 2.27 to 2.28 show the user input interfaces for the program, and the example result of the prediction of migration is shown in Figure 2.29.

45
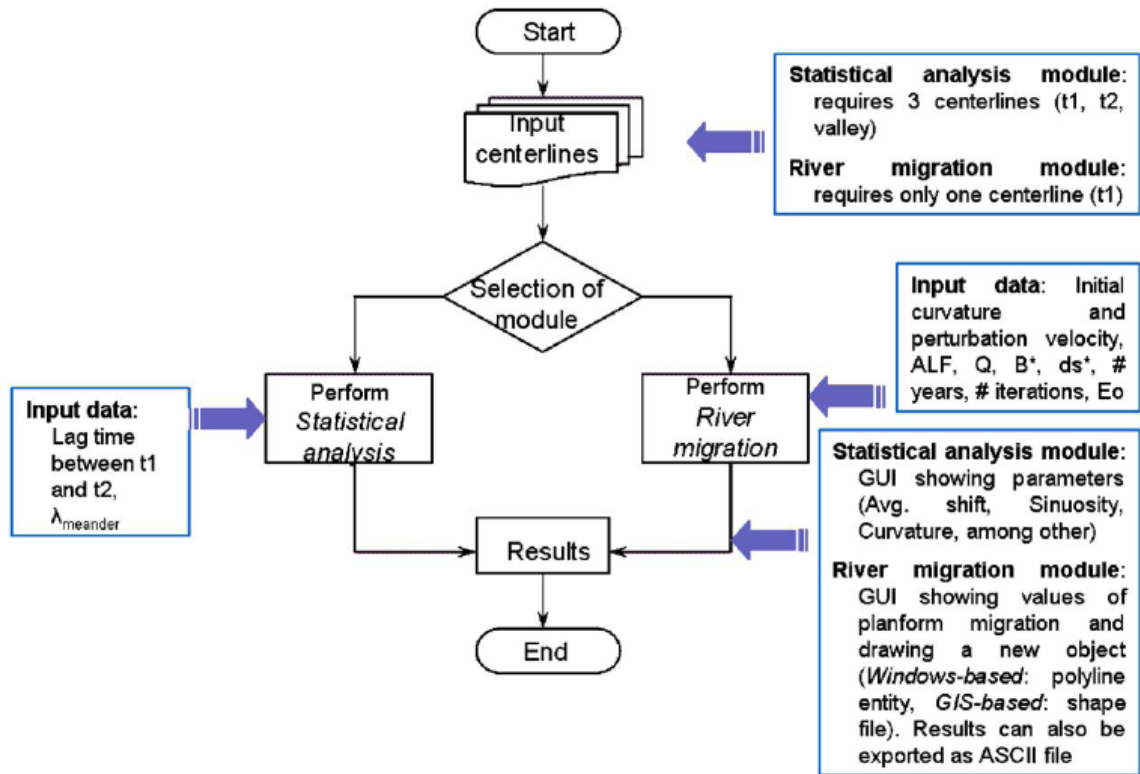
Figure 2.24. Flow Chart of Model Processes (Abad and Garcia, 2006).
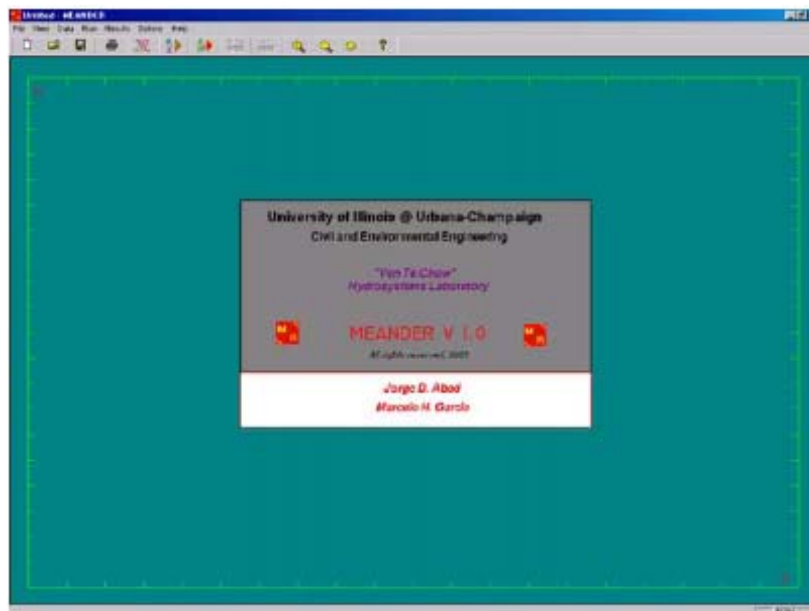
Figure 2.25. Stand-Alone Windows-Based Version (Abad and Garcia, 2006).
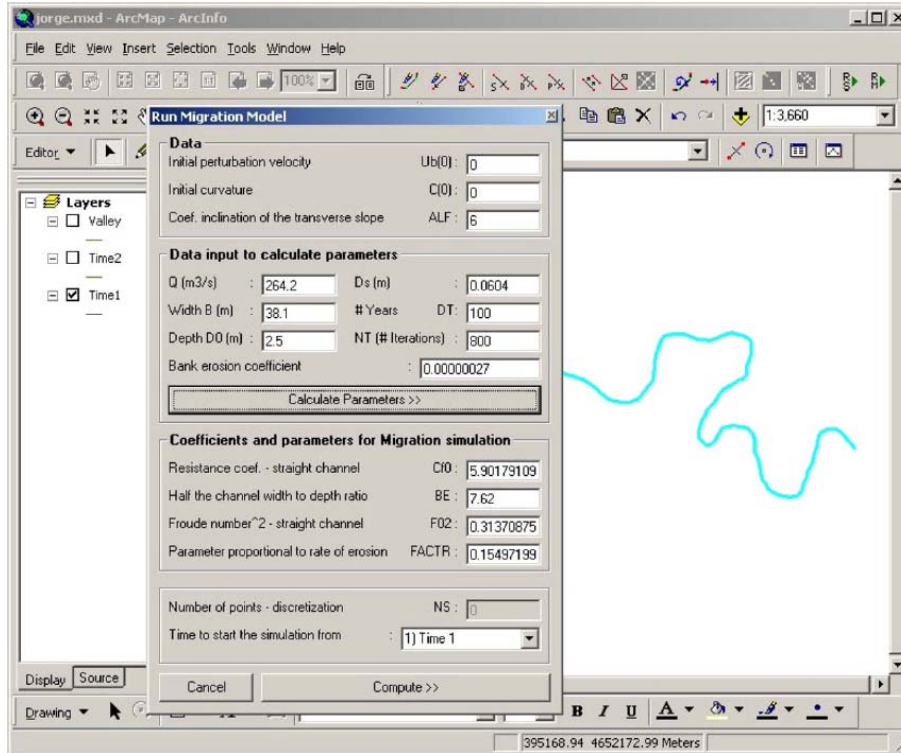
Figure 2.26. GIS-Based Work Environment (Abad and Garcia, 2006).
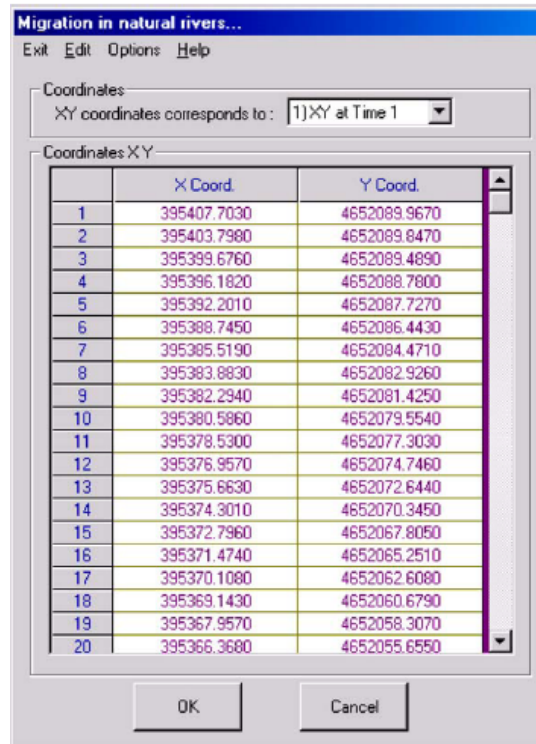
Figure 2.27. User Interface to Input Center line Coordinates (Abad and Garcia, 2006).
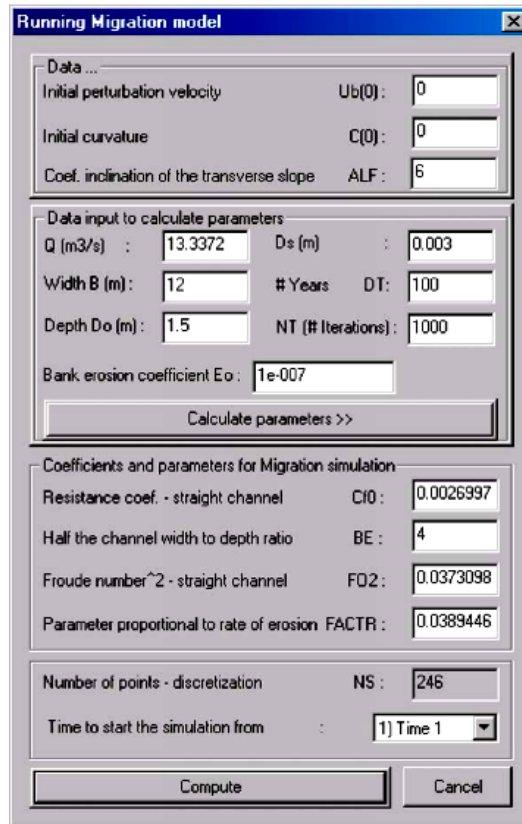
Figure 2.28. User Interface to Run Migration Module (Abad and Garcia, 2006).
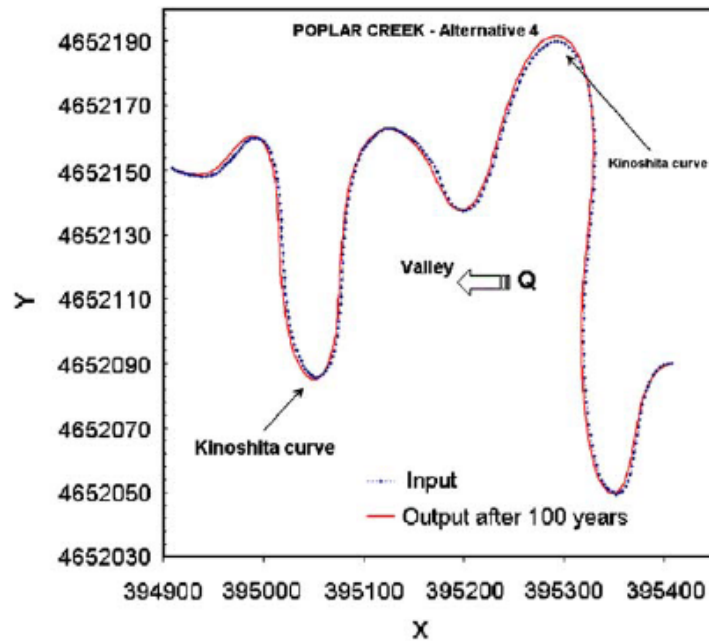
Figure 2.29. Output of Plan form Migration (Abad and Garcia, 2006).

48

CHAPTER 3. METHODOLOGY

3.1 HYPERBOLIC MODEL FOR CHANNEL BANKLINE EROSION DISTANCE

Under high flow rate, a river will erode its bankline and rework the flood plain continuously. The bankline displacement usually contains two components: cross-valley expansion and down-valley translation. Both components make the river more sinuous and extend the length between two reference stations. The increasing channel length increases the friction force on the channel boundaries to counterbalance the stream power, so as to decrease river erodibility. As the river flowrate remains constant, it is expected that the river bankline displacement from its original place will attain an equilibrium state. A hyperbolic process is proposed to estimate the channel bankline migration distance of a cross section,

$$M = \frac{t}{a + bt} \tag{3.1}$$

where M is the bankline migration distance, t is the time, a and b are two constants. The distance increases quickly, responding to the higher stream power in the early stage, and the rate gradually decreases as the channel extends its length and produces larger friction. The two parameters, a and b, are the reciprocal of the initial erosion rate $\dot{M}_i$ and the maximum erosion distance M_{max}, which is the maximum distance when the bankline attains its equilibrium state.

$$\frac{1}{a} = \lim_{t \to 0} \frac{M}{t} = \dot{M}_i, \quad \frac{1}{b} = \lim_{t \to \infty} M = M_{max} \tag{3.2}$$

The two parameters, $\dot{M}_i$ and M_{max}, in the hyperbolic model identify the initial erosion rate and the migration distance of a cross section of the channel as shown in Figure 3.1. Determination of these two parameters is crucial to the prediction of bankline movement. In this study, numerical simulation and EFA test were used to determine the initial migration rate $\dot{M}_i$. Large-scale flume tests were also conducted to investigate the maximum migration distance M_{max} of channel bankline.
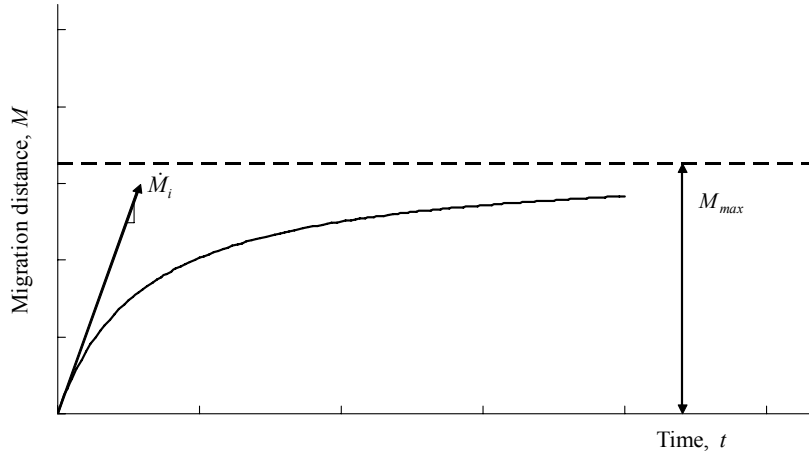
Figure 3.1. Channel Bankline Migration Distance and Hyperbolic Model.

3.2 NUMERICAL SIMULATION

In the present study, the three-dimensional flow chimera RANS method in Chen (1995a, 1995b) and Chen et al. (1997) is used. The computational domain is first divided into a number of smaller grid blocks, which allow complex configurations and flow conditions to be modeled efficiently through the judicious selection of different block topology, flow solvers, and boundary conditions. The chimera domain decomposition technique was used to connect the overlapped grids together by interpolating information across the block boundaries. The Reynolds stresses were evaluated using the two-layer turbulence model of Chen and Patel (1988). The mean flow and turbulence quantities were calculated using the finite-analytical method of Chen et al. (1990). The SIMPLER/PISO pressure-velocity coupling approach of Chen and Patel (1989) and Chen and Korpus (1993) is used to solve for the pressure field. A detailed description of the multiblock and chimera RANS methods is given in Chen and Korpus (1993) and Chen et al. (1997). A useful summary of that method can be found in Nurtjahyo (2002). This summary discusses the governing equations including turbulence modeling (RANS equations), the boundary conditions for the channel bank surface, the river bottom, the outer boundaries, and the free water surface. A more detailed discussion is presented in Chapter 4 of this report.

3.3 EFA TEST

Soil erosion is an interactive process between soil and water occurring at the interface of soil and water. As velocity increases, the shear stress τ imposed by the water on the soil particles becomes large enough to overcome the gravity bonding forces. For coarse-grained soils erosion

occurs by rolling and sliding of particles. Fine-grained soils may erode particle by particle or block of particles by block of particles (electromagnetic and electrostatic forces play an important role) (Briaud et al., 2001a). The threshold shear stress at which erosion is initiated is called the critical shear stress τ_c.

The EFA was invented by Jean-Louis Briaud at Texas A&M University in 1991 (U.S. Patent No. US6260409B1; July 17, 2001). Figure 3.2 shows the conceptual diagram and test section of the machine. The soil sample sits in an American Society for Testing and Materials (ASTM) standard Shelby tube with a 76.2 mm (0.30 inch) outside diameter (ASTM D1587). A piston pushes the sample until it protrudes by 1 mm (0.004 inches) into the flow. The protruding soil erodes under velocities varying from 0.2 m/s to 4 m/s. The procedure for an EFA test is as follows:

1. Place the sample in the EFA, fill the pipe with water, and wait 1 hour.
2. Set the velocity to 0.3 m/s.
3. Push the soil 1 mm into the flow.
4. Record how much time it takes for the 1 mm soil to erode.
5. When the 1 mm of soil is eroded or after 1 hour of flow, whichever comes first, increase the velocity to 0.6 m/s and bring the soil back to a 1 mm protrusion.
6. Repeat step 4.
7. Next, repeat steps 5 and 6 for velocities equal to 1 m/s, 1.5 m/s, 2 m/s, 3 m/s, and 4 m/s.
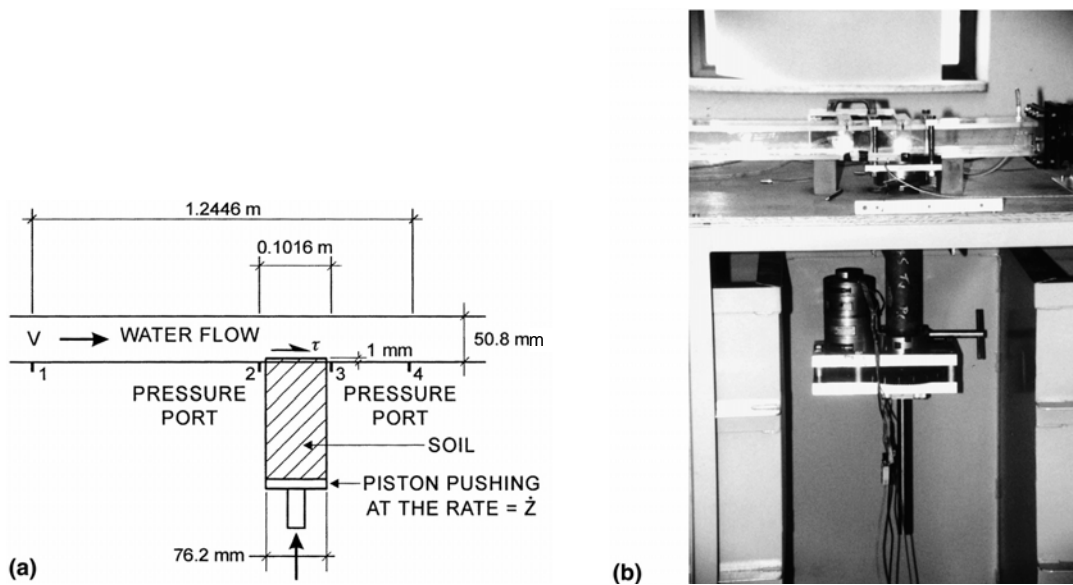
Figure 3.2. EFA Test: (a) Conceptual Diagram; (b) Photograph of Test Section (Briaud, et al., 2001a).

The test result is an erosion rate $\dot{z}$ versus velocity v curve. The erosion rate is the height of the soil eroded divided by the time taken to erode it. Shear stress cannot be measured directly and needs to be solved in an indirect manner. Shear stress at the soil-water interface is caused by the flow, and the magnitude is related to the roughness of soil surface. The pressure difference between points 2 and 3 (Figure 3.2(a)) is caused by the friction across the sample. By drawing a free body diagram, the shear stress can be calculated with reference to the pressure difference. But the pressure head difference is small and fluctuates. It was found that the best way to calculate shear stress is to use the Moody Chart (Moody, 1944; Figure 3.3). The shear stress τ is:

$$\tau = \frac{1}{8} f \rho v^2 \tag{3.3}$$

where τ is the shear stress on the wall, f the friction factor obtained from the Moody Chart, ρ_w mass density of water, and v mean flow velocity in the pipe. On the Moody Chart, Re is Reynolds number; μ_w the dynamic viscosity of water, $v_w = \mu_w / \rho_w$ the kinematic viscosity of water (10^{-6} m^2/s at 20°C), and D the pipe diameter. For non-circular shape, $D = 4A_w / P$ where A_w = cross-sectional flow area and P = wetted perimeter. For a rectangular cross-section pipe, $D = 2ab/(a+b)$, where a and b are dimensions of the sides of the rectangle. ε is the average height of roughness elements. It is taken as $(1/2)D_{50}$, where D_{50} is the mean particle diameter for the soil and ε/D a measure of relative roughness. Figure 3.4 is the result of a test on a clean coarse sand ($D_{50} = 3.375$ mm [0.01 inch]). The critical shear stress for this soil is $\tau_c = 3$ N/m^2.
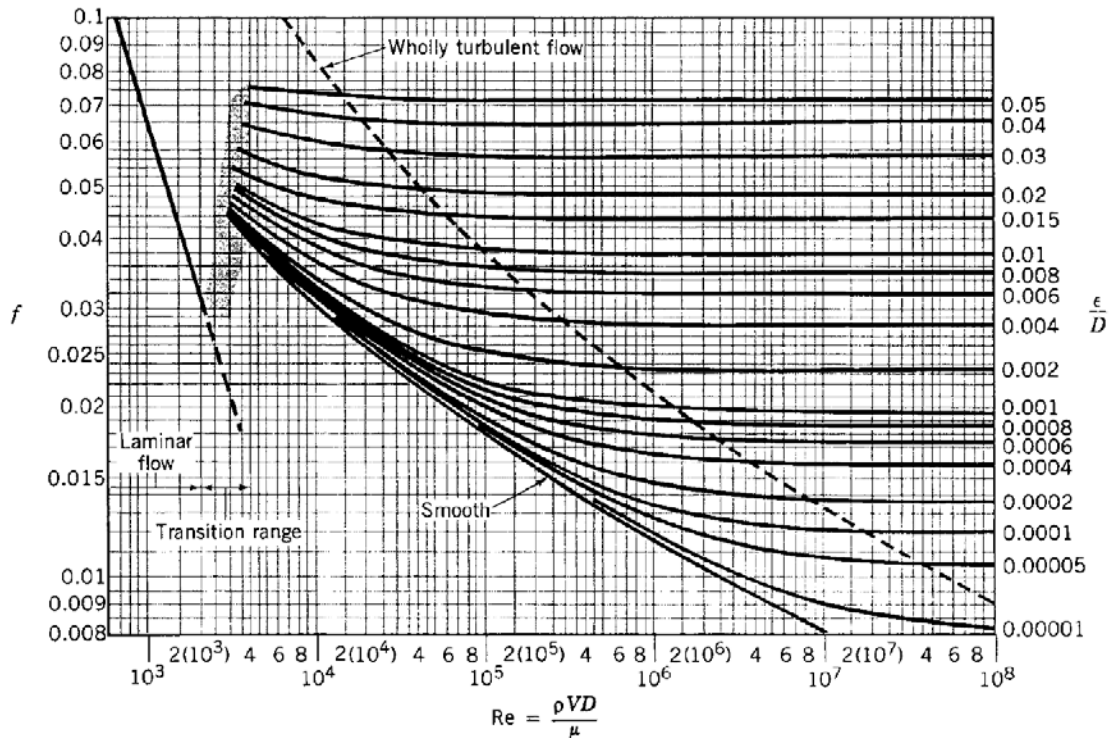
Figure 3.3. Moody Chart (Munson et al., 1990).
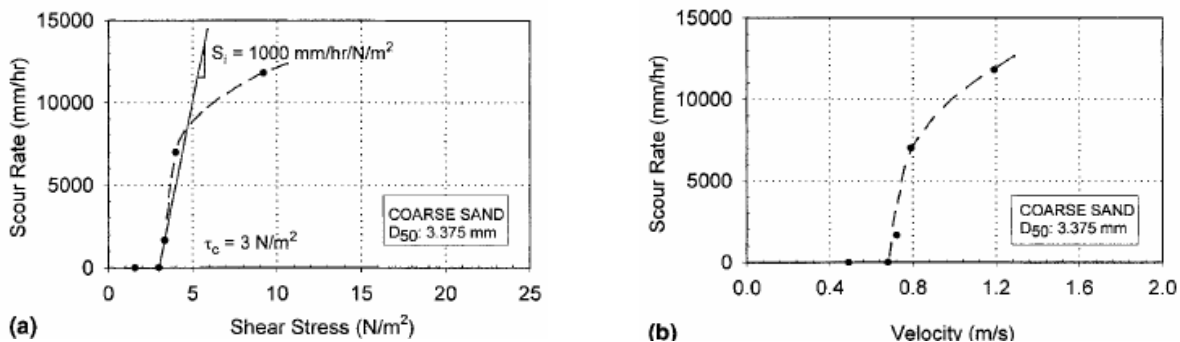
Figure 3.4. Erosion Curve for Coarse Sand (Briaud et al., 2001a).

Many experiments have been done to establish relationships between the erosion function characteristics and common soil properties that can be easily obtained. The erosion function is a non-linear relationship between the erosion rate $\dot{z}$ and the shear stress τ. Critical shear stress τ_c and initial slope of the curve S_i are two of the parameters involved. In order to find the correlation between erodibility and soil parameters, one could try to find the correlation between τ_c, S_i, and soil parameters. For coarse-grained soils, τ_c is proportional to D_{50}. For fine-grained soils, there is no such correlation. Experimental data also show weak correlation between τ_c, S_i, and soil properties such as undrained shear strength, plasticity index, and percentage passing

#200 sieve, etc. So it is not realistic to obtain erodibility from common soil properties. A direct measurement with the EFA for a specific site is favored.

3.4 FLUME TEST

Flume tests are large-scale physical modeling to simulate bankline erosion of curve channels. Based on the physical considerations, the factors that affect the channel bankline migration distance M of any arbitrary position on the channel can be divided into four categories: geometry, hydraulic condition, soil properties, and others not included in the first three categories. Geometry consists of the channel width W, the radius of curvature of the channel bend R, the angle of the channel bend ϕ, and the channel bed slope s. The hydraulic condition includes the fluid density ρ_w, the fluid viscosity μ_w, the average flow velocity U, and the water depth h. The soil property is the relationship between the hydraulic shear stress τ and the soil erosion rate $\dot{z}$; the critical shear stress τ_c at which erosion initiates plays a particularly important role. The other factors include external forcing, vegetation condition, artificial structures, etc. In this study, only the first three categories plus gravitational acceleration g were considered, and the functional relationship can be expressed as

$$M = f_0(W, R, \phi, s, \rho_w, \mu_w, U, h, \tau_c, g) \tag{3.4}$$

After performing the dimensional analysis, the functional relationship between the migration distance and the variables can be expressed as

$$\frac{M}{W} = f_1(\frac{R}{W}, \phi, Fr, s, Re, \frac{h}{W}, \frac{\tau_c}{\rho_w U^2}) \tag{3.5}$$

where $Re = \rho_w U h / \mu_w$ is the Reynolds number and $Fr = U/(gh)^{1/2}$ the Froude number. According to open-channel flow theories, it is known that the water depth h depends on the flow rate Q and the channel bed slope s. Under a constant flow rate and constant channel cross-section condition (and therefore a constant h and U) in the experiments, h can be obtained by adjusting s. This means that s is a dependent variable of U and h and thus can be crossed out in the present study. The Reynolds number is greater than 15,000 in the experiments so the effect of the fluid viscosity may be neglected. The water depth to channel width ratio h/W, was kept constant ($h/W = 1/7.5$) throughout the experiments with h being approximately one order of magnitude smaller than W. We assume such a ratio is close to that of a natural channel while accepting the limits of the physical dimensions in the tests (even though the tests are some of the largest worldwide).

The dimensionless critical shear stress $\tau_c/\rho_w U^2$ is converted into the critical Froude number Frc at which bank erosion is initiated. With these observations, the dimensionless equation is simplified to

$$\frac{M}{W} = f_2(\frac{R}{W}, \ \phi, \ Fr, \ Frc) \tag{3.6}$$

where R/W is the ratio between the radius of curvature of the channel center line and the channel width ϕ, the bend angle Fr, the flow Froude number, and Frc, the critical Froude number. Including the parameter θ to denote the position on the initial channel bankline, the final form of the dimensionless equation is

$$\frac{M}{W} = f_3(\frac{\theta}{\phi}, \ \frac{R}{W}, \ \phi, \ Fr, \ Frc) \tag{3.7}$$

Note that only the initial value in each parameter was used in the study, and θ varies from 0 to ϕ within a curve bend.

3.5 GEOMETRY STUDY

From the previous section, it is known that migration distance M is a function of channel geometry, R/W, and ϕ. Before calculating the migration distance by applying the hyperbolic model, one needs to identify the local geometry of any point on the channel bankline. The purpose of geometry study is to curve fit a channel bankline into several segments with circles and straight lines. The circles is chosen to represent the bend shape due to its simplicity and its claimed effectiveness in literature. An automatic fitting process was also developed to repeat the procedure for a complex hydrograph. The geometry study consists of these steps:

1. Develop a method to fit a circle for a given group of points.
2. Calculate the radius of curvature of each point on the curve.
3. Identify bends for which circles should be fitted.
4. Find the best fit circle at a certain bend.
5. Calculate the bend angle.

A detailed discussion of this section will be described in Chapter 7 of this report.

3.6 APPLICATION OF SRICOS-EFA METHOD TO CHANNEL MIGRATION

The SRICOS-EFA method was developed to determine the scour depth at a cylindrical bridge pier for a constant velocity flow and a uniform soil system (Briaud et al., 1999). The evolution of the pier scour depth with time is predicted by calculating the initial erosion rate and maximum scour depth. The method was adapted in this study by replacing the scour depth with the bankline migration distance.

The major difference in this implementation is that for pier scour, velocity is the only changing parameter, whereas for meander migration, changing parameters also include channel geometry and water depth. If the velocity is constant, there is only one scour depth z versus time t curve for the prediction of pier scour. Scour depth after a certain time can be calculated in one step. For the prediction of meander migration, even though velocity is constant, the geometry and possibly water depth change with time. These parameters need to be updated after each time step. A long time constant velocity needs to be divided into a number of time steps. The migration distance of each step is accumulated, which is similar to using a hydrograph.

A channel curve is simplified into circles and straight lines for easy analysis. The bends and the parts with reasonably large curvature are fitted with circles. The rest is treated as line segments. There might be tens of thousands of time steps for one hydrograph. Manual fitting would make a practical solution not possible. A huge amount of effort has been put into developing automatic fitting techniques and a computer program.

Water depth changes with discharge, velocity, and channel cross section. The prediction needs the water depth at each time step for each point on the channel. It would be too complicated to obtain all these input data. Assumptions are made to simplify the problem. The cross section of the channel is assumed to be trapezoidal and remain the same in the migration process. The average velocity is treated as being the same throughout the channel. With these assumptions, the discharge or velocity versus water depth curve can be developed by running HEC-RAS. Then the needed water depth can be provided numerically.

3.7 RISK ANALYSIS

A meander migrates at a rate controlled by the erosion rate of the soil at the interface between the water and the bank. The hydraulic shear stress imposed by the water is controlled by the velocity of the flow, which depends on the hydrograph of the river. A meander migration prediction

process must therefore consider the hydrograph of the river. This hydrograph is not known since it will occur in the future during the design life of the bridge or of the highway embankment. Since it is not realistic to make a deterministic prediction of a future hydrograph, it is more desirable to make predictions of many equally possible hydrographs in a probabilistic manner. Each hydrograph then moves the river toward a predicted position of the meander and a probabilistic post-process provides a probability that the river will move to a given location at a given time.

3.8 MEANDER PROGRAM

With all the components described above, a computer program was developed as the last step of this project. To apply the methods developed in this research, a user-friendly computer program is necessary to assemble all the steps. The program includes the following components:

- Geometry study. The user can read in the plan form coordinates of a river. The program automatically fits circles to each bend of the river. Radii of curvature and bend angles are obtained accordingly. If a hydrograph is applied, the automatic fitting process is repeated for each time step.
- Input of soil properties. The EFA curves are input here.
- Input of water data. The following information goes here: discharge vs. velocity curve, discharge vs. water depth curve, and hydrograph. The user can choose to do a risk analysis or not. Then the risk analysis period, a hydrograph or Q_{100}, Q_{500} (100/500 year flood), are needed.
- Implementation of the hyperbolic model. With the above information and the equations for τ_{max} and M_{max}, the hyperbolic model is implemented. The code for risk analysis is also here. This process goes on behind the user interface.
- Input Plots. This part graphically gives the user a chance to check whether the input data look correct.
- Output Plots. The migrated channels for a single hydrograph or risk analysis are presented here.

CHAPTER 4. NUMERICAL SIMULATION

Critical shear stress is the threshold to initiate erosion. When the shear stress within the channel exceeds this critical value, a certain erosion rate of the bottom and bank material is established. The numerical simulation calculates the shear stress distribution in the channel. With EFA tests of bank material, the initial migration rate $\dot{M}_i$ of the hyperbolic model can be determined.

4.1 INTRODUCTION

In an earlier TxDOT pier scour project, τ_{max} was defined as the maximum shear stress that occurs at the soil-water interface before the initialization of scour (Chen, 2002). With erosion progressing, scour depth increases gradually and shear stress decreases accordingly until it reaches the critical shear stress τ_c. Since it is not convenient to measure shear stress on the interface, numerical simulation is needed to develop the τ_{max} equation. Numerical simulation can be considered as a computer version of "flume test." A variety of parameters can be chosen and varied in small steps. Many more cases can be conducted in simulation than in actual flume tests. For pier scour, data reduction showed that the most influential factors that affect τ_{max} are velocity and Reynolds number.

The same concept and procedure can be applied to prediction of meander migration. The maximum shear stress τ_{max} corresponds to a certain flow condition, soil property, and channel geometry. Numerical simulation calculates the maximum shear stress along the channel under different flow and geometry conditions. The influence of these factors on maximum shear stress is quantitatively analyzed and an empirical formula can thus be developed.

4.2 EXAMPLE RUNS

The geometry of three example runs is shown in Figure 4.1. These three cases have the same R/W (= 4) with 65°, 120°, and 240° bend angles, respectively. The simulation results of velocity vectors and shear stresses on the channel bank are shown in Figures 4.2 and 4.3.

Numerical Grid: $\phi = 65°$

Numerical Grid: $\phi = 120°$
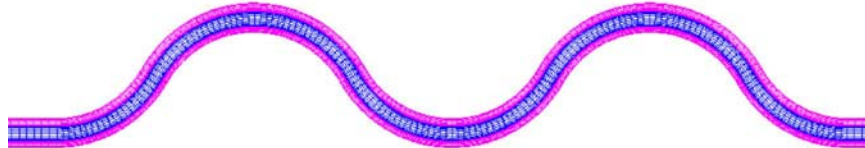
Numerical Grid: $\phi = 240°$
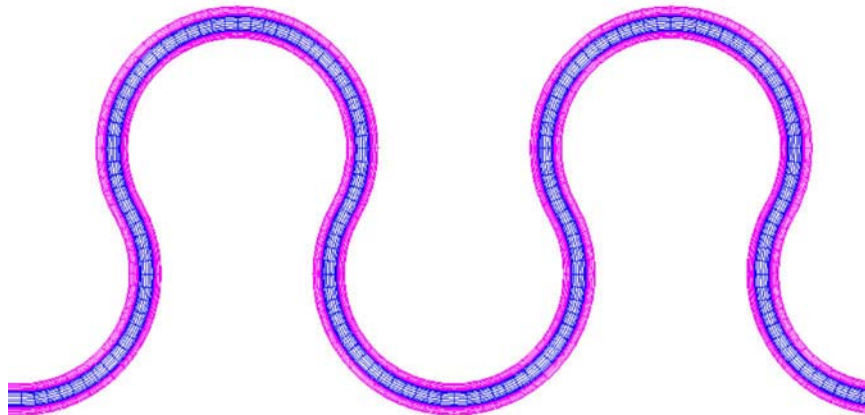
Figure 4.1. Geometry of Numerical Simulation Runs.

Velocity Vectors: $\phi = 65°$
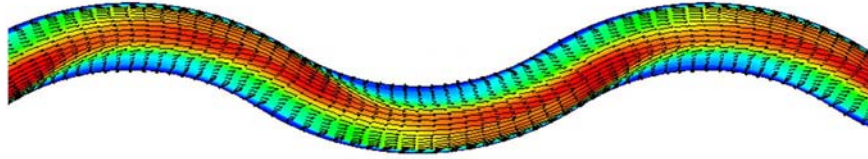
Velocity Vectors: $\phi = 120°$
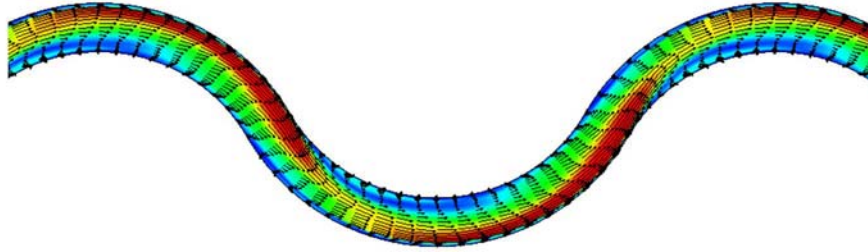
Velocity Vectors: $\phi = 240°$
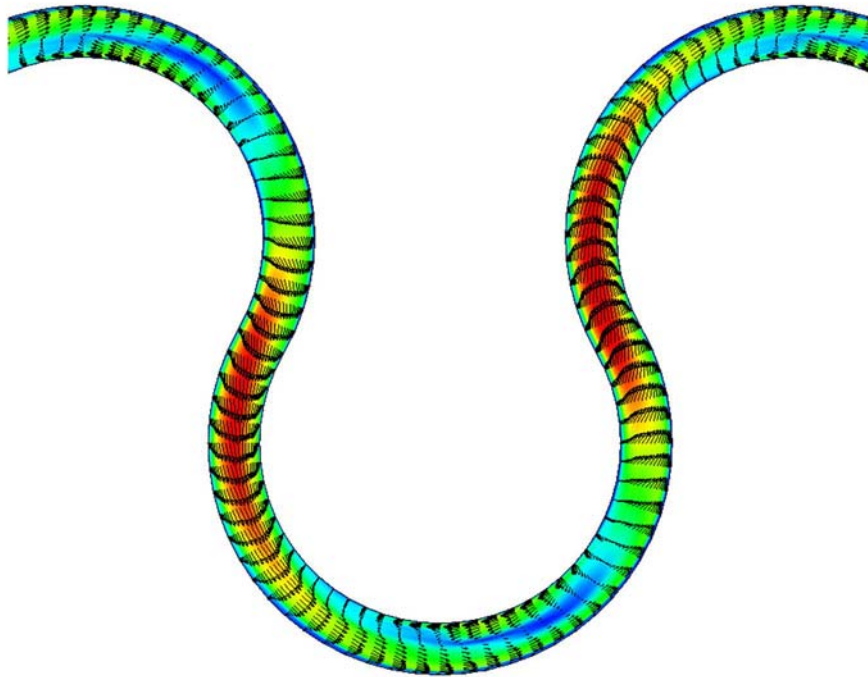
Figure 4.2. Velocity Vectors Obtained in the Numerical Simulations.
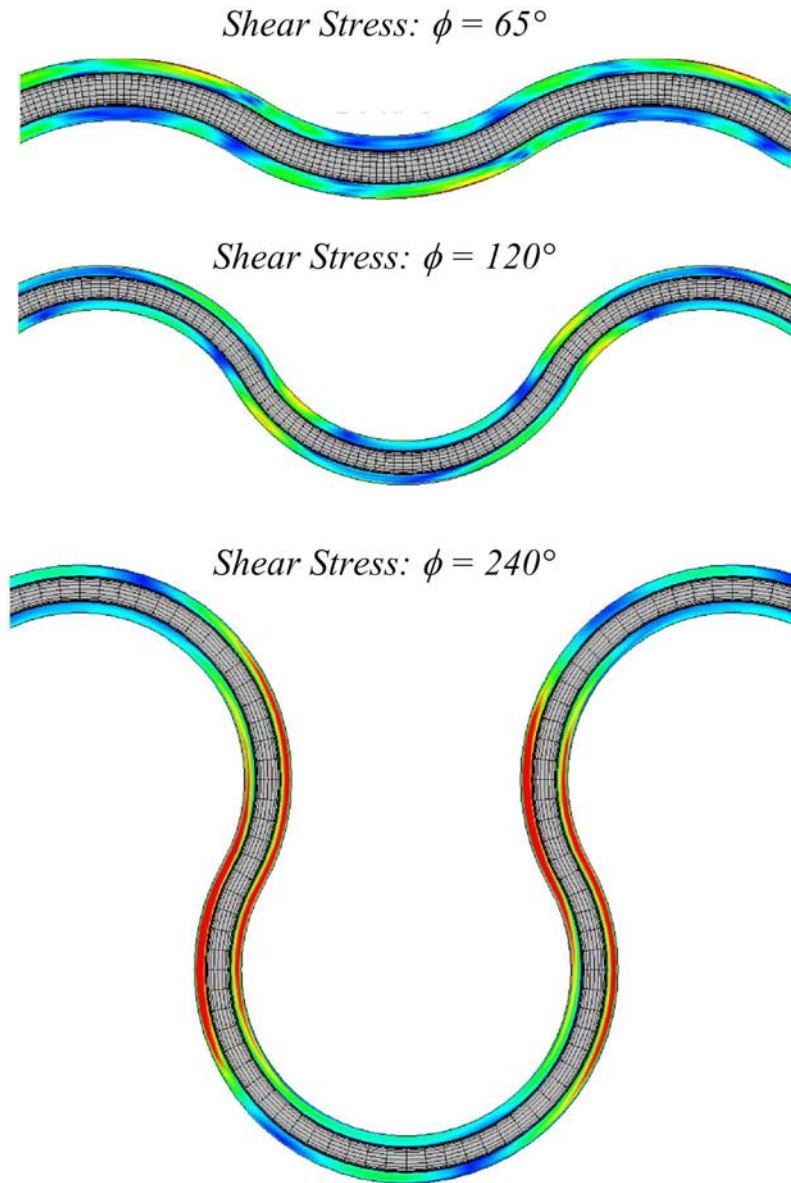
Figure 4.3. Shear Stress Distribution Obtained in the Numerical Simulations.

An example of the bank shear stress along the channel is shown in Figure 4.4. The channel geometry conditions are $R/W = 4$ and $\phi = 180°$. The extreme values at the two ends (i.e., channel inlet and exit) are due to the two boundary conditions of the simulation. On the other hand, the shear stresses in other bends have moderate magnitudes with a periodical pattern. Shear stresses on the alternate banks have the same distribution with an obvious phase angle. τ_{max} on the graph is the maximum shear stress on the cross section of a bank. τ_{avg} is the depth average of the values. It can be seen from the figure that both shear stresses (τ_{max} and τ_{avg}) have similar distributions along the channel. The line segments corresponding to $\theta / \phi = [0\ 1]$ indicate the

location of occurrence of shear stress on a bend. θ denotes the relative location of a point on the bend, the angle between the inflection point and the point of interest. When $\theta = 0$, it indicates the inflection point. When $\theta = \phi/2$, it indicates the middle point of the bend. It is observed from Figure 4.4 and other graphs that the peaks of τ_{max} and τ_{avg} curves often occur at a location close to $\theta/\phi = 1$. A peak means the maximum τ_{max} of a bend, also called τ_{max_max}.
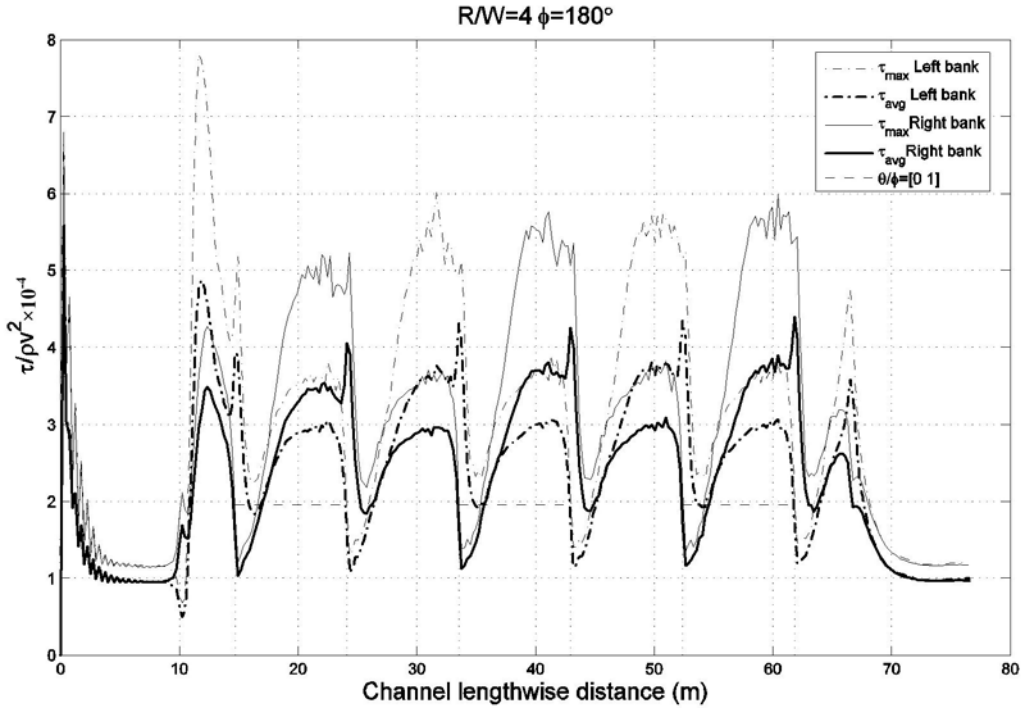
Figure 4.4. Simulated Shear Stress along a Channel.

4.3 ANALYSIS OF RESULTS

The multiple regression involves variables v, R/W, ϕ, and θ. From dimensional analysis and past experience, it can be shown that the dimensionless shear stress $\tau/(\rho v^2)$ is a function of R/W, ϕ, and θ. The regression processes is divided into these steps:

1. Find the relationship between τ_{max_max} and R/W: $\tau_{max\_max}/\rho v^2 = f_1(R/W)$.
2. Find the relationship between τ_{max_max} and ϕ: $\tau_{max\_max}/\rho v^2 = f_2(\phi)$.
3. Find the relationship between the relative location of occurrence of τ_{max_max} and R/W: $\theta_{max}/\phi = f_3(R/W)$.
4. Find the relationship between the relative location of occurrence of τ_{max_max} and ϕ: $\theta_{max}/\phi = f_4(\phi)$.
5. Fit the shear stress distribution of a bend, $\tau_{max}/(\rho v^2) = f_5(\theta/\phi, \theta_{max}/\phi)$.
6. Get the final equation: $\tau_{max}/(\rho v^2) = f_1(R/W) \times f_2(\phi) \times f_5(\theta/\phi, f_3 \times f_4)$.

Figure 4.5 shows the relationship between τ_{max_max} and R/W at a constant ϕ angle of 180° and a velocity of 0.2 m/s. A curve fitting was done for the maximum shear stress. For $R/W \geq 2$, the fitted and the original curves are fairly close. For $R/W < 2$, however, the fitted curve is far lower than the original data. As a matter of fact, geometry of $R/W < 2$ does not often happen in nature. The expression of the fitted curve is:

$$\frac{\tau_{max\_max}}{\rho v^2} = f_1(\frac{R}{W}) = \frac{1}{400(R/W)} \qquad (4.1)$$

Non-dimensionalized shear stress vs. R/W
$\phi=180^o$
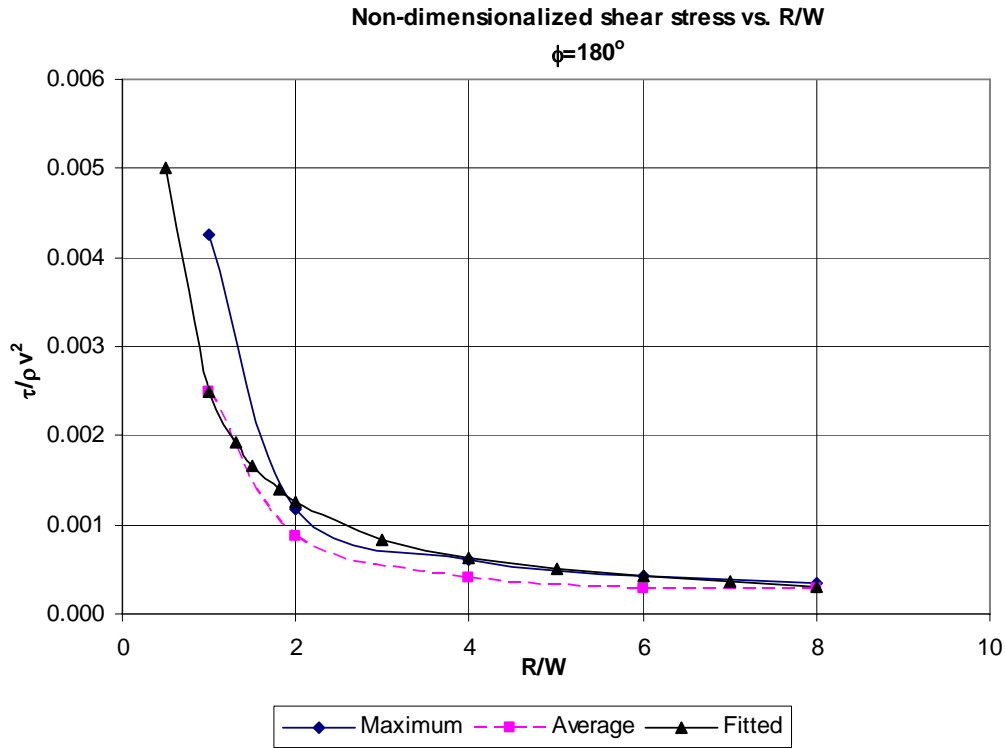
Figure 4.5. Influence of *R/W*.

Figure 4.6 shows the relationship between τ_{max_max} and ϕ angle at a constant radius-to-width ratio of 4 and a velocity of 0.2 m/s. A parabolic curve can be fitted to the data. Since the difference between the maximum and minimum τ_{max_max} values is about 25 percent, a straight line was used instead. So τ_{max_max} was treated as independent of ϕ. The expression of function f_2 is: $f_2(\phi) = 1$.
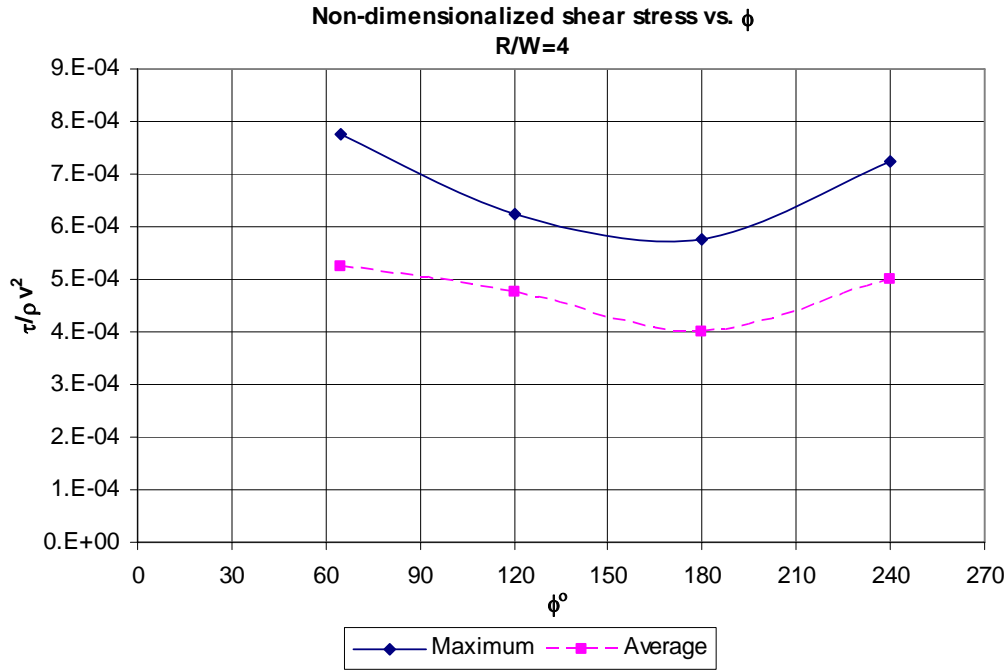
Figure 4.6. Influence of ϕ Angle.

The shear stress distribution of one bend mostly has similar shapes when the influential factors change. It is possible and desirable to find an analytical curve which fits the distribution well. Based on comparison of different type of analytical curves, the probability density function (PDF) of extreme value distribution is found to be a good match for the calculated shear stress. The expression is:

$$y = f(x|\mu, \sigma) = \frac{1}{\sigma} e^{(\frac{x-\mu}{\sigma})} e^{-(e^{(\frac{x-\mu}{\sigma})})} \tag{4.2}$$

Where, μ is the location parameter and σ is the scale parameter. The indicator of relative location on the bend is $x = \theta/\phi$. When $x = \mu$, y reaches maximum value. σ determines the maximum value and the degree of spreading of the curve. Figure 4.7 displays an example of extreme value distribution with $\mu = 1$ and $\sigma = 0.37$.
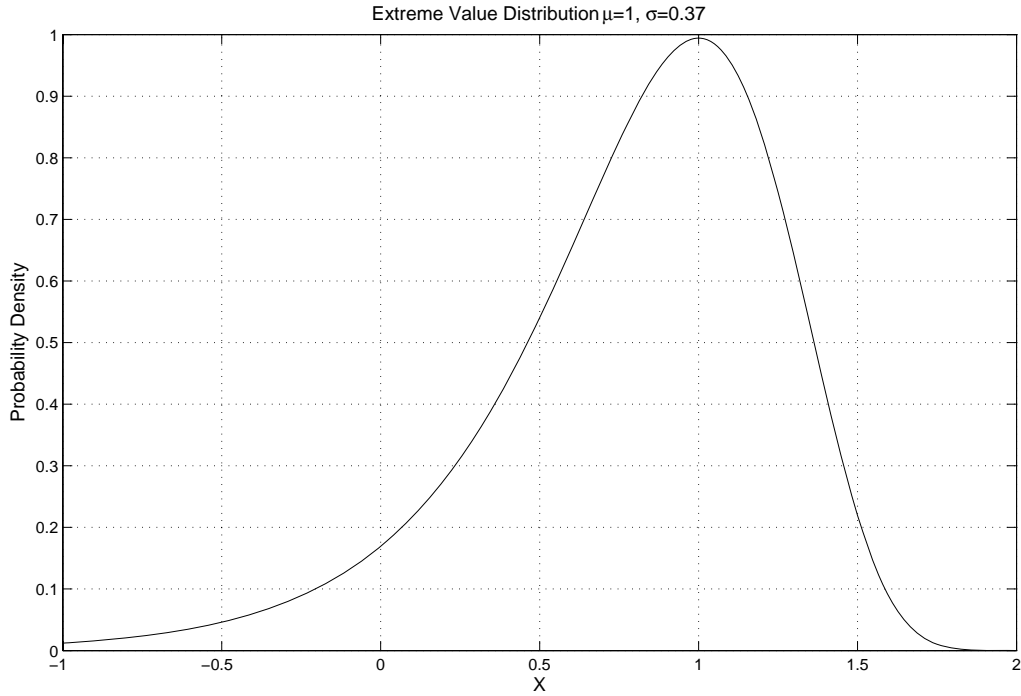
Figure 4.7. Extreme Value Distribution.

Theoretically, σ should also be a function of R/W and ϕ angle. When $\sigma = 0.37$ the maximum value is close to 1 and the degree of spreading is similar to most cases of shear stress distribution. A constant value of $\sigma = 0.37$ is used for the purpose of simplicity while necessary precision is maintained. Figure 4.8 shows the calculated shear stress and fitted curves. A good fit can be observed. The shear stress distribution equation can be expressed as:

$$f_5(\frac{\theta}{\phi}, \frac{\theta_{max}}{\phi}) = \frac{1}{\sigma} e^{(\frac{x-\mu}{\sigma})} e^{-(e^{(\frac{x-\mu}{\sigma})})}$$

$$\sigma = 0.37, \mu = \frac{\theta_{max}}{\phi}, x = \frac{\theta}{\phi}$$

(4.3)
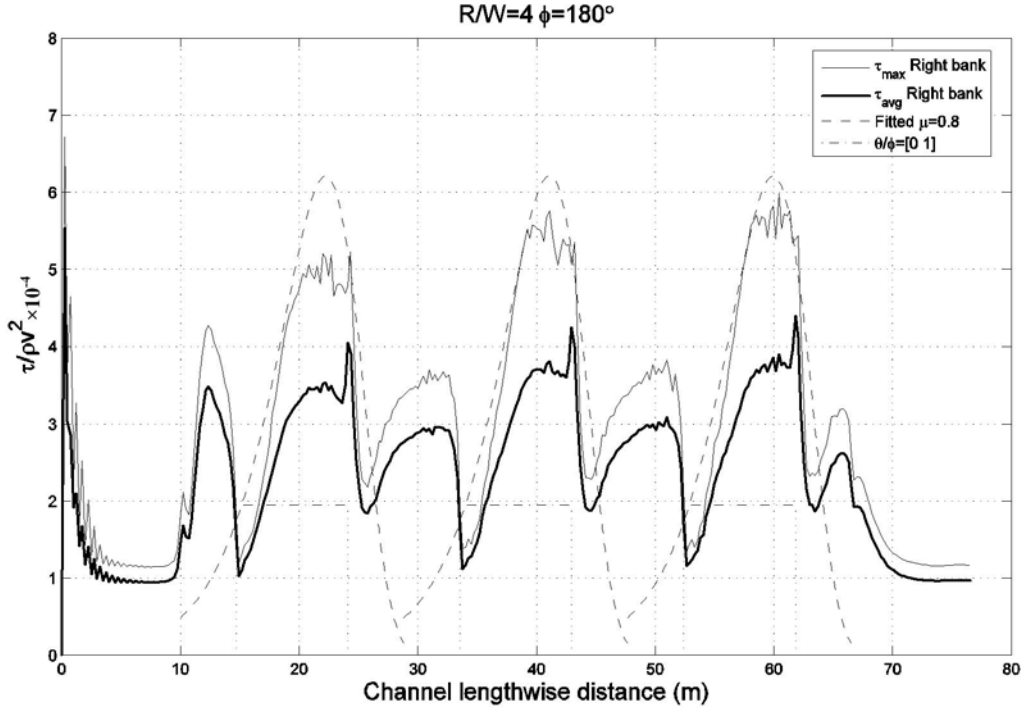
Figure 4.8. Simulated Shear Stress and Fitted Curves.

The next step is to determine the location parameter μ, which is a function of R/W and ϕ angle. The influence of R/W on location parameter μ is shown in Figure 4.9. θ_{max}/ϕ indicates relative location of the peak values. "tao_max" denotes the original data. For the original data, when there is a plateau or several peak values of similar magnitude on the same bend, the location of the peak value of the average shear stress curve is chosen. Curve fitting is a type of simplification. The fitted curve will represent the actual data in the prediction of meander migration. The relative location of the peak values of fitted curves is of greater interest. The relationship between this relative location and R/W is indicated by "Fitted" in Figure 4.9. The θ_{max}/ϕ value corresponds to the peak of the extreme value distribution in Figure 4.8. A straight line is fitted with an $R^2 = 0.9156$. The expression for the location parameter is:

$$\mu = \frac{\theta_{max}}{\phi} = f_3(\frac{R}{W}) = -0.047(\frac{R}{W}) + 1.05 \qquad (4.4)$$
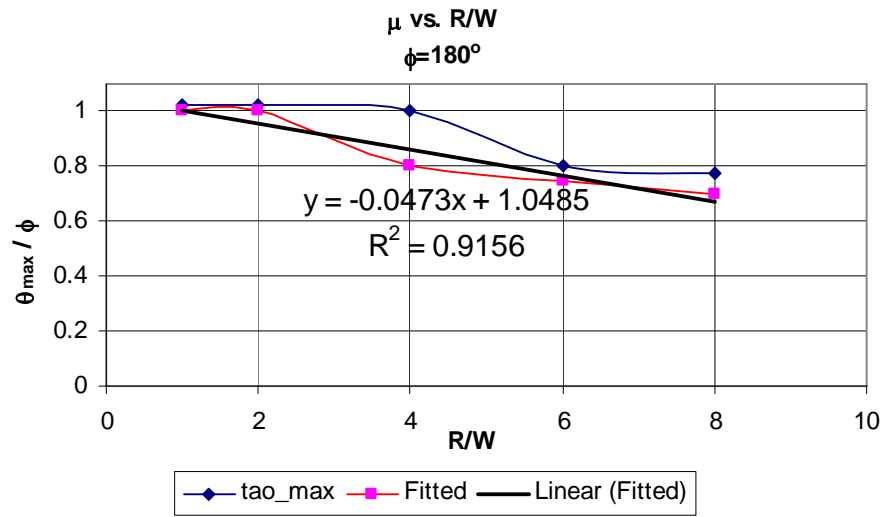
Figure 4.9. Influence of _R/W_ on Location Parameter.

Figure 4.10 shows the relationship between θ_{max}/ϕ and ϕ angle. The curve for the original data ("tao_max") is obtained with the same method as shown in Figure 4.9. The relative location for the peaks of the fitted extreme value distribution changes very little when ϕ angle is less than 120°. When ϕ angle is larger than or equal to 120°, it does not change at all. Thus, the location parameter is considered to be independent of ϕ angle. The expression of function f_4 is $f_4(\phi) = 1$.
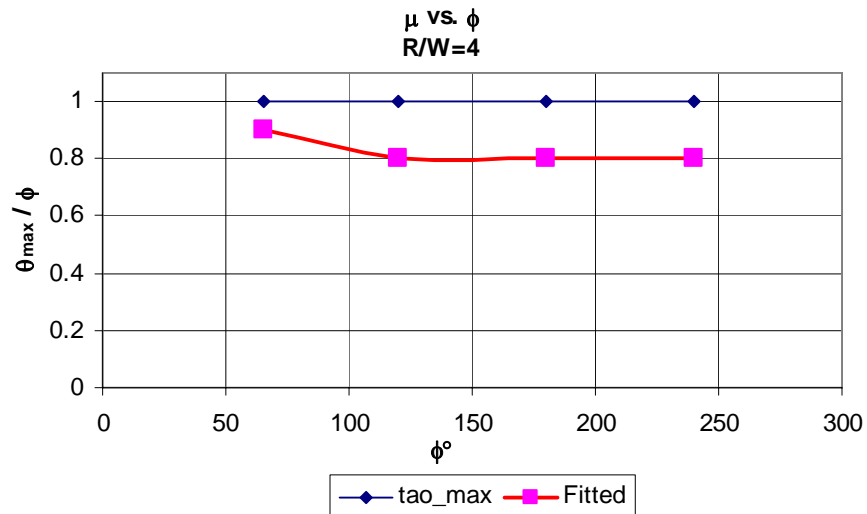
Figure 4.10. Influence of ϕ Angle on Location Parameter.

In numerical simulation, the bank is considered to be perfectly smooth. To account for the roughness in reality, a constant coefficient of c_1, which equals to 8 for sand and 13 for clay, is

68

used. It was also found that a geometry-dependent coefficient c_2 will improve the prediction. Both c_1 and c_2 are determined by verification study.

The last step is to combine the individual relationships and develop a unified equation for $\tau_{max}/(\rho v^2)$ as a function of R/W, ϕ, and θ. The combined form is:

$$\frac{\tau_{max}}{\rho v^2} = f_1(\frac{R}{W}) \times f_2(\phi) \times f_5(\frac{\theta}{\phi}, f_3 \times f_4) \tag{4.5}$$

By substituting corresponding equations, the final equation is expressed as:

$$\frac{\tau_{max}}{\rho v^2} = \frac{c_1 c_2}{400(\frac{R}{W})} \times \frac{1}{\sigma} e^{(\frac{x-\mu}{\sigma})} e^{-(e^{(\frac{x-\mu}{\sigma})})} \tag{4.6}$$

$$\sigma = 0.37, \quad \mu = \frac{\theta_{max}}{\phi} = -0.047(\frac{R}{W}) + 1.05, \quad x = \frac{\theta}{\phi}, \quad c_1 = 8 \tag{4.7}$$

$$c_2 = 0.25\frac{R}{W} - 0.5 \cdots\cdots\cdots (\frac{R}{W} > 6)$$
$$c_2 = 1 \cdots\cdots\cdots\cdots\cdots\cdots (\frac{R}{W} \leq 6) \tag{4.8}$$

The regression is done on a limited number of simulation cases. A systematic matrix will generate maximum shear stress under all possible combinations of conditions. Extreme value distribution is a good match for the shear stress distributions. In some cases the difference between the original data and the fitted curve is quite large. A better fit is suggested.

CHAPTER 5. FLUME TEST IN SAND

From the hyperbolic model, two coefficients, the initial migration rate $\dot{M}_i$ and the maximum migration distance M_{max}, need to be determined. The maximum migration distance M_{max} was obtained from conducting physical modeling. The flume tests described here and in next chapter are two separate yet equally important sets of experiments in non-cohesive and cohesive types of soil, respectively. Based on the dimensional analysis derived in the previous chapter, the maximum migration distance M_{max} is a function of channel geometry, hydraulic conditions, and soil property. Therefore M_{max} is evaluated by varying these three controlling parameters.

5.1 EXPERIMENTAL SETUP

The experiments were conducted in a large basin that is 36.6 m (120 feet) long, 20.9 m (68.5 feet) wide, and 1.5 m (5 feet) deep located in the Haynes Coastal Engineering Laboratory at Texas A&M University. The test area is 27.4 m (90 feet) long, 13.7 m (45 feet) wide, and 0.30 m (1 foot) deep in the basin, which was filled with sand. An idealized channel molded from the sand bed mimicked the natural river erosion process. A constant-head reservoir connected to the entrance of the idealized channel provided the desired constant flowrate. A weir at the end of the channel controlled the water depth in the channel (see Figure 5.1). In order to reduce the scale effect, the channel was designed to maximize the scale while containing at least three curved bends. A straight channel was connected to each end of the curved channel with a transition, which is a curved bend of one-half of the bend angle, ϕ. The straight section was long enough so the flow became fully developed before it entered the first curved bend. The channel has a constant initial cross section in the form of a trapezoid. The cross section has a bottom width of 40.0 cm (15.7 inches), top width of 74.6 cm (29.47 inches), bank slope of 30°, and depth of 15.6 cm (6.1 inches). One typical channel geometry and cross-sectional configuration are shown in Figures 5.2 and 5.3. The parameter θ in the figure is the variable representing the angle and varies from 0 to ϕ in each band. The channel slope was carefully controlled by adjusting the slope of the sand bed to maintain a constant initial water depth of $h = 10$ cm (3.9 inches) along the channel with a maximum discrepancy less than 1.0 cm (0.4 inches) (10 percent of the design depth) in each test case.

Figure 5.1. Water Basin and Flume Test Setup.
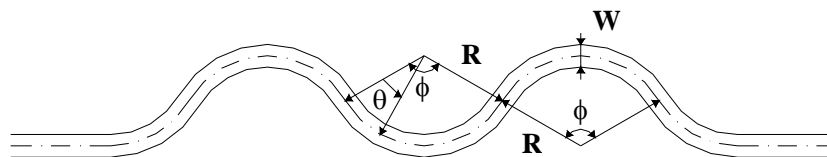
Figure 5.2. Curved Channel Geometry.
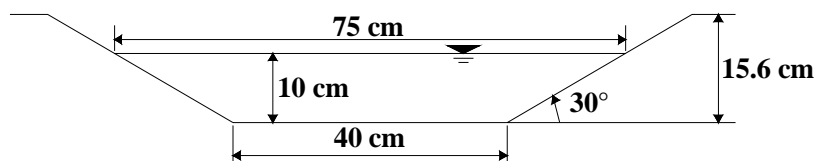
Figure 5.3. Initial Cross-Sectional Configuration.

5.2 SOIL PROPERTIES

Uniform and fine sand with a median grain diameter $D_{50} = 0.32$ mm was used in the tests to minimize the inhomogeneity of material. The curve for grain size distribution obtained from a sieve analysis of the soil samples is shown in Figure 5.4. EFA was developed to measure the erodibility of a soil sample in order to predict the scour depth at bridge piers (Briaud et al., 1999). The test results including the relationships of the soil erosion rate with the mean velocity U and the shear stress τ are shown in Figures 5.5 and 5.6. From these two curves, the critical Froude number Frc was then estimated as 0.14. Note that Frc represents the minimum Froude number to initiate bankline erosion in the tests.
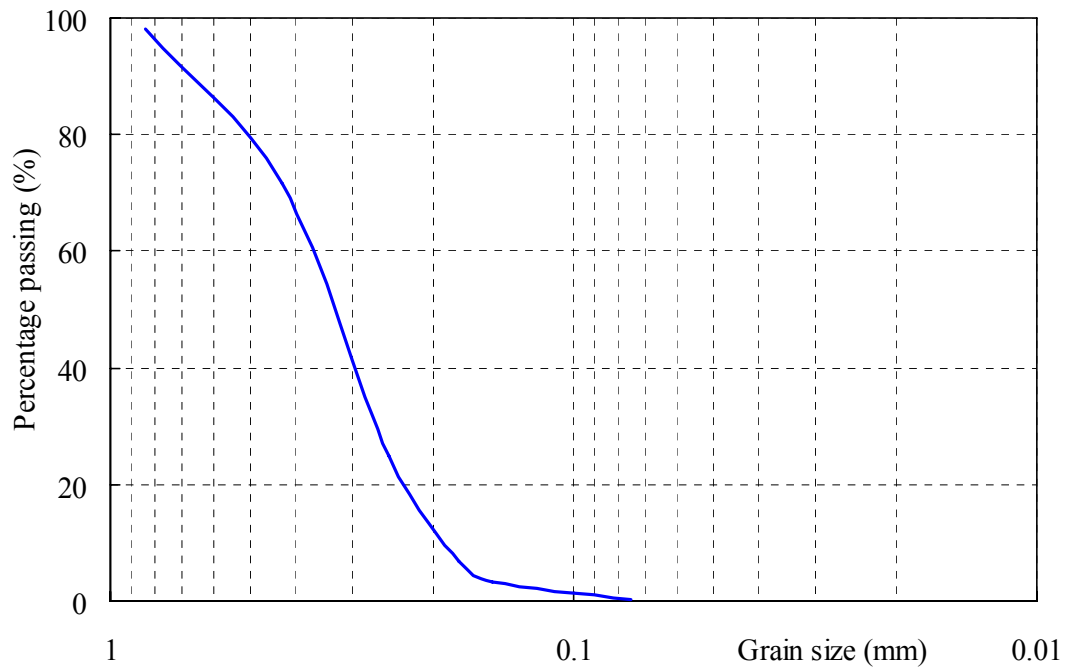
Figure 5.4. Grain Size Distribution.

$\dot{z}$ (mm/hr)
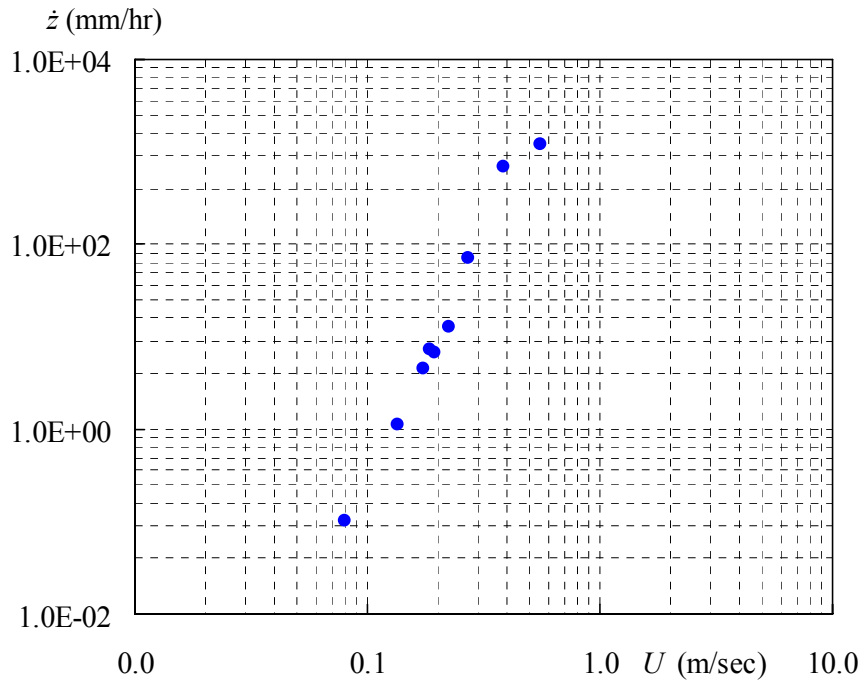
Figure 5.5. EFA Test Results: Soil Erosion Rate versus Mean Velocity.

$\dot{z}$ (mm/hr)
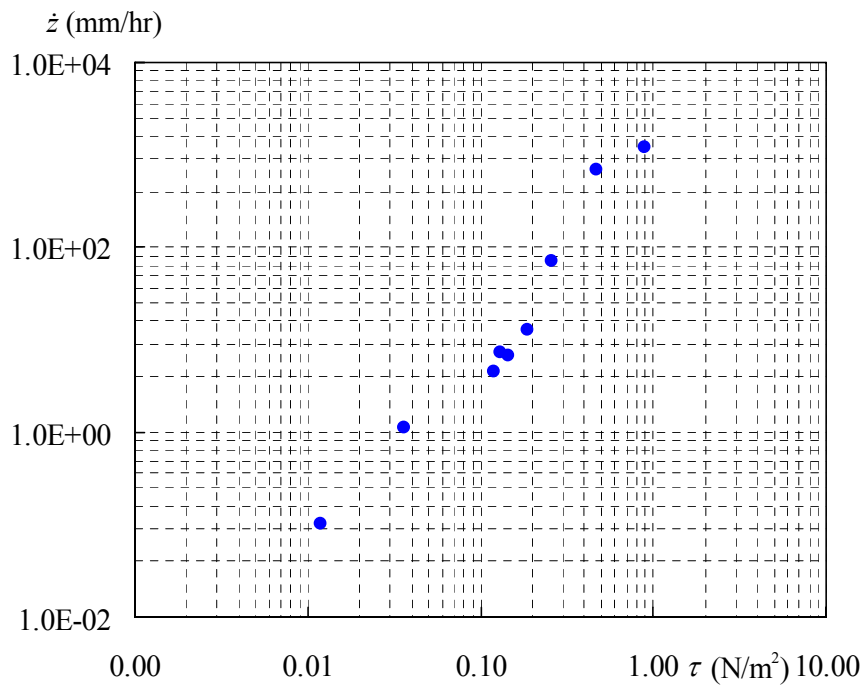
Figure 5.6. EFA Test Results: Soil Erosion Rate versus Shear Stress.

74

5.3 TEST MATRIX

Five different radius-to-width ratios (R/W) and four different bend angles (ϕ) were used in the tests. The hydraulic condition featured four different flow rates; therefore four different Froude numbers (Fr) were varied in the experiments. All the Froude numbers are in the subcritical range. The test matrix with different geometric and hydraulic parameters is shown in Table 5.1. Note that the parameters in Table 5.1 refer to the initial test condition only and do not reflect the later changes due to channel evolution. Also, the last case (case 12) is the repeatability case with the same testing conditions as in case 03. Figure 5.7 plots the designed channel plan forms of all test cases.

Table 5.1. Experimental Conditions.

Case No.	R/W	ϕ	Fr	Frc	Case No.	R/W	ϕ	Fr	Frc
01	2	65°	0.30	0.14	07	4	180°	0.30	0.14
02	3	65°	0.30	0.14	08	4	220°	0.30	0.14
03	4	65°	0.30	0.14	09	4	120°	0.25	0.14
04	6	65°	0.30	0.14	10	4	120°	0.34	0.14
05	8	65°	0.30	0.14	11	4	120°	0.36	0.14
06	4	120°	0.30	0.14	12	4	65°	0.30	0.14
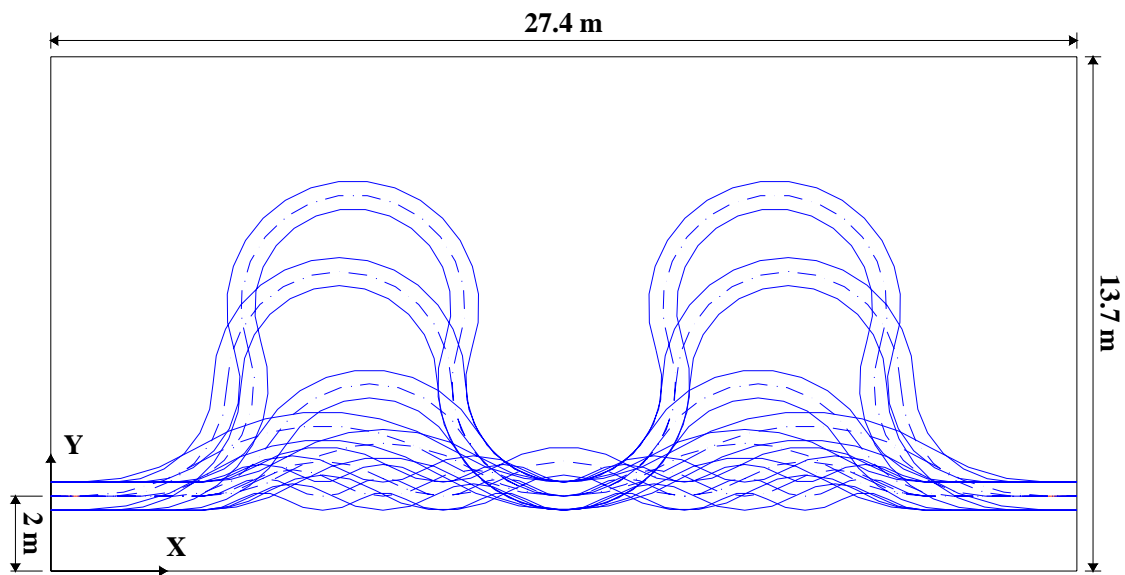
Figure 5.7. Designed Channel Plan forms of All Test Cases.

5.4 TEST PREPARATION

Before the designed curve channel was molded from the sand bed, the channel bed slope was carefully adjusted in order to reach a uniform initial water depth condition along the channel. Manning's equation was used to estimate the necessary channel bed slope. Since Manning's equation calculates the channel bed slope of a straight channel, a sluice gate installed at the channel exit adjusted water depth.

5.5 TEST PROCEDURE AND MEASUREMENTS

The test procedure was standardized in all test cases. The steps in the procedure are listed as follows:
1. Record initial bankline of both banks.
2. Turn on the pump and adjust the flowrate to the target value.
3. Adjust the sluice-gate to reach a uniform initial water depth along the channel.
4. Take pictures of the initial running conditions.
5. Record channel bankline of both banks.
6. Measure water surface elevation along the channel.
7. Measure cross-section profile.

The tests were run at a 10 cm (3.9 inch) initial water depth and 5.6 cm (2.2 inch) free board on the channel banks. The channel bankline and the channel width were defined and measured at the water-bank interfaces and were recorded several times during each test. The measurements were taken with relatively short time steps in the early stage of the tests to resolve the intensive movement of the bankline. In addition to the measurements of bankline, several cross sections were chosen along the channel and the bed profiles mapped. Water elevation was measured at the middle of these cross sections. Each test case was run nonstop until an overflow occurred at any reach of the channel or the bankline movements were less than 1.0 cm (0.4 inches) between consecutive measurements.

5.6 RESULTS

The morphological behavior of a curved channel undergoing a constant flowrate is demonstrated in both the spatial and temporal aspects. Figure 5.8 shows the plan form variations of case 03 ($R/W = 4$, $\phi = 65°$, $Fr = 0.30$) with the bankline at several different instants. In the spatial aspect, the channel bankline expands laterally and translates downstream. The channel migration thus

features two components: cross-valley movement and down-valley movement. The bankline shift starts from the first half of the leading outer bend ($0.0 < \theta/\phi < 0.5$) and ends on the second half of the following inner bend ($1.5 < \theta/\phi < 2.0$). A large displacement occurs behind the apex of the outer bend ($\theta/\phi = 0.5$) with a phase lag to the channel curvature. Both banks have a similar but alternate erosion pattern. In the temporal aspect, the movement of the channel bankline in Figure 5.8 shows that the bankline has a relative large migration rate at the beginning of the test; the rate decreases as the test progresses. Not only did the migration elongate the channel length, it also increased the "sinuosity" of the channel, defined as the ratio of channel length to valley length. Figures 5.9 and 5.10 are the plan form variations of case 06 ($R/W = 4$, $\phi = 120°$, $Fr = 0.30$) and case 08 ($R/W = 4$, $\phi = 220°$, $Fr = 0.30$), respectively.
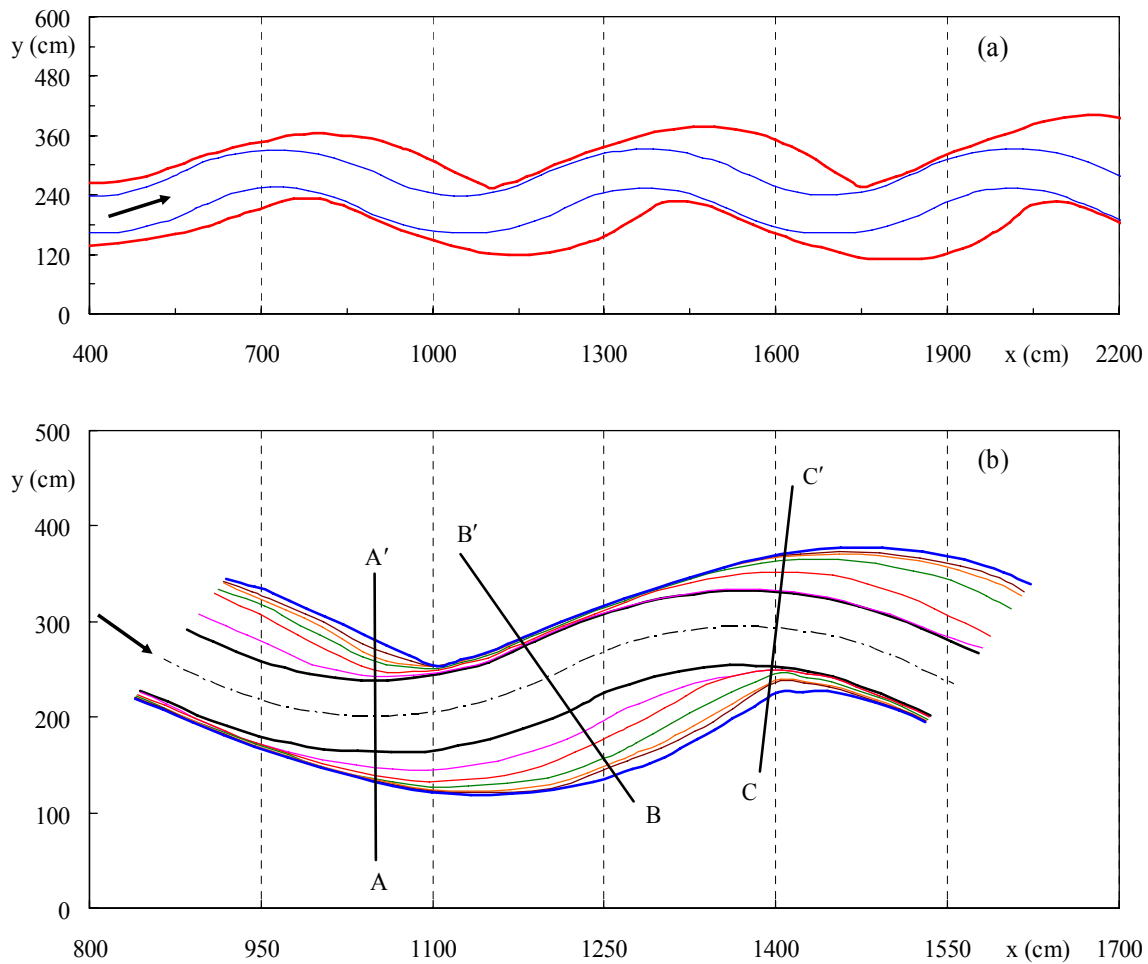
Figure 5.8. Plan form Variations of Case 03: (a) Initial Channel Bankline and Bankline at 51 hours; (b) Banklines of 2nd and 3rd Bends.

77
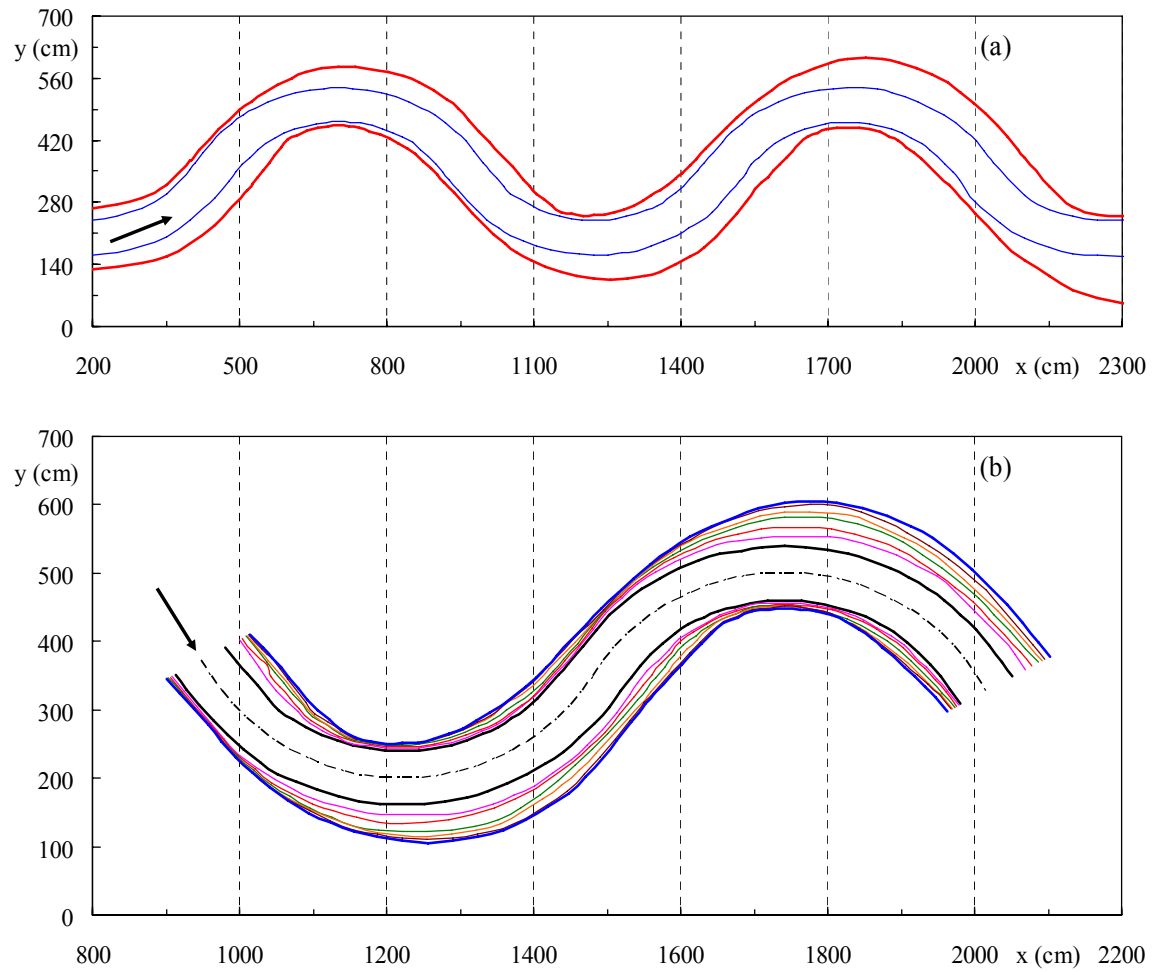
Figure 5.9. Plan form Variations of Case 06: (a) Initial Channel Bankline and Bankline at 30 hours; (b) Banklines of 2nd and 3rd Bends.
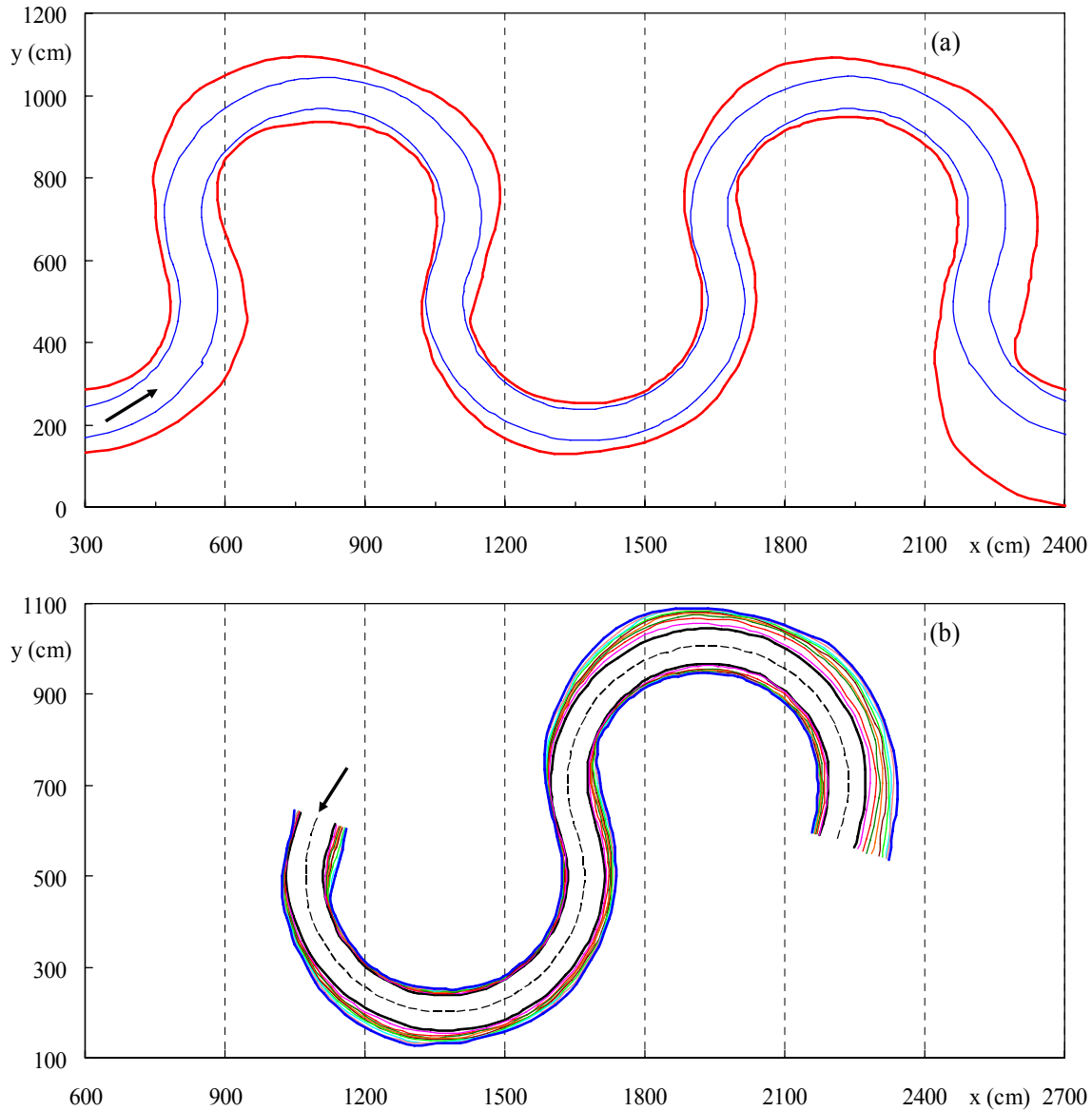
Figure 5.10. Plan form Variations of Case 08: (a) Initial Channel Bankline and Bankline at 147 hours; (b) Banklines of 2nd and 3rd Bends.

Figure 5.11 is a plot of three cross-sectional profiles (A-A', B-B', and C-C') within the second and the consecutive third bends as marked in Figure 5.8(b) (looking downstream). It reveals that all the cross sections have deep pools in front of the toes of the channel outer banks (A', B', and C) and have sand deposits as point bars along the channel inner banks (A, B, and C'). Sediment coming from the upstream and from the collapse of the banks contributes to the increase in bed elevation. Since a relatively high and constant flowrate was used in this study (similar to having a flood lasting for months), the bankline on both sides of the band moved outward and widened with a much greater distance at the outer bank. If the flow rate was reduced in the tests after the

high flowrate, such as in the dry season for a natural channel, the water would flow in the deeper part of the channel and the water-bank interfaces would shift toward the outer bank and expose the inner sand bars. In nature, vegetation may grow and strengthen the soil above the water line in the channel during the dry season and make it harder to erode in the next wet season. The width of the river therefore may not widen as shown in the experiments. This is a feature that these experiments did not reproduce.
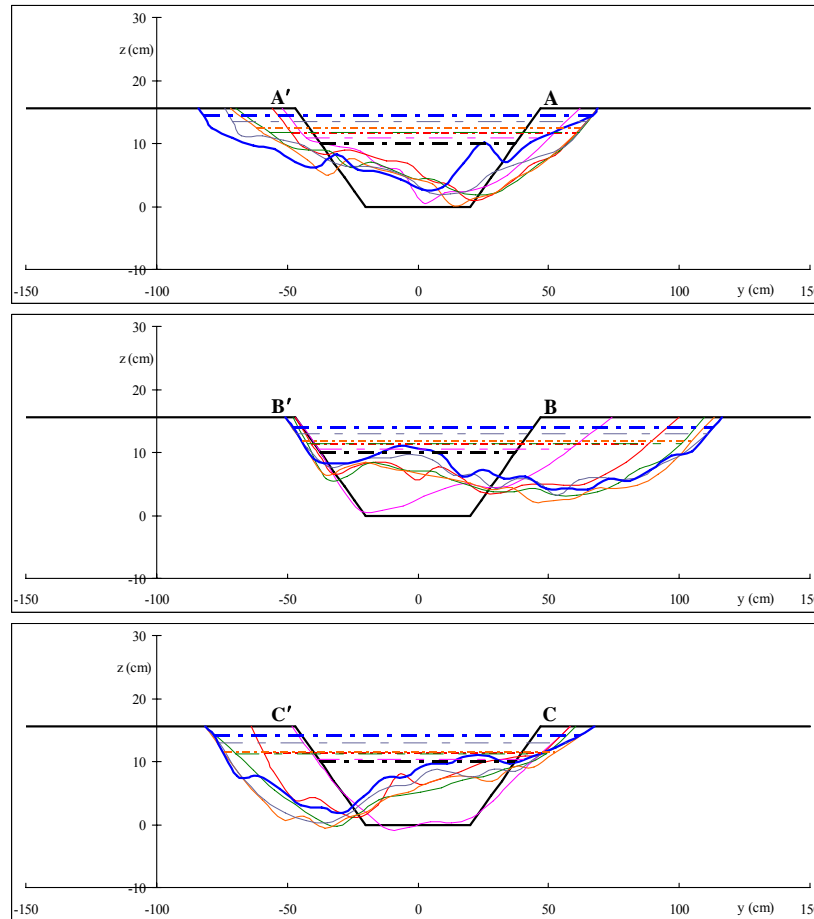
Figure 5.11. Cross-Sectional Profiles of Case 03.

The mean velocities (U) and water elevations (H_w) in different time steps of three selected cross sections are shown in Figure 5.12. In this study, the mean velocity U was calculated as $U = Q/A_w$ with A_w being the wetted cross-sectional area; the water elevation H_w was measured at the middle of the cross section. In the figure, the mean velocity of each cross section decreased and gradually reached a constant value as the bankline erosion process continued. Sediment transport from the upstream and bank collapse caused the water elevation to rise. Interestingly, the elevations among the three cross sections were approximately the same. With the variations of

80

mean velocity and water elevation, the energy slope along the channel, defined as the total head loss over the associated channel length, decreased as the flow continued to erode the channel bankline and elongate the channel. Eventually, an equilibrium state of the channel bankline is expected to be reached. At that time, the displacement of channel bankline should attain maximum value.
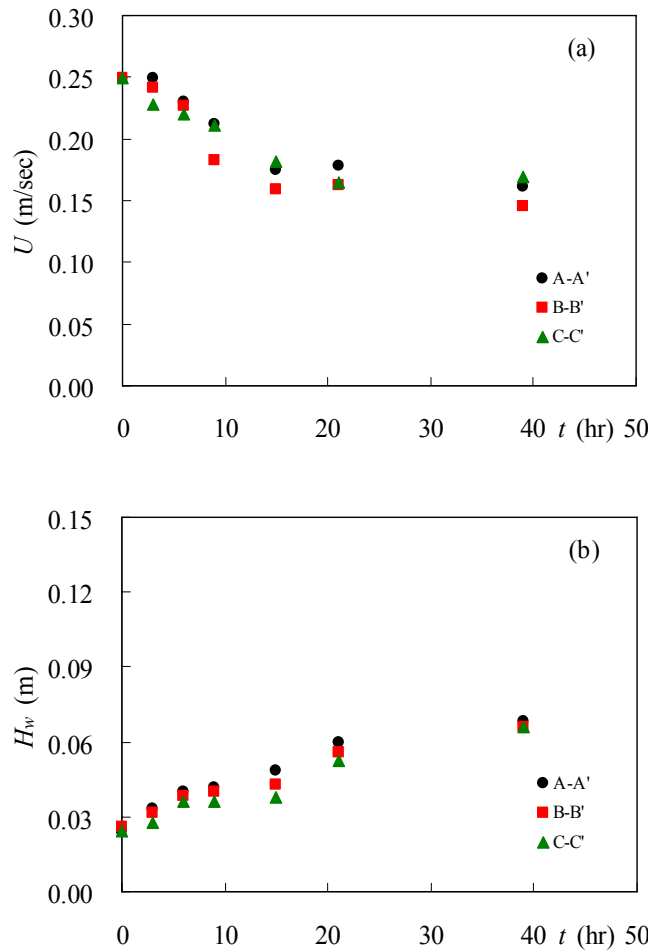
Figure 5.12. Case 03: (a) Mean Velocities, and (b) Water Elevations.

Figure 5.13 shows the channel plan form variations of the four other cases with different R/W values, corresponding to cases 01, 02, 04, and 05 in Table 5.1. The other two parameters, ϕ and Fr, were kept constant in these cases. It is found that the channel bankline in the larger R/W cases ($R/W = 6$ and 8) migrates in both the cross- and down-valley directions. On the contrary, the channel bankline movement in the smaller R/W cases ($R/W = 2$ and 3) is mainly in the down-valley direction. Such a mechanism straightens the channel.
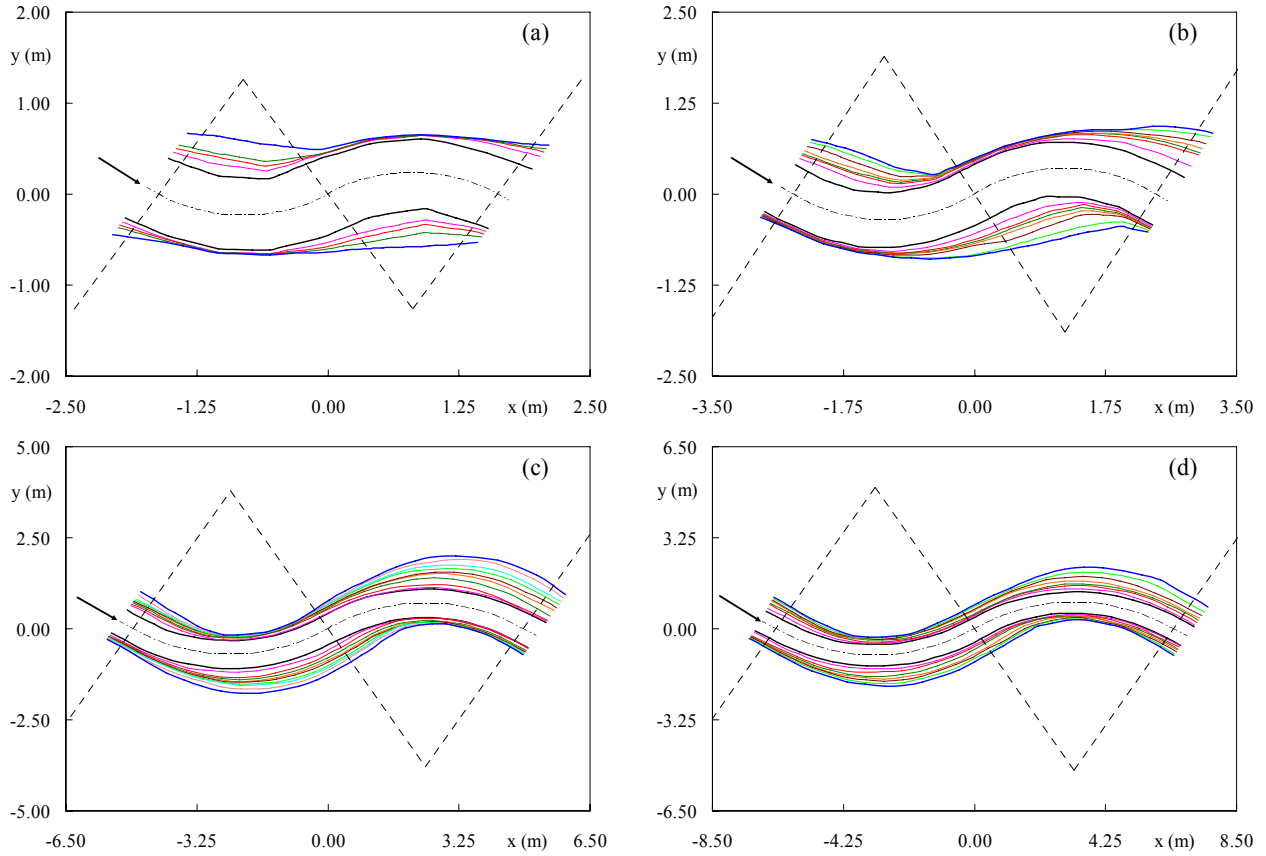
Figure 5.13. Plan Form Evolutions of Different *R/W*: (a) Case 01; (b) Case 02; (c) Case 04; (d) Case 05. Lines Are Measurements Taken from *t* = 0 to *t* = (a) 18 hr, (b) 42 hr, (c) 92 hr, (d) 66 hr.

The bend angle ϕ is another important parameter affecting channel geometry. For channels with the same *R/W*, the one with a greater bend angle ϕ has a longer channel length. Figure 5.14 shows the bank movement for four different bend angles while keeping *R/W* and *Fr* constant. (cases 03, 06, 07, and 08 in Table 5.1) The results show that the channel migration distance and phase lag decrease with the increase in the bend angle. The decrease in phase lag makes the bankline displacement appear more uniform and symmetric for the larger bend angle cases.

82
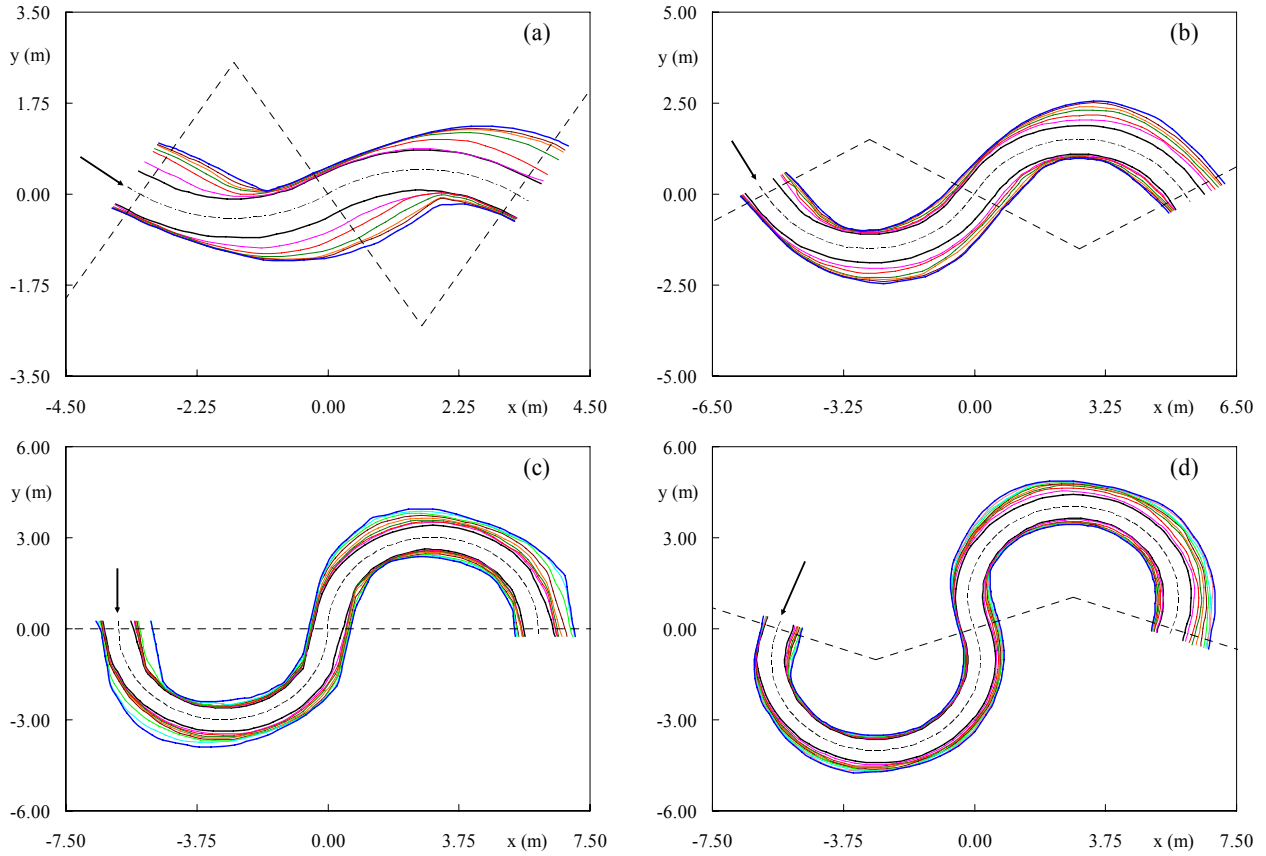
Figure 5.14. Plan form Evolutions of Different ϕ: (a) Case 03; (b) Case 06; (c) Case 07; (d) Case 08. Lines Are Measurements Taken from $t = 0$ to $t =$ (a) 51 hr, (b) 30 hr, (c) 86 hr, (d) 147 hr.

Figure 5.15 compares the channel plan form variations among four different Froude numbers while keeping R/W and ϕ constant (cases 09, 06, 10, and 11 in Table 5.1). The channel bankline demonstrates a very similar pattern among the four cases. The channel bankline movement clearly increases with the Froude number, as expected.
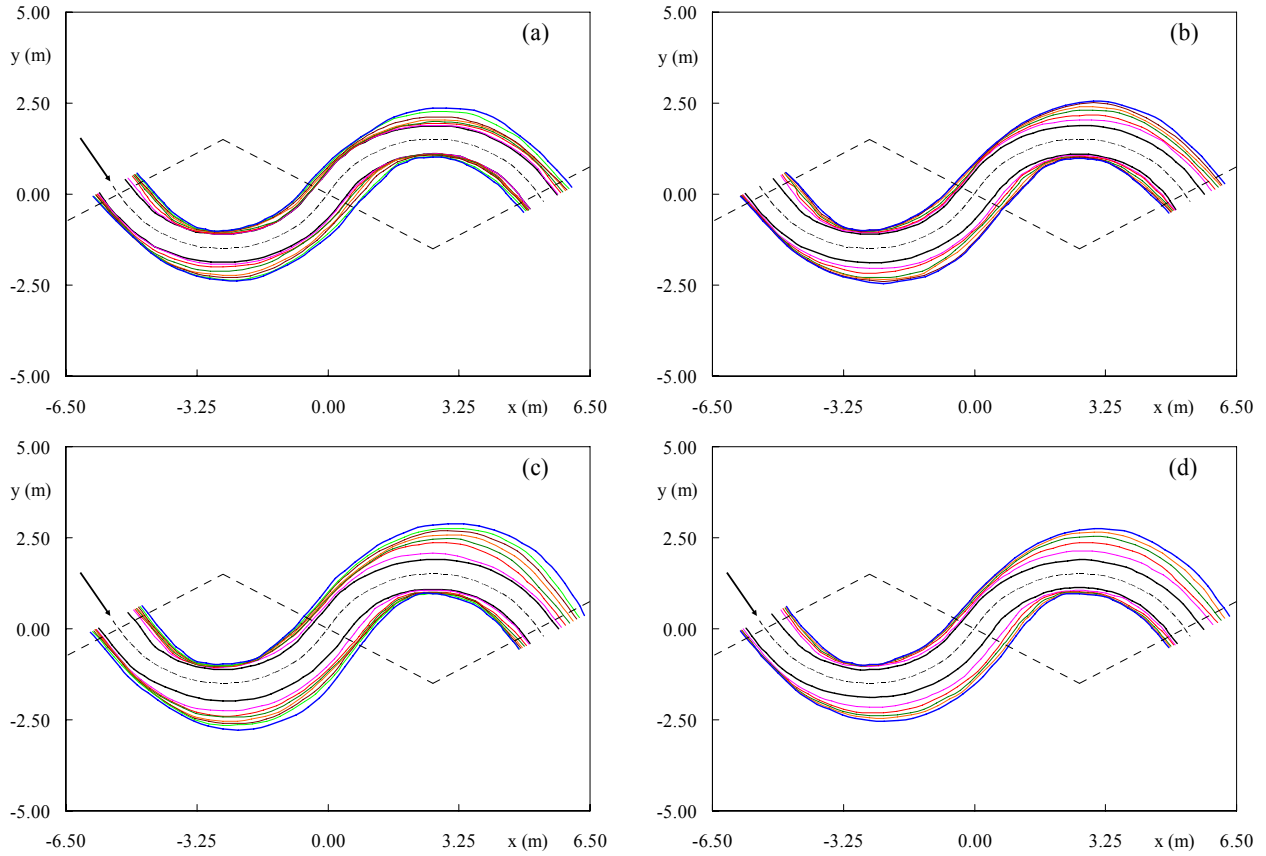
Figure 5.15. Plan form Evolutions of Different *Fr*: (a) Case 09; (b) Case 06; (c) Case 10; (d) Case 11. Lines Are Measurements Taken from *t* = 0 to *t* = (a) 56 hr, (b) 30 hr, (c) 39 hr, (d) 23 hr.

5.7 DATA DEDUCTION

The channel migration distance was measured in the direction perpendicular to the initial channel bank. Using case 03 in Figure 5.8 as an example, the migration distance at five different positions on the right bank is shown in Figure 5.16. Note that when θ/ϕ becomes greater than 1 (e.g., $1.0 < \theta/\phi < 2.0$), it denotes a position in the following inner bend. The figures show that the channel migration rate (slope) is the highest at the early stage of the test, meaning that the channel migration distance increases rapidly within a short period of time. As the flow continues to erode the channel bankline, the rate decreases gradually. A maximum value of the migration distance is expected when the channel reaches an equilibrium state at $t \to \infty$. The data points in Figure 5.16 were then fitted with a hyperbolic function. From the figure, it can be seen that the hyperbolic function is a good approximation in describing the temporal evolution of the bankline migration. The hyperbolic function is expressed in the form:

$$M = \frac{t}{a+bt} \tag{5.1}$$

where M is the channel migration distance, t is time, and a and b are constant. The reciprocals of the two constants in the hyperbolic function are the initial slope at $t = 0$ ($1/a$) and the asymptotic value of the hyperbolic curve at $t \to \infty$ ($1/b$). Therefore, the initial migration rate $\dot{M}_i$ and the maximum migration distance M_{max} at a given cross section can be expressed as $\dot{M}_i = 1/a$ and $M_{max} = 1/b$. In the experiments, the units of M and t are in centimeters and hours, respectively, and the units of $\dot{M}_i$ and M_{max} are in centimeters per hour and centimeters, respectively.
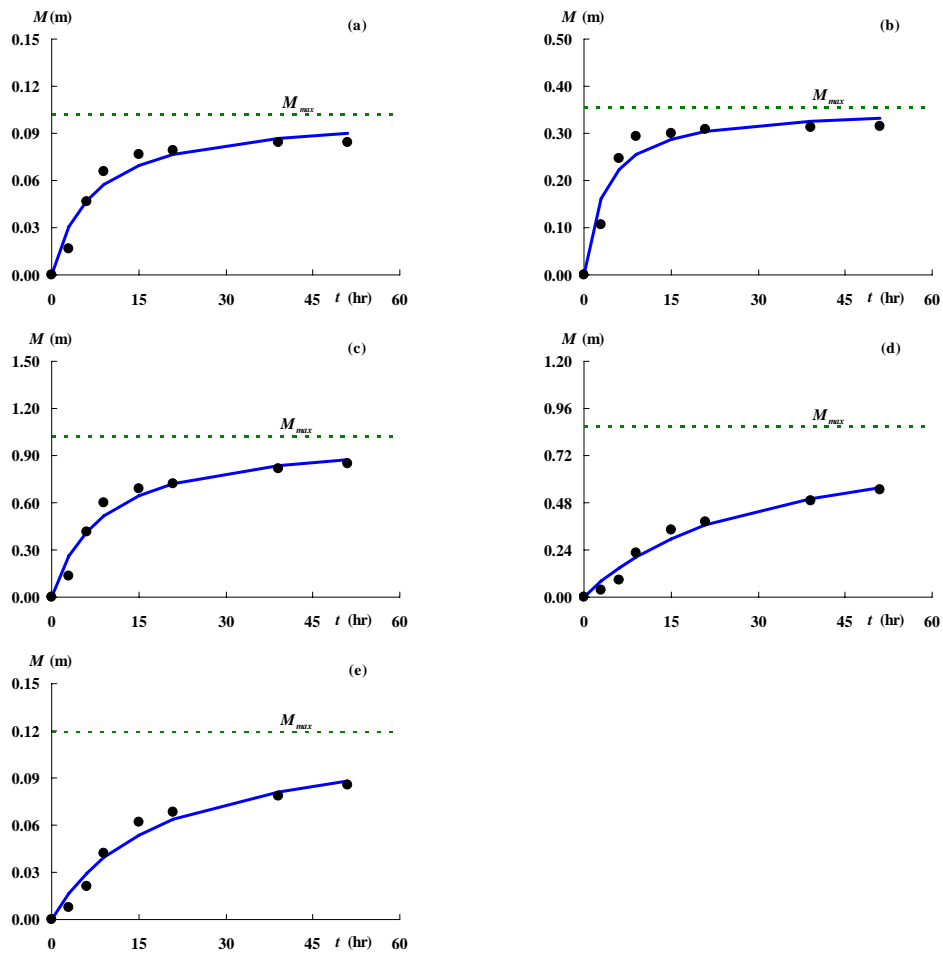
Figure 5.16. Channel Migration Distance at Five Different Cross Sections in Case 03.
(a) $\theta/\phi = 0.0$, (b) $\theta/\phi = 0.5$, (c) $\theta/\phi = 1.0$, (d) $\theta/\phi = 1.5$, (e) $\theta/\phi = 2.0$. Solid Lines Are Hyperbolic Fits.

The maximum migration distance M_{max} at each cross section along the channel was obtained by curve fitting the measured data using the hyperbolic function, as indicated by the solid lines in Figure 5.16. In the experiments, the data from the second outer bank of the channel and the following third inner bank were used. This is to ensure that the fully developed secondary current in the channel was accounted for and the backwater effect from the channel exit was negligible. The non-dimensional results for case 03 are shown in Figure 5.17. Note that in the figure M_{max} is normalized by the initial channel width W. The result shows that M_{max} along the channel has the peak value behind the channel apex ($\theta/\phi = 0.5$) and there exists a phase lag to the channel curvature. Since M_{max} displays the Gaussian distribution, a Gaussian distribution function is used to model the magnitude of M_{max} along the channel bend:

$$\frac{M_{max}}{W} = \hat{A}\exp\left[-0.5\left(\frac{\theta/\phi - \hat{\mu}}{\hat{\sigma}}\right)^2\right] \tag{5.2}$$

where $\hat{A}$ is the maximum value of the distribution, θ/ϕ is the normalized angle, $\hat{\mu}$ is the location of the maximum value in terms of θ/ϕ, and $\hat{\sigma}$ is the standard deviation of θ/ϕ in terms of θ/ϕ. Note that $\theta/\phi > 1$ means a location in the inner bank beyond the target outer bank.
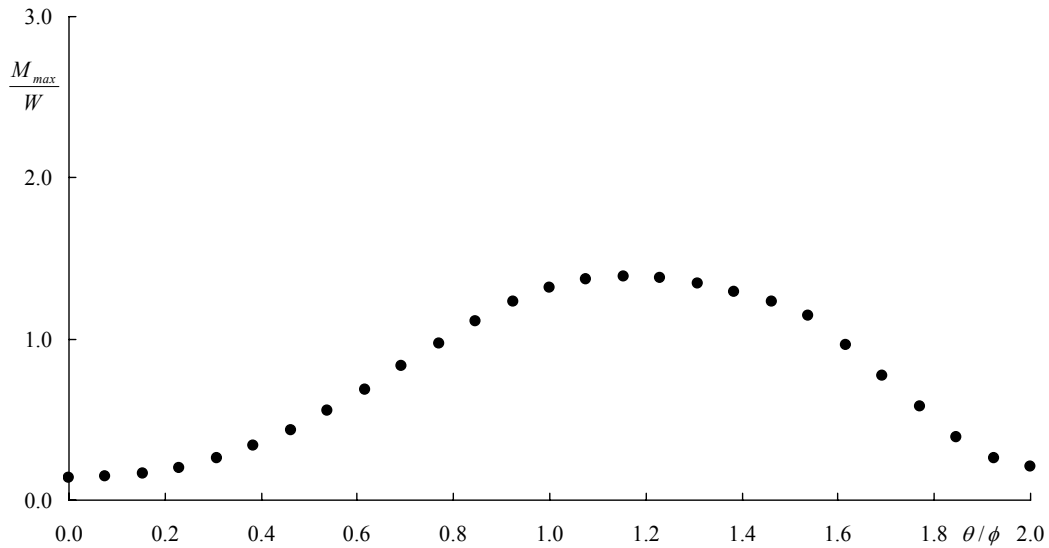
Figure 5.17. M_{max} Distribution along the Channel in Case 03.

In the present study, one case (case 03) was repeated (case 12) to test the repeatability of the experiments. The value of M_{max}, determined by fitting the hyperbolic function, is fitted with the Gaussian function distribution and compared in Figure 5.18. The differences between the two

tests are 0.7 percent for $\hat{A}$, 2.2 percent for $\hat{\mu}$, and 4.7 percent for $\hat{\sigma}$. The relatively small variations demonstrate that the experiment is repeatable and the methodology using the hyperbolic function and Gaussian distribution function may be suitable.
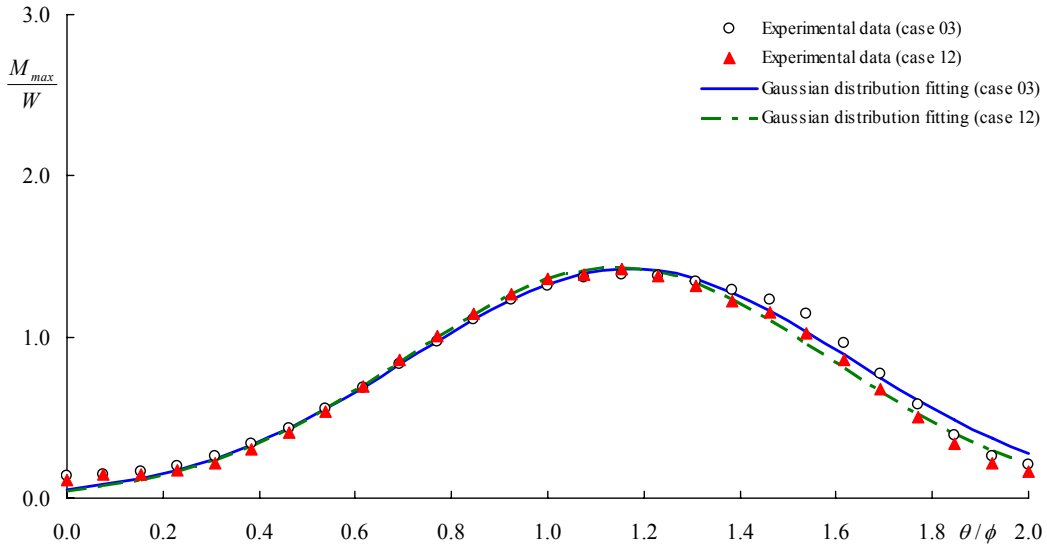
Figure 5.18. Comparison in M_{max} between Case 03 and Case 12 for Repeatability Test.

For a large bend angle ϕ, the maximum migration distance M_{max} along the curved bend shows a "dual-peak" distribution. There are two high value zones for maximum migration distance M_{max} in the leading outer bank and the following inner bend as shown in Figures 5.19 and 5.20. The dual zones of high shear stresses appear in the cases with a bend angle 120° or larger. The second peak is not apparent in the cases with a 65° bend angle. When the flow enters the curved bend, the primary and secondary flows create high shear stresses when the secondary flow is fully developed. If the bend angle is large enough (or the channel length is long enough), the induced helical flow first dissipates its energy and then has enough time and room to regain energy before the flow enters the next bend. After the flow passes the inflection point, the curvature of the following bend induces a centrifugal force in the opposite direction and results in a momentum exchange. This strong momentum exchange creates a second zone of high shear stress in the channel.
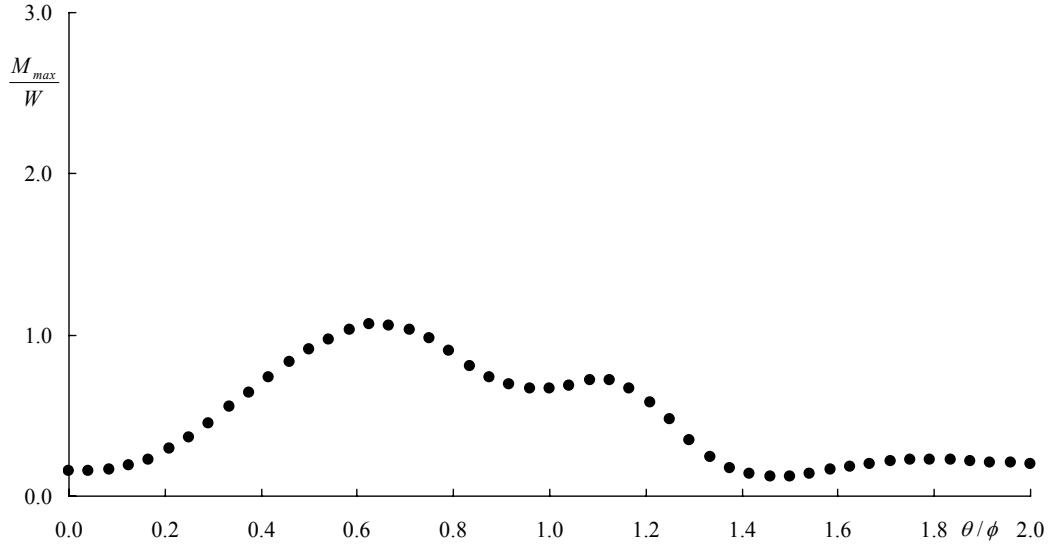
Figure 5.19. M_{max} **Distribution along the Channel in Case 06.**
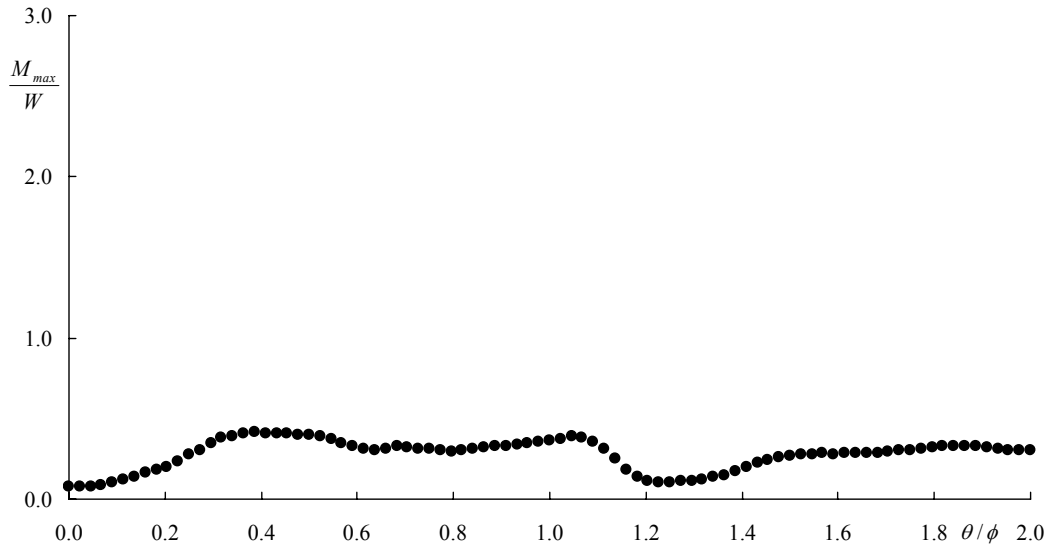
Figure 5.20. M_{max} **Distribution along the Channel in Case 08.**

In order to model the dual-peak behavior, a superposition of two Gaussian distribution functions was used to fit the values for M_{max} along the channel. The formulas can be expressed as:

$$\frac{M_{max}}{W} = \hat{A}_1 \exp\left[-0.5\left(\frac{\theta/\phi - \hat{\mu}_1}{\hat{\sigma}_1}\right)^2\right] + \hat{A}_2 \exp\left[-0.5\left(\frac{\theta/\phi - \hat{\mu}_2}{\hat{\sigma}_2}\right)^2\right] \tag{5.3}$$

where the subscripts 1 and 2 denote the first and second Gaussian distributions.

5.8 PROPOSED EQUATIONS

There are six coefficients in Equation 5.3 that need to be determined. These coefficients are obtained by correlating with the three controlling parameters, R/W, ϕ, Fr and the critical Froude number Frc. From physical considerations and investigations, the near-bank velocity in a cross section is more strongly related to the channel bankline migration than is the mean velocity. A correction parameter β represents the magnitude of the near-bank velocity in terms of the mean velocity. Numerical simulation results show that the correction parameter β is affected by the channel radius curvature R. For the same undisturbed approaching velocity, the centrifugal force in a small R/W channel generates larger near-bank velocity than a large R/W channel. A simple equation to estimate the value of the correction parameter β is shown as follows:

$$\beta = \frac{1}{R/W} + 1 \tag{5.4}$$

With the correction coefficient β being used, the controlling parameters, R/W, Fr, and Frc, can be combined and presented as a single variable βFr-Frc. The effect of R/W is then implicit in the correction coefficient β.

Figure 5.21 shows the relation among the coefficients and βFr-Frc. Note that the band angle is kept at 65° for those cases plotted in the figure so there exists only a single Gaussian distribution, as indicated in Figure 5.17 and Equation 5.2. The results demonstrate the peak value of $\hat{A}$ occurs at βFr-Frc = 0.46, where R/W = 4, and decreases as βFr-Frc and R/W get either smaller or larger. This means a channel has the largest maximum migration distance M_{max} when R/W = 4. Note that the migration direction in the present study is defined as the cross-sectional direction from the center of curvature and perpendicular to the channel initial bankline. The displacement at a given point on the channel bankline contains two components: the lateral expansion (the y-direction displacement in the experiments) and the down-valley translation (the x-direction displacement in the experiments). For channels with a small radius of curvature (such as R/W = 2), the channel bankline displacement is dominated by a down-valley translation with little lateral expansion. As a result, the migration distance remains small as the channel bankline continues to straighten. A similar straightening phenomenon for the large βFr-Frc (small R/W) cases was observed for the location of the peak $\hat{\mu}$ in Figure 5.21(b). The coefficient $\hat{\mu}$ decreases as βFr-Frc increases, which means that the location of the peak moves downstream as R/W decreases. It indicates that the following inner bend may have a large migration rate and a large

migration distance. The standard deviation $\hat{\sigma}$ has a relatively small variation in all the cases, as shown in Figure 5.21(c). The average value is close to 0.5.
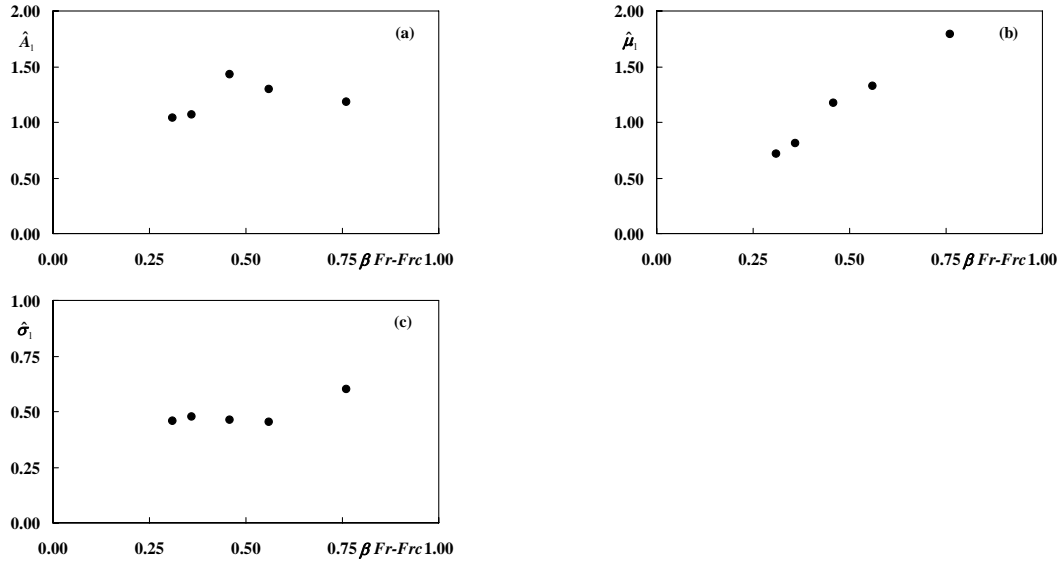
Figure 5.21. Coefficients of Gaussian Distributions versus βFr-Frc.

The maximum migration distance M_{max} is also influenced by the channel bend angle ϕ, as shown in Figure 5.22. As ϕ increases, the amplitude of the first peak ($\hat{A}_1$) decreases; the location of the first peak ($\hat{\mu}_1$) moves upstream toward the front of the outer bank. The second Gaussian distributions for the all bend angles have relatively small and nearly constant peak values except for the 65° case, in which the peak value $\hat{A}_2 = 0$. The ratio of the second peak $\hat{A}_2$ to the first peak $\hat{A}_1$ demonstrates a linearly increasing trend with respect to the bend angle. Similar to the results in Figure 5.21, the first standard deviation $\hat{\sigma}_1$ remains somewhat constant. In the large bend angle cases ($\phi = 120°$, $180°$, and $220°$), the $\hat{\mu}$ values for the second Gaussian distribution ($\hat{\mu}_2$) are less than 2.0, indicating the second peak is within the same channel bend. The location of the second peak ($\hat{\mu}_2$) moves upstream with a slight increase in standard deviation ($\hat{\sigma}_2$) when the channel bend angle increases. As the effect from the second peak becomes more obvious (i.e., ϕ becomes greater), the bankline displacement becomes more uniform and symmetric.
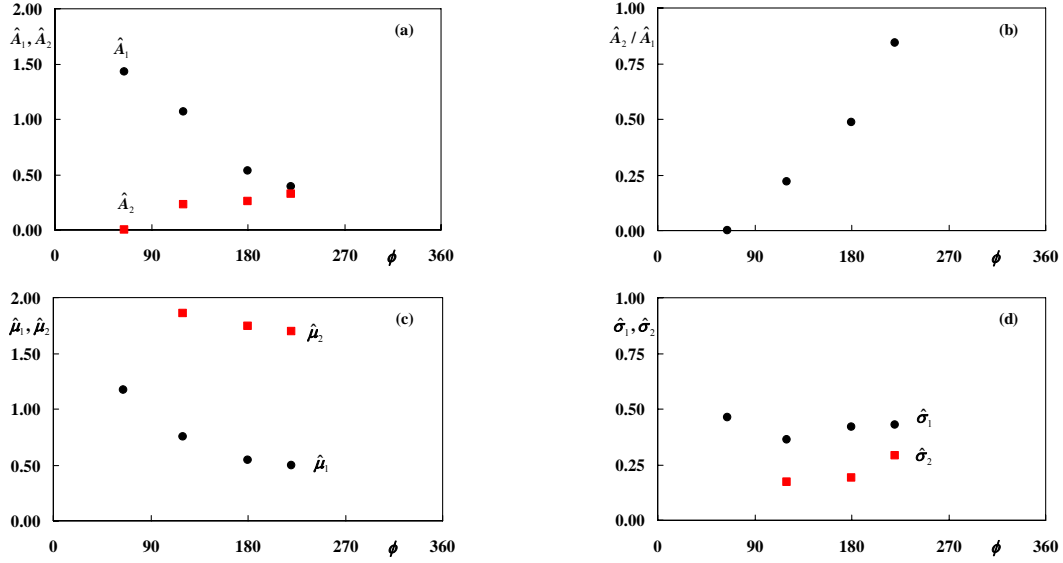
Figure 5.22. Coefficients of Gaussian Distributions versus ϕ.

Based on the results in Figures 5.21 and 5.22, each coefficient in the M_{max} equation (Equation 5.3) is a function of R/W, ϕ, Fr and Frc, and can be obtained using regression analysis with the measured data. The final formulas for these coefficients in the Gaussian distribution functions are expressed as:

$$\beta = \frac{4}{R/W} + 1$$

$$\hat{A}_1 = 19.36(\phi)^{-0.69}(\beta Fr - Frc)^{-0.34} \qquad \text{(for } 2 \leq R/W < 4)$$

$$\hat{A}_1 = 49.41(\phi)^{-0.72}(\beta Fr - Frc)^{0.71} \qquad \text{(for } 4 \leq R/W \leq 8)$$

$$\hat{\mu}_1 = 40.29(\phi)^{-0.69}(\beta Fr - Frc)^{0.92} \tag{5.5}$$

$$\hat{\sigma}_1 = 1.26(\phi)^{-0.19}(\beta Fr - Frc)^{0.25}$$

$$\hat{A}_2 / \hat{A}_1 = 0.01\phi - 0.34$$

$$\hat{\mu}_2 = 4.68(\phi)^{-0.16}(\beta Fr - Frc)^{0.17}$$

$$\hat{\sigma}_2 = 0.01(\phi)^{0.62}(\beta Fr - Frc)^{0.57}$$

Equations 5.2 to 5.5 are therefore the prediction equations for the maximum meander migration. Note that Equation 5.2 should be used if the band angle ϕ is equal or less than 65° (in which only the first Gaussian distribution is needed and $\hat{A}_2 = 0$). For ϕ greater than 65°, Equation 5.3 should be applied.

CHAPTER 6. FLUME TEST IN CLAY

This chapter investigates channel meander migration in clay by conducting physical modeling. The approach is to vary each primary parameter obtained from dimensional analysis while keep the remaining parameters constant. The effect and impact of each individual parameter can therefore be examined to provide a basis for parametric study. The approach is similar to that in Chapter 5 except clay is used.

6.1 EXPERIMENTAL SETUP

The meander experiments in clay were conducted in a large basin that is 22.0 m (72.6 feeet) long, 10.0 m (33 feet) wide, and 0.9 m (3 feet) deep located on the second floor of the Hydromechanics Laboratory at Texas A&M University (Figure 6.1). The basin was filled with approximately 200 tons of sand left from the previous flume tests in order to not only save on clay cost but also to minimize the maintenance effort of keeping moisture on the clay.
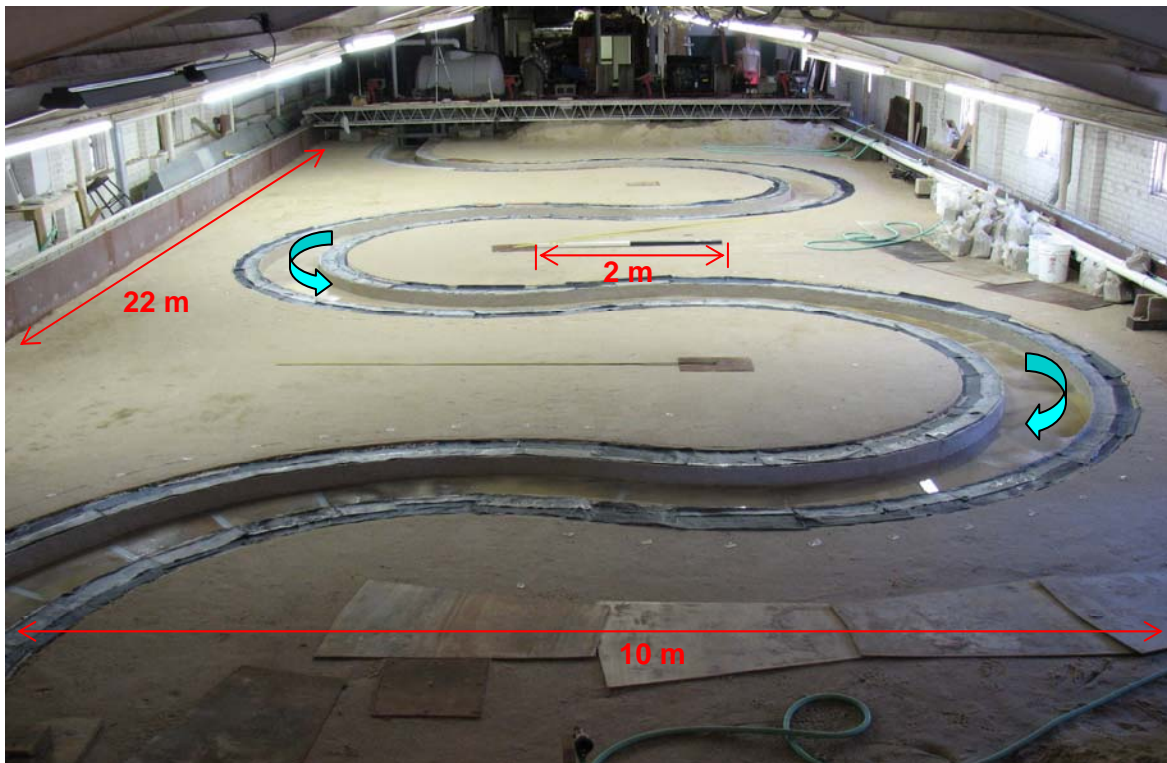
Figure 6.1. Experimental Setup in the Hydromechanics Laboratory.

A guide channel in the sand bed was carved to put the clay banks along the predetermined channel and form the channel geometry in each case. In order to reduce the scale effect, the

channel was designed to maximize the scale ratio while containing at least three curved bends. Figure 6.2 sketches the channel configuration. A straight channel was connected to each end of the curved channel with a transition, which is a curved bend of one-half of the bend angle, ϕ. The straight section was kept long enough so the flow became fully developed before it entered the first curved bend. The initial cross section of the channel is of rectangular shape that has a width of 60.0 cm (23.6 inches) and a depth of 12.0 cm (4.7 inches) (Figure 6.3). Plywood plates were laid at the bottom of the channel so only the banks are erodible.

During the first pre-test with a trapezoidal cross section of the channel, we observed almost no erosion on the side walls along the channel and no lateral movement of the river. Instead we observed erosion of the bottom of the channel. This was attributed to the relatively low shear stress on the walls compared to the higher shear stress on the bottom of the channel. In the second pre-test, we changed the cross-sectional shape from a trapezoidal to a rectangular channel (vertical wall on both sides) to increase the shear stress on the side walls so that the lateral movement of the river could be simulated. This remedy did induce side wall erosion along the channel. However, there was still excessive bottom erosion as well, and this required a huge amount of bottom clay to accommodate this bottom erosion. Since the clay cost and preparation time for the bottom layer were prohibitive, we decided to use a non-erodible bottom such as a thin plastic sheet. In the third pre-test, we changed the bottom material to the plastic sheets. We found the roughness of the plastic was too low compared to that of the clay. As a result, local flow velocity on the bottom increased, causing vibration of the plastic and turbulent flow as well. Therefore, we decided to replace the bottom layer with treated plywood to match the roughness of clay and increase the stiffness to avoid excessive vibration.
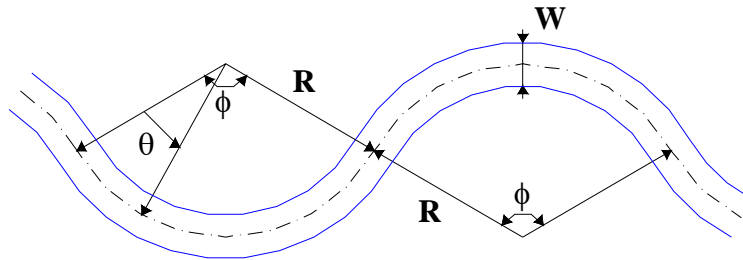
Figure 6.2. Channel Configurations.
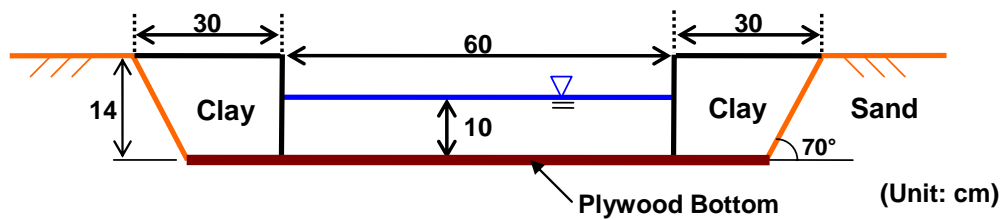
Figure 6.3. Cross Section of the Clay Channel.

The channel slope was carefully controlled by adjusting the slope of the sand bed to maintain a constant initial water depth of $h = 10$ cm (3.9 inches) along the channel with a maximum discrepancy less than 1.0 cm (0.4 inch) (10 percent of the design depth) in each test case. The water circulation system consisted of a pump, a constant-head tank, piping system, a sump in the basement, a clay channel, and two reservoirs before the entrance of the channel and after the exit of the channel. A sluice gate after the downstream reservoir controlled the water depth in the channel. The pump was located on the ground floor, while the basin was on the second floor. Water pumped from the sump in the basement into the constant-head tank through the piping system flowed down to the channel, passing the upstream reservoir (Figure 6.4). A diverting pipe eliminated the excessive pumping capacity. In addition, an overflow pipe located at about 3/4 of the height of the water tank kept the elevation head constant.

Figure 6.4. Upstream Reservoir and Water Tank.

Figure 6.5. Carrier with Laser Sliding on the Bridge for Transverse Coordinate (*y*-direction) Measurement.

Data acquisition during the test included the flowrate, water depth, geometries of the banklines, water surface elevation profile, and water velocity. The same flow meter from the previous sand experiments measured the flow rate in the pipe that directly connected to the upstream reservoir. The flow meter was calibrated before the use. Water depth was measured at the channel center line using a ruler. For the geometry of two banklines, a laser coordinate-measurement system was used, as shown in Figure 6.5. An instrument bridge spanning the flume over the test section mounted the coordinate-measurement system. Two coordinate locating systems were installed with one on one of the side walls for the *x* direction and the other on the bridge for the *y* direction. Once the bridge moved to a pre-designated *x*-coordinate position, the *y* coordinate was obtained by sliding the carrier on the bridge to the interfaces between the clay banks and water.

The water surface elevations were measured for several designated cross sections at certain time intervals. A plumb bob and a digital level measured the changes in water surface elevation throughout the tests, as shown in Figure 6.6. A voltage meter connected to two electrical wires detected current changes between the plumb bob and the wires through the ground when the tip of the plumb bob touched the water surface. In addition, the digital level was used to take readings of relative changes in the elevation from a scale attached to one of the wires. This system avoided possible extensive calibration work since all readings are independent of the measurement locations.
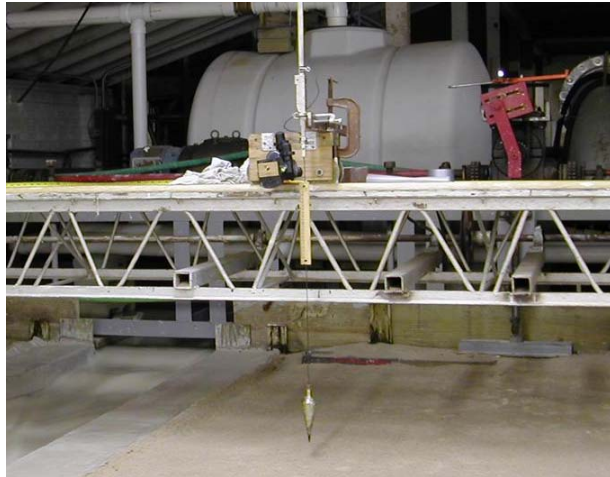
(a) Attached Scale and Plumb Bob	(b) Digital Level

Figure 6.6. Water Elevation Measurement Instrument.

Acoustic Doppler velocimetry (ADV) uses acoustic frequency changes to measure the water velocity at a given point. An ADV probe was installed on a frame on which a tape measure was attached to trace the location of the measurement points within the channel (Figure 6.7).

(a) Installed ADV probe on Frame

(b) Data Acquisition Computer Connected to ADV probe

Figure 6.7. Water Velocity Measurement Instrument.

6.2 SOIL PROPERTIES

The maximum mean velocity from the water supply system was about 55 cm/s due to the limited height of the water tank (525 gallons). Therefore, a more erodible clay type was chosen to initiate the erosion process under the experimental setup. "Grande" clay is the most erodible clay type among the available clays from our clay supplier (located in Austin), so it was used for all the flume tests.

6.2.1 Index List

Grain size distribution analysis including a hydrometer test for the Grande clay was carried out according to the ASTM standard. The result is shown in Figure 6.8.
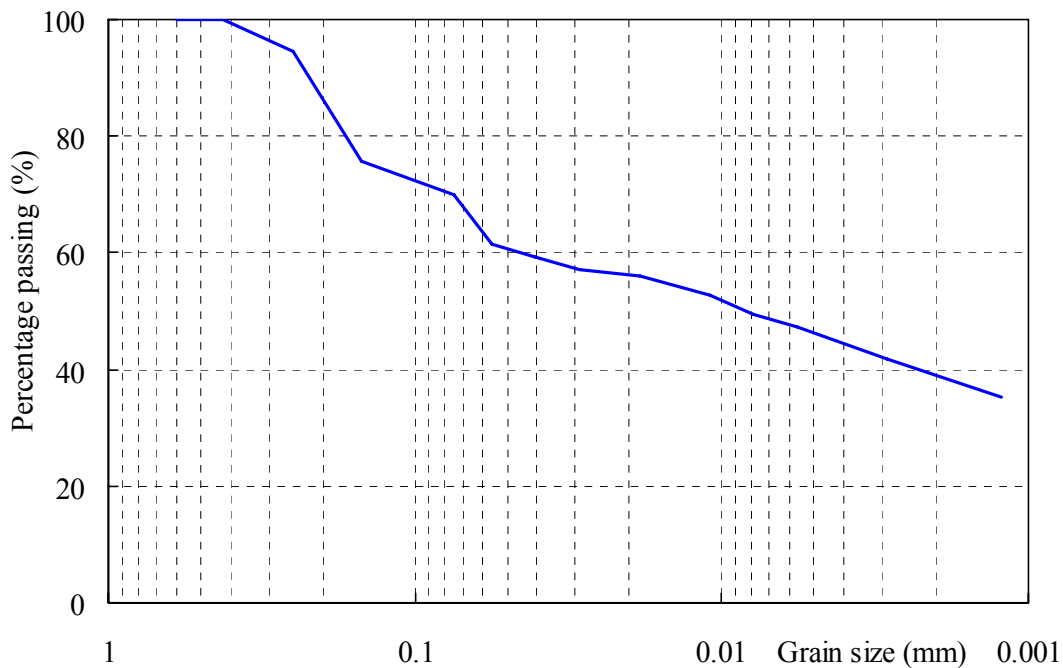
Figure 6.8. Grain Size Distribution Curve of Grande Clay.

6.2.2 Engineering Properties

Geotechnical tests were conducted according to the ASTM standard to obtain the engineering properties of Grande clay. The obtained properties are tabulated in Table 6.1. The vane shear test was also conducted and is shown in the table.

Table 6.1. Geotechnical Properties of Grande Clay.			
Liquid Limit (LL)	Plastic Limit (PL)	Plastic Index (PI)	Shear Strength (kPa)
28.40%	14.55%	13.85%	8.2

6.2.3 Erosion Properties

EFA was developed to measure the erodibility of a soil sample for predicting the scour depth at bridge piers (Briaud et al., 1999). The test results include the relationships of the soil erosion rate (mm/hr) with the mean velocity (m/s) and the shear stress (Pa). The results of the EFA test for Grande clay are shown in Figures 6.9 and 6.10. From the figures, the critical Froude number Frc is estimated as 0.48. The critical Froude number is the minimum Froude number that initiates the bankline erosion in the tests
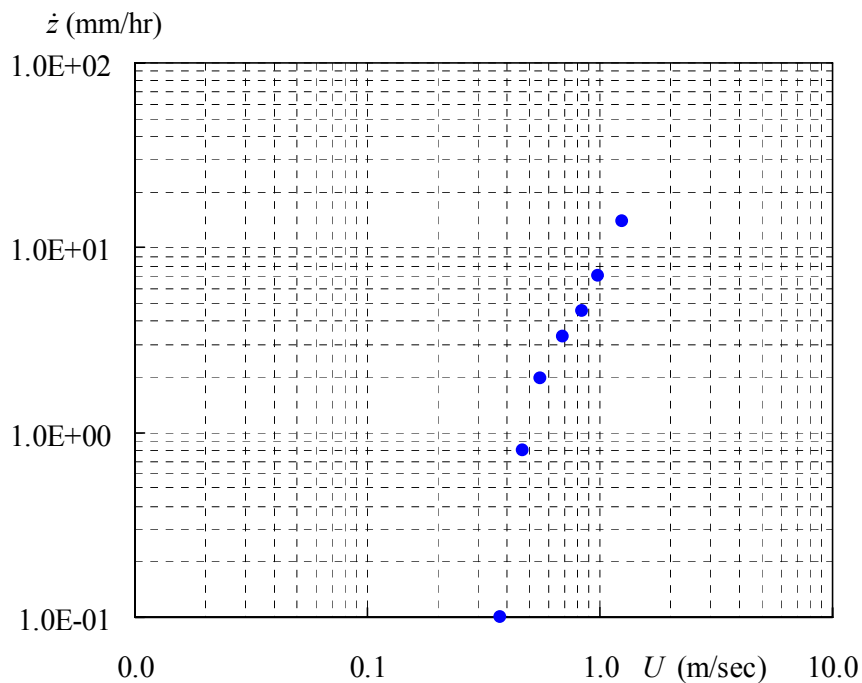
Figure 6.9. Erosion Rate versus Velocity from the EFA Test.
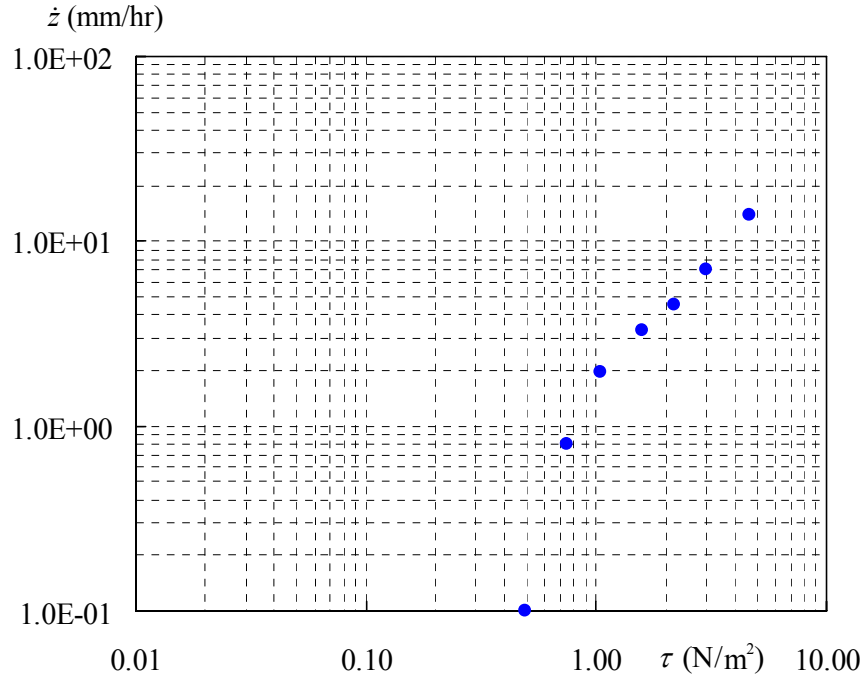
Figure 6.10. Erosion Rate versus Shear Stress from the EFA Test.

6.3 TEST MATRIX

A total of eight flume tests cases were conducted with the parameters shown in Table 6.2. The first three cases are the preliminary tests performed for finding the optimal experimental conditions regarding to the slope of the channel and the cross-sectional shape. After the preliminary tests, five cases were conducted to vary the radius-to-width ratio (R/W) and the bend angle (ϕ). The parameters are defined in Figure 6.2(a) and the geometries of the channel for all cases are plotted in Figure 6.11. The variable θ in the figure represents the angle and varies from 0 to ϕ in each bend. Note that the parameters in Table 6.2 refer to the initial test condition and do not reflect later changes. We did not vary the Froude number in the tests because the critical Froude number is very high and previous tests found the Froude number effect on the maximum meander distance is insignificant (see Chapter 5).

Table 6.2. Test Matrix in Clay Tests.

Case No.	R/W	ϕ	Fr	Fr-Frc
01	4	120°	0.50	0.02
02	4	120°	0.50	0.02
03	6	65°	0.50	0.02
04	4	65°	0.50	0.02
05	6	65°	0.50	0.02
06	2	65°	0.50	0.02
07	4	120°	0.50	0.02
08	4	220°	0.50	0.02
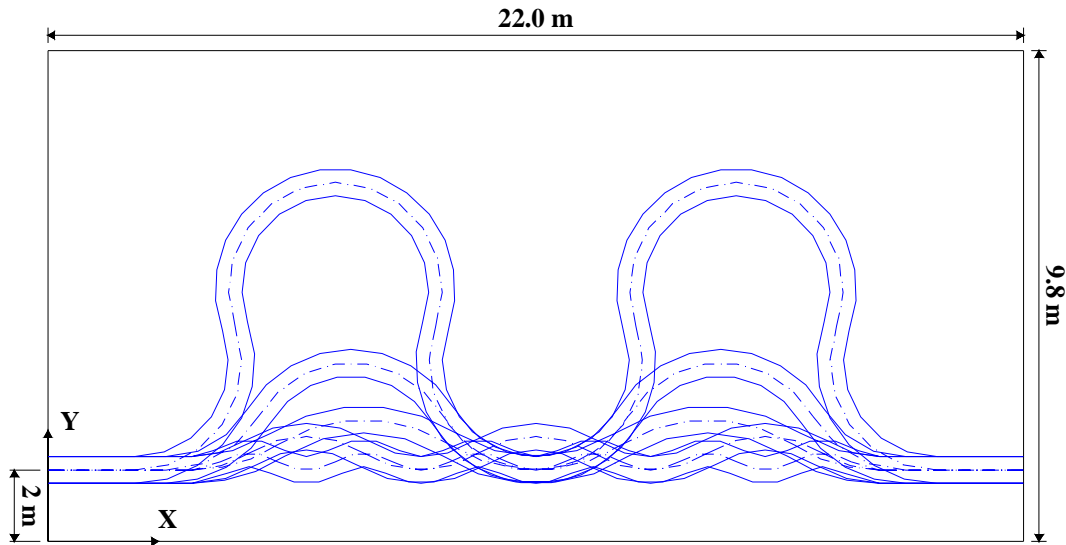
Figure 6.11. Sketches of Plan Forms of All Test Cases.

6.4 TEST PREPARATION

The required channel slope for maintaining a constant water depth along the channel varies case by case since it mainly depends on the geometry of the channel. Therefore, the first step in test preparation is leveling the sand bed. This step includes drawing two reference lines on each flume side wall marking the bed level, flooding the entire test area, and leveling the sand bed by draining water gradually. Once the leveling work was done, the water inside the sand was drained. To make the sand bed more stable, we dug a couple of holes and pumped the water out. Subsequently, the contour of the guide channel in the sand bed was drawn and the sand channel

was carved using a mold and shovels. Figure 6.12 shows the carved guide channel in the sand bed.

Figure 6.12. Carved Guide Channel in the Sand Bed.

Plywood plates were cut according to the shape of the guide channel and laid on the bottom of the channel. This means only the banks were erodible. The Grande clay was delivered in blocks of 25 cm (9.8 inches) × 18 cm (7.1 inches) × 18 cm (7.1 inches). Each block was in a sealed plastic bag. The clay blocks were laid on both sides of the channel using a wooden mold placed on the middle of the channel (Figure 6.13). The finished clay banks were covered with soaked cloths to maintain moisture inside the clay. The cloths were sprayed frequently to retain moisture until the tests started.

Figure 6.13. Laying the Clay Blocks along the Channel.

6.5 TEST PROCEDURES AND MEASUREMENTS

All the flume tests in clay were conducted according to the following procedure:

1. Measure the initial geometry of both banklines (left and right).
2. Turn on the pump and adjust the flow rate to the predetermined value.
3. Adjust the sluice gate to obtain the desired constant water depth of 10 cm (3.9 inches) in the channel.
4. Take pictures of the initial running conditions.
5. Measure the initial water velocity on several predetermined stations.
6. Measure the water surface elevation along the channel.
7. At the next time step, take pictures of the running conditions and shut down the experiment.
8. Measure the geometry of both banklines.
9. Take pictures of the drained channel.
10. Re-start the experiment and measure the water velocity, the water depth, and water surface elevation.
11. Repeat steps 7 to 10 until the experiment is completed.
12. After finish the experiment, measure the cross-sectional profiles.

For each case, the primary measurements were the geometry of the banklines, the water velocity, the water depth, and the water surface elevation.

6.6 RESULTS

The test results of case 08 are presented in this chapter as an example. All the test results for other cases are shown in Appendix B. Two photos in Figure 6.14 show the initial and final conditions of the test. In the photos, most parts of the outer banks were eroded, while the inner banks were mostly intact. This phenomenon can be clearly seen in Figure 6.15, which depicts the measured initial geometry and final geometry on both banklines. The plan form evolution of the second and third bends at several different instants is shown in Figure 6.16. The figure shows the channel bankline expands laterally and translates downstream. The channel migration thus contains two components: cross-valley movement and down-valley movement. The bankline shift starts from the first half of the leading outer bend ($0.0 < \theta/\phi < 0.5$) and ends on the second half of the following inner bend ($1.5 < \theta/\phi < 2.0$). A large displacement occurs behind the apex of the outer bend ($\theta/\phi = 0.5$) with a phase lag to the channel curvature. Both banks have a similar but alternate erosion pattern.

Three cross-sectional profiles looking downstream at stations 1, 4, and 6 are plotted in Figure 6.18. The locations of these stations are shown in Figure 6.17. It reveals that most erosion occurred in the outer banks as expected and the coarse particles in the Grande clay deposited along the inner banks in the channel, although the amount was relatively small in comparison with that in the sand flume tests. Note that Grande clay contains approximately 30 percent fine sand particles as shown in the grain size distribution curve (Figure 6.8). Therefore, some of the sandy particles that are heavier than the clay particles deposited at the inner banks where the velocity is relatively lower, while the finer particles were suspended in the water and carried downstream along the channel.

(a) Initial Condition at $t = 0$ hr

(b) Final Condition at $t = 336$ hr

Figure 6.14. Photos of Clay Test Case 08 ($R/W = 4$, $\phi = 220°$, $Fr = 0.50$).
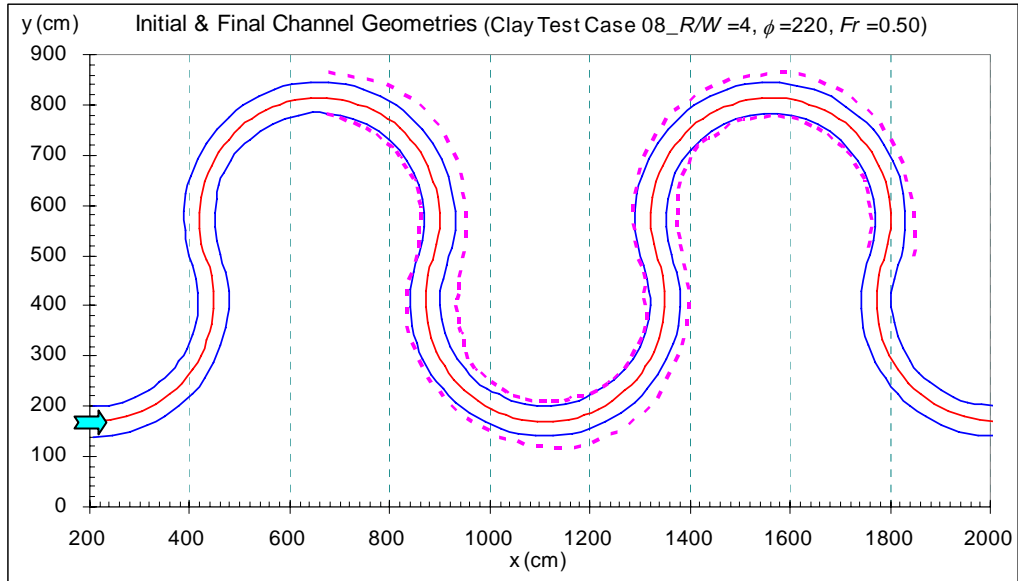
Figure 6.15. Channel Geometry at the Initial Stage and Final (336 hr) Stage (Clay Test Case 08).
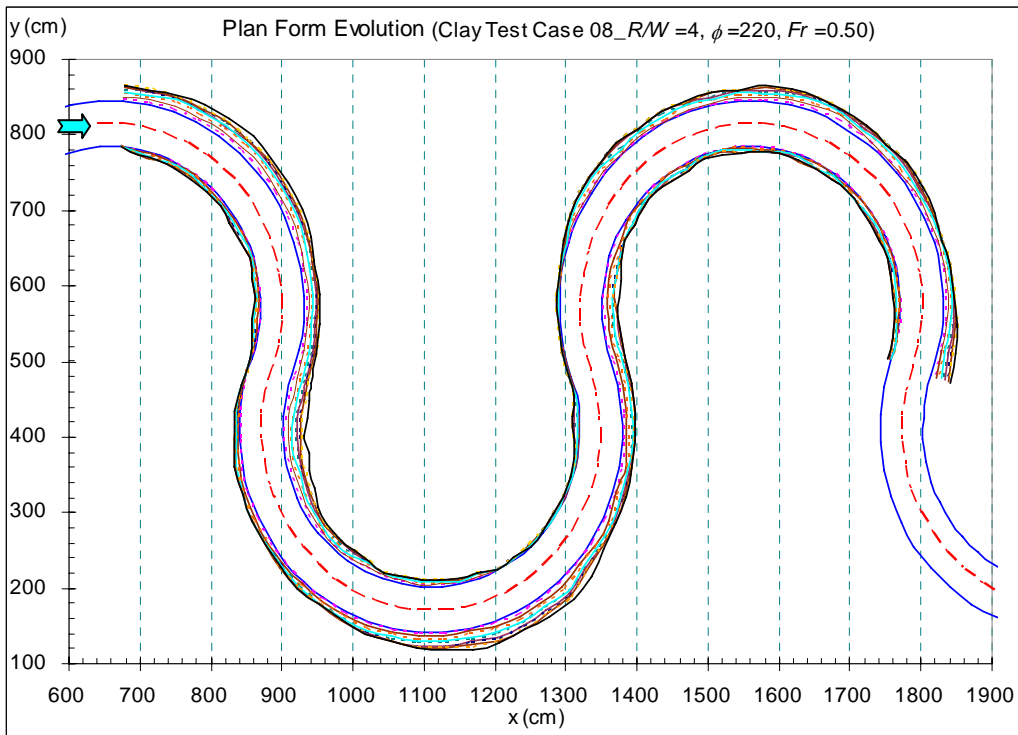
Figure 6.16. Plan Forms Evolution at *t* = 0, 24, 48, 72, 96, 120, 150, 180, 210, 240 and 336 hr (Clay Test Case 08).
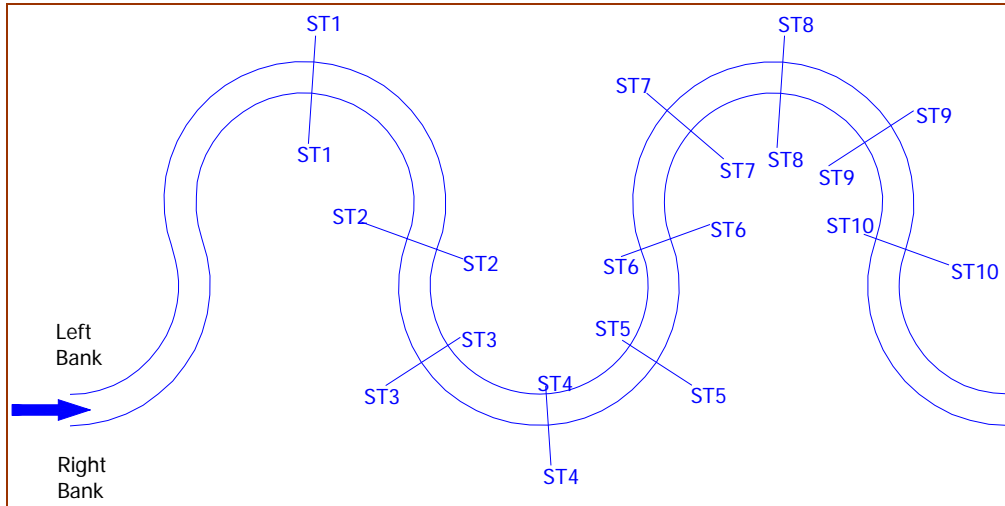
Figure 6.17. Locations of the Predetermined Stations.

(a)

(b)

(c)
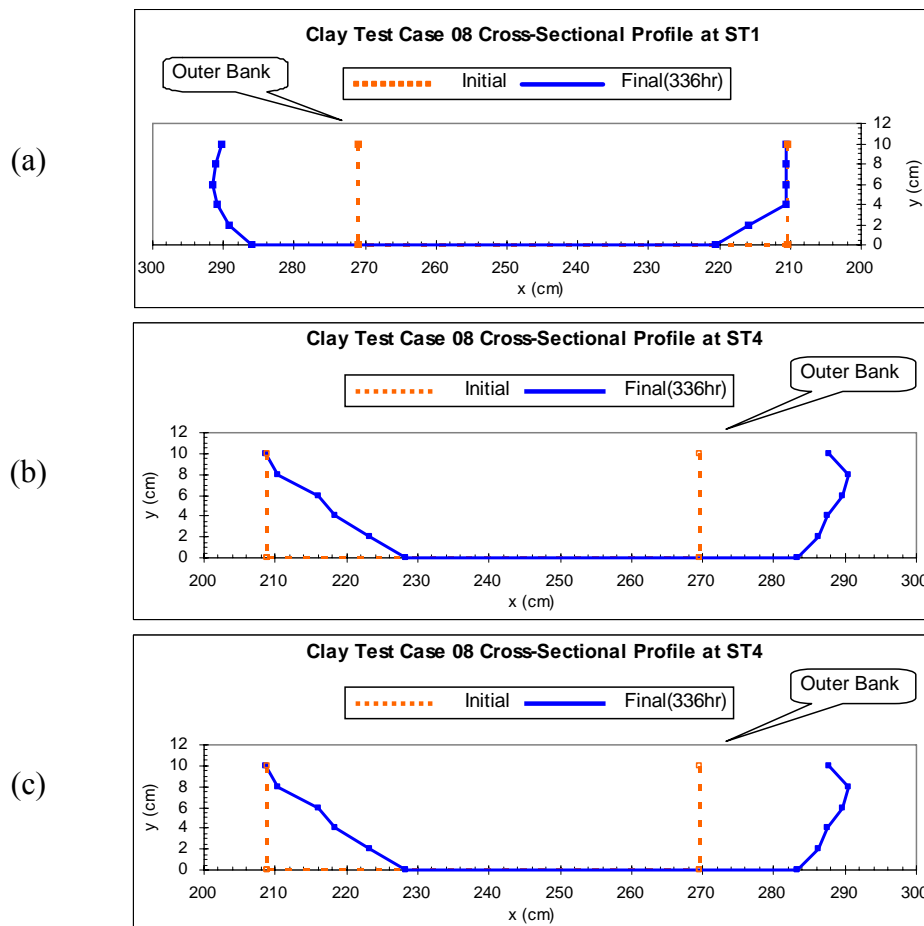
Figure 6.18. Evolution of Cross-Sectional Profiles at Three Stations.

The mean velocities and water elevations in different time intervals at the predetermined stations are shown in Figures 6.19 and 6.20. In this study, the mean velocity U is calculated as $U = Q/A_w$, with A_w being the wetted cross-section area. The water elevation H_w was measured at the middle of the cross section. In the figure, the mean velocity of each station decreased as the bankline erosion process continued. With the variations of mean velocity and water elevation, the energy slope along the channel, which is defined as the total head loss over the associated channel length, decreased as the flow continued to erode the channel bankline and elongate the channel. Eventually, an equilibrium state of the channel bankline is expected to be reached. The displacement of channel bankline is expected to attain the maximum value at that time.
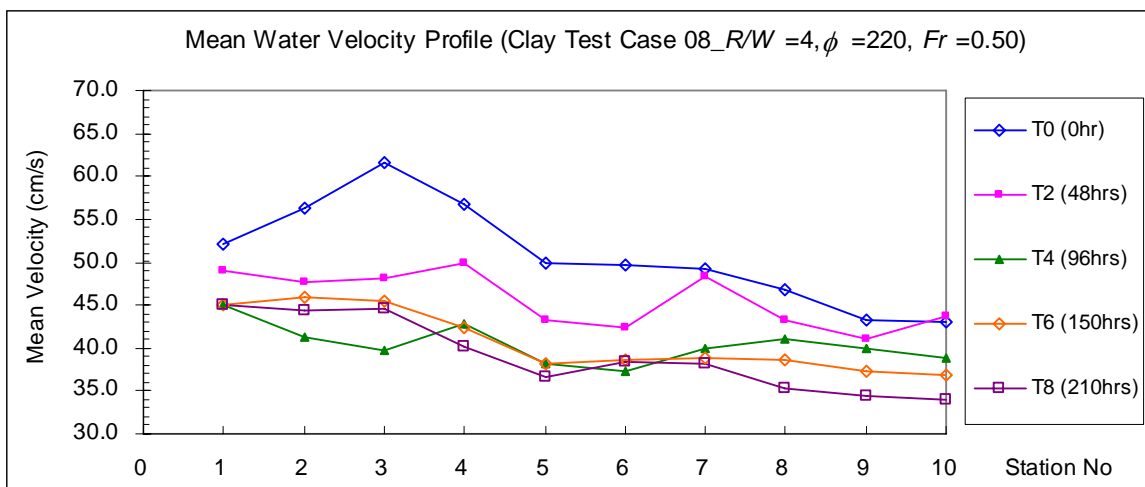
Figure 6.19. Mean Water Velocity Profile (Clay Test Case 08).
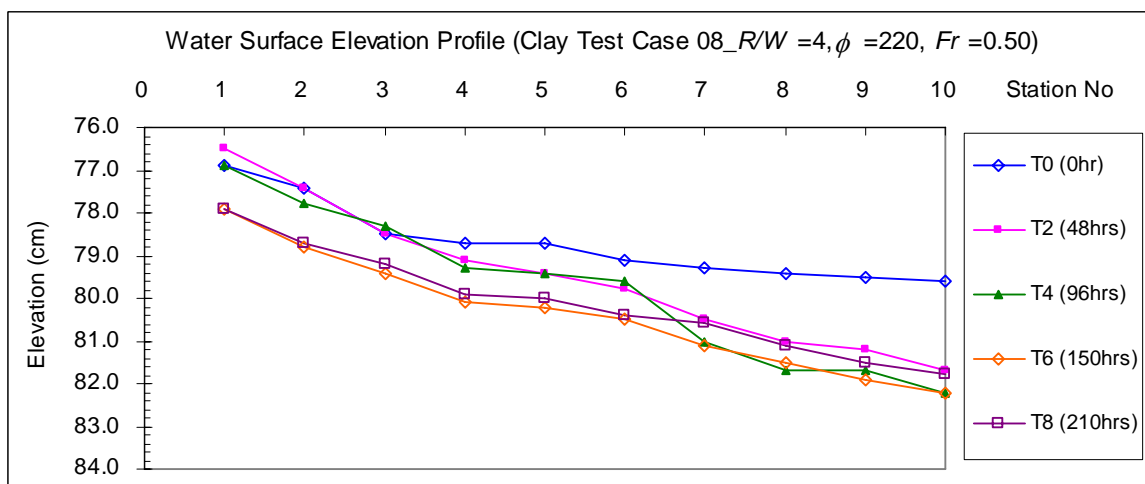
Figure 6.20. Water Surface Elevation Profile (Clay Test Case 08).

6.7 DATA DEDUCTION

The channel migration distance was measured in the direction perpendicular to the initial channel bank. Using case 08 as an example, the migration distance at a cross section on the right bank is shown in Figure 6.21. Note that when θ/ϕ becomes greater than 1 (e.g., $1.0 < \theta/\phi < 2.0$), it denotes a position in the following inner bend. The figure shows that the channel migration rate (slope) is the greatest at the early stage of the test, meaning that the channel migration distance increases rapidly within a short period of time. As the water continues to erode the channel banks, the migration rate tends to decrease gradually. A maximum value of the migration distance is expected when the channel reaches an equilibrium state at $t \rightarrow \infty$. The data points in Figure 6.22 were then fitted with a hyperbolic function. Alternatively, the t/M can be plotted versus the time and then the data can be fitted with a linear equation as shown in Figure 6.21. From these two figures, it can be seen that the hyperbolic function is a good approximation in describing the temporal evolution of channel migration. The hyperbolic function is of the form:

$$M = \frac{1}{a + bt} \tag{6.1}$$

where M is the channel migration distance, t is time, and a and b are constant. The reciprocals of the two constants in the hyperbolic function are the initial slope at $t = 0$ ($1/a$) and the asymptotic value of the hyperbolic curve at $t \rightarrow \infty$ ($1/b$). Therefore, the initial migration rate $\dot{M}_i$ and the maximum migration distance M_{max} at a given cross section can be expressed as $\dot{M}_i = 1/a$ and $M_{max} = 1/b$. In the experiment, the units of M and t are in centimeters and hours, respectively, and the units of $\dot{M}_i$ and M_{max} are in centimeters per hour and centimeters, respectively.
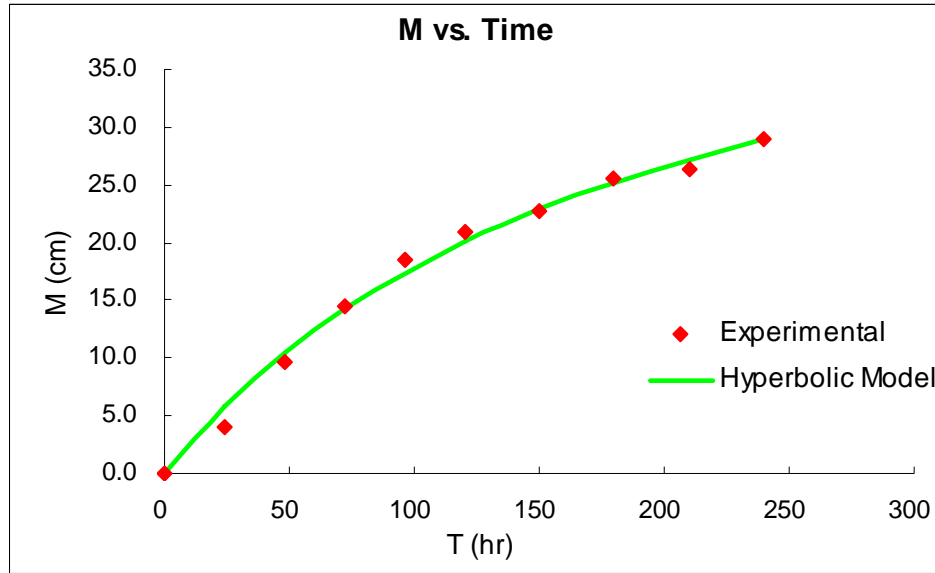
Figure 6.21. Migration Distance versus Time in Clay Test Case 08 (*R/W* = 4, ϕ = 220°, *Fr* = 0.50, θ/ϕ = 0.69).
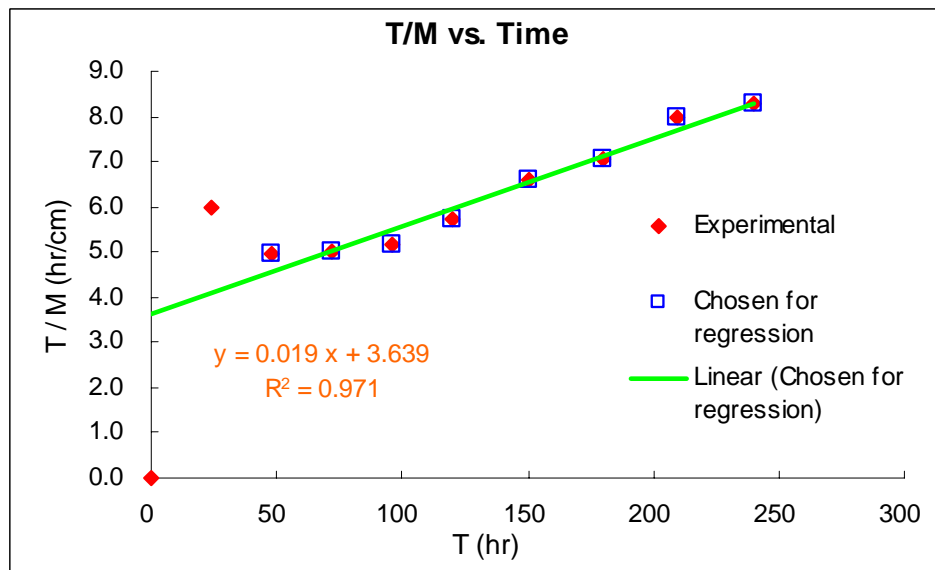
Figure 6.22. *T/M* **versus Time in Clay Test Case 08** (*R/W* = 4, ϕ = 220°, *Fr* = 0.50, θ/ϕ = 0.69).
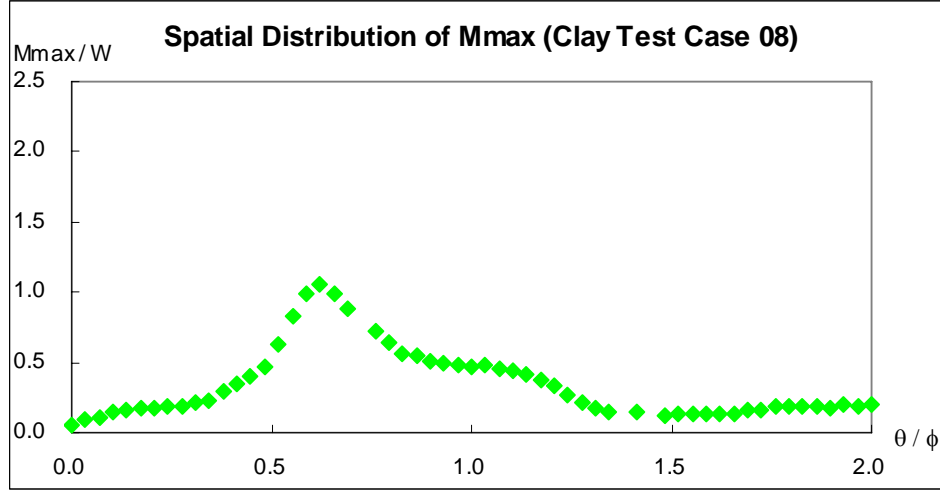
Figure 6.23. M_{max} **Distributions along the Channel for Clay Test Case 08.**

The maximum migration distance M_{max} at each cross section along the channel was obtained by curve fitting the measured data points using the hyperbolic function. The resulting M_{max} is shown in Figure 6.23. Note that M_{max} is normalized by the initial channel width, W. In the experiments, data taken from the second outer bank to the following third inner bank were used in analysis. This is to ensure that the fully developed secondary current in the channel is accounted for and the backwater effect from the channel exit is negligible. The result shows that M_{max} along the channel has the peak value behind the channel apex ($\theta/\phi = 0.5$) and there exists a phase lag to the channel curvature. Although M_{max} in the flume tests in sand displays the Gaussian distribution (see Chapter 5), the typical shape of distribution in the clay tests is somewhat different. A distinct difference is the skewed bell shape of the distribution. To accommodate the skewness, the Pearson IV distribution function is employed:

$$\frac{M_{max}}{W} = a \frac{\left[1 + \frac{\left(\frac{\theta}{\phi} - \frac{ce}{2d} - b\right)^2}{c^2}\right]^{-d} \exp\left[-e\left(\tan^{-1}\left(\frac{\frac{\theta}{\phi} - \frac{ce}{2d} - b}{c}\right) + \tan^{-1}\left(\frac{e}{2d}\right)\right)\right]}{\left(1 + \frac{e^2}{4d^2}\right)^{-d}} \tag{6.2}$$

where a is the maximum value of M_{max}/W, θ/ϕ the normalized angle, b the location (in terms of θ/ϕ) of the maximum value, c and d the coefficients controlling the bandwidth of the distribution, and e the coefficient controlling the skewness of the distribution. It turns out that the Pearson IV

110

function could represent the distribution of M_{max} well in all the cases, shown in Figures 6.24 to 6.28.
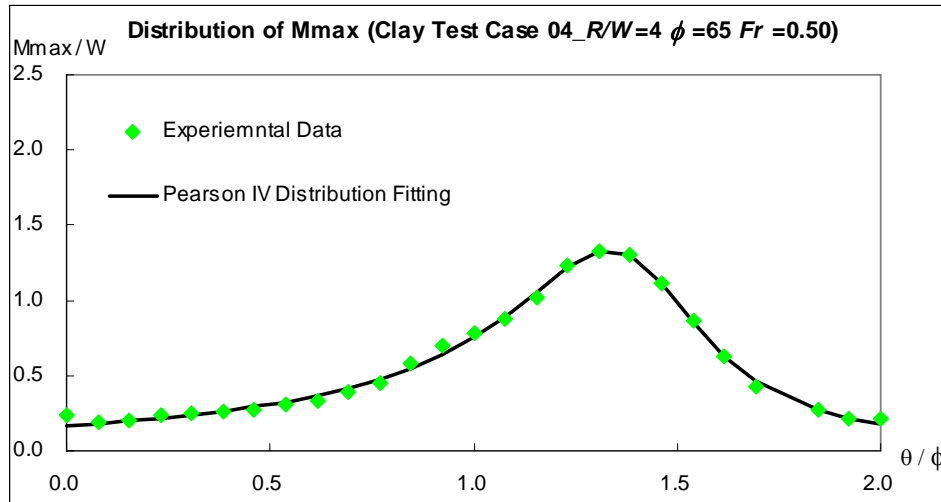
Figure 6.24. Experimental Data and Fitted Curve for M_{max} in Clay Test Case 04.
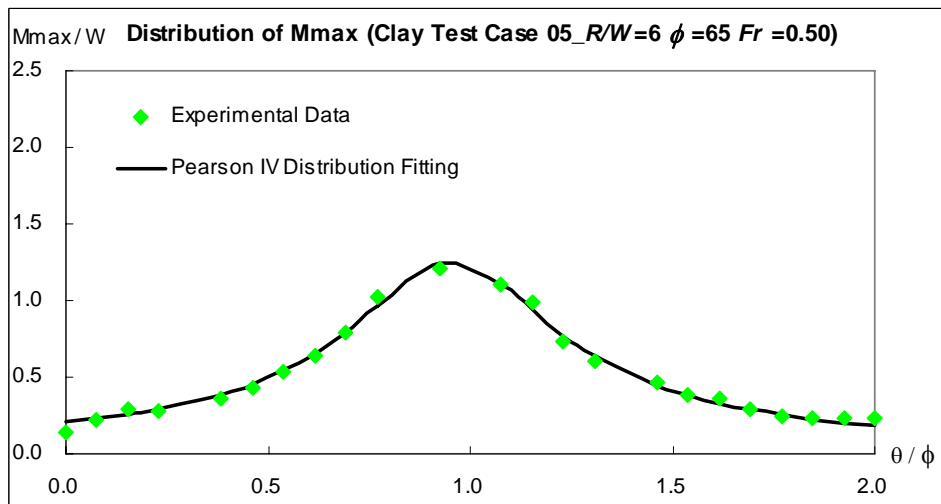
Figure 6.25. Experimental Data and Fitted Curve for M_{max} in Clay Test Case 05.
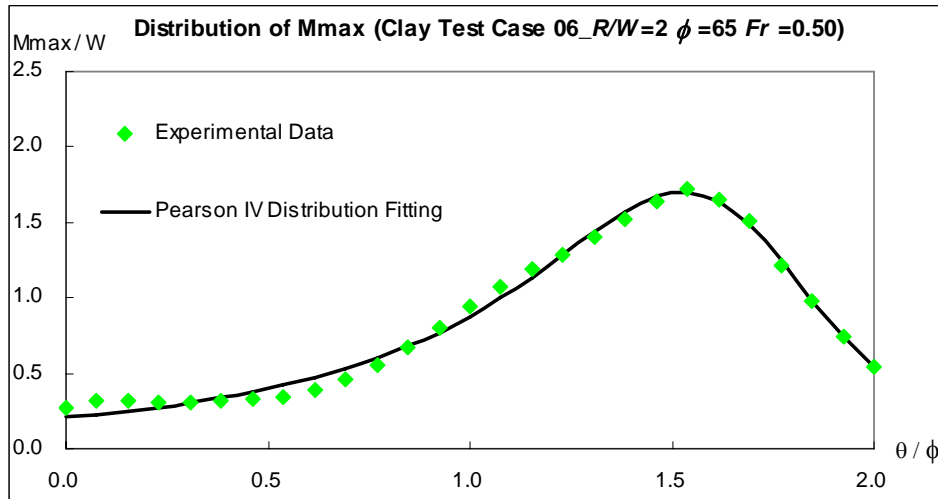
Figure 6.26. Experimental Data and Fitted Curve for *M*_{*max*} in Clay Test Case 06.
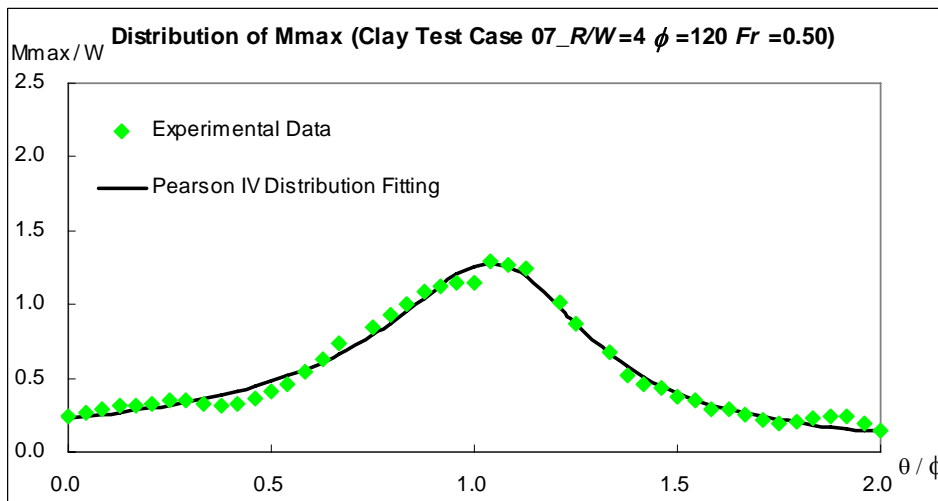
Figure 6.27. Experimental Data and Fitted Curve for *M*_{*max*} in Clay Test Case 07.
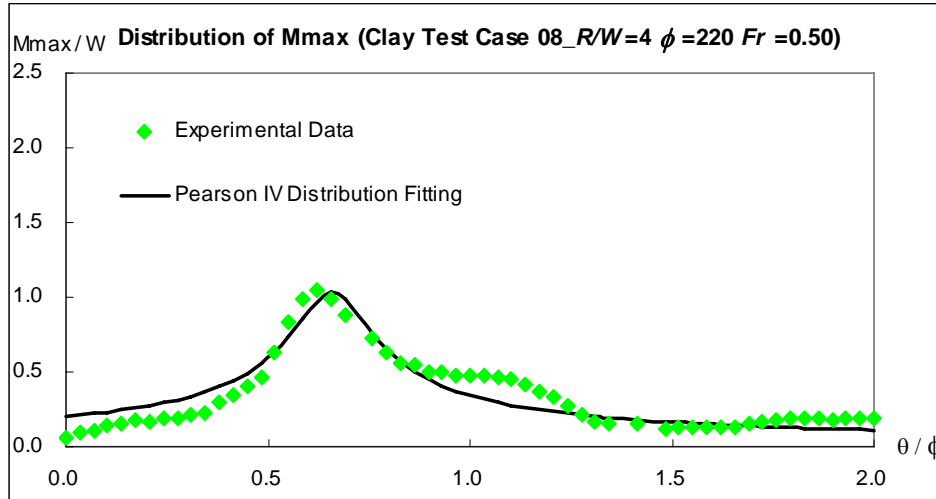
Figure 6.28. Experimental Data and Fitted Curve for M_{max} in Clay Test Case 08.

6.8 PROPOSED EQUATIONS

There are five undetermined coefficients in the proposed prediction equation (Equation 6.2). These coefficients are found by correlating the measurements with the three controlling parameters, R/W, ϕ, Fr and the critical Froude number Frc. The correction parameter β is employed here to relate the near-bank velocity and the mean velocity as described in Chapter 5.

The correlations among the five coefficients and $\beta Fr\text{-}Frc$ were shown in Figure 6.29. The result shows the maximum peak value of M_{max} occurs at $\beta Fr\text{-}Frc = 1.02$ where $R/W = 2$ and decreases as $\beta Fr\text{-}Frc$ decreases. This means a channel has the largest maximum migration distance M_{max} when $R/W = 2$. The similar conclusion has been reported by various researchers such as Hickin and Nanson (1975), even though their concern is the meander migration rate versus R/W. The coefficient b decreases as $\beta Fr\text{-}Frc$ increases, which means that the peak location of M_{max} moves downstream as R/W increases. This indicates that the following inner bend may have a greater migration rate and migration distance. The coefficient c has a relatively small variation in all the cases in Figure 6.29(c). The coefficient d increases as $\beta Fr\text{-}Frc$ increases, as shown in Figure 6.29(d), which implies that meander migration in a channel with a large $\beta Fr\text{-}Frc$ (or R/W) occurs over a longer channel length along the outer bankline. The skewness, controlled by the coefficient e in the M_{max} distribution, reaches maximum value at $\beta Fr\text{-}Frc = 1.02$ ($R/W = 2$) and decreases as $\beta Fr\text{-}Frc$ decreases. Note that the distribution becomes more symmetric when $\beta Fr\text{-}Frc = 0.35$ where R/W = 2.

113
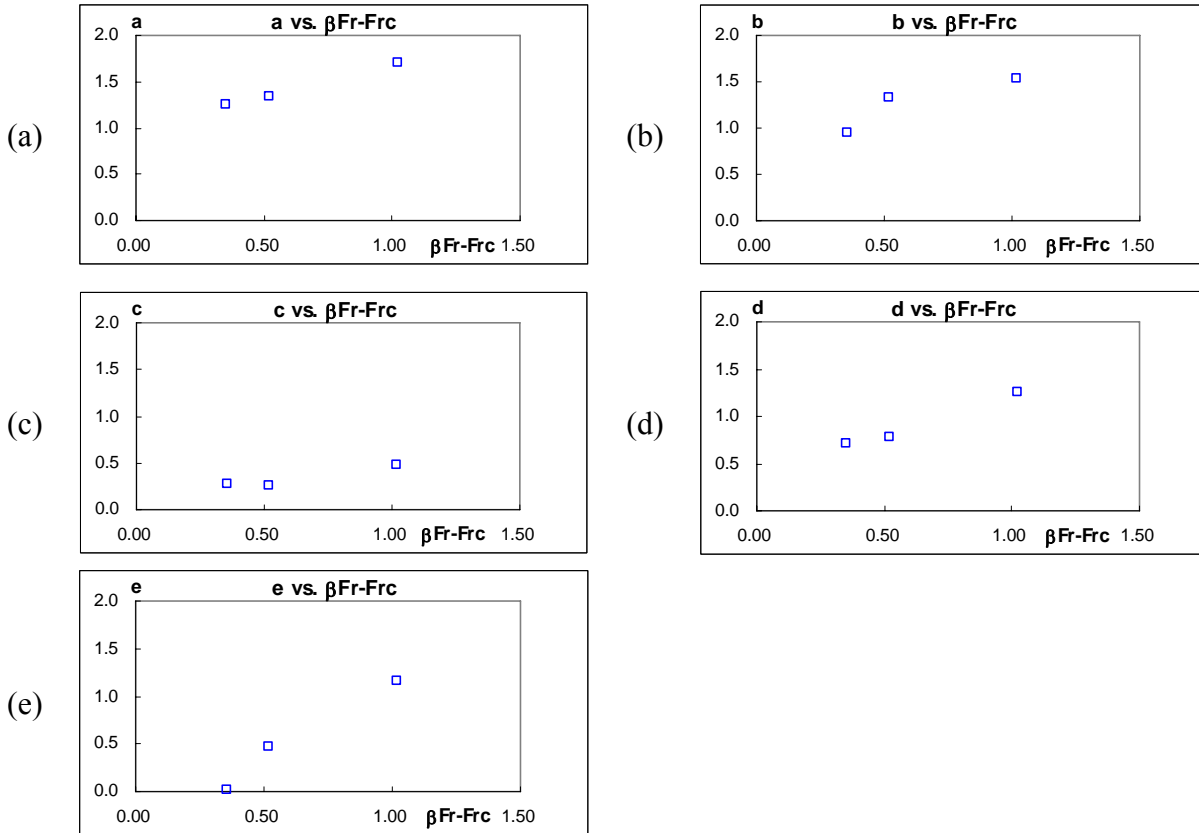
Figure 6.29. Five Coefficients in the Pearson IV Equation versus ($\beta Fr\text{-}Frc$).

The distribution of M_{max} is also influenced by the channel bend angle ϕ, as shown in Figure 6.30. As ϕ increases, the peak value of M_{max} decreases; the location of the peak moves upstream toward the front of the outer bank. The coefficients c and d show similar trends to those in the correlation plots with R/W. In other words, the coefficient c is somewhat constant (Figure 6.30(c)), while the coefficient d increases as R/W increases, as shown in Figure 6.30(d). This means that the migration in a channel with a small R/W occurs over a localized channel length along the outer bankline. The skewness in the M_{max} distribution also shows a similar trend; it reaches maximum value at $\phi = 65°$ and decreases as ϕ increases. Note that the distribution becomes more symmetric when ϕ reaches 220°.
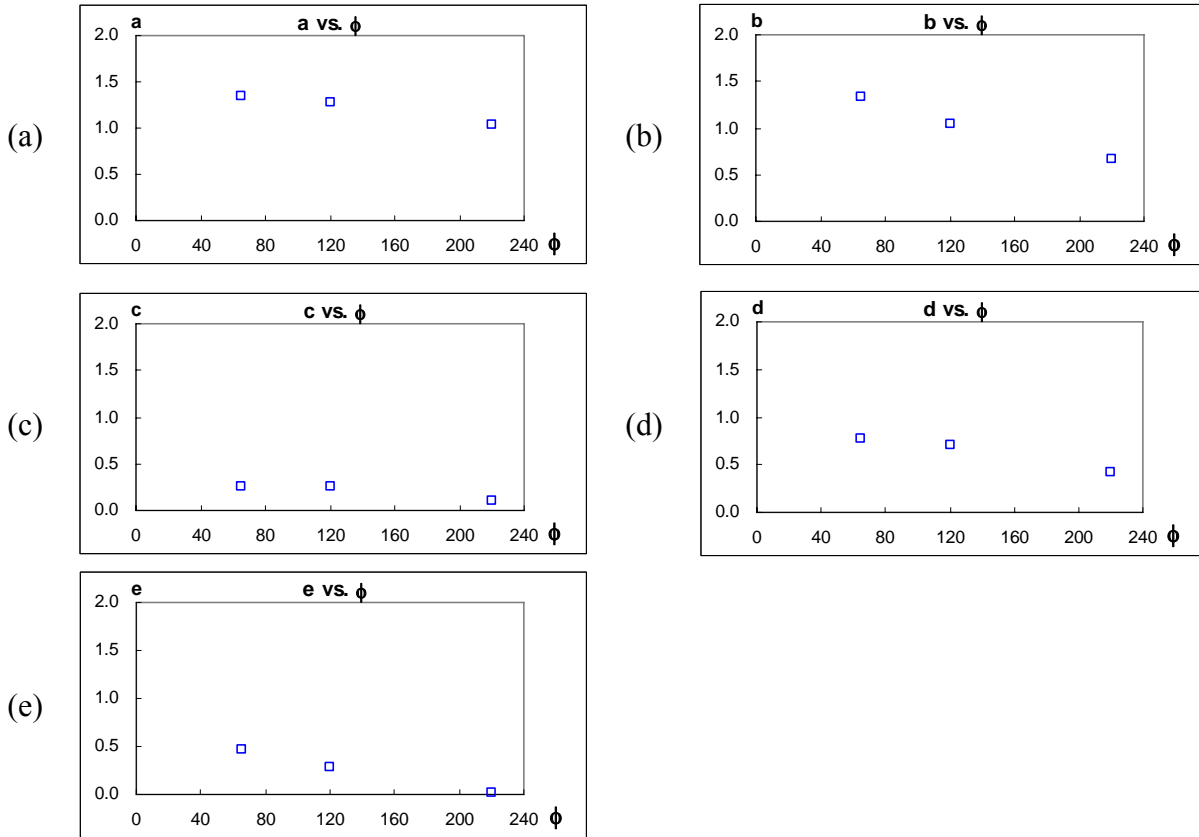
Figure 6.30. Five Coefficients in the Pearson IV Equation versus ϕ.

Based on the results in Figures 6.29 and 6.30, each of the five coefficients in the M_{max} equation is a function of $\beta Fr\text{-}Frc$ and ϕ and can be obtained using regression analysis with the measured data from the flume tests. The final prediction equation with the five coefficients in the Pearson IV distribution function is as follows:

$$\frac{M_{max}}{W} = a \frac{\left[1 + \dfrac{\left(\dfrac{\theta}{\phi} - \dfrac{ce}{2d} - b\right)^2}{c^2}\right]^{-d} \exp\left[-e\left(\tan^{-1}\left(\dfrac{\dfrac{\theta}{\phi} - \dfrac{ce}{2d} - b}{c}\right) + \tan^{-1}\left(\dfrac{e}{2d}\right)\right)\right]}{\left(1 + \dfrac{e^2}{4d^2}\right)^{-d}} \tag{6.3}$$

where,

$$a = 4.325(\beta Fr - Frc)^{0.291}(\phi)^{-0.226}$$

$$b = 1.273(\beta Fr - Frc)^{0.414}[-0.00430(\phi)+1.592]^{0.846}$$

$$c = 4.234[0.325(\beta Fr - Frc)+0.130]^{0.899}[-0.00111(\phi)+0.356]^{1.213}$$

$$d = 1.284[0.846(\beta Fr - Frc)+0.375]^{0.962}[-0.00233(\phi)+0.95]^{1.090}$$

$$e = 2.100[1.637(\beta Fr - Frc)-0.487]^{1.774}[-0.00296(\phi)+0.656]^{0.630}$$

Note: $\beta = \dfrac{4}{R/W} + 1$, and $e = 0$, if $R/W > 6$ or $\phi > 220°$

CHAPTER 7. GEOMETRY STUDY

7.1 FIT A CIRCLE FOR A GIVEN GROUP OF POINTS

7.1.1 A Traditional Method

The equation of a circle is:

$$(x - x_c)^2 + (y - y_c)^2 = R^2 \tag{7.1}$$

To fit a circle for n given points, a traditional least-squares method would tend to minimize one of the following error terms:

$$E_1 = \sum_{i=1}^{n} (R_i - R^*)^2 \tag{7.2}$$

$$E_2 = \sum_{i=1}^{n} \left| R_i - R^* \right| \tag{7.3}$$

$$E_3 = \sum_{i=1}^{n} \left| R_i^2 - R^{*2} \right| \tag{7.4}$$

In these terms, x_c, y_c, R^* are unknowns and $R_i = (x - x_c)^2 + (y - y_c)^2]^{1/2}$. To achieve the minimum value of an error term, the following equations must be solved:

$$\frac{\partial E}{\partial x_c} = 0, \frac{\partial E}{\partial y_c} = 0, \frac{\partial E}{\partial R^*} = 0 \tag{7.5}$$

Error term E_1 gives the simplest form among the three, as shown in what follows:

$$\begin{cases} \sum_{i=1}^{n} (x_i - x_c)(\dfrac{R^*}{\sqrt{(x_i - x_c)^2 + (y_i - y_c)^2}} - 1) = 0 \\[4mm] \sum_{i=1}^{n} (y_i - y_c)(\dfrac{R^*}{\sqrt{(x_i - x_c)^2 + (y_i - y_c)^2}} - 1) = 0 \\[4mm] R^* = \dfrac{1}{n} \sum_{i=1}^{n} \sqrt{(x_i - x_c)^2 + (y_i - y_c)^2} \end{cases} \tag{7.6}$$

Since there are three unknowns and three equations, these equations are theoretically solvable. This method is called a direct solution (Moura and Kitney, 1991). The advantage of this method is that it is straightforward. The disadvantage is that it is not easy to obtain a solution and the computation is time consuming.

7.1.2 Apply the Optimization Toolbox of Matlab

The search for the best circle can also be treated as an optimization problem. The target is to find a circle which gives minimum error. The object function can be any one of Equations 7.2 to 7.4. Equation 7.2 proved to be the most efficient. The optimization toolbox of Matlab has a good solution. Function $x =$ fminunc(fun, x_0, options) was used to find a minimum of an unconstrained multivariable function "fun" whose variables were valid in the range of $(-\infty, +\infty)$. x_0 here indicates the coordinates of the starting point for searching the center of the circle. No searching range needs to be specified. Function $x =$ fmincon(fun, x_0, A, b, A_{eq}, B_{eq}, lb, ub) was used to find a minimum of a constrained multivariable function "fun." x_0 has the same meaning as above. The ranges or constraints of the variables ($lb =$ lower boundary, $ub =$ upper boundary) need to be set, which also constitute a searching range. These two functions have given very precise solutions. They can also fit a very large circle to a group of points in a straight line, as shown in Figure 7.1. Straight line segments are not unusual in river banks. It is not surprising that a regular program would collapse trying to fit a circle to a straight line. Matlab can handle this problem very well. The difference between the solutions of these two functions is tiny. The advantage of this approach is that Matlab is widely available and no complicated programming is needed. However, it is not fast enough. These functions were used until a much better method was found.
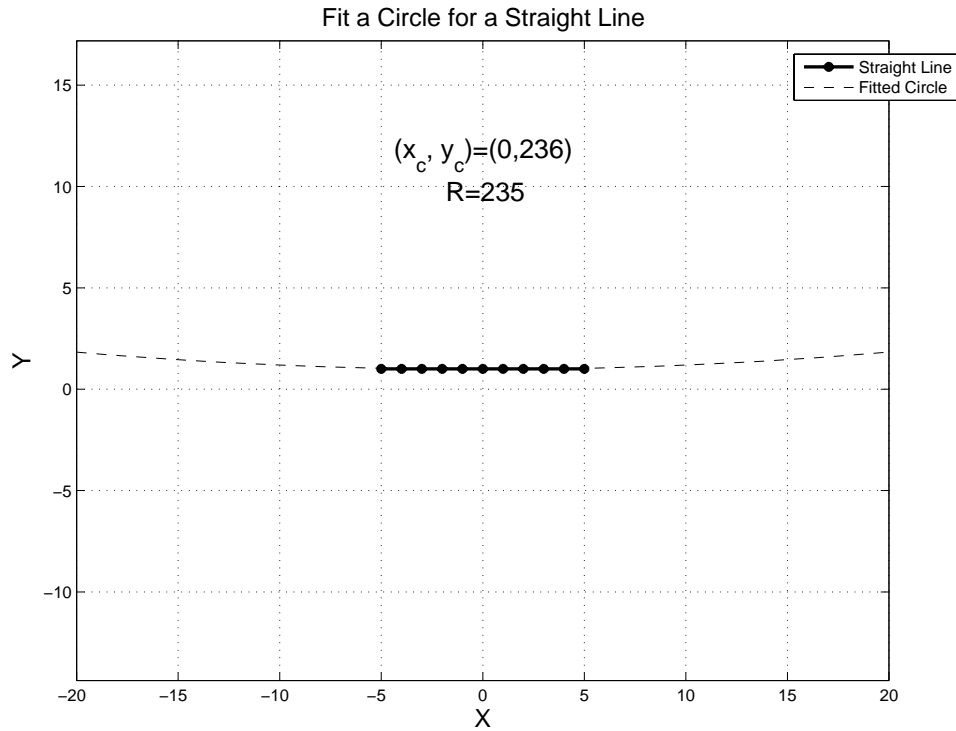
Figure 7.1. Using Matlab to Fit a Circle for a Straight Line.

7.1.3 Linear Least Square Fitting

Rewrite the equation of a circle Equation 7.1 in this form:

$$2x_c x + 2y_c y + R^2 - x_c^2 - y_c^2 = x^2 + y^2 \tag{7.7}$$

Let $a = 2x_c$, $b = 2y_c$, $c = R^2 - x_c^2 - y_c^2$, $z = x^2 + y^2$, the equation can be simplified as:

$$ax + by + c = z \tag{7.8}$$

Plug in the coordinates of the n given points:

$$\begin{cases} ax_1 + by_1 + c \approx z_1 \\ ax_2 + by_2 + c \approx z_2 \\ \vdots \quad \vdots \quad \vdots \quad \vdots \quad \vdots \quad \vdots \quad \vdots \quad \vdots \quad \vdots \quad \vdots \\ ax_n + by_n + c \approx z_n \end{cases} \tag{7.9}$$

There are three unknowns and n equations. This is a typical linear least-squares or linear optimization problem. The equations can be expressed in a matrix form:

$$\begin{bmatrix} x_1 & y_1 & 1 \\ x_2 & y_2 & 1 \\ \vdots & \vdots & \vdots \\ x_n & y_n & 1 \end{bmatrix} \begin{Bmatrix} a \\ b \\ c \end{Bmatrix} \approx \begin{Bmatrix} z_1 \\ z_2 \\ \vdots \\ z_n \end{Bmatrix}, \text{ or} \tag{7.10}$$

$$X A \approx Z \tag{7.11}$$

The sign "$\approx$" indicates it is not an exact linear equation set but an optimization problem. A typical way to solve this problem is to first time the transpose of matrix X to the left side of XA and Z. Then $X^T X$ is a 3 by 3 matrix, and $X^T Z$ is a 3 by 1 vector. Thus $A = [a\ b\ c]^T$ can be solved:

$$A = \begin{Bmatrix} a \\ b \\ c \end{Bmatrix} = \frac{X^T Z}{X^T X} \tag{7.12}$$

Once we solve for a, b, c, we can get $x_c = a/2$, $y_c = b/2$, $R = [c + (a^2 + b^2)/4]^{1/2}$. This method is used in the program.

A straightforward way to solve this linear optimization problem is to explicitly express the error terms and to find the minimum sum square.

$$\begin{cases} ax_1 + by_1 + c = z_1 + e_1 \\ ax_2 + by_2 + c = z_2 + e_2 \\ \vdots \quad \vdots \quad \vdots \quad \vdots \quad \vdots \quad \vdots \quad \vdots \quad \vdots \quad \vdots \\ ax_n + by_n + c = z_n + e_n \end{cases}, \text{ or} \tag{7.13}$$

$$e = X A - Z = \begin{bmatrix} e_1, & e_2, & \cdots\cdots & e_n \end{bmatrix}^T \tag{7.14}$$

T denotes matrix transpose operation. The sum square of the error terms is expressed as:

$$E = \sum_{i=1}^{n} e_i^2 = \sum_{i=1}^{n} (ax_i + by_i + c - z_i)^2 \tag{7.15}$$

Parameters *a*, *b*, and *c* will be obtained by solving equations $\partial E/\partial a = 0$, $\partial E/\partial a = 0$, $\partial E/\partial c = 0$. A simpler solution can be achieved by applying Gauss's *principle of least squares,* which states that the parameters $A = [a\ b\ c]^T$ that make term (Equation 7.15) reach minimum value can also make this term reach minimum value:

$$J = \frac{1}{2} e^T e \tag{7.16}$$

Substituting Equation 7.14 for *e* into Equation 7.16 yields:

$$J = J(A) = \frac{1}{2}(A^T X^T (XA) - 2Z^T XA + Z^T Z) \tag{7.17}$$

In Equation 7.17, $Z^T XA = (Z^T XA)^T = A^T X^T Z$ because they are scalars. If there exist the required parameters $A = [a\ b\ c]^T$, these requirements need to be satisfied:

1. Necessary condition

$$\nabla_A J = \begin{bmatrix} \partial J/\partial a \\ \partial J/\partial b \\ \partial J/\partial c \end{bmatrix} = X^T XA - X^T Z = 0 \tag{7.18}$$

2. Sufficient condition

$$\nabla^2_A J = \frac{\partial^2 J}{\partial A \partial A^T} = X^T X \tag{7.19}$$

must be positive definite. $\nabla_A J$ is the Jacobian and $\nabla^2_A J$ is the Hessian. Any matrix B which satisfies

$$z^T B z \geq 0 \tag{7.20}$$

for all $z \neq 0$ is called positive semi-definite. Let $h = Xz$ be a column vector. It can be easily obtained if the scalar $h^2 = h^T h = z^T X^T Xz \geq 0$. So $X^T X$ is always positive semi-definite. It becomes positive definite when its *n* column vectors are independent, which is not satisfied here. This explains why circles cannot be fit for some cases, say points on a straight line.

From the necessary condition, we can obtain the solution

$$A = (X^T X)^{-1} X^T z \qquad (7.21)$$

which is exactly the same as solution (Equation 7.12). The above clearly shows the correctness of this simple and efficient method used in the program and also explains why the method fails for some cases. When such a condition occurs, the program was designed to report the error and go on to the next fitting.

In deriving the equations listed above, the following matrix calculus differentiation rules (Crassidis and Junkins, 2004) were used:

$$\frac{\partial}{\partial x}(Ax) = A \qquad (7.22)$$

$$\frac{\partial}{\partial A}(a^T Ab) = ab^T \qquad (7.23)$$

$$\frac{\partial}{\partial A}(a^T A^T b) = ba^T \qquad (7.24)$$

$$\frac{\partial}{\partial x}(Ax+b)^T C(Dx+e) = A^T C(Dx+e) + D^T C^T (Ax+b) \qquad (7.25)$$

$$\frac{\partial}{\partial x}(x^T Cx) = (C+C^T)x \qquad (7.26)$$

7.2 CALCULATE RADIUS OF CURVATURE OF EACH POINT ON A CURVE

7.2.1 Obtaining Coordinates of the Banks

The channel curves come from digitized aerial photos and maps. Coordinates are obtained by using the free program WinDIG to digitize the scanned photos and maps. These scanned files are the best clue one can get about the geometry of the channel. The user is encouraged to capture detailed geometry features retained on the electronic image files. The spacing of the digitized points is often uneven and the curves are not smooth. A zigzag can have a big impact on the curvature of the points around it, which may cause fluctuation of curvature in that region. This problem is partially solved by evenly distributing the points. Figure 7.2 shows the smoothing effect.
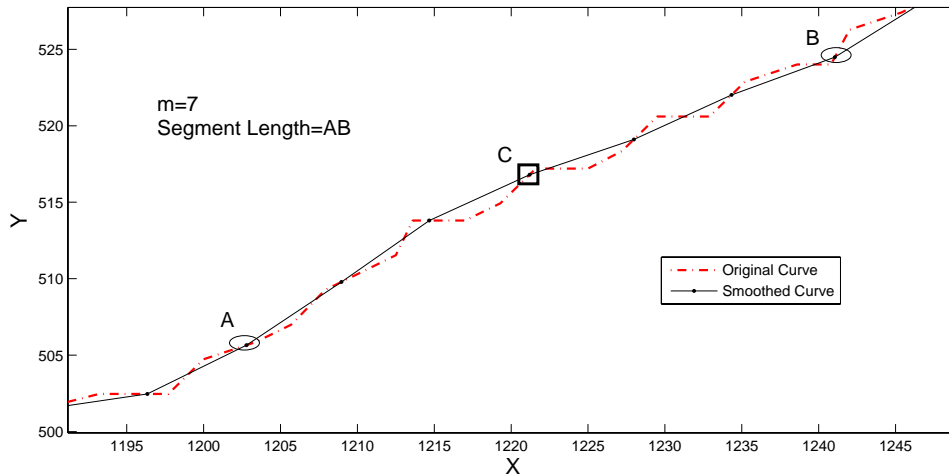
Figure 7.2. Comparison between Original Curve and Smoothed Curve.

The principle of distribution is to maintain a constant total length of the original line segments between two adjacent new points. First calculate total length (L_0) of the original curve. Then determine the number of segments (N) the original curve will be divided into. Start from the first point and travel along the original curve. Stop at distance L_0/N and record the coordinates of this point, which is the second point of the new curve. Then travel a distance of L_0/N again, and the third point will be obtained. Repeat this procedure until the end of the original curve. Since L_0/N is the length along the original curve and may be the summation of several segments, it is not the spacing of the new curve in normal cases.

7.2.2 Equations

For a continuous curve, the equations for the radius of curvature and the curvature are:

$$R = \frac{\sqrt{(1+y'^2)^3}}{y''}, \quad c = \frac{1}{R} = \frac{y''}{\sqrt{(1+y'^2)^3}} \tag{7.27}$$

where, R is the radius of curvature, c the curvature, y the ordinate of the curve, $y' = dy/dx$, and $y'' = d^2y/dx^2$. In civil engineering, when the deflection of a structural element is very small, y' is close to 0. Thus in this case the radius of curvature and curvature can be reasonably approximated as:

123

$$R = \frac{1}{y''}, \quad c = \frac{1}{R} = y'' \tag{7.28}$$

For a bank curve consisting of discrete points, these simplified equations do not apply because the first derivative y' cannot be ignored and sometimes may reach infinity.

7.2.3 Curve Fitting and Important Parameters

The discrete points can be fitted with an analytical curve whose curvature is treated as that of the corresponding points. A long river bank can be fitted with one high-order parabolic curve. The fitting error can be small and an analytical expression of curvature is available for the whole curve. Figure 7.3 shows one of the initial banks of flume test and two fitted parabolic curves of 5th and 7th orders. It is obvious that the higher the order, the closer the fitting will be. However, if the order is higher than 7, the improvement in closeness is hardly noticeable. This can also be seen in Figure 7.4, which shows how the average fitting error decreases with increasing fitting order. But the decreasing trend almost stops after order 7.
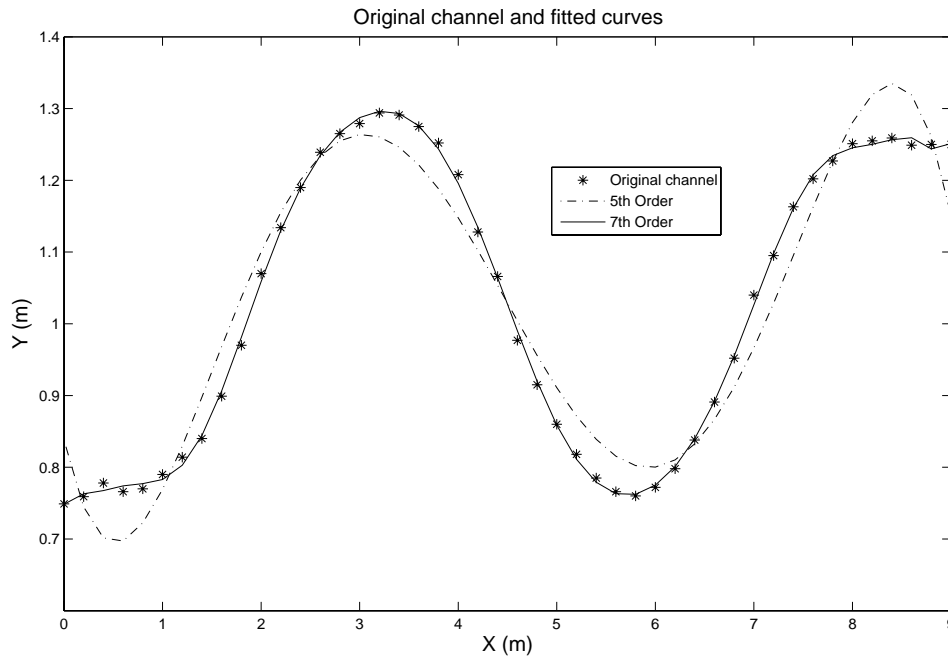
Figure 7.3. Comparison of Parabolic Fittings of Different Orders.
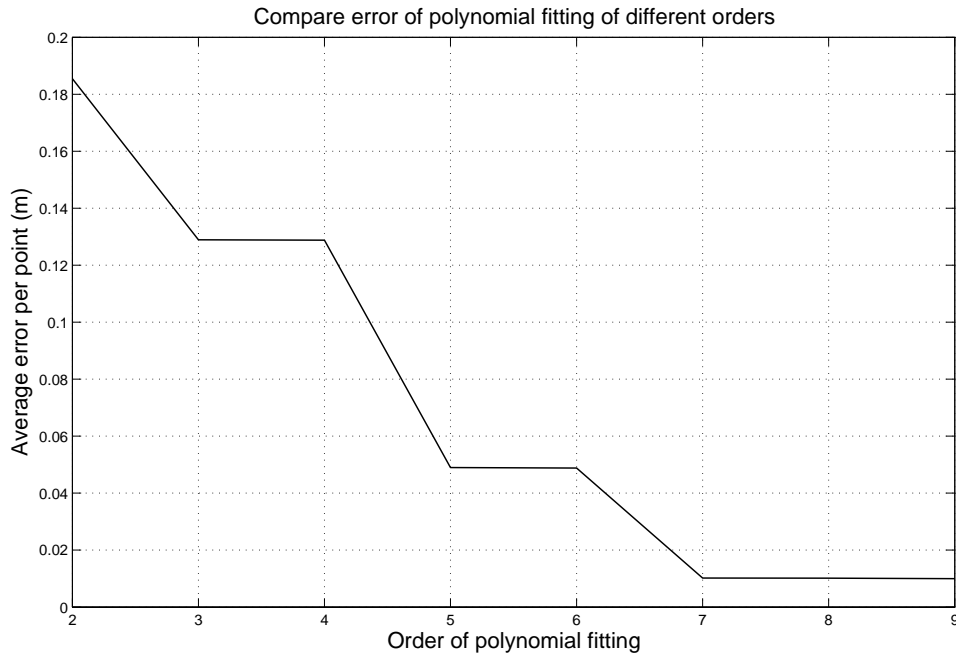
Figure 7.4. Comparison of Errors of Polynomial Fitting of Different Orders.

The idea of using one analytical expression to describe a long channel is tempting. If this goal was achieved, most geometric features of a curve would have been obtained and the task of geometry study can be considered as completed. Figure 7.5 displays a troublesome picture which may diminish this hope. Several orders of parabolic fittings were done to a perfect arc. Although the closeness increases with the order, the fluctuation of radius of curvature increases with the order too. According to the graph, quadratic fitting (2nd order) gives the most stable and closest result. More data points are needed for a high-order parabolic fitting than a quadratic fitting. This means quadratic fitting focuses more on local curvature, which is more suitable to a point in the middle. When the channel curve is not a single-value function of the x coordinate, it has to be broken into several segments in order to be fitted with parabolic curves. Since what is needed is the curvature of each point and high-order parabolic fitting does not provide good results, quadratic fitting is chosen for the calculation.

Figure 7.5. Comparison of *R*s of Different Fitting Orders.

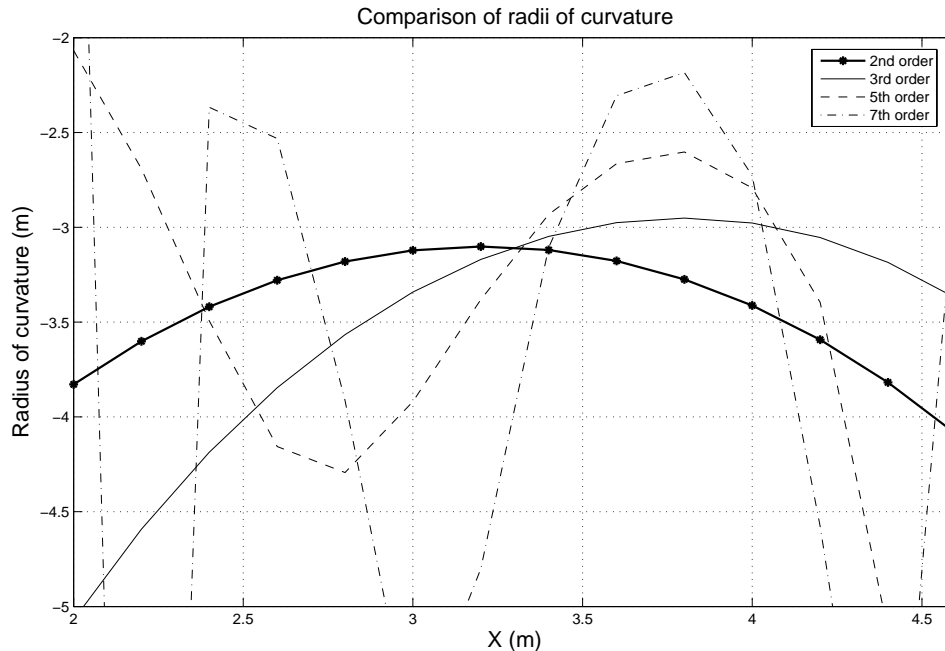A single point alone does not have curvature. Its curvature is determined by a segment that extends from the point in both directions by a certain length (from point A to point B in Figure 7.2). A quadratic curve is fitted to this chosen segment. The curvature of the corresponding point on the fitted curve is treated as that of the point of interest. This process is repeated for each point on the bank.

Before fitting a quadratic curve, two parameters need to be determined. The first is the spacing used to distribute the points; the other is the length of the curve segment for which a quadratic curve is to be fitted, called segment length. The curvature of a river is often related to its average width. These parameters are non-dimensionalized by river width, which can make them independent of a certain case. The spacing coefficient (spacing/width) and segment length coefficient (segment length/width) are therefore used.

With spacing and segment length ready, the number of points "*m*" contained in that segment is determined accordingly. One segment is defined for each point with $(m-1)/2$ points to the left and $(m-1)/2$ points to the right. For the first and last $(m-1)/2$ points, this fitting cannot be carried out. Normally, there is a straight segment at the beginning and at the end. The nearest available radius of curvature can be reasonably assigned to these points. Then each point has a radius of curvature and a curve of the ratio of radius of curvature to channel width (R/W) versus channel lengthwise distance can be drawn. If *m* is not an odd number, use $m+1$ in the program.

126

It can be imagined that large spacing in redistribution can cause the curve to lose local curvature. Very small spacing, on the other hand, has not been found to cause any problem except that it takes more computing time. In cases where an optimum spacing cannot be determined, it would be conservative to pick a small number. In here, 0.1 times the channel width ($0.1W$) is suggested if no experience is available.

Segment length directly affects the quality of the calculated curvature. If it is too short, local curvature dominates, which is sometimes drastically different from the curvature of a reasonably larger range. If it is too long, global curvature dominates and some local curvature may be lost. Then the radius of curvature of an inflection point might be only several times larger than that of other points, although theoretically it should be infinity. The following discussion will show that the major function of the R/W vs. channel length curve is to help identify the approximate range of a bend. A good choice of segment length should make the bends stand out on the R/W curve.

The case of Guadalupe River, Texas, is used for demonstration. The coordinates of a section of the river are processed using the procedures described above. The corresponding average river width is 37.7 m (124.4 feet). As can be seen in Figure 7.6, when segment length is too short ($1.1W$), it is hard to tell where the bends are. Figure 7.8 shows that when segment length is very long ($12.1W$) the R/W vs. channel length curve is much smoother and flatter, but the individual bends are still recognizable. Figure 7.7 is the result of using an appropriate segment length of $4.0W$. Comparing this chart with the original bank geometry shown in Figure 7.15, it can be observed that each significant bend is represented by an arc-shaped curve segment of different size. Therefore, a relatively large segment length can be chosen when not enough knowledge is available for making a decision. Here, $4.0W$ is suggested.

In these figures, MBL stands for minimum bend length, which means that only when the identified bend is longer than MBL will it be considered as a bend.
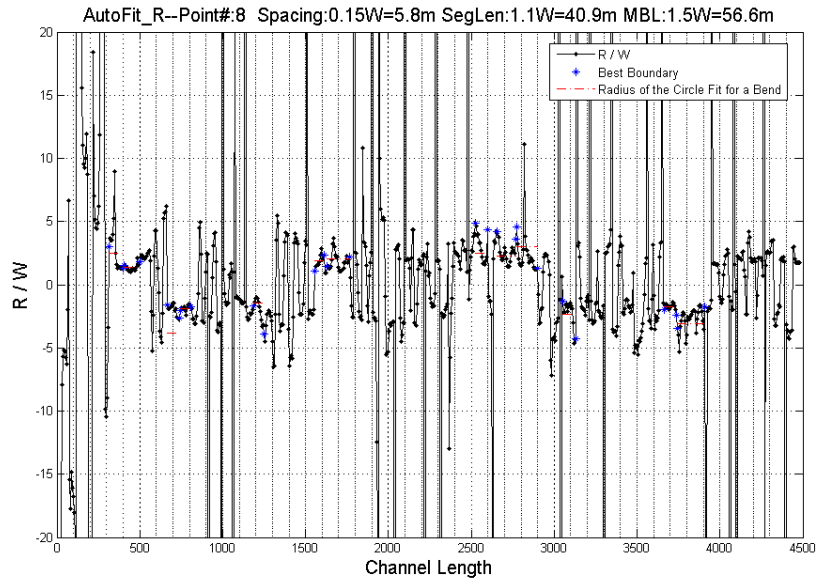
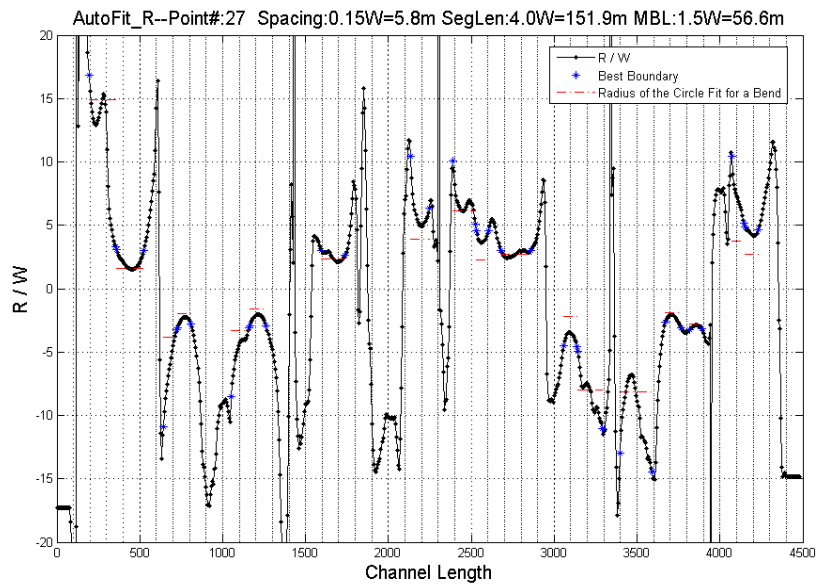**Figure 7.6.** *R/W* **vs. Channel Length, Segment Length = 1.1***W***.**

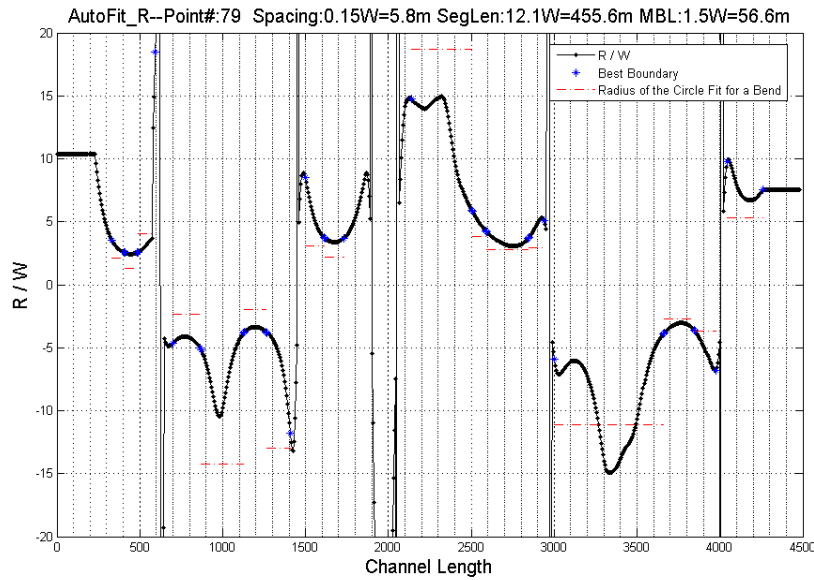**Figure 7.7.** *R/W* **vs. Channel Length, Segment Length = 4.0***W***.**

Figure 7.8. *R*/*W* **vs. Channel Length, Segment Length = 12.1***W*.

7.3 IDENTIFY BENDS FOR WHICH CIRCLES WILL BE FITTED

It is easy for human eyes to tell whether a curve segment is curvy or straight. A computer cannot "see" things this way. Mathematical features about the curve need to be discovered and criteria need to be developed for the computer to make a judgment based on simple logic.

The *R*/*W* vs. channel length curve shows clear features which are related to the bends on the original bank. It is desired to fit circles for those bends. The choice of the portion of a bend for fitting the circle is critical. Before pinpointing the exact segments for fitting those circles, the approximate ranges of the bell-shaped curves need to be identified. Three methods are described below.

7.3.1 Manual Method with AutoCAD

The user directly specifies the region of a bend in AutoCAD. In the early stage of developing this method, it was first thought that the bank needed to be fitted with circles only. Later, the research team decided to do curve fitting for each time step to take into account the importance of geometry. This method was abandoned because the work needs to be repeated thousands of times for a long hydrograph. A human being is not capable of this.
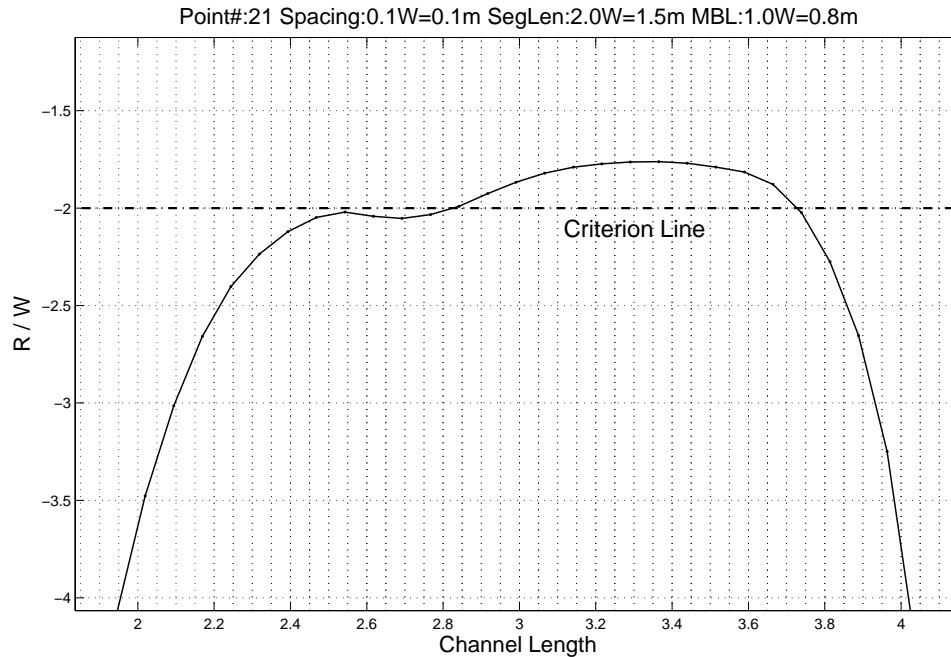
Figure 7.9. Case Showing Sensitivity of Criterion Lines.

7.3.2 Criterion Line Method

The R vs. length curve for an arc is a horizontal line. When a bend on a bank can be reasonably fitted with a circle, its radius of curvature vs. length curve is smooth and of bell shape. The closer the bend is to an arc, the closer the bell-shaped curve is to a horizontal line. Therefore, if a curve segment is found to be of bell shape facing up or down, it most likely corresponds to an obvious bend on the river bank. This method uses three criterion lines (six symmetric lines, as a matter of fact) to identify the bell-shaped segments on the R/W vs. length curve. As shown in Figure 7.10, six lines of $R/W = \pm3, \pm5, \pm8$ were drawn on the graph. In the first loop, all continuous segments between $R/W = 0$ and $R/W = \pm3$ were identified. These segments should be of bell shape and indicate the existence of bends. These segments were marked so that they would not be looked at again in the next loop. In the second loop, the continuous segments left between $R/W = 0$ and $R/W = \pm5$ were identified. This procedure was repeated for $R/W = \pm8$. For each loop there might be new bends identified. The outcome is sometimes very sensitive to the choice of these criterion lines. Figure 7.9 shows a tiny change in the criterion line could lead to quite different result. What is shown is the R/W vs. length curve of a well-behaved bend. But the criterion line of $R/W = -2$ divides it into two arcs, which would cause a problem. If $R/W = -2.2$, this problem can be avoided. So far no method has been developed to decide on the appropriate

numbers. In order to guarantee the inclusion of the desired boundary, the range should be extended by a certain percentage of the bend length.
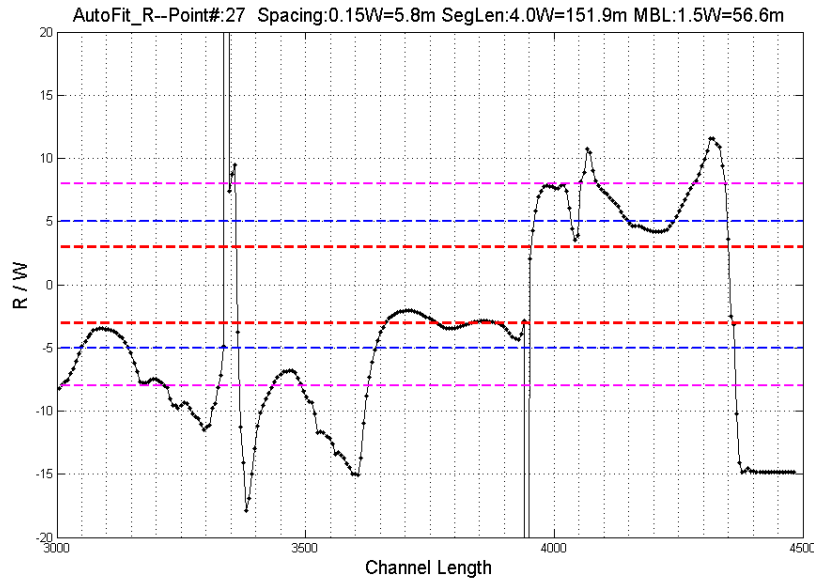

Figure 7.10. Criterion Line Method.

7.3.3 Second Derivative Method

This method identifies the bends by using the curve d^2R/ds^2 vs. channel length, as shown in Figure 7.11. A continuous segment very close to the x axis is considered as a bend. The logic behind this method is that for each bend, the R vs. channel length curve segment is of parabolic shape (bell shape). In parabolic equation $y = ax^2 + bx + c$, 'a' value is extremely small for these curves. So d^2R/ds^2 value is close to 0. The range obtained this way also needs to be extended. When two bends of different radius are right next to each other, this method will fail because there is almost no change in d^2R/ds^2 at the intersection point.
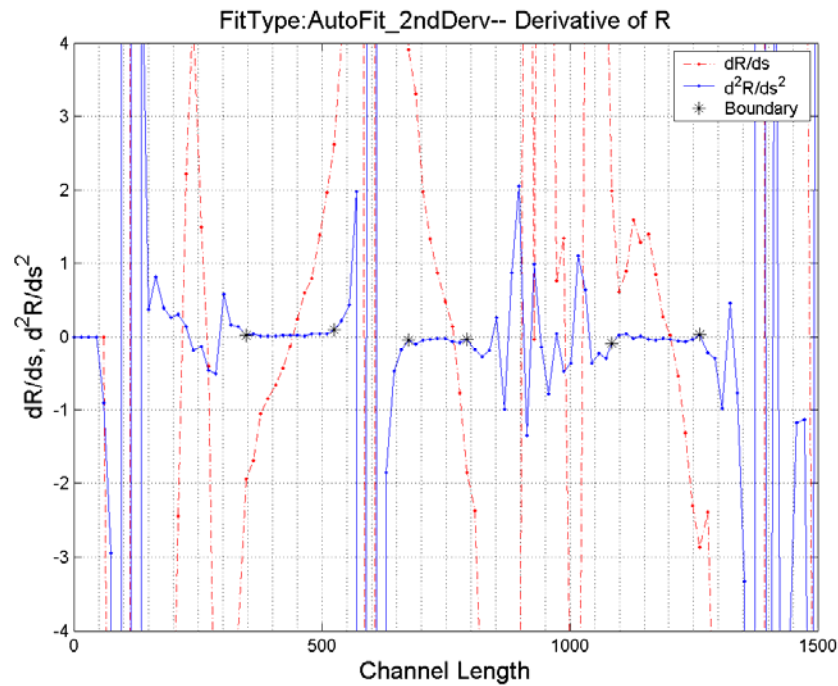
131

Figure 7.11. The Second Derivative of *R* vs. Channel Length.

7.3.4 Change of Sign Method

The initial channel of the flume tests consists of tangent perfect arcs, while the migrated channels can be fitted with tangent arcs. On the *R/W* versus channel length curve, large values occur once or twice around the inflection point. The change of sign can clearly indicate the separation of bends. This method is applicable only when the bends are tangent to each other.

All methods can produce good results in this case. The criterion line method is suggested for its efficiency. The identified range is a two-point boundary. A circle can be fitted to these points. But there is no guarantee that this circle fits the bend best. Further work is needed to pick the best one.

7.4 FIND THE BEST FIT CIRCLE AT A CERTAIN BEND

7.4.1 Producing a Set of Circles for Making a Choice

For a certain bend, dozens of circles can be fitted by using different curve segments. Among them, only one or a few circles really fit the bend. Any of these good circles is called the best fit

132

circle. The arc segment of a best fit circle is supposed to ideally represent the geometry of the bend. To achieve this goal, one should be able to identify which circle is the best before asking the computer to make the same decision. Due to the indistinct boundaries of the bend, there is not an easy formula ready that can tell which circle is the best. Before a sound criterion is established, human vision provides the only judgment whether a fit is good or not. The criteria to be developed will match the visual judgment so that a computer can come up with the same or very close result. It is possible that different people would select different best circles. But it was found that in general people give surprisingly close if not the same estimation about the global closeness between a fitted circle and the original bend.

In Figure 7.12, four out of many circles for that bend were picked for comparison. Circle (a) is a very close fitting regarding the segment used. But only a portion of the bend is used for fitting. It does not reflect the global geometry feature of the bend. Circle (d) reflects more global features but the closeness is not good. Circles (b) and (c) maintain a good balance between bend coverage and closeness. The two circles are so close that it is hard to tell which one is better than the other. Since they are identified using human vision, either one of these two can be called the visually best circle.
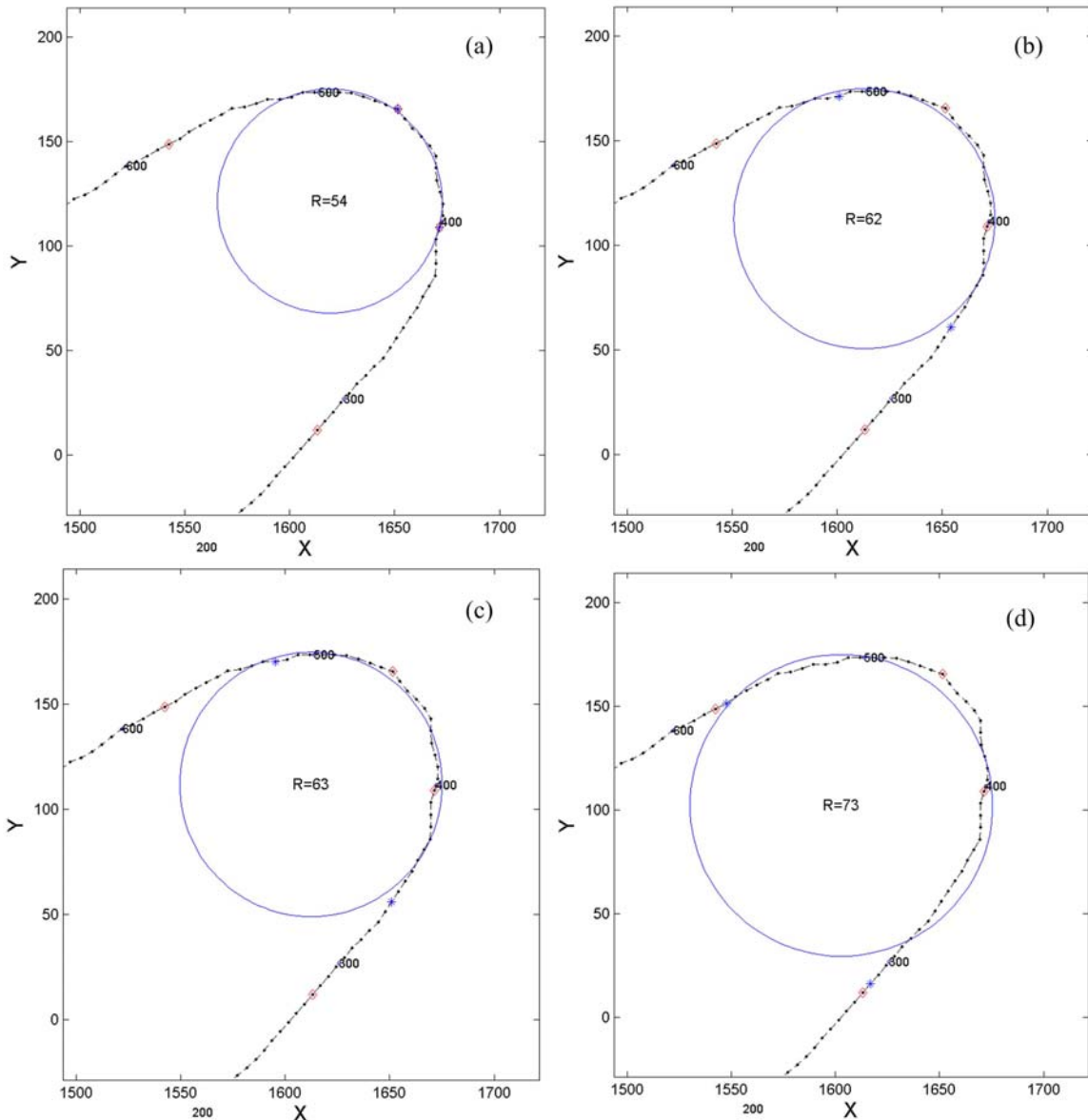
Figure 7.12. Visual Comparison of Fittings.

Figure 7.13 is the *R/W* vs. length curve for the bend shown in Figure 7.12. It helps explain how the set of circles for the bend were obtained. Point A and B were identified by the Criterion Line Method. Then they were extended in both directions by a certain percentage of curve length AB and with the condition that *R/W* should not be larger than 10. Thus, point A was extended to the region from C to E, in which the first correct boundary point was supposed to fall. The second correct boundary point would fall in the region from D to F. The next step was to pick one point from each region and fit a circle. There are 15 points from C to E and 14 points from D to F. So there are 15 × 14 = 210 circles which must include the best fit circle. The *R/W* vs. length curve is almost symmetric to the vertical line passing the lowest point, which indicates the bend can also

134

be symmetric to the point corresponding to the lowest point in Figure 7.13. In the process of producing the set of circles, it is reasonable to pick approximately symmetric points. By starting from point C and D and moving up one point on each side one time, only 15 circles were produced. The computing time was thus greatly shortened without compromising the precision.
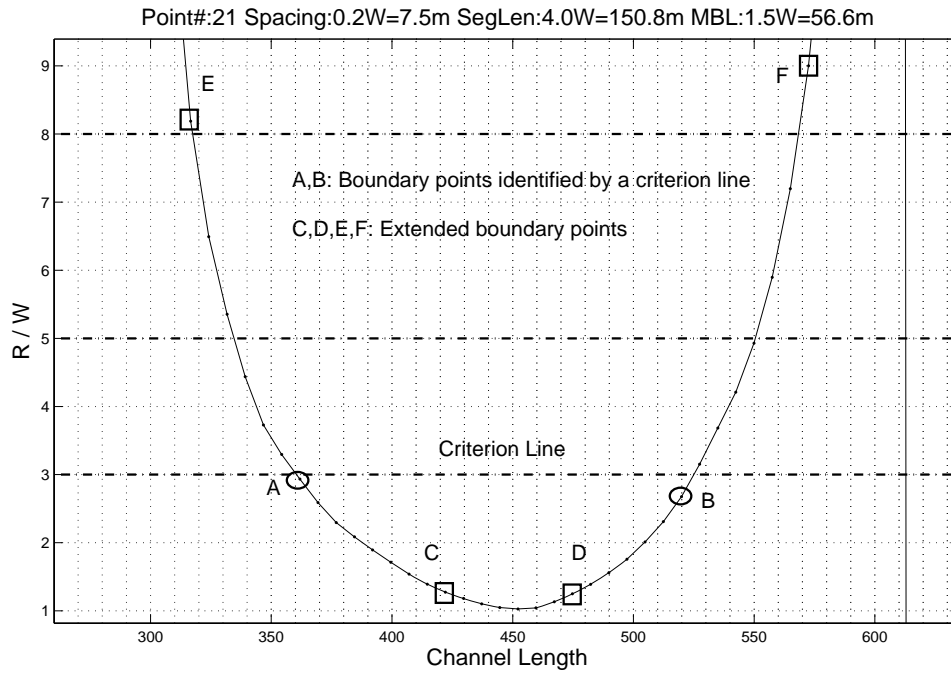

Figure 7.13. Extension of Bend Boundaries.

Finding the best fit circle is the ultimate goal of the geometry study. The challenge is how to numerically describe the visually best circles so that they can be identified by a computer. Several methods have been developed for this goal.

7.4.2 Least Square Error Method

The first method is to make a judgment based on least square error. The most common error term is:

$$ER = \sqrt{\frac{\sum (R^* - R_i)^2}{n}} \tag{7.29}$$

135

where R^* is the radius of the fitted circle, R_i the distance between the center of the fitted circle, and n the number of points used to fit the circle, which is also a measure of bend angle. This error term always tends to pick the shortest possible segment, very likely segments of three points. A circle like the one in Figure 7.12(a) or smaller ones is very likely to be selected. An ideal circle should have a small error (high degree of closeness) and a large n value (for accommodating global geometric features of the bend). The smaller the error is and the larger n value is, the better the circle will be. However, there is a tradeoff between small error and large n value. That is to say if the n value is increased, the error increases accordingly. The degree of closeness should be well balanced against the n value so that a good circle can be produced. Equation 7.29 is not a well-balanced expression, where too much weight is given to the error value. By considering giving some weight to n, this error term is generated:

$$ER = \sqrt{\frac{\sum (R^* - R_i)^2}{n^\alpha}}, \ \alpha > 1 \tag{7.30}$$

If this error term works, there is an optimum α value associated with each bend, and it may vary with bends. Unfortunately, in many cases no α value is available that could produce a best fit circle.

7.4.3 Criterion Line Method

The second method is to use the criterion lines. As described in previous section, three well-placed criterion lines can help identify most of the bends. In some cases good circles can be fitted to the identified bends. The good results normally come from trial and error. A criterion line good for this river may not be suitable for the next river or for the next migrated river. Right now there is no way to calculate the right criterion lines for a river. If this method has to be used, the criterion lines are chosen based on experience and applied to migrating channels. A popular R/W range is from 3 to 8.

7.4.4 Second Derivative Method

The third method is to apply the d^2R/ds^2 vs. channel length curve to identify the exact boundaries. Similar to the Criterion Line Method, this method can identify both the region of the bend and the boundaries for best fit circle. In Figure 7.11, the second derivative of R is close to the x axis for a bend. At the two ends of the bend, the second derivative does not change gradually. There is a sudden jump. The inflection points here happen to be the boundary points

that are looked for. The way to find these segments is the same as using criterion lines. But the criterion lines here have fixed values that are good for most rivers. Two criterion lines are set with $d^2R/ds^2 = 0.3$ and $d^2R/ds^2 = 0.8$. This method works well for the case shown in Figure 7.11. The inherent drawbacks would make it fail for other cases. When the channel curve is not smooth, d^2R/ds^2 fluctuates, causing the result to be unreliable. When two bends of different radius are next to each other or are very close, the method can hardly tell which is which.

7.4.5 Balanced Method

The fourth method is to balance the least error against bend angle with a numerical expression. The expression is:

$$\alpha = \frac{1}{\varphi} + b\sqrt{\frac{\sum_{i=1}^{n}(R_i - R^*)^2}{n}} \, / R^* \qquad (7.31)$$

where, α is the target term, φ the bend angle, R_i the distance between point i and the center, R^* the radius of the fitted circle, n is the number of points used to fit the circle, and b is an empirical coefficient.

In Equation 7.31, α is a combination of the bend angle term and the term of fitting error. The larger the bend angle φ is, the smaller α is; the smaller the fitting error is, the smaller α is. The circle with the smallest α will be treated by Equation 7.31 as the best circle and can be called the numerically best circle. The coefficient b plays a critical role in balancing bend angle and fitting error. A good choice of b would make the numerically best circle the same or very close to the visually best circle.

Figure 7.14 are graphs for the relationship between α value and R. Different b values make the minimum α value to occur at different R. According to visual observation of Figure 7.12 and additional graphs, there are several best fitting circles. The range of radius is from 61 to 64. The b values that make the minimum α value fall in this range are the values being looked for. For this bend, $b = 30$ and $b = 50$ make this happen. If Equation 7.31 does work at some bends, the best b value will differ from bend to bend. So far no other properties of the bend have been associated with the best b values. The determination of b is empirical at this stage. It was found that $b = 100$ gives a relatively good result for many cases. In Figure 7.14, $b = 100$ produces a result of $R = 54$ ($R/W = 54/37.7 = 1.4$). The ideal R/W is $62/37.7 = 1.6$. The difference in R/W

ratio is (1.6 − 1.4)/1.6 = 12.5 percent. For some bends, either term of α or α itself has more than one value corresponding to a single *R*. Although this makes it hard to find the minimum value, the outcome is acceptable. This situation can be avoided by using the ordinal number of the circles as the abscissa. Further work still needs to be done to optimize the solution.
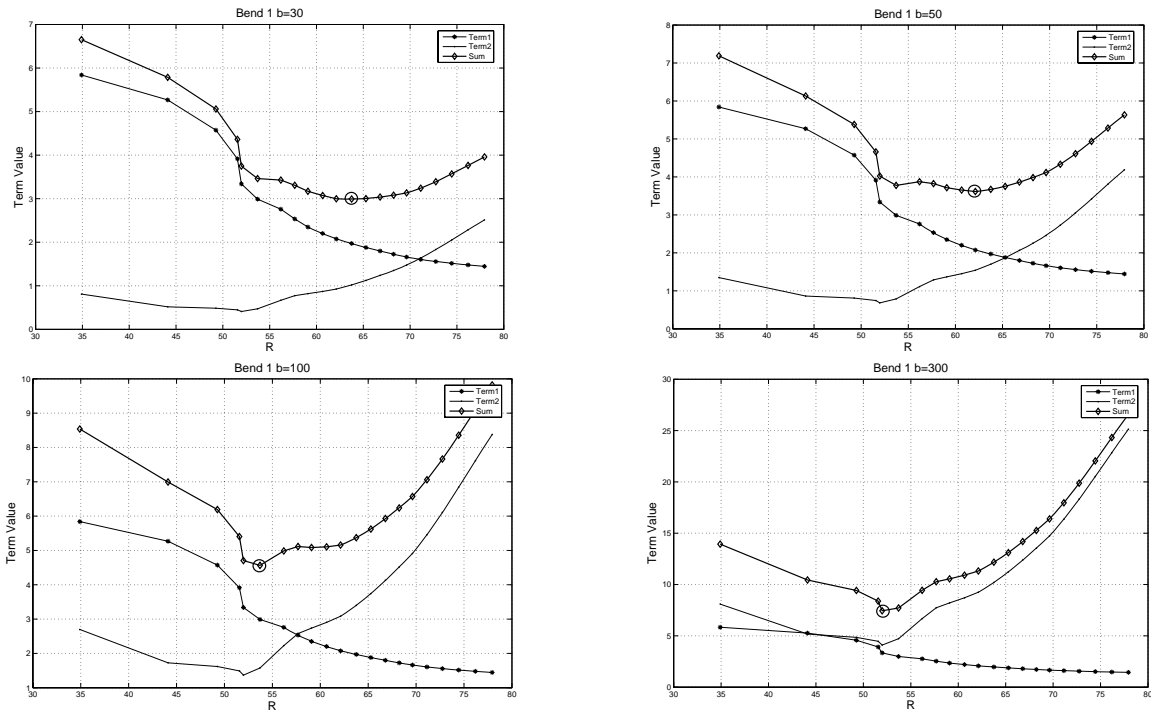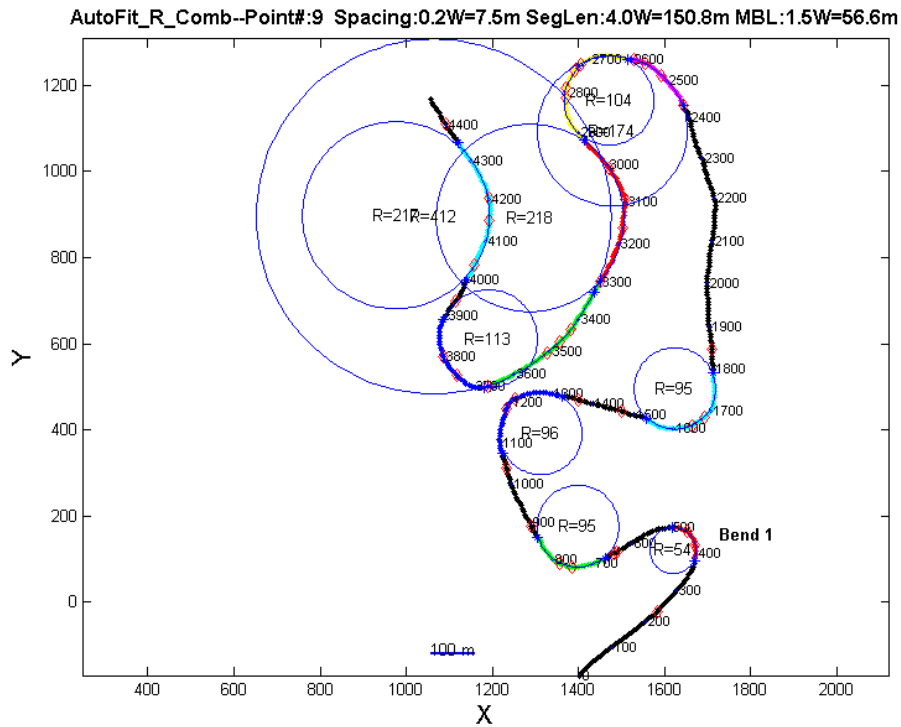

Figure 7.14. Influence of Parameter b.

Figure 7.15. Same *b* Coefficient Applied to All Bends.

7.5 CALCULATE BEND ANGLE

When the best fit circle is available, the bend angle can be calculated based on the two boundary points and the center of the circle. In some cases, the bend angle calculated based on the two straight lines connected with the bend looks more appropriate. The former method was used in the program.

CHAPTER 8. RISK ANALYSIS

8.1 INTRODUCTION

A meander migrates at a rate controlled by the erosion rate of the soil at the interface between the water and the bank. The hydraulic shear stress imposed by the water is controlled by the velocity of the flow, which is dependent on the hydrograph of the river. A meander migration prediction process must therefore consider the hydrograph of the river. This hydrograph is not known because it will occur in the future during the design life of the bridge or of the highway embankment. Because it is not realistic to make a deterministic prediction of a future hydrograph, it is more desirable to make predictions of many equally possible hydrographs in a probabilistic manner. Each hydrograph then moves the river toward a predicted position of the meander and a probabilistic post-process provides a probability that the river will move to a given location at a given time.

8.2 FUTURE HYDROGRAPH

8.2.1 Distribution of Daily Discharge

In order to extract the statistical properties of an existing hydrograph, the type of distribution of the hydrograph should be determined first. It has been observed that a hydrograph fits reasonably well a lognormal distribution. Figure 8.1 is the hydrograph of the Guadalupe River gauge station 08176500 at Victoria, Texas, from December 1, 1934, to September 30, 2002. Figure 8.2 is the probability density function (PDF) of the original data and fitted distribution. Figure 8.3 is the cumulative density function (CDF) of the original data and fitted distribution. These curves show that the daily discharge data can be roughly considered as a log-normally distributed random variable.
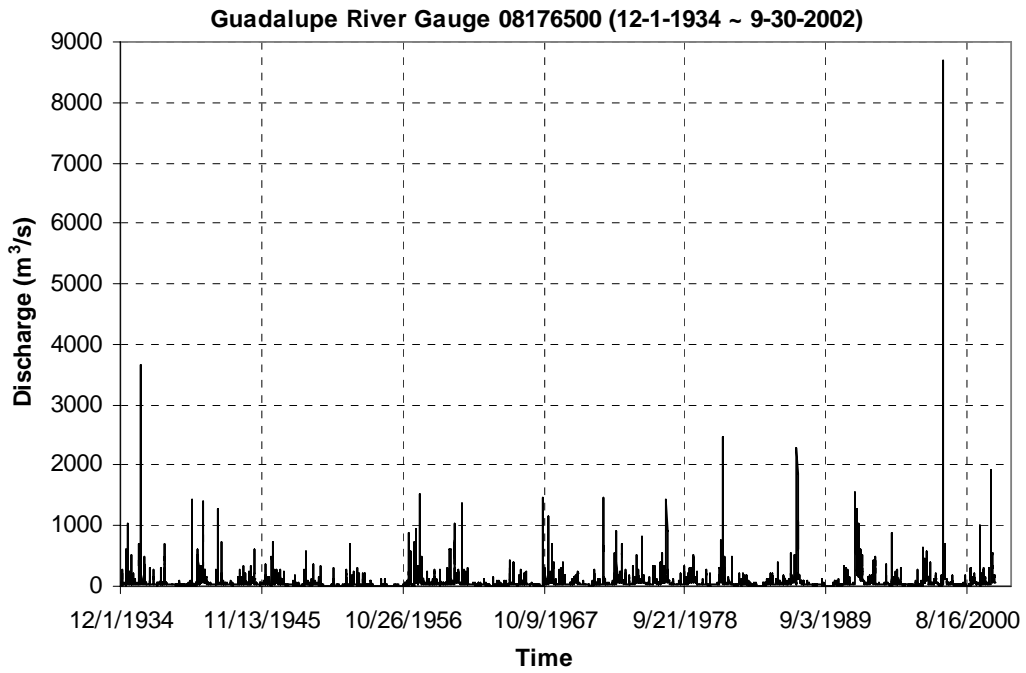
Figure 8.1. Hydrograph of Guadalupe River Gauge Station 08176500.
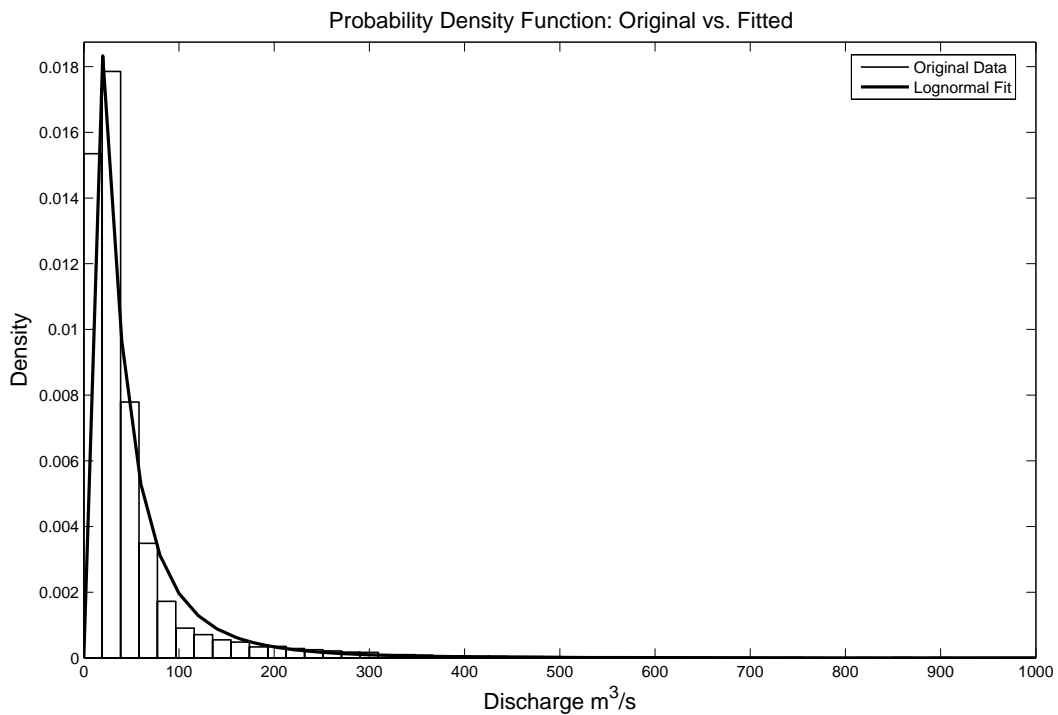
Figure 8.2. PDF of Original Data and Fitted Distribution – Guadalupe River.

142
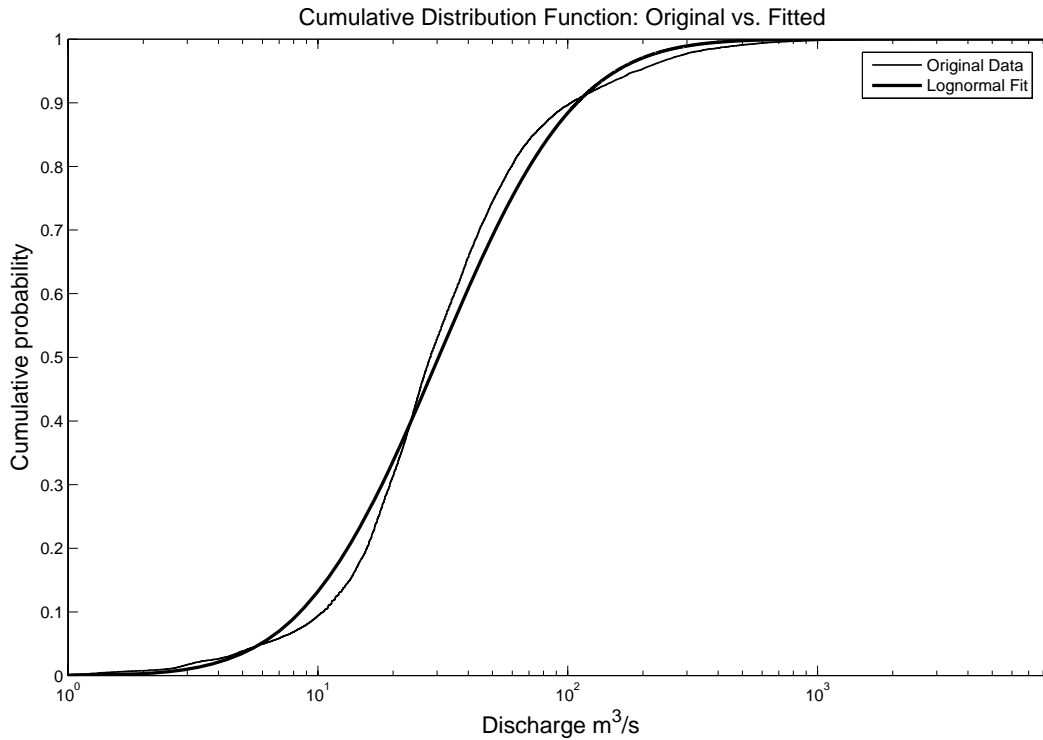
Figure 8.3. CDF of Original Data and Fitted Distribution – Guadalupe River.

Figure 8.4 is the hydrograph from the Potomac River near Washington D.C. Little Falls Pump Station, U.S. Geological Survey (USGS) gage number 01646500. In order to consider the discharge through the Woodrow Wilson Bridge not far downstream, the original flow rate was multiplied by 1.03. The recorded daily flow is from March 1, 1930, to September 30, 2003. Figures 8.5 and 8.6 demonstrate that log-normal distribution fits these data better than the Guadalupe River.
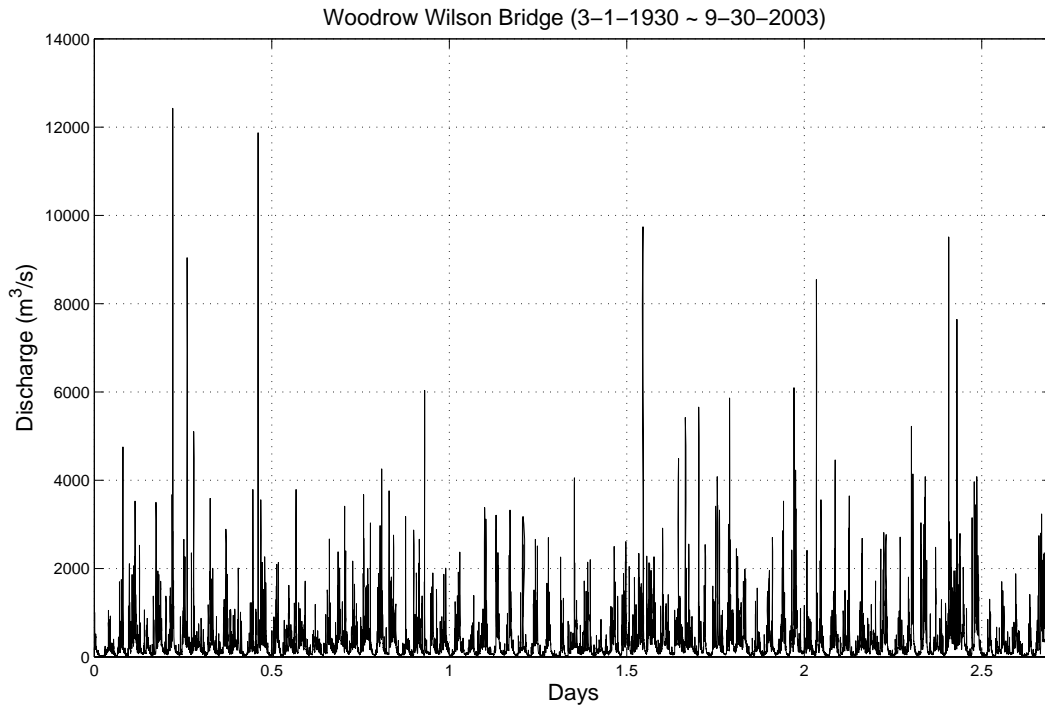
Figure 8.4. Hydrograph of Woodrow Wilson Bridge.
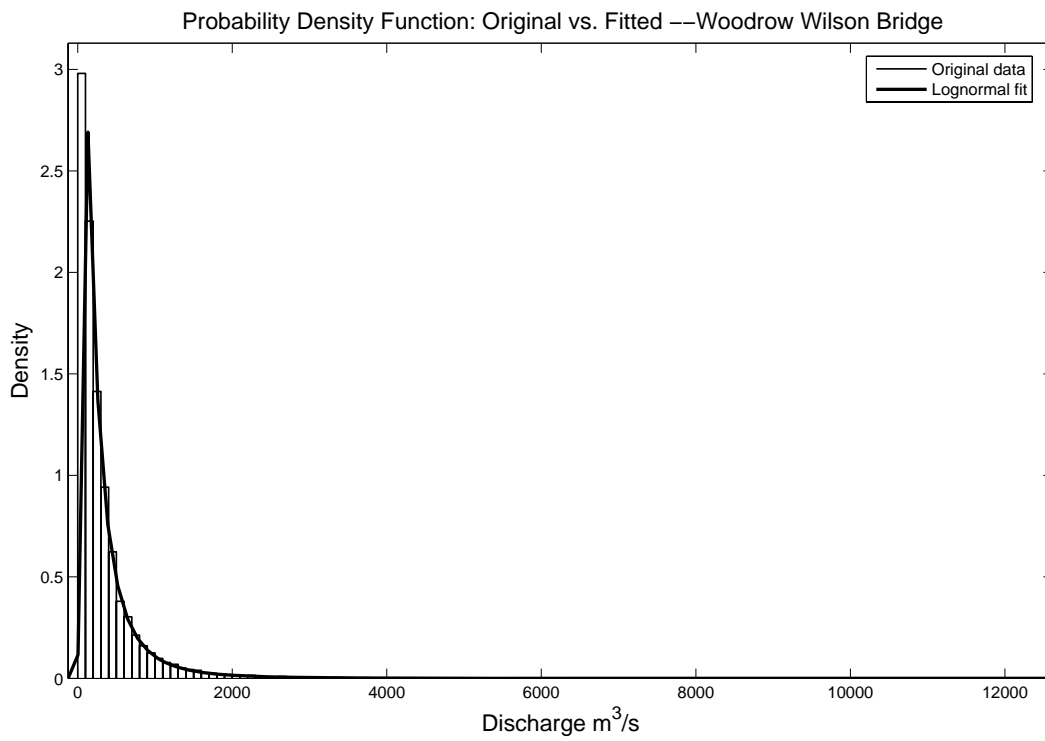
Figure 8.5. PDF of Original Data and Fitted Distribution - Woodrow Wilson Bridge.

144
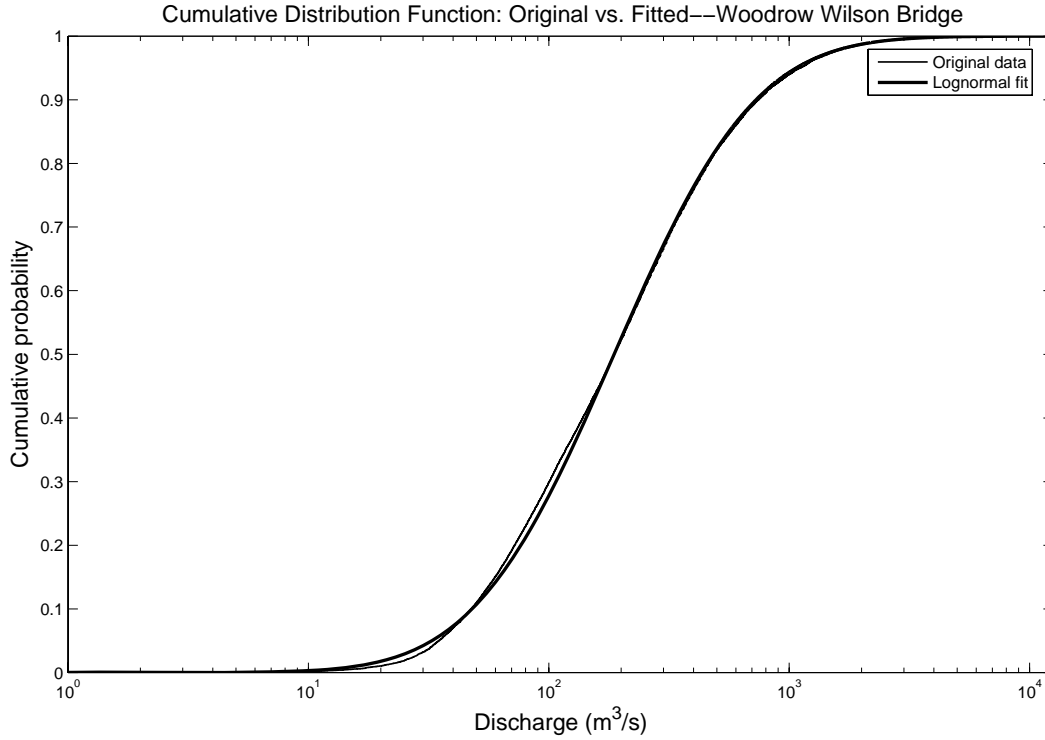
Figure 8.6. CDF of Original Data and Fitted Distribution - Woodrow Wilson Bridge.

Assume Y is a normal random variable. Then $Q = e^Y$ has a lognormal distribution. The probability density function of Q, the flow rate, is:

$$f(Q\,|\,\mu,\ \sigma) = \frac{1}{Q\sigma\sqrt{2\pi}} e^{\frac{-(\ln Q - \mu)^2}{2\sigma^2}} \tag{8.1}$$

Where μ, σ are the mean and standard deviation of Y, the normal random variable. Let m, s be the mean and standard deviation of Q, the lognormal random variable. The following formulas can be derived:

$$m = e^{\mu + \frac{\sigma^2}{2}} \tag{8.2}$$

$$s = e^{\mu + \frac{\sigma^2}{2}} \sqrt{e^{\sigma^2} - 1} \tag{8.3}$$

$$\mu = \ln\left(\frac{m^2}{\sqrt{m^2 + s^2}}\right) \tag{8.4}$$

145

$$\sigma = \sqrt{\ln\left(\left(\frac{s}{m}\right)^2 + 1\right)} \qquad (8.5)$$

The lognormal fitting is performed using Matlab version 7.0.1. The fitted means and standard deviations of the normal random variable Y and lognormal random variable Q for both cases are listed in Table 8.1. For a confidence level of 99%, the ranges of these two parameters for Guadalupe River are:

$$\mu_Y \in [3.399, 3.432], \; \sigma_Y \in [0.982, 1.008]$$

The ranges for Woodrow Wilson Bridge are:

$$\mu_Y \in [5.214, 5.248], \; \sigma_Y \in [1.049, 1.073]$$

This shows that the fitting criteria are well met. Table 8.1 shows a detailed comparison of the mean and standard deviation of the original data and fitted distribution for these two cases.

Table 8.1. Comparison of Statistical Parameters (Unit: m³/s).

	Guadalupe River		Woodrow Wilson Bridge	
	Original Data	Fitted Distribution	Original Data	Fitted Distribution
μ_Y	3.087	3.415	5.244	5.231
σ_Y	1.358	0.996	1.057	1.061
m_Q	55.1	49.9	331.330	328.255
s_Q	*127.2*	*65.1*	475.347	473.746

μ_Y and σ_Y are the mean and standard deviation for the normal variable Y. m_Q and s_Q are the mean and standard deviation for the lognormal variable Q. m_Q and s_Q for the original data are calculated using standard formulas. μ_Y and σ_Y for the original data are calculated using Equations 8.4 and 8.5. The difference of standard deviation s_Q for Guadalupe River is about 50 percent and for Woodrow Wilson Bridge is about 0.3 percent. The hydrograph of Woodrow Wilson Bridge is closer to a lognormal distribution. The fitted parameters for Guadalupe River should be used with caution. The fitting results show that not all hydrographs fit a lognormal distribution. The compromise on the good fit is compensated by the simplicity of the process. The MEANDER program uses m_Q and s_Q for the original data to generate future hydrographs.

8.2.2 Definition of the 100/500-Year Flood

The term "100-year flood" is somewhat misleading. Many people mistakenly think it is a description of the flood that occurs once every 100 years. Instead, it describes a flood elevation that has a 1 percent chance of being equaled or exceeded in any one year. Therefore, "500-year flood" is a flood elevation that has a 0.2 percent (1/500) chance of being equaled or exceeded in any one year. To calculate the probability for a 100-year flood to be equaled or exceeded within a certain period of time, say N years, this formula can be used:

$$p = 1 - (1 - 1/100)^N \tag{8.6}$$

$(1 - 1/100)$ is the probability for a 100-year flood not to occur in one year. $(1 - 1/100)^N$ is the probability for a 100-year flood not to occur in N years. So $p = 1 - (1 - 1/100)^N$ is the probability for a 100-year flood to be equaled or exceeded in N years. The design life of a new bridge is about 75 years, during which the probability for a 100-year flood to occur is $p = 52.9$ percent. If $N = 100$ years, $p = 63.4$ percent.

What is the probability for a 100-year flood to be equaled or exceeded in one day? Assume one year has 365 days. Let p_x denote the unknown. This problem can be solved using Equation 8.6. The probability for the flood to be equaled or exceeded in one day is p_x. The probability for a 100-year flood to be equaled or exceeded in 365 days (one year) is 1/100. The equation can be written as:

$$1/100 = 1 - (1 - p_x)^{365} \tag{8.7}$$

The solution is $p_x = (1/100) \times (1/363.2)$, very close to $(1/100) \times (1/365)$. The probability for a 500-year flood to occur in one day is $p_x = (1/500) \times (1/364.6)$, very close to $(1/500) \times (1/365)$. With this comparison in mind, the approximate values can be used.

8.2.3 Compute Discharge Distribution Based on 100/500-Year Flood

If an existing hydrograph is given, the distribution of daily discharge can be obtained by two methods. One is to do a lognormal fitting and obtain the parameters of mean and standard deviation. The other is to calculate the mean and standard deviation of the hydrograph with the assumption that it follows a lognormal distribution. The latter is used for simplicity and reasonable precision.

In some other cases a hydrograph is not available and only 100-year flood and 500-year flood are provided. The lognormal distribution (μ, σ) needs to be solved based on this information. The two corresponding probabilities of exceedance for a 100-year flood and a 500-year flood have been given in the previous section. For the CDF equation of an analytical lognormal distribution, there are two unknowns and two equations. So the unknowns can be solved as shown below. The CDF of Q can be expressed as:

$$P(Q \le q) = F\langle q|\mu, \sigma\rangle = \frac{1}{\sigma\sqrt{2\pi}}\int_0^q \frac{1}{t}e^{\frac{-(\ln t-\mu)^2}{2\sigma^2}}dt = \frac{1}{\sqrt{2\pi}}\int_0^q e^{-(\frac{\ln t-\mu}{\sqrt{2}\sigma})^2}d(\frac{\ln t-\mu}{\sqrt{2}\sigma})\sqrt{2}$$
$$= \frac{1}{\sqrt{\pi}}\int_{-\infty}^{\frac{\ln q-\mu}{\sqrt{2}\sigma}}e^{-z^2}dz = \frac{1}{2}+\frac{1}{2}erf(\frac{\ln q-\mu}{\sqrt{2}\sigma})$$

(8.8)

The term *erf* indicates the error function. The definition of the error function and inverse error function is as follows:

$$y = erf(x) = \frac{2}{\sqrt{\pi}}\int_0^x e^{-t^2}dt \quad (-\infty < x < +\infty)$$

(8.9)

$$erf(-\infty) = -1, \; erf(\infty) = 1$$

(8.10)

The inverse error function is:

$$x = erf[inv(y)]\cdots(-1 < y < 1)$$

(8.11)

Thus, the cumulative distribution function of a lognormal distribution can be written as:

$$erf[inv(2P-1)] = \frac{\ln q-\mu}{\sqrt{2}\sigma}$$

(8.12)

There are two applications for this formula:
1. Given the distribution (μ, σ) and the probabilities, $P_1(Q \le q_1)$ and $P_2(Q \le q_2)$, the corresponding discharges q_1 and q_2 can be found. This can be used to find Q_{100} and Q_{500}, which will be discussed in the next section.
2. Given two points (q_1, P_1), (q_2, P_2) on the CDF curve, the lognormal distribution (μ, σ) can be solved. Here (Q_{100}, P_{100}), (Q_{500}, P_{500}) are given. The data of the distribution are

148

daily average discharge. The CDF curve based on these data gives the probability for a certain level of discharge not to be exceeded in one day. It makes more sense to use the probability for a 100-year flood (500-year flood) to occur in one day instead of one year. So in the above equations:

$$P_{100} = 1 - (1/100) \times (1/365), \quad P_{500} = 1 - (1/500) \times (1/365)$$

Define:

$$u_{100} = \frac{\ln Q_{100} - \mu}{\sigma} = \sqrt{2} \times erf[inv(2P_{100} - 1)] = 4.03417 \qquad (8.13)$$

Likewise,

$$u_{500} = \frac{\ln Q_{500} - \mu}{\sigma} = \sqrt{2} \times erf[inv(2P_{500} - 1)] = 4.39733 \qquad (8.14)$$

The inverse error function can be solved using any pertinent numeric recipe or Matlab.

$$\sigma = \frac{1}{u_{500} - u_{100}} \ln(\frac{Q_{500}}{Q_{100}}) \qquad (8.15)$$

$$\mu = \ln(Q_{100}) - u_{100} \cdot \sigma \qquad (8.16)$$

Once the mean and standard deviation of the normal variate Y are obtained, the lognormal random variable is determined to be $Q = e^Y$.

8.2.4 Determination of 100-Year Flood and 500-Year Flood

The determination of the 100-year flood and 500-year flood can be based on an existing hydrograph which contains sufficient data. The more data are available, the more accurate the result will be.

Continuous PDF and CDF curves for a hydrograph can be drawn as shown in Figure 8.2 and Figure 8.3. The probability of exceedance curve, which is also called survivor function, is obtained by subtracting CDF from 1, as shown in Figure 8.7. A point (Q, P_Q) means the probability for discharge Q to be equaled or exceeded during a unit of time is P_Q. The unit of

time is the duration of a single Q value. If Q is daily average discharge, the unit of time is one day. The probability for a 100-year flood to be equaled or exceeded in one day is $1/(100 \times 365)$, and the probability for a 500-year flood to be equaled or exceeded in one day is $1/(500 \times 365)$. On an ideal daily flow probability of exceedance curve, the corresponding discharges Q_{100}, Q_{500} are the unknown to be calculated.

A probability of exceedance curve can come from a hydrograph and can also be determined by a given distribution (μ, σ). Lognormal fitting generates μ and σ. The original data also have μ and σ, which are normally different from the fitted results. Figure 8.7 shows these three probability of exceedance curves of Guadalupe River. Any point on the curve of the original data denotes a concept of percentile rather than probability since everything has happened. The other two curves predict the probability for the occurrence of a certain event. Thus, two sets of 100/500-year flood can be obtained and compared.
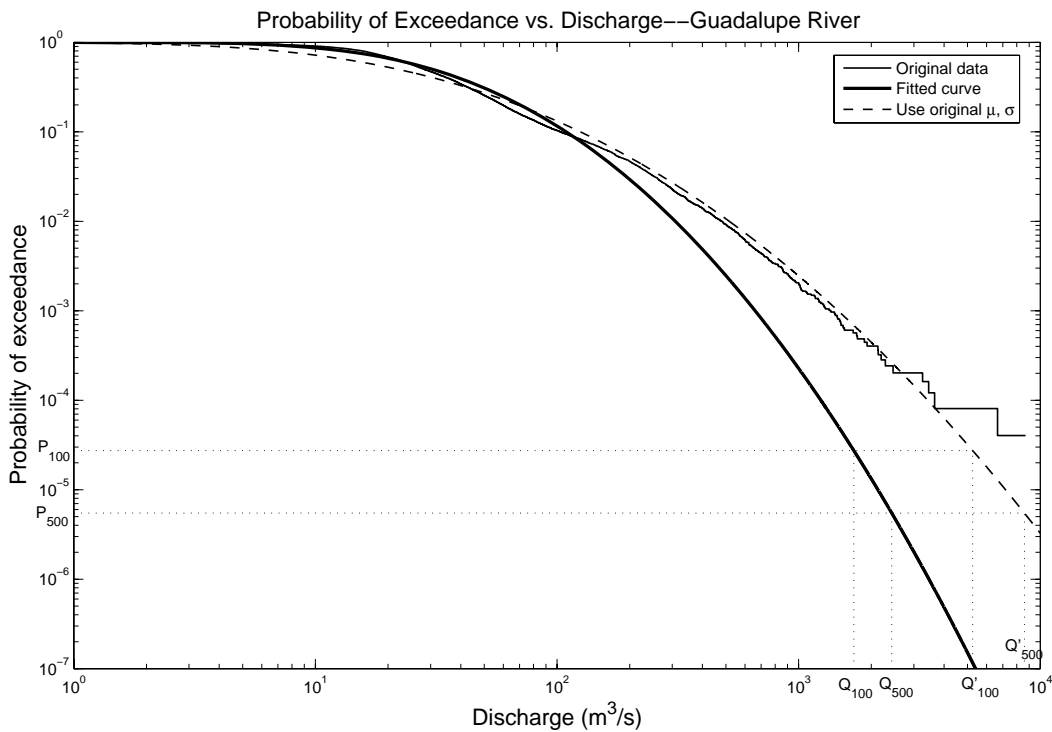
Figure 8.7. Probability of Exceedance Curves - Guadalupe River.

For the hydrograph of Guadalupe River gage station 08176500, if the fitted distribution is used, the 100-year flood and 500-year flood are found to be:

$$Q_{100} = 1692 \text{ m}^3/\text{s}, \ Q_{500} = 2429 \text{ m}^3/\text{s}$$

150

If the lognormal distribution based on the original μ and σ is used, the 100-year flood and 500-year flood are:

$$Q'_{100} = 5251 \text{ m}^3/\text{s}, \ Q'_{500} = 8601 \text{ m}^3/\text{s}$$

The maximum recorded discharge is 8693 m^3/s. According to the fitted curve, the probability for this flow to be equaled or exceeded is $6.8 \times 10^{-9} = (1/400,782) \times (1/365)$, which is a 400,782-year flood. According to the distribution based on the original μ and σ, the probability for the maximum recorded discharge to be equaled or exceeded is $5.3 \times 10^{-6} = (1/518) \times (1/365)$, which is a 518-year flood. It can be seen in Figure 8.7 the curve based on the original μ and σ fits the data record much better when the discharge is larger than 200 m^3/s. Its Q_{100} and Q_{500} are more reasonable.
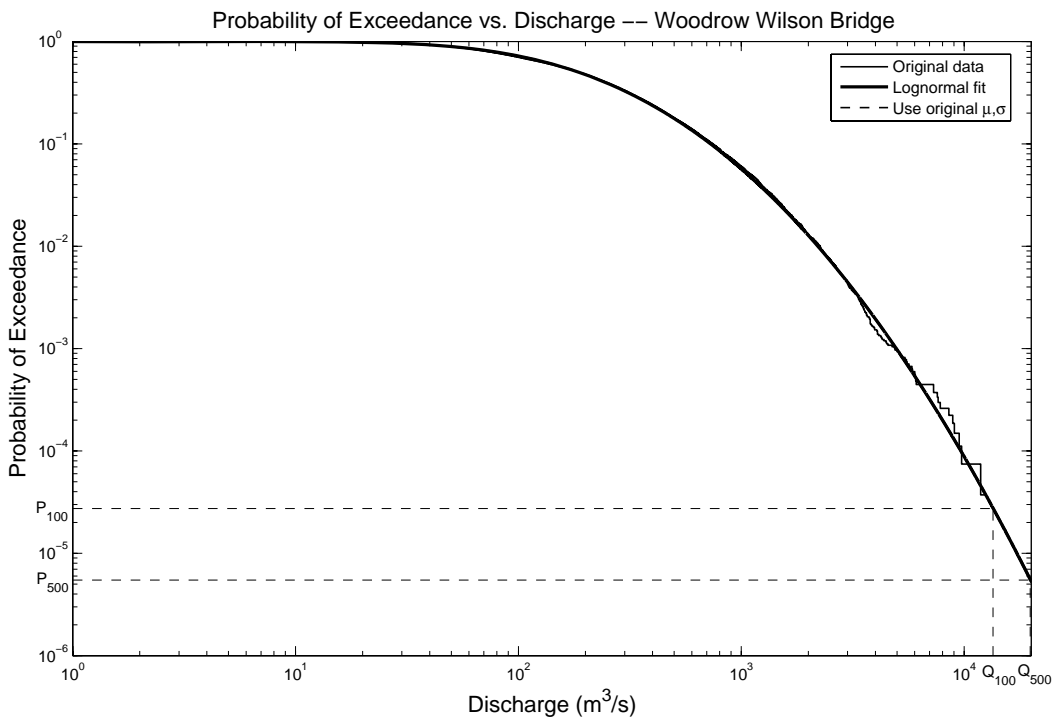
Figure 8.8. Probability of Exceedance Curves – Woodrow Wilson Bridge.

For the case of Guadalupe River the method of using fitted distribution drastically underestimates high-risk floods, which makes this method undesirable. On the hydrograph plot, the maximum flood is a single spike with a magnitude much larger than other peak floods. Spikes like this are critical in estimating 100/500-year flood of the river but are of little

151

importance to the fitting process, which treats each daily flow equally. This explains why good results were not produced by this method.

If the fitted distribution is used for the hydrograph of Woodrow Wilson Bridge, the 100-year flood and 500-year flood are found to be:

$$Q_{100} = 13,513 \text{ m}^3/\text{s}, Q_{500} = 19,865 \text{ m}^3/\text{s}$$

If the lognormal distribution based on the original μ and σ is used, the 100-year flood and 500-year flood are:

$$Q'_{100} = 13,487 \text{ m}^3/\text{s}, Q'_{500} = 19,799 \text{ m}^3/\text{s}$$

The maximum recorded discharge is 12,425 m^3/s. According to the fitted distribution, the probability for this flow to occur is $3.826 \times 10^{-5} = (1/71.6) \times (1/365)$. If the distribution based on the original μ and σ is considered, the probability for this flow to occur is $3.801 \times 10^{-5} = (1/72.1) \times (1/365)$. The closeness of this comparison can also be seen in Figure 8.8. These two curves almost overlap and they fit the original data well. This shows that this hydrograph follows closely the lognormal distribution.

8.2.5 Random Number Generation

With the analytical lognormal distribution function ready, the extraction of the statistical properties of the original data is finished. The next step is to produce future hydrographs by using a random number generation (RNG) technique.

The generation of lognormal random numbers can be a sampling process done on the CDF curve of a lognormal distribution. First, uniformly distributed random numbers in the range of 0 to 1 are generated. Then, these uniform random numbers are applied to the y axis (cumulative probability) of the CDF curve and the corresponding x values (discharge) are the random numbers to be found. An analytical solution can be obtained from Equation 8.12. Given μ, σ, and P, solve for q. This method directly solves the lognormal CDF function and can be easily understood. The drawback is that an inverse error function needs to be solved for each random number, which makes it not efficient even with high-performance computers. Alternatives have been developed to generate random numbers for a normal distribution Y. Lognormal random

numbers are simply e^Y, $e = 2.71828$. The following is a description of the methods used in this research for generating uniform random numbers and normal random numbers.

Linear congruential generators are most commonly used for generating random numbers of uniform distribution. The form is:

$$X_n = a * x_{n-1} + b \bmod M, n = 1, 2, 3\ldots, \text{given } x_0.$$

"mod M" means the right-hand side is first divided by M and then is replaced by the remainder. Let $a = 351$, $b = 42$, $M = 100$, and $x_1 = 81$. A series of random numbers can be obtained: 81, 73, 65, 57, 49, 41, 33, 25, 17, 9, 1, 93, 85, 77, 69, 61, 53, 45, 37, 29, 21, 13, 5, 97, 89, 81⋯.The random numbers start to repeat at a certain point. These numbers are in the range of [0 100]. To obtain random numbers in a given range, transformation is needed. For example, divide each of the random numbers by $M = 100$ to obtain random numbers in the range of [0 1]. Parameters a, b, and M determine the characteristics of the random number generator. The choice of x_0 determines the particular sequence of random numbers that is generated. In the MEANDER program, the values used are: $a = 663608941$, $b = 0$, and $M = 2^{32}$.

Normal random number generators are mostly based on Box-Muller transformation. Box-Muller transformation transforms a two-dimensional continuous uniform distribution into a two-dimensional bivariate normal distribution. If x_1 and x_2 are uniformly and independently distributed between 0 and 1, then z_1 and z_2 as defined below have a <u>normal distribution</u> with <u>mean</u> $\mu = 0$ and <u>variance</u> $\sigma^2 = 1$. Detailed information can be found at <u>*http://mathworld.wolfram.com/Box-MullerTransformation.html*</u>.

$$z_1 = \sqrt{-2\ln x_1}\,\cos(2\pi x_2) \tag{8.17}$$

$$z_2 = \sqrt{-2\ln x_1}\,\sin(2\pi x_2) \tag{8.18}$$

Given two uniform variates generated by the uniform random number generator, two normal variates can be obtained. Free implementation code in C or Fortran language is available on the Internet.

For the two RNGs introduced here, the C RNG (RNG written in C language) is better than the one that directly solves lognormal CDF. Matlab also has a lognormal random number generator

that applies the cutting edge technique in this field. It is used as a benchmark to test the reliability of other two RNGs. Table 8.2 compares the results of four runs of these random number generators. The maximum difference for Q_{100} and Q_{500} between C RNG and Matlab RNG are only 2.45 percent and 4.57 percent, respectively. C RNG is used in the program to avoid calling Matlab code.

Table 8.2. Comparison of Random Number Generators.

Methods	Items	Run 1 Result	Run 1 Error	Run 2 Result	Run 2 Error	Run 3 Result	Run 3 Error	Run 4 Result	Run 4 Error
C RNG	μ_Y	4.9894	0.20%	4.998	0.04%	4.9908	0.18%	4.9919	0.16%
	σ_Y	0.9998	0.02%	1.0012	0.12%	1.0027	0.27%	0.9991	0.09%
	μ_Q	241.3	**2.43%**	245.1	**2.43%**	242.5	0.82%	241.7	1.02%
	σ_Q	312.6	*4.11%*	319.3	0.66%	308.8	*4.57%*	303.3	1.17%
Solve CDF RNG	μ_Y	4.9994	-0.01%	5.0117	0.23%	5.002	0.04%	4.976	-0.48%
	σ_Y	0.9958	-0.42%	1.0047	0.47%	1.0036	0.36%	0.9954	-0.46%
	μ_Q	244.5	-1.96%	249.2	1.44%	244.9	**-1.11%**	236.5	**-3.04%**
	σ_Q	332.8	0.28%	321.4	*-4.95%*	310.4	-2.74%	311.7	*4.22%*
Matlab RNG	μ_Y	5.0011	0.02%	5.0009	0.02%	5.0101	0.20%	4.9851	0.30%
	σ_Y	1.0011	0.11%	1.0049	0.49%	1.0061	0.61%	1.0024	0.24%
	μ_Q	247.3		251.2		244.5		244.2	
	σ_Q	326.0		317.2		295.3		306.9	

Notes:

1.
$$\mu_{Y-error} = (\mu_{Y-RNG} - \mu_{Y-Input}) / \mu_{Y-Input}$$

$$\mu_{Q-error} = (\mu_{Q-CRNG} - \mu_{Q-MTRNG}) / \mu_{Q-MTRNG}$$

2. Input $\mu_Y=5$, $\sigma_Y=1$; Result is the μ_Y, σ_Y, μ_Q, σ_Q of generated random numbers;

3. $Q=e^Y$, Q is the flow, Y is the normally distributed variate.

4. 10,000 random numbers are generated.

5. In "Solve CDF RNG", the most current μ_Q, σ_Q from Matlab RNG are used to calculate the error term for μ_Q, σ_Q, not the values listed in this table.

8.3 GENERATE CUMULATIVE DENSITY FUNCTION (CDF) MAP

A number of equally possible future hydrographs are generated by the random number generating scheme as described in the previous section. For each hydrograph, the MEANDER program predicts the migrated location of the river at the end of the project life. In other words, if 1000 future hydrographs are generated, 1000 rivers are simulated at the different locations according to each hydrograph as shown in Figure 8.9. In the figure, the dotted line represents the initial geometry of the river and the solid lines are the predicted locations of the rivers after a given project life.
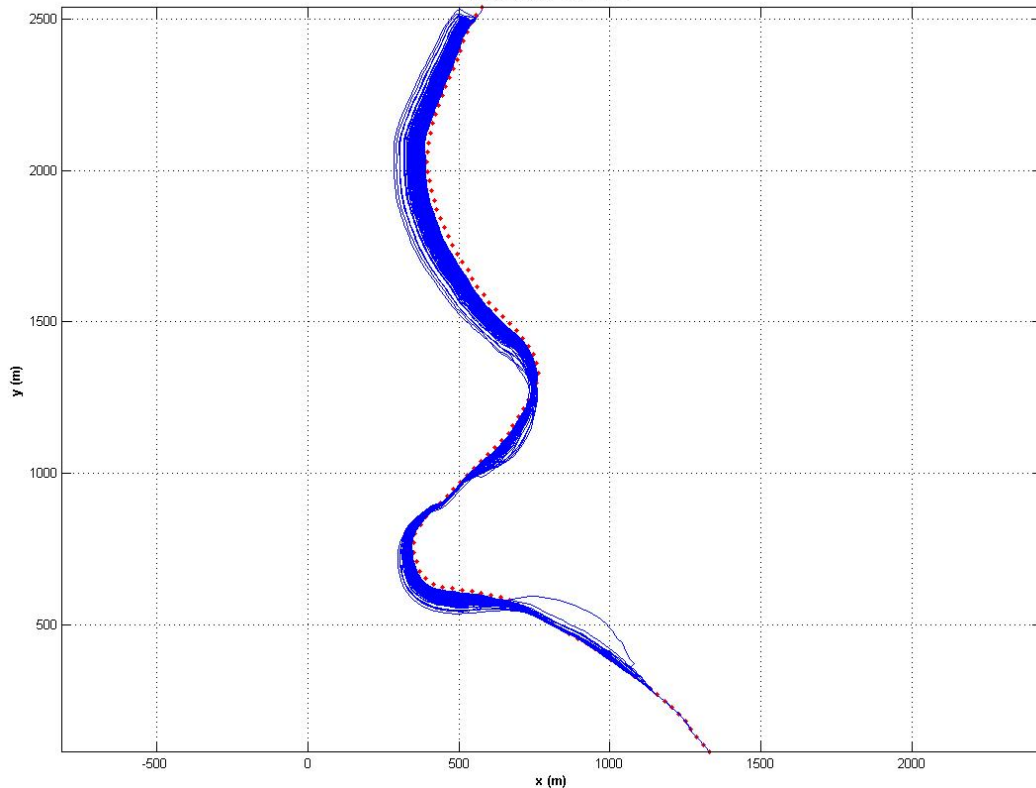
Figure 8.9. Generated Rivers According to the Future Hydrographs.

Once a number of different river geometries are generated as shown above, a post-processing scheme generates the probabilistic information of the prediction results. An independent module for this process using a relatively simple but quite reasonable approach was developed and then incorporated into the MEANDER program. The new methodology of risk analysis in this study can be described by the following steps.

First, a number of reference lines normal to the initial river geometry are generated, and then many small grids along each reference line are created as shown in Figure 8.10. These reference lines and grids on the lines can be used as a domain for calculating the probabilities associated with the predicted locations of the river. The size of each grid is $0.1W$ and the length of the reference line is $4W$ in total, indicating that it is extended to $2W$ in both directions (i.e., right and left) from the initial river. Second, the generated rivers from the previous step are superimposed on the domain as shown in Figure 8.11, and the numbers of crossings of the rivers in each grid are counted. This becomes the probability density function for each reference line. Next, the cumulative distribution function for each reference line can be determined from the PDF obtained in the previous step. Then, all the points that have the same level of probability value (e.g., 1, 10, 30, and 50 percent) on every reference line along the river are connected as shown in

155

Figure 8.12. The connected line represents a certain probability that the initial river will move to the location of the line or further at the end of project life (e.g., 75 years). A series of these lines with the initial geometry of the river can show the general trend of the meander migration of the river with the associated likelihood levels. This is called the CDF map, which is similar to a contour map.
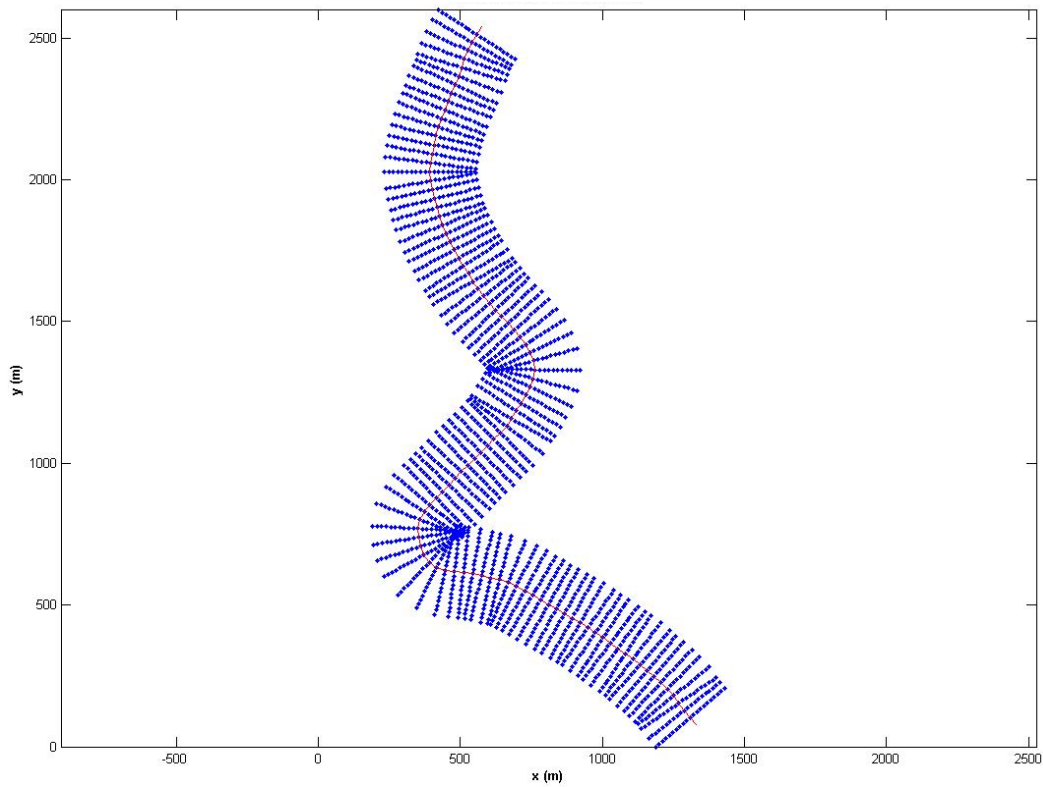
Figure 8.10. Generated Reference Lines along the Initial River.
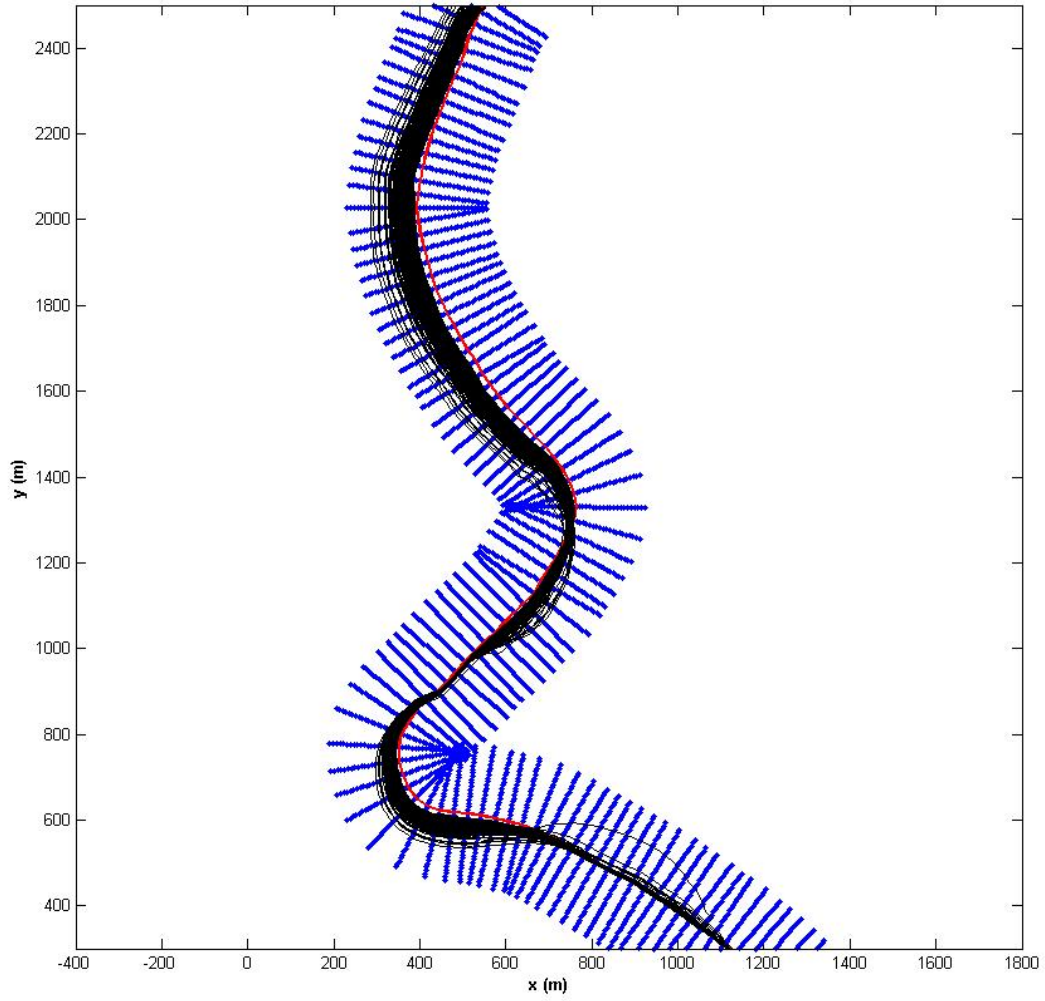
Figure 8.11. Superimposed Rivers on the Domain.
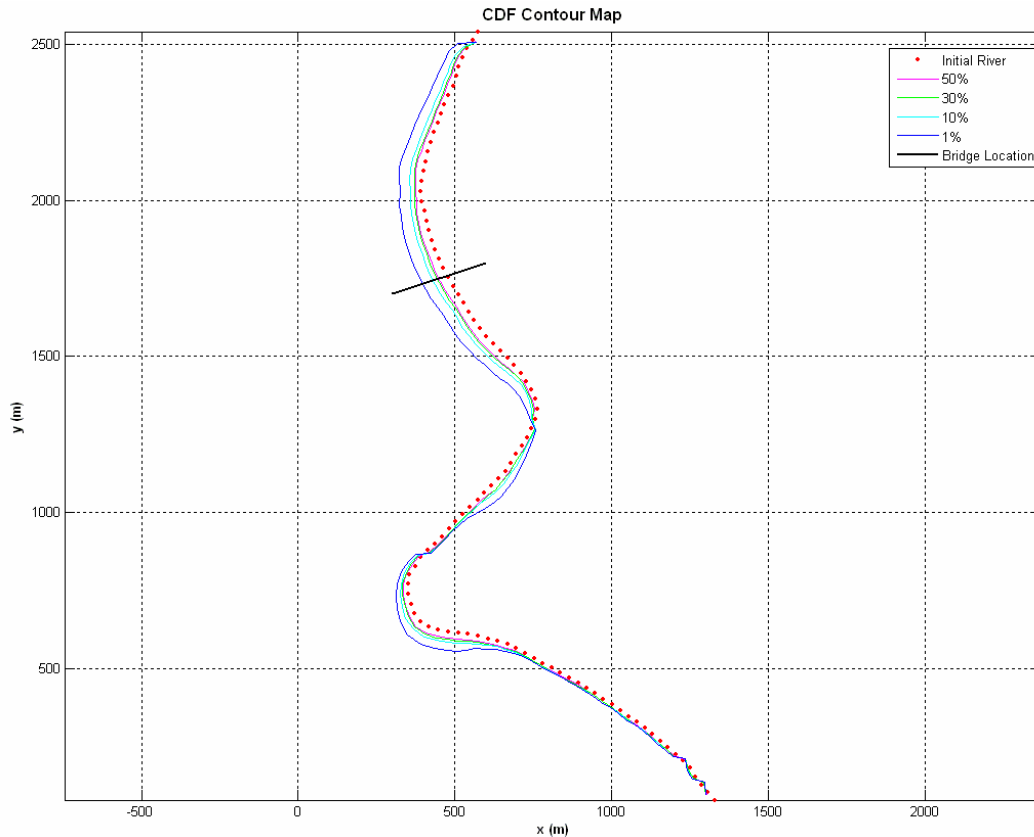
Figure 8.12. Cumulative Density Function Map.

8.4 CALCULATE CUMULATIVE DENSITY FUNCTION FOR A GIVEN BRIDGE DIRECTION

As mentioned in the previous chapter, meander migration can undermine bridge piers and abutments, scour the foundations of parallel highways, and cause loss of useful land. The common concern of these problems might be a specific location as well as a direction of the bank movement. Although the CDF map gives the global picture of the predicted migration movement over the choosen period, it is often insufficient information regarding a specific location and direction. Therefore, a separate CDF for a given location and direction is needed and is determined by interpolation of the CDF map: the x and y coordinates of two end points of interest are specified as input data (Figure 8.12), and then the new CDF is calculated by interpolating the values of two adjacent points on the reference lines. This CDF is plotted with a log scale on the y axis in a new screen so that the user can easily read the associated numbers on the plot as shown in Figure 8.13. In the figure, the highlighted point is read as follows: there is a 1 percent probability that the river will move 82.5 m or further in this direction over the design life of the bridge (e.g., 75 years).

158
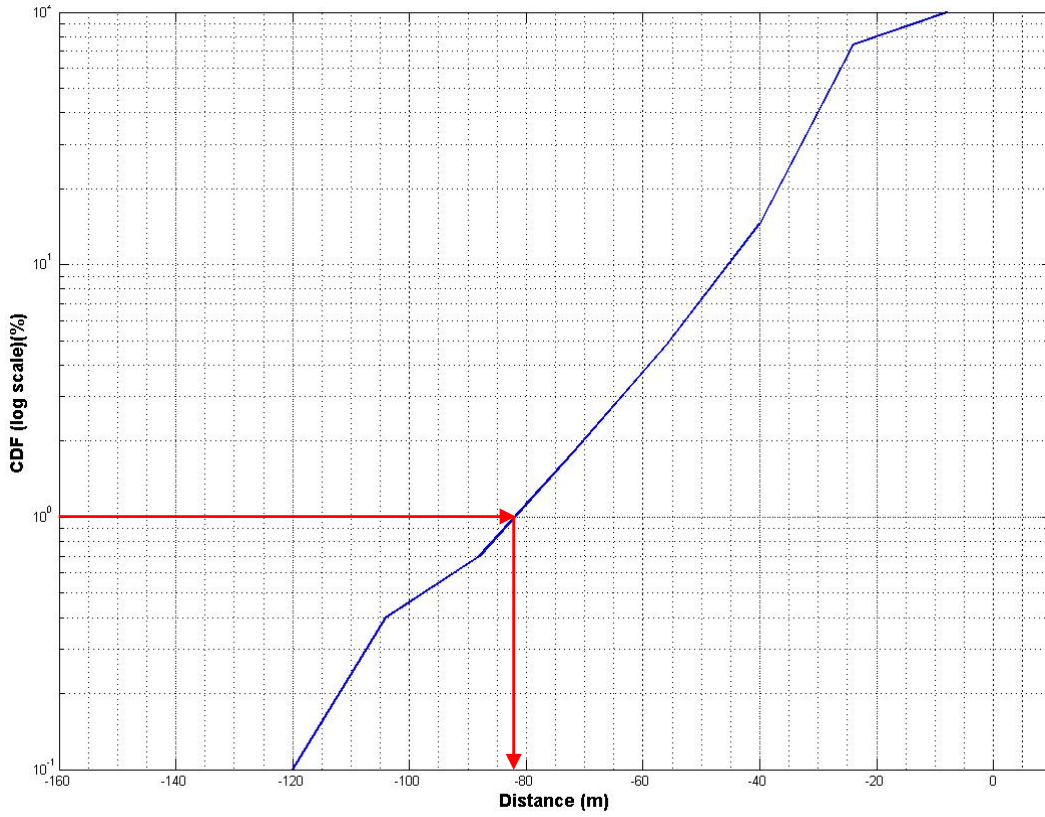
Figure 8.13. CDF Plot for a Given Bridge Direction.

CHAPTER 9. MEANDER PROGRAM

9.1 INTRODUCTION

The MEANDER computer program implements all the methods developed in this project to predict meander migration. It consists of two major components: graphic user interface and numerical implementation. The graphic user interface was adapted from the SRICOS-EFA program. In the SRICOS-EFA program, the GUI takes user input and forms a source data file. Then a FORTRAN program reads the data file, does the computation, and generates output data file. The GUI reads the output file and shows the result graphically. The MEANDER program does all of these things in a more efficient way. The GUI and the implementation of the model are written in C++ and are seamlessly linked together. The part of the geometry study and graphic output are written in Matlab. The Matlab program is compiled and linked to the C++ program so that one executable program is composed of different parts. Transferring data from one module to another is not through a hard drive but through much faster computer memory. Implementation of the model is the kernel of the MEANDER program.

In this chapter a general view of the MEANDER program is given regarding graphic user interface, some programming techniques, and implemented modules. These items will be introduced in order:
- Input and output user interfaces
- Mixed language programming—C++ and Matlab
- Overview of the whole program
    - Implementation of Geometry Study
    - Implementation of the Hyperbolic Model
    - Implementation of the Risk Analysis Module

9.2 GRAPHIC USER INTERFACE (GUI)

Graphic user interface is indispensable to modern computer programs. A lot of resources have been invested into development of the GUI of SRICOS-EFA. The engine of this code is reused with some moderate modifications and additions. A consistent appearance is maintained and programming time is reduced. Figure 9.1 is the main interface of the MEANDER program, which has a look similar to that of the SRICOS-EFA program. All the user interfaces and functions can be accessed either through the menu or the buttons. The user buttons from left to

right correspond to these interfaces: Units, Geometry input, Soil input, Water input, Table input, Plot input, Run function, and Plot output.
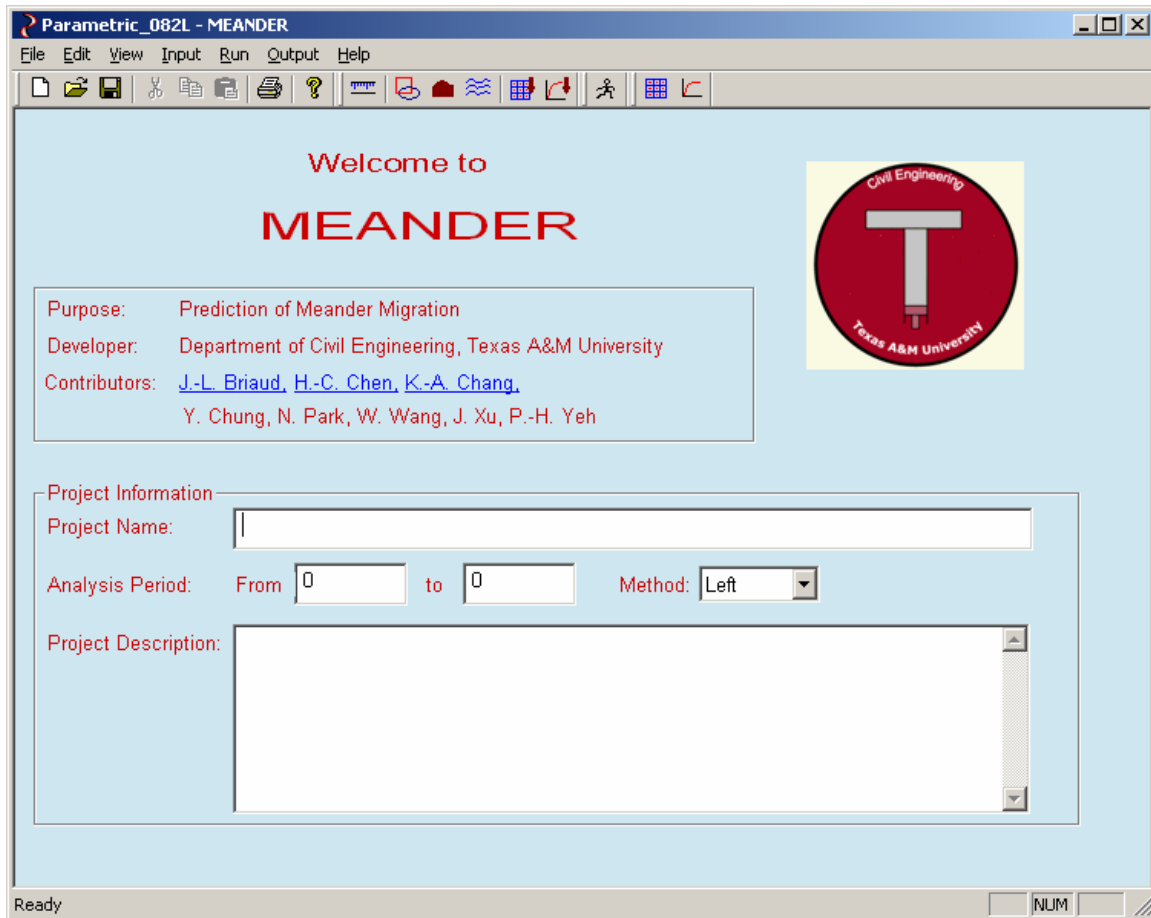
Figure 9.1. Main Interface of the MEANDER Program.

Figure 9.2 shows the unit input dialog. It allows the user to choose a unit system for the computation. There are two unit systems: metric system and U.S. Customary System (English system). The user should be consistent in the units being used. If metric units are chosen, all the input data are implied to have metric units and output is the same. There is an exception for English units: the EFA curve is always in metric units.
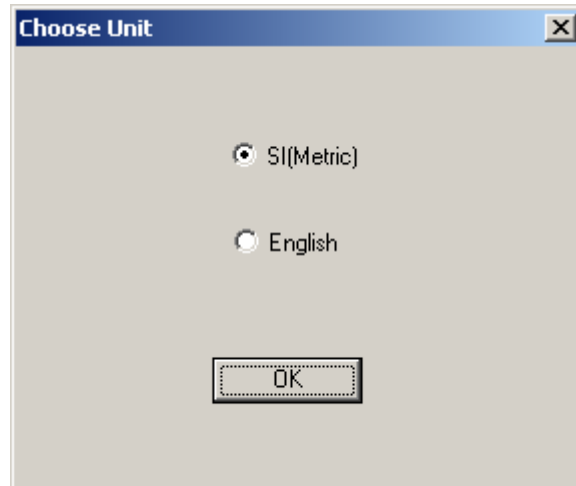
Figure 9.2. Choose Unit.
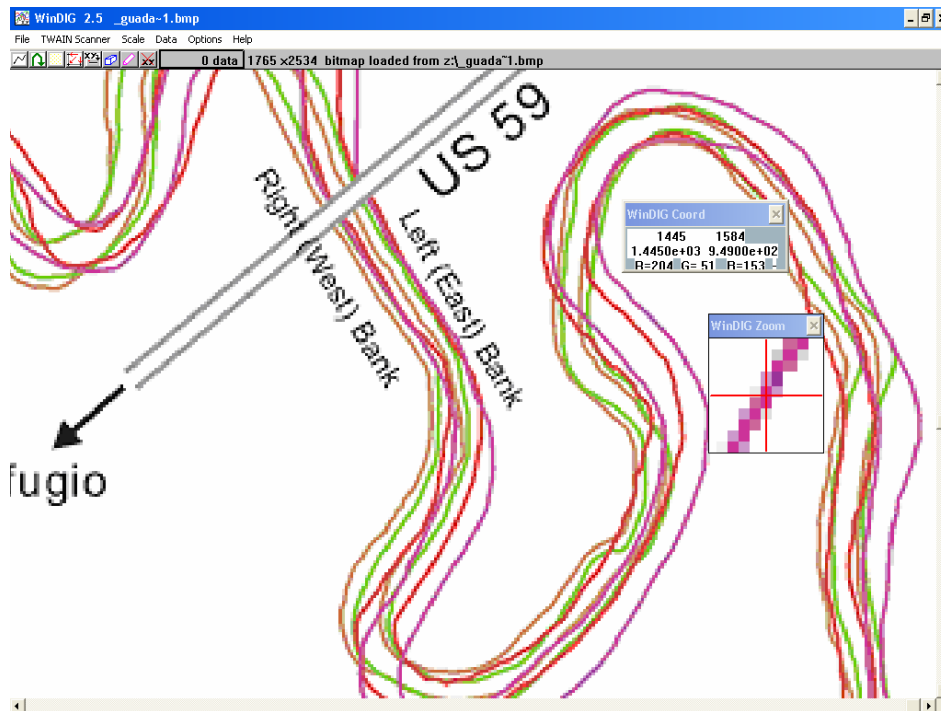
Figure 9.3. Digitize River Banklines with WinDIG Program.

Figure 9.4 is the Geometry Input dialog. The data for the geometry study are entered here. The user needs to input the average river width and the path of coordinate file. Coordinate files can be obtained by digitizing river images with the WinDIG program, which is free software as shown in Figure 9.3. The channel curve will be drawn immediately after the coordinate file is loaded. The given default values for the parameters are based on experience. Adjustments are needed for certain cases. If the "Fit Circles" button is clicked, circles will be fitted and drawn on

the dialog. A better version of figures is shown in two new windows. One is the original channel and fitted circles as shown in Figure 9.5. The other is the *R/W* versus channel lengthwise distance curve as shown in Figure 9.6. These two graphs are drawn by compiled Matlab code, which has a lot of advantages over graphs drawn by C++ code. Besides excellent quality of figures, the user can zoom and pan the graph. It can be exported to any format of raster image or vector image. The coordinates of any point can be displayed at the user's choice.

Before curve fitting is done, the center line or bank of the river is evenly divided into many segments. Spacing is the distance between two adjacent points. *Spacing Coefficient* is the ratio of the spacing to the river width. A default value of 0.2 is given. Reducing the spacing coefficient will smooth the *R/W* vs. channel length curve, but the computation time increases as a result.

Segment length is the length used to calculate the radius of curvature of the middle point. *Segment Length Coefficient* is the ratio of segment length to the river width. It is recommended to use 5. If the segment length coefficient is too small, the bends may not be distinguishable on the *R/W* versus channel length curve. If this value is increased, the bends will become more obvious but the computation time will become longer.

When the length of an identified bend is shorter than a certain value, no circle will be fitted. This value is called minimum bend length. *Minimum Bend Length Coefficient* is the ratio of minimum bend length to the river width. A value of 2 is suggested here. The smaller the value is, the more circles will be generated. If the value is too large, many significant bends will be excluded.

Another way to eliminate an identified bend with a small curvature is to calculate the average distance from a point on the bend to the baseline which connects the first and last point of the bend. If this average distance is smaller than a certain limit, it will be treated as a straight line. The limit is called *Straightness Limit*. If a value of 0 is given, this parameter will be ignored. If the user wants to eliminate some unwanted circles, a number around 5 can be picked. The final desired value can be determined by trial and error.

It is useful to show the channel lengthwise distance on the channel. For this, the user needs to specify the *Tick Spacing*. The given default values come from experience and may not apply to all cases. The values of the criterion line 1 to 3 should be in ascendance order, or it will be ignored. *X0* and *Y0* on the dialogue are the coordinates of the point for which a migration versus time curve will be drawn. It is chosen by the user on the graph of fitted circles as shown in the third circle of Figure 9.5.

If the default settings do not produce a good fit, the user can first adjust the criterion lines based on Figure 9.6. On the *R/W* versus channel length curve, a well-behaved bend appears to be a plateau or a parabolic curve with its vertex close to the horizontal axis (*R/W* = 0). The criterion lines should be adjusted in such a way that the segment between a criterion line and the horizontal axis is longer than the minimum bend length.

Further adjustments that can improve fitting quality include reducing spacing and increasing segment length. Smaller spacing leads to longer computation time, but the *R/W* versus channel length curve becomes smoother. Increasing segment length has the same effect and can effectively reduce sudden jumps on the curve. A very small bend could be better fitted as a part in a larger bend. Setting a reasonable minimum bend length coefficient will help the fitting of the larger bend. Perfect straight lines are rare in river channels; however, not all segments with a curvature need to be fitted with a circle. Choosing a straightness limit can help eliminate the segments that have a reasonable curvature but look straight.
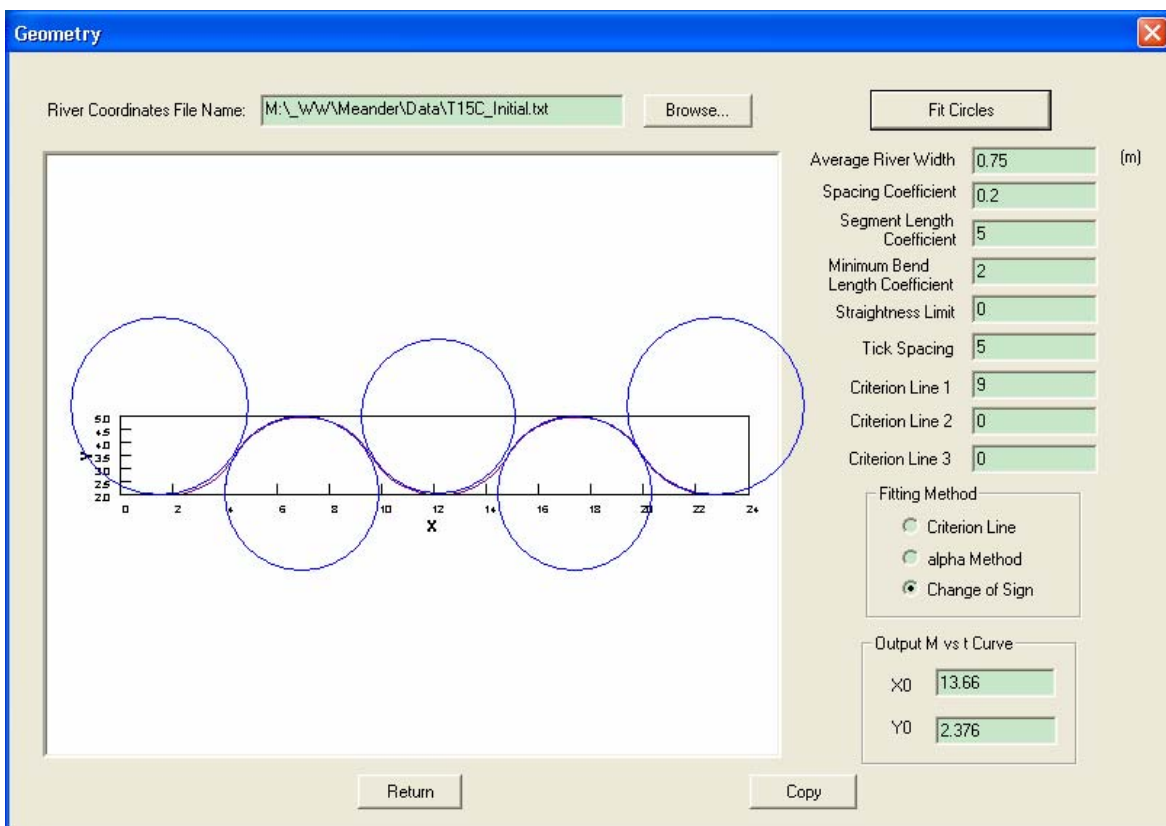
Figure 9.4. Geometry Input.
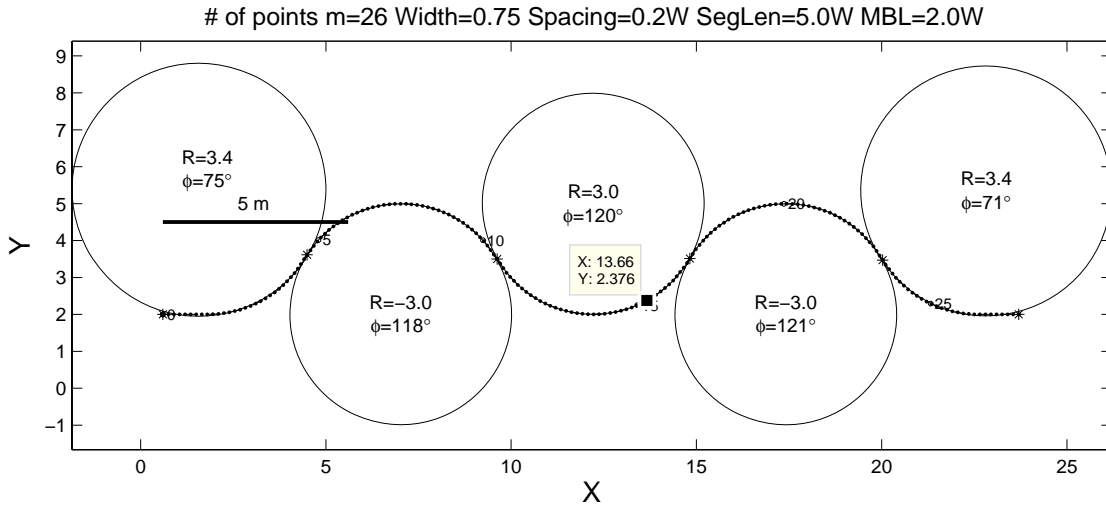
Figure 9.5. Original Channel and Fitted Circles for the Center Line of Flume Test Case 06 in Sand.
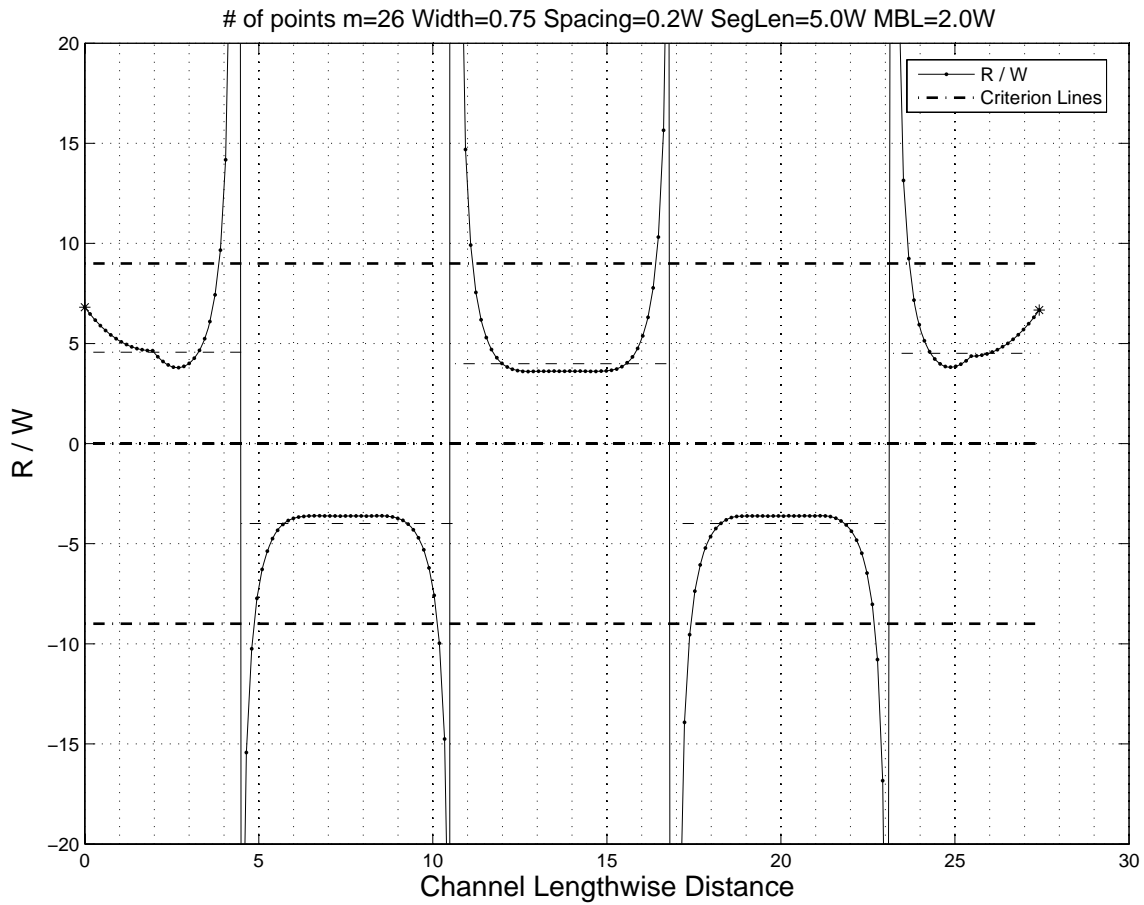
Figure 9.6. *R/W* versus Channel Lengthwise Distance for the Center Line of Flume Test Case 06 in Sand.

166

Figure 9.7 is the soil data input interface. The first item is critical shear stress, which corresponds to a scour rate of 1 mm/hr. The number of points on an EFA curve needs to be specified so that enough space will be allocated on the table. Conventionally, scour rate is in metric units. When looking up a scour rate based on shear stress, linear interpolation is used. Data shown on the dialogue box are for the sand used in the new Coastal Engineering Laboratory. Since the M_{max} equations for sand and clay are different as described in Chapters 5 and 6, the two options for choosing the type of soil are also provided.

Figure 9.7. Soil Data Input.

The interface for entering flow conditions is shown in Figure 9.8. The flow can be in terms of discharge or velocity. For a prediction, three types of analyses are available: constant flow, hydrograph, and risk analysis. The hydrograph used here can be a file directly downloaded from USGS website www.usgs.gov or an edited single-column data file. Each row in a hydrograph has the average flow during one time step, which is specified in the dialog and is normally one day (24 hours). Risk analysis takes as input either a hydrograph or a 100-year and 500-year flood.

Either choice can be used to calculate the probability associated with a certain migration movement of the river over a certain period of time. The Velocity versus Water depth table is used to find the water depth corresponding to a velocity. If the input is discharge, the Discharge versus Velocity table and Discharge versus Water depth table are required. All these tables are obtained from HEC-RAS simulation.

Figure 9.8. Water Data Input.

Figure 9.9 is a dialog box showing previously entered data in a tabular format for easy checking. If a mistake is found, the user can go back to make corrections. Figure 9.10 provides an easier way to check the correctness of the data. Abnormal data can be easily identified on a graph. After the data are entered and checked, the computation process can be started. Upon hitting the "Run" button, the program starts the prediction process.
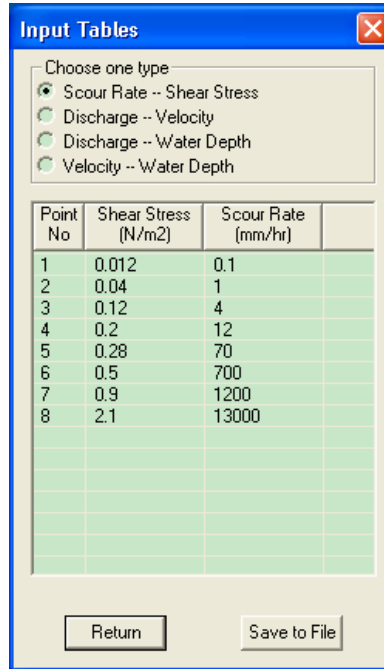
Figure 9.9. Input Tables.

Figure 9.10. Input Plots.

Figure 9.11. Output Table.

Figure 9.11 is the output table that shows the coordinates of the initial channel and the final channel. Accumulated migration distance of each point is on the last column.

The Output Plots dialog box (Figure 9.12) contains four buttons: "Center Line or One Bank", "Both Banks, Risk Analysis", and "M vs. t for one point". All these functions were realized in Matlab. The first button is for showing the migrated channel of each step for the center line or a bank. The third button is to show initial banks, predicted final banks, and measured final banks if data are available. The second button is to run a risk analysis, which requires a specific direction of interest such as a bridge. For the direction of a bridge, the coordinates of two end points on the right and left side from the initial channel need to be specified in the bridge coordinates box. The last button is for showing the migration versus time curve of a selected point.

The trace of a migrating process is shown in Figure 9.13. The black dashed line is the initial center line. Figure 9.14 shows a comparison between predicted and measured final banks. The *Center Line Method* mentioned in the title will be discussed in detail in the next section.

170
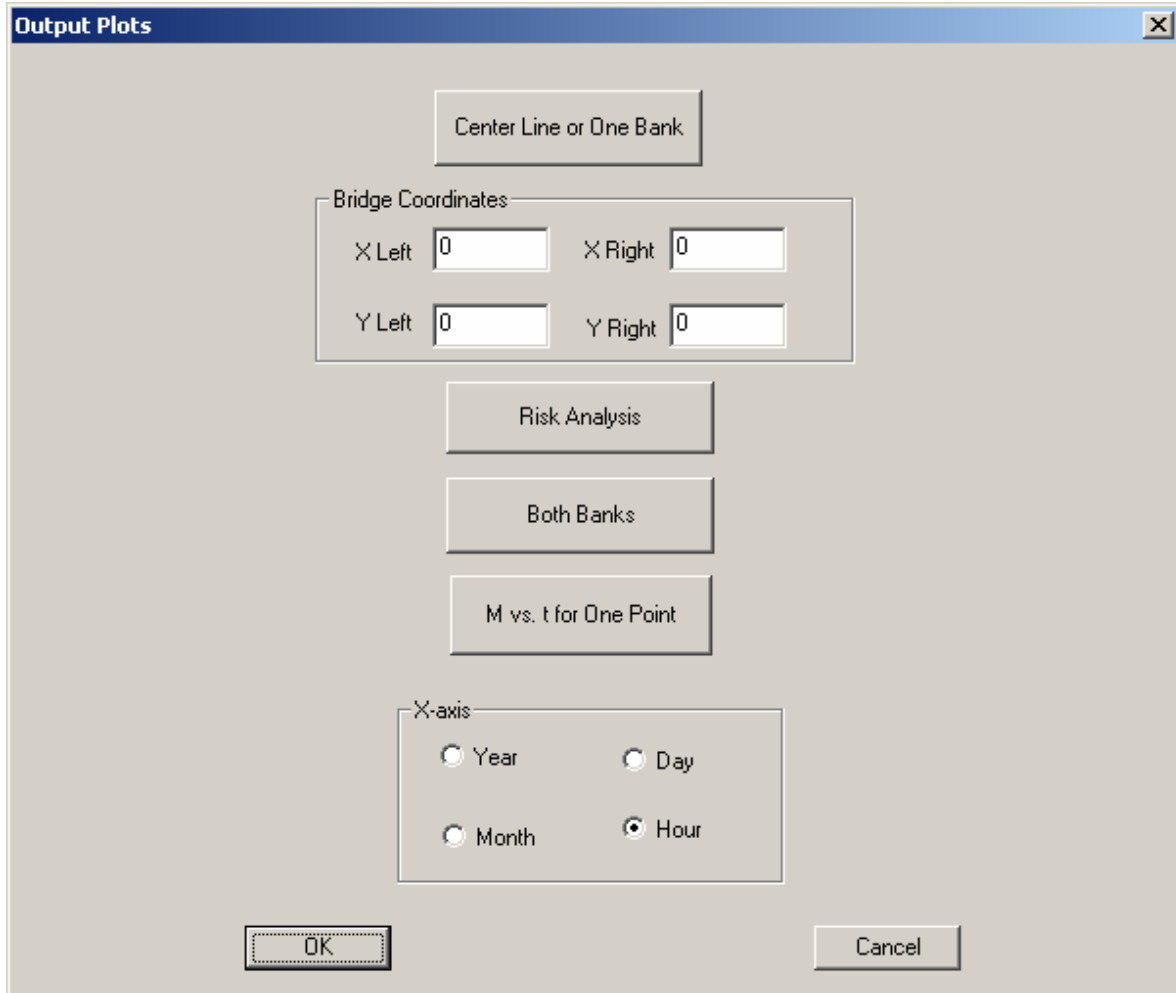
Figure 9.12. Output Plots Dialogue.
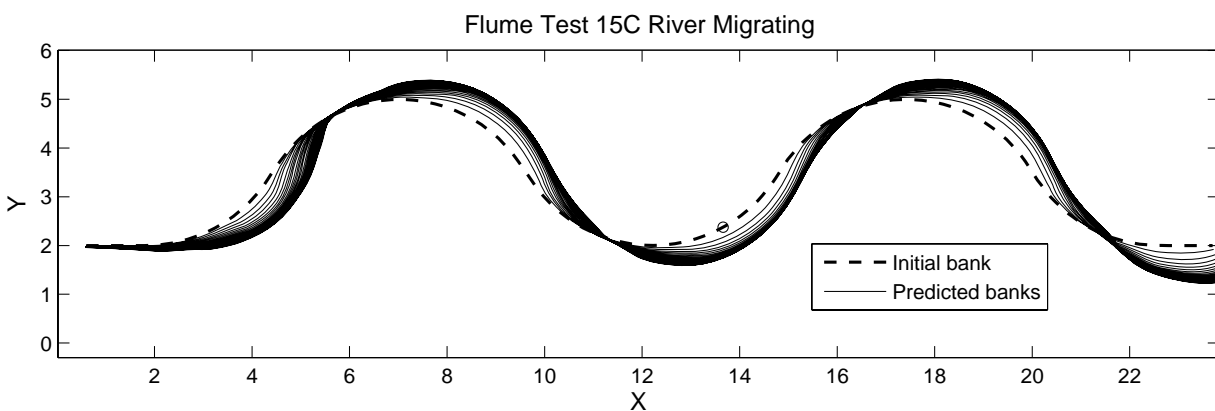
Figure 9.13. Trace of a Migrating Center Line.

171
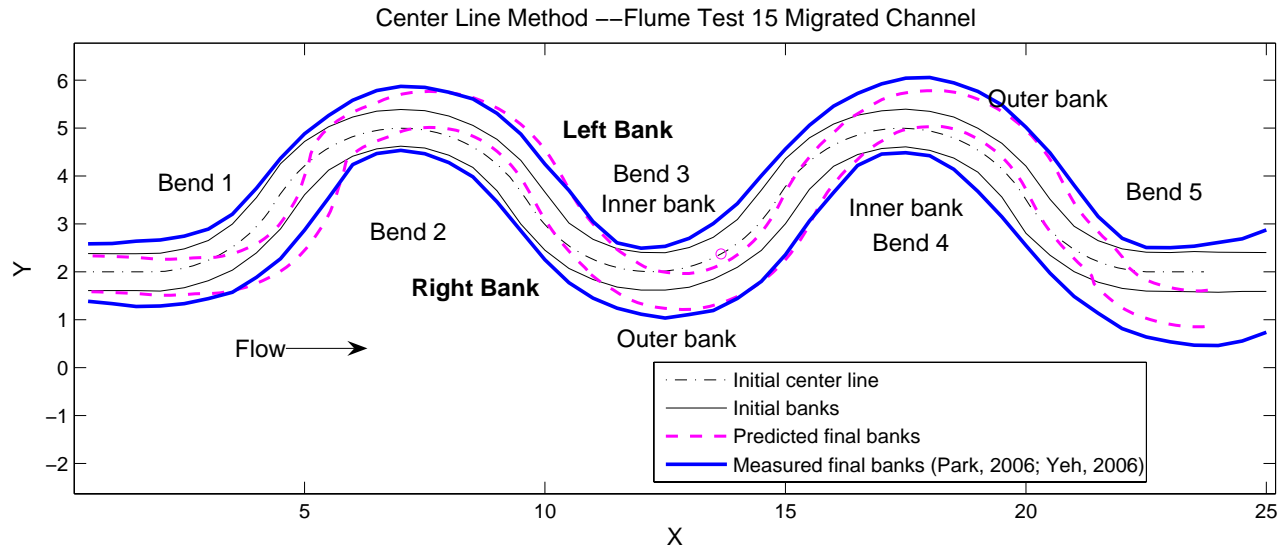
Figure 9.14. Predicted and Measured Banklines Using Center Line Method.

The migration process of an important point along the river is of great interest. The coordinates of this point are entered on the Geometry Input dialog box. The user can obtain the coordinates of a point by clicking the "Data Cursor" button on the Matlab figure and then clicking on the point of interest in any one of Figure 9.5, Figure 9.13, or Figure 9.14. On the Output Plot dialog box, the user first chooses the right unit for time by clicking the appropriate button and then hits the "M vs. t for One Point" button. A curve similar to the one shown in Figure 9.15 will pop up. The location of the chosen point is indicated by a tiny circle in Figure 9.14. At this stage, if the Migration vs. Time curve is needed for another point, the calculation has to be done all over again.
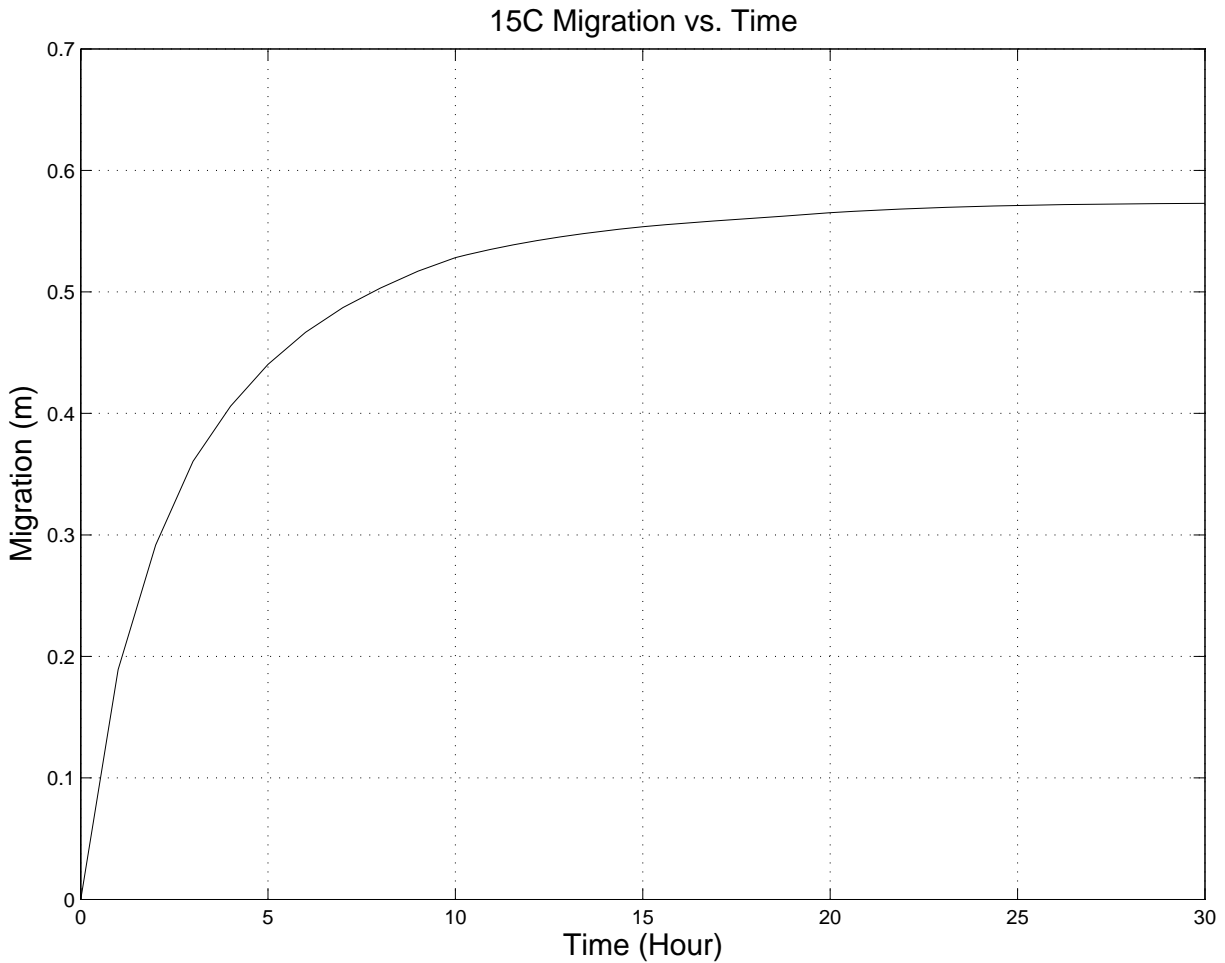
Figure 9.15. Migration versus Time Plot for a Certain Point.

9.3 CENTER LINE METHOD VERSUS BANK METHOD

The initial channel of all flume tests has a well-defined center line. The geometry of a center line is referred as that of the channel because of its constant radius-to-width ratio for all bends. It is natural to use the center line to represent the channel and to do the prediction of migration. However, the model does not have any difficulty in predicting the migration of a single bank. Two approaches are thus available to the user. To distinguish one from the other, when the center line is used it is called Center Line Method. The other method is called Bank Method.

For the Center Line Method the river width has to be assumed as constant since the equations can not predict the change of river width. Channel widening was a common phenomenon in the flume tests. The migration of a bend often goes beyond its two inflection points. The migration of a point on a center line is considered as the superposition of the migration vectors of the two

corresponding bank points. In the calculations, a point on the center line can have two or more migration vectors. One is caused by the bend it is on; the others can be caused by the bend before it or after it. The advantage of this method is that it can simulate that a straight channel can migrate into a sinusoidal channel. The disadvantage of this method is that sometimes superposition can cause a false appearance that the maximum migration is almost reached. The reason is that the difference of the magnitude of two large opposite migration vectors is small. If two consecutive bends are too close, the migration on either sides of the inflection point are of opposition direction, causing the transition part to be more and more distorted from a perfect arc. Thus, the effectiveness of curve fitting decreases with increasing migration. Another difficulty with this method is that it is hard to obtain the center line of a real river. Figure 9.13 shows the trace of predicted center lines coming from an application of the Center Line Method. The predicted banks in Figure 9.14 were obtained by offsetting the center line by a half channel width in both directions.

The Bank Method only calculates the migration of the outer bends. The calculation for one bank is normally done on every other bend of the bank. The influence of an outer bend usually does not go beyond adjacent inner bends. Superposition is not likely to occur for this method. Figure 9.16 shows migrated banks at each time step. Figure 9.17 is a simplified version of Figure 9.16, where only banks of the last time step are kept and highlighted. For the left bank in Figure 9.16, the first, third, and fifth bends are considered to be the active cause of migration. Migration of the second and fourth bend is passively caused by the outer bends next to them. For the right bank in Figure 9.16, the second and fourth bends are considered to be the active cause of migration. Migration of the first, third, and fifth bends is passively caused by the second or fourth bend. Migration of a channel is the result of migration of both banks and not of an imaginary center line. This method simulates the migration phenomenon that really happens in experimental tests and in real rivers. The widening effect can be verified or predicted as shown in Figure 9.17. Without superposition, the calculation can produce more stable results. The disadvantage of this method is that twice the computation time is needed to do a complete prediction.

Development of the M_{max} equation was based on a multiple regression process. The migration of the outer bank and the geometry of the initial center line are used for developing the M_{max} equation. Since the migration of an outer bank can be treated as that of the corresponding center line, the M_{max} equation is the right one for the Center Line Method. In preparing the geometry for a flume test, a bank is obtained by offsetting the center line by half the channel width. The left bank, center line, and the right bank of a bend share the same center but have different radii. The

difference from one to the next is half the channel width. Figure 9.18 shows the geometry of the left bank of flume test case 06 in sand, which can be compared to Figure 9.5 for the center line of the same test. For an ideal situation, the radius of the outer bank is 3.5 and the radius of the inner bank is 2.5. The fitting is not perfect but is very close. To apply the same M_{max} equation for the outer bank, the radius-to-width ratio should be decreased by 0.5. The inner bank remains unchanged, as it has no active migration.
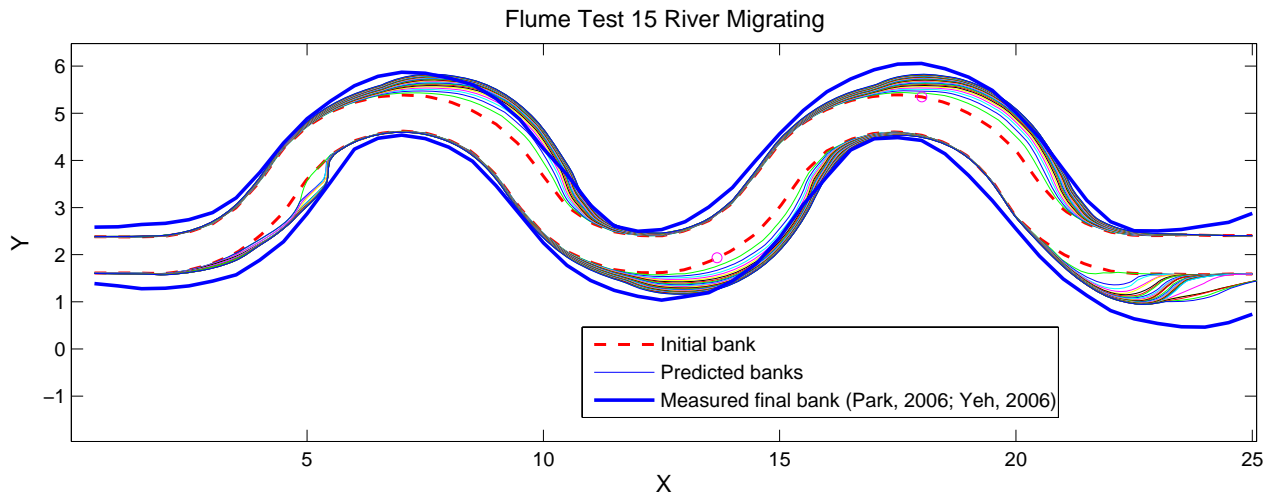
Figure 9.16. Trace of Migrating Banklines.
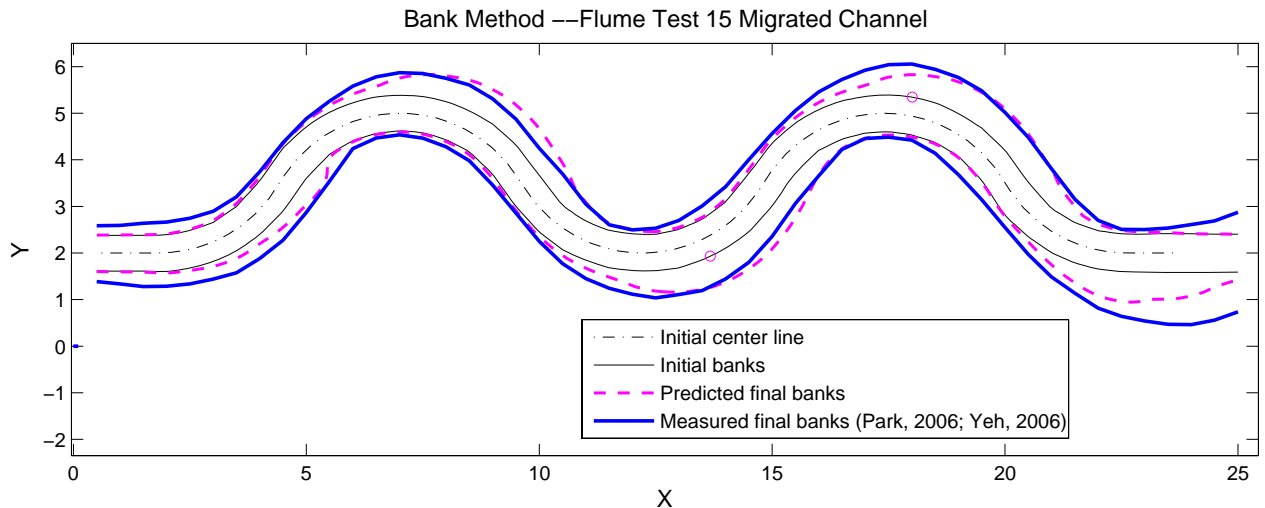
Figure 9.17. Predicted and Measured Banklines Using Bank Method.
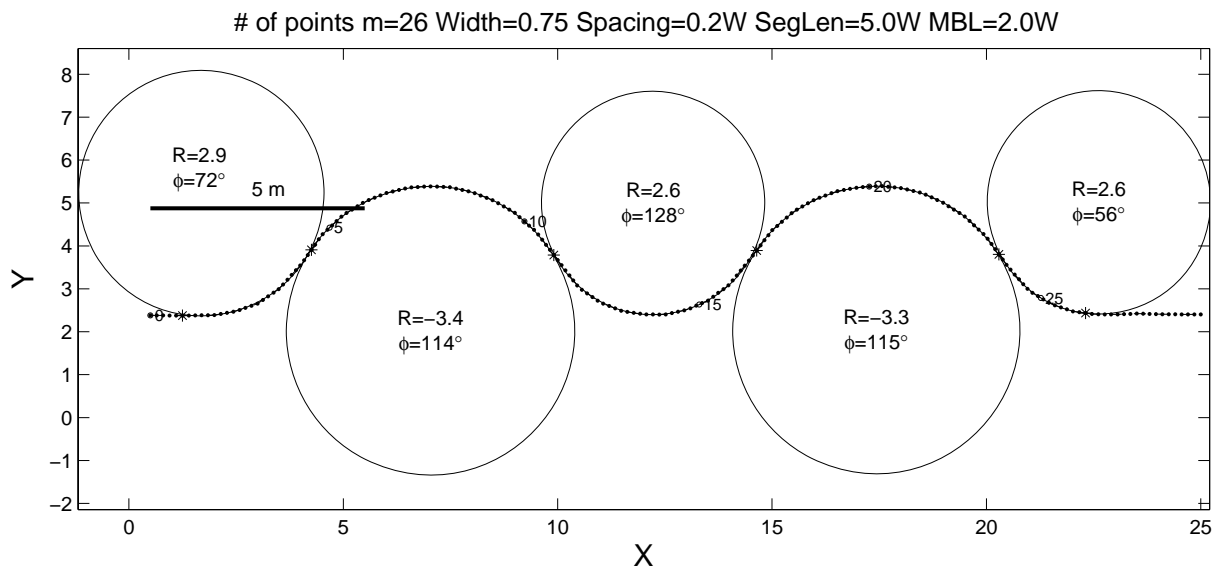
Figure 9.18. Original Channel and Fitted Circles for the Left Bank of Flume Test 15 in Sand.

9.4 MIXED LANGUAGE PROGRAMMING—C++ AND MATLAB

This program could have been written completely in Matlab. Then the GUI code from SRICOS-EFA could not be used and a new GUI would have had to be written in Matlab. It could also have been written completely in C++. Then the code for Geometry Study, which had been written in Matlab, could not be used. The advantages of Matlab, such as a strong functionality in graphic output, debugging, and numerous built-in numerical recipes, etc., would not be utilized. For the MEANDER program, the GUI is in C++ with the application Microsoft Foundation Class (MFC). The implementation of the Hyperbolic Model is in regular C++. The implementation of Geometry Study, Risk Analysis, and graphic output are in Matlab. The program development environment is Visual C++ 6.0 and Matlab 7.0.4 (service pack 2).

Integration of Matlab with C++ is not routine C++ programming or Matlab programming. A good understanding of both languages is extremely helpful. Much time was also spent on solving abnormal problems due to incomplete documentation of Matlab on this issue. Matlab Compiler is an independent module which differs from version to version. The functionality and documentation are also progressing. It is worthwhile to give an explanation from a user's point of view so that later programmers can compile complicated Matlab programs more smoothly.

176

Matlab is a type of interpreting language. Unlike compiling languages like C, C++, or FORTRAN, it is executed line by line when running and has a lower efficiency. A Matlab file has an extension of "m," also called "M-file." M-files cannot run without the Matlab environment. Matlab Compiler takes M-files as input and generates redistributable, stand-alone applications or software components. The resulting applications can be independent of the Matlab environment. The latest version at the time of the study (version 4, going with Matlab 7.0.4) of the Matlab Compiler can support all functionalities of Matlab. The Matlab Compiler can generate these kinds of applications or components:

- Stand-alone applications
- C and C++ shared libraries (dynamically linked libraries (DLLs) on Microsoft Windows)
- Excel add-ins
- Com objects

C++ shared libraries are generated for the MEANDER program. Besides generating the DLL files, The Matlab Compiler also produces an interface function which passes on the input data for the Matlab program and returns the results. A special data type class mwArray was created to do this job. The programmer first converts C++ variables into mwArray type and then converts the results in mwArray type back into C++ type. This process is often written as a user-defined C++ interface function. This function can be called and shared as a regular C++ function.

Conversion of data from one type to the other is the major task of this function. For a scalar or a vector, the conversion is straightforward. For a 2D or 3D array, caution should be taken because C/C++ and Matlab store multiple-dimensional arrays differently. In physical memory a multiple-dimensional array is stored in a column of continuous memory cells. There are two methods to map the one-dimensional (1D) physical index to the multiple-dimensional array index at computer language level. The first method is to store data from row to row, as what C/C++ does. The other is to store data from column to column, which is used by Matlab. Class mwArray has a method SetData to read data from a C/C++ variable and pass it to a mwArray variable. The data are read from a single column physical memory. Then the Matlab mapping method assigns it to an array of Matlab type. A 3D array of dimensions $M \times N \times L$ in C/C++ will be converted into a 3D array of dimensions $L \times N \times M$ in Matlab. However, their storage in the physical memory is of the same order. The GetData method of class mwArray also uses the Matlab mapping method to assign data from a Matlab array to a physical memory, which is for a C/C++ variable.

It is helpful to list a step by step procedure explaining the process of integration. Assume Matlab 7 and Visual C++ 6 are installed. The main MFC project is in folder "Z:_WW\MEANDER\."

177

The subproject in Visual C++ 6 for compiled Matlab program is called GeoRndPrj, which is in folder "Z:_WW\MEANDER\GeoRndPrj\." The interface "GeoRndUI" is a part of the "GeoRndPrj" project.

If it is the first time that the Matlab program is compiled, run the following commands in the Matlab command window first and choose the appropriate C compiler. Here VC++ 6 is used. Then follow the steps listed below.

1. mex –setup.
2. mbuild –setup.
3. Change Matlab work directory to the folder holding the m files. If a file named "mccpath" exists, delete it.
4. Run this command: *mcc -W cpplib:libGeoRnd -T link:lib AutoFit_Run_InVC.m PlotRiver1Curve.m PlotRiverBanks_Main.m PlotMvsT.m plotMgrtForOneFlow.m mLognrnd.m MeshGeneration.m -v -d '<path>\Meander\GeoRndPrj.*' (If a new matlab file is to be added to the work, first copy that file to the current matlab work directory, and include that matlab file in the list of matlab file sin the above command. Next update the GeoRndUI.cpp and GeoRndUI.hpp to contain the interfaces to the added matlab files. Note that the matlab files need to contain functions rather than scripts for it to compile.) Words in italic characters are names decided by the user. "-v" means verbose, which outputs intermediate results in detail. "-d" switch sends output files to the folder after it.
5. Add a static library project to MFC application (MEANDER), GeoRndPrj in here. If "-d" option is not used in step 2, copy generated files libGeoRnd.* to folder ".\MEANDER\GeoRndPrj\."
6. Copy/Move libGeoRnd.ctf and libGeoRnd.dll to folder ".\MEANDER\."
7. Add two files to the subproject "GeoRndPrj." They are "libGeoRnd.lib" and "<Matlab Root>\extern\lib\win32\microsoft\msvc60\mclmcrrt.lib." Build subproject "GeoRndPrj" and GeorndPrj.lib will be generated.
8. Add GeoRndPrj.lib to MEANDER project. In VC++ 6 environment, add "<Matlab Root>\extern\include\" to INCLUDE folder and add "<Matlab Root>\extern\WIN32\MICROSOFT\MSVC60" to LIBRARY folder.
9. Build MEANDER project. The linking process will be done automatically.

9.5 AN OVERVIEW OF THE IMPLEMENTATION OF THE PROGRAM

All the methods have been introduced in previous chapters. The implementation is a description of the same idea in computer languages. A flow chart is an overview of the computer code.

About 14,000 lines of code have been written and checked line by line over a long period of time. Flow charts help introduce important modules, steps, and their functionalities in natural language. Figure 9.19 is the flow chart of the entire MEANDER program. Figure 9.19 gives a good idea about prediction process and what the program can do. To further understand how a specific task is implemented, a more detailed flow chart is needed. Figure 9.20 is the flow chart for the Geometry Study. Figure 9.21 also explains the Geometry Study but from a different perspective. The task is outlined in a problem-solving manner. The major difficulties of certain steps are briefly described. The code that applies the Hyperbolic Model is based on Figure 9.22. The shaded item "One Hydrograph" is a sub-function whose flow chart is Figure 9.23. The function OneHydrograph calculates the migration caused by each time step of a hydrograph and comes up with an accumulated distance. The shaded item "One Flow" in Figure 9.24 is a sub-function of function OneHydrograph( ). "One Flow" calculates the migration of the whole channel caused by the flow of one time step. The flow chart of function OneFlow( ) is shown in Figure 9.24.
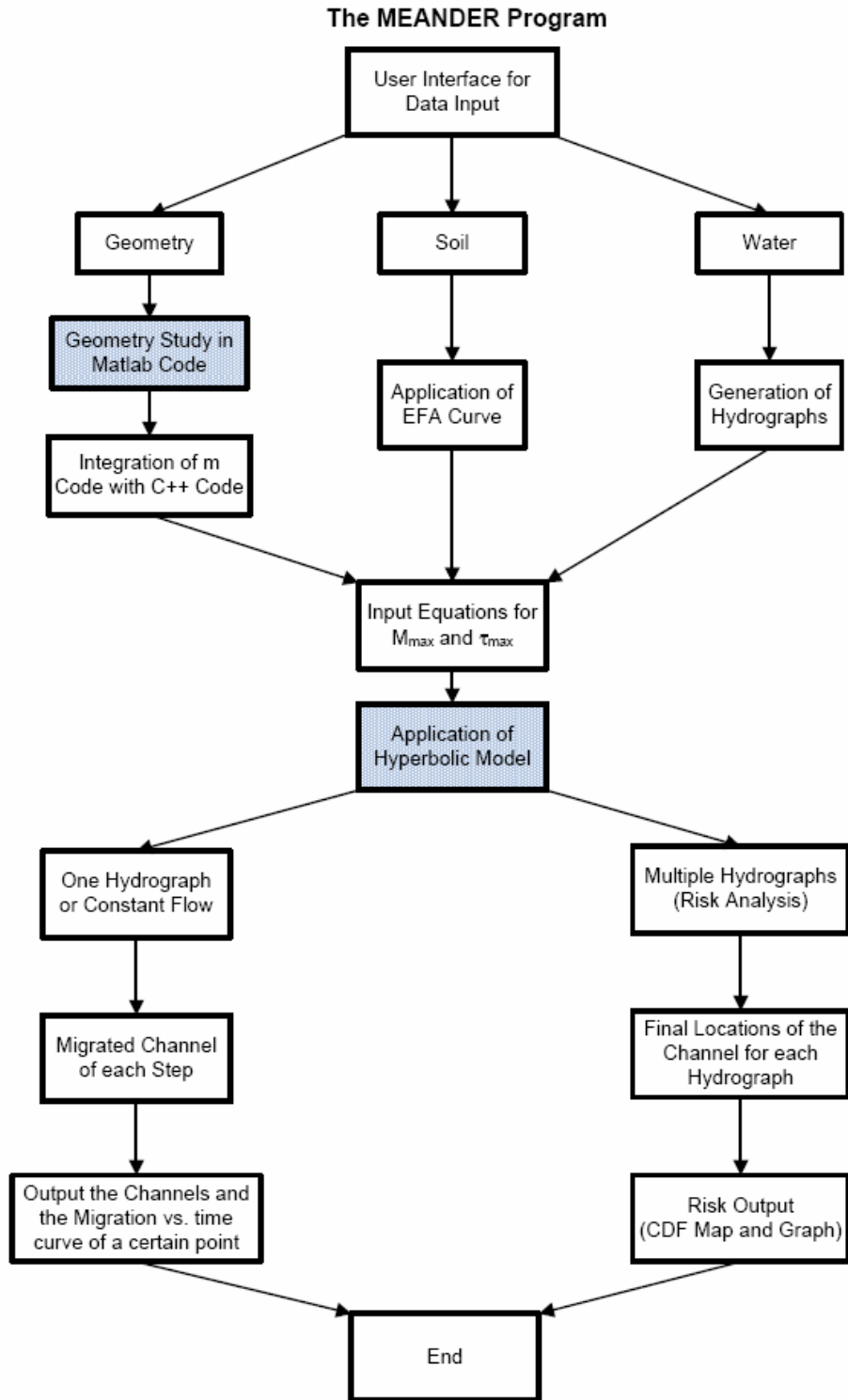
Figure 9.19. Flow Chart of the MEANDER Program.

Geometry Study
Program Written in Matlab Code

```
┌─────────────────────┐
│ Digitize Aerial Photos│
│      and Maps        │
└─────────────────────┘
          │
          ▼
┌─────────────────────┐
│ Calculate Radius of  │
│ Curvature for Each Point│
└─────────────────────┘
          │
          ▼
┌─────────────────────┐
│  Identify Bends of the│
│       Channel        │
└─────────────────────┘
          │
          ▼
┌─────────────────────┐
│ Produce a series of circles,│
│ including the best fit circle│
└─────────────────────┘
          │
          ▼
┌─────────────────────┐
│ Methods for Finding the│
│    Best Fit Circle   │
└─────────────────────┘
```

Criterion Line Method

Least Square Error Method

2nd Derivative of R Method

Balanced Method

Calculate R, ϕ, θ

End
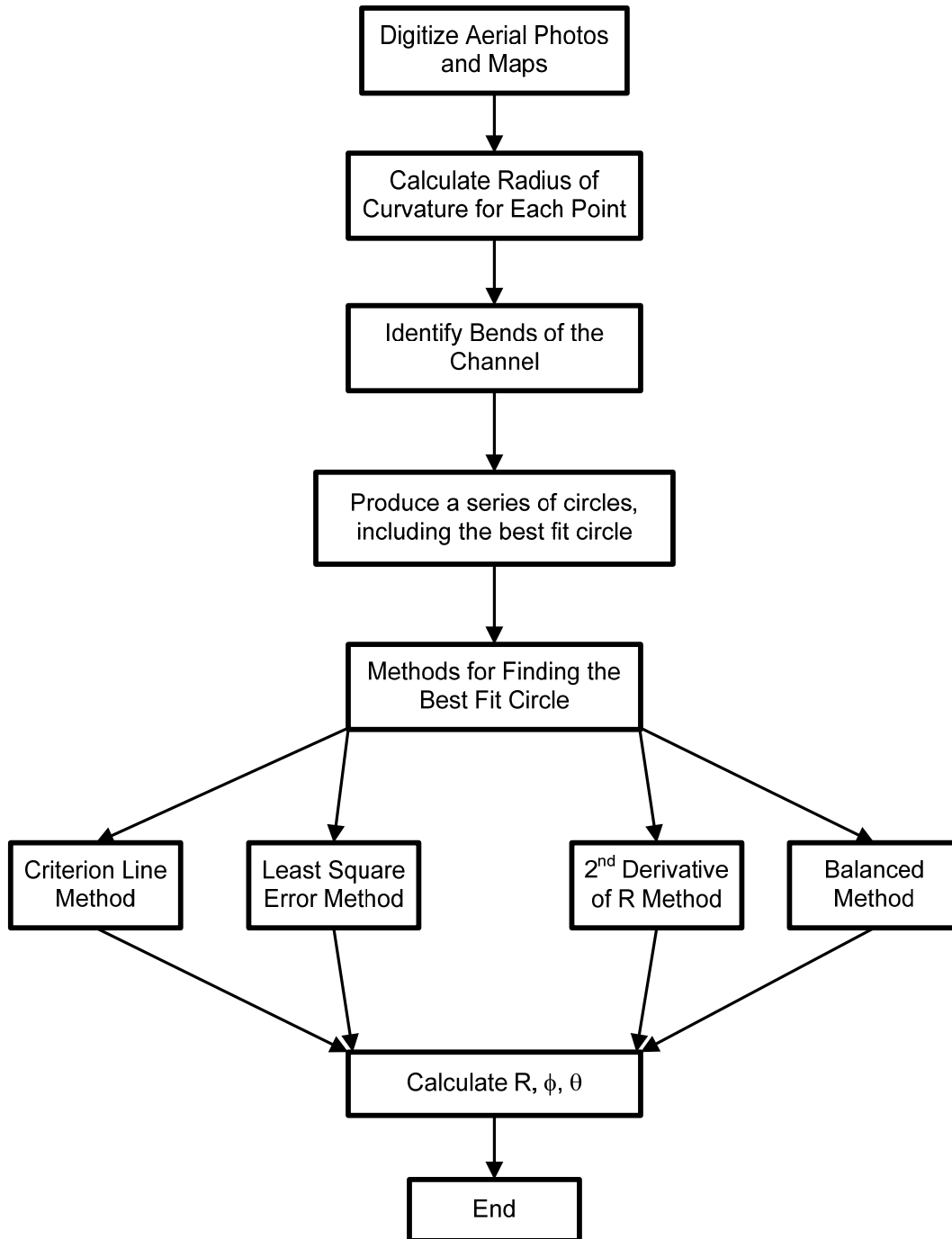
Figure 9.20. Flow Chart of Geometry Study.

Essential Procedures for Geometry Study

```
┌─────────────────────────────────────────────┐
│          Calculate radius of curvature        │
│    Problem: Best segment length for each      │
│                 bend/point                     │
└─────────────────────────────────────────────┘
                      ⇩
┌─────────────────────────────────────────────┐
│      Identify bends, produce many circles in   │
│          which the best circle is.             │
│  Methods: 1. criterion lines 2. Least square   │
│   error 3. second derivative 4. α Method 5     │
│                 Combination                    │
└─────────────────────────────────────────────┘
                      ⇩
┌─────────────────────────────────────────────┐
│   Visually determine: 1. Which circle is the   │
│   best. 2. In some cases two or more circles   │
│            can be equally good.                │
└─────────────────────────────────────────────┘
                      ⇩
┌─────────────────────────────────────────────┐
│   Numerically describe the visually best       │
│   circle. Use these criteria to find the       │
│              circle we want.                   │
└─────────────────────────────────────────────┘
                      ⇩
┌─────────────────────────────────────────────┐
│            Calculate bend angle                │
└─────────────────────────────────────────────┘
```

Figure 9.21. Essential Procedures for Geometry Study.

Application of the Hyperbolic Model
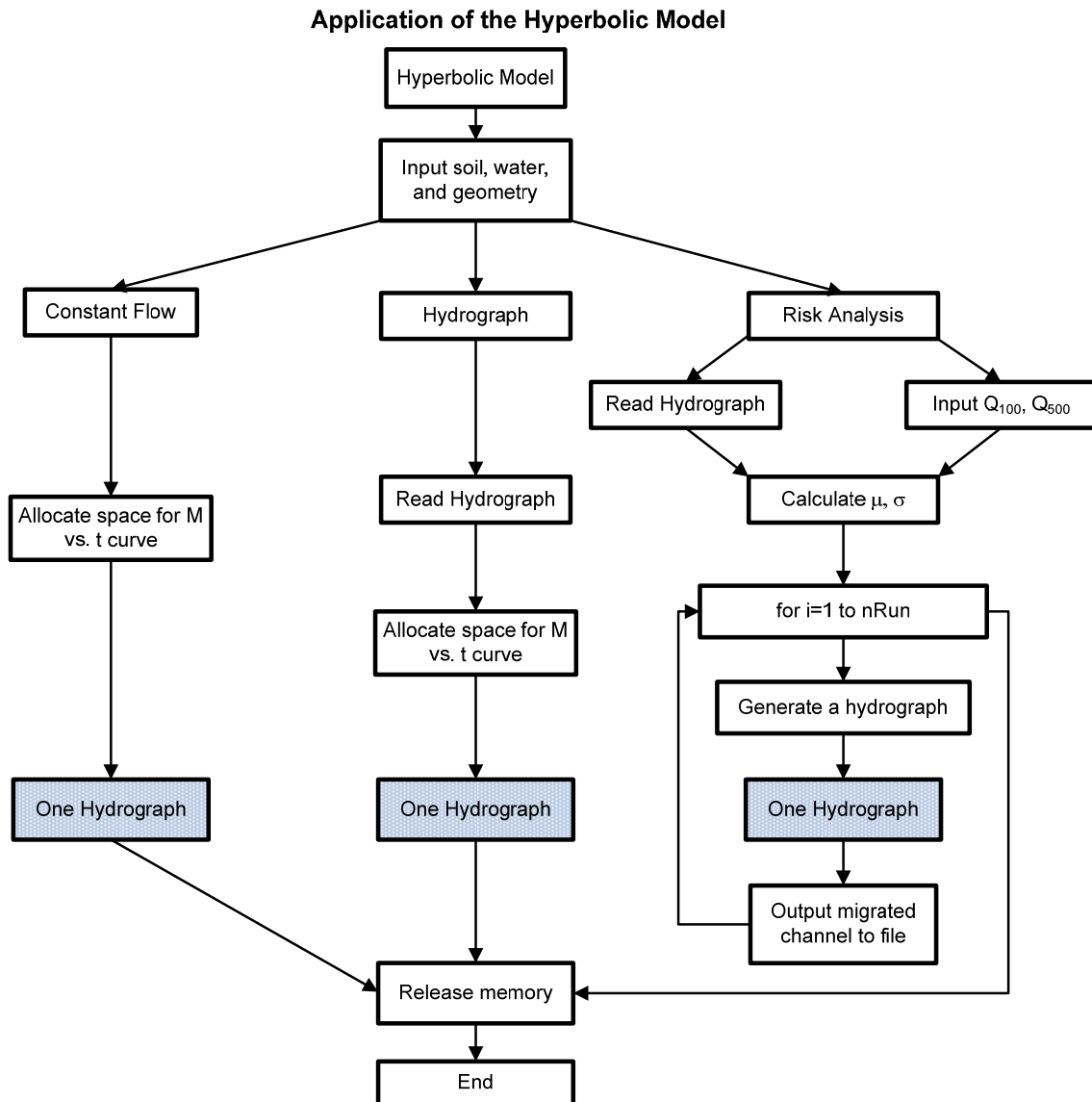
Figure 9.22. Flow Chart of Implementation of the Hyperbolic Model.

Implementation of Function OneHydrograph( )
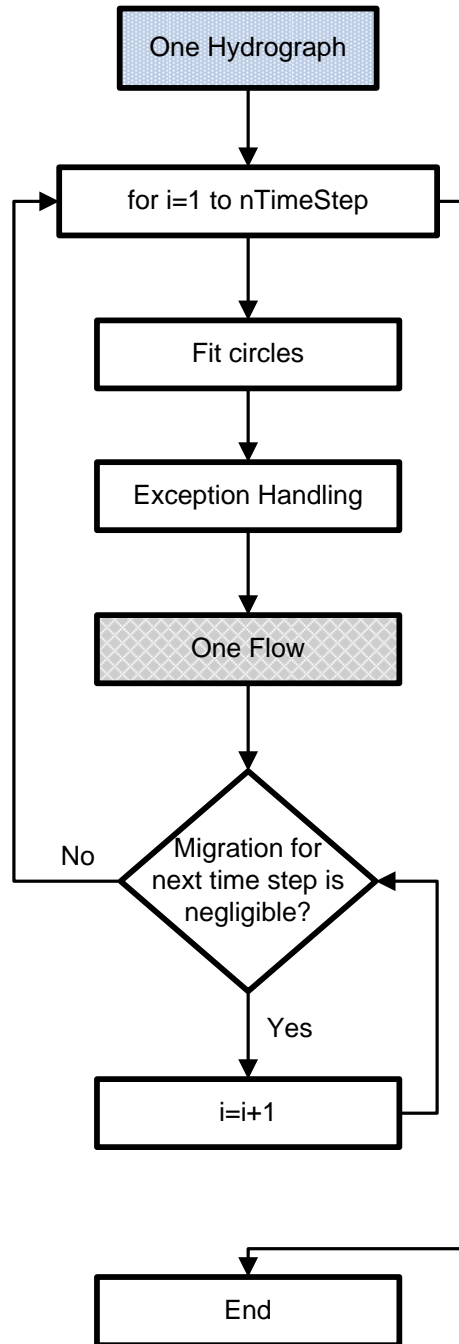
Figure 9.23. Flow Chart of Function OneHydrograph( ).

Implementation of Function OneFlow( )
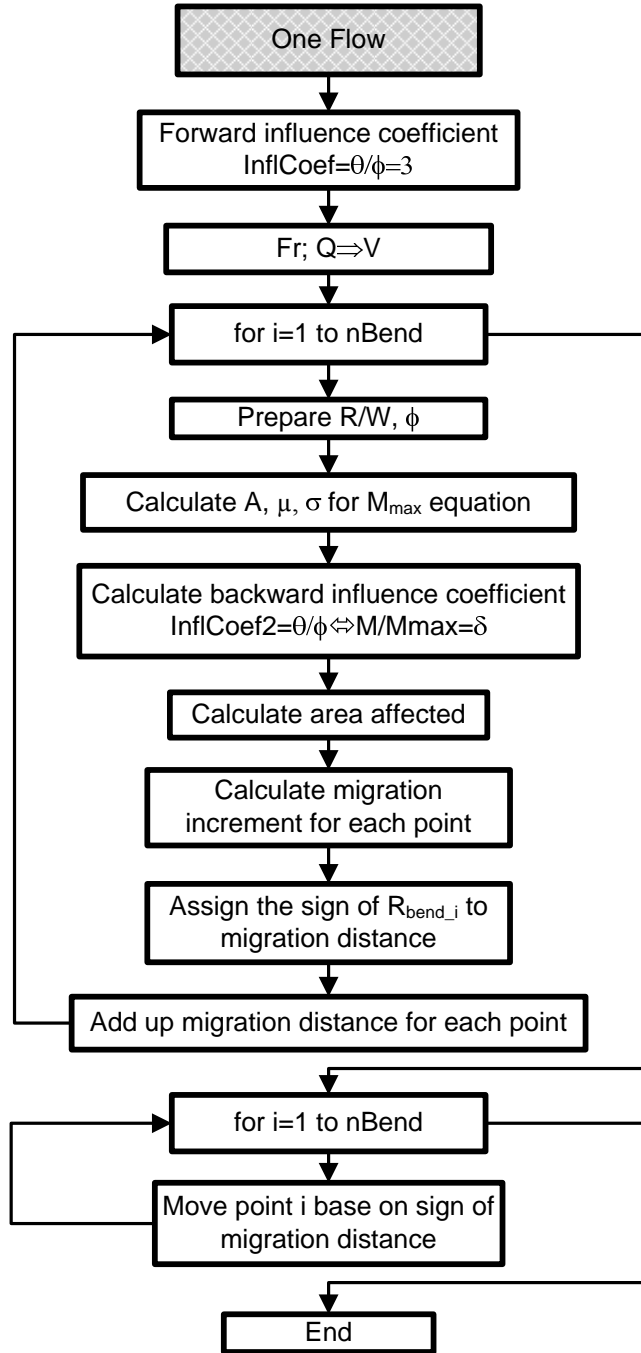
Figure 9.24. Flow Chart of Function OneFlow( ).

CHAPTER 10. EXAMPLE PROBLEMS

10.1 EXAMPLE 1: CONSTANT VELOCITY OPTION

Given:

1. Initial coordinates of the Brazos River center line in 1958 digitized from the map (Figure 10.1), as Figure 10.2:
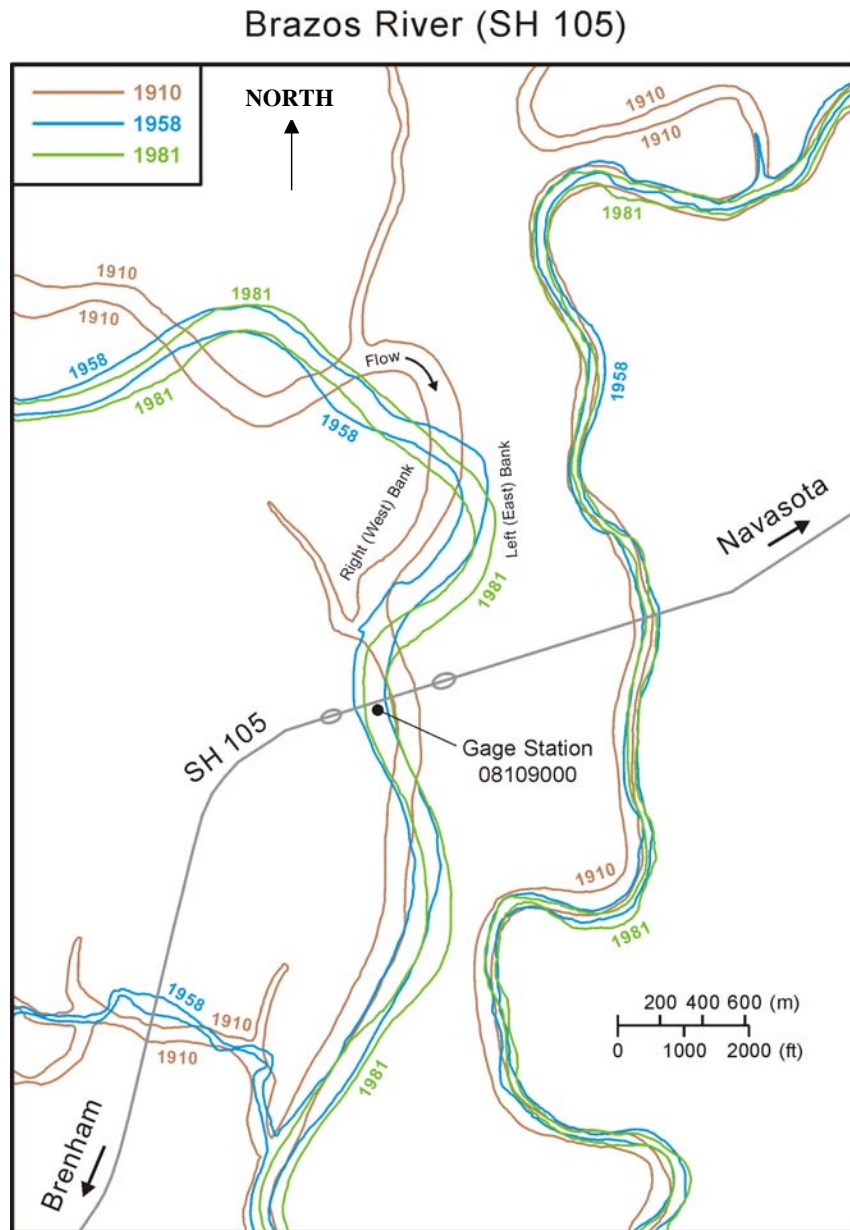
Figure 10.1. Map of the Brazos River (Example 1).
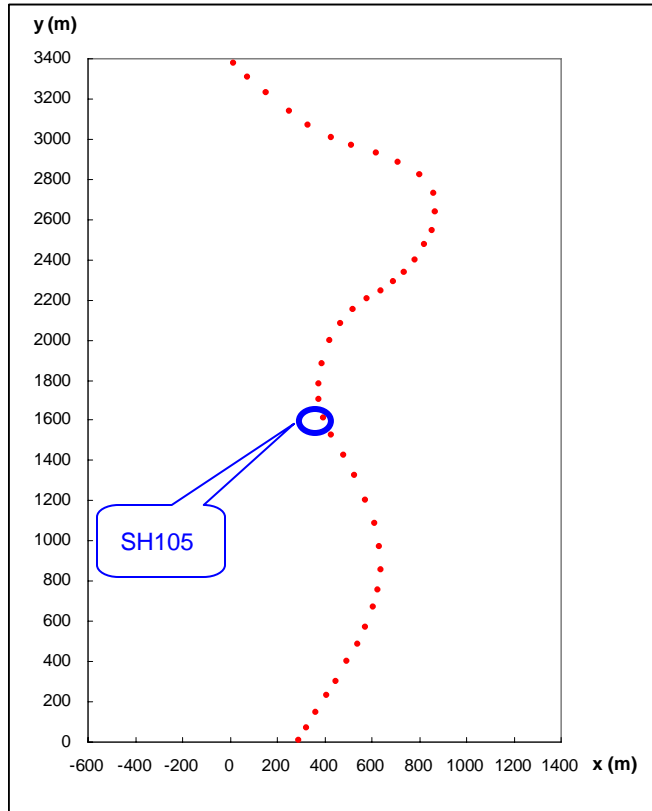
Figure 10.2. Digitized Coordinates of the Brazos River Center Line in 1958 (Example 1).

2. EFA Results shown in Figure 10.3:
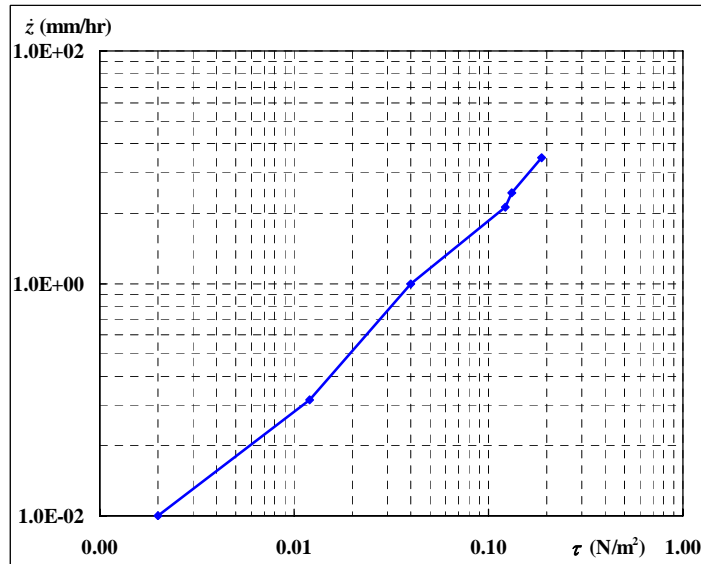
Figure 10.3. Assumed EFA Curve for the Brazos River (Example 1).

3. Constant Flowrate: 200 m³/s from 1958 to 1959.

4. Discharge versus Water depth curve obtained from the HEC-RAS simulation (Figure 10.4):
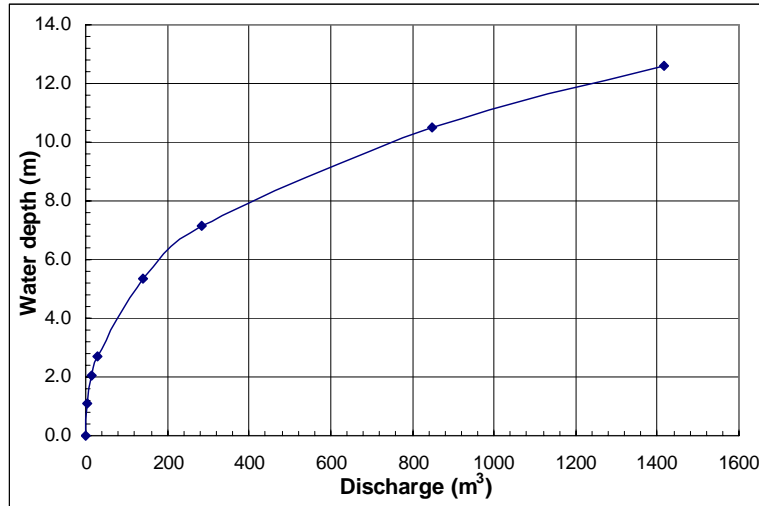
Figure 10.4. Discharge versus Water Depth Curve for the Brazos River (Example 1).

5. Discharge versus Velocity curve obtained from HEC-RAS simulation (Figure 10.5):
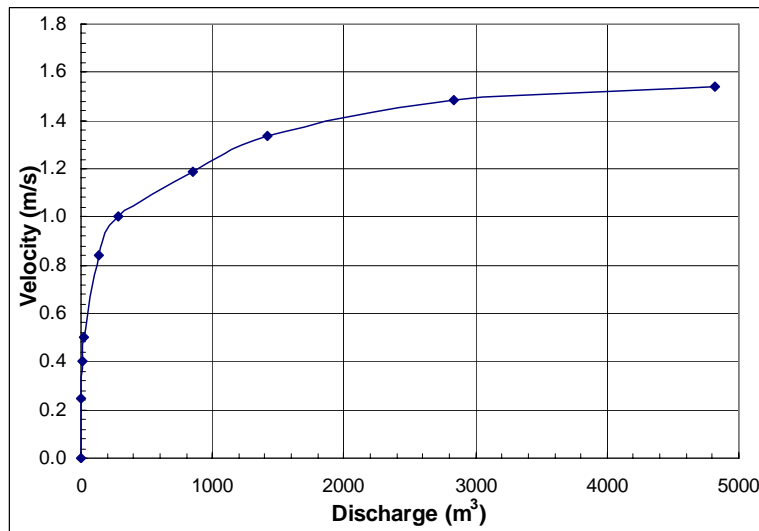
Figure 10.5. Discharge versus Velocity Curve for the Brazos River (Example 1).

Find:

1. Predict the new location of the center line of the Brazos River in 1959.
2. Migration versus Time curve for the SH105 bridge location.

Solution from the MEANDER program:

Use the constant flow option in the MEANDER program.

Results:

After a 1-year period of the flood, the new location of the center line of the Brazos River is shown in Figure 10.6. The exact coordinates of the new and initial locations are generated as a table as shown in Figure 10.7. In the table, the last column shows the accumulated migration distance at each point. The river migrated at the SH105 bridge location toward south by approximately 45 m during one year as shown in Figure 10.8.
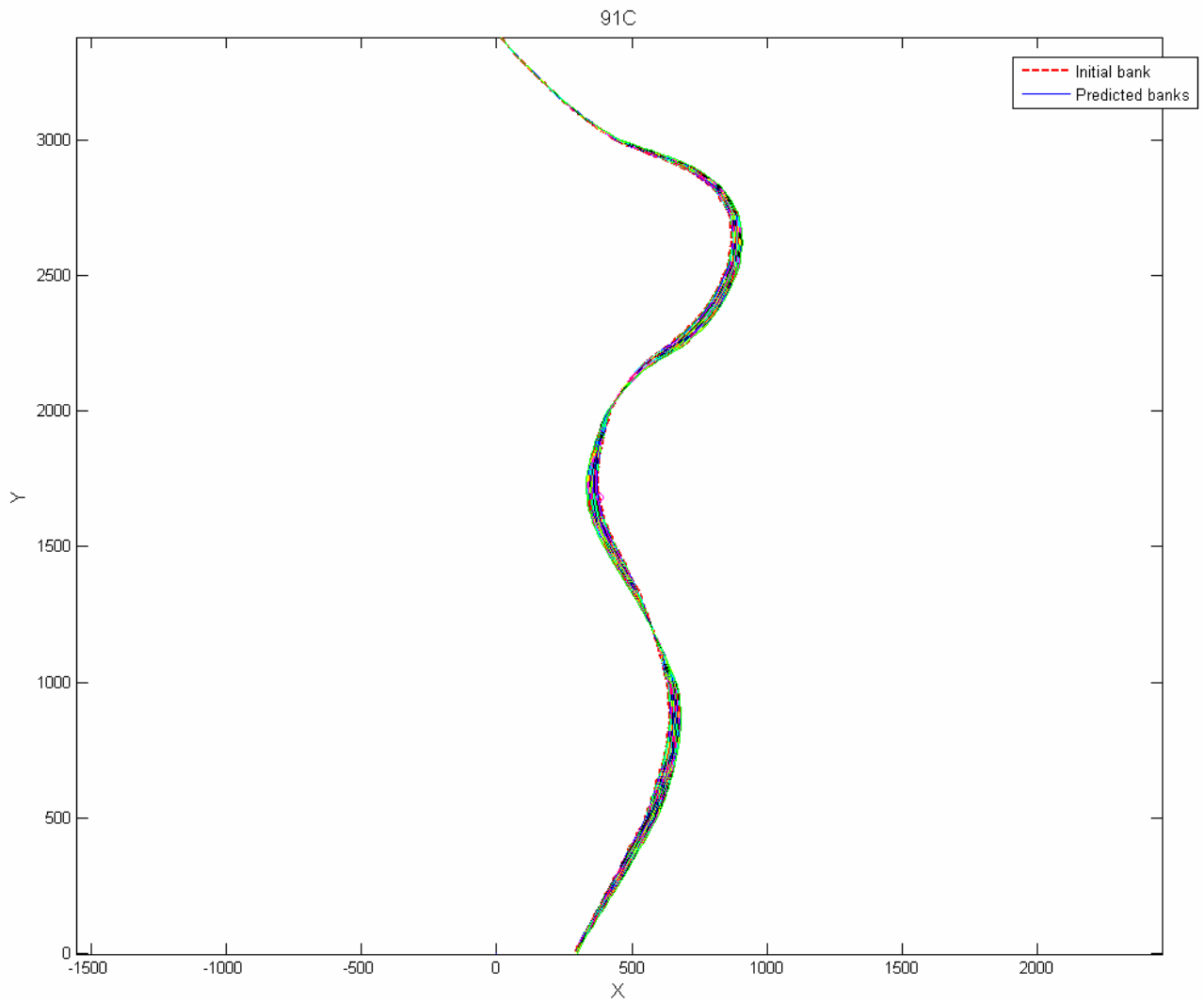
Figure 10.6. Output Plot (Example 1).

Figure 10.7. Output Table (Example 1).
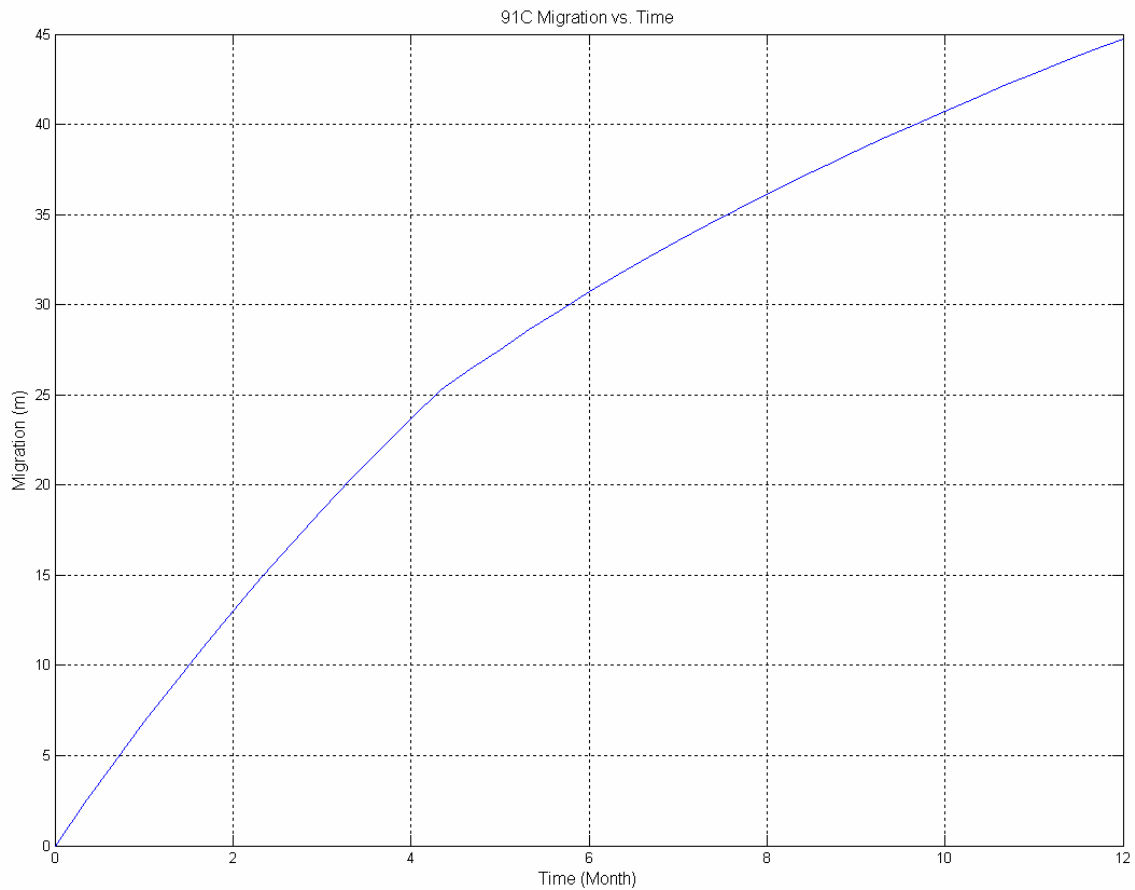
Figure 10.8. Migration versus Time Curve (Example 1).

10.2 EXAMPLE 2: HYDROGRAPH OPTION

Given:

1. Initial coordinates of the Guadalupe River center line in 1959 digitized from the map (Figure 10.9), as Figure 10.10. Note that the US59 bridge has not migrated much since it was located on the straight portion of the river. Therefore, a new bridge location is assumed for Example 2 as shown in Figure 10.10.
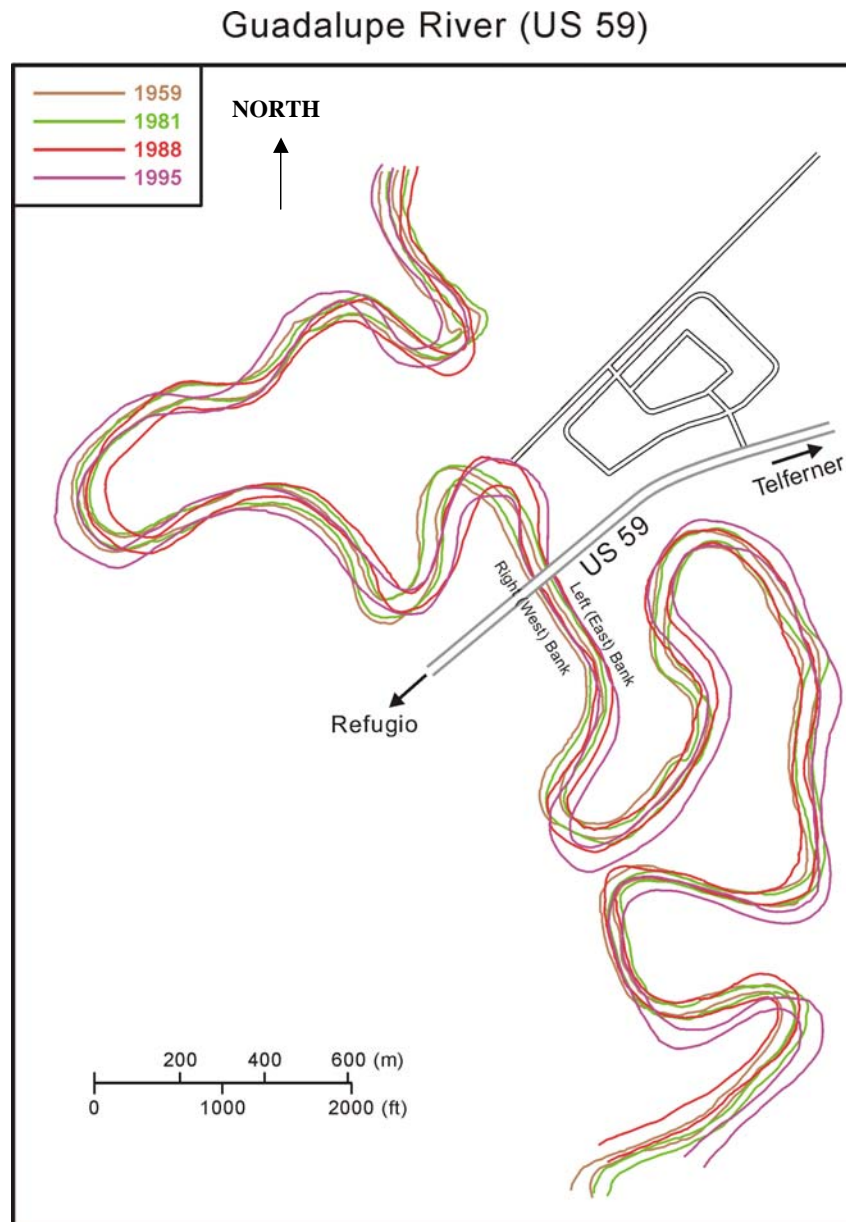
Figure 10.9. Map of the Guadalupe River (Example 2).
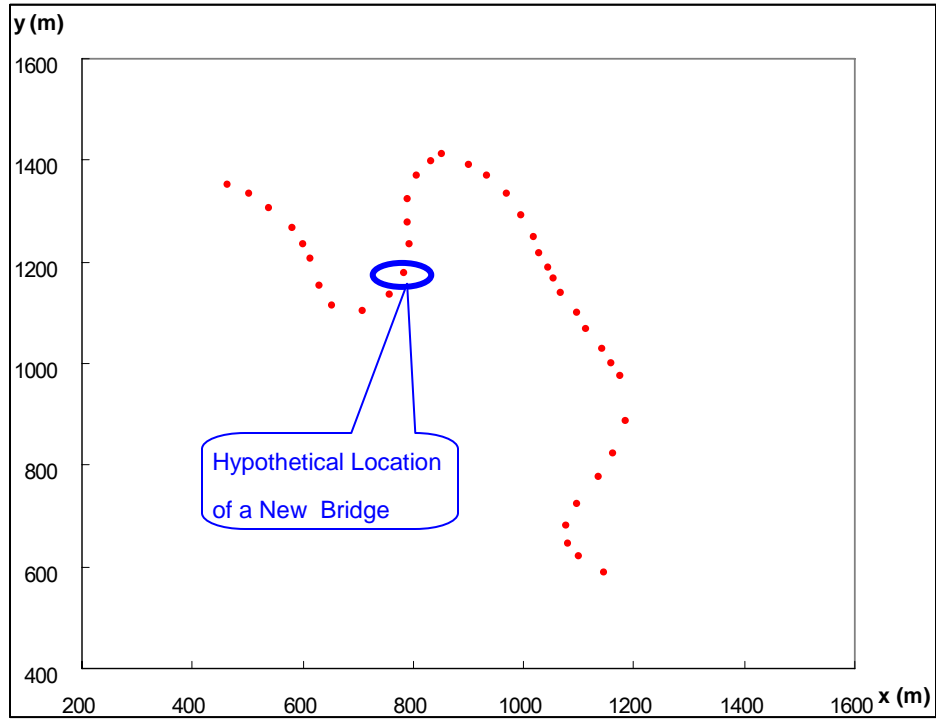
Figure 10.10. Digitized Coordinates of the Guadalupe River Center Line in 1959 (Example 2).

2. EFA Results shown in Figure 10.11:
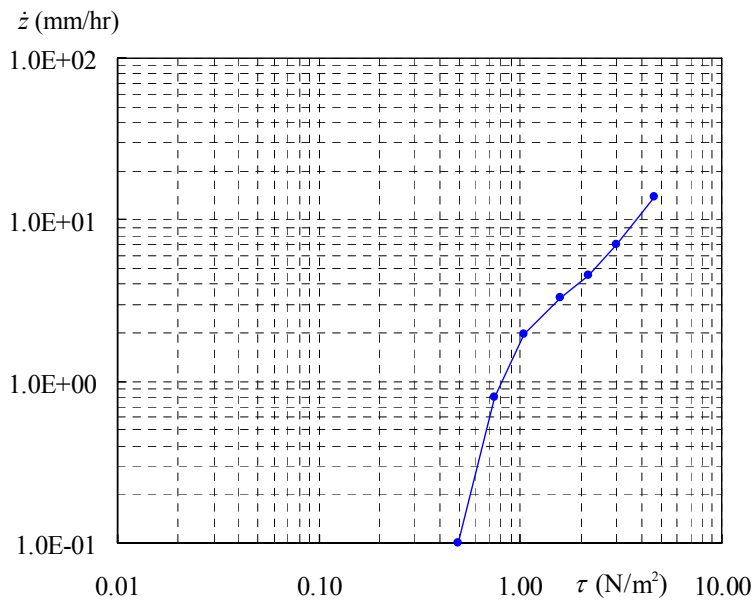
Figure 10.11. Assumed EFA Curve for Guadalupe River (Example 2).

3. Hydrograph of the Guadalupe River at the new bridge location is given in Figure 10.12:
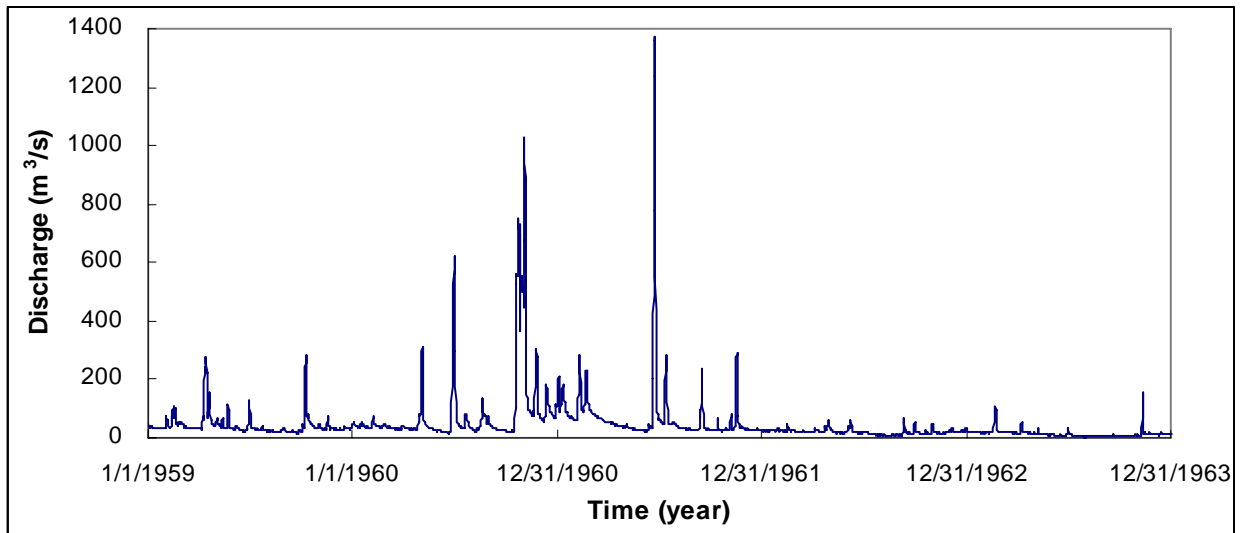
Figure 10.12. Hydrograph of Guadalupe River at the New Bridge Location in 1959.

4. Discharge versus Water depth curve obtained from HEC-RAS simulation (Figure 10.13):
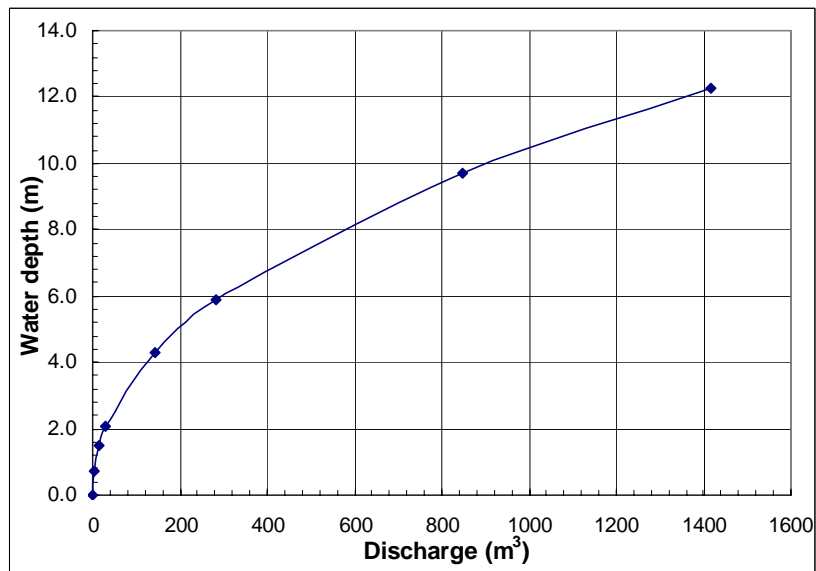
Figure 10.13. Discharge versus Water Depth Curve for the Guadalupe River (Example 2).

5. Discharge versus Velocity curve obtained from HEC-RAS simulation (Figure 10.14):
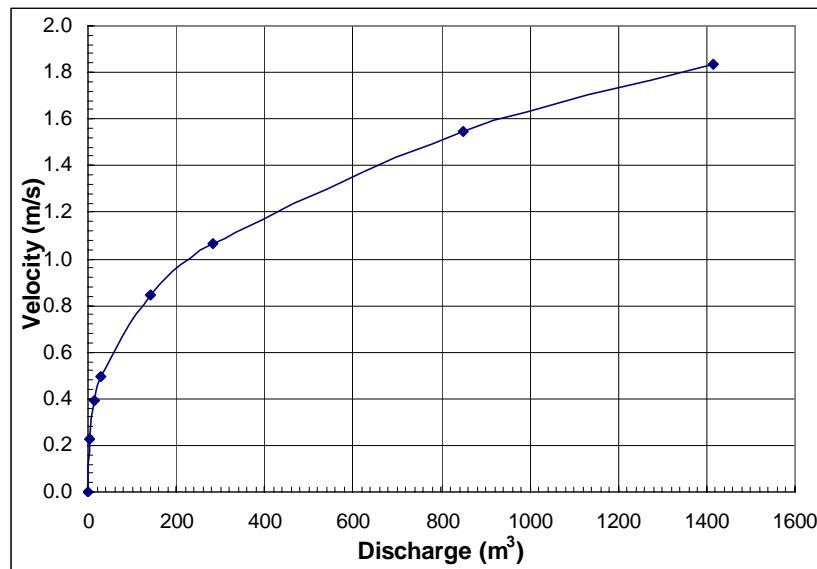
Figure 10.14. Discharge versus Velocity Curve for the Guadalupe River (Example 2).

Find:
1. Predict the new location of the center line of the Guadalupe River at the end of 1963.
2. Migration versus Time curve for the new bridge location during 5-year period.

Solution from the MEANDER program:

Use the hydrograph option in the MEANDER program.

Results:

The migrated location of the center line of Guadalupe River according to the given hydrograph is shown in Figure 10.15. The exact coordinates of the new and initial locations are tabulated in Figure 10.16. In the table, the accumulated migration distance at each point is shown in the last column. The river migrated at the new bridge location toward south by approximately 11.8 m during five years as shown in Figure 10.17. In the figure, the effect of the hydrograph is obvious such that the low flow rate do not cause any migration movement while the big flood moves the river significantly.
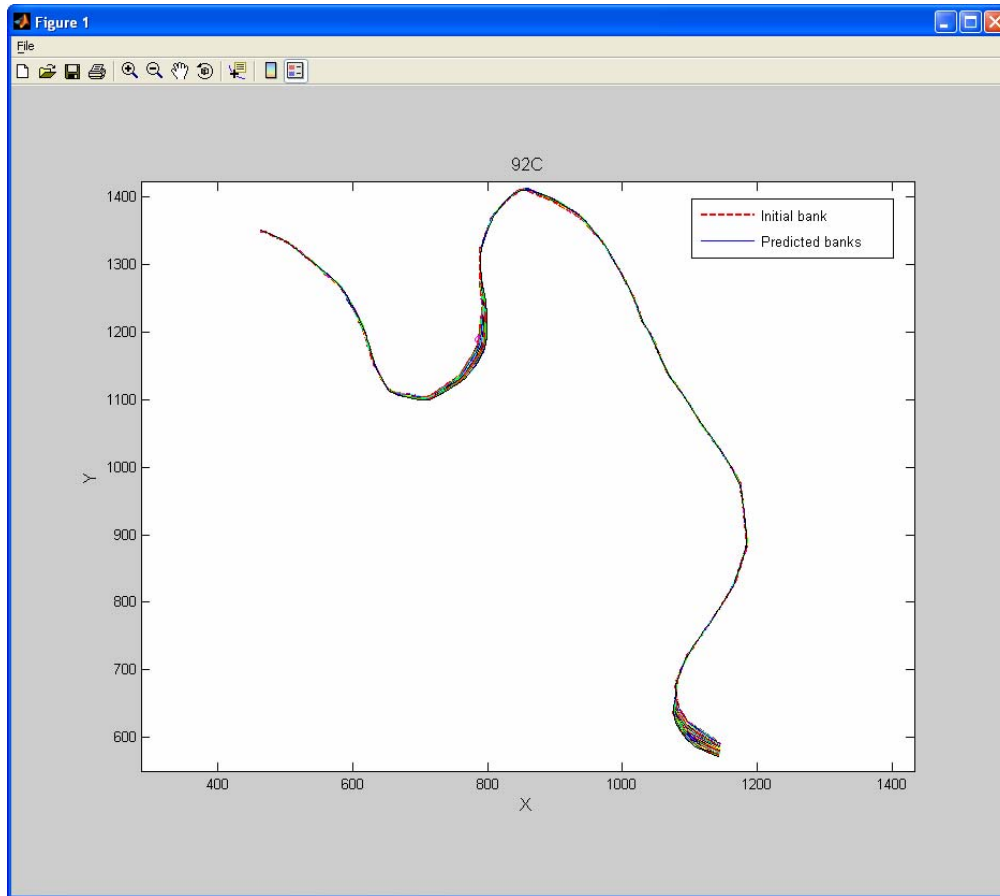
Figure 10.15. Output Plot for Example 2.

Figure 10.16. Output Table for Example 2.

197
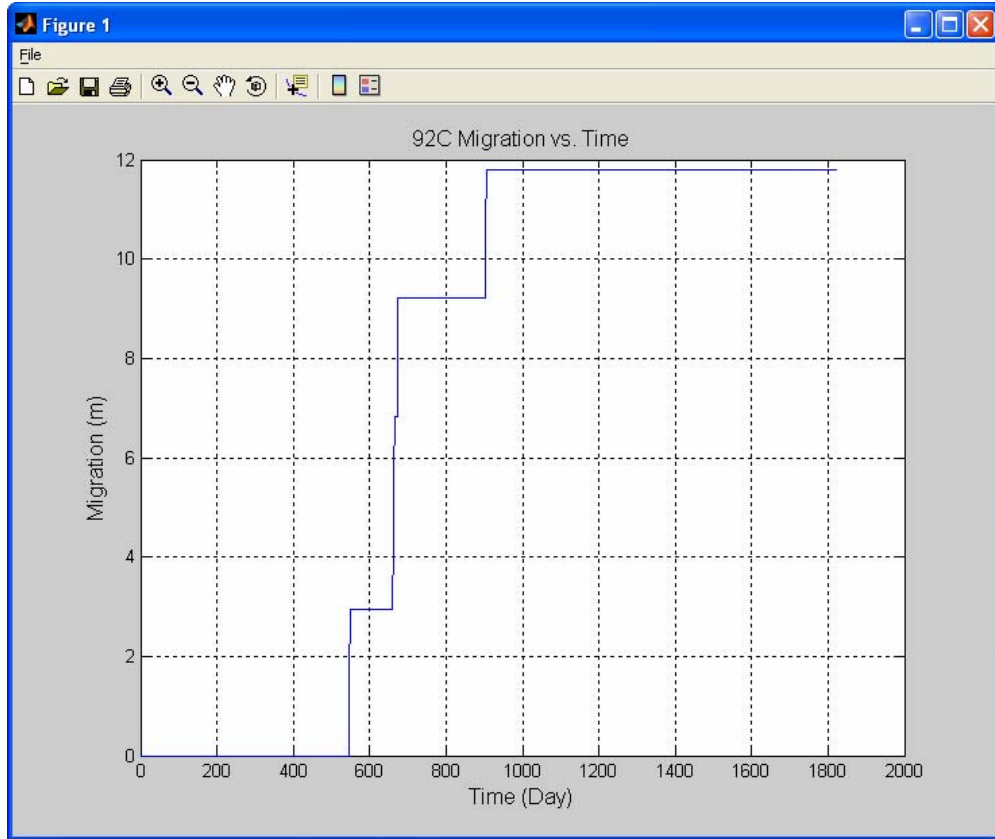
Figure 10.17. Migration versus Time Curve for Example 2.

10.3 EXAMPLE 3: RISK ANALYSIS OPTION

Given:
1. Use the same initial coordinates of the Brazos River center line given in Example 1 (Figure 10.2).
2. Use the same EFA result given in Example 1 (Figure 10.3).
3. Generate the future hydrographs using the following values: Q_{100} = 6000 m^3/s and Q_{500} = 9000 m^3/s.
4. Use the same Discharge versus Water depth curve given in Example 1 (Figure 10.4).
5. Use the same Discharge versus Velocity curve given in Example 1 (Figure 10.5).

Find:
1. Generate the CDF map to show the general trend of the meander migration of the Brazos River with the associated likelihood levels after 180 days.
2. Predict the migration distance at the SH105 bridge location with a 1 percent probability that the river will move to the predicted location or further after 180 days.

***Solution from the MEANDER program*:**

Use the risk analysis option in the MEANDER program.

Results:

The CDF map generated by the MEANDER program is shown in Figure 10.18 and the location of the SH105 bridge is represented by a thick straight line in the same figure. The predicted migration distances at the bridge location after 180 days are shown in Figure 10.19 (CDF plot). According to the CDF plot, the river will migrate 45 m or further in the direction of the bridge with a 1 percent probability. In other words, the river has a 99 percent probability to move 45 m or closer.
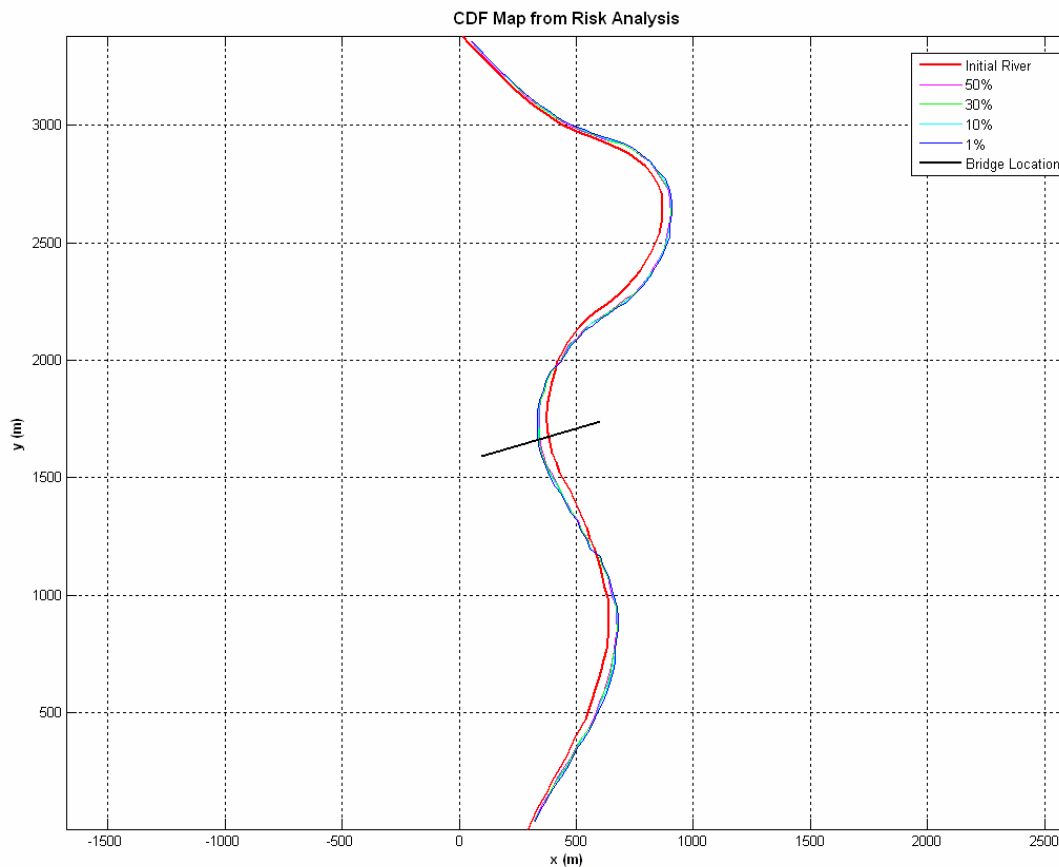
Figure 10.18. CDF Map for the Brazos River (Example 3).
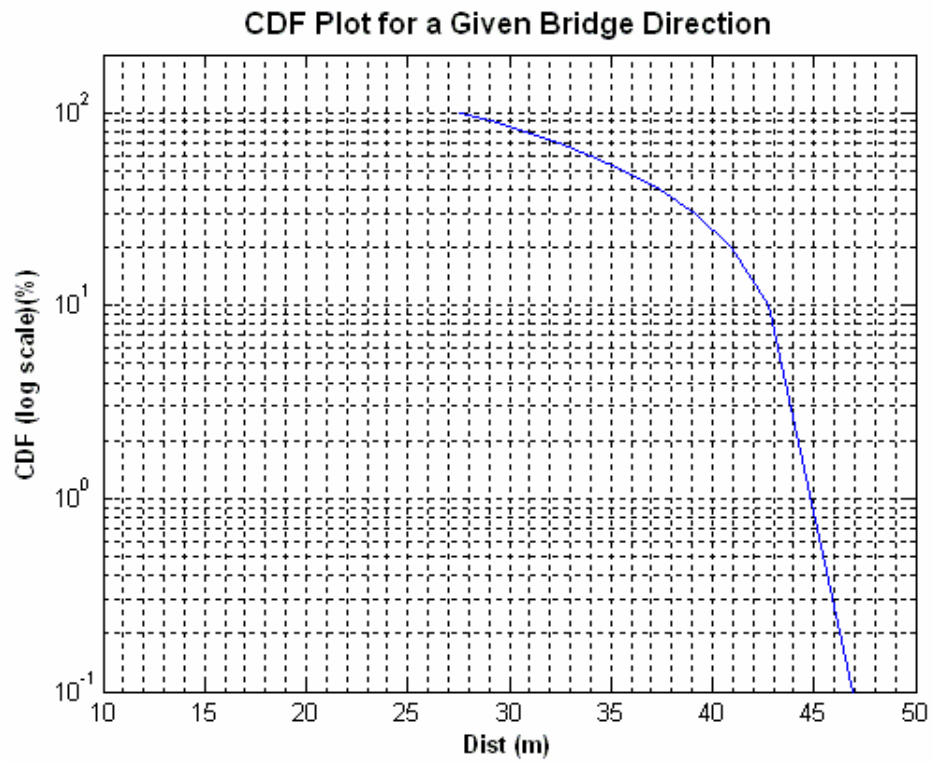
Figure 10.19. CDF Plot for the SH105 Bridge Direction (Example 3).

CHAPTER 11. CONCLUSIONS AND RECOMMENDATIONS

11.1 CONCLUSIONS

This project is to investigate river bankline migration and develop a soil-based guideline for predicting such migration as a function of time. A hyperbolic curve was chosen to estimate the migration displacement with time. This curve is characterized by two parameters: initial migration rate and maximum migration distance. These quantities were to be determined in this project. Numerical simulations with a 3D fluid model were used to obtain the maximum shear stress on the channel boundaries; the erosion function generated by EFA test on the soil material on the site was used to calculate the critical shear stress and the soil erosion rate corresponding to the shear stress. With the results of these two parameters (shear stress from the numerical simulation and EFA test erosion function), the channel bankline initial migration rate was determined. Large-scale flume tests were conducted in the laboratory to simulate real river meander processes and determine the maximum migration distance of the channel bankline needed in the hyperbolic model. Equations for different soils (sand and clay) were thus proposed for the maximum migration distance.

A risk analysis approach and a computer program were also developed in the project. Future hydrographs of the channel flowrate are generated and the corresponding risk is evaluated for the channel bankline movement in a probability approach. The risk that the river bank will reach a given structure can be determined in that fashion. In the last part of this project, all modules were combined in a computer program. User-friendly screens were used in the Windows environment, and documents and examples were attached in the help menu of the program.

11.2 RECOMMENDATIONS

Full-scale verification was not conducted because of limited budget and time. Therefore, full-scale verification which involves sampling work at several river sites for the EFA tests is highly recommended for further validation of the new prediction method.

The input data for the MEANDER program consists of three parts; erodibility of the soil from the EFA test, digitized river coordinates, and hydrograph at a river. Among three input data, digitizing the geometries of the rivers and obtaining the hydrographs at the rivers are time-consuming tasks, especially the digitization work. Therefore, it will be very helpful for the bridge engineers to run the MEANDER program if there are pre-developed databases of

digitized coordinates and hydrographs for the rivers which have a relatively high potential for large migration in Texas.

the Instantaneous Model approach was considered but not completed. The researchers highly recommend that this method be completed and compared with the Hyperbolic Model approach against the full-scale data to choose the better prediction model for meander migration.

The current version of the MEANDER program was developed in the mixed language programming such as Visual C++ and Matlab. If the MEANDER program can be re-written in one language environment, it will be much easier for the future researchers to improve or modify it if necessary.

The run time with a risk analysis option in the MEANDER program might be extremely long if a long time length or a large number of future hydrographs being generated is specified. This might be a problem of the current version of the MEANDER program from a practical standpoint. Therefore, it is highly recommended to optimize the algorithm to reduce computation time.

REFERENCES

Abad, J., and Garcia, M. H. (2004). "Conceptual and Mathematical Model for Evolution of Meandering Rivers in Naturalization Processes." *Proceedings of the 2004 World Water and Environmental Resources Congress: Critical Transitions in Water and Environmental Resources Management*, Salt Lake City, Utah, 2048-2057.

Abad, J., and Garcia, M. H. (2006). "RVR Meander: A Toolbox for Re-Meandering of Channelized Streams." *Computers & Geosciences*, 32, 92-101.

Blondeaux, P., and Seminara, G. (1985). " Aunified Bar-Bend Theory of River Meanders." *Journal of Fluid Mechanics*, 157, 449-470.

Briaud J.-L., Ting, F., Chen, H. C., Gudavalli, R., Perugu, S., and Wei, G. (1999). "SRICOS: Prediction of Scour Rate in Cohesive Soils at Bridge Piers." *Journal of Geotechnical and Environmental Engineering*, ASCE, 125(4), 237-246.

Briaud J.-L., Ting, F., Chen, H. C., Cao, Y., Han, S. W., and Kwak, K. W. (2001a). "Erosion Function Apparatus for Scour Rate Predictions." *Journal of Geotechnical and Geoenvironmental Engineering*, ASCE, 127(2), 105-113.

Briaud J.-L., Chen H.-C., and Park S. (2001b). "Predicting Meander Migration: Evaluation of Some Existing Techniques." *Texas Transportation Institute Report No. 2105-1 for Texas Department of Transportation*, The Texas A&M University System, College Station, Texas.

Briaud J.-L., Chen H.-C., Li, Y., Nurtjahyo, P, and Wang, J. (2003). "Complex Pier Scour and Contraction Scour in Cohesive Soils." *Texas Transportation Institute Report No. 24-15 for National Cooperative Highway Research Program*, The Texas A&M University System, College Station, Texas.

Brice, J. C. (1975). "Airphoto Interpretation of the Form and Behavior of Alluvial Rivers." *Final Report to the U.S. Army Research Office* - Durham, Washington University, St. Louis.

Brice, J. C. (1982). "Stream Channel Stability Assessment." *Federal Highway Administration Report FHWA/RD-82/021*, Washington, D.C., 41.

Brice, J. C., and Blodgett, J. C. (1978). "Countermeasures for Hydraulic Problems at Bridges, Vol. I. Analysis and Assessment. (Final report. Jun 75 – Sep 78)." *Geological Survey Report FHWA/RD-78/162*, Washington, D.C., 187.

Chen, H. C. (1995a). "Submarine Flows Studied by Second-Moment Closure." *Journal of Engineering Mechanics*, 121(10), 1136-1146.

Chen, H. C. (1995b). "Assessment of a Reynolds Stress Closure Model for Appendage-Hull Junction Flow." *Journal of Fluids Engineering*, 117(4), 557-563.

Chen, H. C. (2002). "Numerical Simulation of Scour Around Complex Piers in Cohesive Soil." *First International Conference on Scour of Foundations, ICSF-1,* Vol. 1, Texas A&M University, College Station, Texas, 14-33.

Chen, H. C., and Korpus, R. A. (1993). "A Multi-Block Finite-Analytic Reynolds-Averaged Navier-Stokes Method for 3-D Incompressible Flows." *ASME Journal of Fluids Engineering*, 150, 113-121.

Chen, H.C. and Patel, V.C. (1988). "Near-Wall Turbulence Models for Complex Flows Including Separation." *AIAA Journal*, 26(6), 641-648.

Chen, H. C., and Patel, V. C. (1989). "The Flow around Wing-Body Junctions." *Proc. 4th Symposium on Numer. and Phys. Aspects of Aerodynamic Flows*, Long Beach, CA, 1-15.

Chen, H. C., Chen, M., and Davis, D. A. (1997). "Numerical Simulation of Transient Flows Induced by a Berthing Ship." *International Journal of Offshore and Polar Engineering*, 7(4), 182-191.

Chen, H. C., Patel, V. C., and Ju, S. (1990). "Solutions of Reynolds-Averaged Navier-Stokes Equations for Three-Dimensional Incompressible Flows." *J. of Computational Physics*, 88(2), 305-336.

Crassidis, J. L., and Junkins, J. L. (2004). *Optimal Estimation of Dynamic Systems*, Chapman & Hall/CRC, Boca Raton, Florida.

Darby, S. E., and Thorne, C. R. (1994). "Physically-Based Model of Channel Widening." *Proceedings - National Conference on Hydraulic Engineering*, n pt 2, Buffalo, NY, USA, 944-948.

Darby, S. E., and Thorne, C. R. (1996a). "Numerical Simulation of Widening and Bed Deformation of Straight Sand-Bed Rivers. I: Model Development." *Journal of Hydraulic Engineering*, 122(4), 184-193.

Darby, S. E., Thorne, C. R. and Simon, A. (1996b). "Numerical Simulation of Widening and Bed Deformation of Straight Sand-Bed Rivers. II: Model Evaluation." *Journal of Hydraulic Engineering*, 122(4), 194-202.

Darby, S. E., Alabyan, A. M., and Van de Wiel, M. J. (2002). "Numerical Simulation of Bank Erosion and Channel Migration in Meandering Rivers." *Water Resources Research*, 38(9), 21-221.

Duan, J. G. (1998). "Simulation of Alluvial Channel Migration Processes with a Two-Dimensional Numerical Model." *Ph.D. dissertation*, the Center for Computational Hydroscience and Engineering, the University of Mississippi, University, Mississippi.

Duan, J. G. (2005). "Analytical Approach to Calculate Rate of Bank Erosion." *Journal of Hydraulic Engineering*, 131(11), 980-990.

Duan, J. G., and Julien, P. Y. (2005). "Numerical Simulation of the Inception of Channel Meandering." *Earth Surface Processes and Landforms*, 30(9), 1093-1110.

Duan, J. G., Wang, S. S. Y., and Jia, Y. (2001). "The Applications of the Enhanced CCHE2D Model to Study the Alluvial Channel Migration Processes." *Journal of Hydraulic Research/De Recherches Hydrauliques*, 39(5), 469-480.

Hasegawa, K. (1981). "Bank-Erosion Discharge Based on a Non-Equilibrium Theory." *Proc. JSCE*, Tokyo, 316, 37-50 (in Japanese).

Hickin, E. J., and Nanson, G. C. (1975). "The Character of Channel Migration on the Beatton River, Northeast British Columbia, Canada." *Geological Society of America Bulletin*, 86, 487-494.

Hooke, J. M. (1980). "Magnitude and Distribution of Rates of River Bank Erosion." *Earth Surface Processes*, 5(2), 143-157.

Hudson, P. F., and Kesel, R. H. (2000). "Channel Migration and Meander-Bend Curvature in the Lower Mississippi River Prior to Major Human Modification." *Geology*, 28(6), 531-534.

Ikeda, S., Parker, G., and Sawi, K. (1981). "Bend Theory of River Meanders. I: Linear Development." *Journal of Fluid Mechanics*, 112, 363-377.

Jang, C.-L., and Shimizu, Y. (2005). "Numerical Simulation of Relatively Wide, Shallow Channels with Erodible Banks." *Journal of Hydraulic Engineering*, 131(7), 565-575.

Johannesson, H., and Parker, G. (1989). "Linear Theory of River Meanders." *River Meandering*, *Water Resources Monograph*, vol. 12 (S. Ikeda and G. Parker, eds.), American Geophysical Union, Washington, D.C., 181-213.

Keady, D. M., and Priest, M. S. (1977). "The Downstream Migration Rate of River Meandering Patterns." *Proc. 12th Mississippi Water Resources Conference*, Jackson, Mississippi, 29-34.

Lagasse, P. F., Spitz, W. J., and Zevenbergen, L. W. (2003). "A Methodology for Arcview Tools for Predicting Channel Migration." *ESRI, User Conference Proceedings*, San Diego, California.

Lagasse, P. F., Spitz, W. J., Zevenbergen, L. W., and ZachMann, D. W. (2004a), "Methodology for Predicting Channel Migration." *Report for National Cooperative Highway Research Program Project 24-16*, Owen Ayres & Associates, Inc. Fort Collins, Colorado.

Lagasse, P. F., Spitz, W. J., Zevenbergen, L. W., and ZachMann, D. W. (2004b). "Handbook for Predicting Stream Meander Migration Using Aerial Photographs and Maps." *Report for National Cooperative Highway Research Program Project 24-16*, Owen Ayres & Associates, Inc. Fort Collins, Colorado.

Meyer-Peter, E., and Muller, R. (1948). "Formulas for Bedload Transport." *Proc., 2nd Meeting Int. Assoc. Hydr. Res.*, Stockholm, Sweden, 39-64.

Moody, L. F. (1944). "Friction Factors for Pipe Flow." *Trans. Am. Soc. of Mech. Engrs.*, 66.

Mosselman, E. (1998). "Morphological Modelling of Rivers with Erodible Banks." *Hydrological Processes*, 12(8), 1357-1370.

Moura, L., and Kitney, R. (1991). "A Direct Method for Least-Squares Circle Fitting." *Computer Physics Communications*, 64, 57-63.

Munson, B. R., Young, D. F., and Okiishi, T. H. (1990). *Fundamentals of Fluid Mechanics*, Wiley, New York.

Nagata, N., Hosoda, T., and Muramoto, Y. (2000). "Numerical Analysis of River Channel Processes With Bank Erosion." *Journal of Hydraulic Engineering*, ASCE, 126(4), 243-252.

Nakagawa, H., and Tsujimoto, T. (1980). "Sand Bed Instability due to Bed Load Motion." *Journal of Hydraulic Division*, ASCE, 106(12), 2029-2051.

Nanson, G. C., and Hickin, E. J. (1983). "Channel Migration and Incision on the Beatton River." *Journal Hydraulic Engineering*, ASCE, 109(3), 327-337.

Nanson, G. C., and Hickin, E. J. (1986). "A Statistical Analysis of Bank Erosion and Channel Migration in Western Canada." *Geological Society of America Bulletin*, 97, 497-504.

Nurtjahyo, P. Y. (2002). "Chimera RANS Simulations of Pier Scour and Contraction Scour in Cohesive Soils." *Ph.D. dissertation*, Civil Engineering, Texas A&M University, Texas.

Odgaard, A. J. (1987). "Streambank Erosion along Two Rivers in Iowa." *Water Resources Research*, 23(7), 1225-1236.

Odgarrd, A. J. (1989a), "River-Meander Model. I: Development." *Journal of Hydraulic Engineering*, ASCE, 115(11), 1433-1450.

Odgarrd, A. J. (1989b), "River-Meander Model. II: Applications." *Journal of Hydraulic Engineering*, ASCE, 115(11), 1451-1464.

Olsen, N. R. B. (2003). "Three-Dimensional CFD Modeling of Self-Forming Meandering Channel." *Journal of Hydraulic Engineering*, 129(5), 366-372.

Parker, G., and Andrews, E. D. (1985) "Sorting of Bed Load Sediment by Flow in Meander Bends." *Water Resources Research*, 21, 1361–1373.

Parker, G., Sawai, K., and Ikeda, S. (1982). "Bend Theory of River Meanders. II. Nonlinear Deformation of Finite-Amplitude Bends." *Journal of Fluid Mechanics*, 115, 303-314.

Pizzuto, J. E. (1990). "Numerical Simulation of Gravel River Widening." *Water Resources Research*, 26(9), 1971-80.

Rodriguez, J. F., Bombardelli, F. A., Garcia, M. H., Frothingham, K. M., Rhoads, B. L., and Abad, J. D. (2004). "High-Resolution Numerical Simulation of Flow through a Highly Sinuous River Reach." *Water Resources Management*, 18(3), 177-199.

Rouse, H. (1938). "Experiments on the Mechanics of Sediment Suspension." *Proc. 5th Intern. Cong. for Applied Mech.*, 550-554.

Shen, H. W., Schumm, S. A., Nelson, J. D., Doehring, D. O., Skinner, M. M., and Smith, G. L. (1981). "Methods for Assessment of Stream-Related Hazards of Highways and Bridges." *Report* FHWA-RD-80-160; FCP 35H1-062, Colorado State University, Engineering Research Center, Fort Collins, Colorado, 252.

Sun, T., Meakin, P., and Jossang, T. (2001a). "A Computer Model for Meandering Rivers with Multiple Bed Load Sediment Sizes 1. Theory." *Water Resources Research*, 37(8), 2227-2241.

Sun, T., Meakin, P., and Jossang, T. (2001b). "A Computer Model for Meandering Rivers with Multiple Bed Load Sediment Sizes 2. Computer Simulations." *Water Resources Research*, 37(8), 2243-2258.

U.S. Army Corps of Engineers (1945). "Laboratory Study of the Meandering of Alluvial Rivers." *Technical Report*, U.S. Waterways Experiment Station, Vicksburg, Mississippi.

Van Rijn, L. C. (1989). "Sediment Transport by Currents and Waves." *Technical Report*, H461, Delft Hydraulics, Delft, The Netherlands.

APPENDIX A – FLUME TESTS IN SAND

PHOTOGRAPHS OF THE PREPARATION:

Figure A.1. Filling Sand into the Previous Channel for Next Test.

Figure A.2. Leveling Sand Bed.

Figure A.3. Sketching Channel Contour on the Sand Bed.
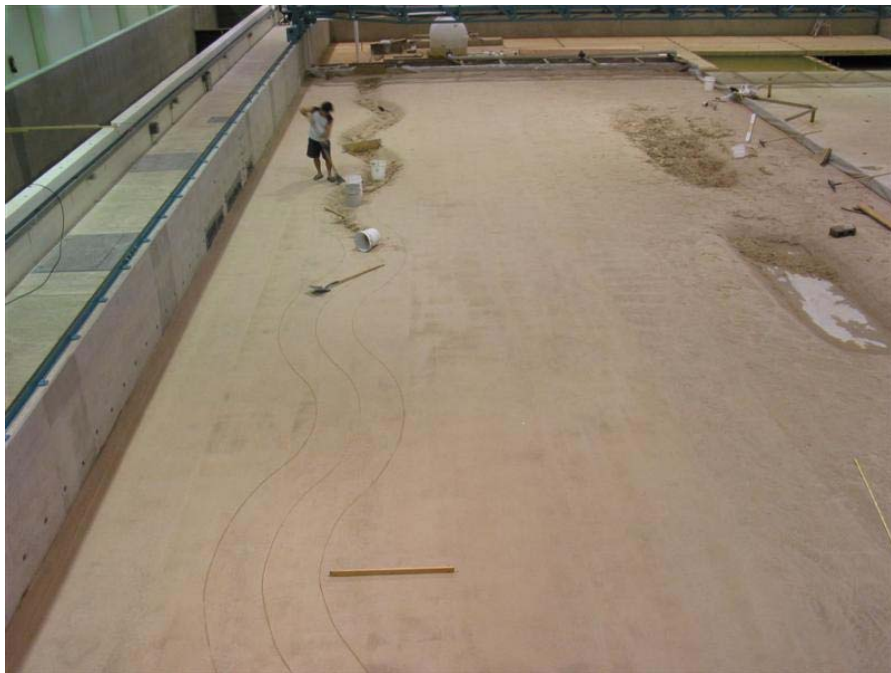
Figure A.4. Digging Sand Channel.

Figure A.5. Completion of the Sand Channel.

Figure A.6. Channel Initial Geometry with Water.

PHOTOGRAPHS OF THE FLUME TESTS:

(a) Initial   (b) Final (t = 42 hr)

Figure A.7. Sand Test Case 02 (R/W = 3, ϕ = 65°, Fr = 0.30).

(a) Initial   (b) Final (t = 92 hr)

Figure A.8. Sand Test Case 04 (R/W = 6, ϕ = 65°, Fr = 0.30).

(a) Initial	(b) Final (t = 30 hr)

Figure A.9. Sand Test Case 06 (R/W = 4, ϕ = 120°, Fr = 0.30).

Figure A.10. Initial Plan Form of Sand Test Case 08 (R/W = 4, ϕ = 220°, Fr = 0.30).

Figure A.11. 147 hr Plan Form of Sand Test Case 08 ($R/W = 4$, $\phi = 220°$, $Fr = 0.30$).

(a) Initial
(b) Final ($t = 56$ hr)

Figure A.12. Sand Test Case 09 ($R/W = 4$, $\phi = 120°$, $Fr = 0.25$).

(a) Initial	(b) Final (t = 23 hr)

Figure A.13. Sand Test Case 11 (R/W = 4, ϕ = 120˚, Fr = 0.36).

FLUME TEST RESULTS:
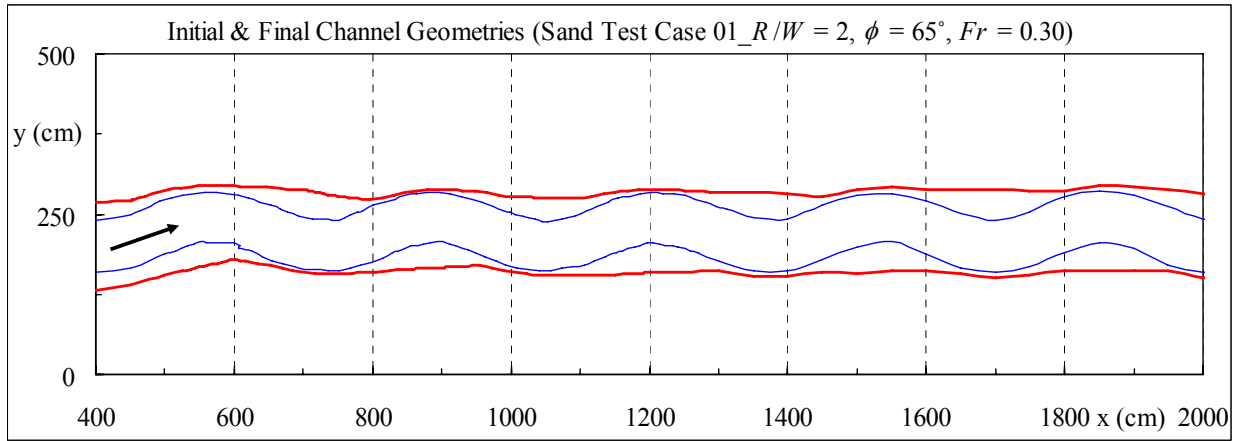
Figure A.14. Channel Geometry at the Initial and Final (18 hr) Stages.
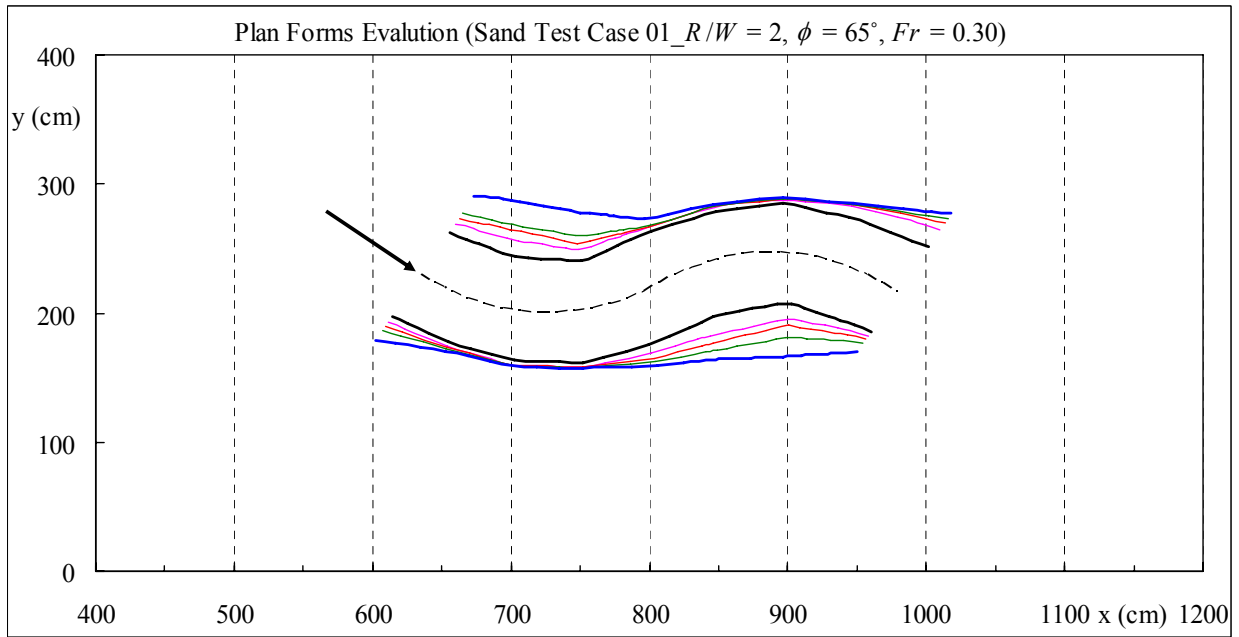
Figure A.15. Plan Forms Evolution at t = 0, 3, 6, 9 and 18 hr.
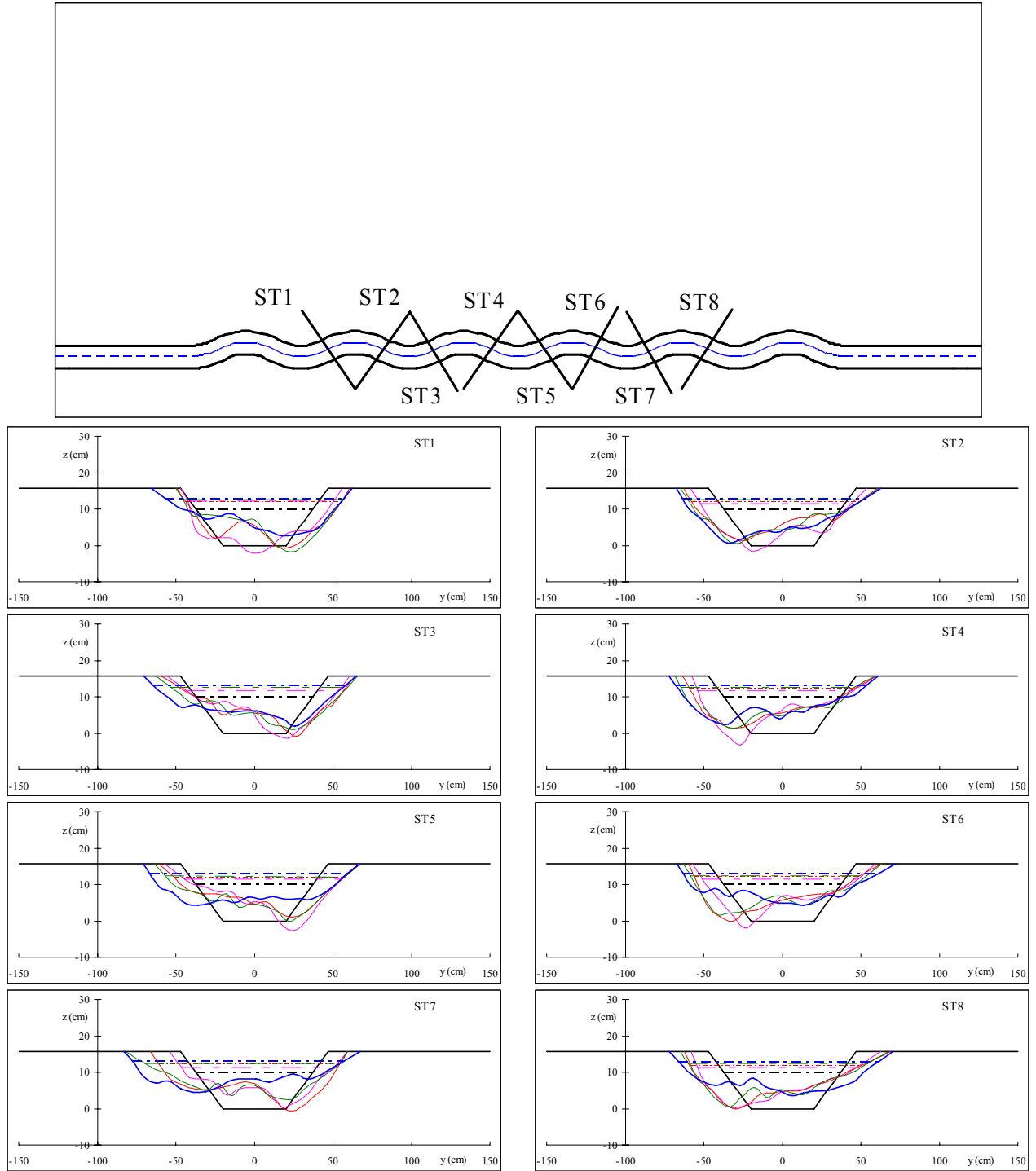
Figure A.16. Channel Cross-Section Profiles (Sand Test Case 01).
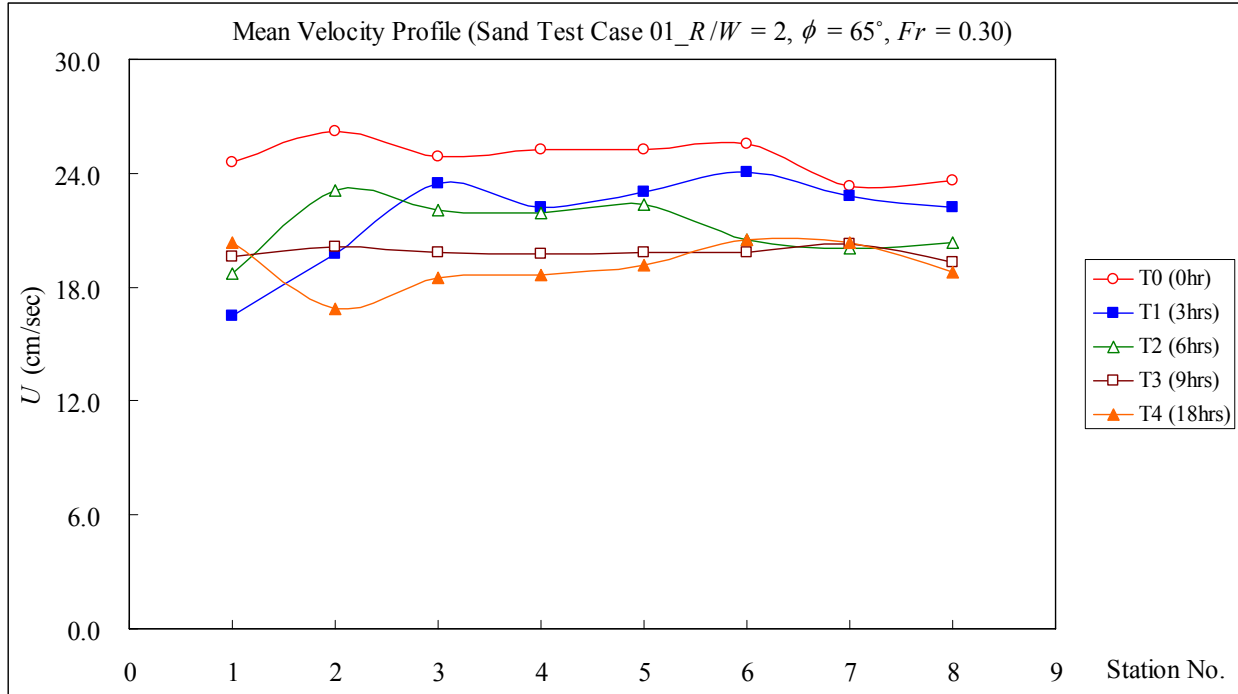
(a) Mean Velocity Profile
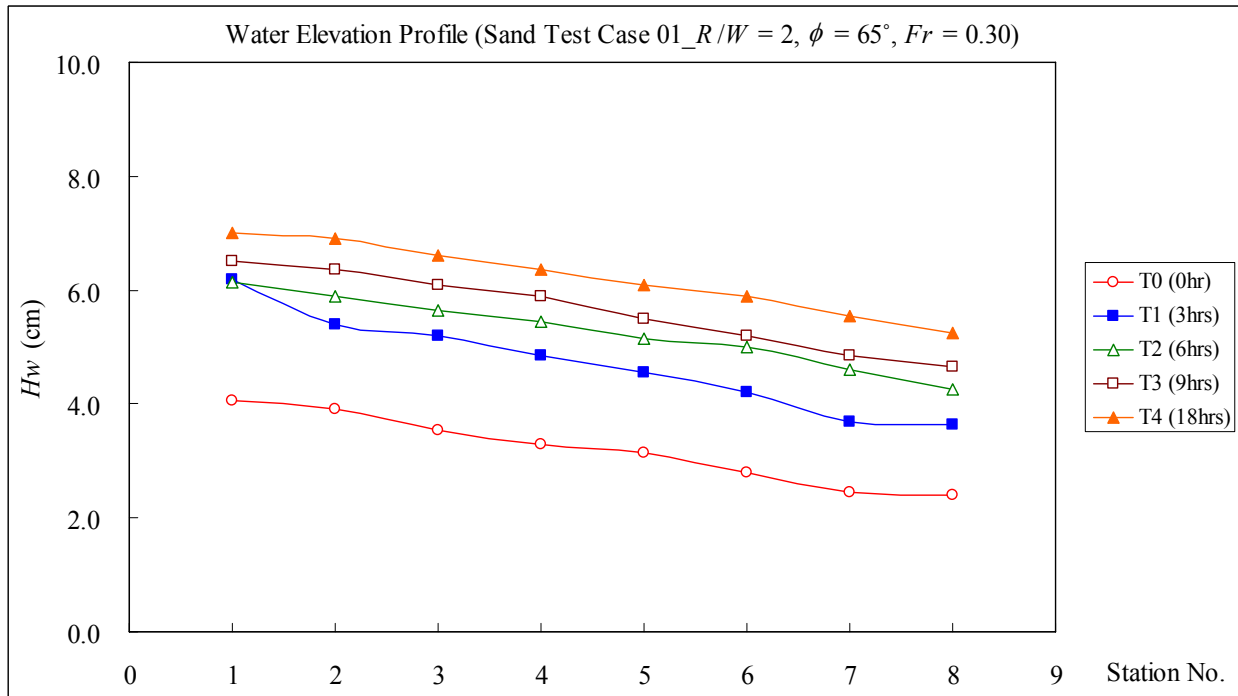
(b) Water Elevation Profile

Figure A.17. Mean Velocity and Water Elevation Measurement Results.
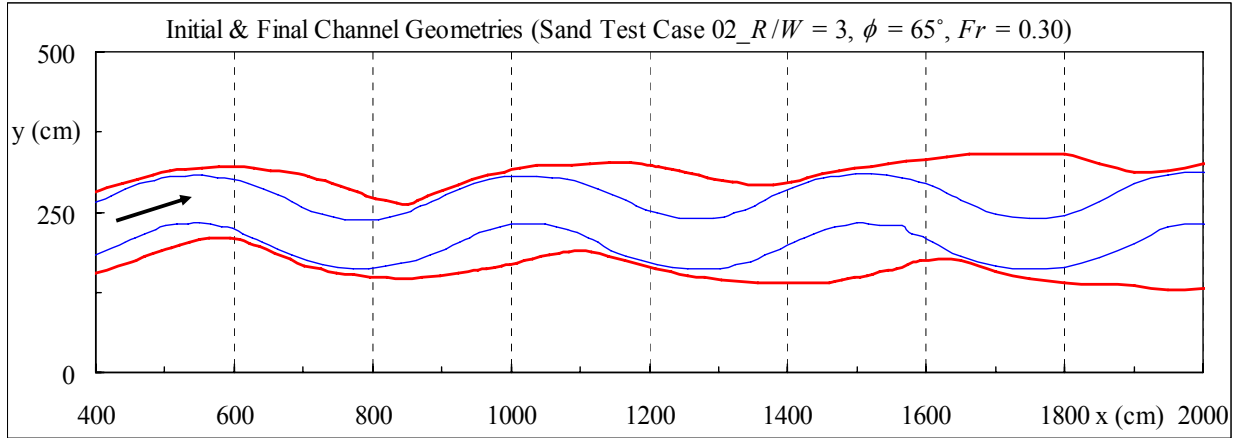
Figure A.18. Channel Geometry at the Initial and Final (42 hr) Stages.
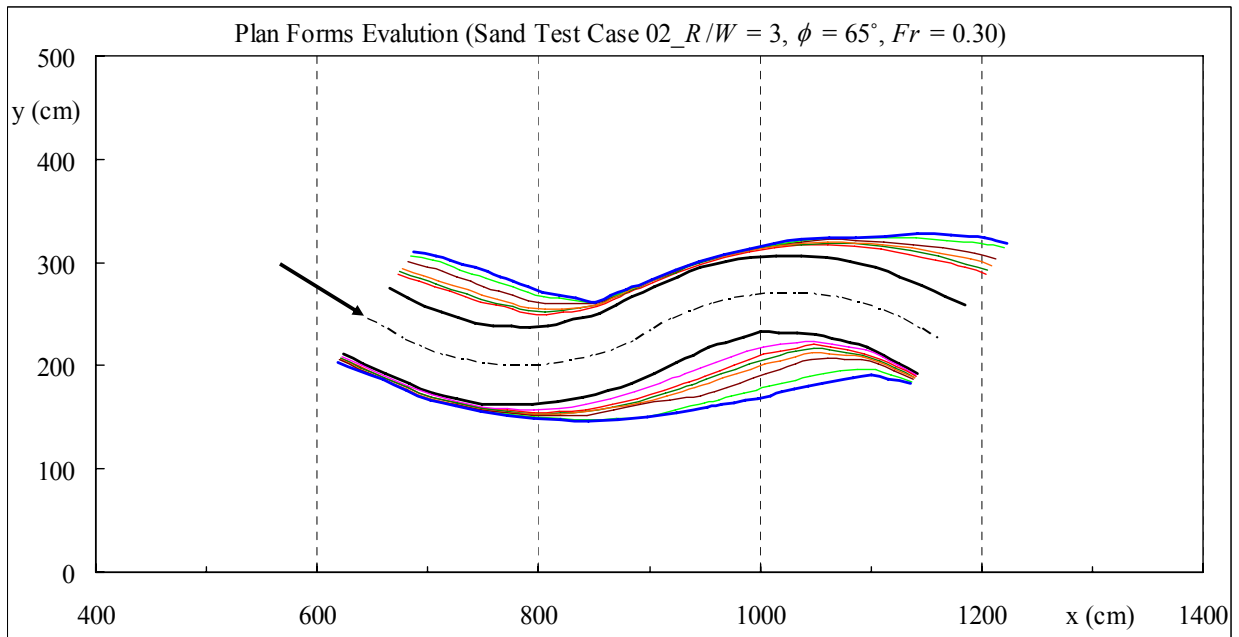
Figure A.19. Plan Forms Evolution at t = 0, 3, 6, 9, 15, 24, 33 and 42 hr.
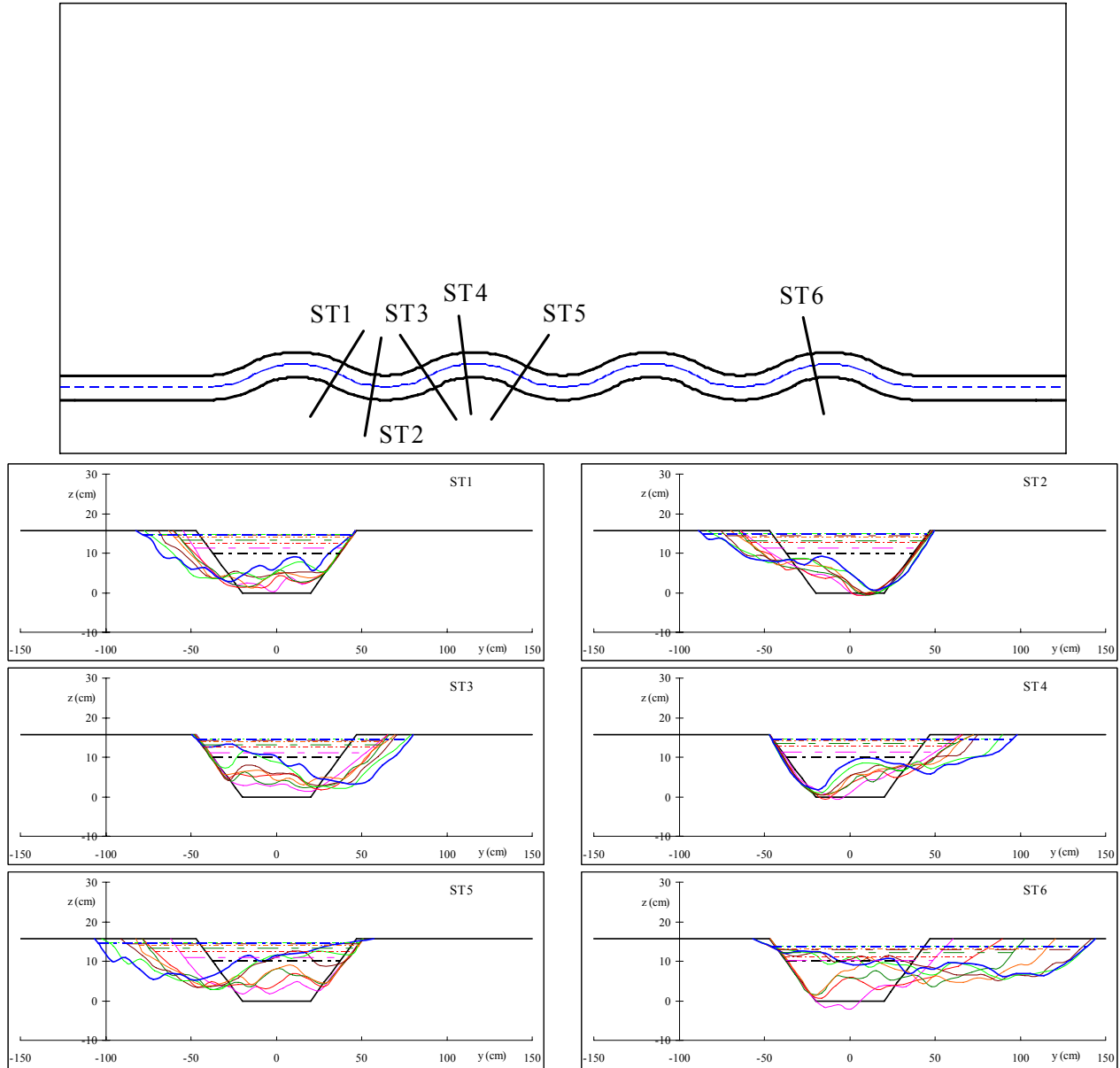
Figure A.20. Channel Cross-Section Profiles (Sand Test Case 02).
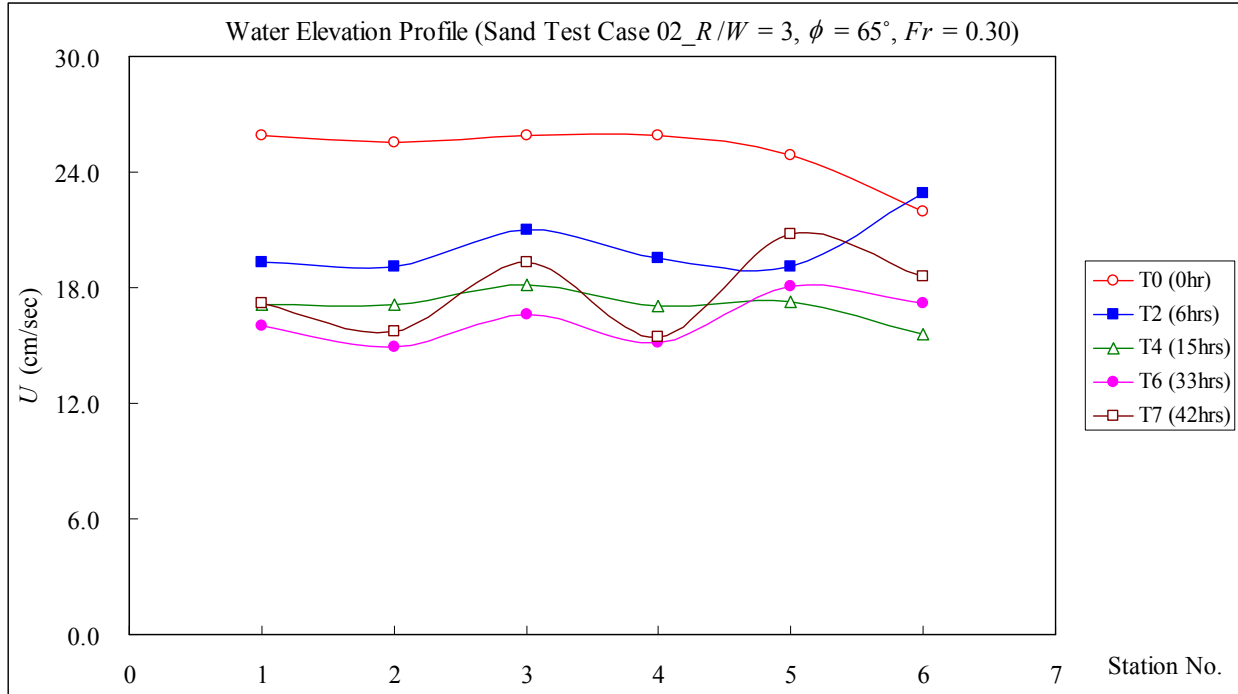
(a) Mean Velocity Profile
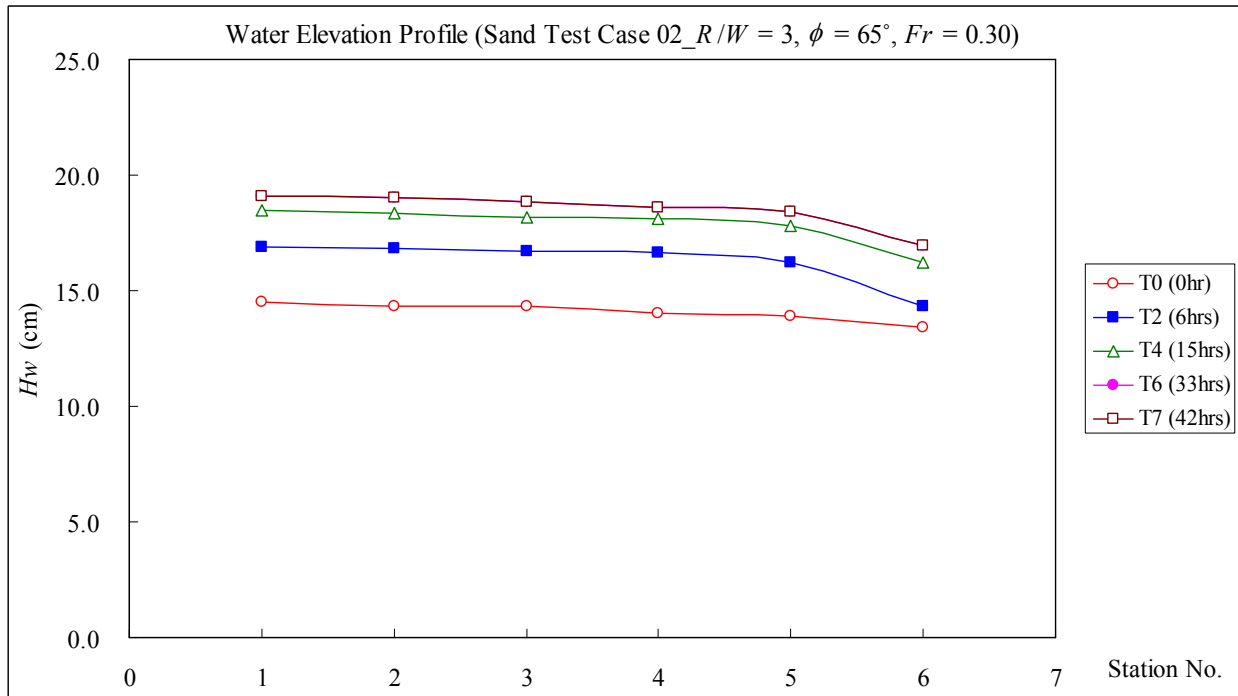
(b) Water Elevation Profile

Figure A.21. Mean Velocity and Water Elevation Measurement Results.
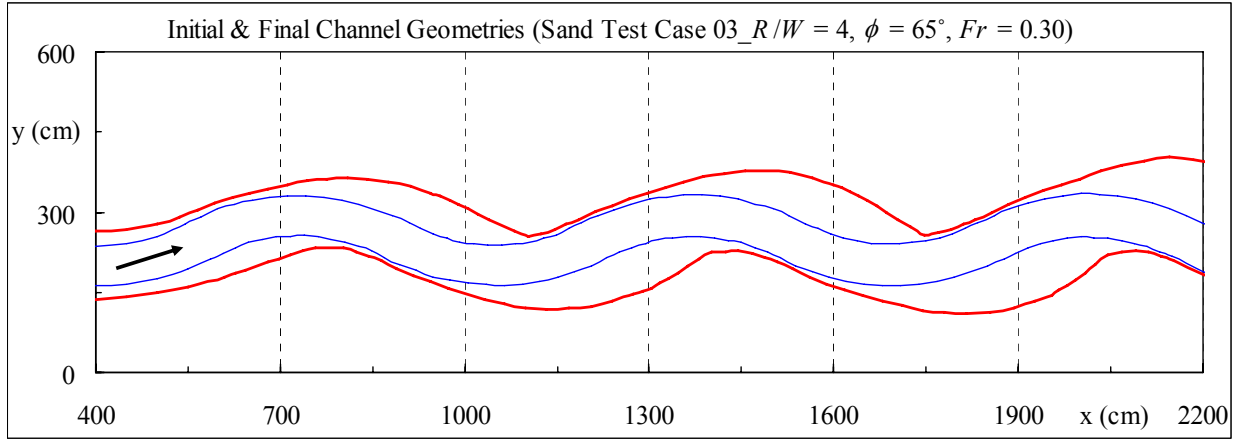
Figure A.22. Channel Geometry at the Initial and Final (39 hr) Stages.
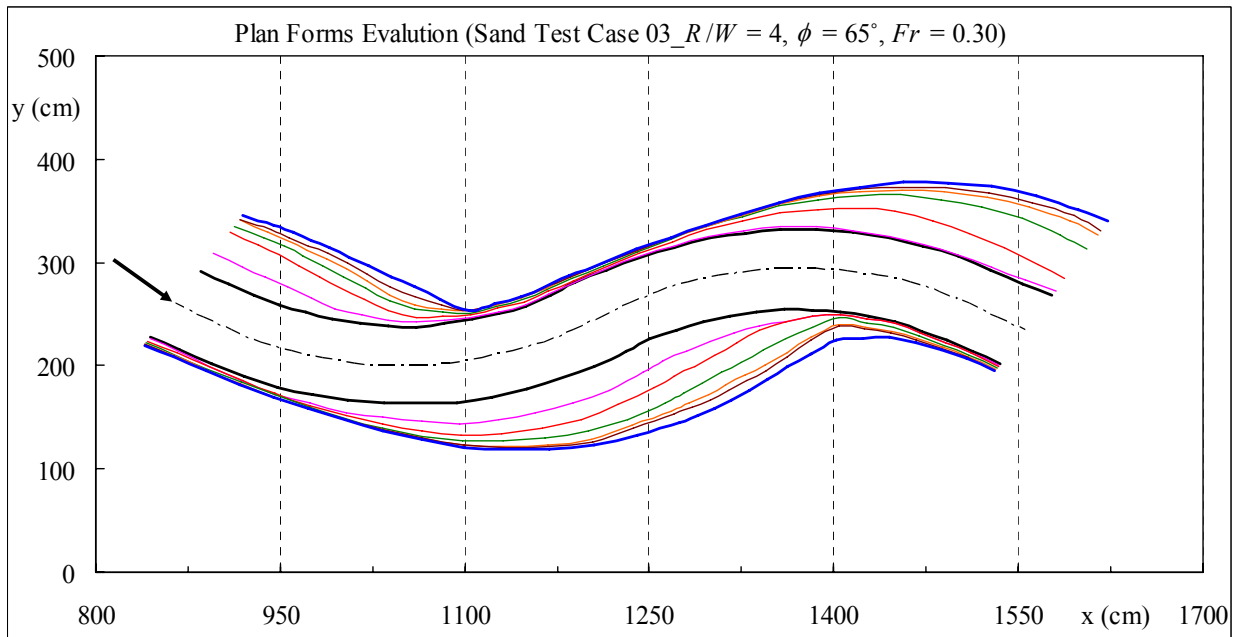
Figure A.23. Plan Forms Evolution at t = 0, 3, 6, 9, 15, 21 and 39 hr.
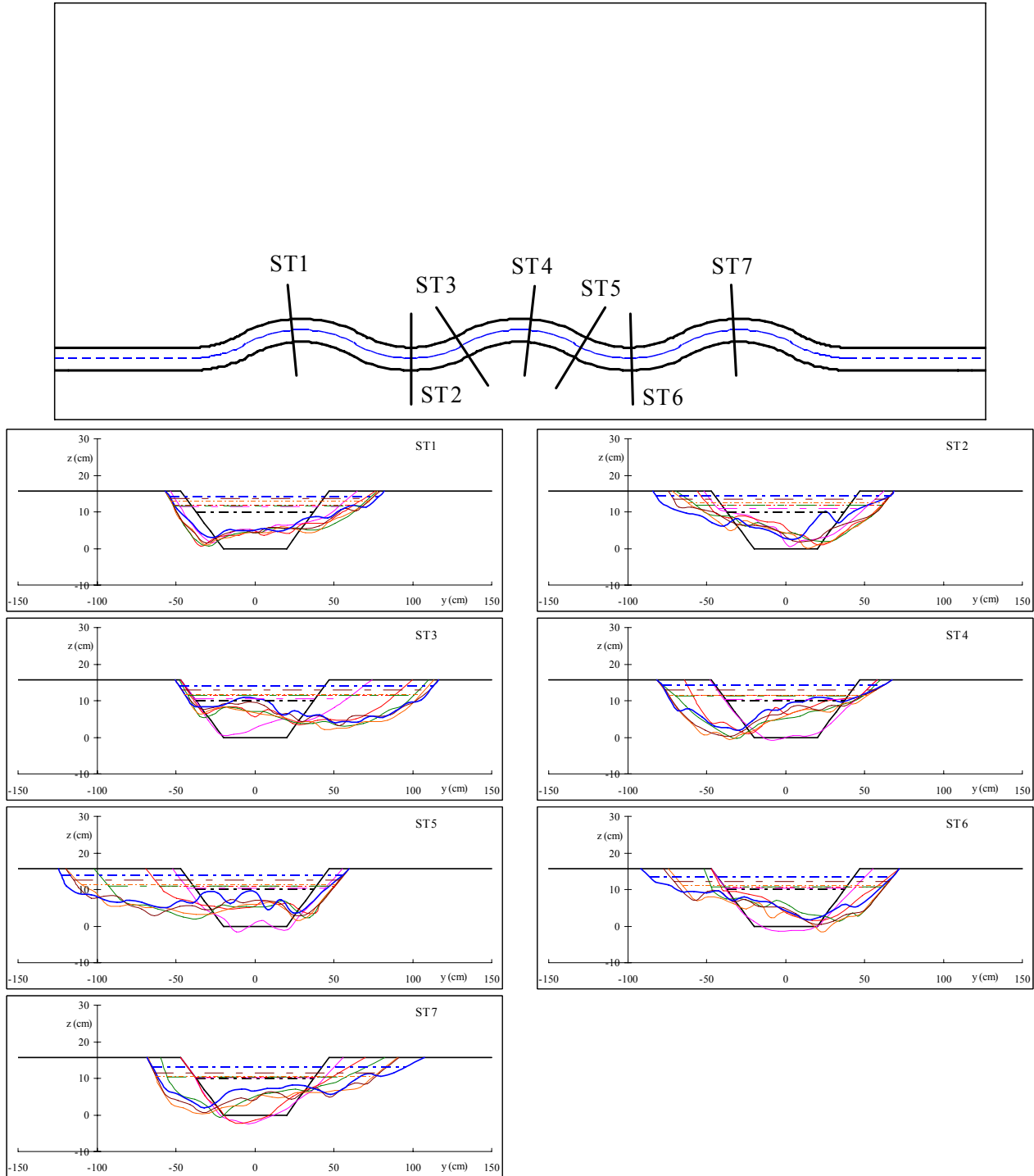
Figure A.24. Channel Cross-Section Profiles (Sand Test Case 03).

223

Water Elevation Profile (Sand Test Case 03_R/W = 4, ϕ = 65°, Fr = 0.30)

(a) Mean Velocity Profile

Water Elevation Profile (Sand Test Case 03_R/W = 4, ϕ = 65°, Fr = 0.30)
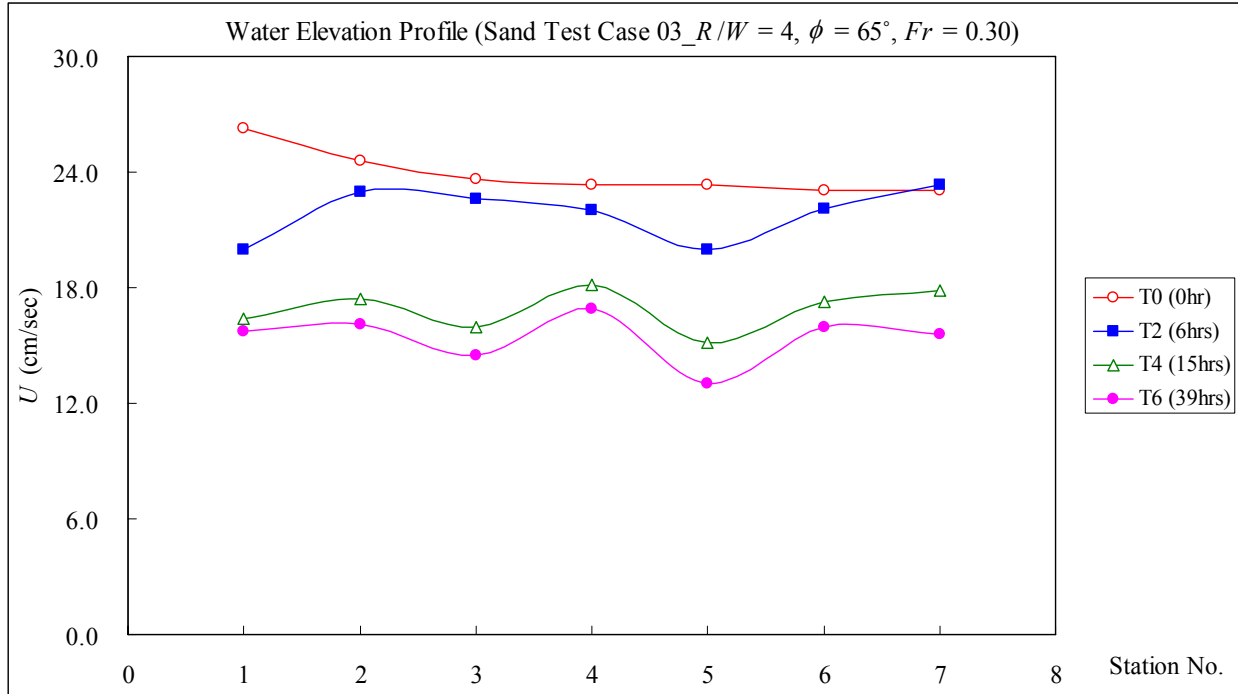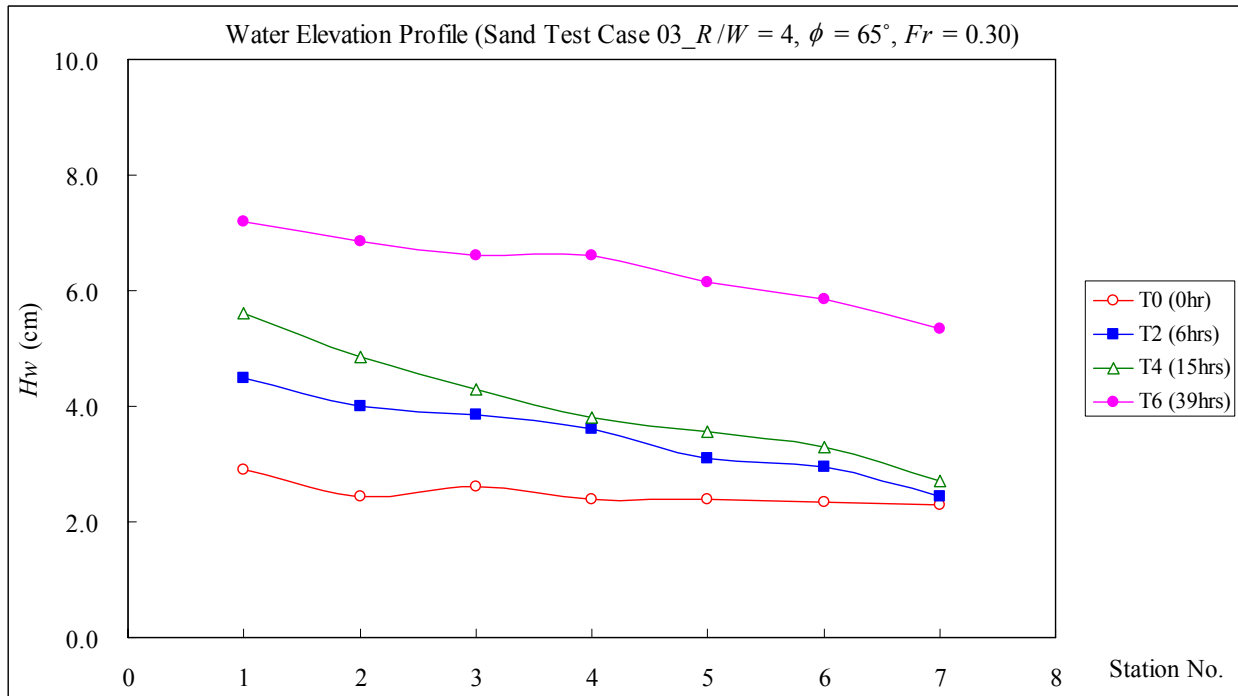
(b) Water Elevation Profile

Figure A.25. Mean Velocity and Water Elevation Measurement Results.
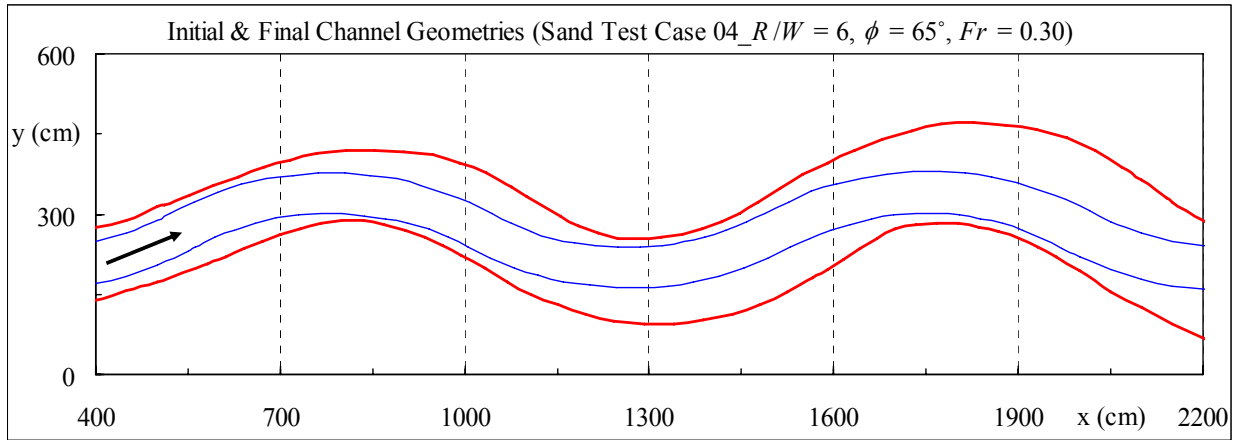
Figure A.26. Channel Geometry at the Initial and Final (92 hr) Stages.
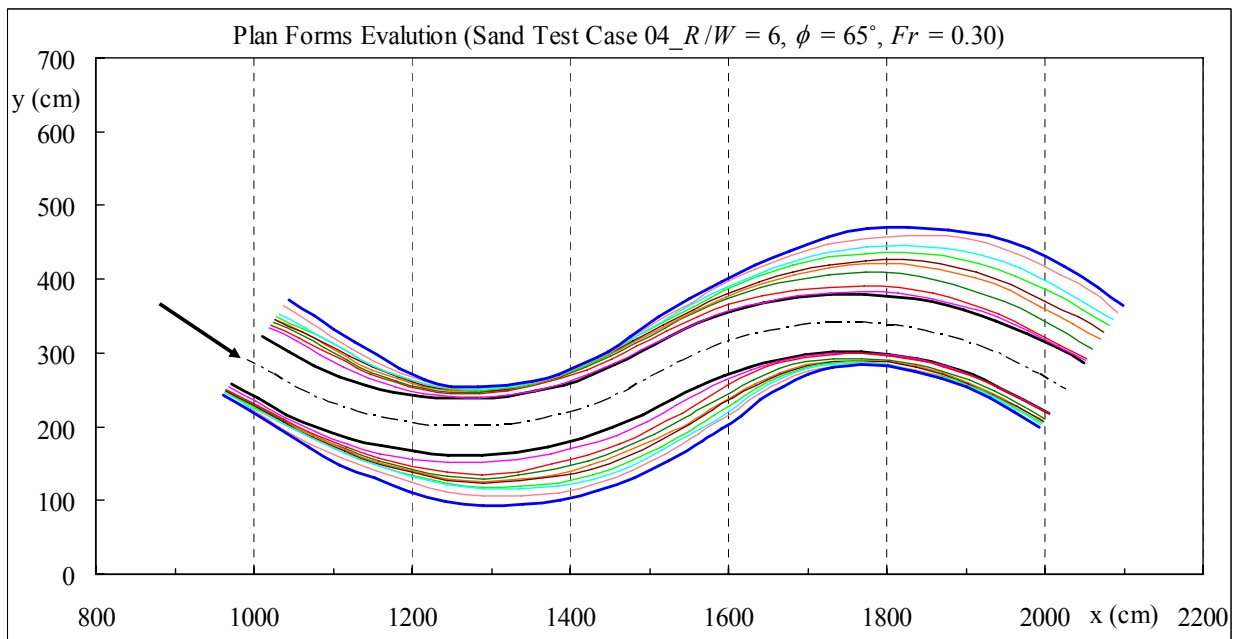
Figure A.27. Plan Forms Evolution at t = 0, 3, 6, 9, 15, 22, 34, 45, 69 and 92 hr.
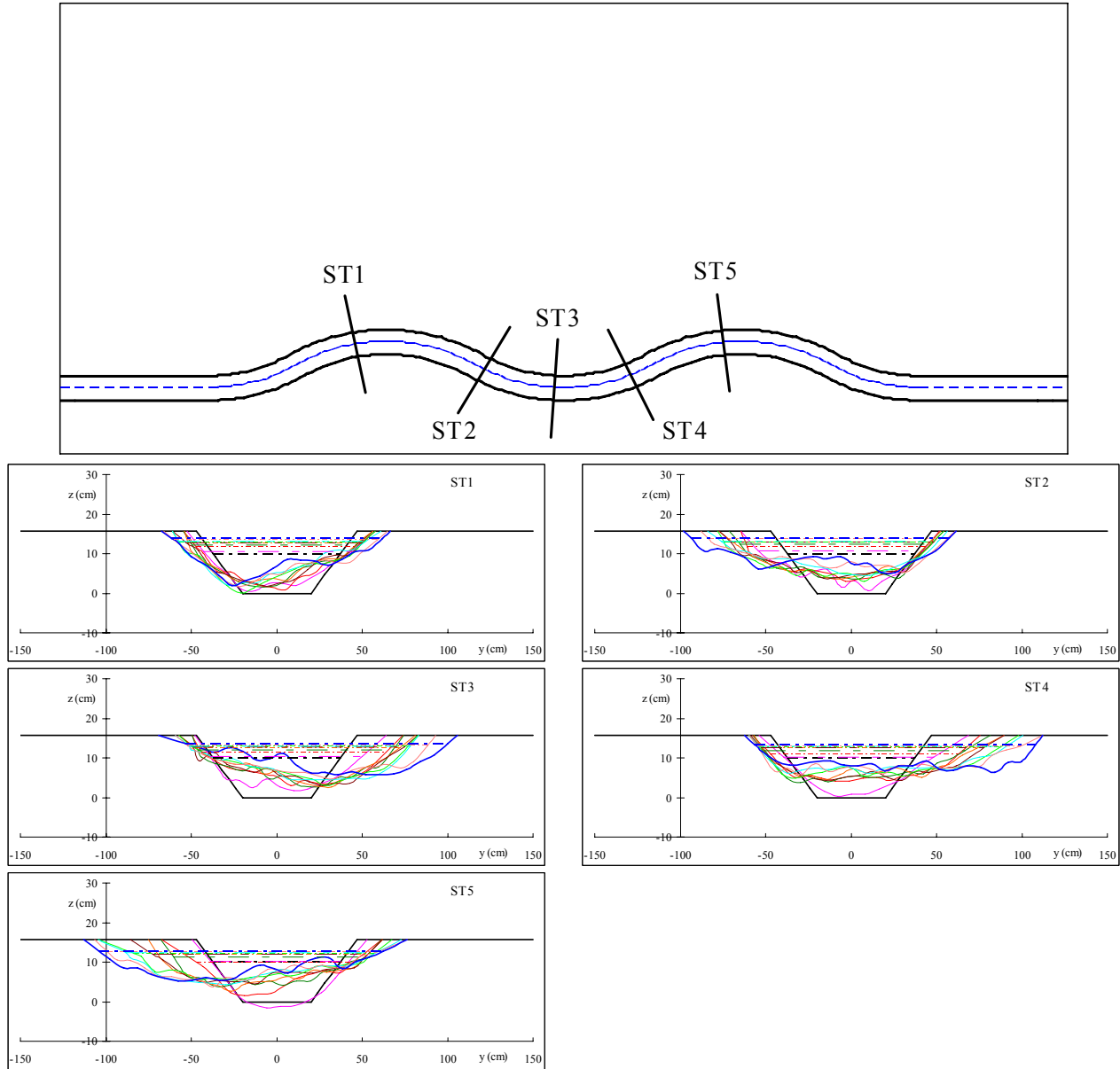
Figure A.28. Channel Cross-Section Profiles (Sand Test Case 04).
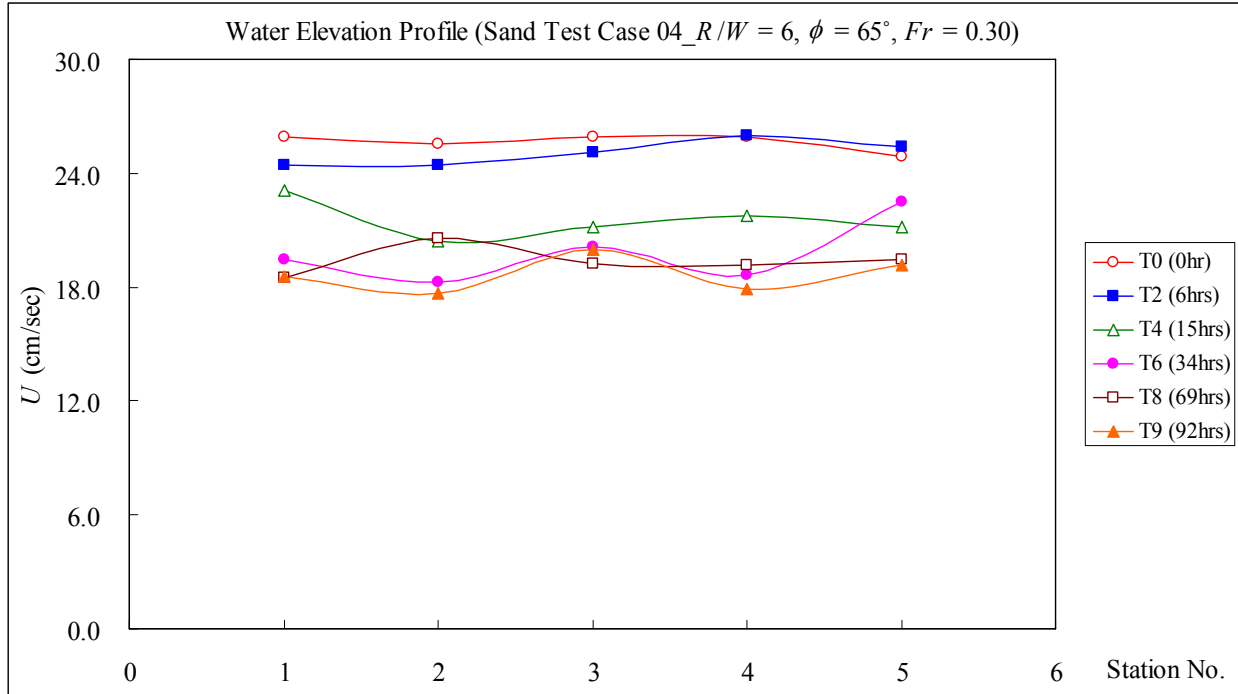
(a) Mean Velocity Profile
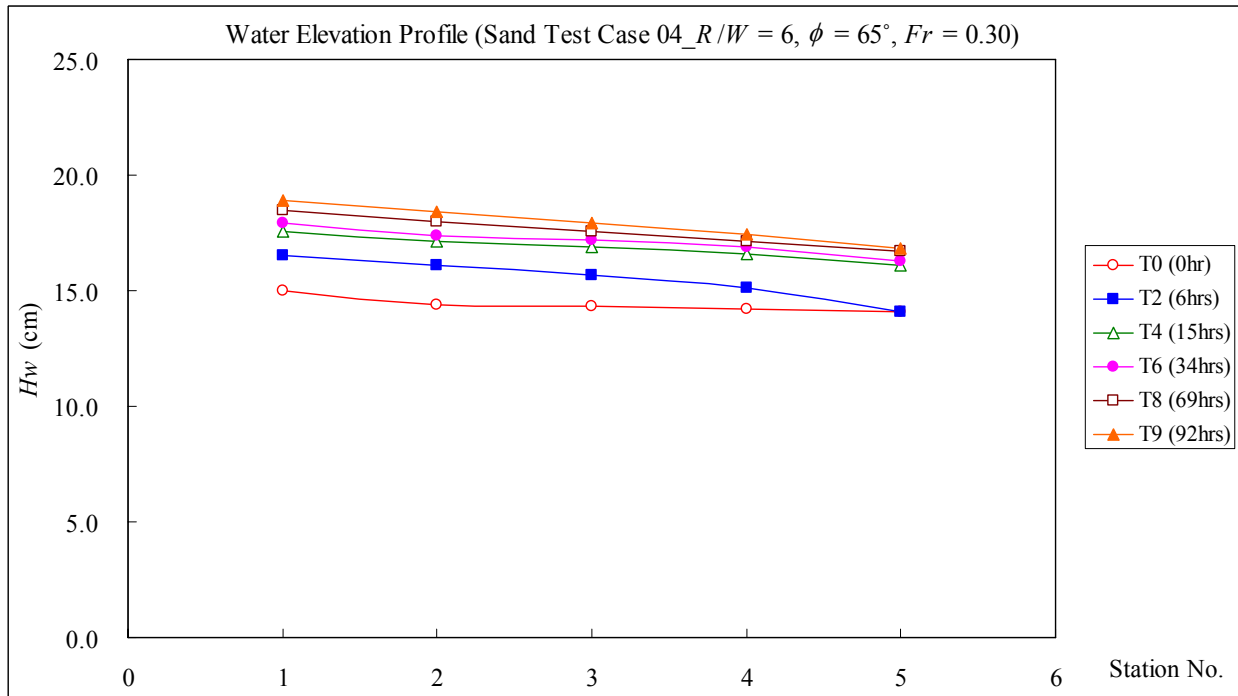
(b) Water Elevation Profile

Figure A.29. Mean Velocity and Water Elevation Measurement Results.

227
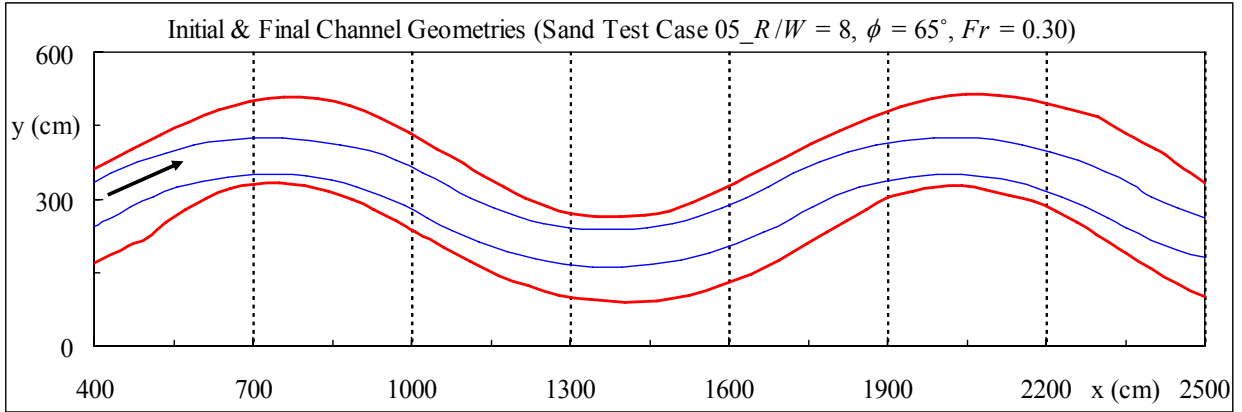
Figure A.30. Channel Geometry at the Initial and Final (66 hr) Stages.
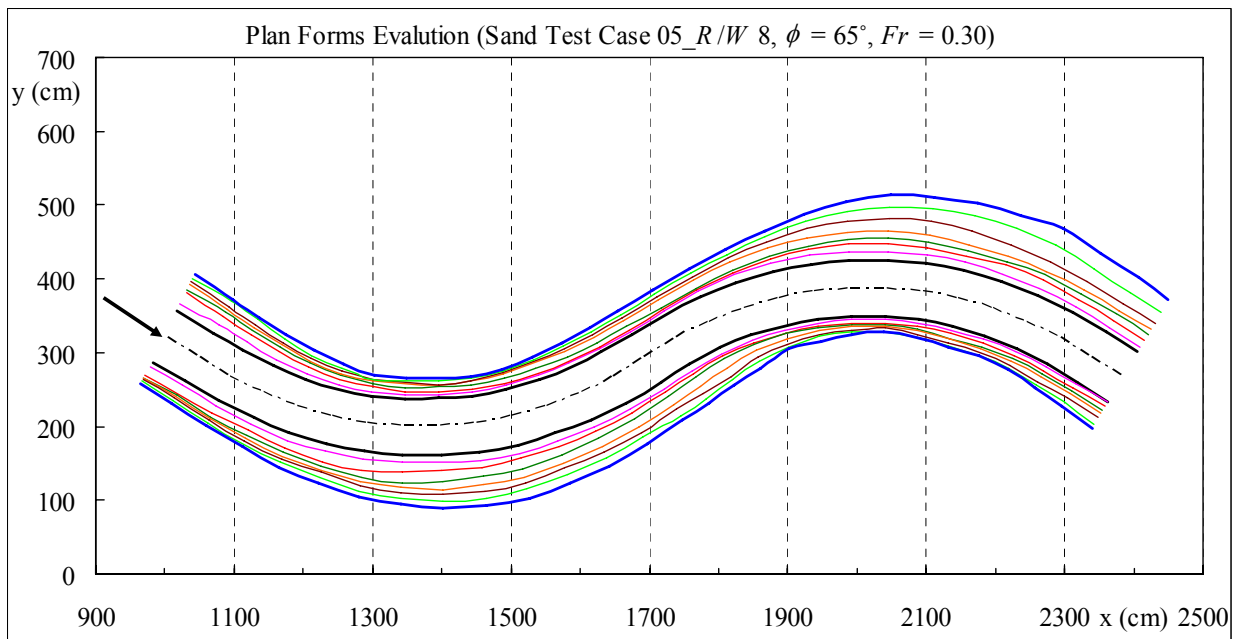
Figure A.31. Plan Forms Evolution at t = 0, 3, 6, 9, 15, 24, 42 and 66 hr.
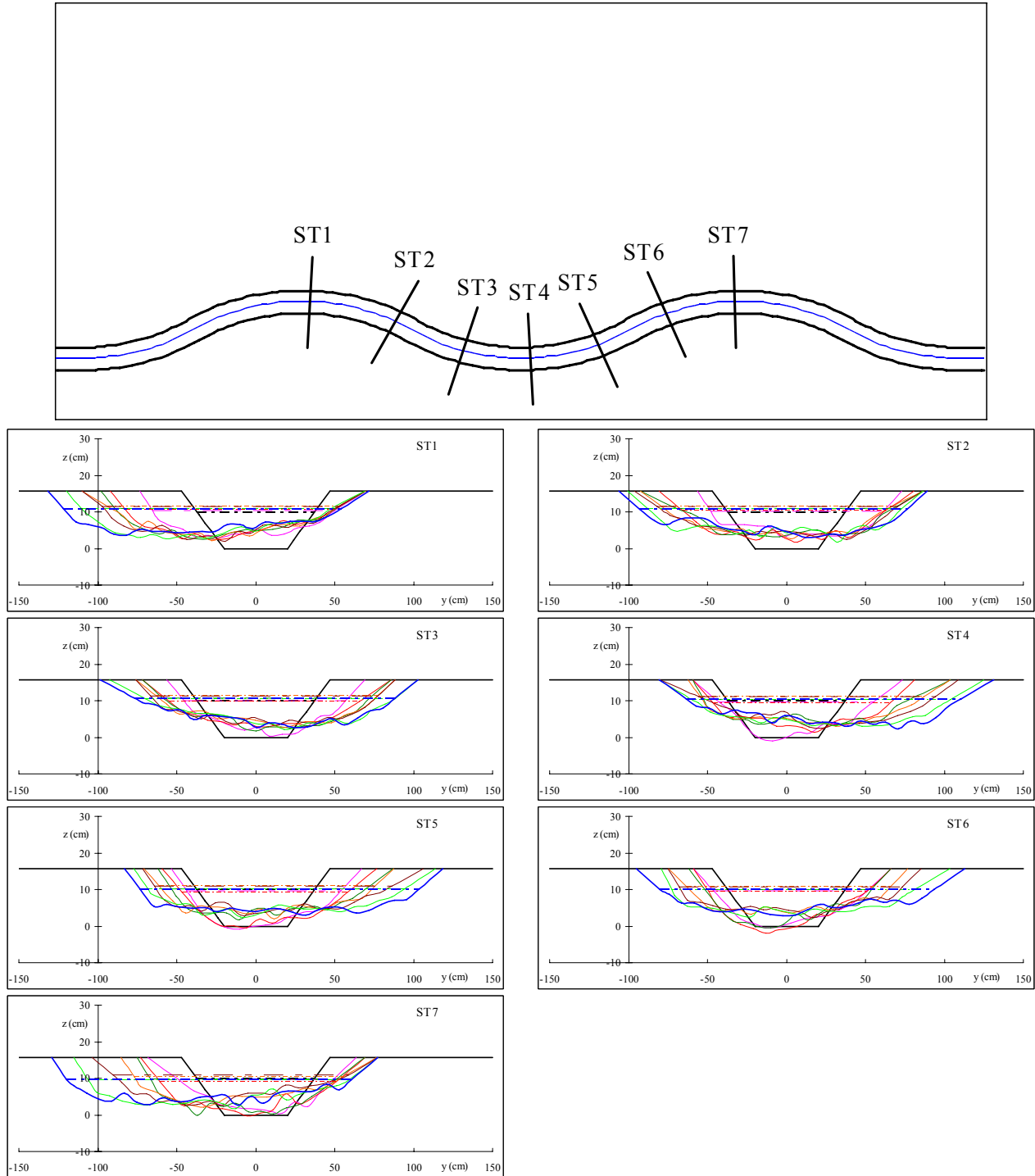
Figure A.32. Channel Cross-Section Profiles (Sand Test Case 05).
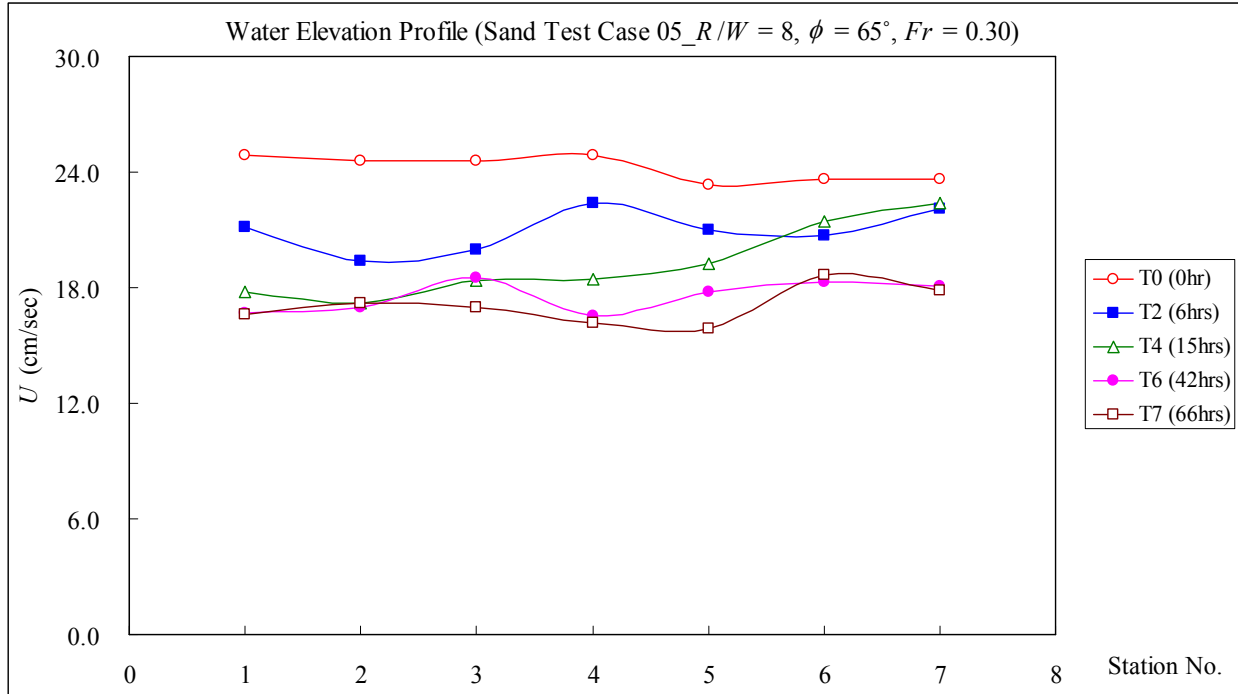
(a) Mean Velocity Profile
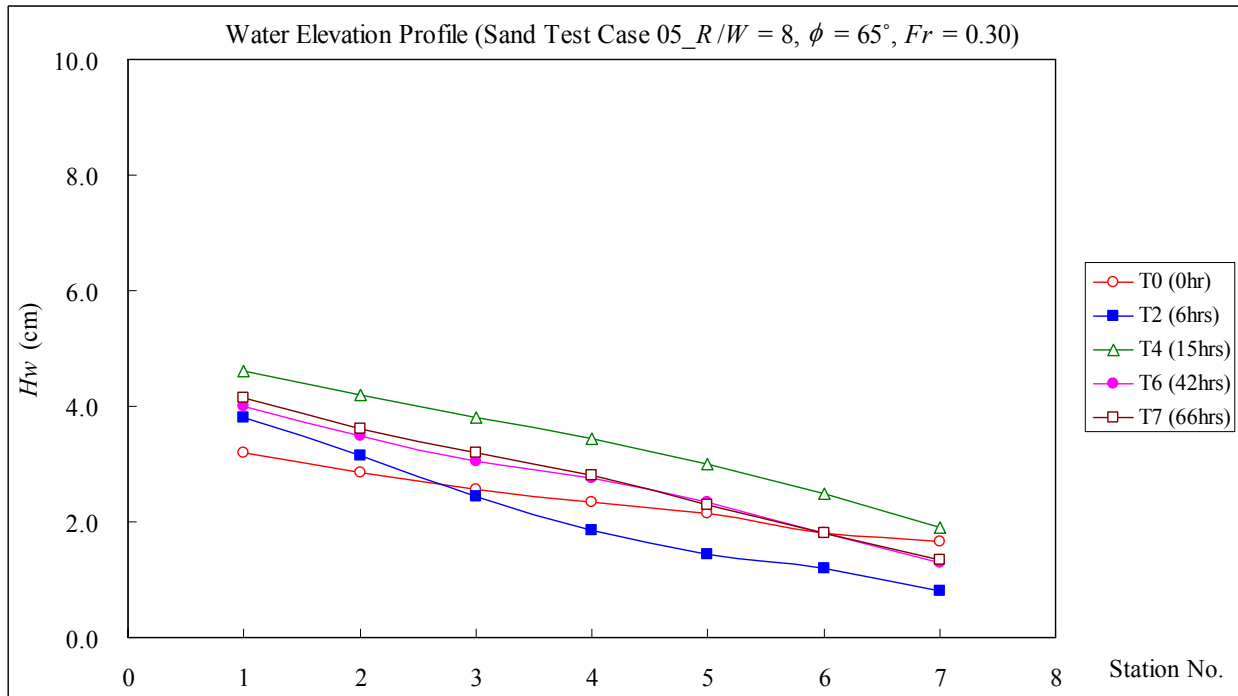
(b) Water Elevation Profile

Figure A.33. Mean Velocity and Water Elevation Measurement Results.
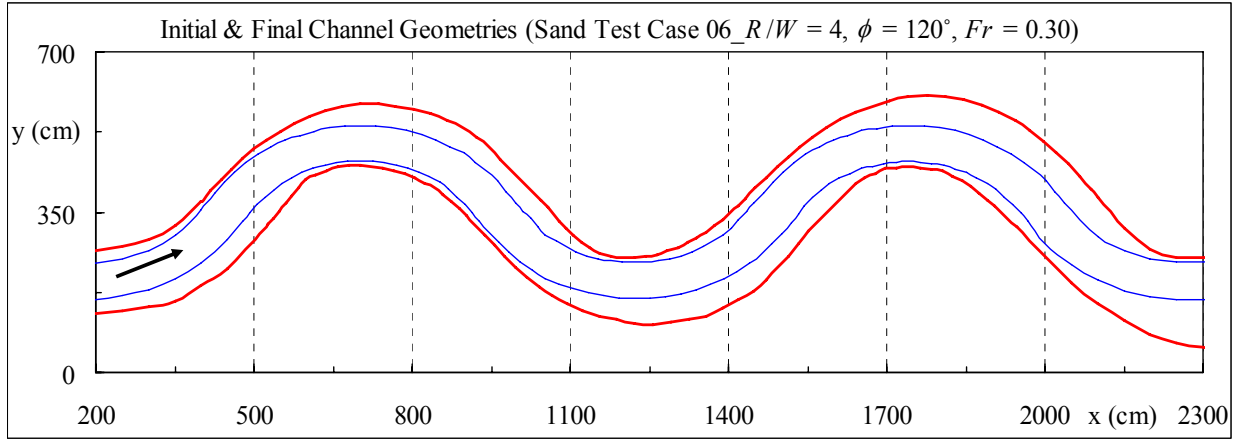
Figure A.34. Channel Geometry at the Initial and Final (30 hr) Stages.
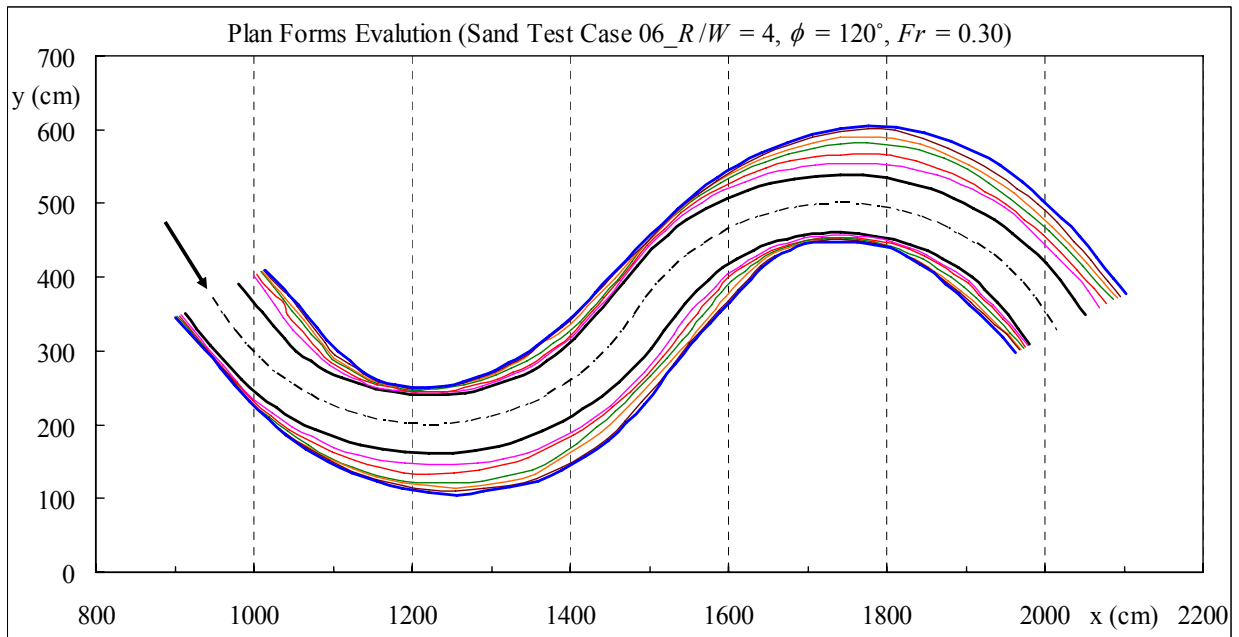
Figure A.35. Plan Forms Evolution at *t* = 0, 3, 6, 12, 18, 24 and 30 hr.
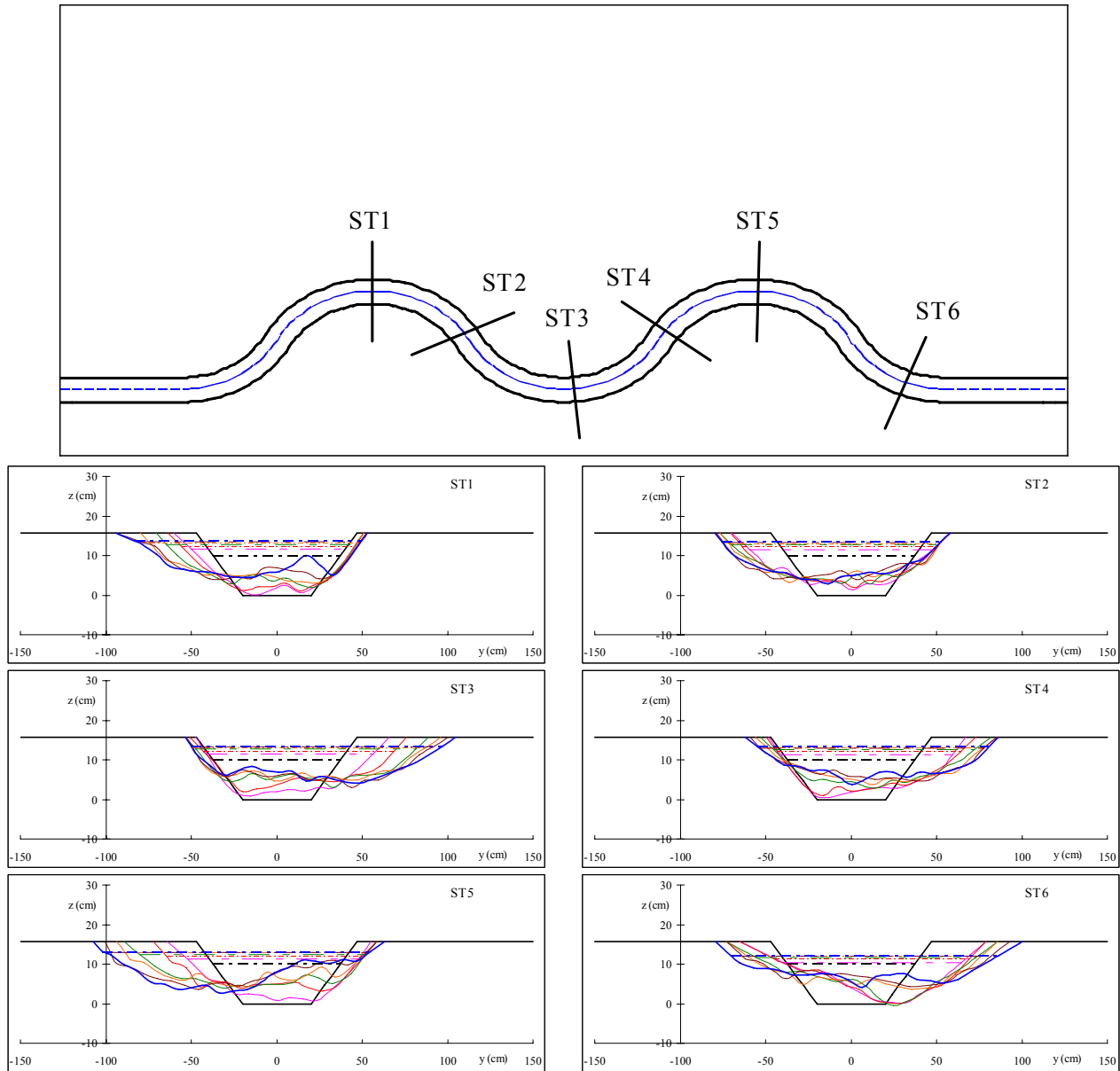
Figure A.36. Channel Cross-Section Profiles (Sand Test Case 06).
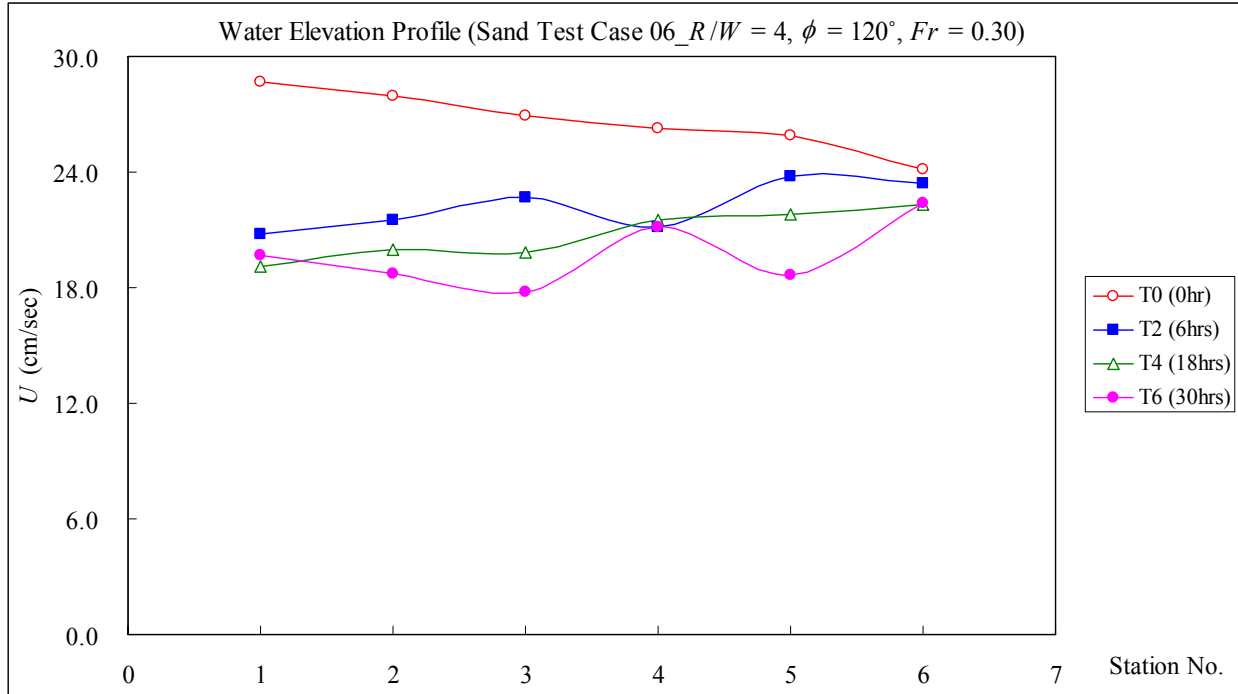
(a) Mean Velocity Profile
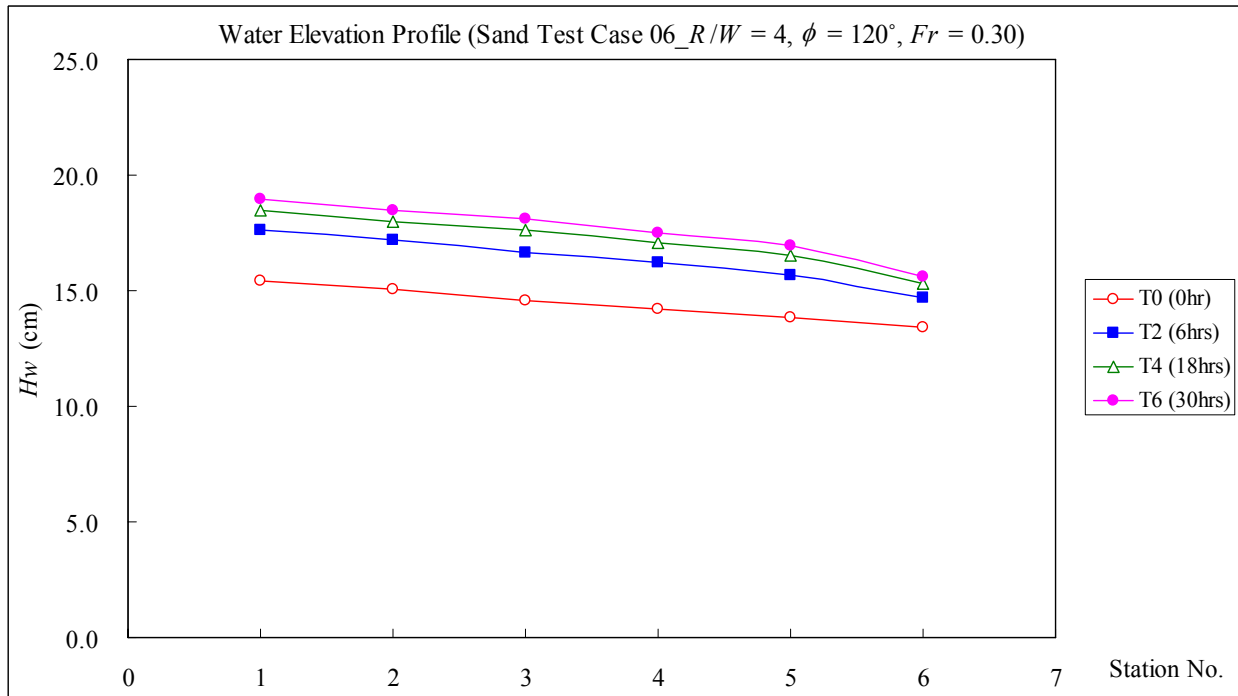
(b) Water Elevation Profile

Figure A.37. Mean Velocity and Water Elevation Measurement Results.
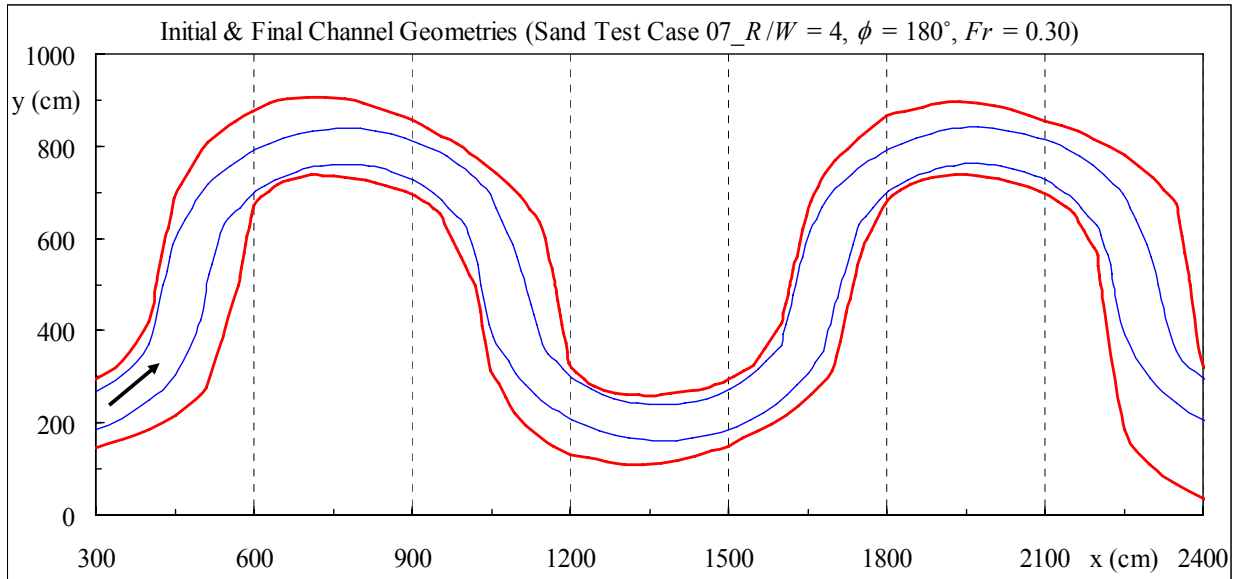
Figure A.38. Channel Geometry at the Initial and Final (86 hr) Stages.
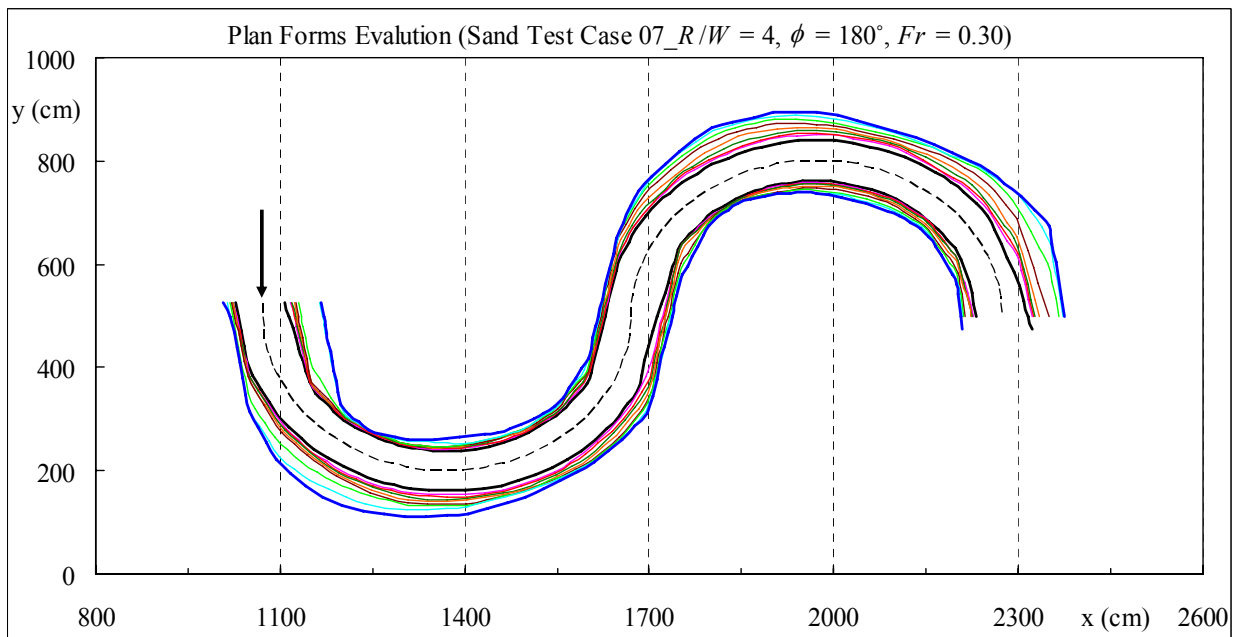
Figure A.39. Plan Forms Evolution at t = 0, 3, 6, 15, 24, 36, 48, 66 and 86 hr.
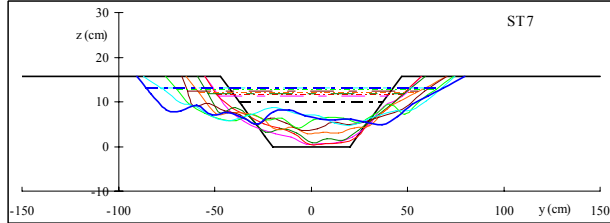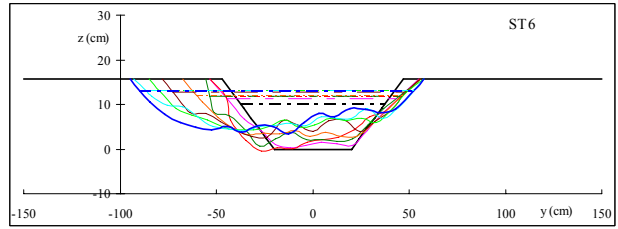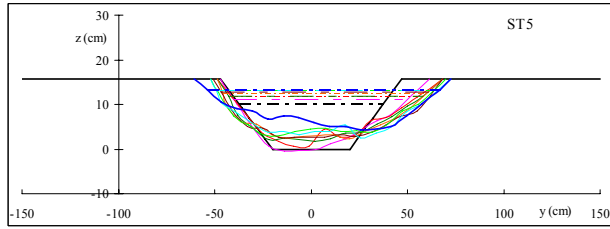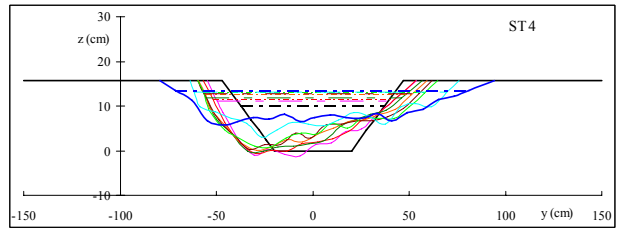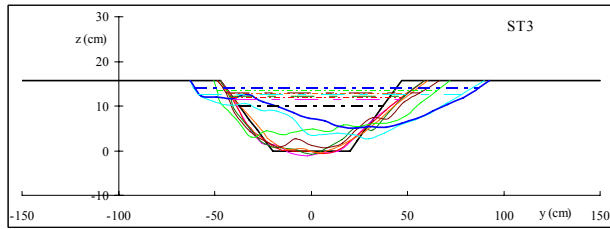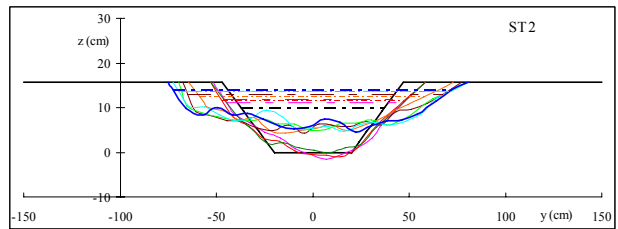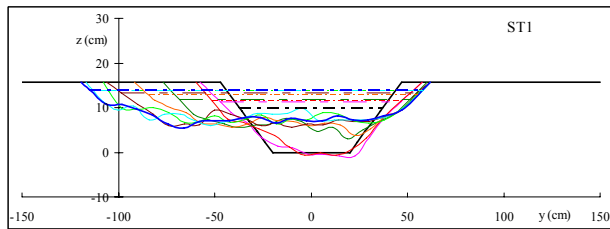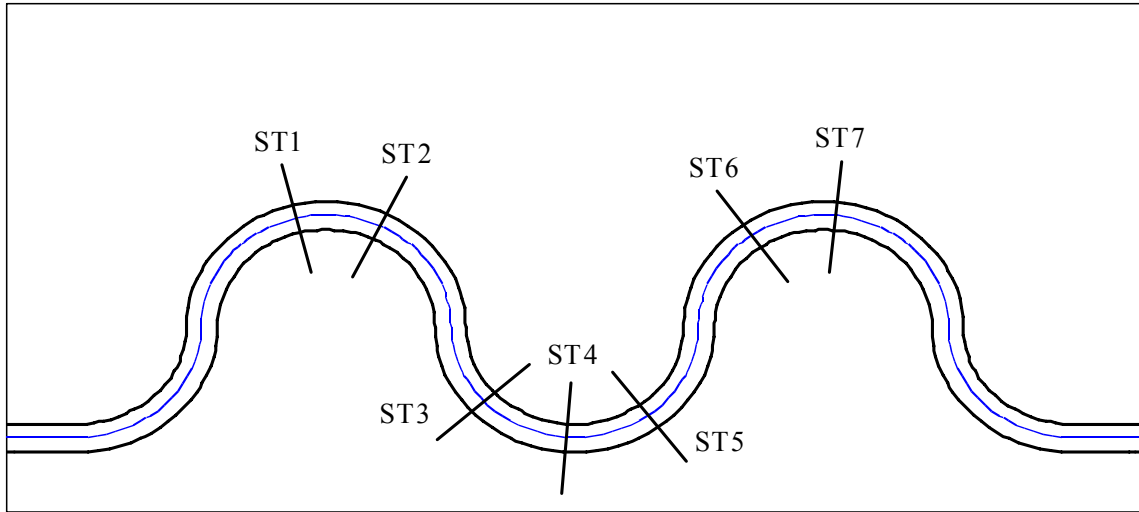
Figure A.40. Channel Cross-Section Profiles (Sand Test Case 07).
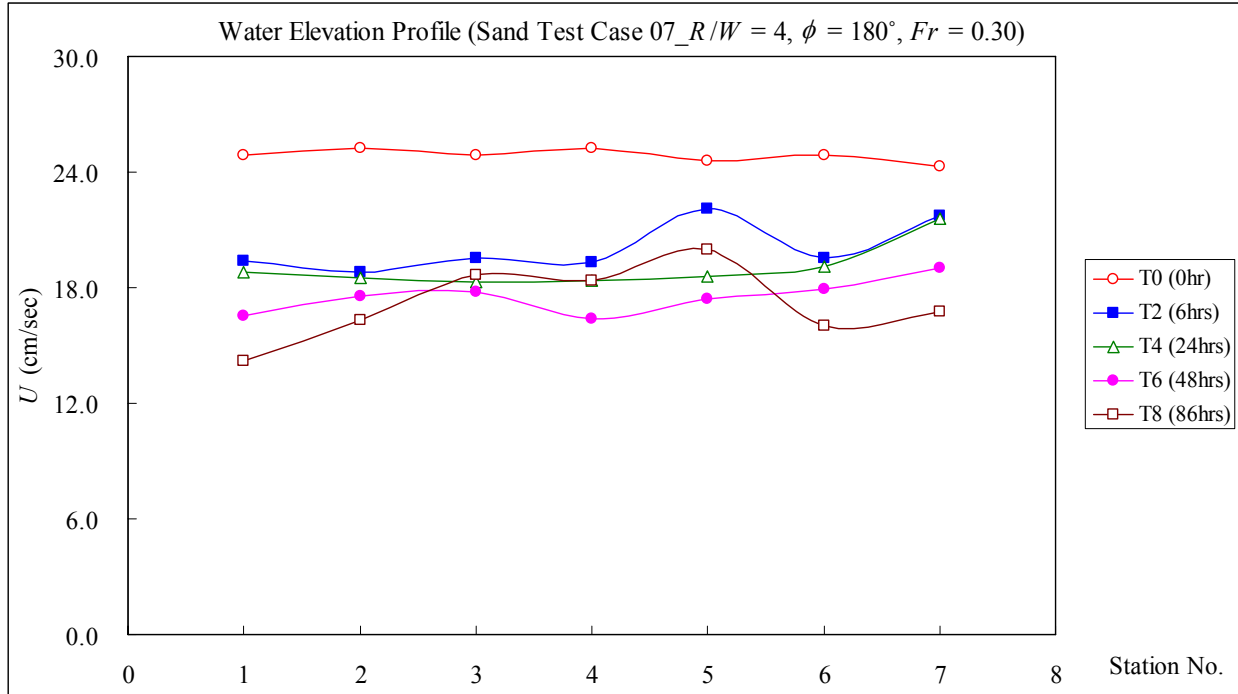
(a) Mean Velocity Profile
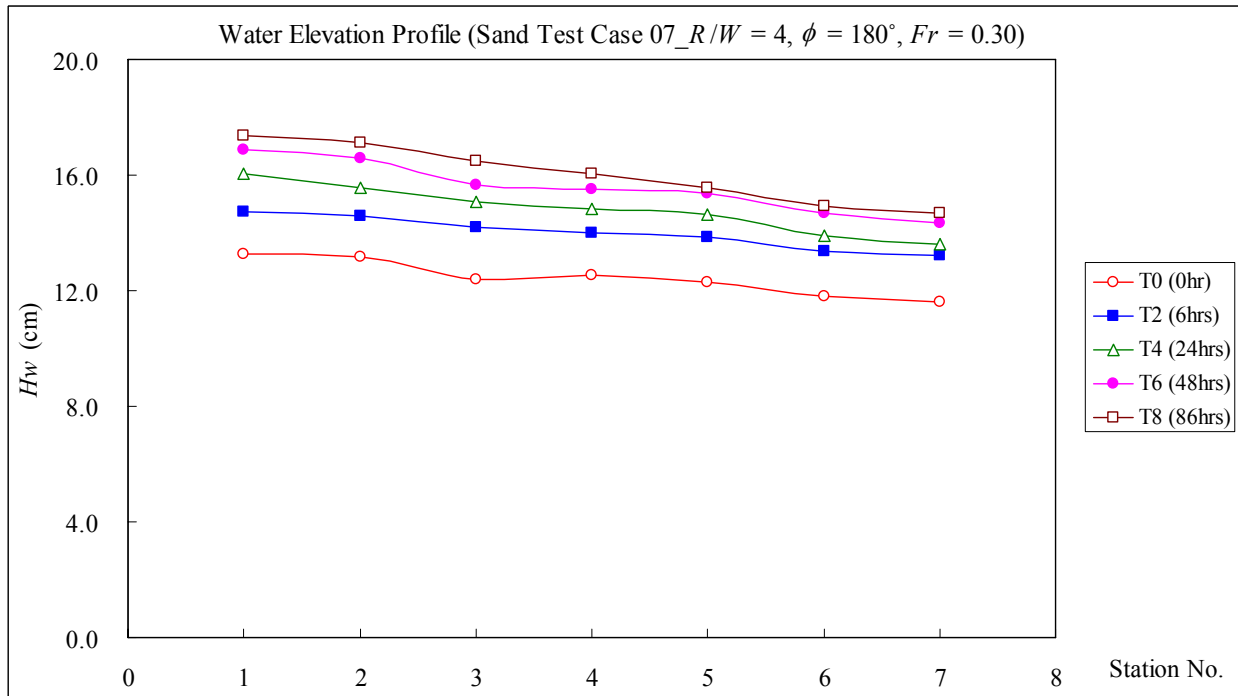
(b) Water Elevation Profile

Figure A.41. Mean Velocity and Water Elevation Measurement Results.
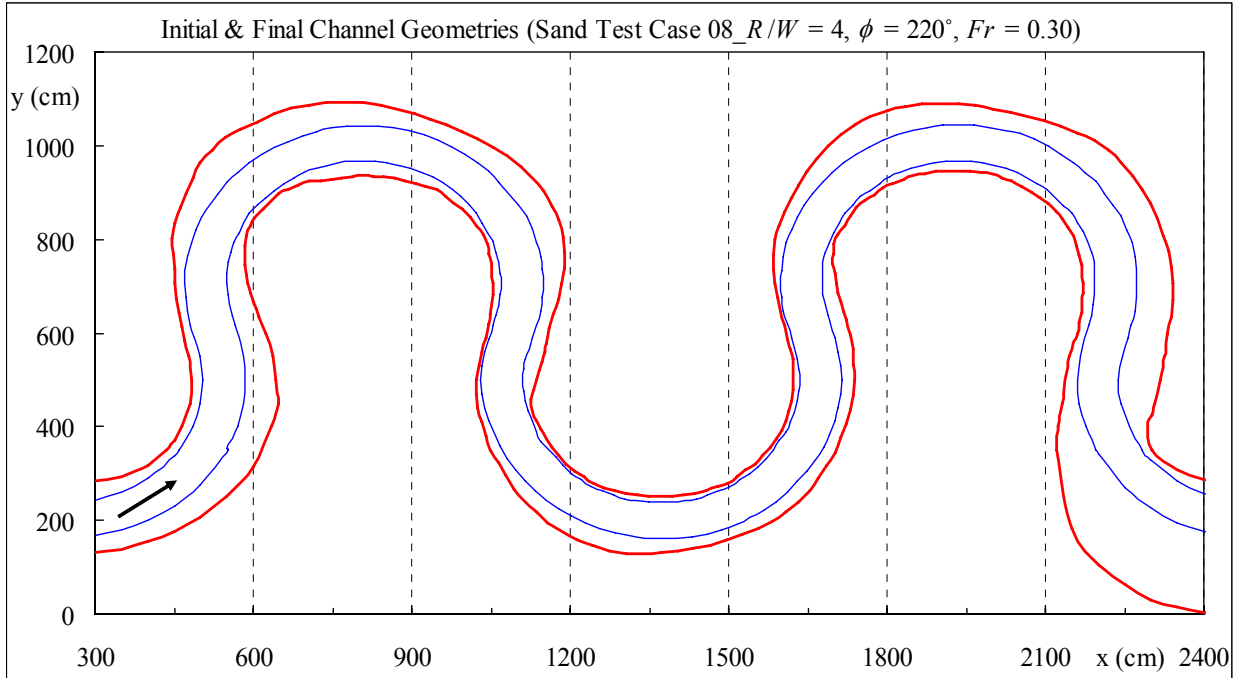
Figure A.42. Channel Geometry at the Initial and Final (147 hr) Stages.
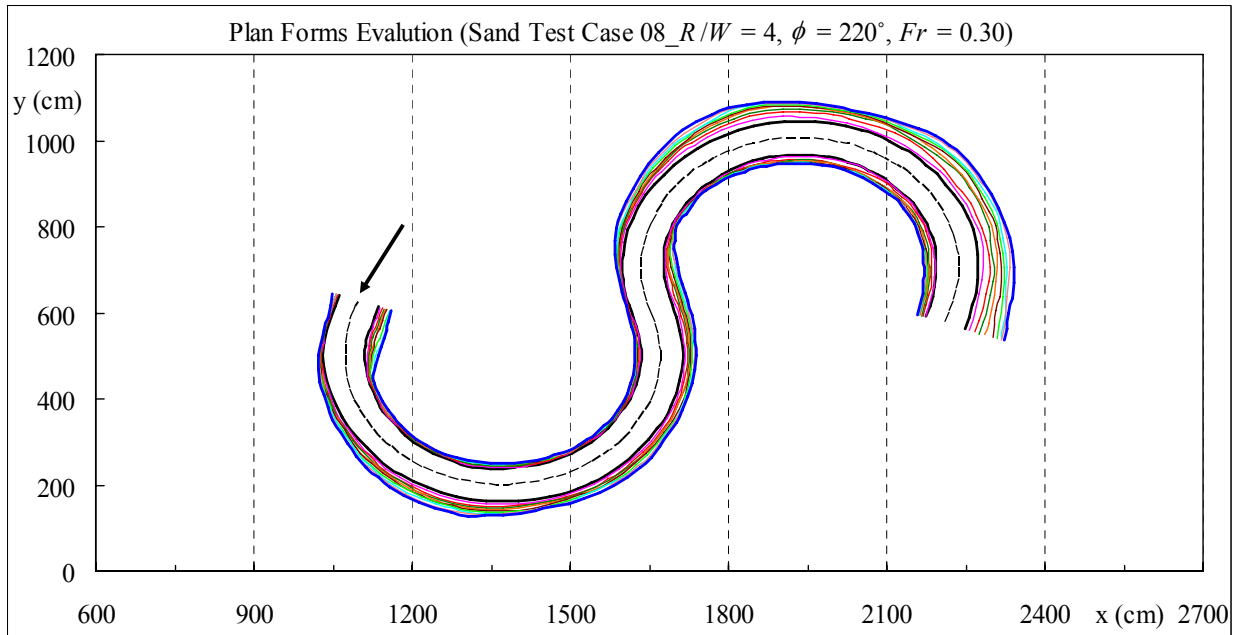
Figure A.43. Plan Forms Evolution at *t* = 0, 3, 9, 18, 30, 48, 69, 96, 123 and 147 hr.
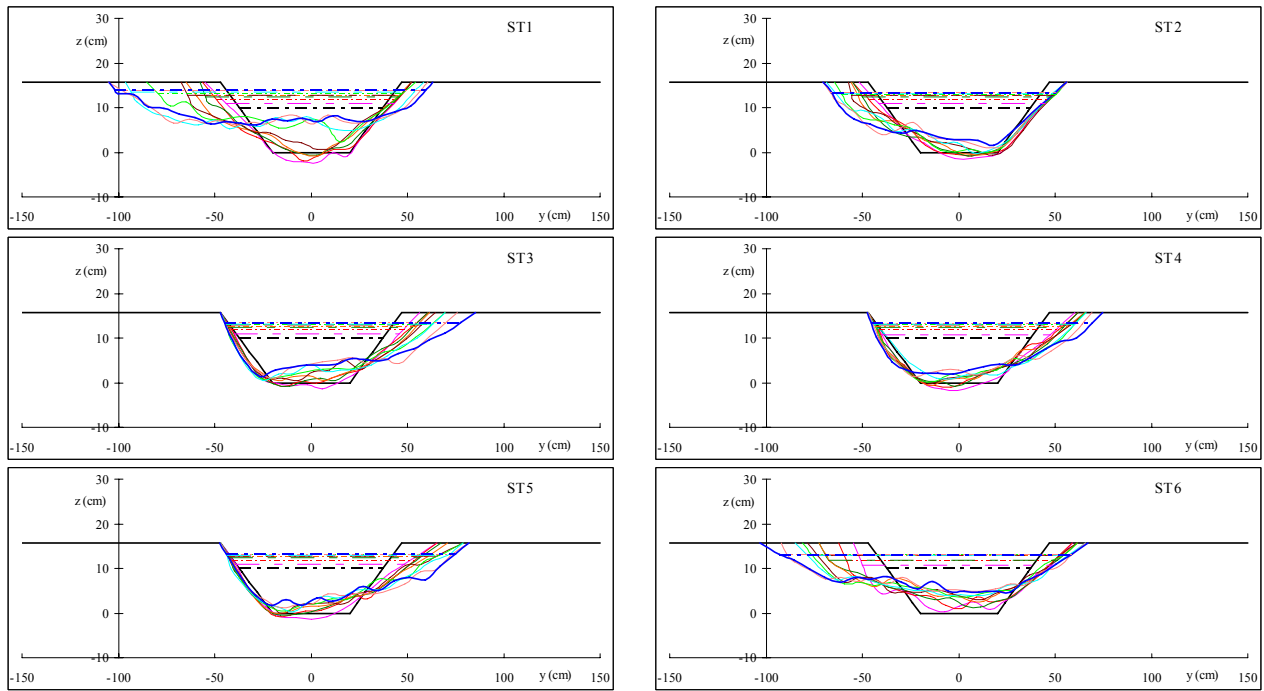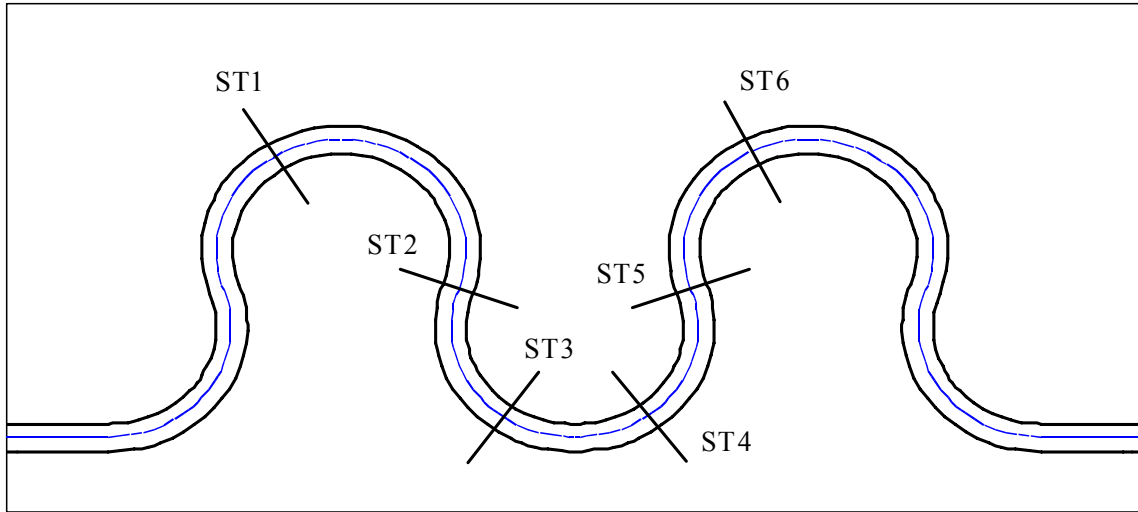
Figure A.44. Channel Cross-Section Profiles (Sand Test Case 08).
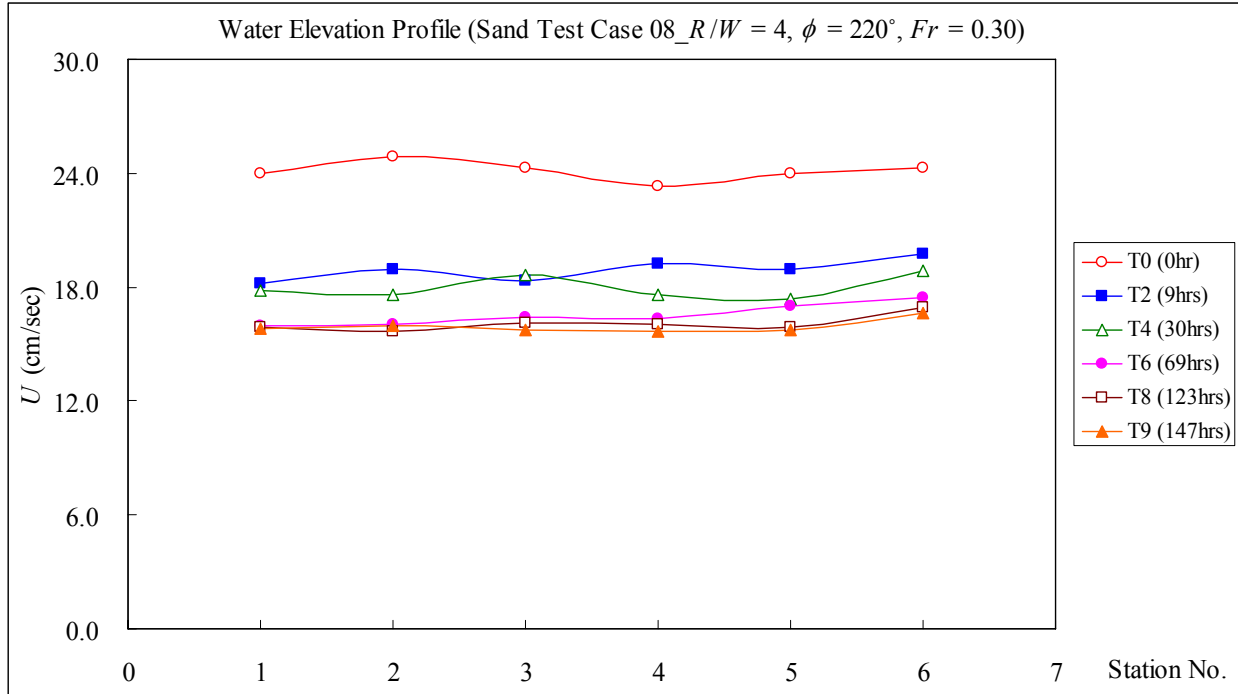
(a) Mean Velocity Profile
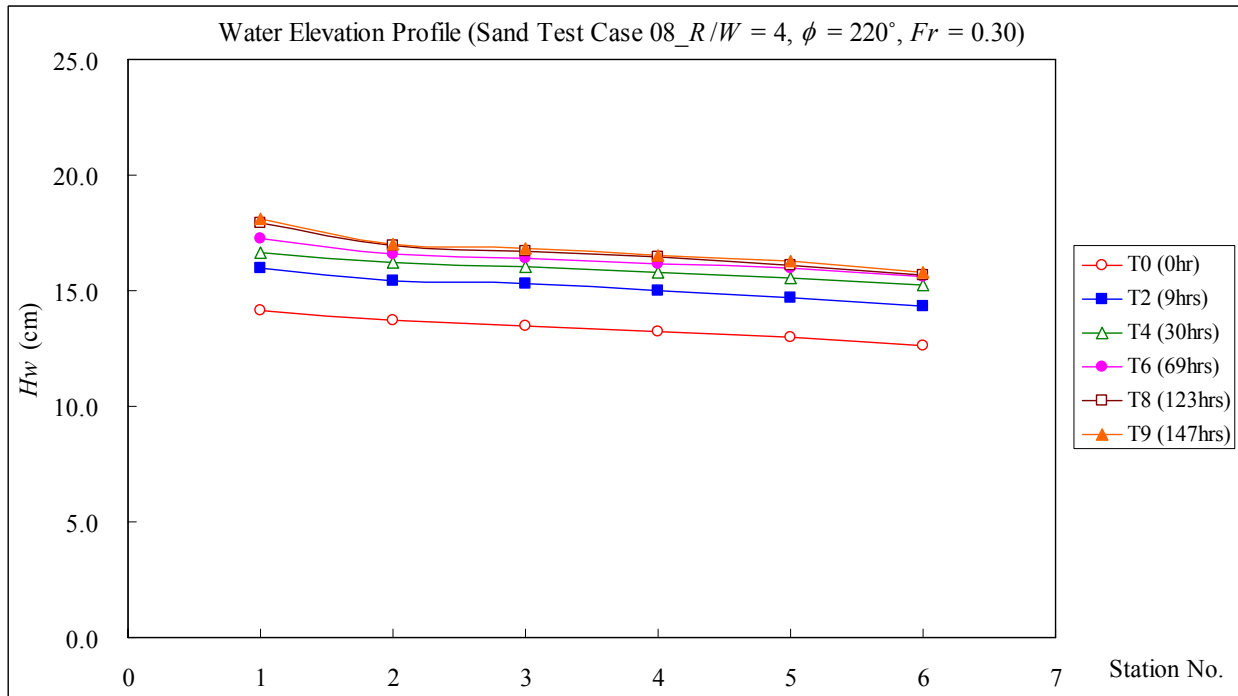
(b) Water Elevation Profile

Figure A.45. Mean Velocity and Water Elevation Measurement Results.
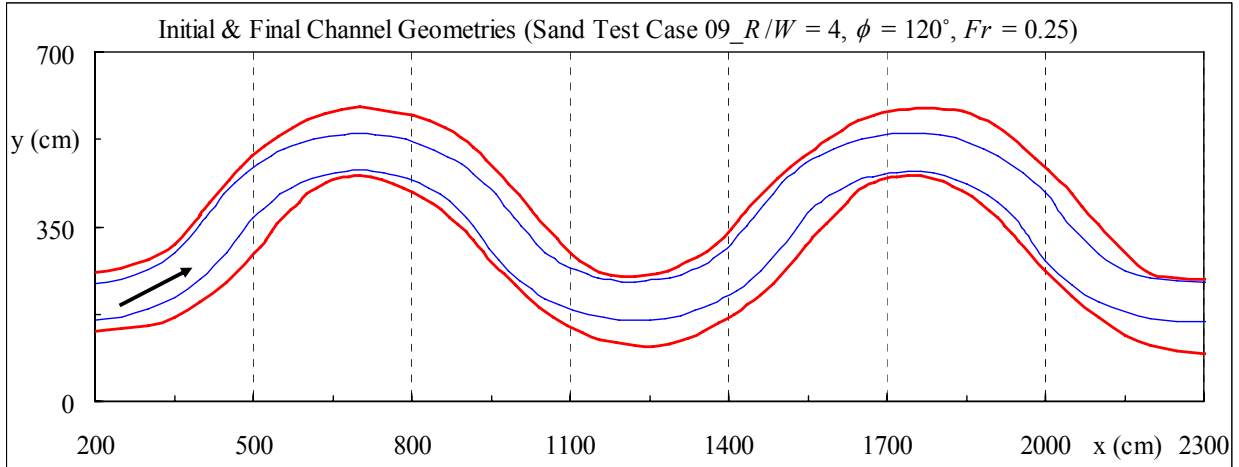
Figure A.46. Channel Geometry at the Initial and Final (56 hr) Stages.
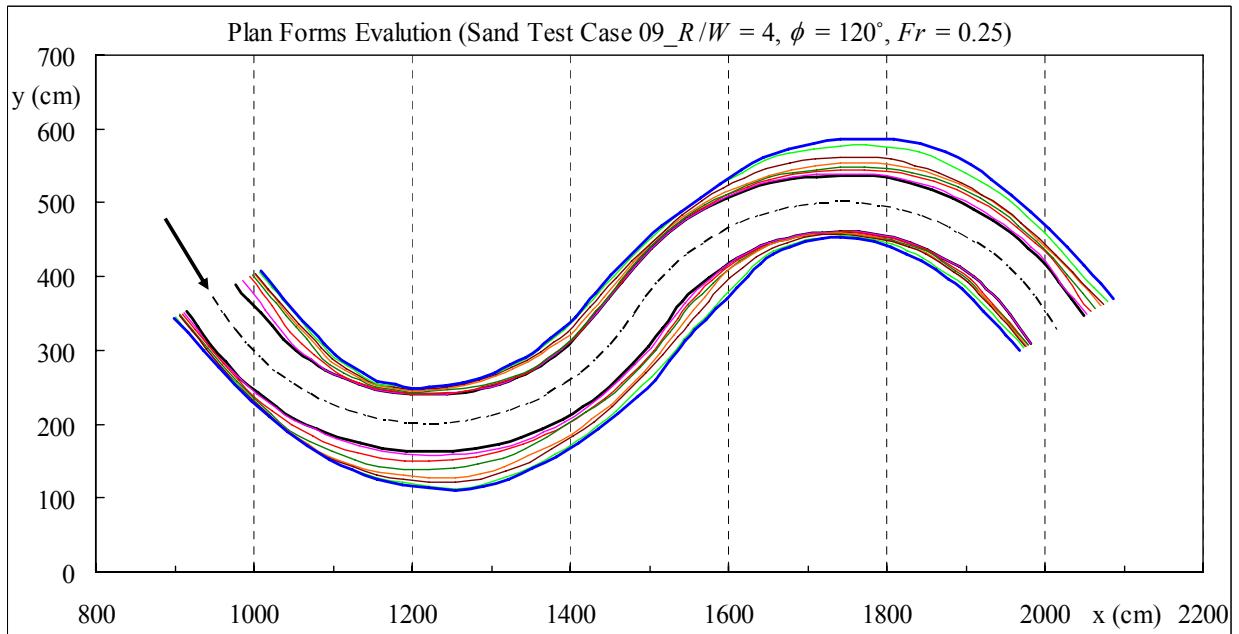
Figure A.47. Plan Forms Evolution at *t* = 0, 4, 10, 16, 24, 32, 44 and 56 hr.

240
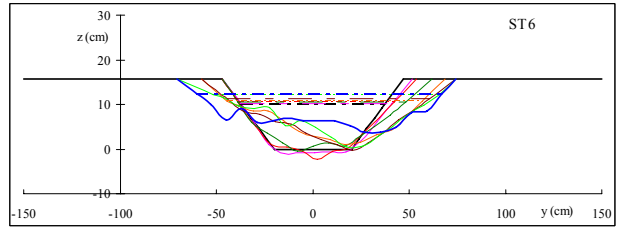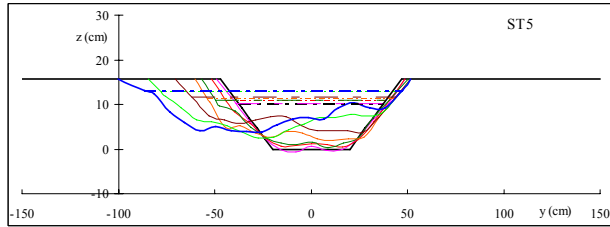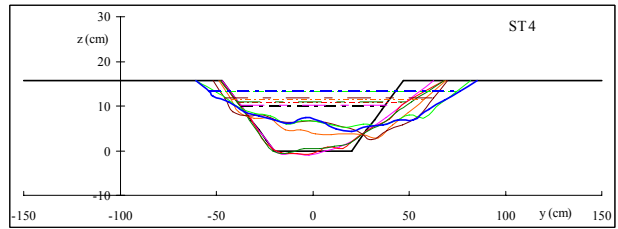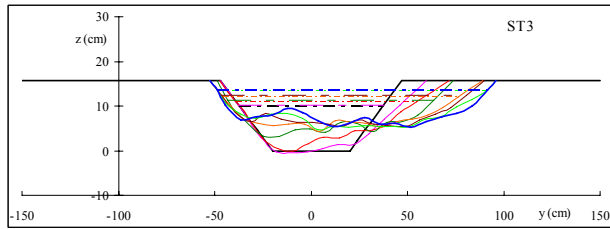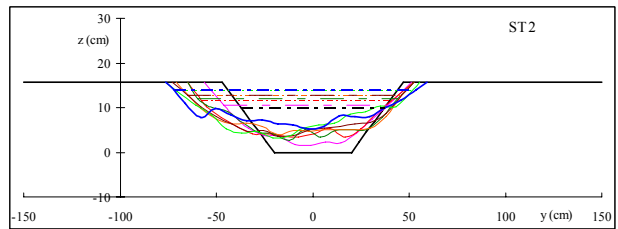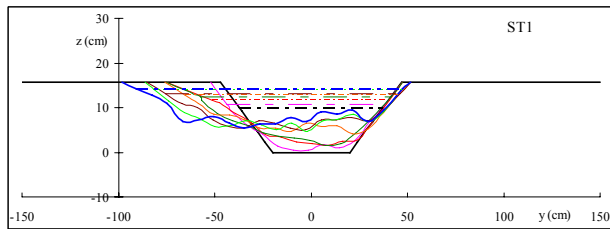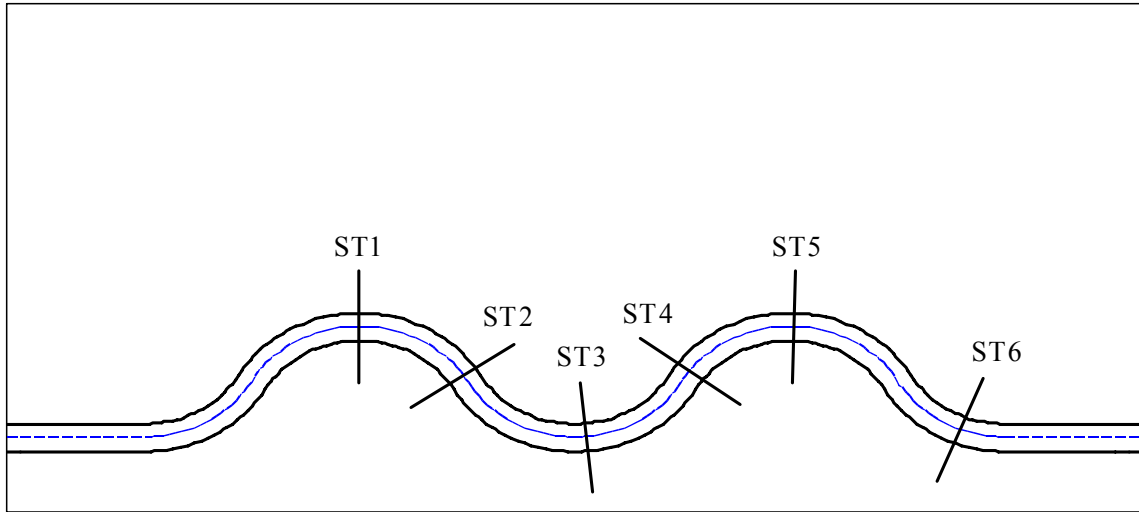
Figure A.48. Channel Cross-Section Profiles (Sand Test Case 09).
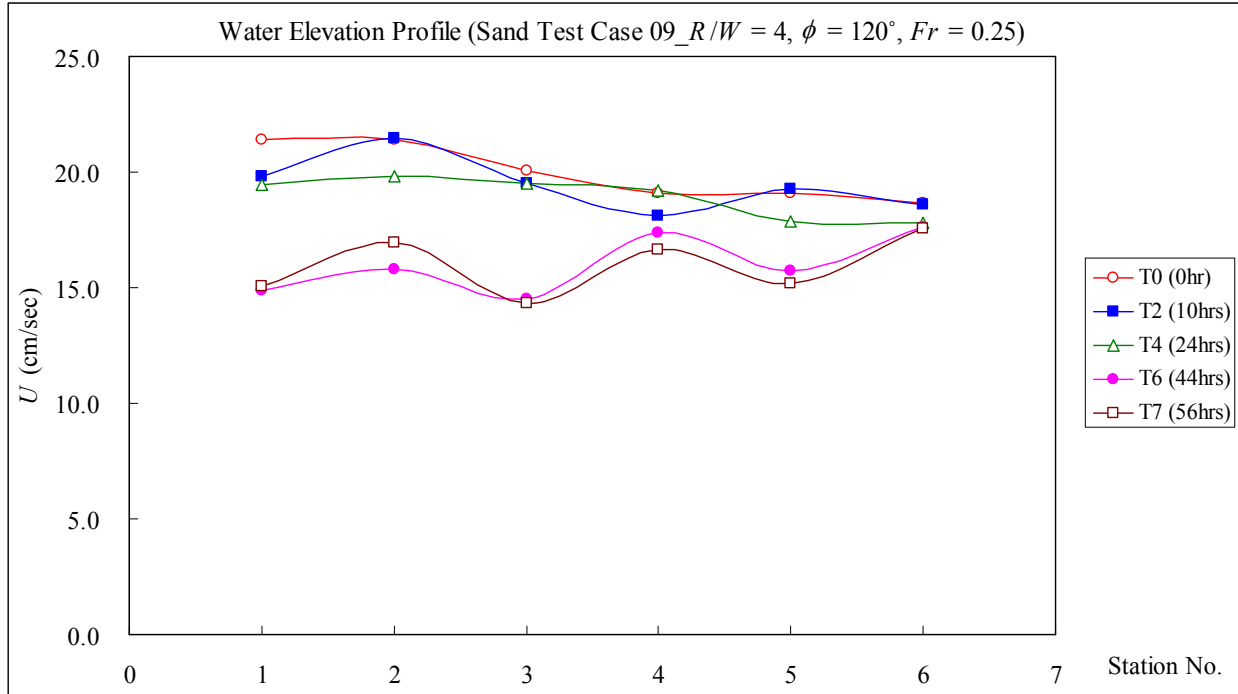
(a) Mean Velocity Profile
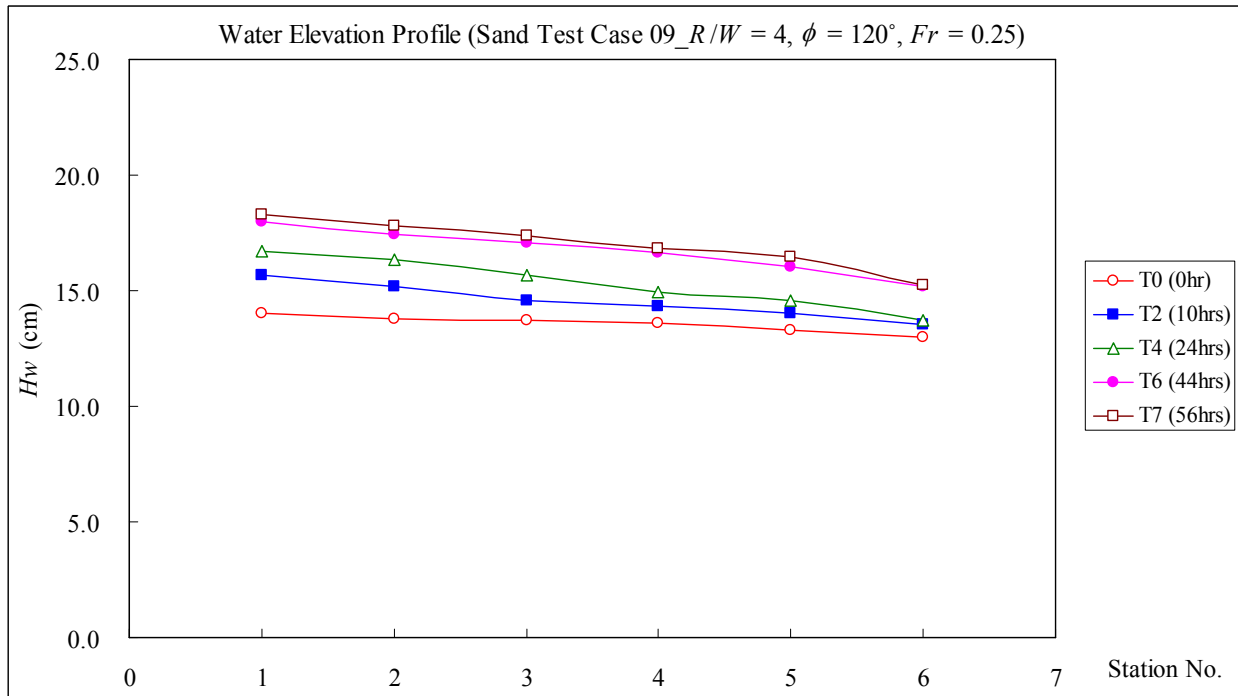
(b) Water Elevation Profile

Figure A.49. Mean Velocity and Water Elevation Measurement Results.
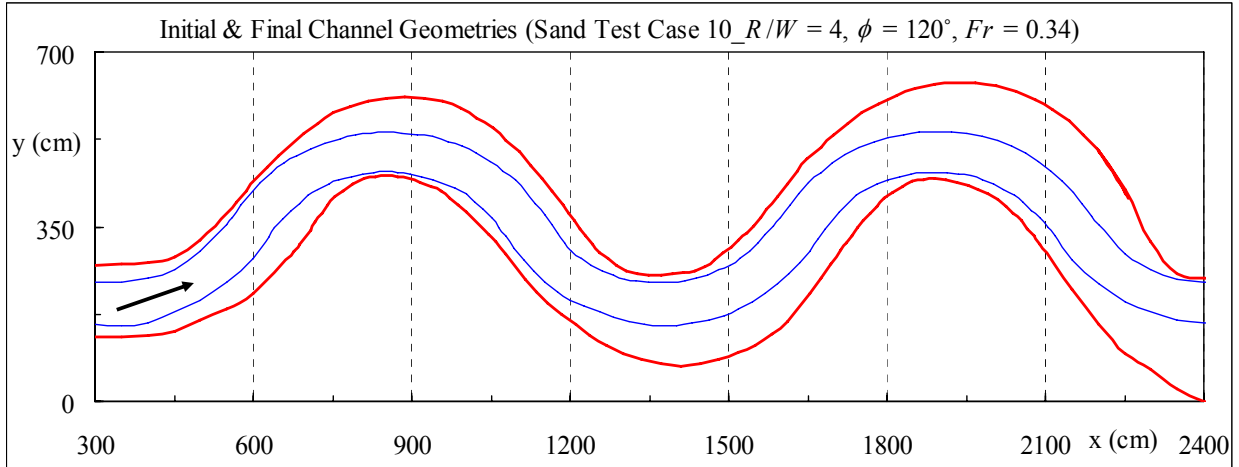
Figure A.50. Channel Geometry at the Initial and Final (39 hr) Stages.
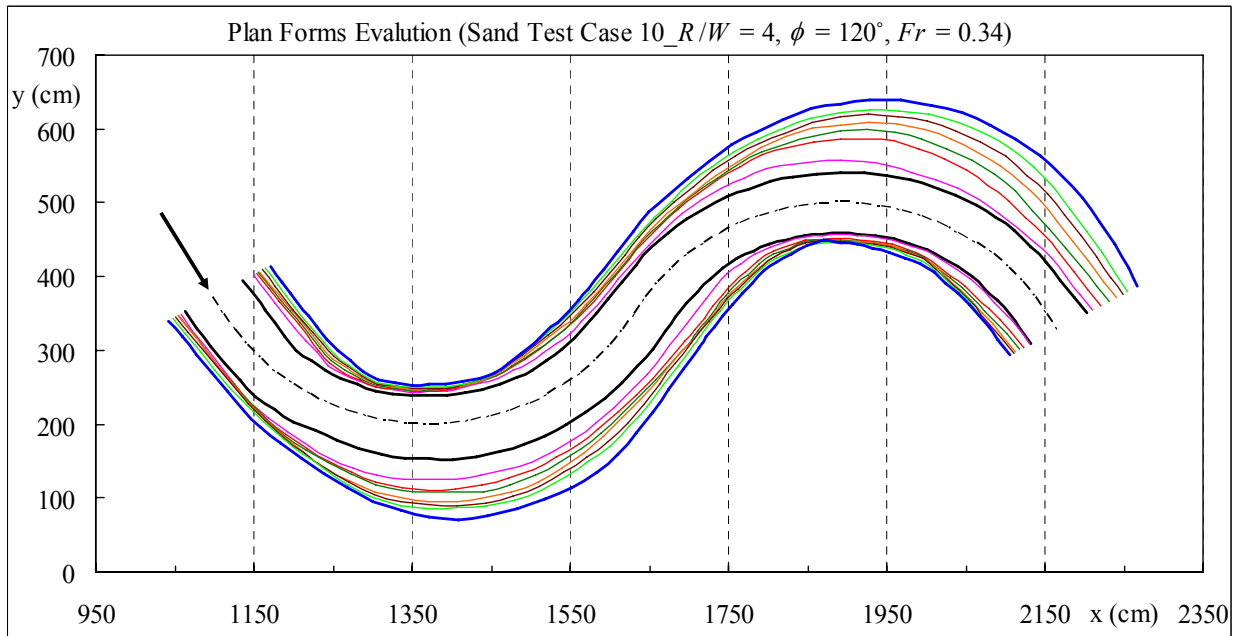
Figure A.51. Plan Forms Evolution at *t* = 0, 3, 6, 9, 15, 21, 27 and 39 hr.

243
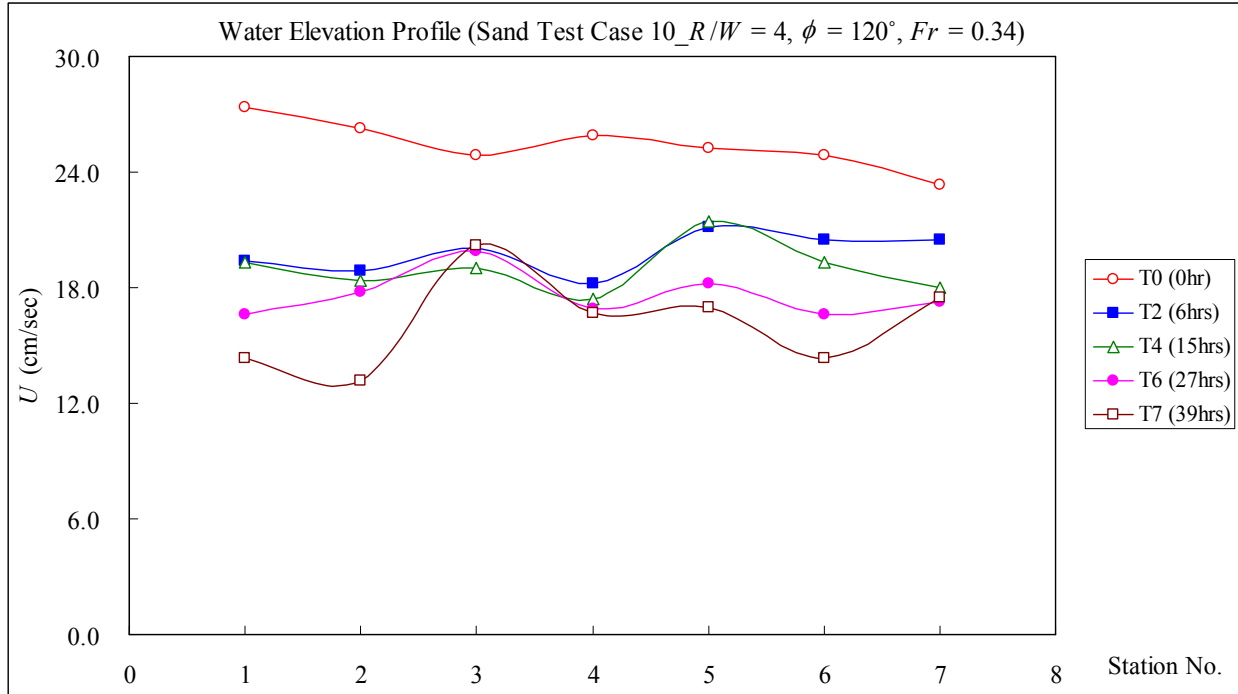
(a) Mean Velocity Profile
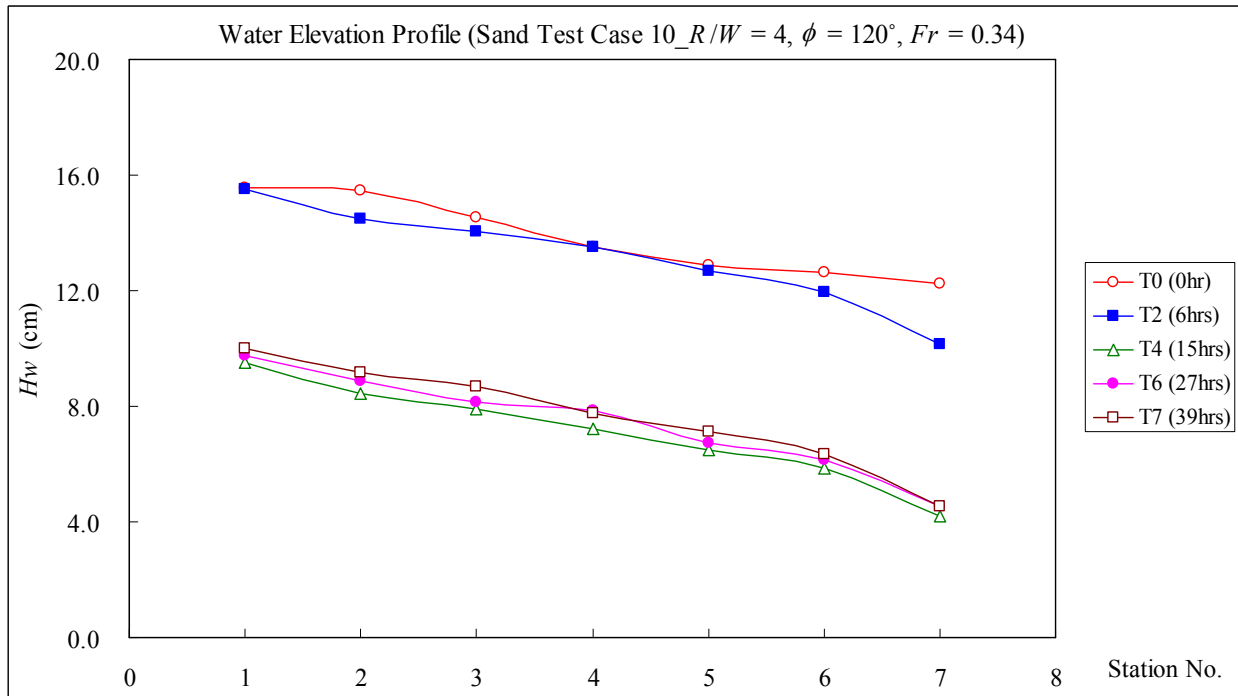
(b) Water Elevation Profile

Figure A.52. Mean Velocity and Water Elevation Measurement Results.
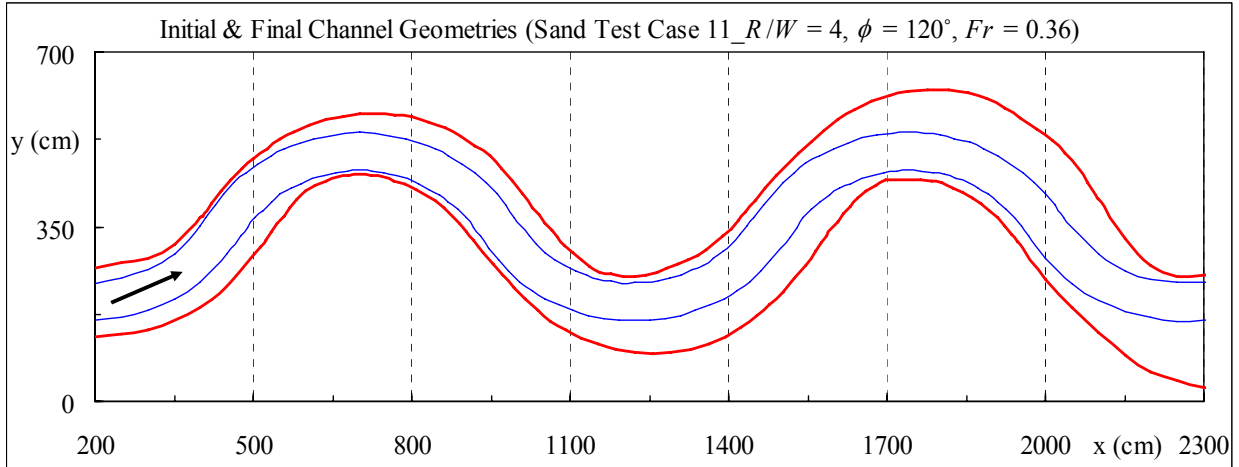
Figure A.53. Channel Geometry at the Initial and Final (23 hr) Stages.
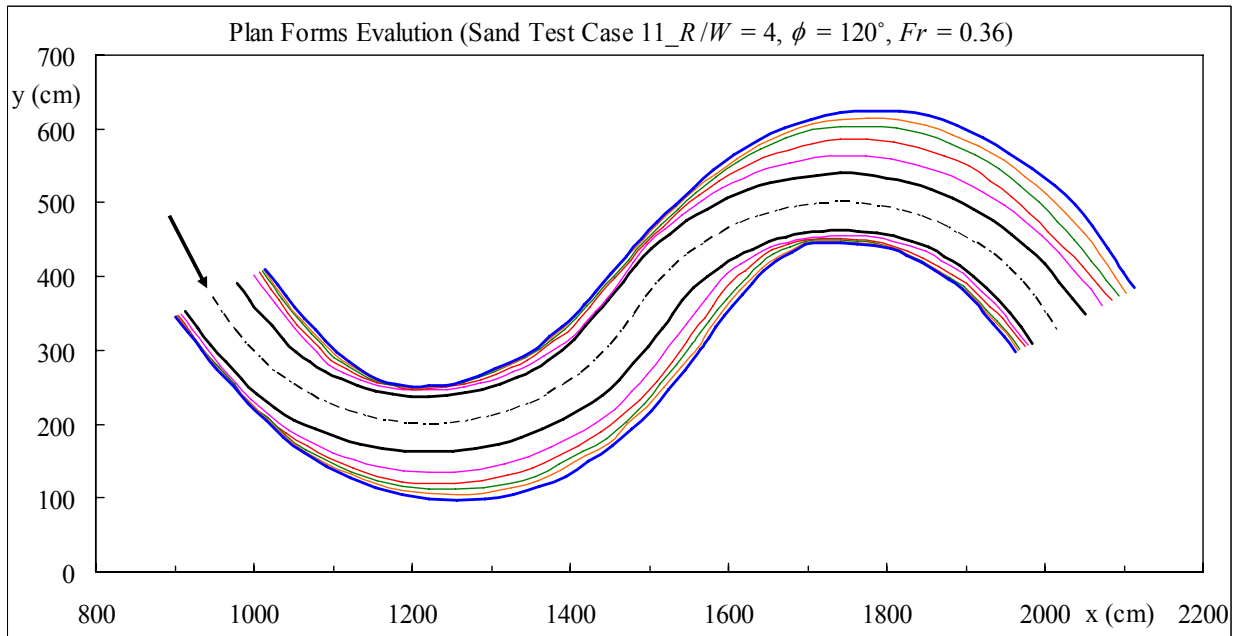
Figure A.54. Plan Forms Evolution at t = 0, 2, 5, 9, 14 and 23 hr.
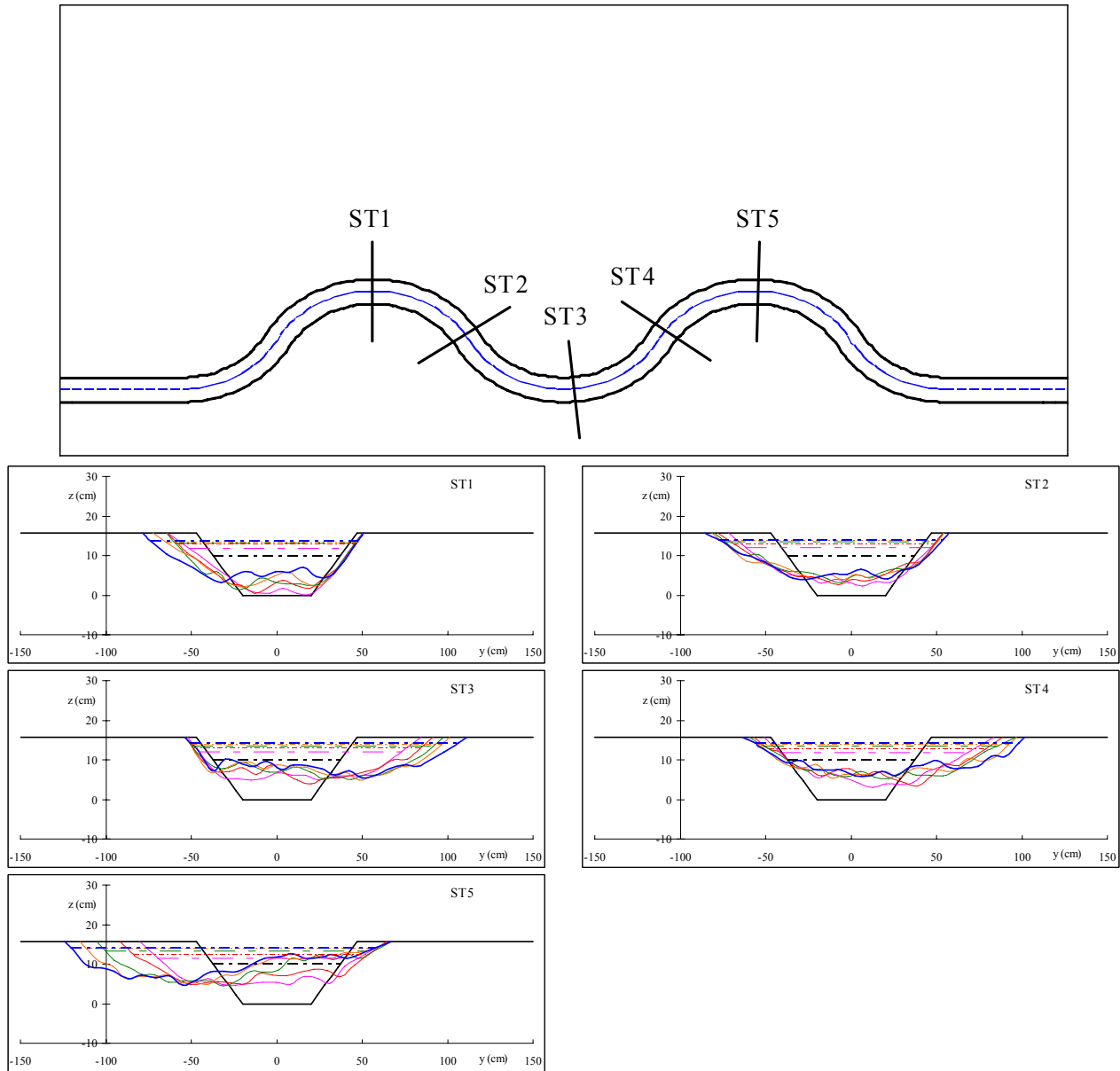
Figure A.55. Channel Cross-Section Profiles (Sand Test Case 11).
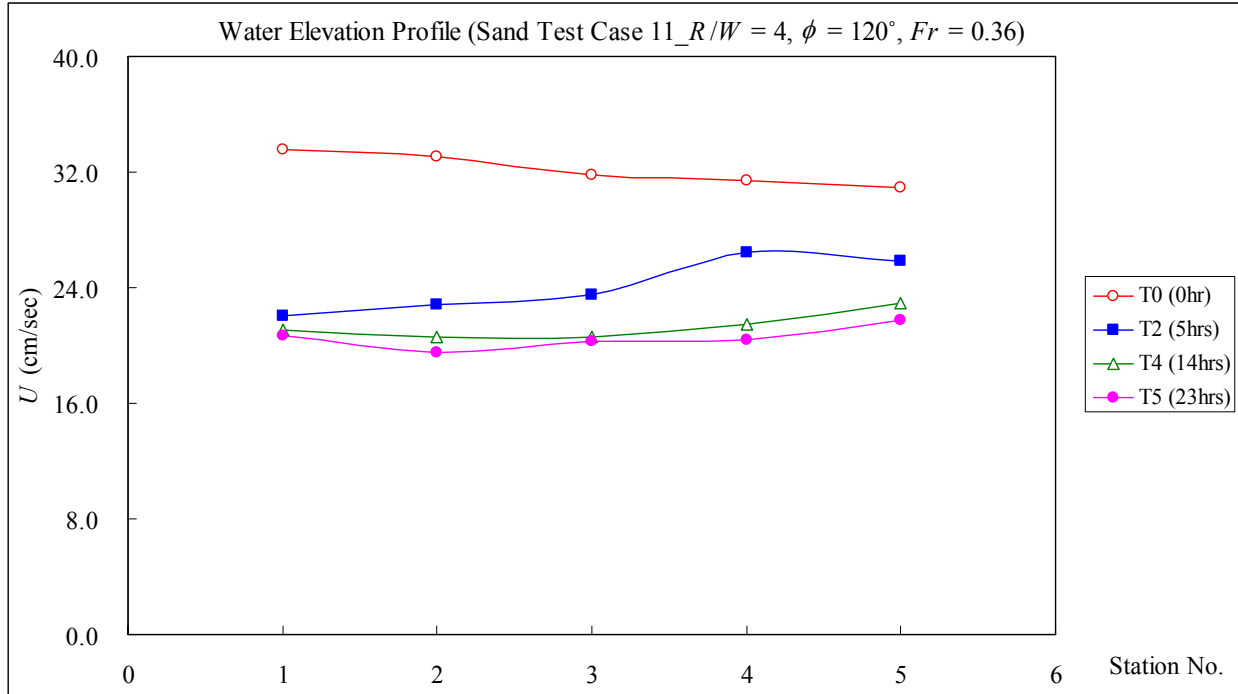
(a) Mean Velocity Profile
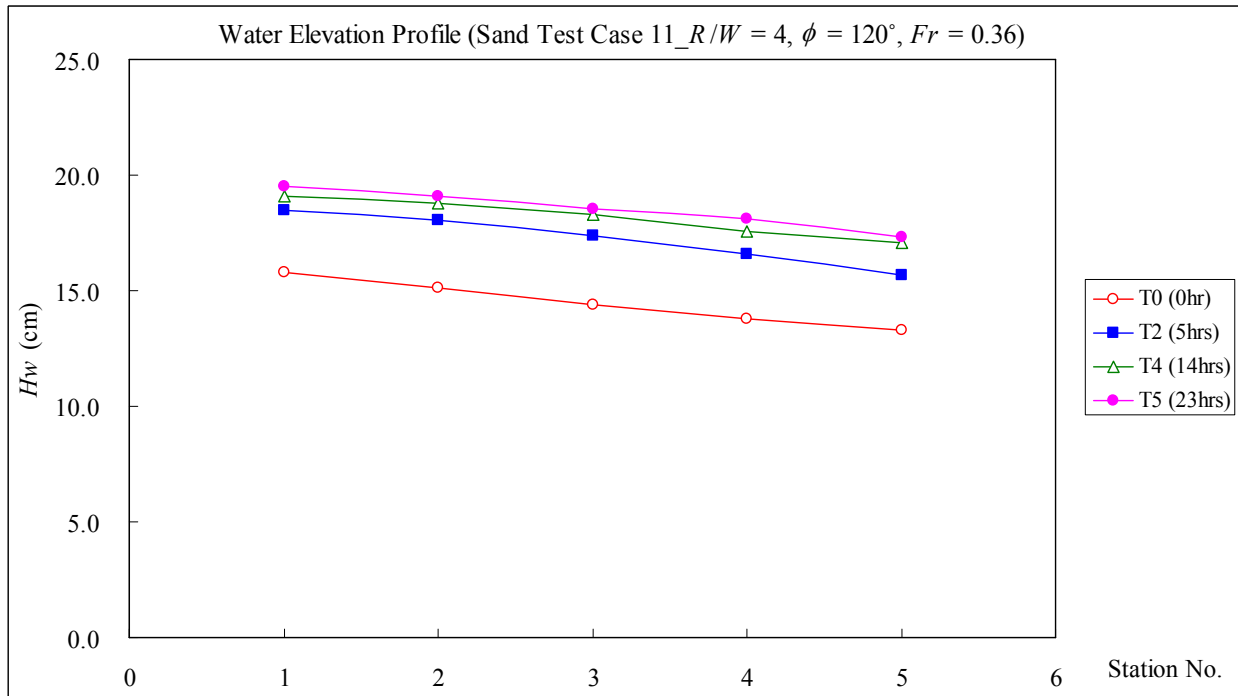
(b) Water Elevation Profile

Figure A.56. Mean Velocity and Water Elevation Measurement Results.
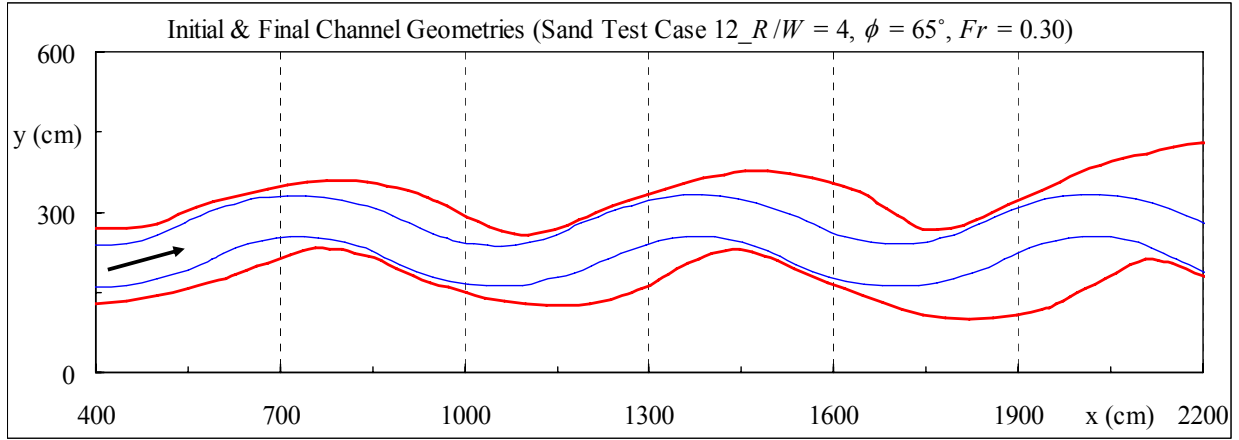
Figure A.57. Channel Geometry at the Initial and Final (45 hr) Stages.
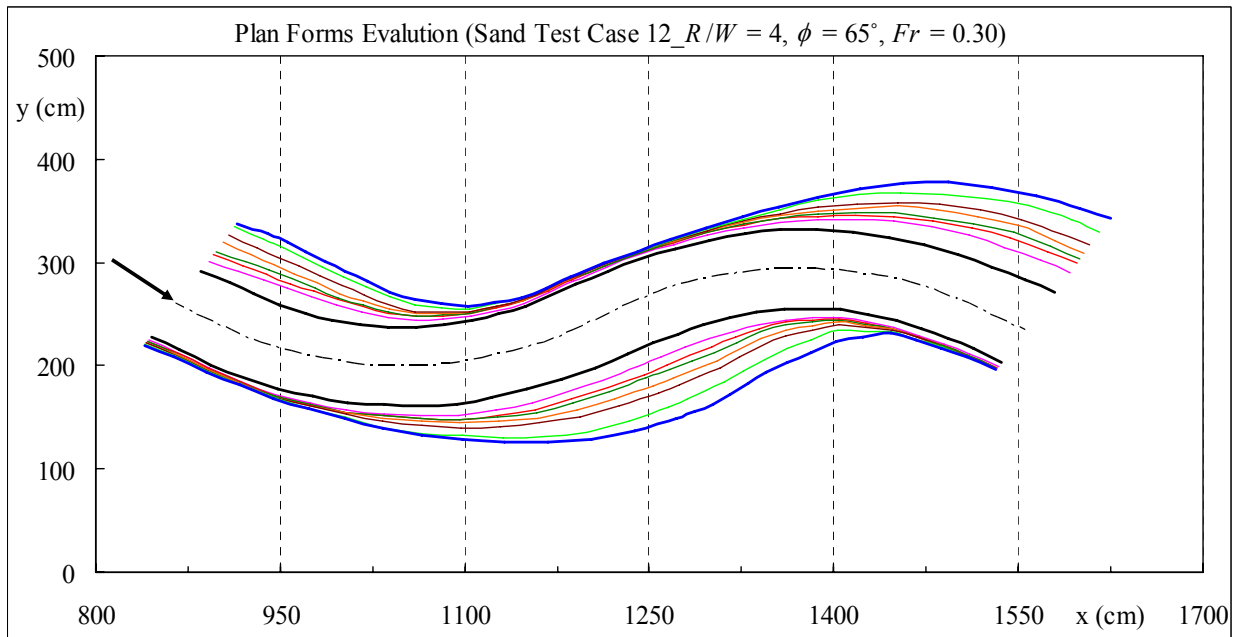
Figure A.58. Plan Forms Evolution at t = 0, 3, 6, 9, 15, 21, 33 and 45 hr.
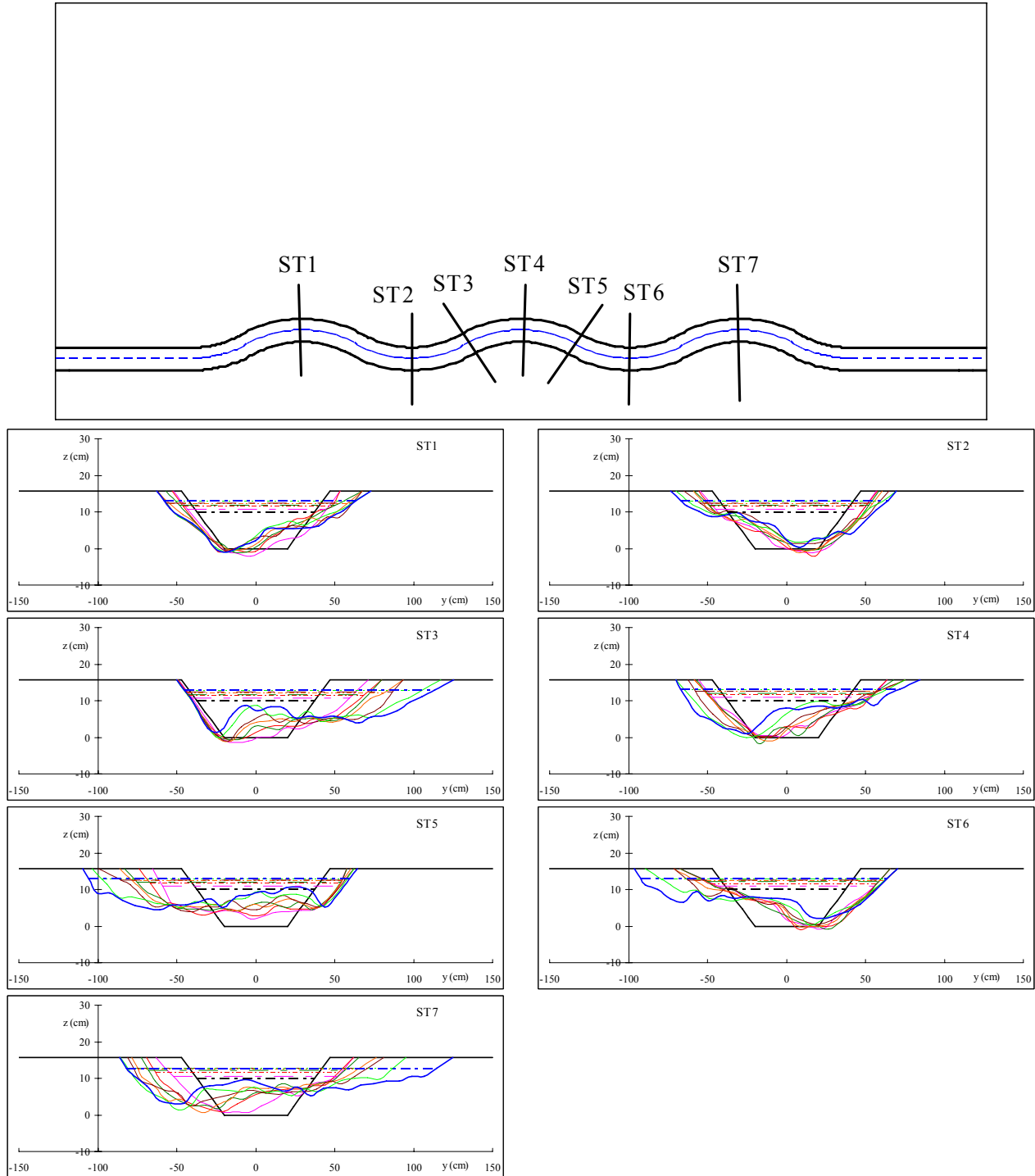
Figure A.59. Channel Cross-Section Profiles (Sand Test Case 12).
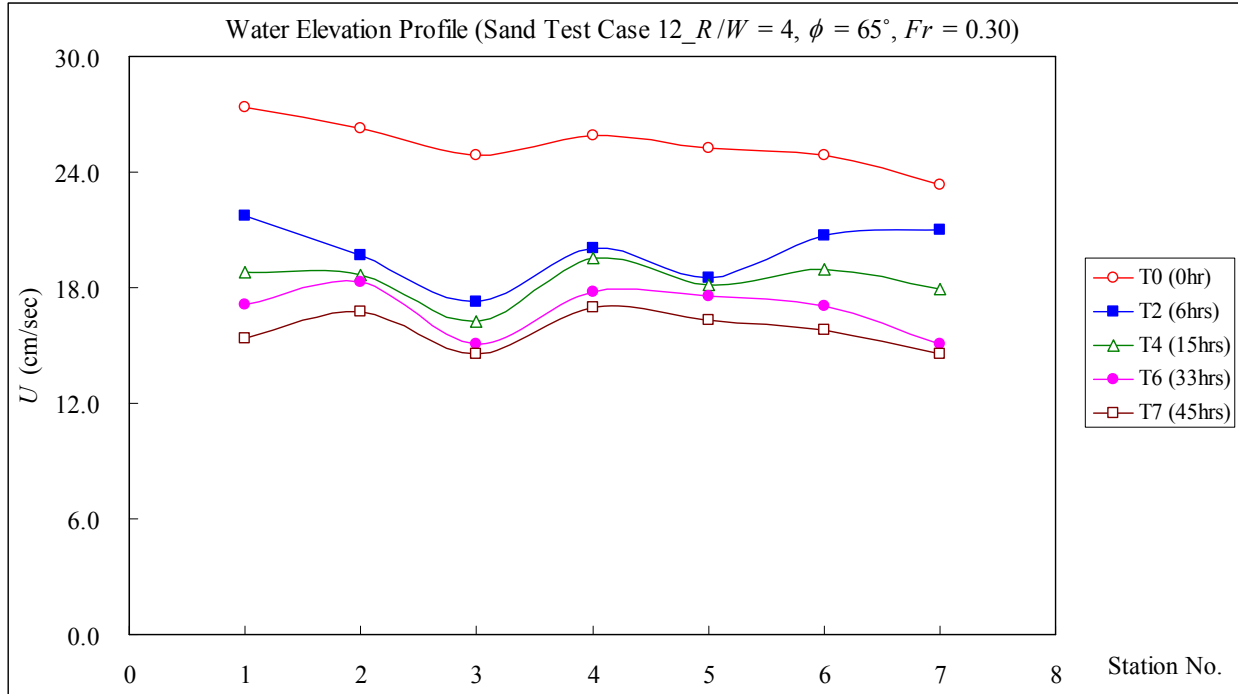
(a) Mean Velocity Profile
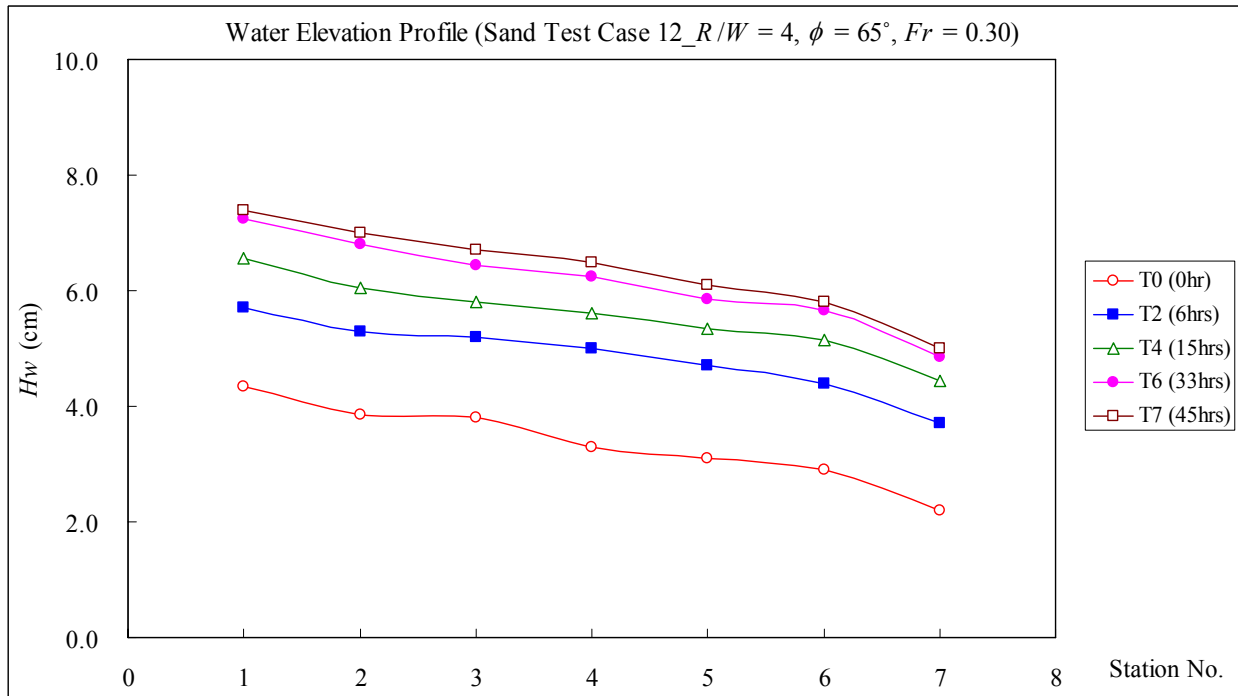
(b) Water Elevation Profile

Figure A.60. Mean Velocity and Water Elevation Measurement Results.

APPENDIX B – FLUME TESTS IN CLAY

PHOTOGRAPHS OF THE PREPARATION:

Figure B.1. Retrieving Clay from the Previous Test.

Figure B.2. Filling the Sand Channel.

Figure B.3. Leveling the Sand Bed.

Figure B.4. Completion of Leveling Work.

Figure B.5. Drawing the Contour of the Sand Channel.

Figure B.6. Digging the Sand Channel.

Figure B.7. Placing the Clay Banks and Covering with Wet Cloth.

Figure B.8. Sprinkling the Clay Banks.

Figure B.9. Completion of the Clay Channel.

Figure B.10. Trial Cross Ssections: (a) Case 01, (b) Case 02, (c) Case 03, and (d) Final. Adapted Cross Section in the Clay Tests.

PHOTOGRAPHS OF THE FLUME TESTS:

<div align="center">

(a) Initial   (b) Final (t = 20 hr)

</div>

Figure B.11. Clay Test Case 01 (R/W = 4, ϕ = 120˚, Fr = 0.50).

Figure B.12. Initial Condition of Clay Test Case 02 (R/W = 4, ϕ = 120˚, Fr = 0.50).

Figure B.13. Final Condition of Clay Test Case 02 (*t* = 106.5 hr).

Figure B.14. Initial Condition of Clay Test Case 03 ($R/W = 6$, $\phi = 65^{\bullet}$, $Fr = 0.50$).

Figure B.15. Final Condition of Clay Test Case 03 ($t = 163.5$ hr).

Figure B.16. Initial Condition of Clay Test Case 04 ($R/W = 4$, $\phi = 65^\bullet$, $Fr = 0.50$).

Figure B.17. Final Condition of Clay Test Case 04 ($t = 268$ hr).

Figure B.18. Initial Condition of Clay Test Case 05 ($R/W = 6$, $\phi = 65^\bullet$, $Fr = 0.50$).
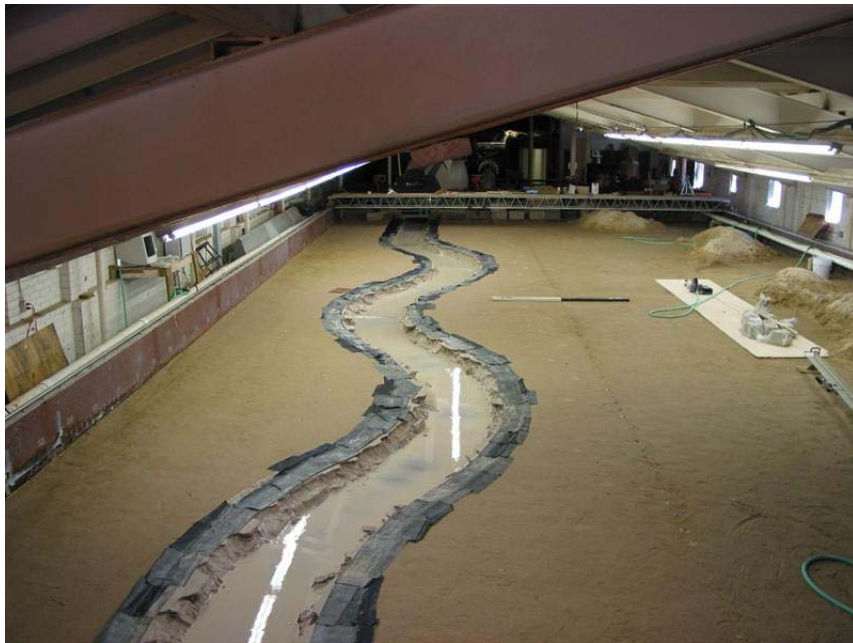
Figure B.19. Final Condition of Clay Test Case 05 ($t = 184$ hr).

Figure B.20. Initial Condition of Clay Test Case 06 ($R/W = 2$, $\phi = 65^{\bullet}$, $Fr = 0.50$).

Figure B.21. Final Condition of Clay Test Case 06 ($t = 180$ hr).

Figure B.22. Initial Condition of Clay Test Case 07 (*R/W* = 4, ϕ = 120$^\bullet$, *Fr* = 0.50).

Figure B.23. Final Condition of Clay Test Case 07 (*t* = 192 hr).

Figure B.24. Initial Condition of Clay Test Case 08 (*R/W* = 4, ϕ = 220$^\bullet$, *Fr* = 0.50).

Figure B.25. Final Condition of Clay Test Case 08 (*t* = 336 hr).

FLUME TEST RESULTS:
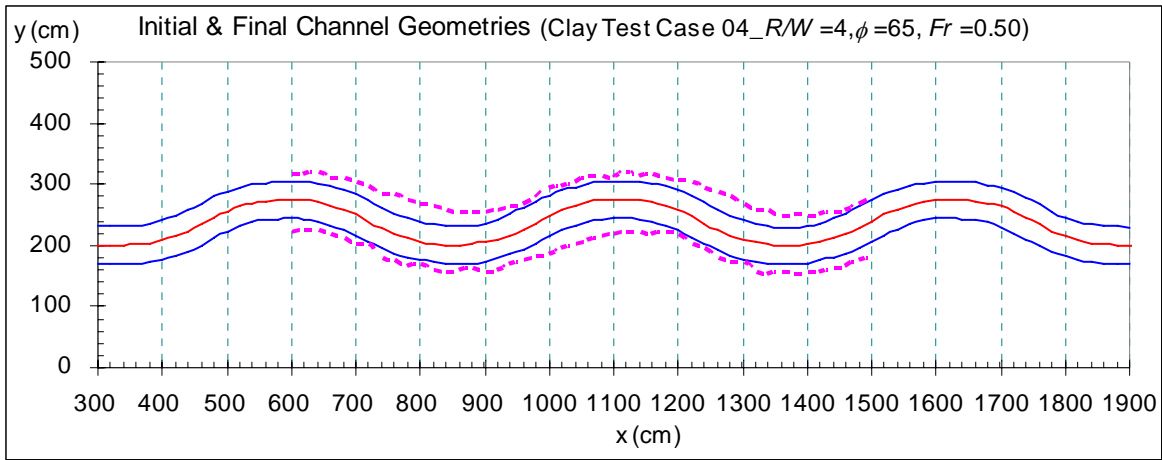
Figure B.26. Channel Geometry at the Initial and Final (268 hr) Stages (Clay Test Case 04).
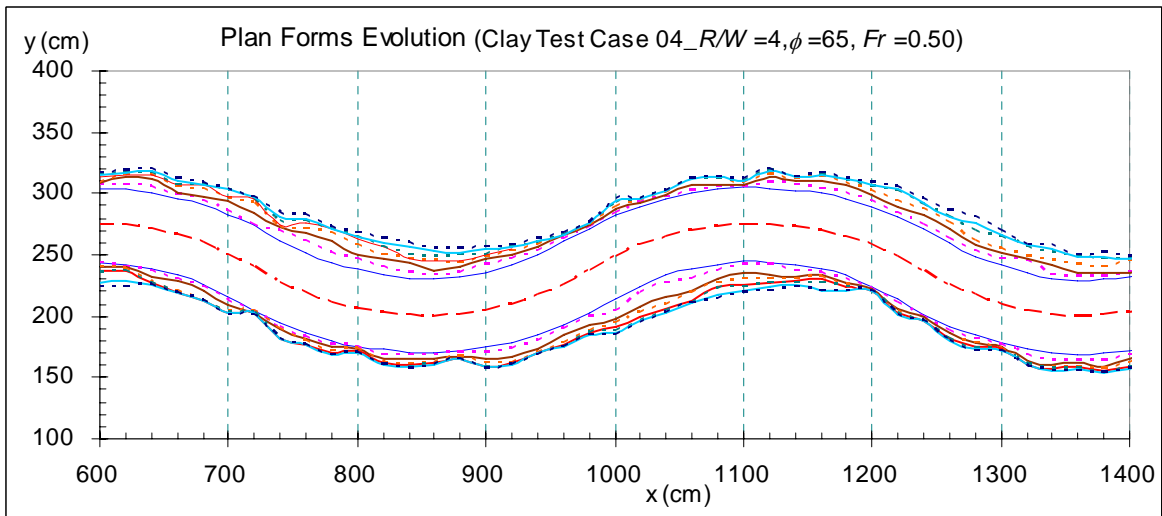
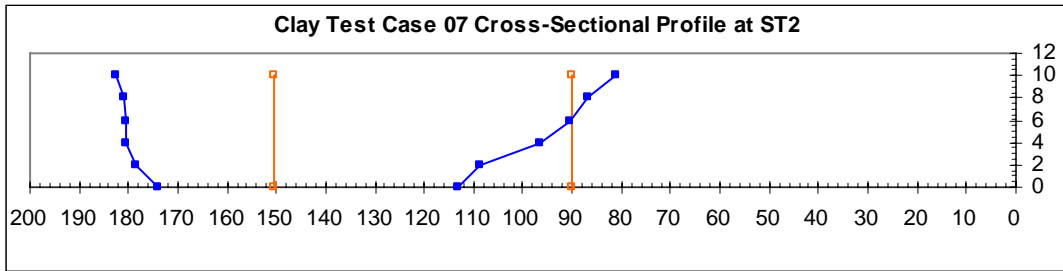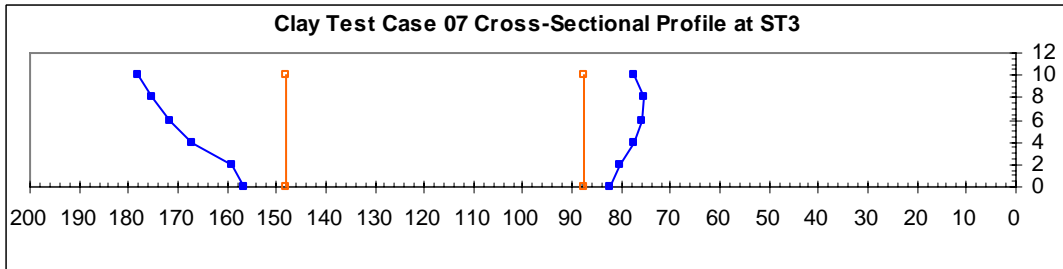**Figure B.27. Plan Forms Evolution at t = 0, 48, 96, 126, 156, 186, 220, and 268 hr (Clay Test Case 04).**
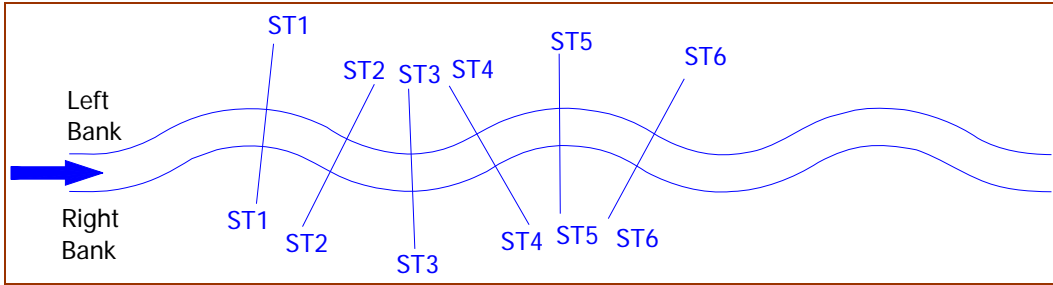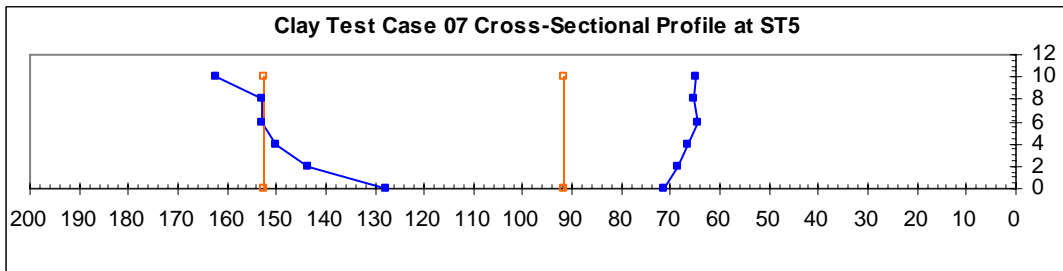
(a) Locations of the Predetermined Stations
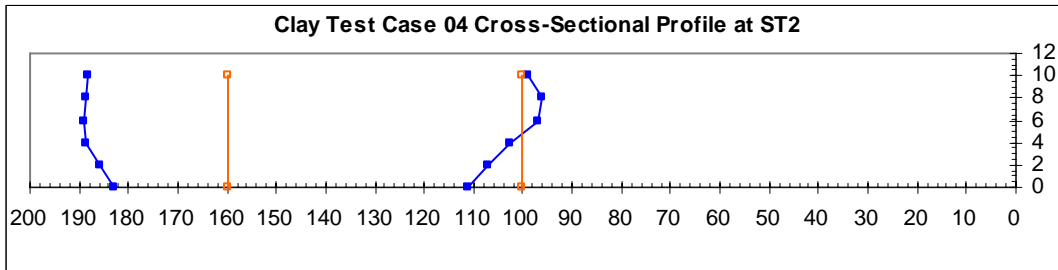
(b) Evolution of cross-sectional profile at station No. 2
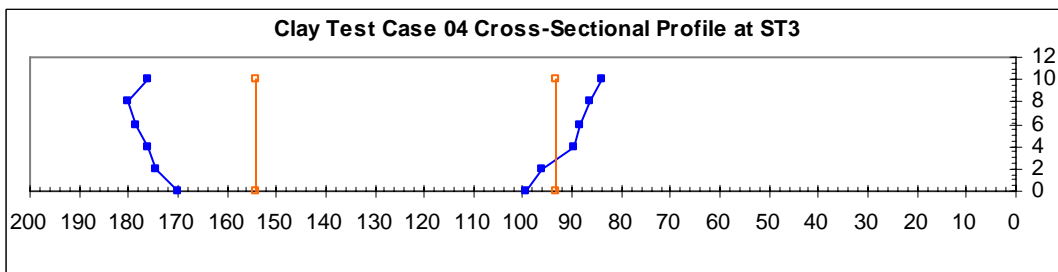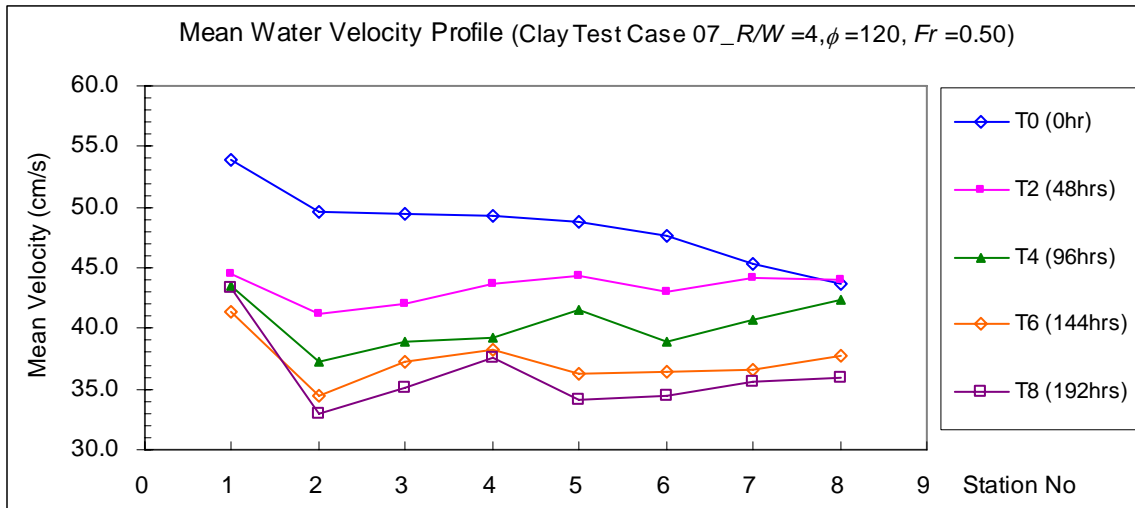

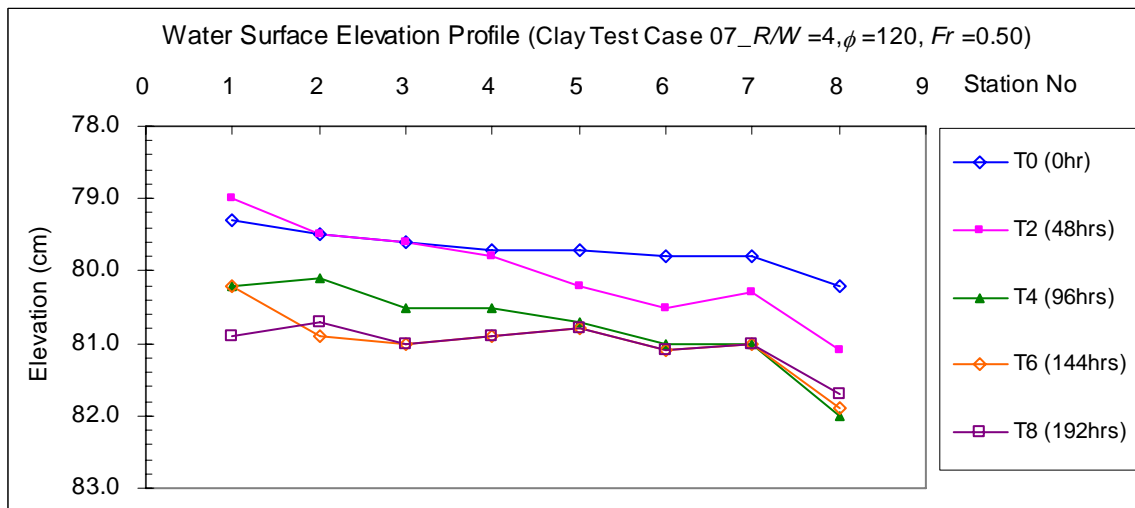(c) Evolution of cross-sectional profile at station No. 3
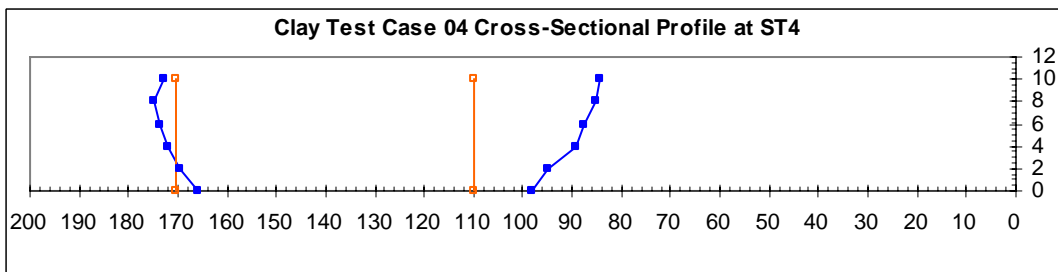
(d) Evolution of cross-sectional profile at station No. 4

Figure B.28. Cross-Sectional Measurement Results
(Clay Test Case 04).
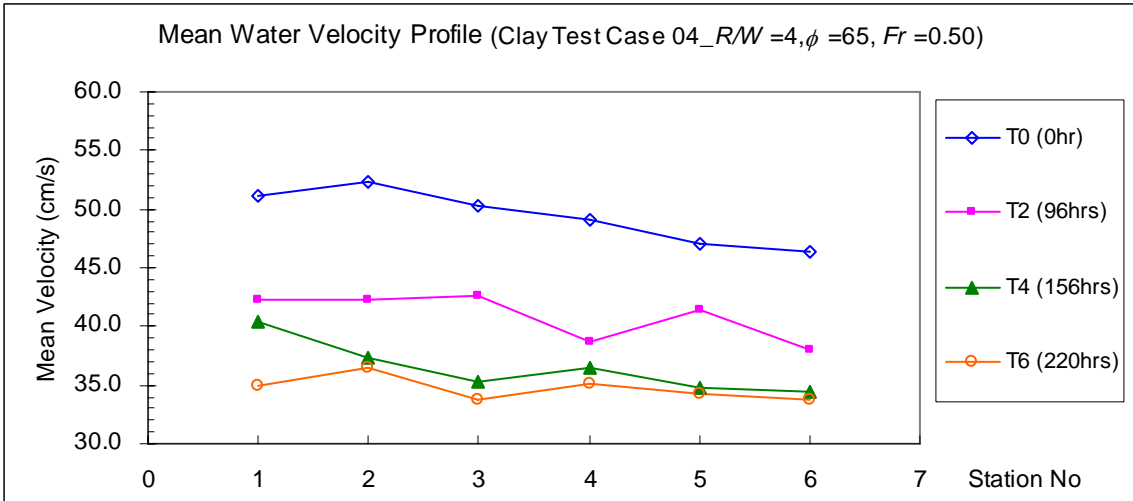
(a) Mean water velocity profile
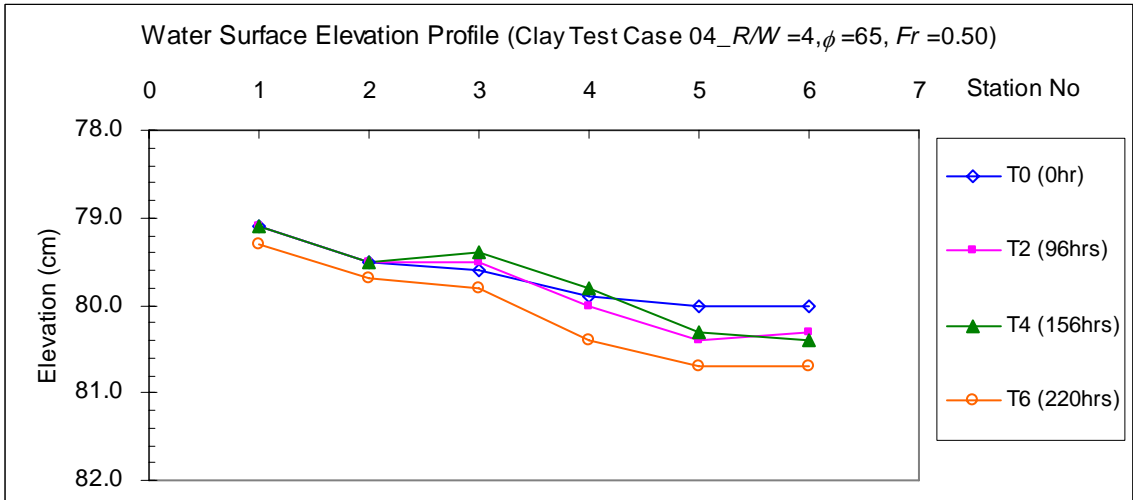
(b) Water surface elevation profile

Figure B.29. Mean Velocity and Water Elevation Measurement Results (Clay Test Case 04).
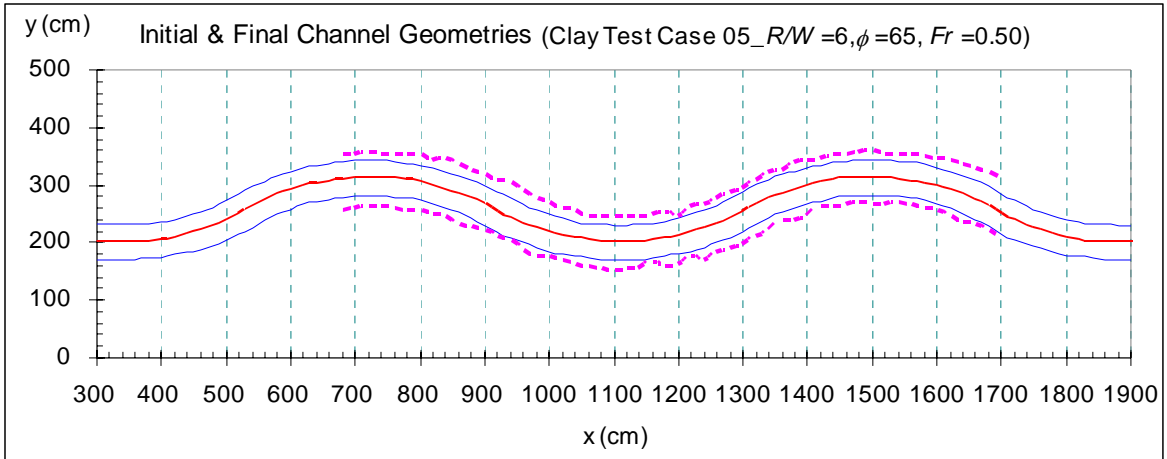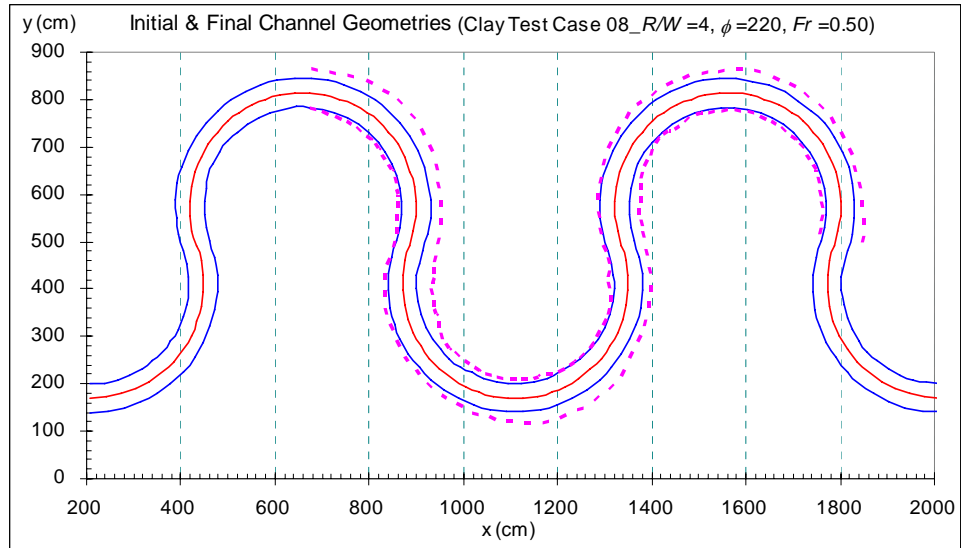
Figure B.30. Channel Geometry at the Initial and Final (260 hr) Stages (Clay Test Case 05).
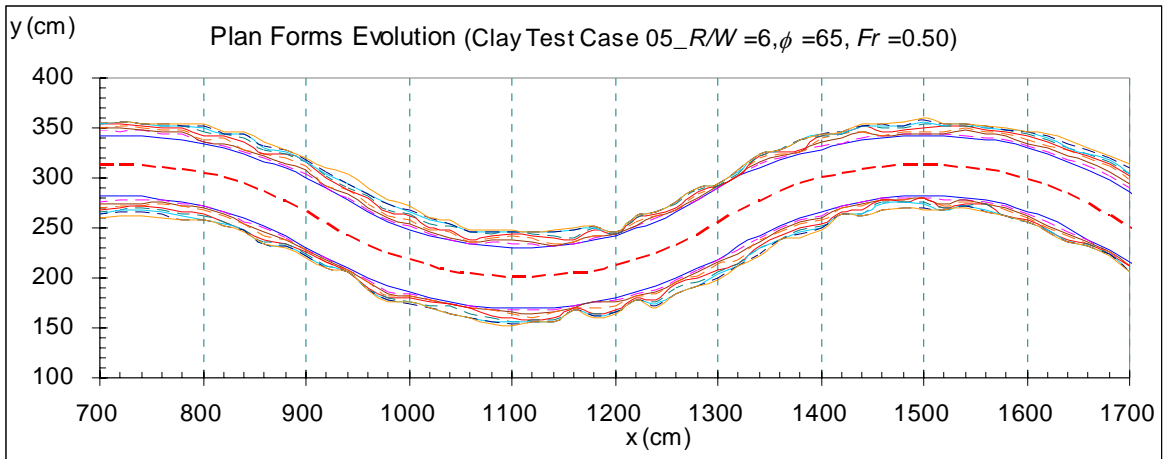
Figure B.31. Plan Forms Evolution at t = 0, 36, 60, 90, 120, 150, 184, 220, and 260 hr (Clay Test Case 05).
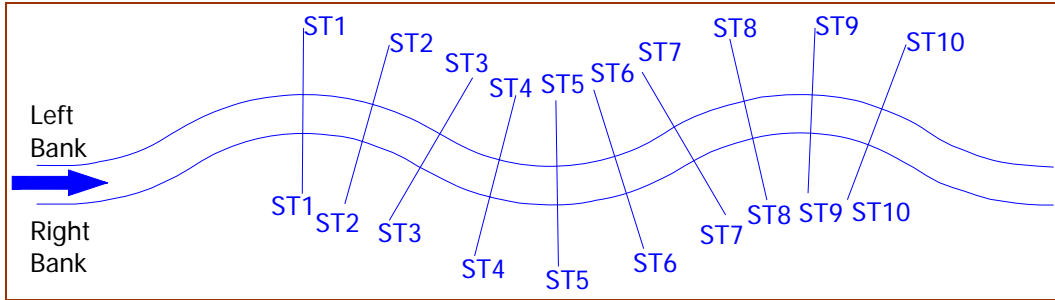
(a) Locations of the Predetermined Stations
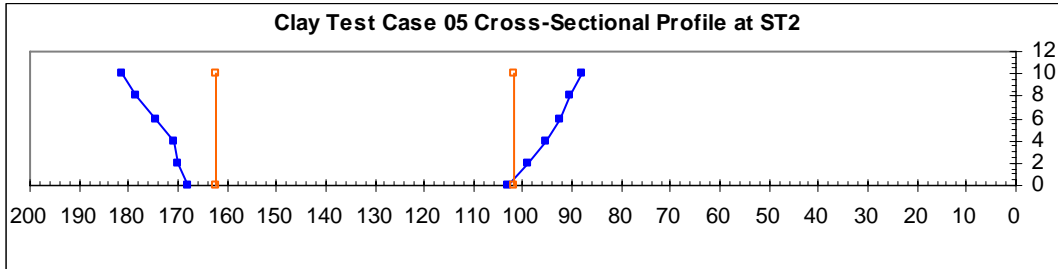
(b) Evolution of cross-sectional profile at station No. 2
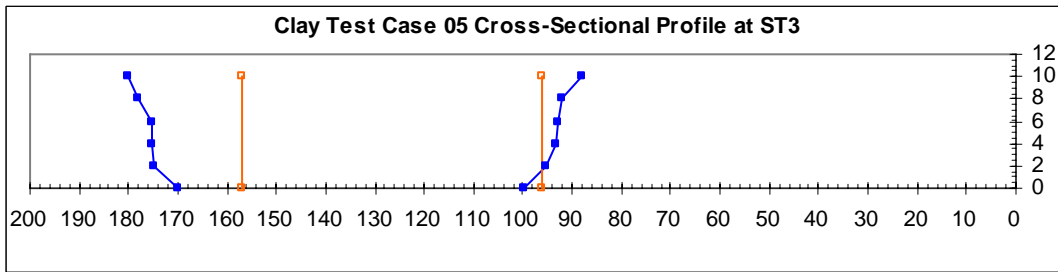
(c) Evolution of cross-sectional profile at station No. 3
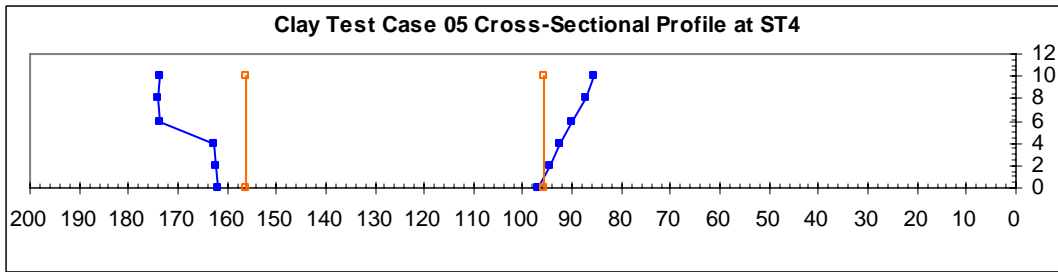
(d) Evolution of cross-sectional profile at station No. 4

Figure B.32. Cross-Sectional Measurement Results
(Clay Test Case 05).
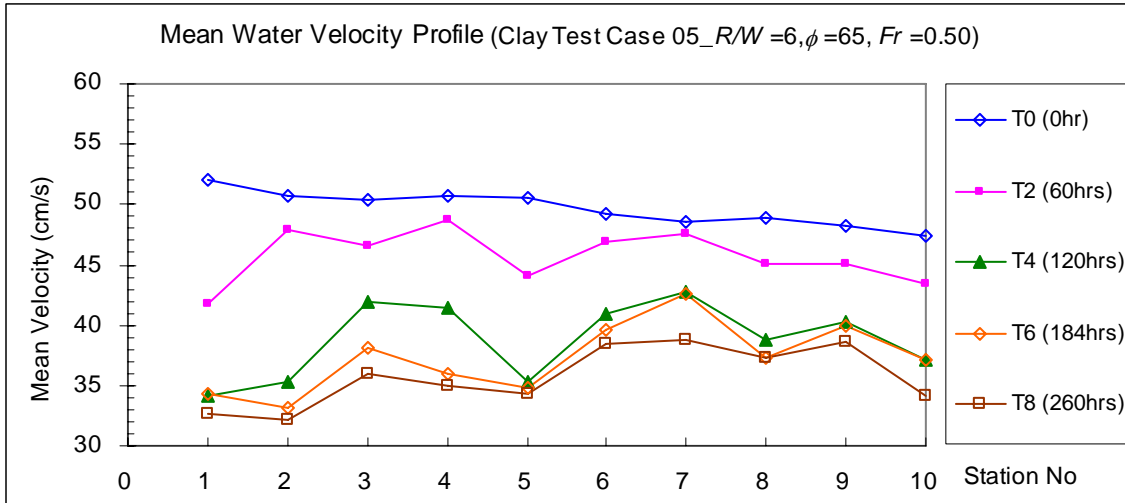
(a) Mean water velocity profile
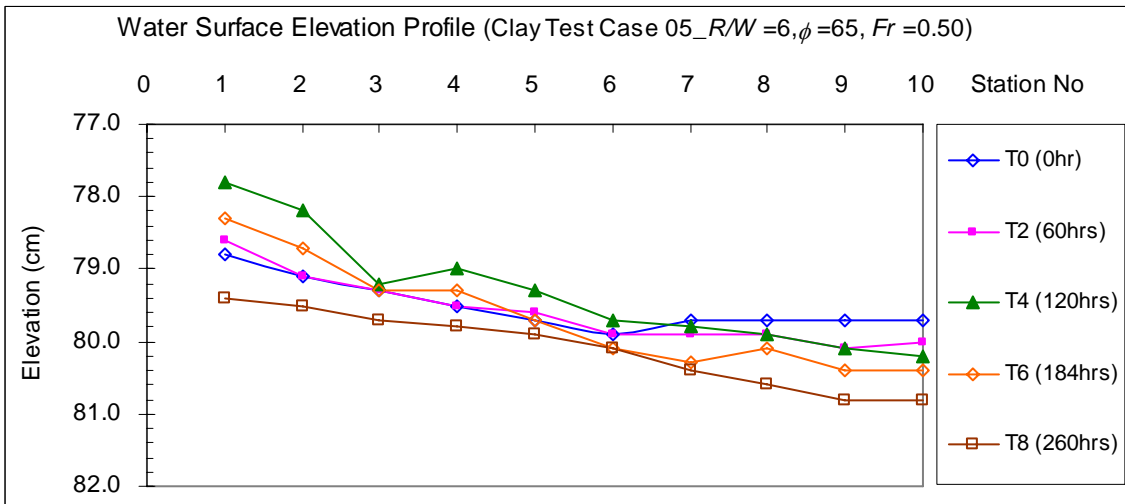
(b) Water surface elevation profile

Figure B.33. Mean Velocity and Water Elevation Measurement Results
(Clay Test Case 05).
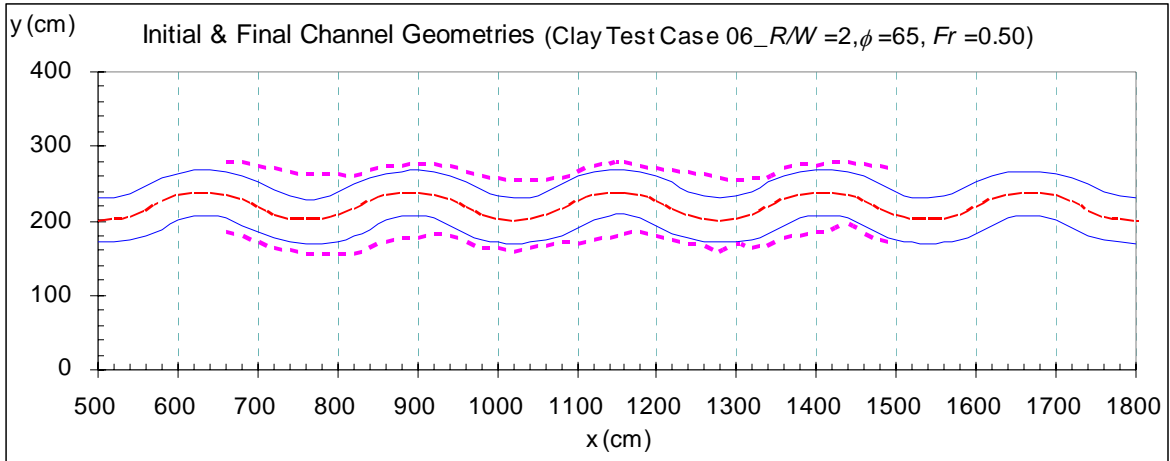
**Figure B.34. Channel Geometry at the Initial and Final (192 hr) Stages
(Clay Test Case 06).**
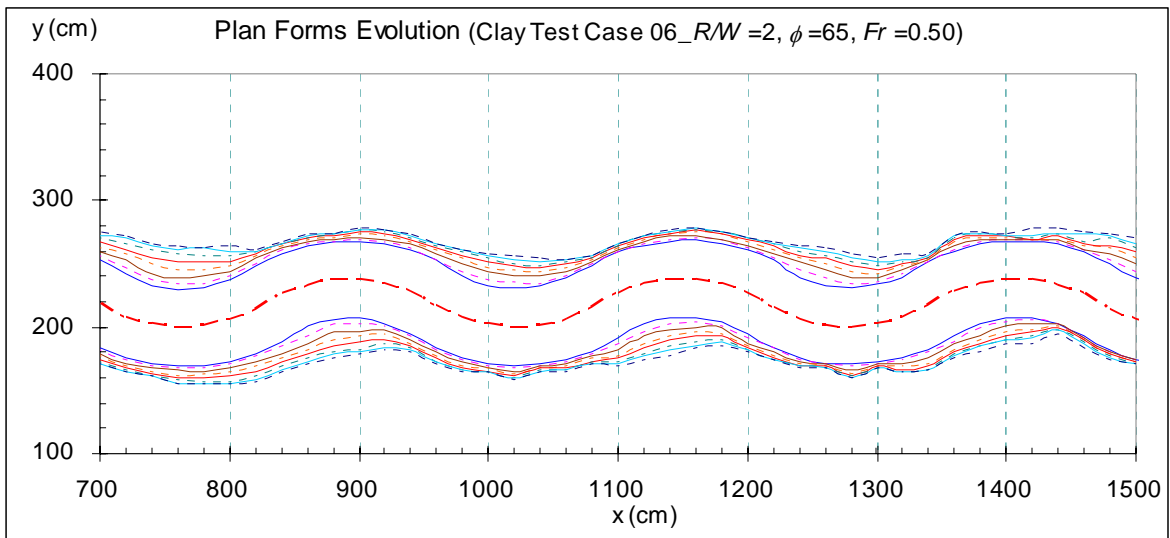
**Figure B.35. Plan Forms Evolution at *t* = 0, 24, 48, 72, 96, 120, 144, and 180 hr
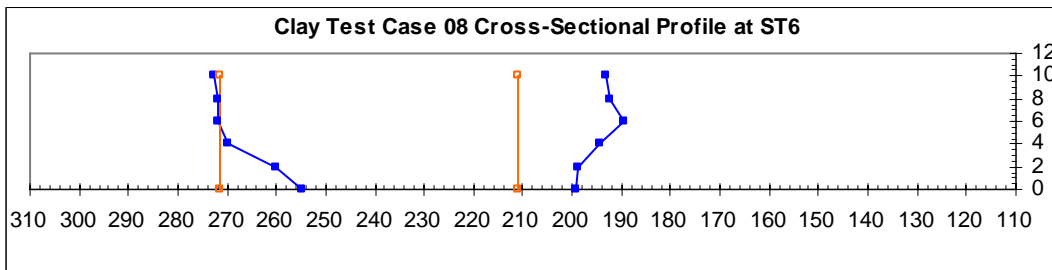(Clay Test Case 06).**
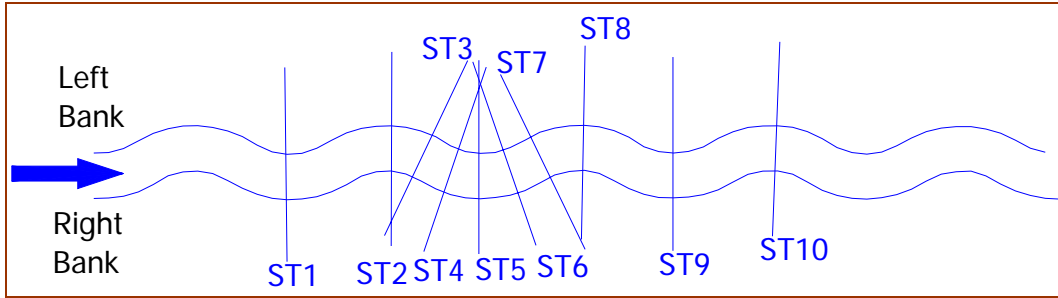
(a) Locations of the Predetermined Stations
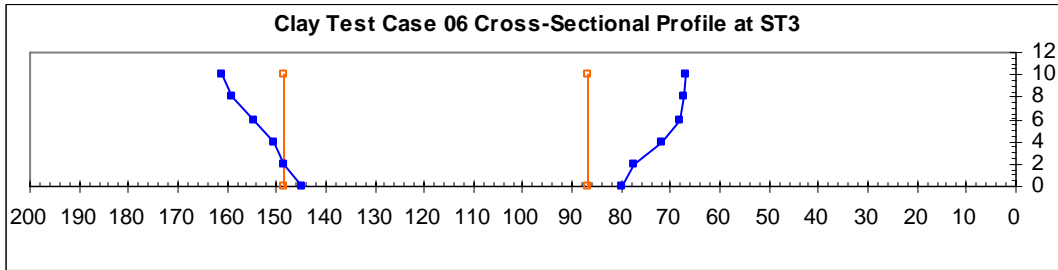
(b) Evolution of cross-sectional profile at station No. 3
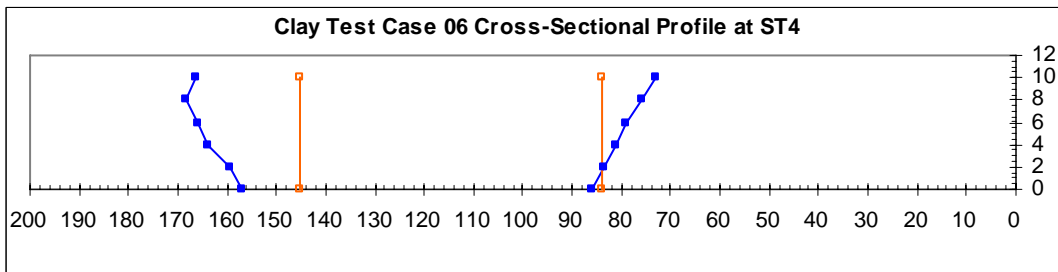
(c) Evolution of cross-sectional profile at station No. 4
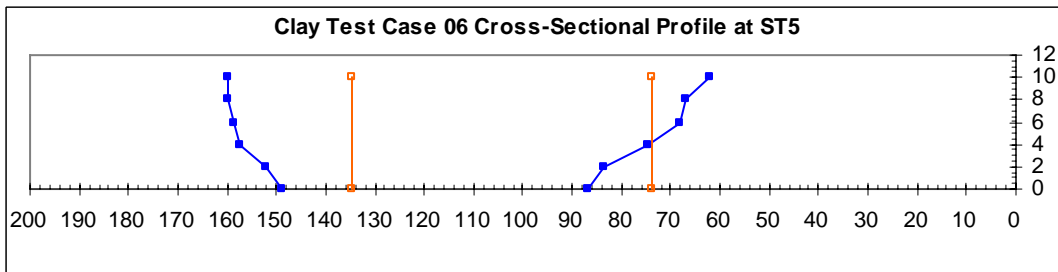
(d) Evolution of cross-sectional profile at station No. 5

Figure B.36. Cross-Sectional Measurement Results
(Clay Test Case 06).
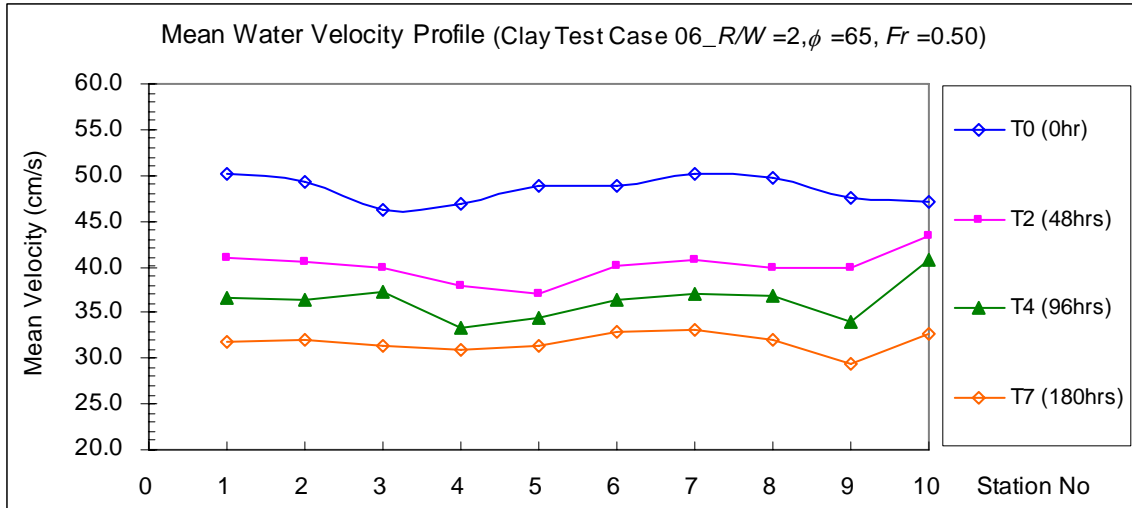
(a) Mean water velocity profile
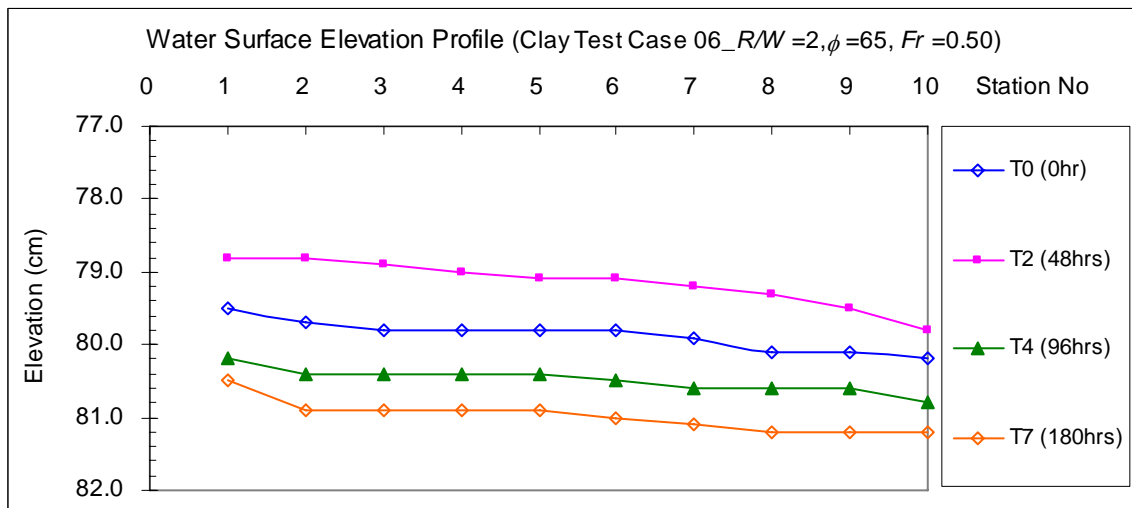
(b) Water surface elevation profile

Figure B.37. Mean Velocity and Water Elevation Measurement Results (Clay Test Case 06).
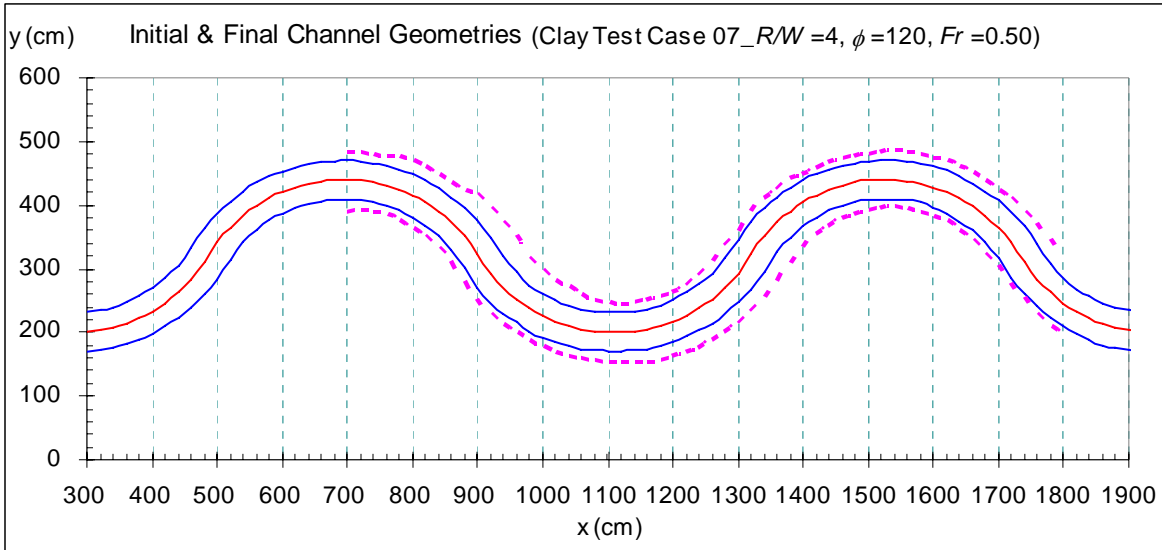
Figure B.38. Channel Geometry at the Initial and Final (192 hr) Stages (Clay Test Case 07).
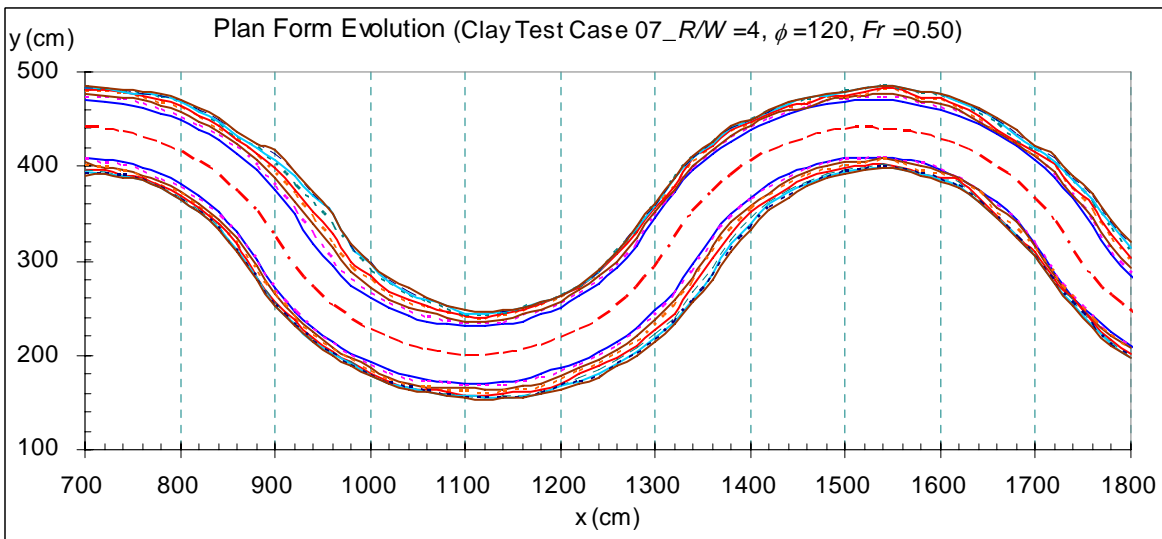
Figure B.39. Plan Forms Evolution at $t = 0, 24, 48, 72, 96, 120, 144, 168,$ and 192 hr (Clay Test Case 07)
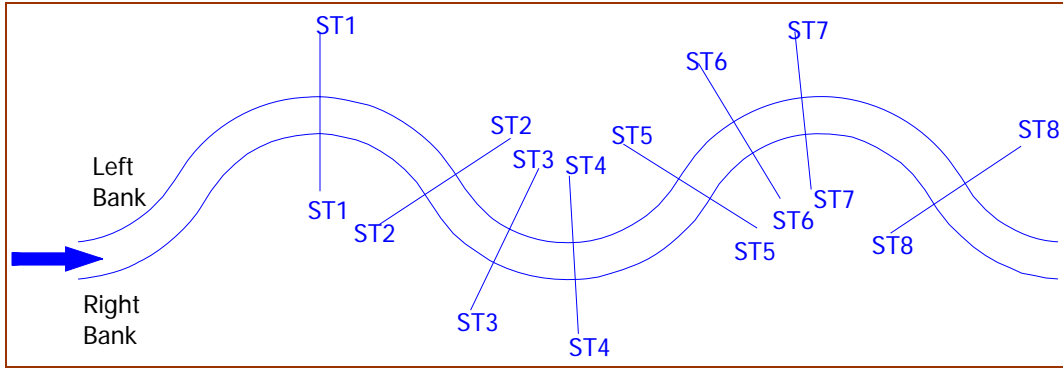
274

(a) Locations of the Predetermined Stations

(b) Evolution of cross-sectional profile at station No. 2

(c) Evolution of cross-sectional profile at station No. 3

(d) Evolution of cross-sectional profile at station No. 5

Figure B.40. Cross-Sectional Measurement Results
(Clay Test Case 07).

275

(a) Mean water velocity profile

(b) Water surface elevation profile

Figure B.41. Mean Velocity and Water Elevation Measurement Results (Clay Test Case 07).

276

Figure B.42. Channel Geometry at the Initial and Final (336 hr) Stages (Clay Test Case 08).
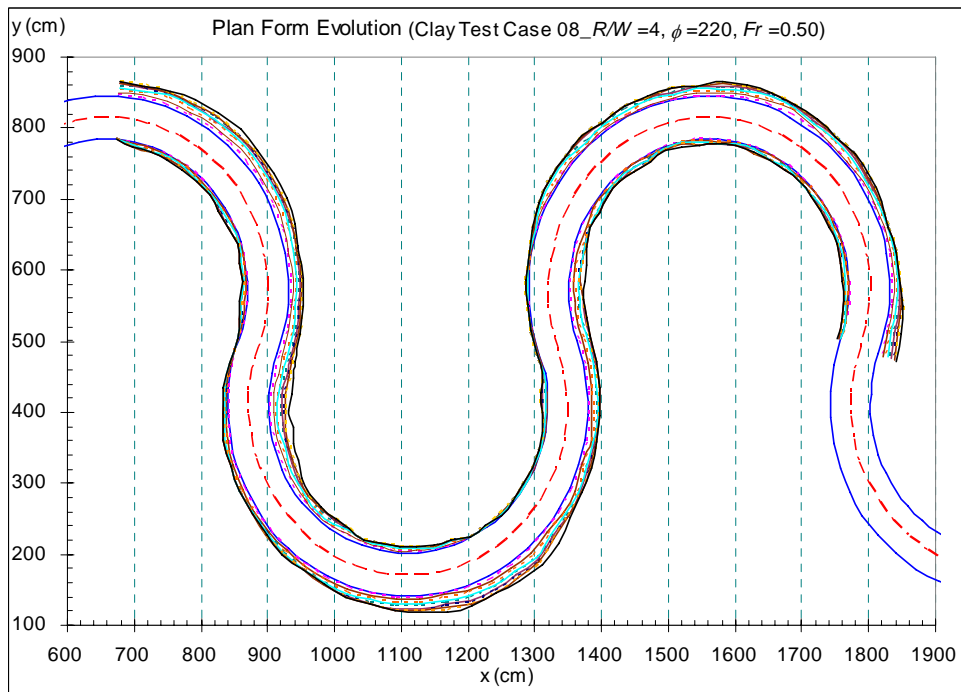
Figure B.43. Plan Forms Evolution at *t* = 0, 24, 48, 72, 96, 120, 150, 180, 210, 240 and 336 hr (Clay Test Case 08).
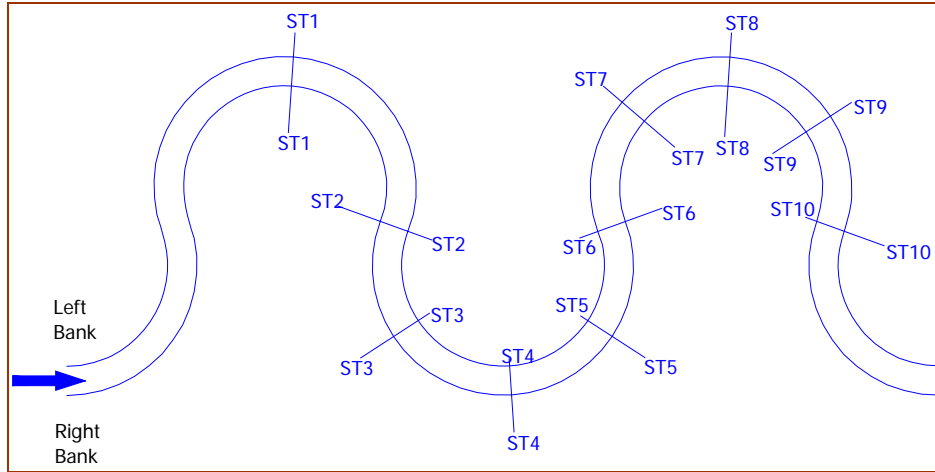
(a) Locations of the Predetermined Stations
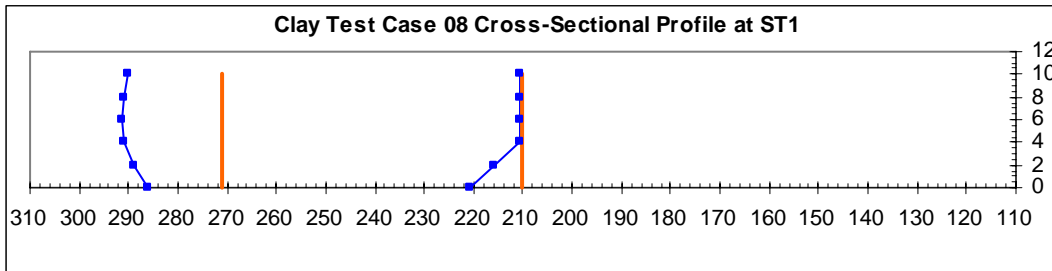
(b) Evolution of cross-sectional profile at station No. 1
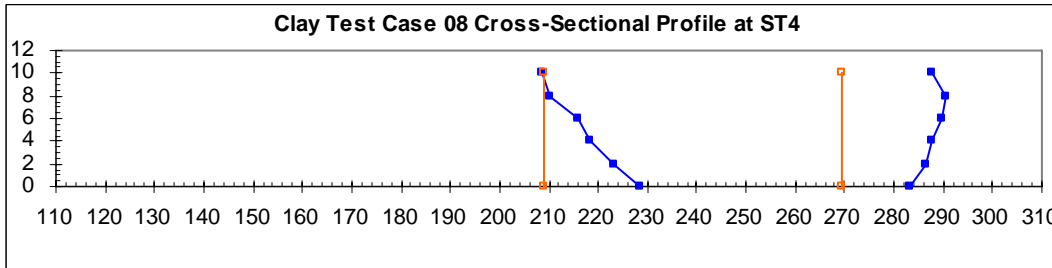
(c) Evolution of cross-sectional profile at station No. 4

(d) Evolution of cross-sectional profile at station No. 6

Figure B.44. Cross-Sectional Measurement Results
(Clay Test Case 08).
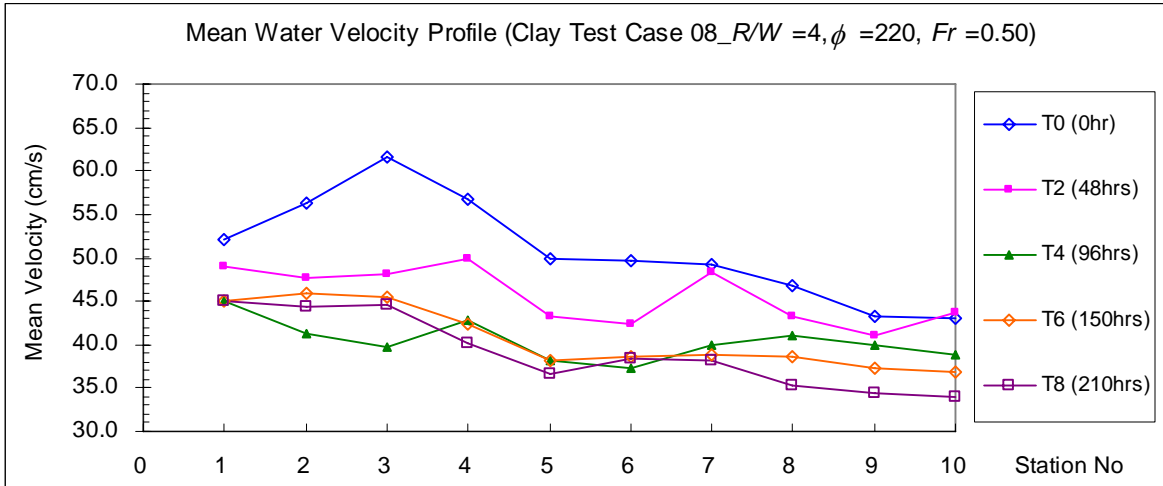
(a) Mean water velocity profile
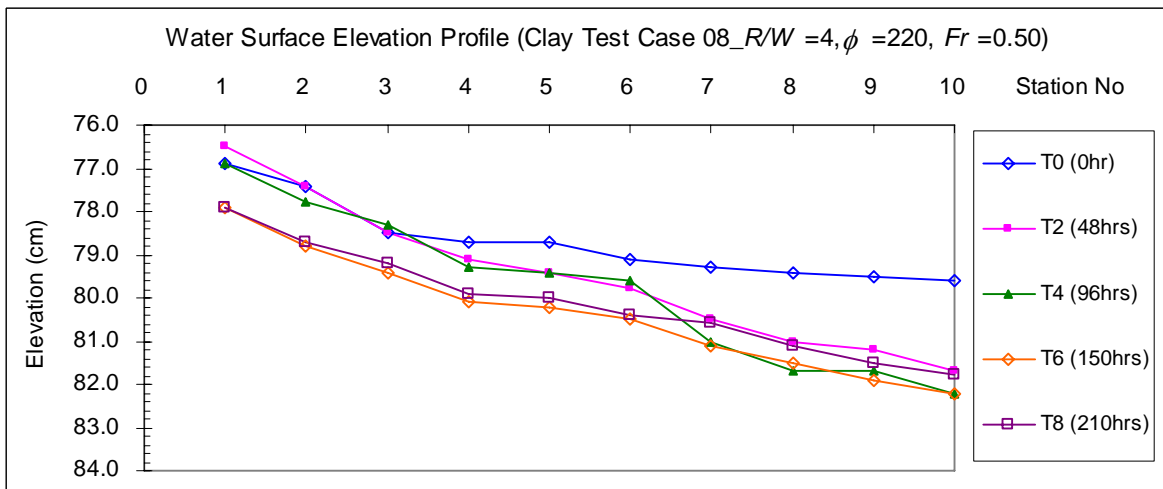
(b) Water surface elevation profile

Figure B.45. Mean Velocity and Water Elevation Measurement Results (Clay Test Case 08).

279

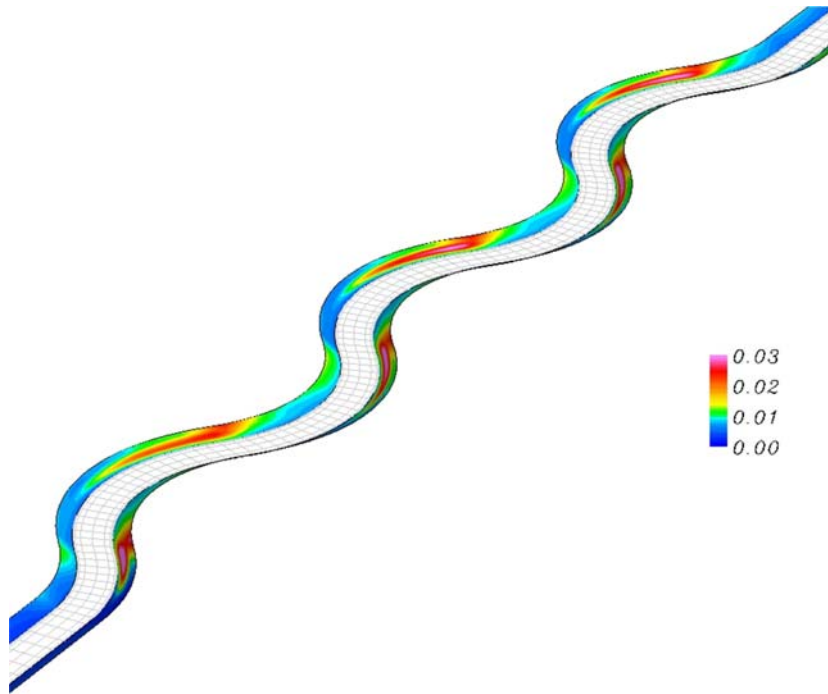# APPENDIX C – EXAMPLE RUNS OF NUMERICAL SIMULATION
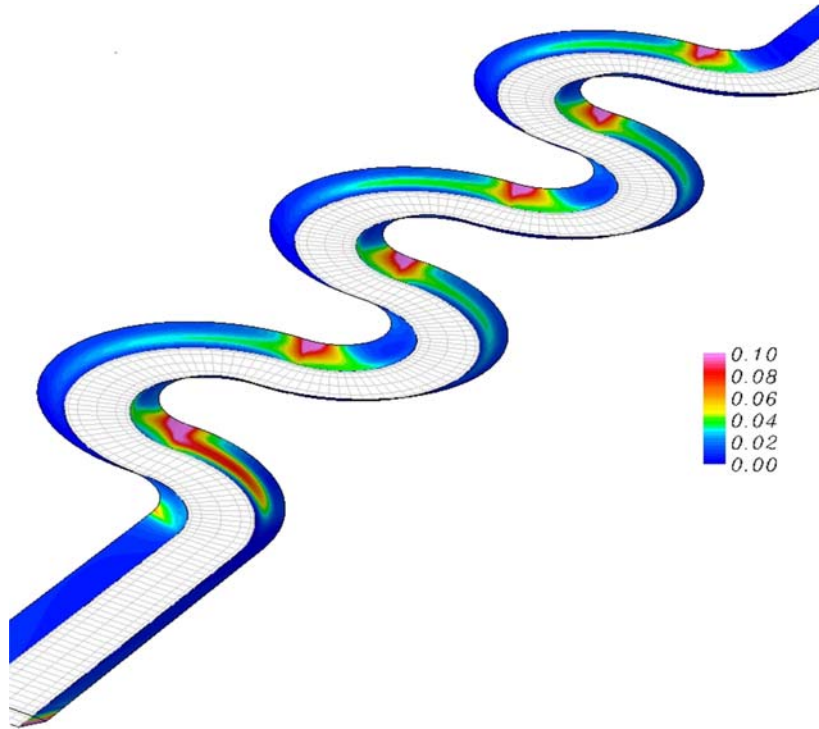
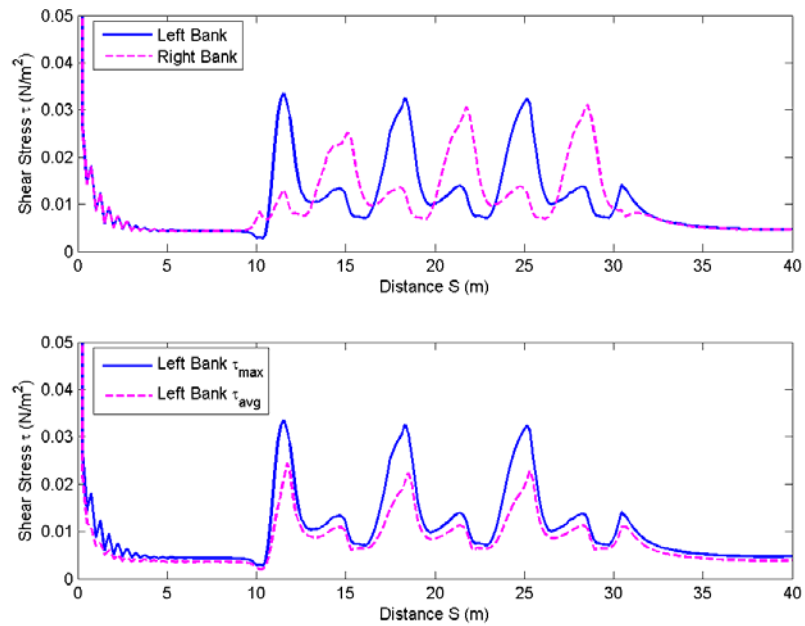**Figure C.1. Simulation Bank Shear Stress ($R/W = 1$, $\phi = 180°$).**
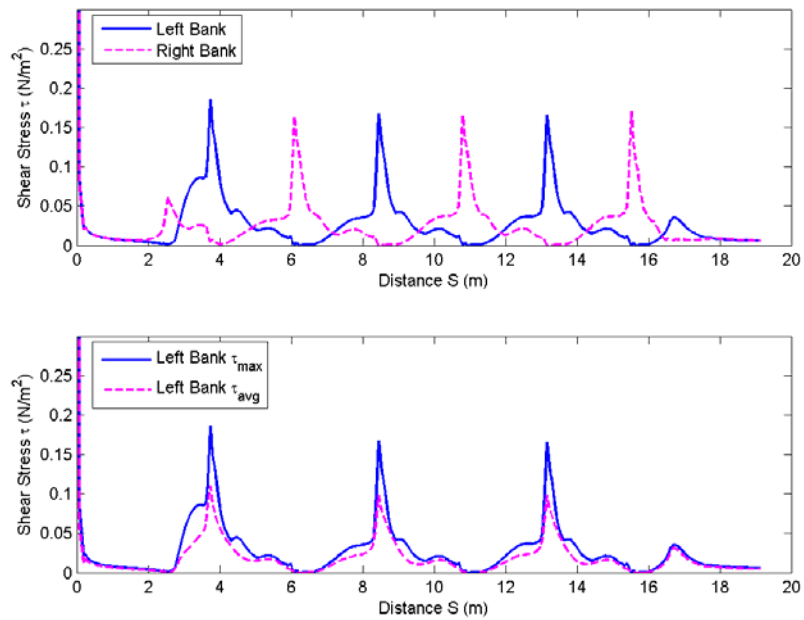
Figure C.2. Shear Stress Distribution on Both Banks along the Channel ($R/W = 1$, $\phi = 180°$).
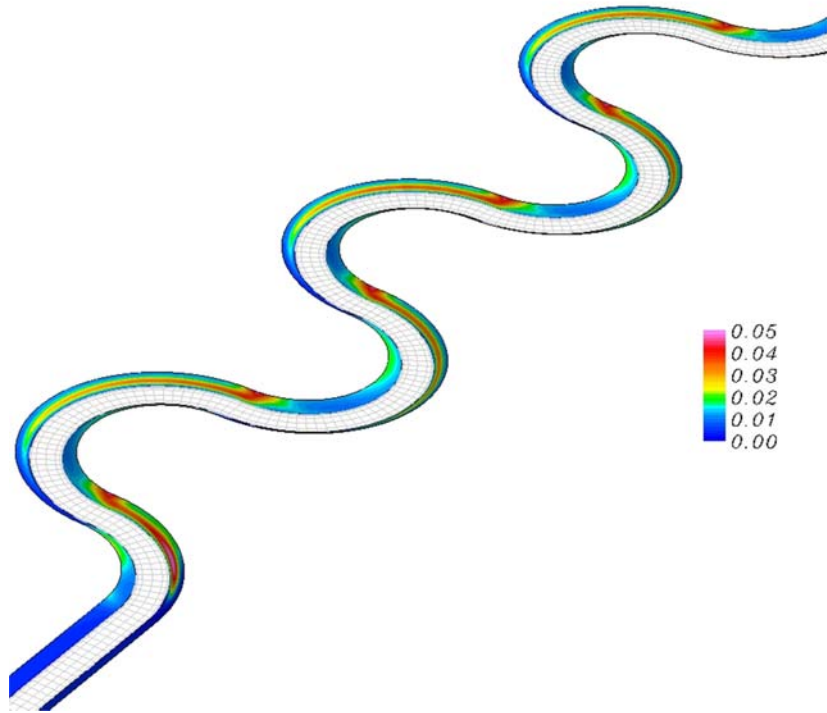
Figure C.3. Simulation Bank Shear Stress ($R/W = 2$, $\phi = 180°$).
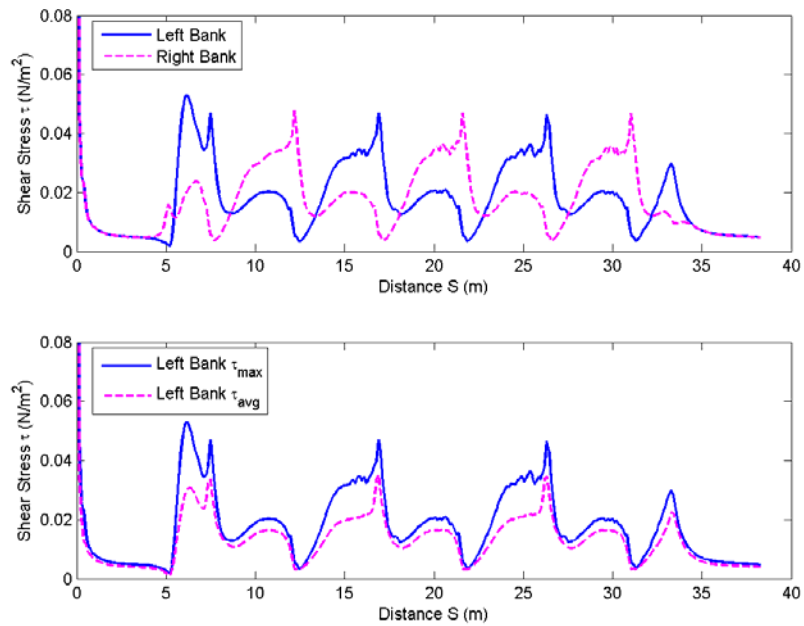
Figure C.4. Shear Stress Distribution on Both Banks along the Channel ($R/W = 2$, $\phi = 180°$).

Figure C.5. Simulation Bank Shear Stress ($R/W = 4$, $\phi = 65°$).

Figure C.6. Shear Stress Distribution on Both Banks along the Channel ($R/W = 4$, $\phi = 65°$).

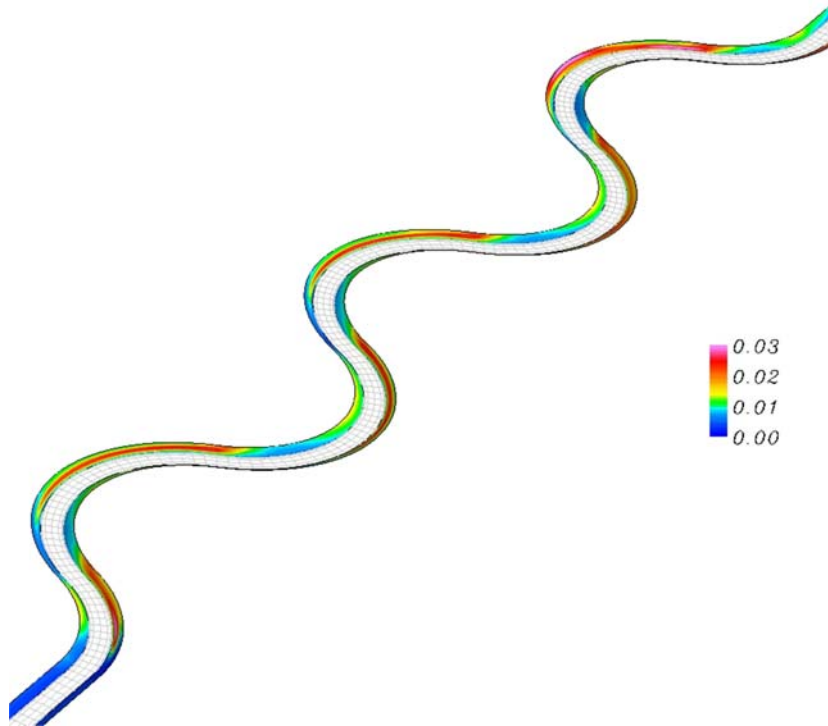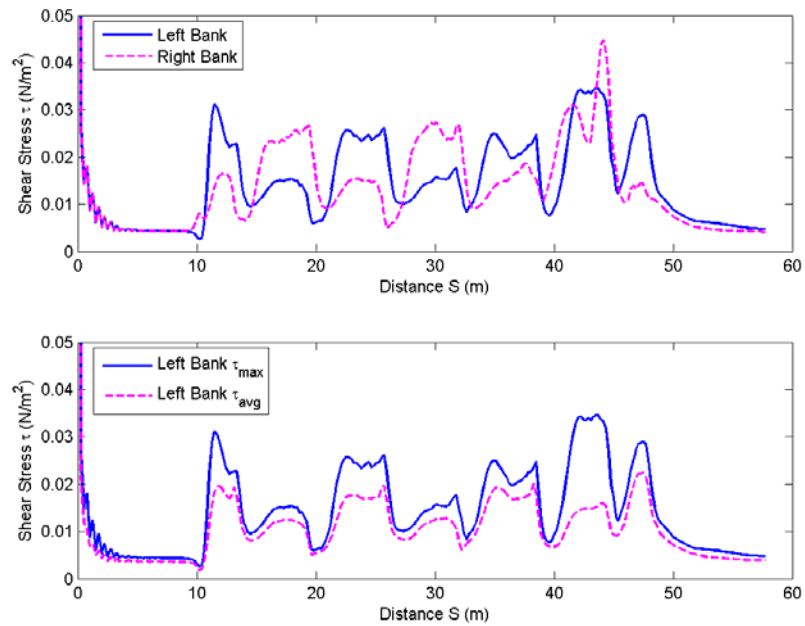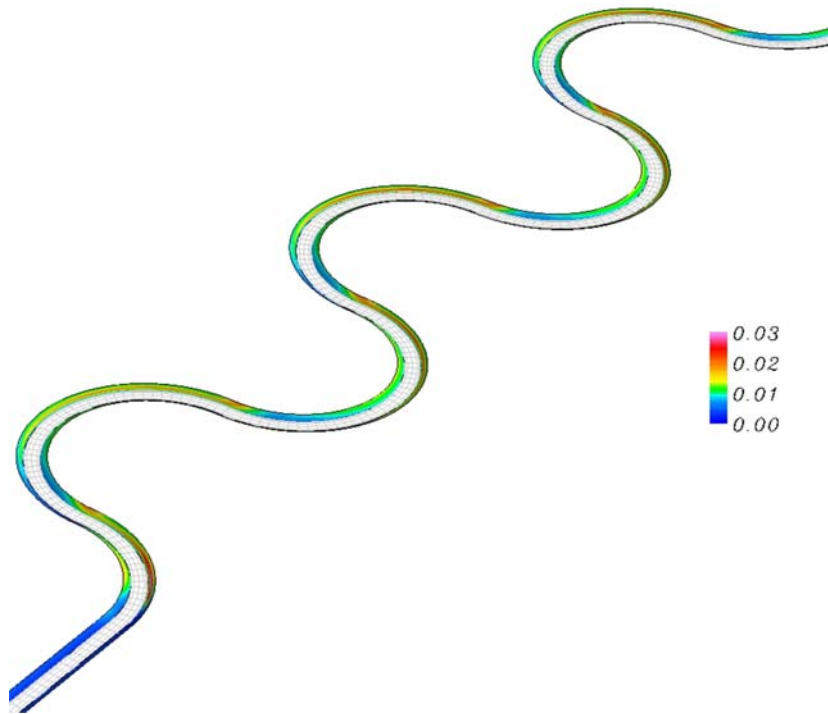**Figure C.7. Simulation Bank Shear Stress ($R/W = 4$, $\phi = 120°$).**

Figure C.8. Shear Stress Distribution on Both Banks along the Channel ($R/W = 4$, $\phi = 120°$).

284

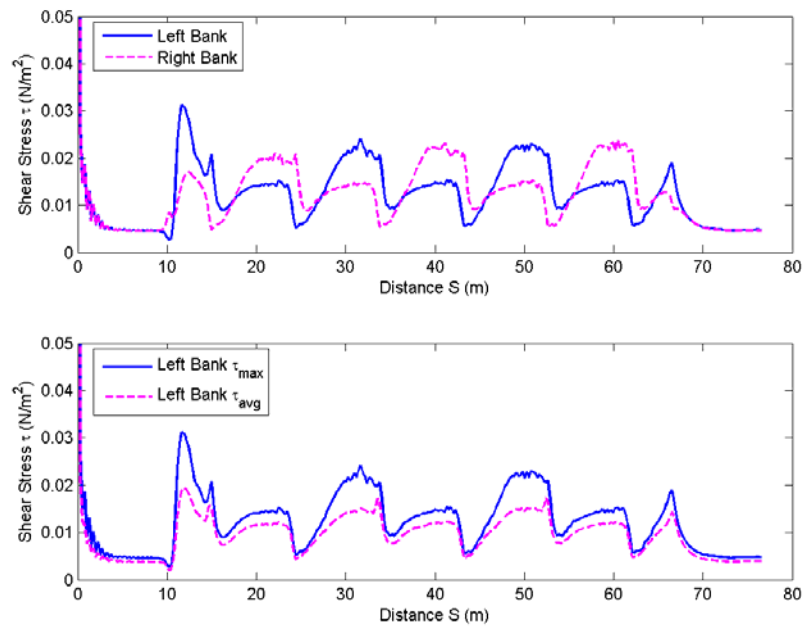**Figure C.9. Simulation Bank Shear Stress ($R/W = 4$, $\phi = 180°$).**

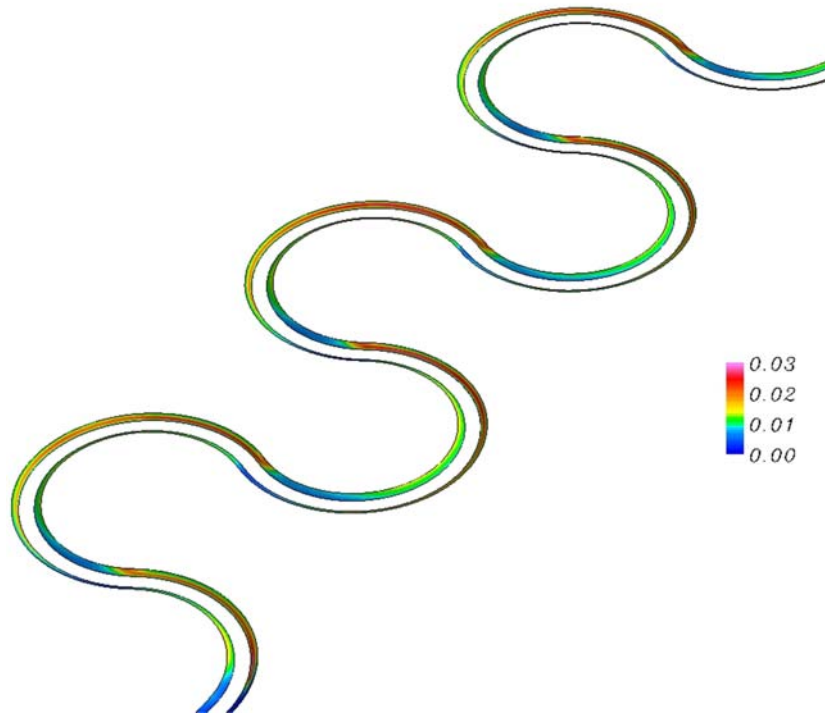**Figure C.10. Shear Stress Distribution on Both Banks along the Channel ($R/W = 4$, $\phi = 180°$).**

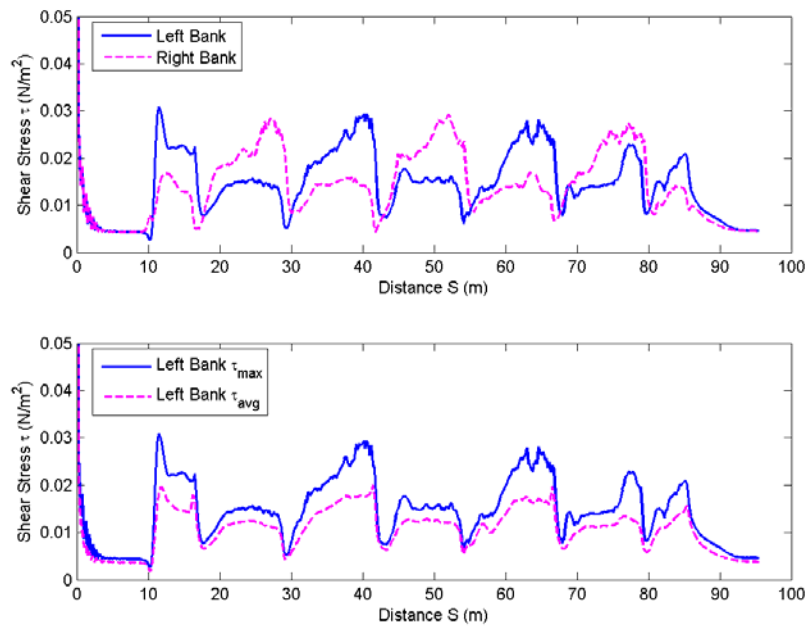**Figure C.11. Simulation Bank Shear Stress ($R/W = 4$, $\phi = 240°$).**

Figure C.12. Shear Stress Distribution on Both Banks along the Channel
($R/W = 4$, $\phi = 240°$).

Figure C.13. Simulation Bank Shear Stress ($R/W = 6$, $\phi = 180°$).

Figure C.14. Shear Stress Distribution on Both Banks along the Channel ($R/W = 6$, $\phi = 180°$).

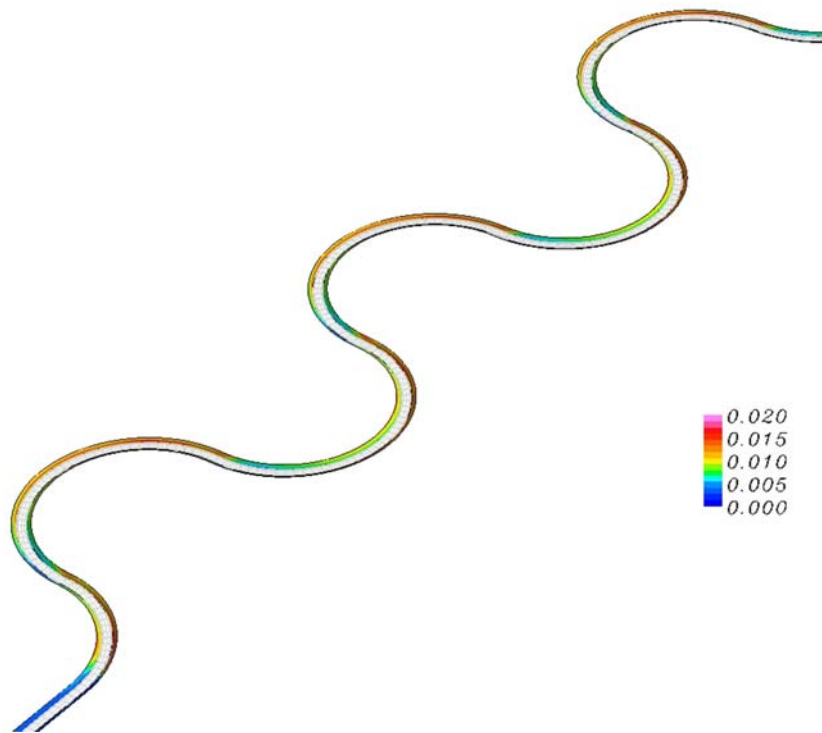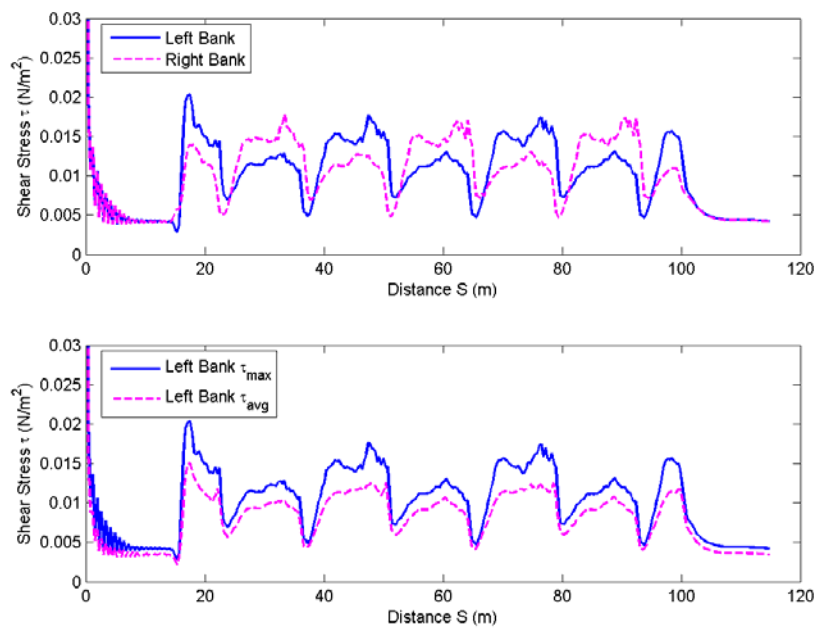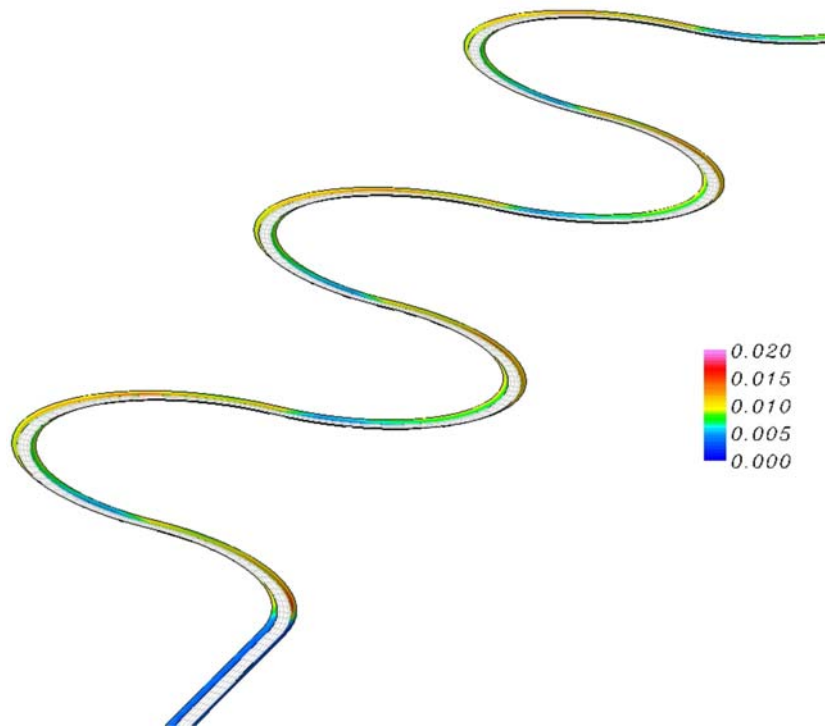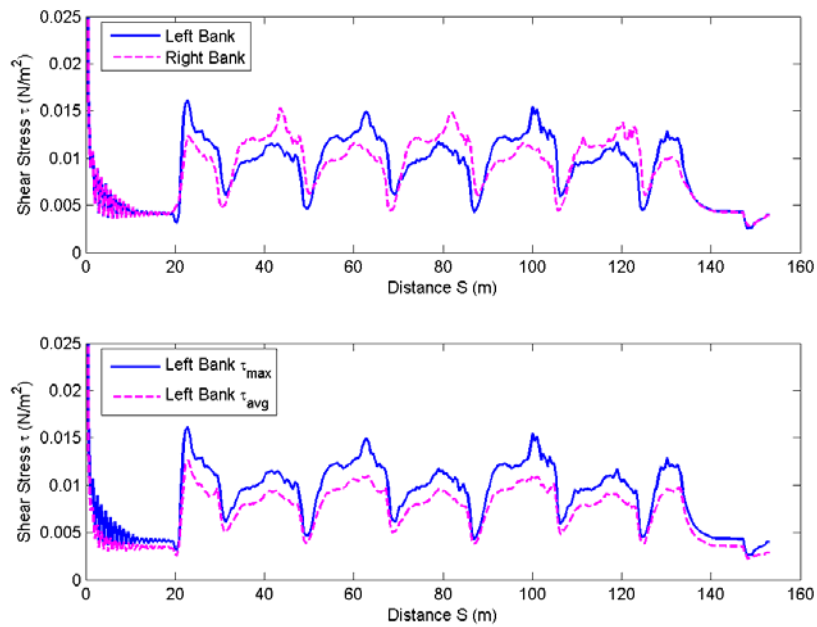**Figure C.15. Simulation Bank Shear Stress ($R/W = 8$, $\phi = 180°$).**

Figure C.16. Shear Stress Distribution on Both Banks along the Channel ($R/W = 8$, $\phi = 180°$).
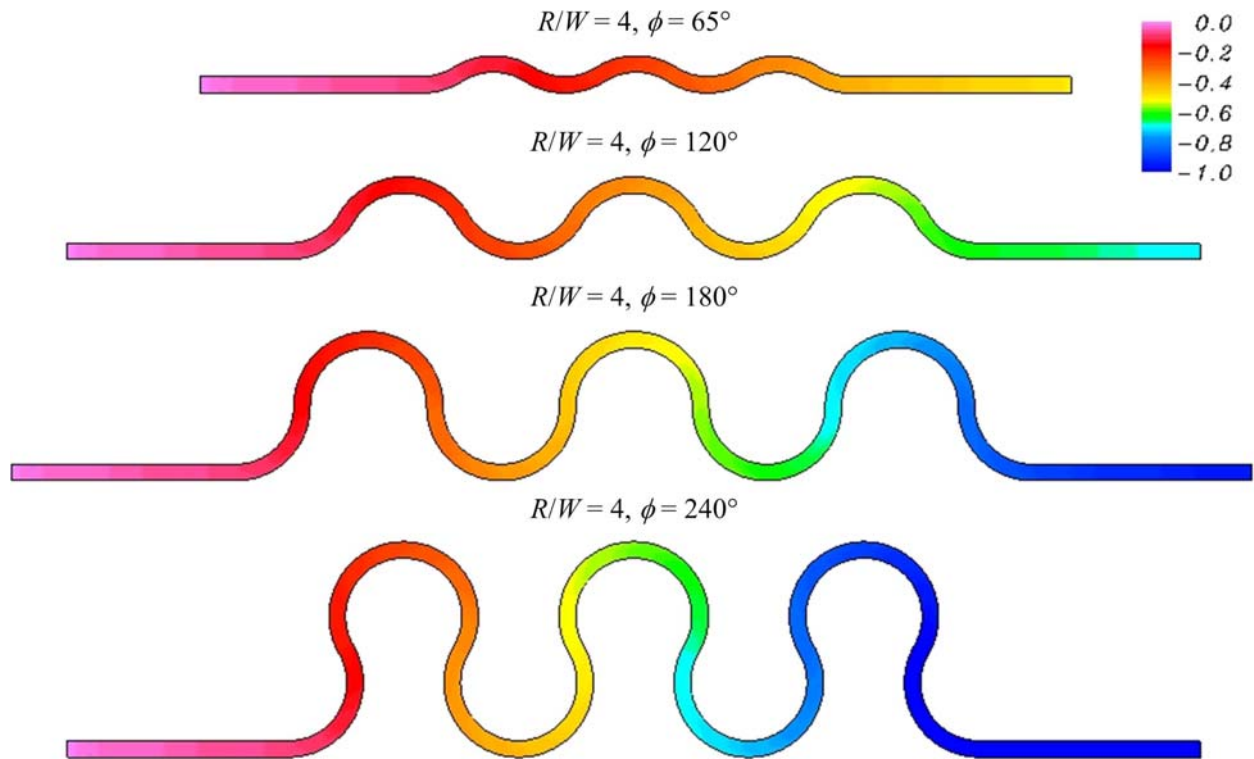
Figure C.17. Free Surface Elevation Contours;
R/W = 4, *ϕ* = 65°, 120°, 180° and 240°.

Figure C.18. Free Surface Velocity Magnitude Contours;
$R/W = 4$, $\phi = 65°$, $120°$, $180°$ and $240°$.

$R/W = 4, \phi = 65°$

$R/W = 4, \phi = 120°$

$R/W = 4, \phi = 180°$

0.05
0.04
0.03
0.02
0.01
0.00

$R/W = 4, \phi = 240°$

Figure C.19. Shear Stress Contours on Channel Banks;
$R/W = 4$, $\phi = 65°$, $120°$, $180°$ and $240°$.

Figure C.20. Free Surface Elevation Contours;
R/W = 1, 2, 4, 6, 8 and ϕ = 180°.

Figure C.21. Free Surface Velocity Magnitude Contours;
$R/W = 1, 2, 4, 6, 8$ and $\phi = 180°$.

APPENDIX D – MEANDER PROGRAM USER'S MANUAL

Introduction

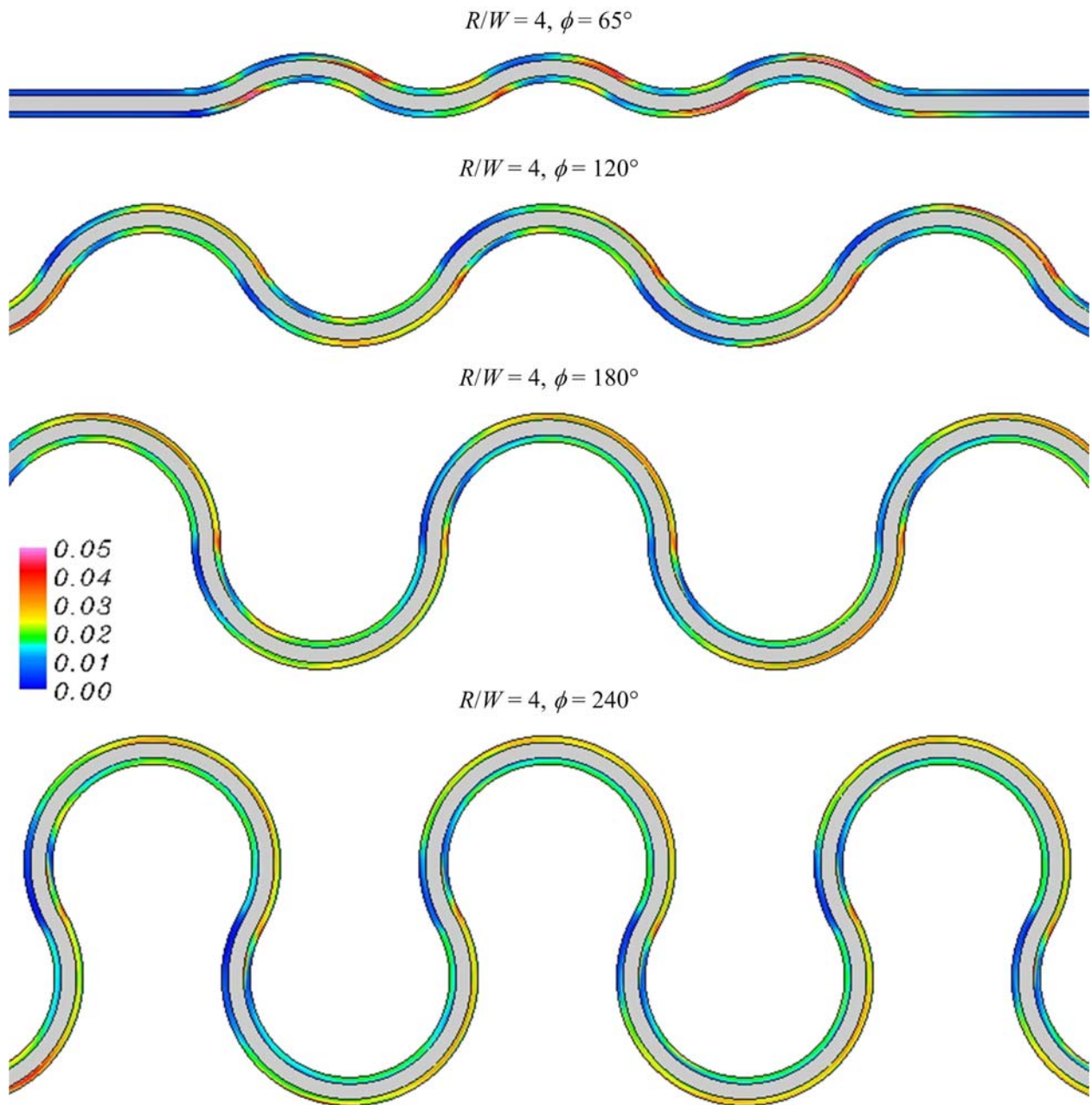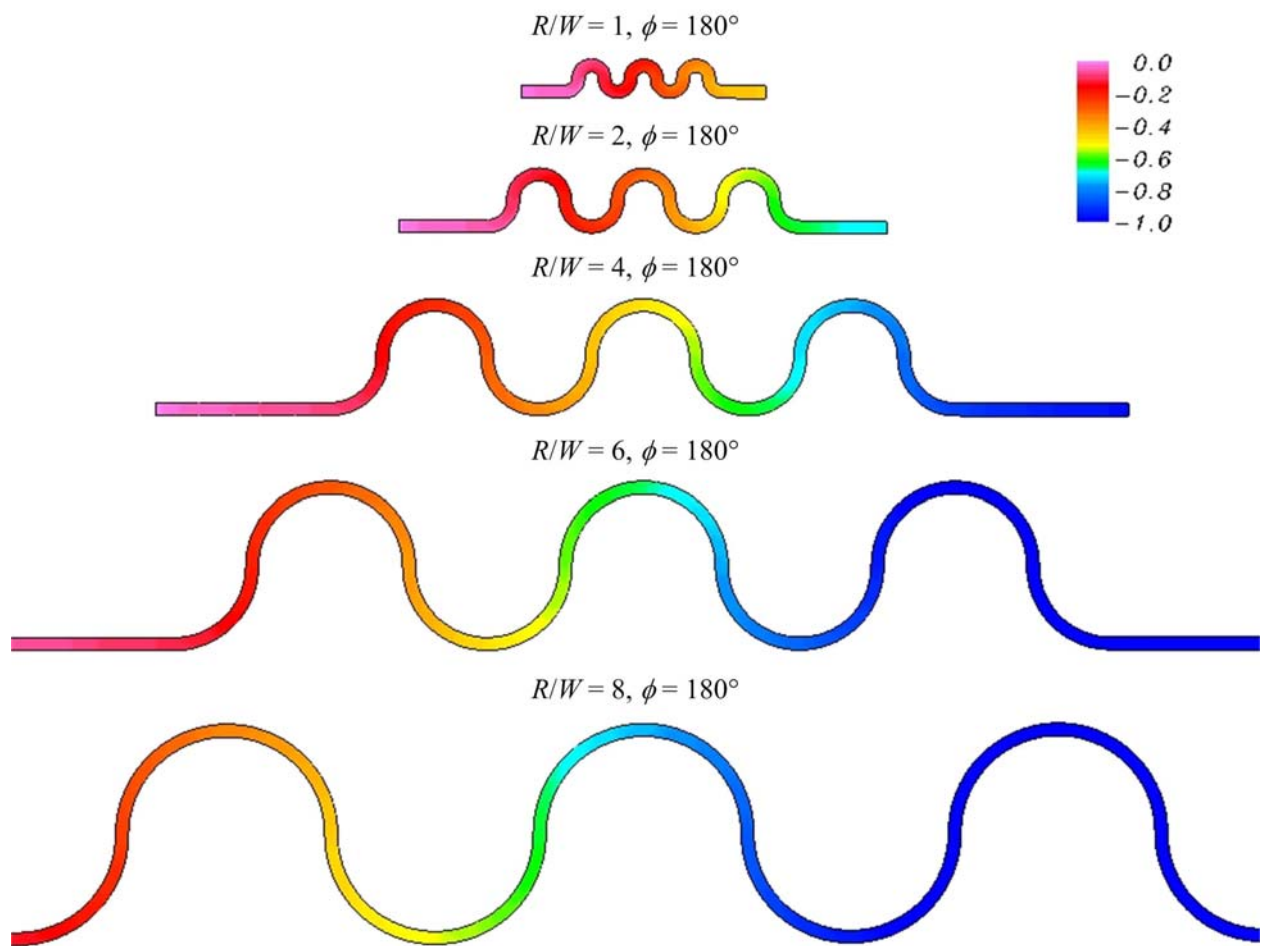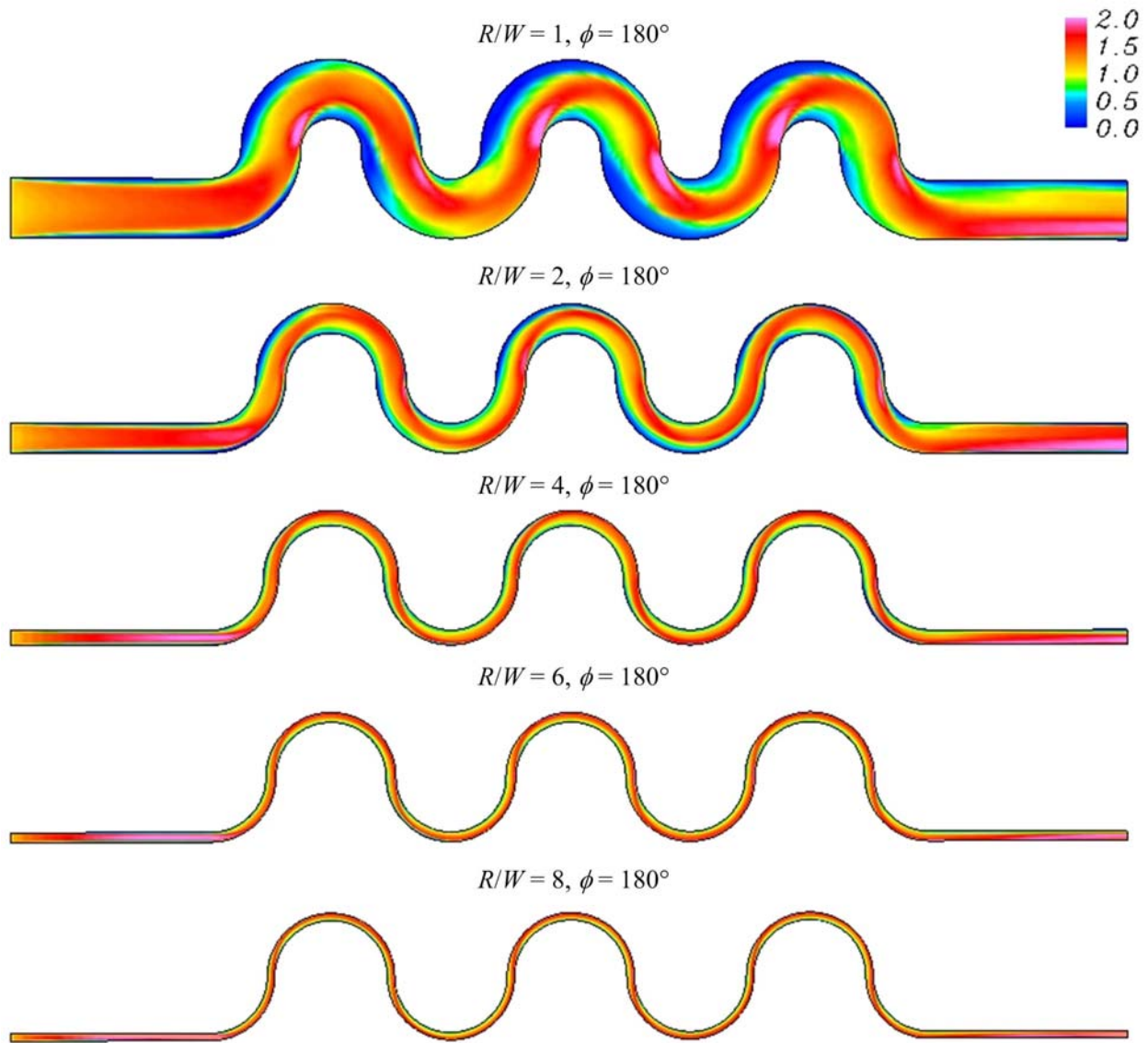The MEANDER program is a product of the TxDOT-sponsored project: Establish Guidance for Soils Properties–Based Prediction of Meander Migration Rate. The program consists of: graphic interface for data input, implementation of the prediction model, and graphic interface for data output. The code was written in Visual C++ and Matlab. The Matlab code was compiled and seamlessly linked with Visual C++ code.

The program takes the data of soil, water, and geometry and calculates the migration of a river after a certain period of time. The flow can be a constant discharge or a hydrograph. The output plots include the migrated channel and the original channel and the migration versus time curve for a selected point. The prediction can also be made based on a probabilistic approach where a hydrograph or a 100-year flood and a 500-year flood is needed to provide the risk level. The output plot shows the probability of a selected point reaching a certain location and further.

Installation

Because of the amount of computation involved, a high-performance computer (1 GB RAM, 2.8 GHz central processing unit [CPU] or better) is recommended. The operating system should be Windows XP or a newer version. The installation folder contains the following files:

libGeoRnd.ctf
libGeoRnd.dll
MCRInstaller.exe
MEANDER.exe
UserManual.mht
Tutorial.mht
Meander Report.pdf
ReadMe.txt

The two files "libGeoRnd.ctf" and "libGeoRnd.dll" are the run-time libraries for the compiled Matlab code. "MCRInstaller.exe" enables the program to run independent of Matlab and needs to be installed before the program can run. "UserManual.mht" is the user manual for this program. "Tutorial.mht" is a step by step example for the case of Brazos River. "Meander Report.pdf" is the final report for this project.

It is required to build a folder named "Data" in the same directory as these files. Output data files will go here. Once the program is running, the folder "libGeoRnd_mcr" will be generated, which contains some required libraries for the program. This folder needs to be deleted when the executable (i.e., Meander.exe) is replaced by a newer version.

Starting a New Project

This is a process of entering all the needed input data, running the program, and getting output results. Each time the program starts, the main interface as shown in Figure D.1 pops up and a new project is opened.

Method is a pull down list control. If the center line of a river is used to calculate migration, it is called Center Line Method. If a bank is used, it is called Bank Method. There are three items on the list: *Center*, *Right*, and *Left*. The default setting is Center Line Method. If the user wants to use Bank Method, *Right* or *Left* needs to be chosen.

The project name should be formatted in order to facilitate easy graphic output. If the coordinates of measured migrated channels are available, the project name should start with a number between 1 and 99. If the Center Line Method is used, the name ends with letter "C." Otherwise, the name ends with "L" or "R." In this case, a project name looks like "15C" or "15L." The corresponding coordinate files should be in the following file names and be in the "Data" folder:

T15C_Initial.txt

T15R_Initial.txt

T15L_Initial.txt

T15R_Final.txt (measured coordinates)

T15L_Final.txt

If no measured final channels are available, the project name should start with letter "P" and followed by a number between 1 and 999. The last letter is "C" if the Center Line Method is used and is "L" or "R" if the Bank Method is used. In this case, a project name looks like "P101C" or "P101L." The coordinate files for the initial channel should be in the following names and be in the "Data" folder:

P101C_Initial.txt

P101L_Initial.txt

P101R_Initial.txt

If the user does not have the data, the files are still needed, but the two column coordinates can be for any points close to the channel.
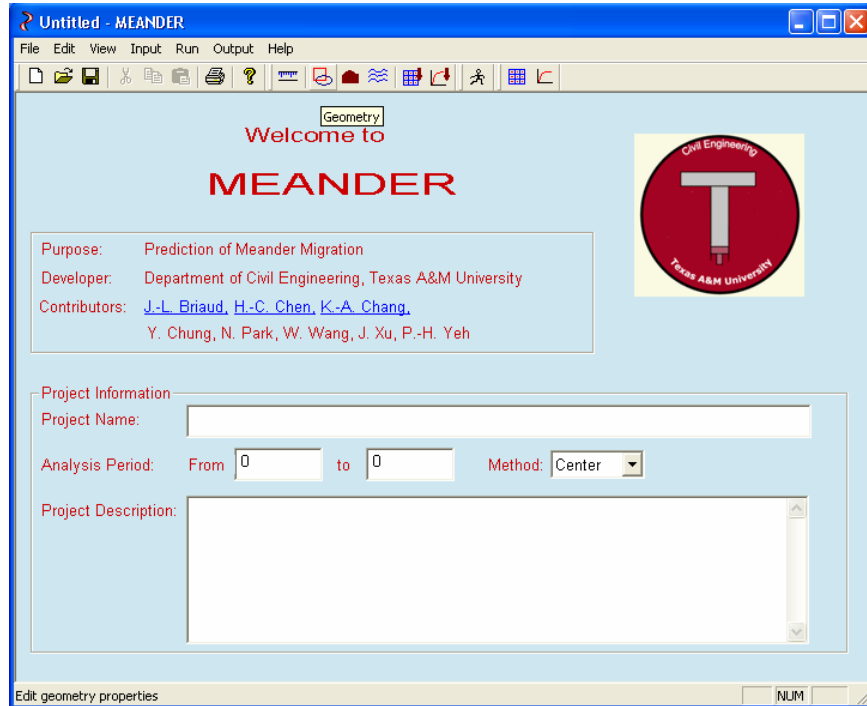
Figure D.1. Main Interface.

Units

Figure D.2 shows the unit input dialog. It allows the user to choose a unit system for the computation. There are two unit systems: metric system and U.S. Customary System (English system). The user should be consistent in the units being used. If metric units are chosen, all the input data are implied to have metric units and output is the same. There is an exception for English units, that the EFA curve is always in metric units.
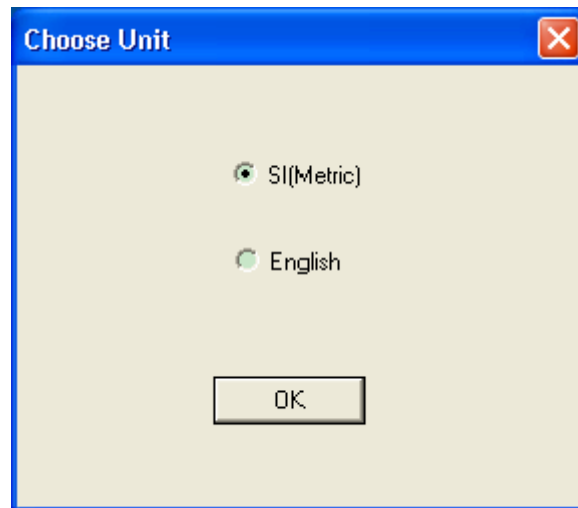

Figure D.2. Choose a Unit.

Geometry

Figure D.3 shows the interface for geometry input. The coordinates of the channel and the parameters needed for fitting circles are entered here. The coordinates should be in the order of from upstream to downstream. Getting to know something about the geometry study is helpful in understanding the parameters listed here. A set of default values for the parameters are given. The *Copy* button allows copying the fitted plot to other documents such as a Microsoft Word file.

The purpose of geometry study is to simplify the geometry of a real river into arcs and lines. The first step is to obtain the coordinates of a channel. The curve can be smoothed by redistributing the points (Figure D.4). A single point (Point C) alone does not have curvature. Its curvature is determined by a segment that is extended from the point in both directions by a certain length (from C to A and from C to B). A quadratic curve is fitted to this chosen segment AB, the length of which is called *segment length*. The curvature of the corresponding point on the fitted curve is treated as that of the point of interest (Point C). This process is repeated for each point on the bank.

Spacing Coefficient is the ratio of spacing to river width, while spacing is the distance between two adjacent points. A default value of 0.2 is given. Reducing the spacing coefficient increases the performance to some degree, but the computation time also increases as a result.

Segment Length Coefficient is the ratio of segment length to river width. It is recommended to use 5. If the segment length coefficient is too small, the bends may not be distinguishable on the R/W versus channel length curve. If this value is increased, the bends become more obvious but the computation time increases.

When the length of an identified bend is shorter than a certain value, no circle will be fitted. This value is called minimum bend length. *Minimum Bend Length Coefficient* is the ratio of minimum bend length to river width. A value of 2 is suggested here. The smaller the value is, the more bends are generated. If the value is too large, many significant bends are excluded.

Another way to eliminate an identified bend with small curvature is to calculate the average distance from a point on the bend to the baseline which connects the first and last point of the bend. If this average distance is smaller than a certain limit, it is treated as a straight line. The limit is called *Straightness Limit*. If a value of 0 is given, this parameter is ignored. If the user wants to eliminate some unwanted circles, a value around 5 can be picked. The final desired value can be determined by trial and error.

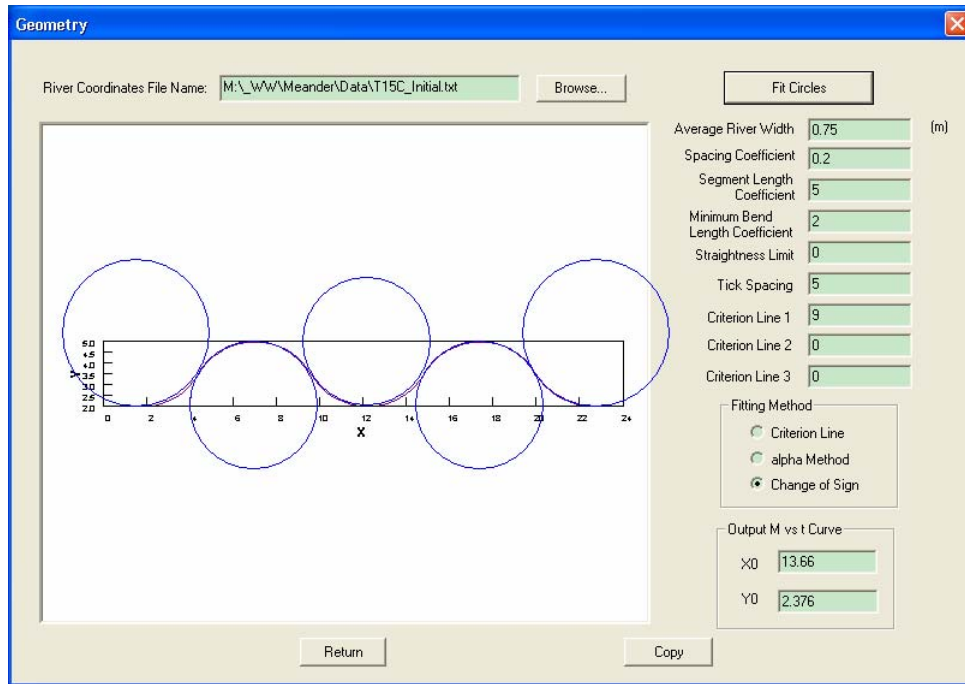It is nice to show channel lengthwise distance on the channel. Then the user needs to specify *Tick Spacing*.
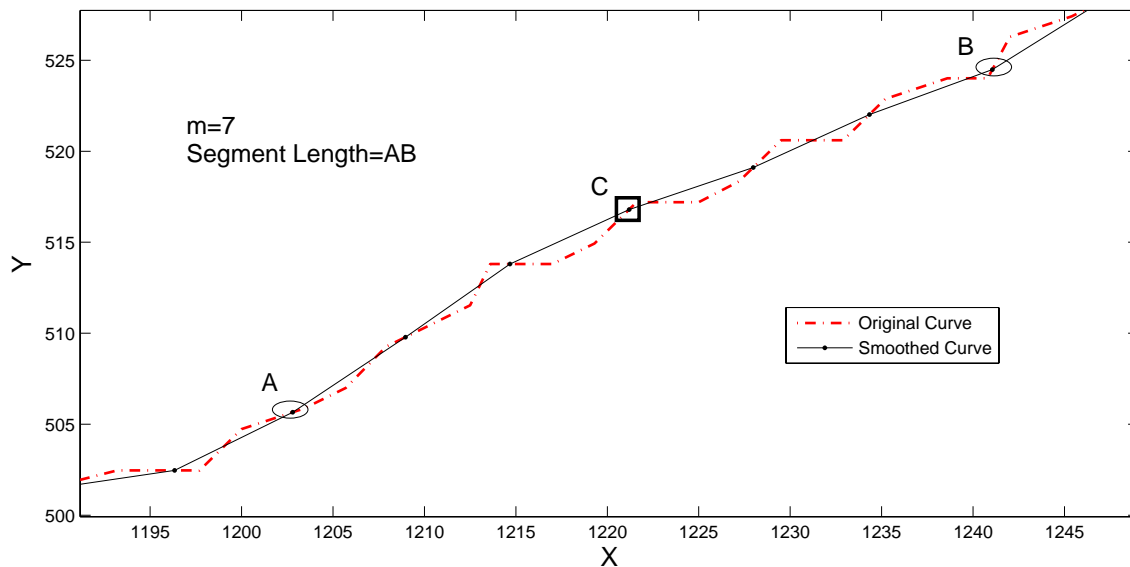
Figure D.3. Geometry Interface.

Figure D.4. Redistribute the Points.

Three fitting methods are used in this program. Figure D.1 shows how the *Criterion Line Method* is implemented. The *R* vs. length curve for an arc is a horizontal line. When a bend on a bank can be reasonably fitted with a circle, its radius of curvature vs. length curve is smooth and of bell shape. The closer the bend is to an arc, the closer the bell-shaped curve is to a horizontal

line. Therefore, if a curve segment is found to be of bell shape facing up or down, it most likely corresponds to an obvious bend on the river bank. This method uses three criterion lines (six symmetric lines, as a matter of fact) to identify the bell-shaped segments on the R/W vs. length curve. As shown in Figure D.5, six lines of $R/W = \pm 3, \pm 5, \pm 8$ were drawn on the graph. In the first loop, all continuous segments between $R/W = 0$ and $R/W = \pm 3$ were identified. These segments should be of bell shape and indicate the existence of bends. These segments were marked so that they will not be looked at again in the next loop. In the second loop, the continuous segments left between $R/W = 0$ and $R/W = \pm 5$ were identified. This procedure was repeated for $R/W = \pm 8$. For each loop there might be new bends identified. So far the choice of the numbers is based on experience. The values of the criterion line 1 to 3 should be in ascendance order, or it will be ignored.
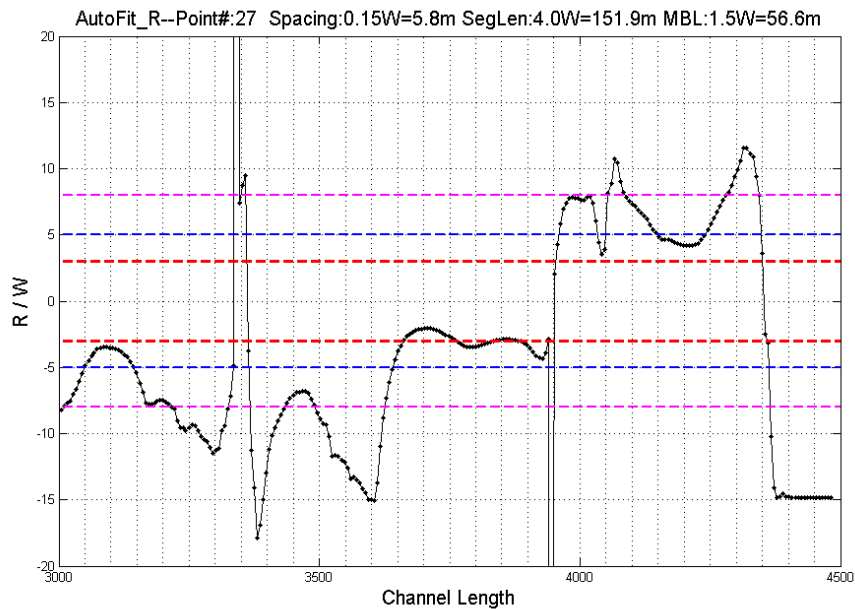

Figure D.5. Criterion Line Method.

The *Balanced Method* is applied to achieve a balance between closeness of fitting and the length of the arc. A best fit circle is found when the following α term reaches a minimum value.

$$\alpha = \frac{1}{\varphi} + b\sqrt{\frac{\sum_{i=1}^{n}(R_i - R^*)^2}{n}} \, / R^*$$

Where,

α.   Target term

300

ϕ: Bend angle

b: Empirical coefficient

R_i: The distance between point i and the center

R^*:   Radius of the fitted circle

n: Number of points used to fit the circle

The *Change of Sign Method* is good for flume tests. The initial channel of flume tests consists of tangent perfect arcs, while the migrated channels can be fitted with tangent arcs. On the R/W versus channel length curve, large values occur once or twice around the inflection point. The change of sign can clearly indicate the separation of bends. This method is applicable only when the bends are tangent to each other.

X0 and *Y0* on the dialog are the coordinates of the point for which a migration versus time curve will be drawn. It is chosen by the user on the graph of fitted circles as shown in the third circle of Figure D.6.

If the Fit Circles button is clicked, fitted circles will be plotted on the Geometry dialogue and plots of Figure D.6 and Figure D.7 will be generated. The user can adjust the parameters based the output.
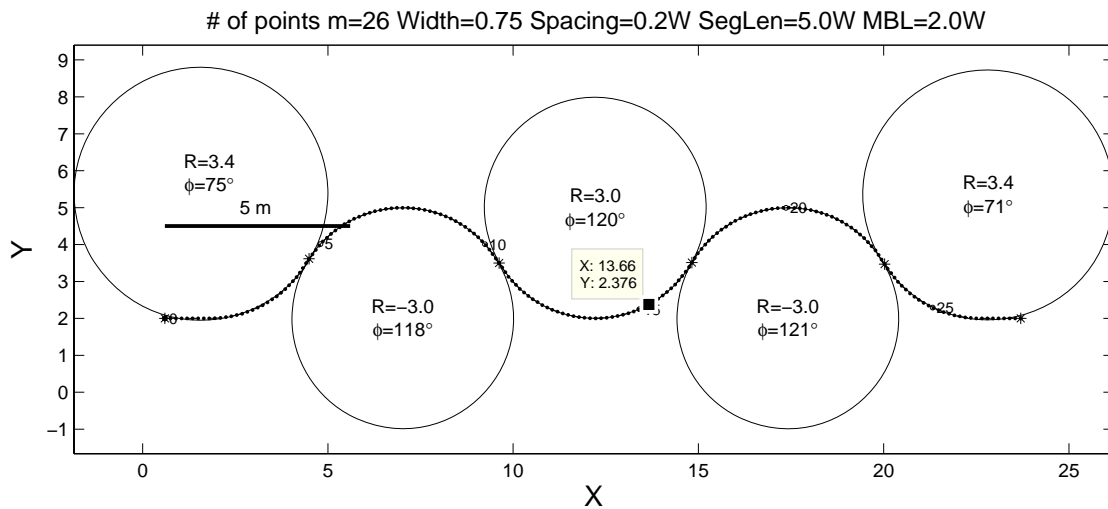

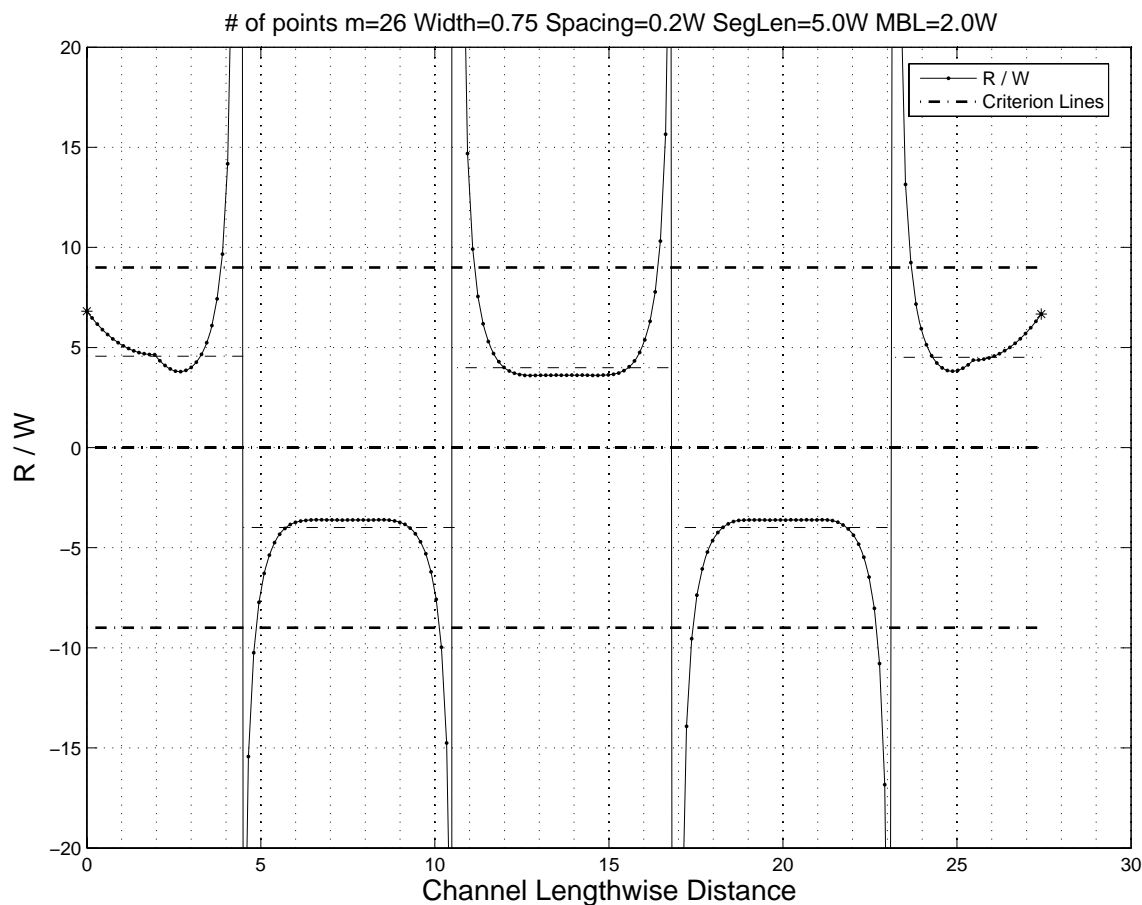**Figure D.6. Original Channel and Fitted Circles.**

Figure D.7. *R/W* versus Channel Length.

If default settings do not produce good fitting results, the user can first adjust criterion lines based on the Figure D.7. On the *R/W* versus channel length curve, a well-behaved bend appears to be a plateau or a parabolic curve with its vertex close to the horizontal axis (*R/W* = 0). The criterion lines should be adjusted in such a way that the segment between a criterion line and the horizontal axis is longer than the minimum bend length.

Further adjustments that can improve fitting quality include reducing spacing and increasing segment length. Smaller spacing leads to longer computation time, but the *R/W* versus channel length curve becomes smoother. Increasing segment length has the same effect and can effectively reduce sudden jumps on the curve. A very small bend could be better fitted as a part in a larger bend. Setting a reasonable minimum bend length coefficient will help the fitting of the larger bend. Perfect straight lines are rare in river channels; however, not all segments with a curvature are good to be fitted with a circle. Choosing a straightness limit can help eliminate the segments that have a reasonable curvature but look straight.

Soil Data

Figure D.8 is the soil data input interface. The first item is critical shear stress, which corresponds to a scour rate of 1 mm/hour. The number of points on an EFA curve needs to be specified so that enough space will be allocated on the table. Conventionally, scour rate is in metric units. When looking up a scour rate based on shear stress, linear interpolation is used. Finally, an appropriate type of the soil needs to be specified (sand or clay).

Figure D.8. Soil Data Input.

Water Data

The interface for entering flow conditions is shown in Figure D.9 to Figure D.16. The expression for the critical Froude number is:

$$Fr_c = \frac{v_c}{\sqrt{gy}}$$

Where,

Fr_c: Critical Froude number

v_c: Critical velocity

g: Acceleration of gravity

y: Water depth

The flow can be in discharge or velocity. For doing a prediction, three types of analyses are available: constant flow (Figure D.9), hydrograph (Figure D.10), and risk analysis (Figure D.11 and Figure D.12). The hydrograph used here can be a file directly downloaded from USGS website www.usgs.gov or an edited single-column data file. Each row in a hydrograph has the average flow during one time step which is specified in the dialog and is normally one day (24 hours). Risk analysis takes as input either a hydrograph (Figure D.11) or a 100-year and 500-year flood (Figure D.12). Either choice can be used to calculate the risk level a river underwent during a certain period of time in history. It is assumed that the river will be at the same risk level during the predicted period in the future. The Velocity versus Water depth table is used to find the water depth corresponding to a velocity. If the input is discharge the Discharge versus Velocity table and Discharge versus Water depth table are required. All these tables are obtained from HEC-RAS simulation. The input of flow can also be in velocity as shown in Figure D.13.

Figure D.9. Water Data: Discharge and Constant Flow.

Figure D.10. Water Data: Discharge and Hydrograph.

Figure D.11. Water Data: Discharge and Risk with Hydrograph.

Figure D.12. Water Data: Discharge and Risk with Q_{100}, Q_{500}.

Figure D.13. Water Data: Constant Velocity.

Input Tables and Plots

Figure D.14 is a dialog showing previously entered data in a tabular format for easy check. If a mistake is found, the user can go back to make corrections. Figure D.15 provides an easier way to check the correctness of the data. Abnormal data can be easily identified on a graph. After the data are entered and checked, the computation process can be started. Upon hitting the *Run* button, the program starts the prediction process.
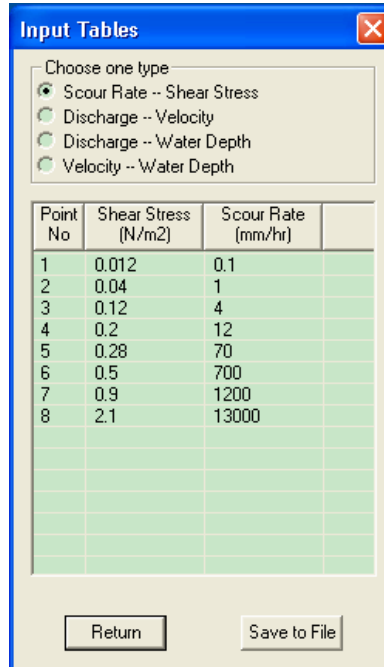
Figure D.14. Input Tables.
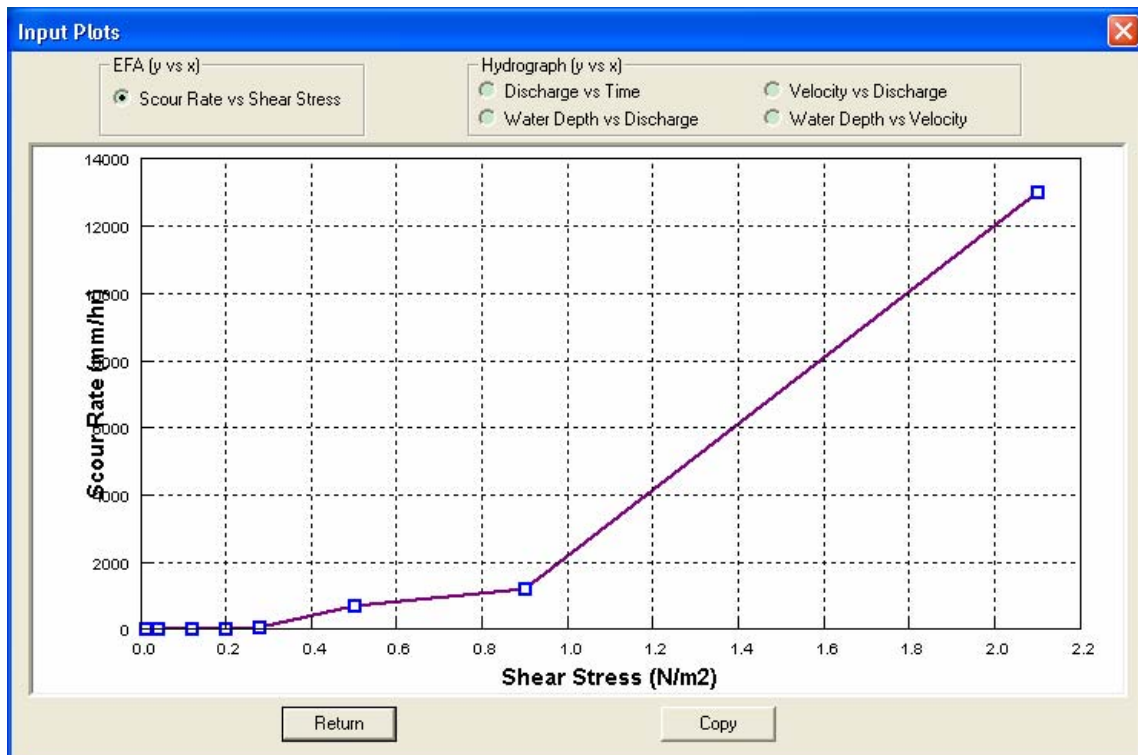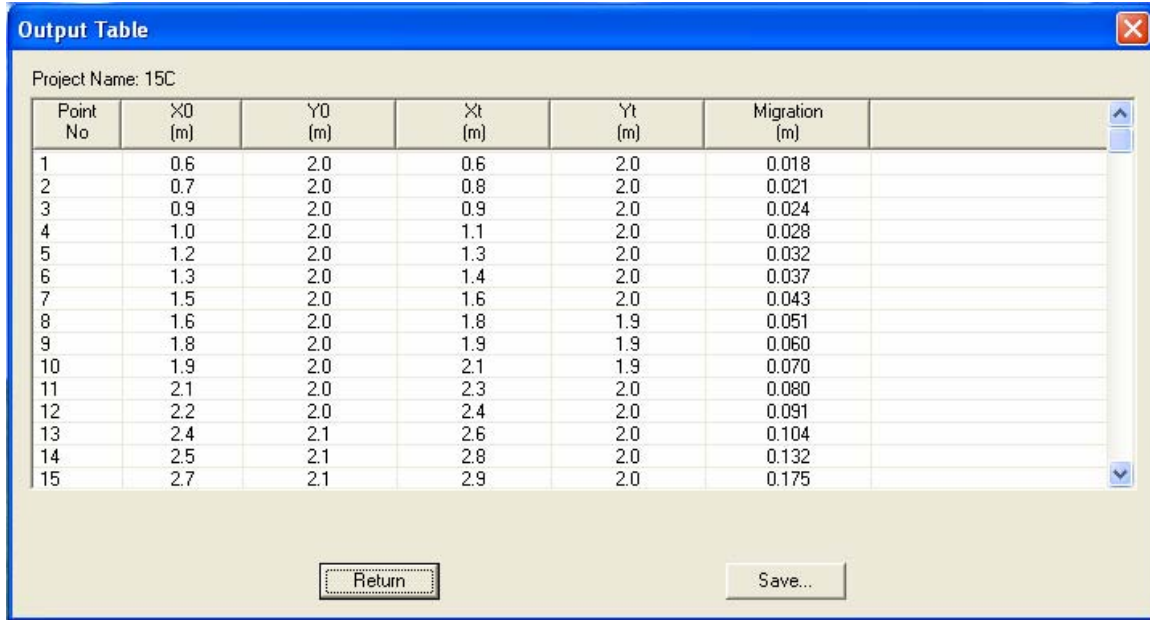
Figure D.15. Input Plots.

Output Table

Figure D.16 is the output table that shows the coordinates of the initial channel and the final channel. Accumulated migration distance of each point is on the last column.

Figure D.16. Output Table.

Output Plots

The Output Plots dialog Figure D.17 contains four buttons: *Center Line or One Bank*, *Both Banks*, *Risk Analysis*, and *M vs. t for one point*. All these functions were realized in Matlab. The first button is for showing the migrated channel of each step for the center line or a bank (Figure D.18). The second button is to show initial banks, predicted final banks, and measured final banks if data are available (Figure D.19 and Figure D.20). The third button is to run a risk analysis, which requires a specific direction of interest such as a bridge. For the direction of a bridge, the coordinates of two end points on the right and left side from the initial channel need to be specified in the bridge coordinates box. The right side is the right side of a person looking downstream. Once the button is hit, the simulation will took several minutes depending on the number of the future hydrographs. For the output of the risk analysis, two separate screens will be generated as shown in Figures 21 and 22. The last button is for showing the migration versus time curve of a selected point (Figure D.23). Note that this function does not work for a risk analysis option.
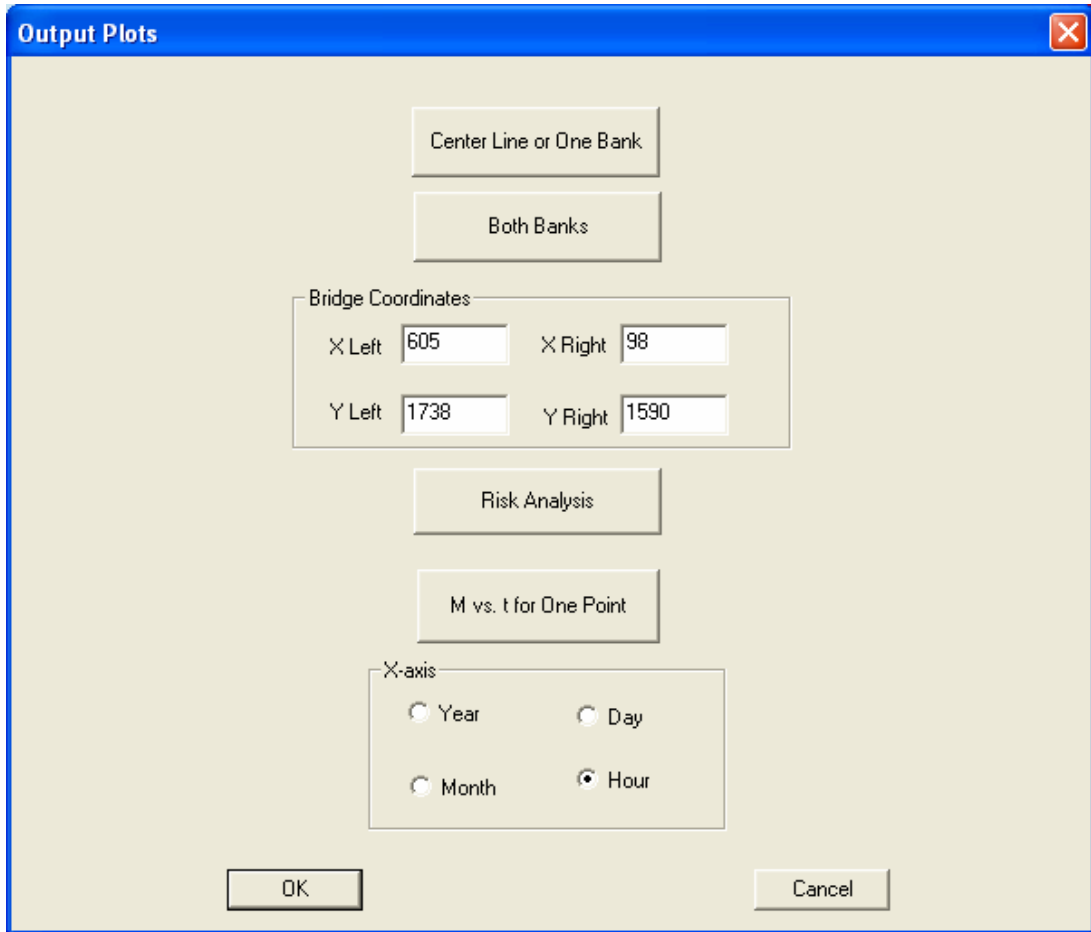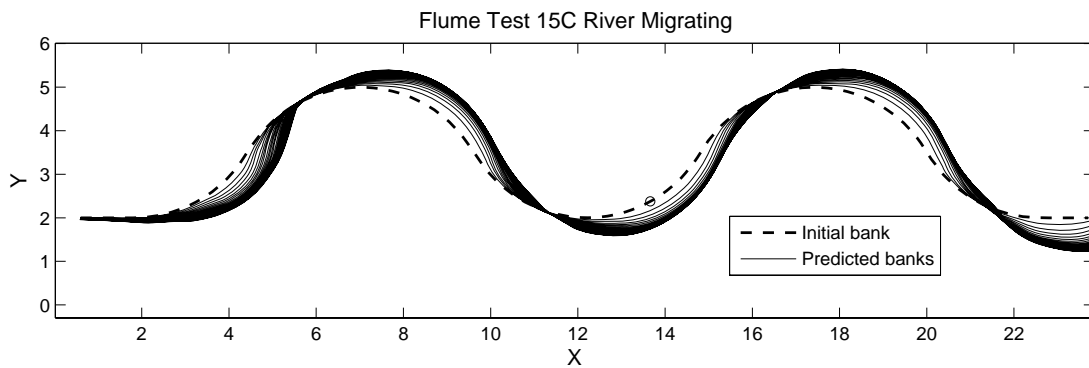
Figure D.17. Interface of Output Plots.
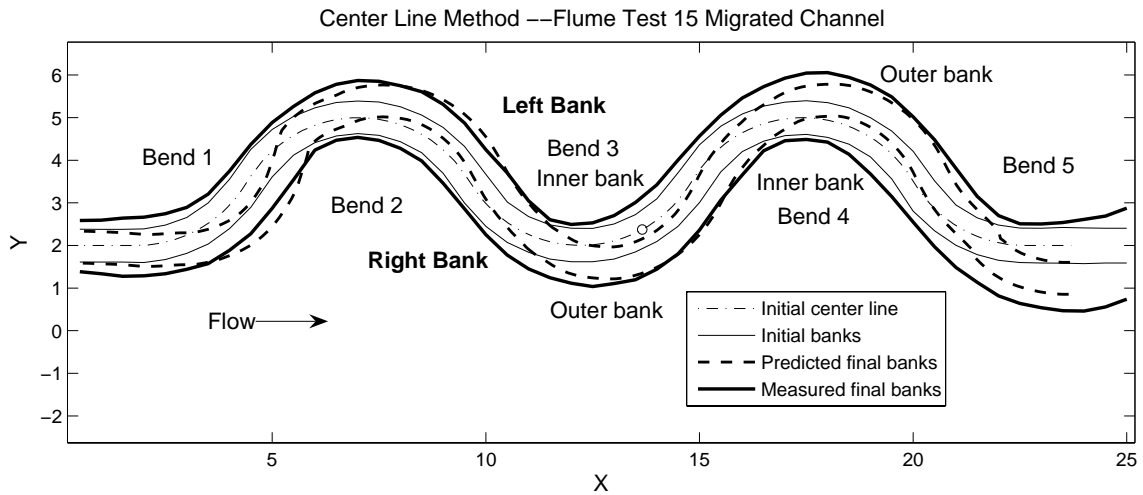

Figure D.18. Migrated Channel of Each Step.

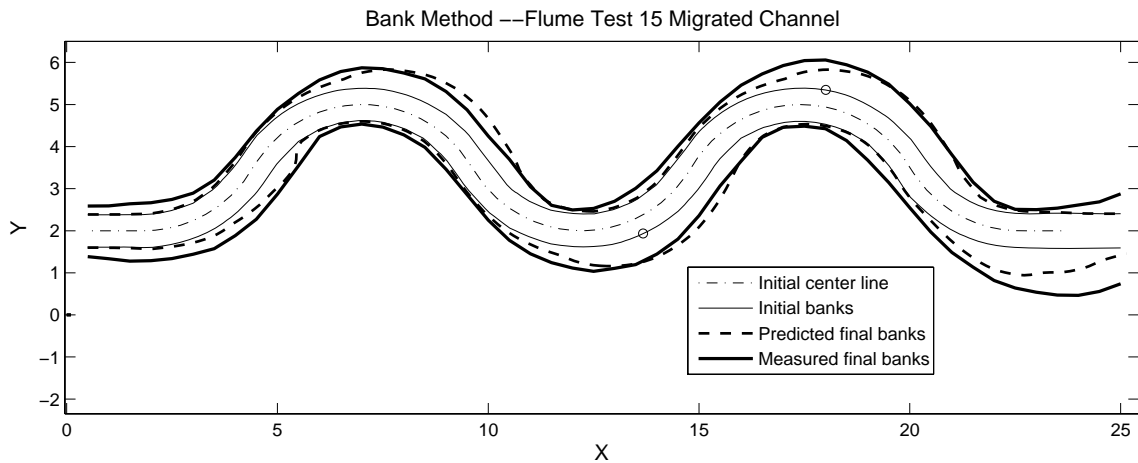**Figure D.19. Initial and Final Banks, Center Line Method.**

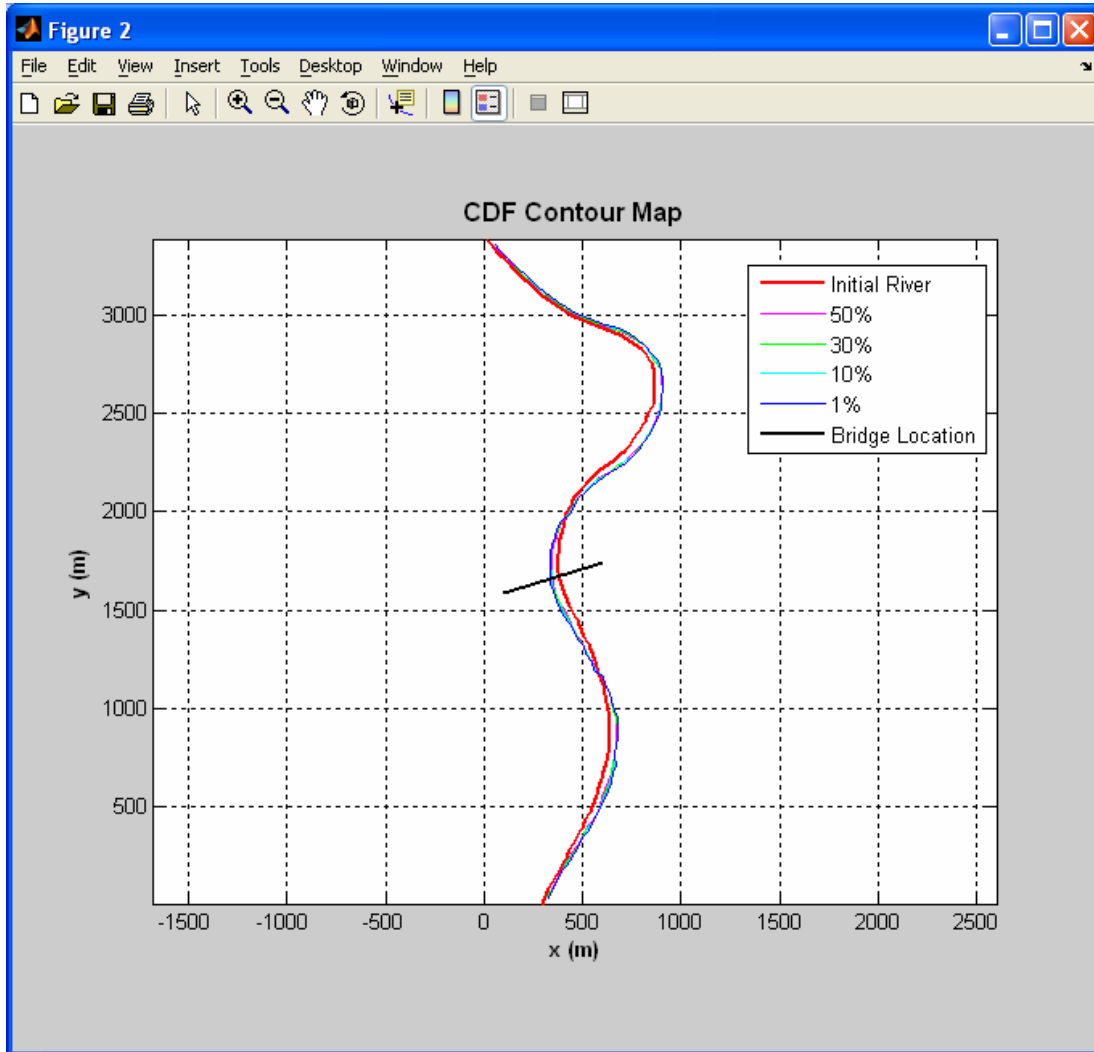**Figure D.20. Initial and Final Banks, Bank Method.**
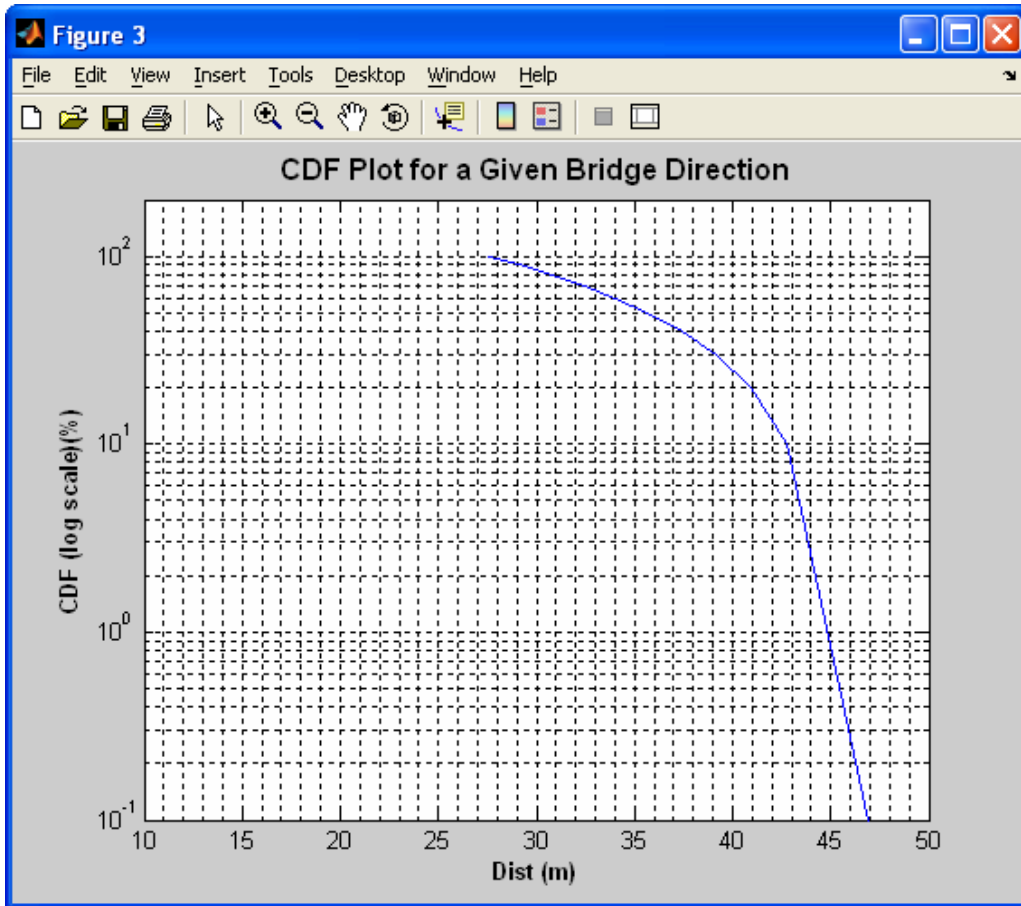
312

Figure D.21. CDF Map.
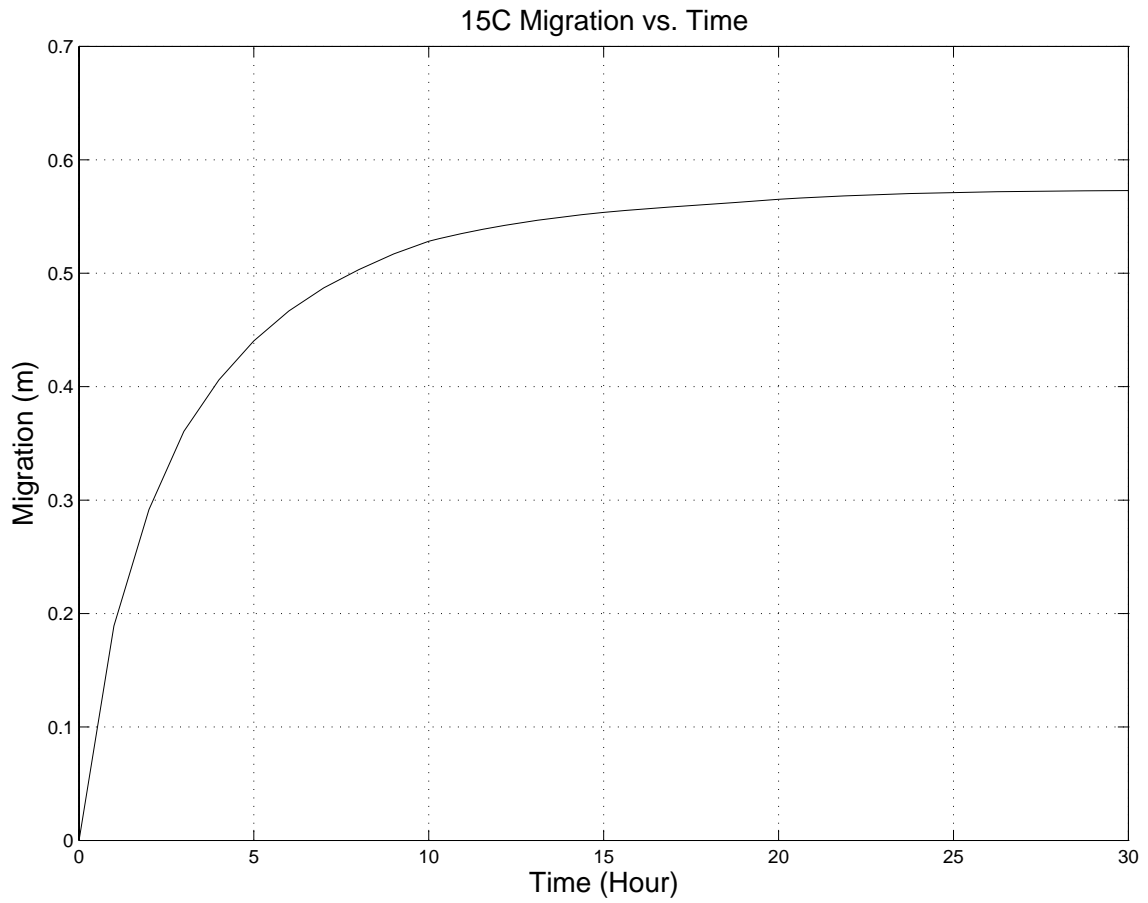
Figure 22. CDF Plot for a Given Bridge Direction.

Figure D.23. Migration versus Time of a Selected Point.